ARO 38728.1-PH-CF

1998

Technical

Digest Series

Volume 10

Diffractive Optics and Micro-Optics

Technical Digest

June 8–11, 1998

Kona Surf Hotel
Kailua Kona, Hawaii

Postconference Edition

Sponsored by
Optical Society of America

OSA®
Optical Society of America

REPORT DOCUMENTATION PAGE

Form Approved
OMB No. 0704-0188

1. REPORT DATE (DD-MM-YYYY)	2. REPORT DATE	3. DATES COVERED (From - To)
22-06-99	June 22, 1999	May 4, 1998 - May 3, 1999

4. TITLE AND SUBTITLE

Organization of the 1998 Diffractive Optics and Micro-Optics Topical Meeting

5a. CONTRACT NUMBER

DAAG55-98-1-0346

5b. GRANT NUMBER

DAAG55-98-1-0346

5c. PROGRAM ELEMENT NUMBER

5d. PROJECT NUMBER

5e. TASK NUMBER

5f. WORK UNIT NUMBER

6. AUTHOR(S)

Stephen Fantone

7. PERFORMING ORGANIZATION NAME(S) AND ADDRESS(ES)

Optical Society of America
2010 Massachusetts Ave., NW
Washington DC 20036

8. PERFORMING ORGANIZATION REPORT NUMBER

AR038728.1-PH-CF

9. SPONSORING/MONITORING AGENCY NAME(S) AND ADDRESS(ES)

US Army Research Office
PO Box 12211
Research Triangle Park, NC 27709-2211

10. SPONSOR/MONITOR'S ACRONYM(S)

11. SPONSORING/MONITORING AGENCY REPORT NUMBER

12. DISTRIBUTION AVAILABILITY STATEMENT

Approved for public release
Distribution unlimited

13. SUPPLEMENTARY NOTES

The views, opinions, and/or findings contained in this report are those of the author(s) and should not be construed as an official Department of the Army position, or decision, unless so designated by other documentation.

14. ABSTRACT

The Diffractive Otics and Micro-Optics Topical Meeting brought together scientists and engineers of various backgrounds to discuss new developments in the various aspects of diffractive and refractive micro-optics. These included modeling and design, fabrication and replication technology, and applications and products.

15. SUBJECT TERMS

16. SECURITY CLASSIFICATION OF:			17. LIMITATION OF ABSTRACT	18. NUMBER OF PAGES	19a. NAME OF RESPONSIBLE PERSON
a. REPORT	b. ABSTRACT	c. THIS PAGE			Stephen Fantone
unclassified	unclassified	unclassified	UL		19b. TELEPONE NUMBER (Include area code) 202/223-8130

Standard Form 298 (Rev. 8-98)
Prescribed by ANSI-Std Z39-18

DTIC QUALITY INSPECTED 4

Diffractive Optics and Micro-Optics

Postconference Edition

Technical Digest

June 8–11, 1998

Kona Surf Hotel
Kailua-Kona, Hawaii

1998 OSA Technical Digest Series
Volume 10

Partial support provided by
Army Research Laboratory
Army Research Office
OMRON Corporation
Honeywell
Rochester Photonics Corporation
Digital Optics Corporation

Sponsored by
Optical Society of America
2010 Massachusetts Avenue, NW
Washington, DC 20036-1023

OSA

Articles in this publication may be cited in other publications. To facilitate access to the original publication source, the following form for the citation is suggested:

Name of Author(s), "Title of Paper," in *Diffractive Optics and Micro-Optics*, Vol. 10, OSA Technical Digest Series, (Optical Society of America, Washington DC, 1998), pp. xx-xx.

Optical Society of America

ISBN

Conference Edition	1-55752-551-X
Postconference Edition	1-55752-552-8
1998 Technical Digest Series	1-55752-521-8

Library of Congress Catalogue Card Number

Conference Edition	98-85326
Postconference Edition	98-85327

Printed in the U.S.A.

Contents

Technical Program Committee

J. Allen Cox, *General Chair, Honeywell Inc., USA*

Hans Peter Herzig, *Program Chair, University of Neuchatel, Switzerland*

Joseph N. Mait, *Program Chair, U.S. Army Research Laboratory, USA*

Shigeru Aoyama, *Omron Corporation, Japan*

Madeleine B. Fleming, *3M Company, USA*

Michael T. Gale, *Centre Suisse d'Electronique et de Microtechnique (CSEM), Switzerland*

Michael Hutley, *National Physics Laboratory, U.K.*

Juergen Jahns, *University of Hagen, Federal Republic of Germany*

Gina R. Kritchevsky, *Donnelly Corporation, USA*

James R. Leger, *University of Minnesota, USA*

Lifeng Li, *University of Arizona, USA*

Robert Magnusson, *University of Texas-Arlington, USA*

Jim Moharam, *CREOL, University of Central Florida, USA*

G. Michael Morris, *University of Rochester, USA*

Dan Raguin, *Rochester Photonics, USA*

Terry Clark Smith, *Torrance, California, Technical Council Representative*

Donald Sweeney, *Lawrence Livermore National Laboratory, USA*

S. Ura, *Osaka University, Japan*

Agenda

■ Monday
■ June 8, 1998

Koa Room

8:15am–8:30am
Opening Remarks

8:30am–10:00am
DMA ■ Theory 1
J. Allen Cox, *Honeywell Inc., Presider*

8:30am (Invited)
DMA1 ■ Grating diffraction analysis: Maxwell's equations or Kirchhoff diffraction integral, M.G. Moharam, S. Dunn, *CREOL, Univ. Central Florida.* We discuss the implications of the approximations inherent in the Kirchhoff's integral-based scalar diffraction analysis methods as compared to Maxwell's equation-based rigorous methods for the analysis and design of diffractive optical elements. **(p. 2)**

9:00am
DMA2 ■ Mathematical modeling of diffractive gratings, Gang Bao, *Univ. Florida.* A new variational approach is presented. Model formulation, numerical solution, and convergence of the approach in both TE and TM polarizations are discussed. **(p. 4)**

9:15am
DMA3 ■ Reformulation of the Fourier modal method for surface-relief anisotropic gratings, Lifeng Li, *Univ. Arizona.* The Fourier modal method for anisotropic surface-relief gratings is reformulated by the use of the correct Fourier factorization rules. Numerical convergence is greatly improved. **(p. 7)**

9:30am
DMA4 ■ Applicability of the method of reduction in the Fourier modal method, Lifeng Li, *Univ. Arizona.* The applicability of the method of reduction (approximation by matrix truncation) in the Fourier modal method for modeling diffraction gratings is established by using a classical theorem of H. von Koch. **(p. 10)**

9:45am
DMA5 ■ Perturbation theory—a unified approach to describe diffractive optical elements, Markus Testorf, *Univ. Massachusetts–Lowell.* An extension of Kirchhoff's approximation for optically thick diffraction screens is derived. The perturbation approach is explicitly applied to problems of diffractive optics and micro-optics. **(p. 13)**

Reception Lanai
10:00am–10:30am
Coffee Break

Koa Room

10:30am–12:00m
DMB ■ Subwavelength Structures 1
Joseph N. Mait, *U.S. Army Research Laboratory, Presider*

10:30am (Invited)
DMB1 ■ Applications of guided-mode resonant filters to VCSELs, Robert A. Morgan, J. Allen Cox, Robert Wilke, Carol Ford, *Honeywell Technology Center.* A brief summary of both VCSEL technology and guided-mode grating resonant filters (GMGRFs) is presented. We then discuss benefits and issues of integrating the two technologies with design and fabrication results. **(p. 18)**

11:00am
DMB2 ■ Guided-mode resonant filters incorporating the Brewster effect, R. Magnusson, D. Shin, Z.S. Liu, *Univ. Texas at Arlington.* A new type of high-efficiency, low-sideband, guided-mode resonance reflection filter incorporating the Brewster effect is predicted theoretically and verified experimentally. **(p. 21)**

11:15am
DMB3 ■ Guided-mode resonance filters generated with genetic algorithms, S. Tibuleac, D. Shin, R. Magnusson, *Univ. Texas at Arlington;* C. Zuffada, *Jet Propulsion Laboratory.* Design of guided-mode resonance reflection and transmission filters is demonstrated utilizing a genetic algorithm to optimize the physical parameters of multilayer diffractive structures. **(p. 24)**

11:30am
DMB4 ■ Study of the resonant behavior of waveguide-gratings increasing the angular tolerance of guided-mode filters, F. Lemarchand, A. Sentenac, H. Giovannini, *Univ. St. Jérôme, France.* Resonances of waveguide gratings having two modulations of different period are studied. Their angular tolerance is much larger than that obtained with a single modulation. **(p. 27)**

11:45am
DMB5 ■ Subwavelength structured narrow-band integrated optical grating filters, Eric Grann, David E. Holcomb, Raymond A. Zuhr, *Oak Ridge National Laboratory;* M.G. Moharam, *CREOL, Univ. Central Florida.* A unique type of narrow-band integrated optical filter is investigated based on embedding a subwavelength resonant grating structure within a planar waveguide. **(p. 30)**

12:00m–1:30pm
Lunch Break

Koa Room

1:30pm–3:00pm
DMC ■ Design
Daniel H. Raguin, *Rochester Photonics, Presider*

1:30pm (Invited)
DMC1 ■ Chromatic compensation of free-space light propagation combining diffractive and refractive lenses: achromatic Fresnel and Fourier applications, P. Andrés, *Univ. de Valencia, Spain;* V. Climent, *Univ. Jaume I, Spain.* The remarkable properties shown by our lens setups designed for chromatic-dispersion compensation of light diffraction are applied for implementing several achromatic diffraction-based applications with color objects. **(p. 34)**

2:00pm
DMC2 ■ Multilevel diffraction gratings in the resonance domain: rigorous optimization by simulated annealing, Eero Noponen, *Helsinki Univ. of Technology, Finland.* Simulated annealing is applied to optimize resonance-domain diffraction gratings with multilevel staircase profiles, and is shown to be significantly more efficient than gradient method. **(p. 37)**

2:15pm
DMC3 ■ Interference effects in diffractive beam-shaping elements, Markus Rossi, Thomas Hessler, *Centre Suisse d'Electronique et de Microtechnique, Switzerland.* The spatial distribution and interference effects of stray light in beam-shaping elements in micro-systems fabricated by direct laser-beam writing have been analyzed, controlled, and reduced. **(p. 40)**

2:30pm
DMC4 ■ Stratified diffractive-optic approach for creating high-efficiency gratings, Diana M. Chambers, *Micro Craft, Inc.;* Gregory P. Nordin, *Univ. Alabama in Huntsville.* Volume grating behavior can be achieved with diffractive-optic techniques by interleaving binary grating layers with homogeneous layers in a stratified diffractive-optic grating. **(p. 43)**

2:45pm
DMC5 ■ Two-level binary diffractive optical elements for symmetric line-pattern generation from laser diodes, Michael A. Golub, *Holo-Or, Ltd., Israel.* Diffractive elements with only two phase levels generate symmetrical patterns (cross, rectangle) with 80–85% efficiency. Applications for diode laser pointing and CO_2 laser focusing considered. **(p. 46)**

Reception Lanai
3:00pm–3:30pm
Coffee Break

Koa Room

3:30pm–5:00pm
DMD ■ Optical Interconnects 1
M.G. (Jim) Moharam, *University of Central Florida, Presider*

3:30pm (Invited)
DMD1 ■ Polarization-selective diffractive optical elements and applications, Y. Fainman, F. Xu, R. Tyan, D. Marom, P. Shames, P.C. Sun, *Univ. California–San Diego;* J. Ford, A. Krishnamoorthy, *Bell Laboratories, Lucent Technologies;* A. Scherer, *Caltech.* Polarization selective diffractive optical elements will be introduced, describing design, rigorous modeling, and their microfabrication approaches. We will describe the utilization of these diffractive optical elements in optoelectronic packages for specific applications. **(p. 50)**

4:00pm
DMD2 ■ Substrate-mode polarization-controlled optical switch with sandwich reflection holograms, V. Moreau, Y. Renotte, Y. Lion, *Univ. Liège, Belgium;* S. Habraken, *Centre Spatial de Liège, Belgium.* We present the design and optical performances of an original 2×2 polarization-controlled switch based on substrate-mode holography. In-line integration of more complex devices are proposed. **(p. 53)**

4:15pm

DMD3 ■ Novel multichannel WDM-PON demultiplexer using an AWG and diffractive optical elements, E. Pawlowski, M. Ferstl, H. Hellmich, B. Kuhlow, G. Przyrembel, C. Warmuth, *Heinrich-Hertz-Institut für Nachrichtentechnik Berlin GmbH, Germany;* J.R. Salgueiro, *Univ. Santiago de Compostela, Spain.* An integrated WDM-PON demultiplexer is presented. The device is used to distribute 1.3-μm wavelength signals and to multiplex an eight-channel WDM spectrum at 1.55-μm wavelength. **(p. 56)**

4:30pm

DMD4 ■ Grating coupler utilizing third-order diffraction, Shogo Ura, Takayoshi Fujii, Toshiaki Suhara, Hiroshi Nishihara, *Osaka Univ., Japan.* Efficiency enhancement of third-order grating coupler was designed and demonstrated. Output coupling efficiency of 40% was experimentally obtained with 1.86-μm grating period for 0.82-μm wavelength. This design scheme is attractive for future integrated-optic applications using ultraviolet wavelength. **(p. 59)**

4:45pm

DMD5 ■ Planar-integrated optical systems for pulse shaping, Markus Testorf, *Univ. Massachusetts–Lowell;* Ulf Österberg, *Dartmouth College.* We discuss an integrated design of an optical setup for pulse-shaping applications. Our approach is based on the concept of planar-integrated free-space optics. **(p. 62)**

■ Tuesday
■ June 9, 1998

Koa Room

8:30am–10:00am
DTuA ■ Theory 2
Lifeng Li, *University of Arizona, Presider*

8:30am
DTuA1 ■ Symmetry of the field transmitted by periodic metallic grids, A. Sentenac, D. Maystre, *Univ. St. Jérôme, France.* Study of the modes inside the grid through-holes permits us to determine a large range of grating parameters for which four transmitted equal-efficiencies orders are obtained. **(p. 66)**

8:45am
DTuA2 ■ Electromagnetic analysis of waveguide Bragg reflectors, Pasi Vahimaa, Jari Turunen, *Univ. Joensuu, Finland.* Rigorous diffraction theory is used to compute the efficiency of waveguide Bragg reflectors as a function of the number of periods, and to model fabrication errors. **(p. 69)**

9:00am
DTuA3 ■ Numerical simulation of binary lenses by direct solution of the Helmholtz equation, G. Ronald Hadley, *Sandia National Laboratories.* We numerically compute diffraction efficiencies of low F-number (<1.5) eight-level binary lenses by direct solution of the scalar Helmholtz equation followed by wide-angle BPM. **(p. 72)**

9:15am
DTuA4 ■ Analysis and modeling of nonparaxial diffractive optical elements on curvilinear surfaces, Michael A. Golub, Israel Grossinger, *Holo-Or, Ltd., Israel.* Kirchhoff integral for diffractive microrelief on steep nonparaxial curved substrate is reduced to single Fourier transform. Several orders in diffractive-refractive multilens optical system are analyzed. **(p. 75)**

9:30am
DTuA5 ■ Super-resolving filters as diffractive-optical elements, C.J.R. Sheppard, *Univ. Sydney, Australia.* Super-resolving filters can be regarded as diffractive-optical elements. The complete system can thus be regarded as a hybrid system. **(p. 78)**

9:45am
DTuA6 ■ Superresolution in computer-generated holograms, Yasuhiro Takaki, *Nihon Univ., Japan.* Resolvable points of computer-generated holograms' diffraction images overlap and interfere with one another. By controlling the interference, diffraction intensity distribution can be controlled with high density. **(p. 80)**

Reception Lanai
10:00am–10:30am
Coffee Break

Koa Room

10:30am–12:00m
DTuB ■ Subwavelength Structures 2
Robert Magnusson, *University of Texas at Arlington, Presider*

10:30am (Invited)
DTuB1 ■ Fabrication of functional optical structures based on photonic crystals, A. Scherer, A. Yariv, B. D'Urso, O. Painter, C.C. Cheng, *Caltech;* Y. Fainman, *UC–San Diego;* E. Yablonovich, *UCLA.* We have developed techniques to fabricate photonic crystals within functional semiconductor materials to reflect, polarize, and filter light. Here, we will describe the fabrication methods and the observed performance of these devices. **(p. 84)**

11:00am
DTuB2 ■ Fabrication and simulation of blazed gratings with inherent antireflection structured surfaces, Fredrik Nikolajeff, *Univ. Minnesota;* Claus Heine, *Balzers Ltd., Liechtenstein.* We present a novel scheme for the fabrication of diffractive optical elements with inherent antireflection or polarizing properties. Simulated and experimentally measured results are given. **(p. 85)**

11:15am
DTuB3 ■ Scalar-based design of binary subwavelength diffractive lenses, Joseph N. Mait, *U.S. Army Research Laboratory;* Dennis W. Prather, *Univ. Delaware;* Mark S. Mirotznik, *Catholic Univ. America.* We present a technique for the design of binary subwavelength diffractive lenses based on the combination of two approximate theories, scalar diffraction theory, and effective medium theory. Design examples are presented. **(p. 88)**

11:30am
DTuB4 ■ Three-dimensional vector-based analysis of subwavelength diffractive optical elements using the finite-difference-time-domain method, Mark S. Mirotznik, *Catholic Univ. America;* Joseph N. Mait, William A. Beck, *U.S. Army Research Laboratory;* Dennis W. Prather, *Univ. Delaware.* Here we present the use of the finite-difference-time-domain (FDTD) method for the analysis of two-dimensional subwavelength diffractive optical elements. FDTD is a computationally practical method for performing three-dimensional infinitely periodic and finite aperiodic SWDOEs. A specific example is given of a binary subwavelength lens. **(p. 91)**

11:45am
DTuB5 ■ Vector-based analysis of axially symmetric and conducting diffractive lenses, Dennis W. Prather, Shouyuan Shi, *Univ. Delaware;* Mark S. Mirotznik, *Catholic Univ. America;* Joseph N. Mait, *U.S. Army Research Laboratory.* We present the electric-field integral equation as it applies to the analysis of three-dimensional perfectly conducting diffractive lenses. Simulations of binary and eight-level lenses are presented. **(p. 94)**

12:00m–1:30pm
Lunch Break

Koa Room

1:30pm–3:00pm
DTuC ■ Optical Interconnects 2
James R. Leger, *University of Minnesota, Presider*

1:30pm (Invited)
DTuC1 ■ Diffractive optics for optical interconnects, Hudson Welch, Eric Johnson, Michael Feldman, *Digital Optics Corp.* Abstract not available. **(p. 98)**

2:00pm
DTuC2 ■ Two-dimensional micro-optical interconnects for a multiprocessor system, U. Danzer, J. Schwider, *Univ. Erlangen-Nürnberg, Germany.* Two realized micro-optical interconnection systems, a 128-channel point-to-point interconnection system and a two-dimensional space-invariant optical star network will be shown. **(p. 99)**

2:15pm
DTuC3 ■ Hybridization of Fresnel diffractive microlenses and VCSEL arrays for free-space optical interconnections, Michel Fraces, Jean-Pierre Bouzinac, Pascal Churoux, *ONERA/CERT/DOTA, France.* To solve the latency problem for connecting multichip modules on face-to-face PC boards, we propose to image vertical-cavity surface-emitting lasers (VCSEL) linear arrays onto corresponding PIN photodiode arrays by using diffractive microlenses. The microlens arrays were stuck onto the VCSEL ones to form monolithic optoelectronic devices. Experimental results are presented. **(p. 102)**

2:30pm
DTuC4 ■ Reconfigurable optical interconnects in free-space optical processing modules based on polarization-selective diffractive optical elements, Hugo Thienpont, Nancy Nieuborg, Alain Goulet, Pawel Koczyk, Cathleen De Tandt, Willy Ranson, Roger Vounckx, Irina Veretennicoff, *Vrije Univ. Brussel, Belgium;* Andrew Kirk, *McGill Univ., Canada;* Paul Heremans, *IMEC, Belgium;* Maarten Kujik, *IMEC, Belgium.* We demonstrate a reconfigurable optical fanout element and a switchable logical inverter between planes of optical thyristors using polarization-selective diffractive-optical elements. **(p. 105)**

2:45pm
DTuC5 ■ Demonstration of a monolithic micro-optical bridge for free-space intrachip interconnects, H. Thienpont, G. Verschaffelt, R. Buczynski, P. Tuteleers, P. Vynck, V. Baukens, S. Kufner, M. Kufner, A. Hermanne, J. Genoe, D. Coppée, R. Vounckx, I. Veretennicoff, *Vrije Univ. Brussel, Belgium;* P. Heremans, *IMEC, Belgium.* We demonstrate the proof-of-principle of optical intrachip interconnects by establishing a 1 Mbit/s digital data link between two optoelectronic transceivers positioned on a same chip. **(p. 108)**

Reception Lanai
3:00pm–3:30pm
Coffee Break

Koa Room

3:30pm–4:30pm
DTuD ■ Poster Preview
G. Michael Morris, *University of Rochester, Presider*

3:30pm
DTuD1 ■ Optical elements for elimination of on-axis visible transmission, Luzhong Cai, Chunfei Li, Jinhua Zhao, Hua-kuang Liu, *Univ. South Alabama.* We have investigated transmitted spectra of optical elements including the phase gratings and Fabry-Perot etalon and found design parameters for eliminating/reducing on-axis broadband visible transmission. **(p. 112)**

3:32pm
DTuD2 ■ Generic approach to relate surface-relief profile height and the phase function of diffractive-optical element, Michael A. Golub, *Holo-Or, Ltd., Israel.* Actual beam propagation inside diffractive microrelief is reduced to the phase jump on the substrate surface. Microrelief height considered versus local beam slope angles. **(p. 115)**

3:34pm
DTuD3 ■ New theoretical method for nonuniform gratings investigation, G.G. Karapetyan, *State Engineering Univ. of Armenia.* A new method for nonuniform gratings theoretical investigation is presented. For this type of gratings the average permittivity, local period, and depth of modulation are arbitrary and slowly varied along the grating. The analytical formulaes of reflectance and transmittance in all-frequency interval are obtained for the first time to our knowledge. **(p. 118)**

3:36pm
DTuD4 ■ A contribution to the analysis of relief diffraction gratings, I. Richter, Z. Ryzí, P. Fiala, *Czech Technical Univ.* Diffraction characteristics of periodic diffractive structures with various relief profiles for both TE and TM polarizations are studied using several different theoretical approaches. **(p. 120)**

3:38pm
DTuD5 ■ Rigorous coupled-wave diffraction analysis of stratified volume photopolymer holograms, Yukihiro Ishii, *Univ. of Industrial Technology, Japan;* Toshihiro Kubota, *Kyoto Institute of Technology, Japan.* We develop a rigorous coupled-wave model to analyze the diffraction properties of stratified volume photopolymer holograms. The numerical and experimental angular selectivities of stratified holograms are shown. **(p. 123)**

3:40pm
DTuD6 ■ Binary high-efficiency single-order gratings for beam switching, Hartmut Bartelt, Tilman Glaser, Siegmund Schroeter, *Institut fuer Physikalische Hochtechnologie, Germany.* The combination of two binary high-frequency diffraction gratings is used for beam switching achieving good efficiency with small mechanical shifts in the nanometer range. **(p. 126)**

3:42pm
DTuD7 ■ A wedge made in an artificial dielectric, Costantino Giaconia, R. Torrini, S. Murad, C.D.W. Wilkinson, *Univ. Glasgow, U.K.* A wedge made in an artificial dielectric is presented. Such a grating exhibits a diffraction efficiency well above 80%. **(p. 129)**

3:44pm
DTuD8 ■ High-efficiency binary blazed grating waveguide couplers, Michael D. Watson, Helen Cole, *NASA Marshall Space Flight Center;* Mustafa Abushagur, *Univ. Alabama in Huntsville;* Paul R. Ashley, *U.S. Army Missile Command.* Blazed grating equations are related to artificial index grating equations to produce binary blazed grating equations yielding a periodic pattern emulating the blazed grating. **(p. 130)**

3:46pm
DTuD9 ■ Arrays of infrared micropolarizers, Gregory P. Nordin, Jeffrey T. Meier, Panfilo Deguzman, *Univ. Alabama in Huntsville;* Blair Barbour, Michael W. Jones, *Nichols Research Corp.* We report the design and fabrication of an array of wire-grid micropolarizers with different angular orientations for the 3–5-μm wavelength region. **(p. 133)**

3:48pm
DTuD10 ■ Novel polarizers using 2D bandgap structures, Tetze Hamano, *Telecommunications Advancement Organization of Japan (TAO) and Communications Research Laboratory (CRL), Japan;* Masayuki Izutsu, *CRL, Japan.* We propose a polarizer using a two-dimensional photonic bandgap structure. A maximum 40 dB extinction ratio of two orthogonal polarized waves was calculated numerically by finite-difference time-domain method using a square lattice structure. **(p. 136)**

3:50pm
DTuD11 ■ Color pseudo-nondiffracting beams generated by diffractive phase elements, Bi-Zhen Dong, Rong Liu, Ben-Yuan Gu, Guo-Zhen Yang, *Academia Sinica, China.* Generation of color pseudo-nondiffracting beams (PNDBs) by using diffractive phase elements in a polychomatic light illuminating system is, to our knowledge, first proposed. Numerical evaluations of the axial- and transverse-intensity distributions of the diffractive field show that all the beams obtained behave as the characteristic of the PNDBs well. **(p. 139)**

3:52pm
DTuD12 ■ Optical wavelet transform with use of a computer-generated hologram, Guo-Zhen Yang, Yan Zhang, Ben-Yuan Gu, Bi-Zhen Dong, *Academia Sinica, China.* We propose a new scheme to design the computer-generated hologram for achieving the wavelet transform. The present method is analyzed and a computer simulation is given. **(p. 142)**

3:54pm
DTuD13 ■ Locating rotation-invariant optical correlation, Yan Zhang, Ben-Yuan Gu, Bi-Zhen Dong, Guo-Zhen Yang, *Academia Sinica, China.* An approach, which is the combination of the fractional correlation and the method of the circular harmonics decomposition, is proposed to achieve the locating rotation-invariant optical correlation. The method is analyzed and computer simulations are given. **(p. 145)**

3:56pm
DTuD14 ■ Character display unit using a binary phase hologram array and an LC-SLM, Nam Kim, Bong-Gyun Kang, *Chungbuk National Univ., Korea;* Ho-Hyung Suh, Duck-Hee Lee, *Electronics and Telecommunications Research Institute, Korea.* We have demonstrated the character display unit that combines the dynamic property of the LC-SLM with the high-efficiency property of the phase hologram fabricated by photolithography. **(p. 148)**

3:58pm
DTuD15 ■ Beam steering in the spectrum of a liquid crystal spatial light modulator, Peder Rodhe, *Halmstad Univ., Sweden.* Spectrally dependent beam steering by an array of liquid crystal pixels is investigated. Desired diffraction characteristics are accomplished by a given pixel sequence of baseband phase. **(p. 151)**

4:00pm
DTuD16 ■ Paper withdrawn.

4:02pm
DTuD17 ■ Binary zone plate array for a parallel joint transform correlator system: design and evaluation, Asako Hashimoto, Kyoko Koda, Kashiko Kodate, *Japan Women's Univ., Japan;* Roshan Thapliya, Takeshi Kamiya, *Univ. Tokyo, Japan.* Introducing an optimizing design, eight-level binary zone plate array (η = 88%) was fabricated and applied to parallel facial recognition with satisfactory discrimination and reasonable throughput (1.8 s/face). **(p. 155)**

4:04pm
DTuD18 ■ Polarization analysis for detection of molecular reactions, E.-B. Kley, B. Schnabel, *Friedrich Schiller Univ., Germany;* U. Riß, *DER-Dr. Riss Ellipsometerbau GmbH, Germany.* A micro-optical polarimeter based on subwavelength metal stripe gratings as well as its application for molecular reactions detection will be described. **(p. 158)**

4:06pm
DTuD19 ■ A confocal profilometer using microlens arrays, M. Eisner, N. Lindlein, J. Schwider, *Univ. Erlangen-Nürnberg, Germany.* Confocal microscopy works with Nipkow-disc scanning of the field of view. This can be avoided by using a microlens in conjunction with a suitable stop array. **(p. 161)**

4:08pm
DTuD20 ■ Spectral calibration of MODIS bands using the SRCA, Harry Montgomery, *NASA Goddard Space Flight Center;* Nianzeng Che, *Swales Aerospace;* Jeff Broser, *Hughes STX.* The Spectro-Radiometric Calibration Assembly (SRCA) on-board MODIS utilizes a didymium glass as wavelength calibrator. The wavelength self-calibration capability provides information about MODIS band shift on-orbit. **(p. 164)**

4:10pm
DTuD21 ■ Reactive ion etching: a versatile fabrication technique for micro-optical elements, Margit Ferstl, *Heinrich-Hertz-Institut für Nachrichtentecknik Berlin GmbH, Germany.* Various optical elements, e.g., microlenses, high-frequency gratings, arrayed-waveguide gratings, strongly differing in shape, feature size (down to 100 nm) etc. were fabricated in silica and silicon. **(p. 167)**

4:12pm
DTuD22 ■ Diffractive-focusing elements for signal purposes produced by *e*-beam lithography, Zbynek Ryzi, F. Matejka, *Czech Holography s.r.o, Czech Republic.* Design and production of a diffractive-focusing element for signal lights with LED as a light source. A binary relief structure fabricated by an *e*-beam lithography is chosen. **(p. 170)**

4:14pm
DTuD23 ■ Photodeposition technique for restoring holographic films of polydiacetylene, Hossin Abdeldayem, Mark S. Paley, William Witherow, Donald O. Frazier, *NASA-Marshall Space Flight Center.* We present a novel photodeposition technique for depositing a permanent storing holographic grating, made of a thin film of a polydiacetylene derivative. **(p. 172)**

4:16pm
DTuD24 ■ Fabrication of microprisms of planar-optical interconnections using analog gray-scale lithography with high-energy beam sensitive glass, Ch. Gimkiewicz, D. Hagedorn, J. Jahns, *Fernuniversität Hagen, Germany;* E.B. Kley, F. Thoma, *Friedrich-Schiller-Univ. Jena, Germany.* The fabrication of microprism arrays using analog lithography and their use for light-efficient planar optical interconnections will be described. Experimental results will be presented. **(p. 175)**

4:18pm
DTuD25 ■ GRIN-lens-based optical interconnection systems for planes of micro emitters and detectors: microlens arrays improve transmission efficiency, Valérie Baukens, A. Goulet, H. Thienpont, I. Veretennicoff, *Vrije Univ. Brussel, Belgium;* W.R. Cox, C. Guan, *MicroFab Technologies, Inc.* We present a compact hybrid optical system, combining large-diameter GRIN lenses and microlens arrays, to interconnect planes of microemitters and detectors. **(p. 177)**

4:20pm
DTuD26 ■ Visible testbed projector with replicated DOE, C. Bill Chen, Ronald G. Hegg, Todd Johnson, Bill King, David F. Rock, *Raytheon Sensors and Electronic Systems;* Robert Spande, *US Army.* This paper focuses on the need and proper application of DOE's in visible systems and on the nature and performance of the projector optical design and test results. **(p. 180)**

Koa Room

4:30pm–5:00pm
Diffractive Beauty Contest

Koa Room

5:00pm–7:00pm
DTuD ■ Poster Session

Luau Gardens

7:00pm–8:30pm
Conference Reception

Wednesday
June 10, 1998

Koa Room

8:30am–10:00am
DWA ■ Micro Optics
Madeleine B. Fleming, *3M Company;* Hudson Welch, *Digital Optics Corp., Presiders*

8:30am (Invited)
DWA1 ■ Micromachining for micro-optics, Ming Wu, *UC–Los Angeles.* We report on the application of the emerging micromachining technology for fabrication of micro-optics as well as its integration with microactuators for adaptive control and dynamic alignment. **(p. 182)**

9:00am
DWA2 ■ Integrated micro-optical systems fabricated by replication technology, M.T. Gale, M. Rossi, *Centre Suisse d'Electronique et de Microtechnique, Switzerland;* L. Stauffer, M. Scheidt, J.R. Rogers, *Leica Geosystems AG, Switzerland.* Integrated micro-optical systems fabricated by replication into a thin polymer film on a glass slab have been investigated and developed for applications in sensor microsystems. **(p. 183)**

9:15am
DWA3 ■ Mass-transport gallium-phosphide refractive micro-lenses for diode-array reconfiguration, T.A. Ballen, J.R. Leger, *Univ. Minnesota.* Transformation of a linear laser diode array by mass-transport-method off-axis aspheric lenses and prisms is described. Aspehric lens design and prism experimental results are included. **(p. 186)**

9:30am
DWA4 ■ Vector radiation coupling method for high-efficiency and high-uniformity lightguide, Masayuki Shinohara, Masataka Tei, Shigeru Aoyama, Masashi Takeuchi, *Omron Corp., Japan.* A novel method for vector radiation coupling using a concentric chirped microlens array to achieve high efficiency and high uniformity is proposed. **(p. 189)**

9:45am
DWA5 ■ Diode laser illuminated automotive brake lamp using a linear fanout diffractive-optical element, J.T. Remillard, *Ford Motor Co.;* M.A. Marinelli, *Visteon, Exterior Systems Engineering;* T. Fohl, *Technology Integration Group;* D.A. O'Neil, *O'Neil Engineering.* Diffractive-optical elements have been incorporated in novel, diode laser illuminated automotive brake lamps. They offer significant advantages compared to conventional automotive lamps. **(p. 192)**

Reception Lanai
10:00am–10:30am
Coffee Break

Koa Room

10:30am–12:00m
DWB ■ Applications 1
Michael T. Gale, *CSEM Centre Suisse d'Electronique et de Microtechnique, Switzerland, Presider*

10:30am (Invited)
DWB1 ■ Holographic optical element for a dual-focus optical head, Yoshiaki Komma, Shin-ichi Kuwamoto, Hideki Aikou, Kenichiro Urairi, Michihiro Yamagata, Yasuhiro Tanaka, *Matsushita Electric Industrial Co., Japan.* Grating profile of a holographic optical element used for reading both 0.6-mm disk and 1.2-mm disk was optimized to suppress unnecessary stray diffracted light. **(p. 196)**

11:00am
DWB2 ■ Counterfeit-deterrents for surface-relief diffractive optical elements, Daniel H. Raguin, Robert McGuire, Geoffrey Gretton, *Rochester Photonics Corp.* Counterfeit-deterrent schemes are presented for surface-relief DOEs. Identification markings are integrated that do not alter the DOE's primary function, yet serve to identify the company that fabricated the original DOE master. **(p. 200)**

11:15am
DWB3 ■ Dual-element diffractive-element algorithm for beam shaping and phase encryption, Eric Johnson, Adam Fedor, *Digital Optics Corp.* This paper illustrates a technique for phase encryption and beam shaping using two diffractive elements in a cascaded optical system. **(p. 203)**

11:30am
DWB4 ■ Diffractive-optic power monitor for use with a VCSEL source, B. Fritz, J.A. Cox, T. Werner, J. Gieske, *Honeywell Technology Center.* A diffractive-optical element to be used as a power monitor for use with a vertical-cavity surface-emitting laser (VCSEL) source has been designed, fabricated, and tested. **(p. 206)**

11:45am
DWB5 ■ Waveguides and diffractive elements for noncontact sensors: analysis, Lars Lading, Palle G. Dinesen, Jens-Peter Lynov, *Risoe National Laboratory, Denmark;* Jan S. Hesthaven, *Brown Univ.* Noncontact sensors are miniaturized by combining planar waveguides and surface diffractive structures. A new pseudospectral time-domain modeling of multiplexed waveguide structures is applied. **(p. 209)**

12:00m–1:30pm
Lunch Break

Koa Room

1:30pm–3:00pm
JWC ■ Joint Session with International Optical Design Conference
J. Allen Cox, *Honeywell Inc., Presider*

1:30pm (Invited)
JWC1 ■ Diffractive optics in the Thomson Group, J. Rollin, *Thomson CSF Optronique, France;* C. Puech, *Angenieux, France;* P.J. Rogers, *Pilkington Optronics, U.K.* The paper deals with diffractive surfaces used in optical designs: fabricated devices operating in the IR wavebands are detailed and their manufacture in Thomson is described. **(p. 214)**

2:00pm
JWC2 ■ Ring-toric optics in optical data storage applications, Michael R. Descour, Daniel I. Simon, *Univ. Arizona.* The design, fabrication, and characterization of a diffractive ring-toric lens as a focus- and track-error-sensing element is presented. The sensitivity of this technique is evaluated. **(p. 217)**

2:15pm
JWC3 ■ Talbot array illuminators for high intensity compression ratios, Werner Klaus, *Ministry of Posts and Telecommunications, Japan;* Kashiko Kodate, *Japan Women's Univ.* We present theoretical evaluations of the efficiency, discuss some fabrication issues, and show experimental results of Talbot array illuminators designed for high compression ratios (>1000). **(p. 219)**

2:30pm
JWC4 ■ Super resolution and Dammann gratings, Adolf W. Lohmann, David Mendlovic, Zeev Zalevsky, *Tel-Aviv Univ., Israel.* Early super resolution experiments by Lukosz, Grimm, and Lohmann can be improved quantitatively by Dammann gratings. We also added conceptual advances. **(p. 222)**

2:45pm
JWC5 ■ Design of holographic optical beam splitters based on thin-grating sequential-diffraction technique, Michael R. Wang, *Univ. Miami.* A thin-grating sequential-diffraction technique is used to analyze Bragg diffractions by superimposed transmission phase gratings and to design holographic optical beam splitters. **(p. 225)**

Reception Lanai
3:00pm–3:30pm
Coffee Break

Koa Room

3:30pm–5:00pm
DWD ■ Fabrication 1
Shigeru Aoyama, *Omron Corporation, Presider*

3:30pm (Invited)
DWD1 ■ Paper withdrawn.

4:00pm
DWD2 ■ Fabrication of large circular diffractive optics, James H. Burge, *Univ. Arizona.* New equipment and techniques were developed and demonstrated for fabricating circular diffractive optics onto curved surfaces up to 1.8 m in diameter. **(p. 231)**

4:15pm
DWD3 ■ New convex grating types manufactured by electron beam lithography, Paul D. Maker, Richard E. Muller, Daniel W. Wilson, Pantazis Mouroulis, *Jet Propulsion Laboratory.* High-performance blazed gratings have been fabricated on convex surfaces by electron beam lithography, for use in an instrument to be flown on NASA's NM-EO1 spacecraft. **(p. 234)**

4:30pm
DWD4 ■ Fabrication of blazed holographic optical elements on oxygen-free copper by ultrahigh precision cutting, Shin-ya Morita, *Univ. Tokyo* and *Kanagawa Academy of Science and Technology* and *The Inst. of Phys. & Chem. Res. (RIKEN), Japan;* Yutaka Yamagata, *Kanagawa Academy of Science and Technology* and *RIKEN, Japan;* Toshiro Higuchi, *RIKEN* and *Univ. Tokyo, Japan.* We developed a novel method to fabricate blazed holographic optical elements on oxygen-free copper by ultrahigh precision cutting with single crystalline diamond cutting tool. **(p. 237)**

4:45pm
DWD5 ■ Single-step etching fabrication of diffractive microlens on high-energy-beam-sensitive glass, Michael R. Wang, Heng Su, *Univ. Miami.* A maskless single-step laser-assisted chemical etching technique has been studied and used for the fabrication of sixteen-phase-level diffractive microlens on an ion-exchanged high-energy beam-sensitive glass. **(p. 240)**

Thursday
June 11, 1998

Koa Room

8:30am–10:00am
DThA ■ Metrology and Testing
Hans Peter Herzig, *University of Neuchatel, Switzerland, Presider*

8:30am (Invited)
DThA1 ■ Diffraction efficiency limitations on visually coupled hybrid optics, Brian H. Tsou, *Air Force Research Laboratory;* Carl R. Ingling, Jr., Julie Beegan, *Ohio State Univ.* Using a psychophysical scale based on direct magnitude estimation of image quality, we compare images produced by hybrid optics and conventional eyepieces. **(p. 244)**

9:00am
DThA2 ■ Optical measurement of the global and local geometry of grating structures, Peter Blattner, S. Traut, H.P. Herzig, *Univ. Neuchatel, Switzerland.* In this paper different optical characterization methods for measuring the local and global relief parameters of phase and amplitude gratings are presented. **(p. 247)**

9:15am
DThA3 ■ Optical testing of technical surfaces with diffractive-optical elements, Sven Brinkmann, Thomas Dresel, Roland Schreiner, Johannes Schwider, *Univ. Erlangen-Nürnberg, Germany.* Grazing incidence interferometry with computer-generated holograms allows a single-step testing of entire mantle surfaces of workpieces for macroscopic surface deviations with submicron precision. **(p. 250)**

9:30am
DThA4 ■ Neural networks as a statistical model for optical scatterometry, Ilkka Kallioniemi, Jyrki Saarinen, Erkki Oja, *Helsinki Univ. of Technology, Finland.* Neural networks are successfully used as nonlinear models to predict simultaneously even five diffraction grating topology parameters from scatterdata with <10 nm accuracy. **(p. 253)**

9:45am
DThA5 ■ Evaluation of a diamond-cut large-groove grating for near-infrared spectroscopy, Miwa Goto, Masatoshi Imanishi, Fumihide Iwamuro, Toshinori Maihara, *Kyoto Univ., Japan.* We have developed a large-groove grating by a diamond-cut method. The measured diffraction efficiency is compared with that of a numerical computation. **(p. 256)**

Reception Lanai
10:00am–10:30am
Coffee Break

Koa Room

10:30am–12:00m
JThB ■ Joint Session with International Optical Design Conference
Michael Missig, *Opkor Inc., Presider*

10:30am (Invited)
JThB1 ■ Diffractive optics: from basic research to practical applications, G. Michael Morris, *Univ. Rochester and Rochester Photonics Corp.* The features and limitations of various mastering and replication techniques used to produce surface-relief diffractive optical elements are described. Key research results that have led to practical applications of diffractive optics technology are emphasized. **(p. 260)**

11:00am
JThB2 ■ Low-distortion imaging spectrometer designs utilizing convex gratings, Pantazis Mouroulis, *Jet Propulsion Laboratory.* Imaging spectrometer designs capable of submicron distortion in both spectral and spatial directions are described, utilizing novel types of convex electron-beam-lithography-generated gratings. **(p. 263)**

11:15am
JThB3 ■ Laser printer scan lens with diffractive optics, Kevin J. McIntyre, G. Michael Morris, *Univ. Rochester;* Susan Dunn, Karen Rumsey, Ken Ossman, *Xerox Corp.* Experimental results are presented for a 600 dpi laser printer scan lens utilizing diffractive optics technology. This novel lens requires neither a toroidal surface nor a cylindrical field mirror. **(p. 266)**

11:30am
JThB4 ■ Hybrid optics in dual waveband infrared systems, A.P. Wood, P.J. Rogers, *Pilkington Optronics, U.K.;* P.B. Conway, P.A. Manning, *Defence Research Agency, U.K.* The fundamental diffraction-based performance limitations of hybrid lenses in dual-band infrared systems are examined. An objective lens example has been manufactured and evaluated. **(p. 269)**

11:45am
JThB5 ■ A new approach to correct chromatic aberrations utilizing a hybrid surface, C. Gary Blough, *Melles Griot.* A unique approach to correct optical systems for chromatic aberrations is generated by combining equal and opposite amounts of refractive and diffractive optical power on a single surface. **(p. 272)**

12:00m–1:30pm
Lunch Break

Koa Room

1:30pm–3:00pm
DThC ■ Fabrication 2
Gina R. Kritchevsky, *Donnelly Corp., Presider*

1:30pm (Invited)
DThC1 ■ Micro-jet printing of refractive microlenses, W. Royall Cox, Ting Chen, Chi Guan, Donald J. Hayes, Rick E. Hoenigman, *MicroFab Technologies, Inc.;* Brian T. Teipen, Duncan L. MacFarlane, *Univ. Texas at Dallas.* Refractive microlenses printed onto optical substrates, GRIN lenses, LEDs, diode lasers and detectors can provide low-cost enhancements of coupling efficiencies in optoelectronic systems and packages. **(p. 276)**

2:00pm
DThC2 ■ Different concepts for the fabrication of hybrid (refractive/diffractive) elements, H.P. Herzig, Ph. Nussbaum, A. Schilling, S. Traut, I. Philipoussis, C. Ossmann, R. Völkel, *Univ. Neuchâtel, Switzerland;* M. Rossi, *CSEM, Switzerland;* H. Schift, *Paul Scherrer Inst., Switzerland.* Different concepts for the fabrication of hybrid elements are investigated. The diffractive elements are realized on the planar and on the curved surface of microlenses. **(p. 279)**

2:15pm
DThC3 ■ Diffraction characteristics of thick phase volume hologram recorded in photo-thermo-refractive glass, S. Dunn, M.G. Moharam, L. Glebov, K.A. Richardson, *CREOL, Univ. Central Florida.* We characterize high-resolution and high-efficiency thick volume phase holograms in photothermo-refractive (PTR) silicate glasses fabricated and processed at CREOL. Diffraction efficiency and angular selectivity measurements are presented. **(p. 282)**

2:30pm
DThC4 ■ One-step fabrication of a high-efficiency flat-top beam shaper, Xu Guang Huang, Michael R. Wang, *Univ. Miami.* We report the realization of a high-efficiency diffractive-optics beam shaper on an ion-exchanged high-energy beam sensitive (HEBS) glass using laser-assisted chemical etching technique. **(p. 285)**

2:45pm
DThC5 ■ Effects of fabrication errors on Talbot array illuminators, Thomas J. Suleski, *Digital Optics Corp.* Fabrication errors have unusual and undesirable effects on the performance of Talbot array illuminators. Theoretical and experimental data are presented to explore the effects of fabrication errors on these devices. **(p. 288)**

Reception Lanai
3:00pm–3:30pm
Coffee Break

Koa Room

3:30pm–5:00pm
DThD ■ Applications 2
Shogo Ura, *Osaka University, Japan, Presider*

3:30pm (Invited)
DThD1 ■ Diffractive and microoptics at Centro Ricerche Fiat: implemented technologies and applications in the transport industry and general lighting, P. Perlo, P.M. Repetto, S. Sinesi, V. Lambertini, C. Bigliati, *Centro Ricerche Fiat, Italy.* Emphasis on the design methodologies and on the technologies implemented to rapidly manufacture large nonrepeated cluster is given. The development of systems based on diffractive and micro-optics for the motorcycle, automotive and general lighting industries is presented. Considerations on their use over the more conventional approaches conclude the paper. **(p. 292)**

4:00pm
DThD2 ■ High-efficiency transmission diffractive grating and grating lens of the megajoule laser final optic assembly, Alain Adolf, Arnaud Dulac, Eric Journot, *CEA/LV-DLP/SCSL, France.* We describe the design and fabrication processes and compare theoretical calculations with experimental results for the two diffractive elements. **(p. 293)**

4:15pm
DThD3 ■ Design of diffractive-optical elements for mode shaping within custom laser resonators, Ian M. Barton, Mohammad R. Taghizadeh, *Heriot-Watt Univ., U.K.* Diffractive-optical elements are designed using numerical optimization algorithms that customize the shape of the fundamental mode of a laser resonator. Experimental verification is presented. **(p. 296)**

4:30pm
DThD4 ■ Diffractive elements for the generation of propagation-invariant, rotating, and self-reproducing fields, S.N. Khonina, V.V. Kotlyar, V.A. Soifer, *Russian Academy of Sciences;* P. Pääkkönen, J. Lautanen, M. Honkanen, M. Kuittinen, J. Turunen, *Univ. Joensuu, Finland;* A.T. Friberg, *Royal Institute of Technology, Sweden.* Diffractive elements fabricated by electron beam lithography are used to demonstrate superpositions of Bessel field modes with wave vectors on one or several Montgomerys rings. **(p. 299)**

4:45pm
DThD5 ■ Liquid crystal blazed grating beam deflector, Xu Wang, Demetri Psaltis, *California Institute of Technology;* Daniel W. Wilson, Richard E. Muller, Paul D. Maker, *Jet Propulsion Laboratory.* A liquid crystal blazed grating beam deflector, which consists of a stack of liquid crystal and PMMA composite blazed gratings has been developed. Four steering angles with approximately 70% diffraction efficiency are achieved within a 15 V voltage. **(p. 302)**

Diffractive Optics and Micro-Optics

Theory 1

Monday, June 8, 1998

J. Allen Cox, Honeywell, Inc.
Presider

DMA
8:30am–10:30am
Koa Room

Grating diffraction analysis: Maxwell's equations or Kirchhoff diffraction integrals

M. G. Moharam and S. Dunn
Center for Research and Education in Optics and Lasers,
University of Central Florida
Orlando, Florida 32816-2700
(407) 823-6833, Fax (407) 823-6810, email: moharam@creol.ucf.edu

Introduction:

Scalar diffraction theory is widely used to design and analyze diffractive optical elements. This approach has been the approach of choice for it is easy to use, lacks computation strain, and more importantly, offer some direct approach for the design of diffractive elements. The validity and, therefore, the usability of the scalar diffraction approaches are based on the assumption that the smallest feature in the diffractive element is much greater than the wavelength of incident light. However, recent advances in the fabrication techniques have resulted in producing diffractive optical elements with small feature sizes of wavelength and subwavelength dimensions and scalar diffraction approaches may not be applicable. Rigorous diffraction analysis techniques have been developed and/or refined to analyze these wavelength size structures. These methods include rigorous coupled-wave theory, modal approach, method of moments, and other differential and integral methods. These electromagnetic theory based approaches provide powerful, accurate, and relatively efficient analysis methods. However, they do not provide satisfactory tools for the systematic design of diffraction elements.

Approach

The objective of this work is to provide an insight into the scalar diffraction formulations to help determine the conditions under which these scalar approaches may be applied with reasonable accuracy. We will attempt to identify and delineate the inherent fundamental "physical" approximations in the scalar

formulation of Kirchhoff and Rayleigh-Sommerfeld integrals from those approximations performed to simplify the formulation and/or to obtain close-form solution for the diffraction problem. The fundamental diffraction problem consists of two parts. They are: 1) determining the effect of introducing the diffractive structure upon the electromagnetic fields immediately behind and in front of the structure and 2) determining how the field will propagate away from the diffractive structure in either direction.

The propagation part is relatively well recognized, if not fully understood. Approximations in this part are predominantly the "mathematical" kind that lead to simplifications in the formulations including those for far-field Fraunhofer diffraction and near-field Fresnel diffraction. However these mathematical approximations are precisely the cause for the various wave front various aberrations of optical imaging systems ignored when making the Fresnel and the Fraunhofer approximations. These approximations are not necessary and can be avoid with additional modest effort in the numerical calculations of the diffraction patterns.

However, the first part of the diffraction problem, which is imposing a field distribution immediately behind/before the diffractive structure, is the fundamental physical approximation in all scalar diffraction integral theories. This is true for Kirchhoff, and Rayleigh-Sommerfeld, and similar scalar integrals. It is clearly the main and very significant difference between the scalar methods and electromagnetic based techniques, where the field at the diffractive structure is rigorously calculated.

We will discuss the implications of the approximations inherent in the Kirchhoff's integral based scalar diffraction analysis methods specifically as related to forcing a field distribution at the aperture. These imposed field distribution and the resulting diffraction characteristics will be compared by those obtained by electromagnetics based rigorous coupled-wave technique. The insight gained into the scalar diffraction formulations will help provide a better understanding to he conditions under which these scalar approaches may be applied with reasonable accuracy.

Mathematical Modeling of Diffractive Gratings

Gang Bao
Department of Mathematics
University of Florida
Gainesville, FL 32611

1. Introduction. Since 1990, the electromagnetic theory of gratings has received considerable attention from the applied mathematics community. Several approaches and numerical methods have been developed, including integral equation methods Dobson and Friedman [9], analytical continuation method Bruno and Reitich [7], and variational methods Dobson [8], Abboud [1], and Bao [3]. Significant results on existence, uniqueness, and convergence of solutions of the Maxwell equations have been obtained. We refer to Bao, Dobson, and Cox [5] for a survey of recent mathematical and computational results. A good introduction to the problem of electromagnetic diffraction through periodic structures can be found in Petit [12]. See also Gaylord and Moharam [10], Li [11], ... for other approaches, particularly along the line of differential methods.

Here, we present a new variational approach based on least-squares finite element methods, drawn largely from our recent work [4] [6]. We highlight the main steps of this approach as well as the convergence properties. In particular, optimal convergence rates may be obtained in both TE and TM cases. We also discuss the computational aspects of the approach. Our numerical experiments indicate that the least-squares finite element methods are accurate and efficient.

2. The scattering problem. We assume that the media are nonmagnetic with a unit magnetic permeability, and no external charge or current is present. Then the electromagnetic fields satisfy the following time harmonic (time dependence $e^{-i\omega t}$) Maxwell equations: $\nabla\times E - i\omega H = 0$, $\nabla\times H + i\omega\epsilon E = 0$, where E and H are the electric and magnetic field vectors, respectively, ω is angular frequency. The geometry and material properties are characterized completely by the dielectric coefficient $\epsilon(x)$, $x = (x_1, x_2, x_3)$. The periodicity of the structure is also characterized by the dielectric coefficient. In the two dimensional setting, we assume that the medium and grating surface are constant in the x_2 direction. It follows that the solution of the diffraction problem can be written as a sum of TE (*transverse electric*) and TM (*transverse magnetic*) polarized solutions: In the TE case, the electric field is pointed along the x_2 direction, the Maxwell equations may be further reduced to $(\Delta + \omega^2\epsilon)u = 0$, $E = u(x_1, x_3)\vec{x}_2$. In the TM case, the magnetic field is pointed along the x_2 direction, thus $\nabla\cdot(\frac{1}{\epsilon}\nabla u) + \omega^2 u = 0$, $H = u(x_1, x_3)\vec{x}_2$.

The periodicity of the structure and material allows us to compute the solutions in a single period. The fundamental step of the variational approach is to reduce the problem to a bounded domain or cell. This can be done by introducing a pair of transparent boundary conditions resulting from the radiation condition, Green's functions, and quasi-periodicity properties of the solutions[8][5].

We consider the simple situation of linear gratings in TM polarization. Assume that the medium and grating structure are invariant in the x_2 direction.

Let a plane wave $u_I = e^{(i\alpha x_1 - i\beta_1 x_3)}$ be incident on the grating surface S_1 from the top, where $\alpha = \omega\sqrt{\varepsilon_1}\sin\theta$, $\beta_1 = \omega\sqrt{\varepsilon_1}cos\theta$, and $\theta \in (-\frac{\pi}{2}, \frac{\pi}{2})$ is the angle of incidence. Assume that some possibly nonhomogeneous material lies in between S_1 and S_2. Let Ω_1, Ω_2, Ω_0 denote the regions above S_1, below S_2, between S_1 and S_2, respectively. The dielectric coefficient ε is defined to be ε_1 in $\bar{\Omega}_1$; ε_0 in Ω_0; ε_2 in $\bar{\Omega}_2$, where ε_1, ε_2 are fixed positive constants, ε_0 is a bounded function which satisfies $\inf_{(x_1,x_3)\in\Omega_0} Re\,\varepsilon_0(x_1,x_3) > 0$, and $Im\,\varepsilon_0(x_1,x_3) \geq 0$. We are interested in quasiperiodic solutions u, *i.e.*, $ue^{-i\alpha x_1}$ are 2π periodic in x_1. So we may restrict our attention to a single period.

Introduce the notations $\Gamma_1 = \{x_3 = b,\ 0 < x_1 < 2\pi\}$, $\Gamma_2 = \{x_3 = -b,\ 0 < x_1 < 2\pi\}$, $\Omega = \{0 < x_1 < 2\pi, -b < x_3 < b\}$, $\nabla_\alpha = \nabla + i(\alpha, 0)$, $u_\alpha = ue^{-i\alpha x_1}$, where b is a positive constant such that S_1, S_2 lie strictly between Γ_1 and Γ_2.

Let $a = 1/(\omega^2\epsilon)$, $a_j = 1/(\omega^2\epsilon_j)$, $j = 0, 1, 2$. The scattering problem in the TM case can be formulated as follows (Bao [2]):

$$\begin{aligned}\nabla_\alpha\cdot(a_j\nabla_\alpha u_\alpha^j) + u_\alpha^j &= 0 \text{ in } \Omega_j,\ \ j = 0,\,1,\,2\,,\\ [u_\alpha] &= 0 \text{ on } S_j,\ \ j = 1,\,2,\end{aligned}$$

$$
\begin{aligned}
n_j \cdot [a\nabla_\alpha u_\alpha] &= 0 \text{ on } S_j, \\
\left(T_1^\alpha - \frac{\partial}{\partial n_1}\right) u_\alpha^1 &= 2i\beta_1 e^{-i\beta_1 b} \text{ on } \Gamma_1, \\
\left(T_2^\alpha - \frac{\partial}{\partial n_2}\right) u_\alpha^2 &= 0 \text{ on } \Gamma_2,
\end{aligned}
$$

where $u_\alpha^j = u_\alpha|_{\Omega_j}$, $j = 0, 1, 2$, n_j is the unit outward normal to Ω_j, $j = 1, 2$, and the symbol $[\cdot]$ denotes the jump of a function across the specified surface. For a function g on Γ_j, define the operator T_j^α by

$$
(T_j^\alpha g)(x_1) = \sum_{n \in Z} i\beta_j^{(n)}(\alpha) g^{(n)} e^{inx_1},
$$

where $g^{(n)}$ is the Fourier transform of g, and

$$
\beta_j^{(n)}(\alpha) = \begin{cases} \sqrt{\omega^2\varepsilon_j - (n+\alpha)^2} & \text{if } \omega^2\varepsilon_j > (n+\alpha)^2, \\ i\sqrt{(n+\alpha)^2 - \omega^2\varepsilon_j} & \text{if } \omega^2\varepsilon_j < (n+\alpha)^2. \end{cases}
$$

Note that a slight modification of the expression of $\beta_2^{(n)}$ would be needed for complex ε_2,.

3. Least-squares finite element methods. In order to introduce the approach, it is crucial to view the grating problem as an interface problem with interfaces S_1, S_2. The first step is to rewrite the interface problem as a first order system of u, ϕ and to formulate it as a least-squares problem. Let $\phi^j = a_j \nabla_\alpha u_\alpha^j$, $j = 0, 1, 2$. We have

$$
\begin{aligned}
\nabla_\alpha \cdot \phi^j + u_\alpha^j &= 0 \text{ in } \Omega_j, \quad j = 0, 1, 2, \\
a_j \nabla_\alpha u_\alpha^j - \phi^j &= 0 \text{ in } \Omega_j, \quad j = 0, 1, 2, \\
[u_\alpha] &= 0 \text{ on } S_j, \quad j = 1, 2, \\
[n \cdot \phi] &= 0 \text{ on } S_j, \quad j = 1, 2, \\
a_1 T_1 u_\alpha^1 - n_1 \cdot \phi^1 &= f \text{ on } \Gamma_1, \\
a_2 T_2 u_\alpha^2 - n_2 \cdot \phi^2 &= 0 \text{ on } \Gamma_2,
\end{aligned}
$$

where $f = 2ia_1\beta_1 e^{-i\beta_1 b}$.

Let $V = \{u \in L^2(\Omega) : u^j = u|_{\Omega_j} \in H_p^1(\Omega_j),\ j = 0, 1, 2\}$, where $L^2(\Omega)$ contains all the square integrable functions in Ω, $H_p^1(\Omega_j)$, the Sobolev space of order one, contains complex 2π-periodic (in x_1) square integrable functions, whose first order derivatives are also square integrable. Denote $W = \{\phi \in (L^2(\Omega))^2 : \phi^j = \phi|_{\Omega_j} = H_p(div, \Omega_j),\ j = 0, 1, 2\}$, where $H_p(div, \Omega_j) = \{\phi \in (L^2(\Omega_j))^2 :\ \nabla \cdot \phi \in L^2$ and ϕ is 2π periodic in x_1 $\}$. Define the least-squares functional $J(v, \psi; f)$ by

$$
\begin{aligned}
&\sum_{j=0}^{2} (\|\nabla_\alpha \cdot \psi^j + v^j\|_{L^2(\Omega_j)}^2 + \|a_j \nabla_\alpha v^j - \psi^j\|_{L^2(\Omega_j)}^2) + \sum_{j=1}^{2} (\|[v]\|_{H^{1/2}(S_j)}^2 \\
&+ \|[n \cdot \psi]\|_{H^{-1/2}(S_j)}^2) + \|a_1 T_1 v^1 - n_1 \cdot \psi^1 - f\|_{H^{-1/2}(\Gamma_1)}^2 + \|a_2 T_2 v^2 - n_2 \cdot \psi^2\|_{H^{-1/2}(\Gamma_2)}^2.
\end{aligned}
$$

Note that the jump conditions are built in the functional. The L^2, $H^{-1/2}$, $H^{1/2}$ norms are standard and may be computed via the Fourier transform.

The least-squares minimization problem is to find $u \in V$, $\phi \in W$, such that

$$
J(u, \phi; f) = \inf_{v \in V, \psi \in W} J(v, \psi; f).
$$

Taking the variation of J with respect to v, ψ, we obtain an equivalent variational problem: find $u \in V$, $\phi \in W$ such that

$$
B(u, \phi; v, \psi) = \langle f, a_1 T_1 v^1 - n_1 \cdot \phi^1 \rangle_{-\frac{1}{2}, \Gamma_1},\ \forall v \in V,\ \psi \in W,
$$

where

$$B(u,\phi;v,\psi)=\sum_{j=0}^{2}\{(\nabla_\alpha\cdot\phi^j+u^j,\ \nabla_\alpha\cdot\psi^j+v^j)_{0,\Omega_j}+(a_j\nabla_\alpha u^j-\phi^j,\ a_j\nabla_\alpha v^j-\psi^j)_{0,\Omega_j}\}+$$

$$\sum_{j=1}^{2}\{\langle[u],[v]\rangle_{\frac{1}{2},S_j}+\langle[n\cdot\phi],\ [n\cdot\psi]\rangle_{-\frac{1}{2},S_j}+\langle a_jT_ju^j-n_j\cdot\phi^j,\ a_jT_jv^j-n_j\cdot\psi^j\rangle_{-\frac{1}{2},\Gamma_j}\}.$$

Here $<\cdot>_{-\frac{1}{2},\Gamma_j}$, $<\cdot>_{\frac{1}{2},\Gamma_j}$, $<\cdot>_{-\frac{1}{2},S_j}$, $<\cdot>_{\frac{1}{2},S_j}$ are inner products in the specified spaces which are defined by Fourier transforms (series), and $(\cdot)_{0,\Omega_j}$ denotes the L^2 inner product.

Let V_h, W_h be finite dimensional subspaces of V, W, respectively. Here h is the mesh size from partitioning Ω into subdomains. A least-squares finite element approximation $(u_h,\ \phi_h)$ of $(u,\ \phi)$ may be obtained by solving

$$B(u_h,\phi_h;v_h,\psi_h)=\langle f,a_1T_1v_h^1-n_1\cdot\phi_h^1\rangle_{-\frac{1}{2},\Gamma_1},\ \forall v_h\in V_h,\ \psi\in W_h,$$

which gives rise to a system of linear equations. An important property of the least-squares finite element formulation is that the resulting system is symmetric, positive definite, and thus can be solved efficiently by various existing preconditioning techniques.

In addition, it is shown in [6] that under some mild assumptions

$$||u-u_h||_{H_p^1(\Omega)}+||\phi-\phi_h||_{H_p(div,\Omega)}\le Ch\ ,$$

where the constant is independent of h. In fact, better convergence results can be expected with more regular grating surfaces. In contrast, no convergence rate is available in the TM case for the standard finite element method [2].

Our approach has the following advantages: The problem may be discretized on both sides of the interface and the jump conditions are enforced through the least-squares functional. In particular, different finite element spaces may be easily used on two sides of the interface. The interface can be a curved surface. Both electric and magnetic fields can be determined simultaneously, which avoids the unstable numerical differentiation process. With sufficiently smooth interfaces, significantly better estimates can be expected. Note that even with a smooth interface, standard finite element may not have good convergence results.

Finally, in TE polarization, due to more regular global solutions, a different (non-interface type) least-squares finite element method may be employed [4]. We believe that the general ideas also apply to crossed gratings and nonlinear gratings.

REFERENCES

[1] T. Abboud, *Electromagnetic waves in periodic media*, in Second International Conference on Mathematical and Numerical Aspects of Wave Propagation, ed. by R. Kleinman et al, SIAM, Philadelphia, 1993, 1–9.

[2] G. Bao, *Numerical analysis of diffraction by periodic structures: TM polarization*, Numer. Math. **75** (1996), 1-16.

[3] G. Bao, *Variational approximation of Maxwell's equations in biperiodic structures*, SIAM J. Appl. Math. **57** (1997), 364-381.

[4] G. Bao, Y. Cao, and H. Yang, *Numerical solution of diffraction problem by a least-squares finite element method*, SIAM J. Sci. Comput., submitted.

[5] G. Bao, D. Dobson, and J. A. Cox, *Mathematical studies of rigorous grating theory*, J. Opt. Soc. Am. **A 12**(1995), 1029–1042.

[6] G. Bao and H. Yang, *A least-squares finite element analysis for diffraction problems*, Math. Comp., submitted.

[7] O. P. Bruno and F. Reitich, *Numerical solution of diffraction problems: a method of variation of boundaries*, J. Opt. Soc. Amer. A. **10** (1993), 1168-1175.

[8] D. Dobson, *Optimal design of periodic antireflective structures for the Helmholtz equation*, Euro. J. Appl. Math. **4** (1993), 321-340.

[9] D. Dobson and A. Friedman, *The time-harmonic Maxwell equations in a doubly periodic structure*, J. Math. Anal. Appl. **166** (1992), 507-528.

[10] T. K. Gaylord and M. G. Moharam, *Analysis and applications of optical diffraction by gratings*, IEEE Proceedings, Vol. 73 No. 5 (1985), 894-937.

[11] L. Li, *A model analysis of lamellar diffraction gratings in conical mountings*, J. Mod. Opt. **40**, 553–573 (1993).

[12] *Electromagnetic Theory of Gratings*, Topics in Current Physics, Vol. 22, edited by R. Petit, Springer-Verlag, Heidelberg, 1980.

Reformulation of the Fourier modal method for surface-relief anisotropic gratings

Lifeng Li
Optical Sciences Center, University of Arizona, Tucson, Arizona 85721
Tel: (520) 621-1789, Fax: (520) 621-4358

1. Introduction

Surface-relief gratings made with anisotropic materials are finding more applications. An example is grooved magneto-optic disks as data storage media. The present work is a reformulation of the couple-wave method, for solving the anisotropic grating problem, that is described in Refs. 1-3. [Since the method essentially is a modal method relying on expanding both the electromagnetic fields and the permittivity function into Fourier series, here it is referred to as the Fourier modal method (FMM).] It originated from the work documented in Refs. 4-7. Recently Lalanne and Morris[4], and Granet and Guizal[5] simultaneously reformulated the conventional FMM for isotropic gratings in TM polarization. As a result, the convergence of the method for highly conducting metallic gratings was greatly improved. Auslender and Hava[6] also reported the same reformulation. The findings of these authors were mathematically justified and summarized in the form of three Fourier factorization rules[7]. The use of these factorization rules has led to improvement of convergence in two other cases: the C method for gratings with sharp edges[8] and the FMM for crossed gratings.[9] This conference paper briefly reports yet another successful application of the factorization rules. A detailed exposition will soon appear elsewhere.[10]

2. Statement of the Problem

The grating geometry is shown in Fig. 1. In this paper a tilde is used to denote a tensor in the three-dimensional space. With the exception of the incident medium, every region in the grating structure can be either isotropic, uniaxial, or biaxial. The basic grating problem is to determine the diffraction efficiencies and states of polarization of the propagating diffraction orders.

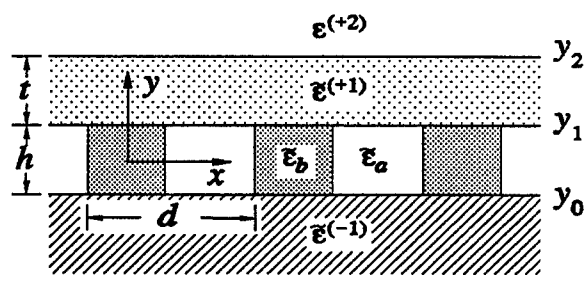

Fig. 1. Geometry of the anisotropic grating.

3. Eigen Solutions in a Homogeneous Anisotropic Medium

In an anisotropic grating structure there are usually some homogeneous anisotropic layers. This is true at least when the substrate is anisotropic. In order to write down the Rayleigh expansions for the fields, one must solve the eigenvalue problem for the plane waves in an anisotropic medium. To do so one solves, implicitly or explicitly, a fourth order polynomial that is called the Booker quartic.[11] From a geometrical point of view, the solution of the Booker quartic amounts to the following operation. First, cut the wave vector surface[12] with the plane that contains the y axis and vector $\boldsymbol{b} = k_x\hat{\mathbf{x}}$ (assuming non-conical incidence). An example of such a cut is illustrated in Fig. 2. Then, parallel to the y axis draw a line passing through the tip of $\boldsymbol{b}$. The ordinates of locations where the line pierces the wave vector surface give the real solutions of the Booker quartic.

Of the four solutions of the Booker quartic, two solutions correspond to upward propagating or decaying plane waves; the other two correspond to downward propagating or decaying plane waves. The physics of the problem requires that, in the substrate, the up-waves be discarded and the down-waves be kept. Thus, the identification of the directions of the waves is important. The task of identifying the

directions of the propagating plane waves in an anisotropic medium seems to have been handled by previous authors in manners that ranged from careless to over-conservative. Indeed, one often finds in the literature statements like: A $k_y > 0$ corresponds to an up-wave and a $k_y < 0$ corresponds to an down-wave. Such a statement, although true for an isotropic medium, is not always true for an anisotropic medium. It suffices to note that for a given $\boldsymbol{b}$ it is possible that three k_y values have the same sign. Examples of this possibility are shown in Fig. 2 by lines PP′ and QQ′. On the other hand, other authors calculate the y components of all Poynting vectors in order to classify the solutions. This approach is reliable but inefficient and not so elegant. A simple and reliable set of identification criteria are given in Ref. 10.

4. Fourier Analysis in the Grating Region

In the conventional treatment[1-3] of the FMM Fourier expansions of the electromagnetic fields and the permittivity function are directly substituted into the standard form of the two Maxwell's equations involving curl operators. After the elimination of the y components of the fields, a matrix eigenvalue equation is obtained,

$$A \cdot (E_z, H_z, H_x, E_x)^{\mathrm{T}} = \lambda\,(E_z, H_z, H_x, E_x)^{\mathrm{T}},$$

where λ is the eigenvalue, superscript T indicates matrix transpose, and A is a 4×4 block matrix whose expressions can be found in Refs. 1-3. Here it is only necessary to pointed out that A in general depends on the Fourier expansions of all 9 elements of the tensorial permittivity function $\boldsymbol{\varepsilon}(x)$.

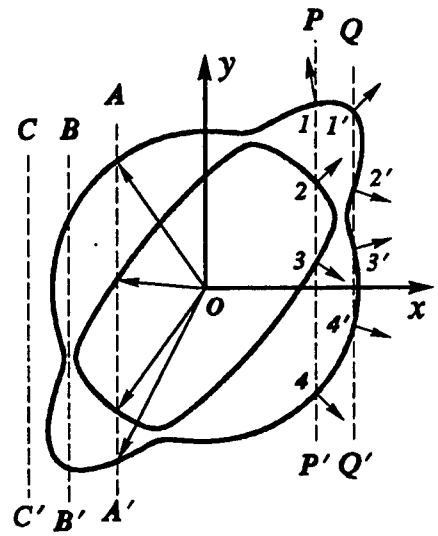

Fig. 2. Geometric interpretation of solutions of the Booker quartic.

The conventional FMM converges slowly for surface-relief gratings when the permittivity contrast in the grating region is high. This is because the conventional formulation uses the Fourier expansions of the permittivity tensor elements without due considerations of the continuity characteristics of the products in which they appear. A reformulation of the FMM following the theorems and methodology presented in Ref. 7 shows that the expressions of matrix A given in Ref. 1-3 are still valid, provided that everywhere in these expressions $[\![\varepsilon_{ij}]\!]$ are replaced by Q_{ij}, where Q_{ij} are elements of the 3×3 block matrix

$$Q = \begin{pmatrix} \left[\!\left[\frac{1}{\varepsilon_{11}}\right]\!\right]^{-1} & \left[\!\left[\frac{1}{\varepsilon_{11}}\right]\!\right]^{-1}\left[\!\left[\frac{\varepsilon_{12}}{\varepsilon_{11}}\right]\!\right] & \left[\!\left[\frac{1}{\varepsilon_{11}}\right]\!\right]^{-1}\left[\!\left[\frac{\varepsilon_{13}}{\varepsilon_{11}}\right]\!\right] \\ \left[\!\left[\frac{\varepsilon_{21}}{\varepsilon_{11}}\right]\!\right]\left[\!\left[\frac{1}{\varepsilon_{11}}\right]\!\right]^{-1} & \left[\!\left[\frac{\varepsilon_{21}}{\varepsilon_{11}}\right]\!\right]\left[\!\left[\frac{1}{\varepsilon_{11}}\right]\!\right]^{-1}\left[\!\left[\frac{\varepsilon_{12}}{\varepsilon_{11}}\right]\!\right] + \left[\!\left[\frac{\varepsilon_{11}\varepsilon_{22} - \varepsilon_{21}\varepsilon_{12}}{\varepsilon_{11}}\right]\!\right] & \left[\!\left[\frac{\varepsilon_{21}}{\varepsilon_{11}}\right]\!\right]\left[\!\left[\frac{1}{\varepsilon_{11}}\right]\!\right]^{-1}\left[\!\left[\frac{\varepsilon_{13}}{\varepsilon_{11}}\right]\!\right] + \left[\!\left[\frac{\varepsilon_{11}\varepsilon_{23} - \varepsilon_{21}\varepsilon_{13}}{\varepsilon_{11}}\right]\!\right] \\ \left[\!\left[\frac{\varepsilon_{31}}{\varepsilon_{11}}\right]\!\right]\left[\!\left[\frac{1}{\varepsilon_{11}}\right]\!\right]^{-1} & \left[\!\left[\frac{\varepsilon_{31}}{\varepsilon_{11}}\right]\!\right]\left[\!\left[\frac{1}{\varepsilon_{11}}\right]\!\right]^{-1}\left[\!\left[\frac{\varepsilon_{12}}{\varepsilon_{11}}\right]\!\right] + \left[\!\left[\frac{\varepsilon_{11}\varepsilon_{32} - \varepsilon_{31}\varepsilon_{12}}{\varepsilon_{11}}\right]\!\right] & \left[\!\left[\frac{\varepsilon_{31}}{\varepsilon_{11}}\right]\!\right]\left[\!\left[\frac{1}{\varepsilon_{11}}\right]\!\right]^{-1}\left[\!\left[\frac{\varepsilon_{13}}{\varepsilon_{11}}\right]\!\right] + \left[\!\left[\frac{\varepsilon_{11}\varepsilon_{33} - \varepsilon_{31}\varepsilon_{13}}{\varepsilon_{11}}\right]\!\right] \end{pmatrix},$$

and $[\![f]\!]$ is the Toeplitz matrix generated by the Fourier coefficients of function $f(x)$.

It is emphasized that the above expression of matrix Q is mathematically derived following the theory of Ref. 7. One may recall that the authors of Refs. 4-6 found the correct formulation of the FMM for isotropic gratings more or less empirically. If one were to find the correct expression of A empirically, he would be facing an impossible task. The tensor elements ε_{ij} appear in the old A matrix in 36 places. If for every ε_{ij} appearing as a numerator he would experiment with $[\![\varepsilon_{ij}]\!]$ and $[\![1/\varepsilon_{ij}]\!]^{-1}$, and for every ε_{ij}

appearing as a denominator he would experiment with $[\![1/\varepsilon_{ij}]\!]$ and $[\![\varepsilon_{ij}]\!]^{-1}$, then he would have 2^{36} = 68,719,476,736 experiments to perform, an astronomical figure! Moreover, the correct answer is even not among these huge number of possibilities.

5. Numerical Example

The example is built upon a celebrated test case for evaluating the convergence of the FMM for isotropic gratings[4,5,13]. The only difference here is that an anisotropic dielectric material is added, filling the grating grooves and leaving a one-wavelength thick layer above the grating. The biaxial tensor of this fictitious material is characterized by $\varepsilon_{11} = 2.25$, $\varepsilon_{22} = 2.56$, $\varepsilon_{33} = 2.89$, $\varepsilon_{12} = 0.04$, $\varepsilon_{23} = 0.16$, and $\varepsilon_{13} = 0.36$. Figure 3 compares the convergence of the old and the new FMM. The truncation order N is one-fourth of the dimension of matrix A. Note that because of the arbitrary orientation of the permittivity tensor a TE (or TM) incident plane wave excites both TE and TM polarized diffracted orders.

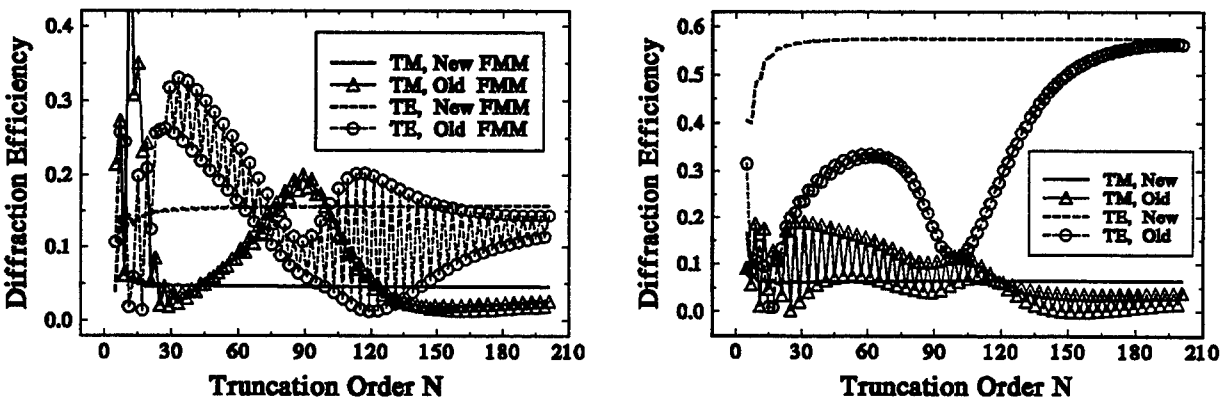

(*a*) (*b*)

Fig. 3. Comparison of convergence of the 0 order (*a*) and the − 1st order (*b*) diffraction efficiencies computed by the old and new formulations of the FMM, for a metallic lamellar grating coated with an anisotropic layer. The incident polarization is TE.

6. Conclusion

The Fourier modal method for anisotropic surface-relief gratings has been reformulated by using the correct Fourier factorization rules of Ref. 7. It is shown that the newly formulated FMM converges much faster than the old formulation when the permittivity contrast in the grating groove region is large. Highly conducting lamellar gratings coated with anisotropic materials, the analysis of which was impractical by using the old FMM, can now be analyzed easily with the new FMM.

References

1. K. Rokushima and J. Yamakita, *J. Opt. Soc. Am.*, **73**, 901 (1983).
2. E. N. Glytsis and T. K. Gaylord, *J. Opt. Soc. Am.* A, **4**, 2061 (1987).
3. S. Mori, K. Mukai, J. Yamakita, and K. Rokushima, *J. Opt. Soc. Am.* A, **7**, 1661 (1990).
4. Ph. Lalanne and G. M. Morris, *J. Opt. Soc. Am.* A, **13**, 779 (1996).
5. G. Granet and B. Guizal, *J. Opt. Soc. Am.* A, **13**, 1019 (1996).
6. M. Auslender and S. Hava, *Opt. Lett.*, **21**, 1765 (1996).
7. L. Li, *J. Opt. Soc. Am.* A, **13**, 1870 (1996).
8. L. Li and J. Chandezon, *J. Opt. Soc. Am.* A, **13**, 2247 (1996).
9. L. Li, *J. Opt. Soc. Am.* A, **14**, 2758 (1997).
10. L. Li, *J. Mod. Opt.* 1998 Special Issue on Diffractive Optics (to be published).
11 H. G. Booker, *Proc. Roy. Soc. London*, A, **155**, 235 (1936).
12. H. C. Chen, *Theory of Electromagnetic Waves* (New York: McGraw-Hill, 1983).
13. L. Li and C. W. Haggans, *J. Opt. Soc. Am.* A, **10**, 1184 (1993).

Applicability of the method of reduction in the Fourier modal method

Lifeng Li
Optical Sciences Center, University of Arizona, Tucson, Arizona 85721
Tel: (520) 621-1789, Fax: (520) 621-4358

1. Introduction

The Fourier modal method (FMM) is one of the simplest and most effective methods for modeling diffraction gratings. Burckhardt's paper[1], published in 1966, marked the beginning of this method. In Burckhardt's work, a volume grating of lossless, sinusoidally varying permittivity was considered. Later Kaspar[2] extended Burckhardt's work to lossy and non-sinusoidal volume gratings. Apparently unaware of Burckhardt and Kaspar's work, Peng *et al.*[3] also proposed the Fourier modal method; however, they refrained from applying it to surface-relief gratings (see next section). Apparently unaware of the concerns of Peng *et al.*, Knop[4] extended Burckhardt's work to rectangular surface-relief gratings. Moharam and Gaylord[5] took one step further. They applied the FMM to analyze surface-relief gratings of arbitrary profile.

In the FMM, both the electromagnetic fields and the permittivity function in the grating region are expanded into Fourier series. A matrix eigenvalue problem is obtained upon substituting the Fourier series into Maxwell's equations; hence the name Fourier modal method. In order to solve the eigenvalue problem numerically the coefficient matrix must be judiciously truncated (Mathematically this is called the method of reduction). With the sole exception of Peng *et al.*, no authors on the subject have expressed any concern over the legitimacy of using the method of reduction. Even in the recent reformulation of the method[6-9], the legitimacy remained unquestioned.

The researchers seem to have put their faith in the physics of the problem or in the satisfactory performance of the numerical codes. However, there are at least three good reasons to investigate the applicability of the method of reduction: 1. To develop the FMM into a scientific method (not just an engineering tool) it is necessary to lay it on a solid mathematical ground. 2. The applicability study will pave the road to a mathematical analysis of the convergence characteristics of the FMM, which may eventually lead to an *a priori* criterion for determining optimum truncation. 3. Such a study potentially could also suggest new approximation methods.

2. A Discussion of Peng *et al.*[3]

The 1975 paper of Peng *et al.* is of great importance in the theory of gratings. It contains a large number of significant results. Pertinent to the present subject is the paragraph containing inequality (24), in which they mathematically justified the use of the method of reduction in the FMM for certain types of gratings. To my knowledge, this is the first and the only effort of the kind made by an author on the FMM.

However, I find the discussion of Peng *et al.* in that paragraph both peculiar and unfortunate. I say that it is peculiar because, according to Kantorovich and Krylov,[10] inequality (24) gives the condition for the linear system to be regular. However, regularity only assures the solvability of the linear system by the method of successive approximation. It does not assure the convergence of the infinite determinant. Based on this inequality, they concluded that for surface-relief gratings "other mathematical techniques

for determining the characteristic solutions in the grating region have to be employed". With the benefit of the developments in the FMM over more than 20 years since the publication of that paper, we now know that this statement is incorrect. I say that it is also unfortunate because in Section 6 of the same chapter that they referenced, printed in small type, Kantorovich and Krylov mentioned a theorem of H. von Koch. This theorem is all we need to establish the applicability of the method of reduction in the FMM, at least in TE polarization, for gratings of any index distributions.

3. A Theorem of H. von Koch

Let A_{ik}, $i, k = -\infty, \ldots, -1, 0, +1, \ldots, +\infty$, be a double sequence of complex numbers.

Theorem (H. von Koch)

For the determinant of A_{ik} and all its minors to converge absolutely, it is sufficient that the product of the diagonal elements converges absolutely and that the sum of the squares of the non-diagonal elements converges absolutely.

4. Application to the Fourier Modal Method

4.1 *TE polarization*

The matrix eigenvalue equation in TE polarization is normally written as[1-4,8,9]

$$\sum_n \left(\xi_{m-n} - \alpha_m^2 \delta_{mn} \right) E_{zn} = \rho E_{zm}, \tag{1}$$

where ρ is the eigenvalue, $\alpha_m = \alpha_0 + m K$, $\xi(x) = \varepsilon(x)\mu k_0^2$ (Gaussian system of units is used here), and the rest of the symbols take their usual meanings. Assuming that $\xi_0 - \alpha_m^2 - \rho \neq 0$, $\forall\, m$, we can rewrite Eq. (1) in a more convenient form:

$$\sum_n \left(\delta_{mn} + \frac{\xi'_{m-n}}{\xi_0 - \alpha_m^2 - \rho} \right) E_{zn} = 0, \tag{2}$$

where $\xi'_m = \xi_m$ if $m \neq 0$, and $\xi'_0 = 0$. For gratings of any kind, volume or surface-relief, the Fourier coefficient of $\xi(x)$ tends to zero at least as fast as $1/n$ as $n \to \infty$. Thus by von Koch's theorem it is easy to see that the method of reduction can be applied to the solution of Eq. (1) or (2).

4.2 *TM polarization*

The matrix eigenvalue equation in TM polarization should be written as[6-9]

$$\sum_n \left[\!\left[\frac{1}{\xi} \right]\!\right]^{-1}_{mn} \sum_p \left(\delta_{np} - \alpha_n [\![\xi]\!]^{-1}_{np} \alpha_p \right) H_{zp} = \rho H_{zm}, \tag{3}$$

where $[\![\xi]\!]$ denotes the matrix with elements $\xi_{mn} = \xi_{m-n}$. For simplicity we only consider the case of $\alpha_m \neq 0$, $\forall\, m$. Then Eq. (3) is equivalent to

$$\sum_n \left[\delta_{mn} + \sum_p \frac{1}{\alpha_m} \xi_{m-p} \frac{1}{\alpha_p} \left(\rho \left[\frac{1}{\xi} \right]_{p-n} - \delta_{pn} \right) \right] H_{zn} = 0. \tag{4}$$

Note that compared with Eq. (2) there is an extra summation over p in Eq. (4). Let $A_{mn}^{(P)}$ be the matrix elements obtained by summing over p from $-P$ to $+P$, and $\|A_{mn}^{(P)}\|_{-N}^{N}$ be the truncated determinant with $|m| \leq N$ and $|n| \leq N$. Then from von Koch's theorem it follows that, for a fixed P, $\|A_{mn}^{(P)}\|_{-N}^{N}$ converges as $N \to \infty$. However, since we normally truncate the three indices m, n, and p simultaneously to the same integer in numerical computations, what we really want to know is if $\|A_{mn}^{(N)}\|_{-N}^{N}$ converges as $N \to \infty$. In von Koch's theorem A_{ik} is assumed to be independent of matrix truncation, so the theorem is not directly applicable to the present situation. Nonetheless, a detailed

analysis along the line that von Koch arrived at his theorem shows that the answer to the above question is positive. Therefore the method of reduction is also applicable to TM polarization.

5. Discussion

Without much further analysis, Eqs. (2) and (4) already tell us mathematically many facts that we have known from numerical experience.

5.1. *Convergence difference between TE and TM*

It is well known that for a surface-relief grating the FMM converges faster in TE polarization than in TM polarization. This can be seen from the fact that the non-diagonal matrix elements in Eq. (2) tend to zero like $1/[m^2(m-n)]$ as $m \to \infty$ and $n \to \infty$, whereas the non-diagonal matrix elements in Eq. (4) tend to zero like $[(\ln|n|)/n + (\ln|m|)/m] / [m(m-n)]$.

5.2 *Influence of the permittivity difference on numerical convergence*

For a surface-relief grating the non-diagonal matrix elements in Eq. (2) are proportional to $\Delta\varepsilon$, the permittivity difference. In TM polarization the asymptotically dominant contribution to the non-diagonal matrix elements is proportional to $(\Delta\varepsilon)^2$. Thus the greater the permittivity difference is, the less diagonally dominant the coefficient matrices become, and the slower the convergence of the eigen-solutions is.

5.3. *Influence of the magnitude of the eigenvalues on numerical convergence*

An independent analysis or numerical experiments will show that $\rho \sim -(nK)^2$ for an eigenvalue with a sufficiently large order number n, assuming that the eigenvalues are ordered in increasing magnitude. Therefore, from both Eqs. (2) and (4) it can be seen that with a large eigenvalue it takes a larger truncation number N for the peripheral elements of the matrices to have sufficiently small values than it takes with a small eigenvalue. Thus the higher order numerical eigenvalues converge slower than the lower order eigenvalues. This conclusion agrees with numerical observations.

6. Conclusion

The applicability of the method of reduction in computing the eigen-solutions in the FMM is established by using a classical theorem of H. von Koch. This work may serve as a starting point of a mathematical study of the convergence characteristics of the method.

Incidentally, a similar analysis can be easily made to justify the use of the method of reduction in the coordinate transformation method of Chandezon *et al*[11].

References

1. C. B. Burckhardt, *J. Opt. Soc. Am.* **56**, 1502 (1966).
2. F. G. Kaspar, *J. Opt. Soc. Am.* **63**, 37 (1973).
3. S. T. Peng, T. Tamir, and H. L. Bertoni, *IEEE Trans. Microwave Theory Tech.* **23**, 123 (1975).
4. K. Knop, *J. Opt. Soc. Am.* **68**, 1206 (1978).
5. M. G. Moharam and T. K. Gaylord, *J. Opt. Soc. Am.* **72**, 1385 (1982).
6. Ph. Lalanne and G. M. Morris, *J. Opt. Soc. Am.* A **13**, 779 (1996).
7. G. Granet and B. Guizal, *J. Opt. Soc. Am.* A **13**, 1019 (1996).
8. L. Li, *J. Opt. Soc. Am.* A **13**, 1870 (1996).
9. M. Auslender and S. Hava, *Opt. Lett.* **21**, 1765 (1996).
10. L. V. Kantorovich and V. I. Krylov, *Approximation Methods of Higher Analysis* (Interscience, New York, 1964), Chap. I, Sec. 2, pp. 20-44.
11. J. Chandezon, D. Maystre, and G. Raoult, *J. Optics* (Paris) **11**, 235 (1980).

Perturbation theory - a unified approach to describe diffractive optical elements

Markus Testorf
University of Massachusetts-Lowell, Department of Electrical Engineering
One University Ave., Lowell, MA 01854, USA
phone: (508) 934-3300; fax: (508) 934 3027; e-mail: markus.e.testorf@dartmouth.edu

1. Introduction

The conceptual advantage of Kirchhoff's approximation[1] for the description of optical elements and systems is the intensive use of the Fourier transformation[2]. Its simple mathematical relations can be used to predict spatially distributed light signals in any plane of an optical system. An analysis in terms of Fourier optics and, more specific, the paraxial approximation is even appropriate if more rigorous calculations are required to achieve a desired accuracy for the design of the system.

Kirchhoff's approximation involves the description of diffractive optical elements as thin elements. Here we seek for an extension, which considers the effect of a finite thickness of optical elements. Differently from reference 3, where an extension of the Kirchhoff diffraction theory for surface relief structures is obtained on the basis of the first Born approximation, we adapt time-dependent perturbation theory of quantum mechanics to obtain an unified description for a large variety of diffraction phenomena. The applications we discuss show that a description of optically thick elements can be achieved preserving the simplicity and intuitive character of Fourier optics.

2. z-dependent perturbation theory of diffraction

In optical applications one space coordinate, for instance z, usually serves as the optical axis along which the propagation of the two-dimensional complex amplitude is observed. For a weakly scattering object in free space described by the refractive index distribution n(x,y,z) Helmholtz' equation can be written as

$$\left[H_0 + H'\right]u(x,y,z) \;=\; -\frac{\partial^2}{\partial z^2}u(x,y,z) \tag{1}$$

where u(x,y,z) is the complex amplitude and with the wave number $k_0=2\pi/\lambda$, we have

$$H_0 \;=\; \frac{\partial^2}{\partial x^2}+\frac{\partial^2}{\partial y^2}+k_0^2; \qquad H' \;=\; k_0^2\left(n^2-1\right) \tag{2}$$

The fundamental solutions of the z-independent equation, H'=0, are plane waves and any solution can be expressed as a superposition of these solutions

$$u(x,y,z) \;=\; \int_{-\infty}^{\infty}\int_{-\infty}^{\infty} a(\nu,\mu)\exp\left[i2\pi(\nu x+\mu y)\right]\exp\left[\pm i2\pi\beta z\right]d\nu d\mu \tag{3}$$

The propagation constant β and the spatial frequencies ν, μ are connected through $\beta^2+\nu^2+\mu^2=1/\lambda^2$. Assuming a small perturbation we expect that the complex amplitude can still be obtained as a superposition of the undisturbed solutions, but with a z-dependent plane wave spectrum $a(\nu,\mu,z)$. Substituting Eq. (3) into Eq. (1), multiplying with the complex conjugate of the output plane wave and integrating over both lateral coordinates we find

$$-\frac{\partial^2}{\partial z^2}a(\nu',\mu',z)\pm i4\pi\beta'\frac{\partial}{\partial z}a(\nu',\mu',z)=\int_{-\infty}^{\infty}\int_{-\infty}^{\infty}a(\nu,\mu,z)\,\tilde{H}'(\nu'-\nu,\mu'-\mu,z)\exp\left[\pm i2\pi(\beta-\beta')z\right]d\nu d\mu \tag{4}$$

The z-dependency of the plane wave spectrum is expressed as a set of coupled differential equations. The coupling strength is determined by the Fourier transform of the perturbation operator H'(x,y,z). Eq. (4) can be the starting point of a coupled wave analysis[4]. To emphasize the perturbation approach, we neglect the second derivative in Eq. (4), i.e. a smooth change of the coefficients is assumed. For a simplified notation, we only consider a single

incident plane wave $a(\nu,\mu, 0) = \delta(\nu-\nu_0,\mu-\mu_0)$. We also assume, that the intensity of the incident wave does not change significantly while passing the object. Integrating the remaining terms with respect to z, only considering plane waves propagating in positive z - direction, we obtain

$$a(\nu,\mu,z) = -\frac{i}{4\pi\beta}\int_0^z \tilde{H}'(\nu-\nu_0,\mu-\mu_0,z')\exp\left[-i2\pi(\beta-\beta_0)z'\right]dz' + \delta(\nu-\nu_0,\mu-\mu_0) \tag{5}$$

The delta-function corresponds to the incident beam. Eqs. (4) and (5) can be interpreted as follows: The plane wave spectrum behind the object can be calculated as the convolution of the incident plane wave spectrum with the three dimensional Fourier transformation of the perturbation. In comparison, for thin elements the input spectrum is convoluted with the two dimensional Fourier transform of the transparency. For dielectric optical fibers a perturbation expression similar to Eq. (5) is derived in reference 5. Then, the plane waves in Eqs. (3) - (5) are replaced by the transverse eigen functions of the undisturbed waveguide.

3. Applications

A. Equivalence of z-dependent perturbation theory and the first Born approximation

In quantum mechanics a formal equivalence between the time-dependent perturbation theory and the first Born approximation can be derived[6]. Similarly, Eq. (5), can be compared to the first Born approximation which has already been used to describe volume holograms[7]. In fact, Eq. (5) yields the scattering amplitude as a superposition of the incident wave and the scattered field. Despite this formal equivalence, the z-dependent perturbation approach is derived from a quite different point of view: While the Born formulation is based on Green's function, and thus starts from a spherical wave expansion, the z-dependent perturbation theory departs from an expansion in terms of the eigen functions of the problem, i.e. plane waves for free space optics. Hence, both perturbation methods are related like the spherical wave approach of the Huygens-Fresnel-Kirchhoff diffraction theory and the plane wave description of the Rayleigh-Sommerfeld-Debye diffraction theory[8]

Furthermore, the equivalence of both approaches becomes evident for the calculation of the plane wave spectrum behind a thick surface relief structure. The perturbation operator H' is

$$H'(x,y,z) = \begin{cases} k_0^2(n^2-1); & 0 \le z \le h(x,y) \\ 0; & \text{otherwise} \end{cases} \tag{6}$$

where h(x,y) is the local thickness of the element. Neglecting the bias in the zero order diffraction amplitude and assuming the incident beam propagating on-axis the plane wave spectrum behind the element is

$$a(\nu,\mu) = \frac{k_0^2(n^2-1)}{2(2\pi)^2}\int_{-\infty}^{\infty}\int_{-\infty}^{\infty}\frac{\exp\left[-i2\pi(\beta-\beta_0)h(x,y)\right]}{\beta(\beta-\beta_0)}\exp\left[-i2\pi(\nu x+\mu y)\right]dxdy \tag{7}$$

This result was already obtained in the framework of the first Born approximation to extend the thin element approximation[3]. Eq. (7) can be also used as a starting point to derive the thin element expression[3].

B. Absorbing screens and Babinet's principle

A thick absorbing screen can be considered by a complex refractive index distribution in Eq. (6). As an illustrating example, which provides insight into the structure of the perturbation operator for absorbing screens we derive the expression for a thin transparency. For small diffraction angles the propagation constant β can be treated as a constant. For a transmittance t(x,y) and a perturbation operator

$$H'(x,y,z) = -i4\pi\beta\left[1-t(x,y)\right]\delta(z) \tag{8}$$

Eq. (5) yields the plane wave spectrum of t(x,y). H'(x,y,z) basically is the inverse of the transmission function which is defined zero for opaque areas and one for openings. Thus, the relation between the transmission function and the perturbation operator is ruled by Babinet's effect[1,8]. The term for the incident wave, i.e. the delta function in Eq. (5), then compensates for the additional zero order contribution caused by an inverse screen.

C. Pseudo-deep holograms and planar-integrated micro-optics

The perturbation approach can also be applied to a class of problems where the diffractive element is basically thin, but tilted by an angle α with respect to the optical axis. One application are so-called pseudo-deep holograms[9,10]. Neglecting constant factors the perturbation operator for a pseudo-deep hologram reads

$$H'(x,y,z) = \left[t(x,y)-1\right]\delta(y-z/\tan\alpha) \tag{9}$$

i.e. a thin transparency is rotated in the y-z plane. For a pseudo-deep hologram the Fraunhofer diffraction pattern at $\mu = 0$ is considered as output. With the help of Eq. (5) we obtain

$$a(\nu,0) = \iint t(x,z/\tan\alpha)\exp\left[-i2\pi(\beta z+\nu x)\right]dx\,dz \tag{10}$$

Eq. (10) describes the reconstruction of a pseudo-deep hologram, where t(x,y) again is the transmission function. It illustrates how the diffraction amplitude for μ=0 depends on the two dimensional transparency and refers to the response of a volume hologram in one lateral dimension[10].

Optical elements which are rotated with respect to the optical axis play an important role in planar-integrated free-space optics[11]. The perturbation approach provides the straightforward possibility to extend Eqs. (9) and (10) to tilted elements which are thin compared to their lateral extension, though their optical thickness cannot be neglected. For planar optics an improved description of the optical elements is obtained and hence a more accurate design.

4. Conclusion

We presented a perturbation description of problems in scalar diffraction theory. This approach was developed analogous to the time-dependent perturbation theory of quantum mechanics. It is aimed to extend Kirchhoff's approximation to include thick diffractive optical elements. We calculated various diffraction problems including the plane wave spectrum behind thick diffraction screens. This illustrates, that the perturbation approach allows an unified description of these problems. The transition amplitudes in the plane wave spectrum are obtained as the three dimensional Fourier transformation of the element. Thus, this extension of Kirchhoff's theory can be used without sacrificing the simplicity of Fourier optics.

The application which were discussed are only a small selection of problems which can be treated within this framework. In addition, the perturbation approach can provide links to alternative extensions of the Kirchhoff approximation[12] or might be useful for numerical simulations. Though we only discussed objects in free space, perturbation theory is well suited to calculate diffraction in laterally modulated media. For planar-integrated micro-optics, the idea of embedding free-space optics into a modulated medium was proposed recently[13].

References

1. J. D. Jackson, *Classical Electrodynamics*, John Wiley and Sons, New York 1975, chapters 7-9.
2. J. Goodman, *Introduction to Fourier Optics*, McGraw Hill, New York 1968.
3. W. Singer, K.-H. Brenner, J. Opt. Soc. Am. A **12**, 1913-1919 (1995).
4. H. Kogelnik, Bell Syst. Tech. J. **48**, 2909-2947 (1969).
5. D. Marcuse, *Theory of dielectric optical waveguides*, Academic Press, New York 1974, chapter 3.
6. A. Messiah, *Quantum mechanics*, Vol. 2, North-Holland Pub. Co., Amsterdam 1962, chapters 17 and 19.
7. D. Gabor, G. W. Stroke, Proc. Royal Soc. of London, A **304**, 275-289 (1968).
8. A. Lohmann, *Optical Information processing*, Erlangen 1986, chapters 16 and 22.
9. Y. N. Denisyuk, N. M. Ganzherli, Opt. Eng. 31, 731-738 (1992).
10. A. W. Lohmann, V. Arrizón, J. Mod. Opt., 43, 2381-2402 (1996).
11. J. Jahns, A. Huang, Appl. Opt. **28**, 1602-1605 (1989).
12. G. Swanson, MIT Technical Report **914** (1991).
13. S. H. Song, E.-H. Lee, U. Jung, K. H. Lee, M. Cho, OSA Annual Meeting 1997, Conference Program, WS8.

Diffractive Optics and Micro-Optics

Subwavelength Strucutres 1

Monday, June 8, 1998

Joseph N. Mait, U.S. Army Research Laboratory
Presider

DMB
10:30am–12:00m
Koa Room

Applications of Guided-mode resonant filters to VCSELs

Robert A. Morgan, J. Allen Cox, Robert Wilke, and Carol Ford
Honeywell Technology Center, 12001 State Highway 55, Plymouth, MN 55441

Within the last 2 years Vertical Cavity Surface Emitting Lasers (VCSELs) have emerged from the research laboratory into the commercial marketplace as the component of choice for numerous applications, supplanting both LED and edge-emitting sources. The enormous success of VCSELs is attributed, in part, to their premium performance, producibility, and packaging perks. Namely, significantly lower operating currents and power dissipation at Gb/s data rates; wafer-level batch fabrication, testing, and utilization of the existing LED and III-V manufacturing infrastructure; more efficient coupling into fibers and simplified drive electronics.[1] These attributes result directly from the laser's inherent vertical geometry. This vertical cavity is essentially a zero-order thin-film Fabry-Perot transmission filter, utilizing integral quarter-wave high-reflectance (> 99%) interference stacks referred to as distributed Bragg reflectors (DBRs). On a parallel front, it has recently been suggested that high reflectivity possible from guided-mode grating resonant filters (GMGRFs)[2-4] may likewise serve to construct the high-Finesse vertical cavity, requiring minimal layers. These "resonant reflectors" may be designed to provide ultra-narrow bandwidth filters for a selected center wavelength and polarization with ≅100% in-band reflectance and ~30dB sideband suppression. These are very attractive properties for VCSELs and offer the potential as an enabling tool for modal engineering.

Much of the complexity of commercial-grade VCSELs lies in their epitaxial structure. Over 200 AlGaAs hetero-layers, in excess of 7 μm thick, are required to construct the vertical cavity. To obtain the low threshold currents (1-5mA), these VCSELs utilize small-volume, high-Finesse cavities. To obtain lasing from thin, ≅100-Å thick, active regions (typically 1 - 3 quantum wells) very high reflectivity (> 99%) DBRs are needed. This necessitates >20 quarter-wave periods, >2.5μm thick. The gain-guided area is defined by proton bombardment through the top DBR. Annular metal contacts are utilized to enable current injection concomitant with light transmission.[1] The resulting planar structure is limited to diameters in excess of 10μm (20μm typical) due in part to the lateral straggle effects of proton implantation (roughly equal to the depth). These VCSELs operate in a single (dual polarization) longitudinal mode determined from the Fabry-Perot resonance, but are inherently multi-transverse mode (diameter >> λ). Although this characteristic is employed to circumvent modal noise in multi-mode fiber data links, many applications require a well-behaved modal and linear polarization mode.

Research-grade VCSELs, utilizing dielectric-apertures formed by selective oxidation of buried high Aluminum-containing AlGaAs layer(s)[5] have enabled an order of magnitude reduction in the VCSEL diameter, concomitant with a similar reduction in threshold current. These 0.1-mA threshold current VCSELs are especially encouraging for multi-element VCSEL array applications. However, state-of-the-art commercial- and research-grade VCSELs both require several microns of epi-structure growth whose optical thickness predominantly determines the emission wavelength. Furthermore, reproducibly well-controlled single polarization and transverse mode operation remains elusive. The unique reflectance characteristics of the recently discovered guided-mode resonances in dielectric waveguide gratings, as detailed in [2] and [3], offer a potential solution to

these impasses. This resonance is achieved by matching a first-order evanescent ($\lambda/n > \Lambda$) grating wavevector to a propagating waveguide mode. Since the latter depends on polarization, the reflectance is inherently polarization-selective. The resonant wavelength is determined primarily by the grating period and the bandwidth primarily by the modulation of grating refractive index. Note that the lithographically-defined wavelength/polarization control may be readily exploited for wavelength/polarization division multiplexed arrays. Furthermore, this exceptional performance is obtained in a very thin structure, typically ~ 300 nm.

In [4], a peak reflectivity ≅90% at 633nm was demonstrated in a GMGRF fabricated holographically. Here we report similar reflectivities in GMGRFs fabricated by direct-write electron-beam lithography and dry etching. The resonant wavelength was designed to be ≅850 nm, amenable to VCSEL applications. A three-film multilayer waveguide design, depicted in Figure (1a), was used to facilitate imposing both the resonance condition and the out-of-band antireflection condition.[2] The reflectance given in Figure (1a) was simulated using a rigorous Maxwell solver code (MAXFELM). The back surface of the fused quartz substrate was coated with a standard broadband AR coating to minimize Fresnel reflection. The top film is sputtered SiO2 films 2 and 3 are sputtered blended oxides. The design assumed E|| polarization; i.e., the electric field vector is parallel to the grating lines. A detailed design sensitivity analysis determined wavelength tuning with incident angle ~7 nm/deg. 2-mm square gratings with a nominal 480nm pitch were fabricated in the top film of the 3-layer waveguide stack to create a resonant structure. The measured film indices were: film 1 - 1.49; film 2 - 2.106; and film 3 - 2.016.

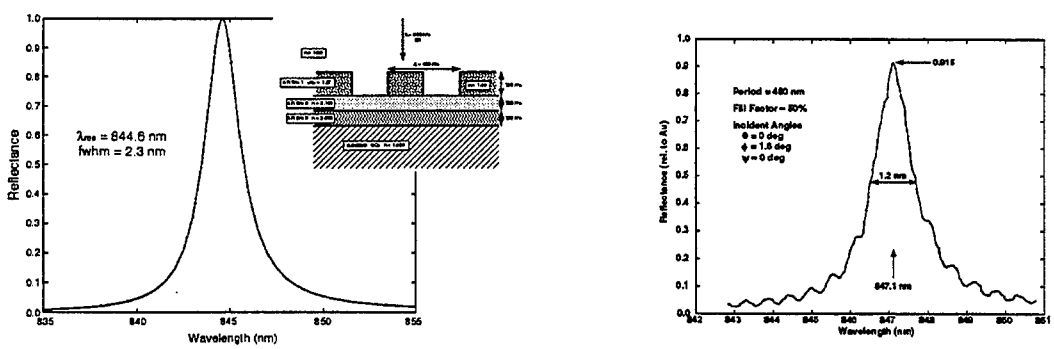

Figure (1a) Design and simulated reflectivity. (1b) Measured reflectivity at normal incidence.

The experimental reflectance measured relative to a gold mirror reference is given in Figure (1b). The wavevector of the incident light lay in a plane normal to the surface of the substrate and parallel to the grating lines ($\theta = 0$). The wavevector was inclined ϕ~1.6 deg in this plane relative to the surface normal in order to direct the beam onto a detector. The peak reflectance of ~90% is achieved when $\psi = 0$ (Fig. 1b). An ≅10% scatter loss is attributed to grating-line roughness which was observed in SEM photos. To vary the angle ψ between the polarization vector and the grating lines, the substrate was rotated about the incident wavevector. The GMGRF reflectance for $\psi = 15^0$ is given in Figure 2. As anticipated, increasing ψ suppresses the reflectance of the TE resonant wavelength and a TM resonance emerges.

In order to integrate a GMGRF into a VCSEL, several significant technical challenges must be overcome. Primary among these is the degrading effect of absorption and scatter on the resonant reflectivity. This is illustrated by the simulation in Figure 3. Here reflectance curves

were calculated assuming two values (0 and 10^{-5}) for the imaginary component of the refractive index in all three layers of the waveguide-grating structure. In the resonant grating structure, ≅5% absorption is evident, two orders of magnitude higher than for the absorption (0.05%) in the same three AR layers sans grating. Since $k=10^{-5}$ corresponds to a minimal conductivity required to inject current through the mirror into the active region, this result demonstrates that the GMGRF cannot serve as the solitary feedback mirror for electrically injected VCSELs.

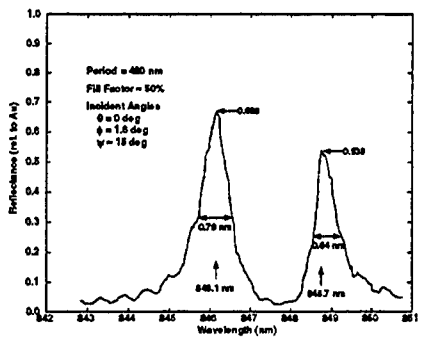

Figure 2 Measured reflectance for ψ = 15⁰.

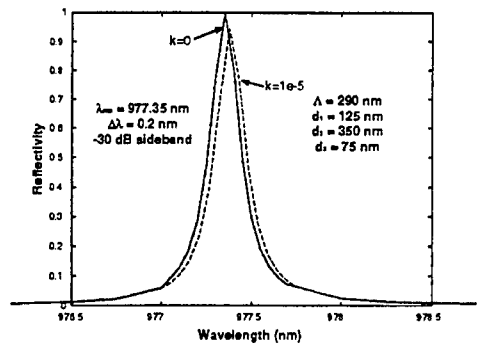

Figure 3 Effect of absorption in a GMGRF.

As is common with most resonance phenomena, guided-mode grating resonant filters exhibit not only extraordinary ideal performance attributes, but suffer from high sensitivity to loss mechanisms such as scatter and absorption. The latter tempers realistic expectations for the practical application of a GMGRF structure to electrically-injected VCSELs, particularly in terms of surrogating the semiconductor DBR stack. In practice, unavoidable losses from both scatter and absorption are encountered: the former from imperfections introduced during grating fabrication, and the latter from the conductivity required for through mirror electrical injection.. With this in mind, we propose to reduce the sensitivity to loss with a hybrid approach consisting of a resonant reflector structure with ~ 5 periods of a conventional semiconductor DBR similar to the hybrid - dielectric/semiconductor BBR approach described in reference [6].

There are several other issues that are expected to challenge the integration of GMGRFs with VCSELs. The high refractive index of III-V materials leads to small grating periods; e.g., a resonance λ= 850 nm requires a 480 nm period in fused quartz, which is reduced to a period of 250 nm for GaAs. This high resolution further compounds the fabrication difficulty. Direct-write, electron-beam lithography does not scale up easily to large volume manufacturing.. Phase mask lithography could represent a viable alternative, but it is relatively new and untested. A thermal stress mismatch between the dielectric and III-V materials also poses a reliability concern.

1. R.A. Morgan, et.al., in SPIE Vol. 2683-04 (SPIE, Bellingham, WA, 1996).
2. S.S. Wang and R. Magnusson, Appl. Opt. 32 (14), 2606-13 (1993).
3. S.S. Wang and R. Magnusson, Appl. Opt. 34 (14), 2414-20 (1995).
4. S. Peng and G.M. Morris, OSA Technical Digest Series (OSA, Washington DC, 1996), p. 257.
5. K.L. Lear, et. al., Elec. Lett., Vol. 31, pp. 208-209 (1995).
6. R. A. Morgan, et. al, Appl. Phys. Lett, Vol. 66, pp. 1157-1159 (1995).

Guided-mode resonant filters incorporating the Brewster effect

R. Magnusson, D. Shin, and Z. S. Liu

Department of Electrical Engineering, The University of Texas at Arlington, Arlington, Texas 76019
Phone : (817) 272-3474, Fax : (817) 272-2253, Email : magnusson@uta.edu

Guided-mode resonance (GMR) effects are observed in dielectric and semiconductor thin-film structures comprising diffractive and waveguide layers[1,2]. High-efficiency resonances are realizable under zero-order conditions imposed by a diffractive element with suitably high spatial frequency such that all higher-order diffracted waves are evanescent. For parametric conditions such that one of these evanescent waves couples to a (leaky) waveguide mode, a resonance occurs with associated strong power exchange between the propagating zero-order waves. This resonance coupling effect is typically represented as spectral (with constant angle of incidence) or angular (with constant wavelength) variation of the diffraction efficiency of the transmitted and reflected waves. Theoretical and experimental studies[1-10] have illustrated the feasibility of utilizing this basic effect for numerous applications[11].

Although the Brewster effect is defined for a planar interface, Brewster-like minimum reflection is still obtainable for layered structures, in general. In this paper, we show theoretically and experimentally that if the layer is a waveguide grating, a GMR reflection filter can be realized at Brewster incidence. Thus, instead of the zero reflection expected for a TM-polarized wave at Brewster-angle incidence on a planar interface in classical optics, a high-efficiency band-limited reflection occurs. Also, a desirable filter response with a symmetrical lineshape and low-sideband reflection is shown to be obtainable using this simple antireflection (AR) strucure in addition to generally used multilayer structures[2,12,13].

Figure 1 illustrates a numerically calculated (rigorous coupled-wave analysis[14]) example of an angular resonance (width of ~0.4°) occurring at the Brewster angle of 57.88° in a single-layer, asymmetric, planar waveguide grating. It is seen that the Brewster-angle zero reflection is defeated by the GMR effect. This is because the guided-mode resonance arises on coupling of the first evanescent diffraction order to a leaky waveguide mode. Consequently, in contrast to the classical picture of a TM-polarized wave at a dielectric interface, the zeroth reflected order is reradiated efficiently in the specular direction even though the polarization vector of the incident wave in the layer is oriented along the direction of reflection. The corresponding spectral response in Fig. 2 reveals a single resonance peak associated with the TM_0 waveguide mode excited by the incident wave at Brewster incidence. Since the value of the Brewster angle for a given structure is rather insensitive to the wavelength, such a filter exhibits low-reflectance sidebands over extended wavelength regions.

To verify the predicted high TM reflection efficiency at the Brewster angle, a double-layer GMR filter is designed using a photoresist coupling grating on a HfO_2 waveguide layer deposited on a fused-silica substrate as indicated in Fig. 3. The grating is recorded holographically using a HeCd laser (λ=442 nm) with the grating period of 455 nm to produce a resonance with the incident continuous-wave Nd:YAG laser beam (λ=1064 nm) at the Brewster angle of 50.2°. The Gaussian laser beam is well collimated with ~1 mm beam diameter. The measured filter response is symmetric with a 94.2% peak reflection efficiency at $\theta = 50.2°$ and exhibits low sidebands of ~2% reflectance over a range of ~12°. Figure 3 also shows a calculated curve that has been fitted to the experimental data. The nominal values of waveguide- and photoresist film thicknesses are used but the grating period is changed from the nominal value of 455 nm to 453.2 nm to bring the theoretical and experimental peaks into coincidence. The grating is modeled as a sinusoidal surface-relief grating which yields an excellent agreement between measured and calculated resonance linewidths as shown in Fig. 3.

Figure 4(a) shows the TE polarization (i. e., no Brewster effect) reflectance of the filter described in Fig. 3. The measured resonance efficiency peak reaches 80.3% at $\theta = 39.6°$. The theoretical response is calculated for the parameter values that yielded the fit in Fig. 3, resulting in a ~0.5° deviation from the measured response. Systematic small variations of the device parameters may bring both the TM and TE data sets into agreement with theory; this is not attempted here. The small experimentally observed undulations are due to Fabry-Perot resonances originating in the substrate. The calculated curve in Fig. 4(a) corresponds to an infinitely-thick substrate whereas Fig. 4(b) shows the effect of including the substrate in the analytical model. The high (~10%) experimental sideband reflectance depicted in Fig. 4(a) is clearly due to the substrate quantitatively matching that of Fig. 4(b) on the average.

The experimental results in this paper pertain to layered GMR devices with spatially distinct coupling and waveguiding layers. At resonance, the HfO_2 film carries most of the guided-mode power with the evanescent-field tail of the mode interacting with the grating. Nevertheless, as illustrated in this paper, in spite of a lack of complete overlap of the mode and the diffractive layer, high efficiencies (>90%) can be obtained in practice. Previous research yielding comparable values of experimental resonance efficiencies[7,15] employed GMR structures where the waveguide and grating were one and the same.

1. R. Magnusson and S. S. Wang, "New principle for optical filters," *Appl. Phys. Lett.*, **61,** 1022-1024 (1992).
2. S. S. Wang and R. Magnusson, "Design of waveguide-grating filters with symmetrical line shapes and low sidebands," *Opt. Lett.* **19**, 919-921 (1994).
3. A. Hessel and A. A. Oliner, "A new theory of Wood's anomalies on optical gratings," *Appl. Opt.* **10,** 1275-1297 (1965).
4. L. Mashev and E. Popov, "Zero order anomaly of dielectric coated gratings," *Opt. Commun.* **55,** 377-380 (1985).
5. S. Zhang and T. Tamir, "Spatial modifications of Gaussian beams diffracted by reflection gratings," *J. Opt. Soc. Amer.* A **6**, 1368-1381 (1989).
6. I. A. Avrutsky and V. A. Sychugov, "Reflection of a beam of finite size from a corrugated waveguide," *J. Mod. Optics*. **36**, 1527-1539 (1989).
7. M. T. Gale, K. Knop, and R. H. Morf, "Zero-order diffractive microstructures for security applications," *Proc. SPIE on Optical Security and Anticounterfeiting Systems* **1210**, 83-89 (1990).
8. S. Peng and G. M. Morris, "Experimental demonstration of resonant anomalies in diffraction from two-dimensional gratings," *Opt. Lett.* **21**, 549-551 (1996).
9. A. Sharon, D. Rosenblatt, A. A. Friesem, H. G. Weber, H. Engel, and R. Steingrueber, "Light modulation with resonant grating-waveguide structures," *Opt. Lett.* **21**, 1564-1566 (1996).
10. S. Tibuleac and R. Magnusson, "Diffractive narrow-band transmission filters based on guided-mode resonance effects in thin-film multilayers," *IEEE Photonics Tech. Lett.*, **9**, 464-466 (1997).
11. S. S. Wang and R. Magnusson, "Theory and applications of guided-mode resonance filters," *Appl.Opt.* **32**, 2606-2613 (1993).
12. S. S. Wang and R. Magnusson, "Multilayer waveguide-grating filters," *Appl. Opt.* **34**, 2414-2420 (1995).
13. D. Shin, S. Tibuleac, T. A. Maldonado, and R. Magnusson, "Thin-film multilayer optical filters containing diffractive elements and waveguides," *Proc. SPIE on Optical Thin-films V: New Developments* **3133**, 273 (1997).
14. T. K. Gaylord and M. G. Moharam, "Analysis and applications of optical diffraction by gratings," *Proc. IEEE* **73**, 894-937 (1985).
15. R. Magnusson, S. S. Wang, T. D. Black, and A. Sohn, "Resonance properties of dielectric waveguide gratings: Theory and experiments at 4-18 GHz," *IEEE Trans. Antennas Propagat.* **42**, 567-569 (1994).

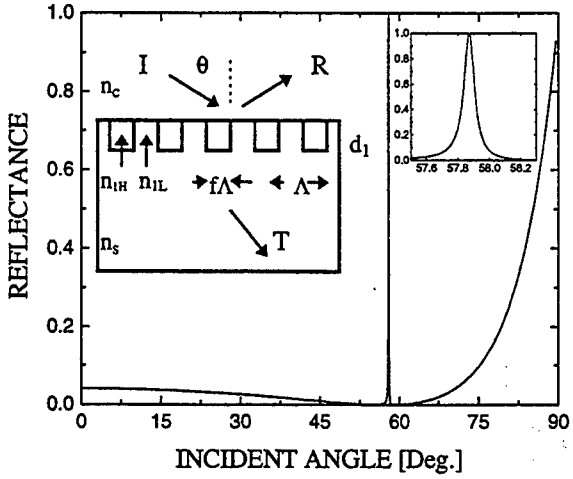

Fig. 1. Angular response of a single-layer guided-mode resonance filter for a TM polarized incident wave with 632.8 nm wavelength. The parameters are n_c=1.0, n_s=n_{1L}=1.52, n_{1H}=2.0, f=0.5, d_1=178.1 nm, and Λ=266.2 nm.

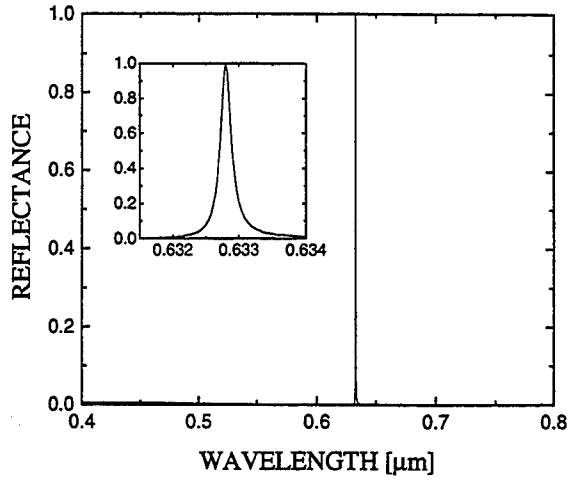

Fig. 2. Spectral response of the single-layer filter given in Fig. 1 for a TM polarized wave incident at an angle of θ=57.88°.

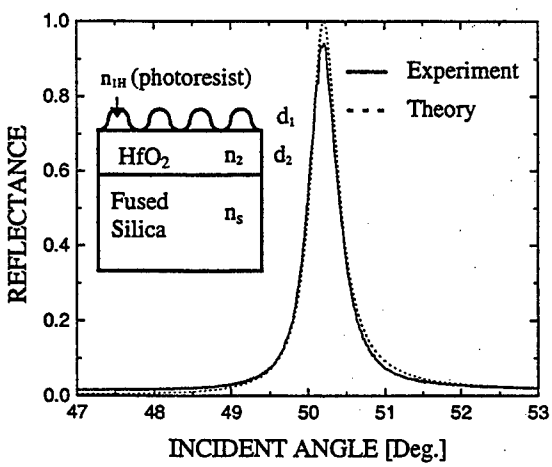

Fig. 3. Comparison of the experimentally measured and theoretically calculated angular response of a double-layer guided-mode resonance filter for a TM polarized incident wave. The parameters used to fit the measured reflectance curve are n_c=n_{1L}=1.0, n_{1H}=1.63, n_2=1.97, n_s=1.45, d_1=175 nm, d_2=260 nm, Λ=453.2 nm.

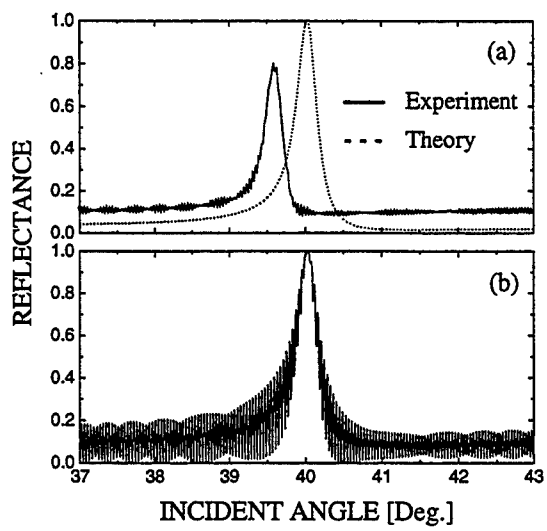

Fig. 4. (a) Comparison of the experimentally measured and theoretically calculated angular response of a double-layer guided-mode resonance filter for a TE polarized incident wave. The parameters are the same as in Fig. 3. (b) Angular response of the same filter including the substrate with thickness 2015 μm.

Guided-mode resonance filters generated with genetic algorithms

S. Tibuleac, D. Shin, and R. Magnusson
Department of Electrical Engineering,
The University of Texas at Arlington,
Arlington, Texas 76019

C. Zuffada
Jet Propulsion Laboratory
California Institute of Technology
Pasadena, California 91109

This paper focuses on the application of genetic algorithms to the study and design of reflection and transmission filters based on the guided-mode resonance (GMR) effect in waveguide gratings.[1-3] As genetic algorithms are well suited for problems with multidimensional, large search spaces[4], they may be used effectively for optical filter design involving multiple periodic and homogeneous layers. In this work, the genetic algorithm library PGAPACK[5] is combined with a forward code based on rigorous coupled-wave analysis[6] in a new computer program that optimizes the merit function of a multilayer diffractive optical structure. Thus, a GMR-filter response with a given central wavelength, linewidth and sideband levels can be specified with a corresponding diffractive structure yielding approximately the specified response provided by the program. The net effect of this approach is that the inverse problem of finding a structure (i. e., layer thicknesses, refractive indices, fill factors, grating period) that yields a given filter response can be solved. In addition to providing useful filter designs, this approach may aid in the discovery of diffractive structures with profiles that may differ significantly from those ordinarily treated.

Current knowledge about the guided-mode resonance effects provides guidelines in the search for a desired filter structure by utilizing thin-film interference and waveguide concepts to find approximate filter characteristics.[1-3] However, practical design of guided-mode resonance filters remains an iterative process where the physical parameters of the diffractive structure are determined by repeatedly solving coupled differential equations with different waveguide-grating parameters until the desired filter characteristics (center wavelength, linewidth, sideband level, filter range and lineshape) are obtained. The ability of genetic algorithms to perform a parallel search in a parameter space and find the global minimum of a merit function in an effective and efficient manner makes it an attractive optimization tool for design of guided-mode resonance filters. Johnson and Abushagur[7] demonstrated the ability of a microgenetic algorithm to find a guided-mode reflectance resonance at a given wavelength by optimizing a dual-surface corrugated grating. The results of the optimization indicate a response with a 100% resonance at the desired wavelength but also other adjacent peaks, asymmetrical sidebands with high reflectance.[7] In the microwave spectral region, a genetic algorithm optimization routine utilizing method of moments for electromagnetic field calculations for design of guided-mode resonance transmission filters was reported by Zuffada et al.[8] and Tibuleac et al.[9] Optimization of the refractive indices, thickness and fill factor of a binary grating in a continuous parameter space yielded a high-efficiency transmission filter peaking at 6.65 GHz in the range 6.25 - 7.14 GHz[9].

In this paper, optical reflection and transmission filters are obtained by optimizing the grating period, the thicknesses, fill factors, phase shifts and refractive indices of a multilayer structure to minimize the difference between the reflection or transmission reference data specified by the user and the response of the structure generated by the genetic algorithm. The refractive indices are selected from a set of discrete values while the geometrical parameters are searched in continuous ranges defined by the user. To test the performance of the optimization algorithm a set of 50 unequally distributed reflectance points are selected from a known reflection filter response and used as input reference data for the genetic algorithm. The thickness is allowed to vary in the range 50-350 nm, while the fill factor is searched in the range 0.1 - 0.9. The refractive indices are selected from a set of 13 values ranging from 1.3 - 2.5 in increments of 0.1. The grating period, incident angle, cover and substrate refractive indices are fixed. Figure 1 illustrates the response of the single-layer waveguide grating generated by the genetic algorithm and the reference data. The program found the same refractive indices as the structure used to generate the reference data, the thickness to within 0.15 % and the fill factor deviating by 9.5 %. The deviations arise mostly in the resonance region which is explained by the high sensitivity of the peak location and linewidth to slight changes in layer thickness and fill factor. Using the same reference data as in the example of Fig. 1 but different genetic algorithm input parameters, two other solutions are found consisting of single-layer gratings with the same grating period, incident angle, and substrate and cover refractive indices. One solution has high and low refractive indices $n_H = 2.5$, $n_L = 2.4$, thickness $d = 221.1$ nm, and fill factor $f = 0.369$, while the other has the grating parameters: $n_H = 2.0$, $n_L = 1.6$, $d = 278.5$ nm, $f = 0.811$. The generation of several alternative solutions is important in practical applications where material and technological constraints may exclude the fabrication of some design solutions. Guided-mode resonance transmission filters in the visible spectral region can also be designed with the genetic algorithm optimization. A preliminary result of a double-layer transmission filter design with center wavelength of 550 nm, ~ 70 % efficiency, and 0.65 nm linewidth is shown in Fig. 2. The solution is found in the physical parameter space defined by the following ranges for grating period 270 nm $< \Lambda <$ 330 nm, thickness 100 nm $< d <$ 500 nm, and fill factor $0.1 < f < 0.9$, and using the same set of refractive index values as in the reflection filter examples. The genetic algorithm program developed is versatile and can be applied for design of other multilayer structures with homogeneous and grating layers such as fan-out gratings, anti-reflection coatings, high-reflectors, polarizing elements, beam-splitters, and edge filters.

1. S. S. Wang and R. Magnusson, "Design of waveguide-grating filters with symmetrical line shapes and low sidebands," Opt. Lett. **19**, 919-921 (1994).
2. S. S. Wang and R. Magnusson, "Multilayer waveguide-grating filters," Appl. Opt. **34**, 2414-2420 (1995).
3. S. Tibuleac and R. Magnusson, "Diffractive narrow-band transmission filters based on guided-mode resonance effects in thin-film multilayers," IEEE Phot. Tech. Lett **9**, 464-466, (1997).
4. D. Goldberg, *Genetic Algorithms in Search, Optimization, and Machine Learning*, Addison-Wesley, Reading, Mass., 1989.
5. D. Levine, "Users guide to the PGAPack parallel genetic algorithm library," *Argonne National Laboratory* - 95/18, January 1996.

6. T. K. Gaylord and M. G. Moharam, "Analysis and applications of optical diffraction by gratings," Proc. IEEE **73**, 894-937 (1985).
7. E. G. Johnson and M. A. G. Abushagur, "Microgenetic-algorithm optimization methods applied to dielectric gratings," J. Opt. Soc. Am. A **12**, 1152-1160 (1995).
8. C. Zuffada, T. Cwik and C. Ditchman, " Synthesis of novel all-dielectric grating filters using genetic algorithms," IEEE Antennas and Propagation Society International Symposium, Montreal, Canada, July 1997, Conference Proceedings **3**, 1676-1679 (1997).
9. S. Tibuleac, R. Magnusson, T. A. Maldonado, D. Shin, and C. Zuffada, "Direct and inverse techniques of guided-mode resonance filters designs," IEEE Antennas and Propagation Society International Symposium, Montreal, Canada, July 1997, Conference Proceedings **4**, 2380-2383 (1997).

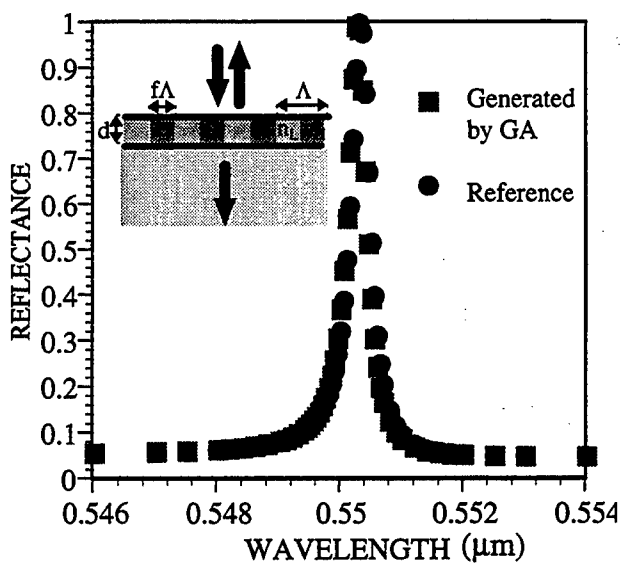

Fig. 1. Reflectance of a guided-mode resonance filter generated by the genetic algorithm and reference reflectance. The parameters of the grating used to generate the reference reflectance are: $n_H = 2.1$, $n_L = 2.0$, $d = 134$ nm, $f = 0.5$. The parameters of the grating generated by the genetic algorithm are: $n_H = 2.1$, $n_L = 2.0$, $d = 133.8$ nm, $f = 0.547$.

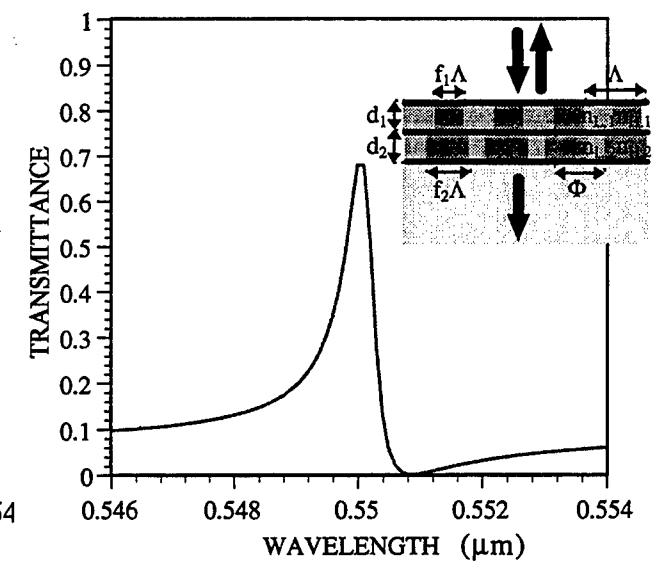

Fig. 2. Transmission filter in the optical spectral region generated by genetic algorithm optimization of 2 grating layers. The parameters of the structure are: $\Lambda = 326.5$ nm, $n_{H,1} = 2.5$, $n_{L,1} = 1.9$, $d_1 = 191.6$ nm, $f_1 = 0.373$, $n_{H,2} = 2.4$, $n_{L,2} = 1.5$, $d_2 = 203.3$ nm, $f_2 = 0.408$, $\Phi = 158°$.

Study of the resonant behavior of waveguide-gratings

Increasing the angular tolerance of guided-mode filters

F. Lemarchand, A. Sentenac and H. Giovannini

Laboratoire d'Optique des Surfaces et des Couches Minces, Ecole Nationale Supérieure de Physique de Marseille, Université de St Jérôme, 13 397 Marseille.

E-mail : anne.sentenac@enspm.u-3mrs.fr, *Tel : (33) 4 91 28 87 14, Fax : (33) 4 91 28 80 67*

Studies of anomalies of the reflection and transmission curves of waveguide-gratings have demonstrated unique filtering capabilities of these structures. Vincent and Nevière [1] showed that the excitation of a leaky mode in the system can lead to 100% reflectance at a given wavelength under certain condition of symmetry. A comparative study of guided-mode resonance filters with classical multilayers design shows that the latter requires considerably more layers to yield equivalent narrow-band linewidths [2]. However, contrary to thin-films filters, waveguide-gratings are very sensitive to the angle of the incident wave. Hence, the narrow-band filter suffers significant reduction in the peak reflectance, even if the incident optical beam is wide [3].

In this work, we study the resonant behavior of wave-guide gratings by focusing on the dispersion relations of the guided modes in the homogenized structure and the changes induced by the periodic perturbation. We plot in Fig. (1) the dispersion curves of an unperturbed structure supporting only one TE mode. The guided-mode expression, written in a form adapted to a periodic problem with period d,

$$E(x,y) = \exp(ikx)f(x,y) \text{ where } f(x+d,y) = f(x,y) = \sum f_n(y)\exp(inKx) \text{ with } K=2\pi/d, \quad (1)$$

is solution of the homogeneous equation

$$\Delta E+\varepsilon(x,y)(\omega/c)^2E = 0 \text{ with } \varepsilon(x+d,y) = \varepsilon(x,y). \quad (2)$$

When both forward and backward guided modes are excited by the grating (at the intersection of the solid curves in Fig. 1), stop-bands are produced that flatten the dispersion curves (dash lines in Fig. 1). The angular tolerance of the system is thus expected to increase in these regions [4]. Note that the dispersion curves, drawn schematically in Fig. 1, are obtained by taking k real in Eq. (1) and searching ω complex that satisfies Eq. (2). This technique permits to delimit

clearly the forbidden frequency gaps, [1]. Unfortunately, the interaction between the two branches at the second order stop-band ω_2, (which corresponds to the usual configuration of filtering at normal incidence) is negligeable and the curves are not modified [5].

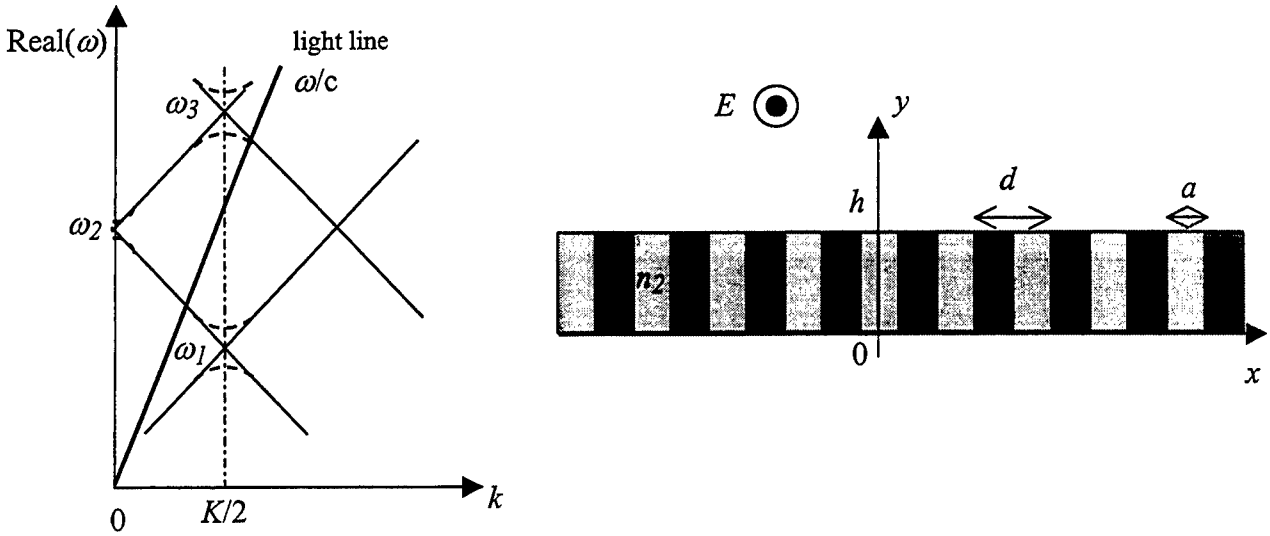

Fig. 1 (solid line) Dispersion curves of the homogenized structure
(dash lines) Changes induced by the periodic modulation of the dielectric constant

It is preferable to use the system near the first or third order stop-band. In the latter case, the wave vector of the incident wave is taken equal to $K/2$ (-1 Littrow mounting) and two reflected and transmitted orders are diffracted [4]. To get only one diffracted mode, we focus on the first order stop-band. This portion of dispersion curve lies outside the light lines and so cannot couple to photon even after scattering by the grating. Following [5] we introduce another periodic perturbation with a longer period $d'=2d$ on the top of the modulated waveguide. In terms of dispersion relation, this new periodicity amounts to translate and duplicate the curves of Fig. 1 by the factor $K'=K/2=2\pi/d'$.

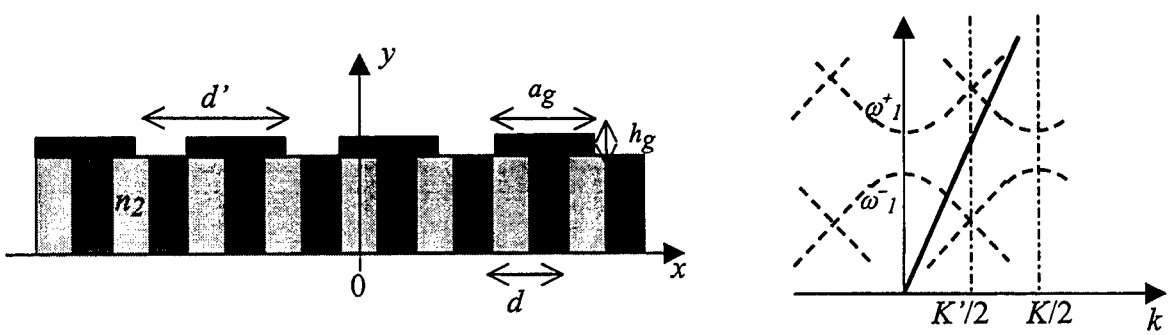

Fig. 2 : the double grating structure and the dispersion curves

Note that the double grating structure is neither symmetrical nor antisymmetrical so that both the lower and upper branches can be excited under normal incidence [1]. The height h_g, the dielectric constant ε_g and the width a_g of the top grating of period d' act on the coupling (and leaking) of the mode, i. e. the bandwidth of the filter. The dielectric contrast of the modulated waveguide acts on the gap width (ω^+_1, ω^-_1). In Fig. 3a we plot the reflectivity versus the wavelength of the structure depicted in Fig. 2 illuminated under normal incidence. Two anomalies appear on both sides of the resonant wavelength of the homogenized system ($\lambda_1 = 1$ with these parameters). In Fig. 3b, the reflectivity is plotted versus the angle of incidence at the resonant frequency ω^-_1. The angular tolerance of the double grating is 6 times greater than that obtained with a single-modulation waveguide filter (Fig. 1) having an equivalent frequency linewidth.

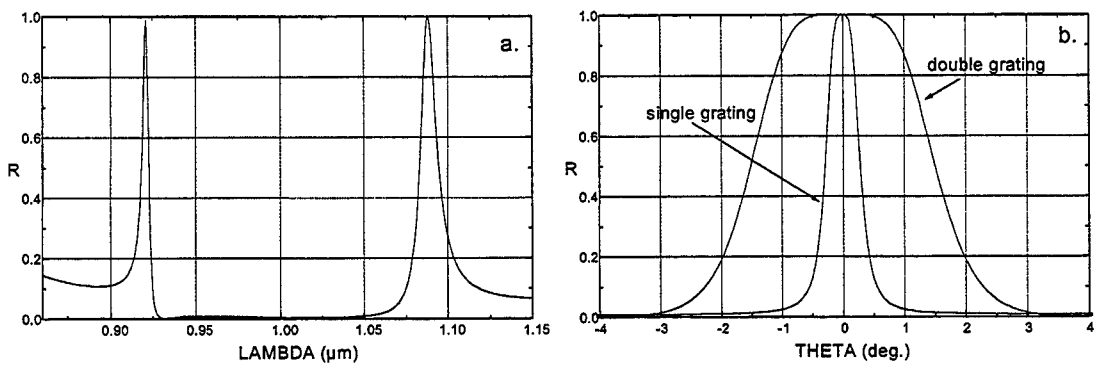

Fig. 3 Reflectivity of the double grating depicted in Fig. 2

Bottom grating $\varepsilon_1=1.5$, $\varepsilon_2=3$, $h=0.309$, $d=0.3935$, $a=d/2$. Top grating : $\varepsilon_g=2$, $h_g=0.041$, $d'=0.787$, $a_g=d'/2$

Single grating with equivalent frequency bandwidth : $\varepsilon_1=2$, $\varepsilon_2=2.5$, $d=0.787$, $a=d/2$, $h=0.309$

Until now, we have studied a problem invariant along the z axis. However, the incident beam is three-dimensional and the conical angular tolerance has to be checked. The use of bi-periodic grating [3] should even improve this result. To this aim, study of the three-dimensional dispersion relation for both 1D and 2D gratings will be presented.

[1] P. Vincent and M. Neviere, Appl. Phys. 20, 345-351 (1979)
[2] S. Tibuleac and M. Magnusson, J. Opt. Soc. Am. A 14 1617-1626 (1997)
[3] S. Peng and G. M. Morris, J. Opt. Soc. Am. A 13 993-1005 (1996)
[4] T. Tamir and S. Zhang J. Opt. Soc. Am. A 14, 1607-1616 (1997)
[5] W. L. Barnes, T. W. Preist, S. C. Kitson and J. R. Sambles, Phys. Rev. B 54 , 6227-6244 (1996)

Subwavelength Structured Narrow-band Integrated Optical Grating Filters

Eric B. Grann[1], David E. Holcomb[1], Raymond A. Zuhr[2], and M. G. Moharam[3]
[1]Instrumentation and Controls Division, [2]Solid State Division
Oak Ridge National Laboratory, Oak Ridge, TN 37831-6004
phone: (423) 574-5679 fax: (423) 574-1249 email: granneb@ornl.gov

[3] University of Central Florida
Center for Research and Education in Optics and Lasers (CREOL)

1.0 Introduction

A unique type of narrow-band integrated optical filter is investigated based on embedding a subwavelength resonant grating structure within a planar waveguide. Current integrated narrow-band optical filters are limited by their size, density of devices that can be produced, overall performance, and ability to be actively altered for tuning and modulation purposes. In contrast, the integrated optical filters described in this work can have extremely narrow bandwidths - on the order of a few angstroms. Also, their compact size enables multiple filters to be integrated in a single high density device for signal routing or wavelength discrimination. Manipulating any of the resonant structure's parameters will tune the output response of the filter, which can be used for modulation or switching applications.

Previous work on subwavelength resonant grating structures have concentrated solely on large planar surfaces (not confined to a waveguide for an integrated optical device). A subwavelength grating structure is a zeroth order diffraction grating that can be represented by an effective uniform homogeneous material (n_{eff}).[1-3] Under particular structural configurations ($n_o < n_{eff} > n_2$), subwavelength structured surfaces exhibit a resonance anomaly which results in a strong reflection in an extremely narrow bandwidth.[4,5]

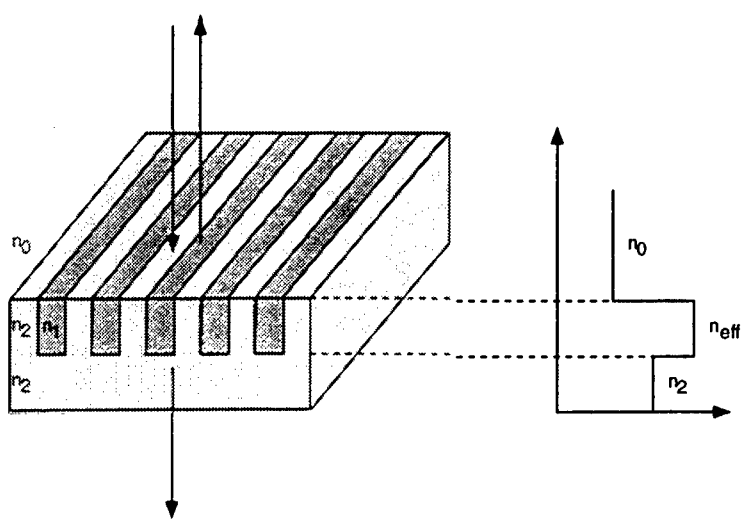

Figure 1 - Planar Surface Subwavelength Resonance Filter

This resonance phenomenon occurs when a surface propagating field is trapped within the grating region due to total internal reflection. If this trapped field is coupled into the mode of the effective waveguide, the field will resonant and redirect all of the energy backwards. This resonance effect results in a total reflection of the incident field from the surface, which is extremely sensitive to wavelength (narrow-band reflection filter).

The following example demonstrates the performance of a planar surfaced resonant grating structure. The parameters of the structure are $n_o = 1.0$, $n_1 = 1.52$, $n_2 = 1.62$, d = 1032nm, and Λ = 1017nm, where d is the thickness of the resonant region and Λ is the period of the grating. Figure 2 illustrates the response of the resonant filter. Note that the bandwidth of the filter is on the order of a few angstroms.

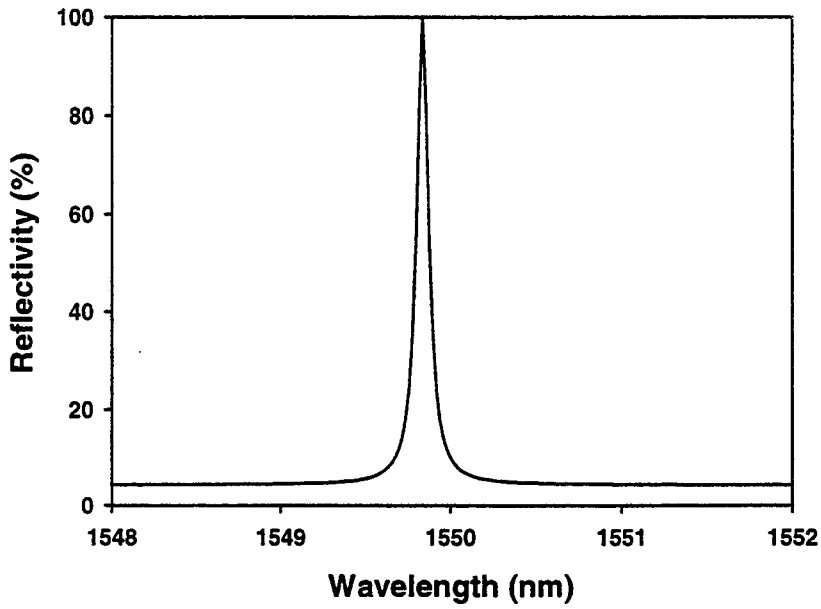

Figure 2 - Spectral response of the designed resonant filter ($\lambda_{resonance}$ = 1549.8nm)

2.0 Device Description

The device investigated is based on embedding a subwavelength resonant structure within a planar waveguide to create an integrated narrow-band optical filter. Figure 3 provides a conceptual illustration of an embedded resonant structure within a planar waveguide.

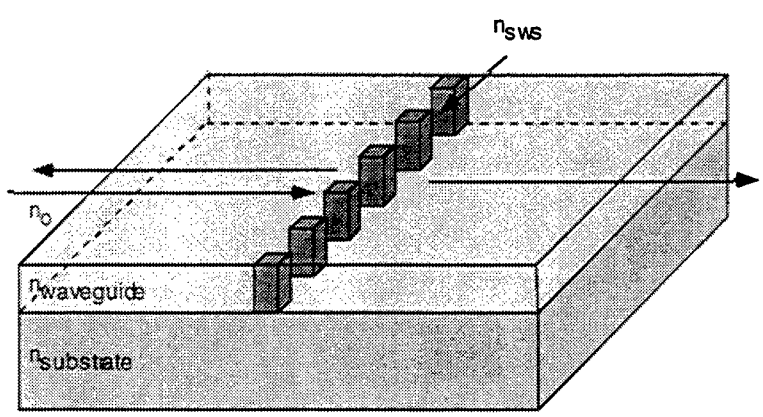

Figure 3 - Embedded Subwavelength Resonant Structure within a Planar Waveguide

In order to create a resonance effect, $n_{sws} > n_{waveguide}$, where n_{sws} is the refractive index of the subwavelength structured elements and $n_{waveguide}$ is the refractive index of the waveguide region. Also, in order to propagate the field within the planar waveguide region, $n_o < n_{waveguide} > n_{substrate}$.

Key Features:
1) Minimal sideband reflections. Since the resonant structure is buried within a waveguiding region, both the input and output regions of the resonant filter have the same material characteristics. Therefore, by designing the filter thickness to be approximately ½ wavelength thick, an incident field will experience minimal or no Fresnel reflections away from the resonance peak.

2) Spatial control: Resonant structures can be placed at a particular angle with respect to the incident field to redirect the resonant energy to another portion of the planar waveguide.

3) High Packing Density: The resonant structure is thin (~ ½ wavelength thick) and thus allows for a high packing density where multiple resonant filters are produced in a single planar waveguide device to perform a number of functions. Each filter can be designed for a particular wavelength, enabling the separation of a multi-wavelength input optical signal. Crossed resonant structures (i.e. two or more resonant structures which cross each other) can also be used with minimal cross-talk between structures.

4) Tunability: Manipulating any of the parameters of the resonant structure (angle of incidence, refractive indices, grating spacing, grating period, grating thickness) can result in a tuning of the output response.

Potential applications:
1) Wavelength division multiplexing / demultiplexing (WDM)
2) Tunable narrow-band integrated optical filter
3) Optical signal routing
4) Integrated optical modulator
5) Integrated optical switch
6) Spectroscopic analysis
7) Biological and chemical integrated optical sensors
8) Optical computing

3.0 Conclusions

A unique type of narrow-band integrated optical filter is being investigated based on embedding a subwavelength resonant grating structure within a planar waveguide. These integrated optical filters offer several advantages over existing filter technologies, and have the potential to play a significant role in future integrated optical systems. A prototype device is currently being constructed for operation near 1550nm.

---

1. S. M. Rytov, "Electromagnetic properties of a finely stratified medium," *Soviet Physics JETP*, vol. 2, pp. 466-474, 1956.
2. D. L. Brundrett, E. N. Glytsis, and T. K. Gaylord, "Homogeneous layer model for high-spatial- frequency dielectric surface-relief gratings: conical diffraction and antireflection designs," *Applied Optics*, vol. 33, No. 13, pp. 2695-2706, 1994.
3. Eric B. Grann, M. G. Moharam, and Drew A. Pommet, "Artificial uniaxial and biaxial dielectrics with use of two-dimensional subwavelength binary gratings," *Journal of the Optical Society of America*, vol. 11, No. 10, pp. 2695-2703, 1994.
4. R. Magnusson, S. S. Wang, T. D. Black, and A. Sohn, "Resonance properties of dielectric waveguide gratings: Theory and experiments at 4-18 Ghz," *IEEE Transactions on Antennas and Propagation*, vol. x, pp. xx-xx, 1994.
5. S. Peng and G. M. Morris, "Resonance phenomenon in two-dimensional-grating diffraction," 1995 Annual Meeting of the Optical Society of America, Portland, Oregon.

Diffractive Optics and Micro-Optics

Design

Monday, June 8, 1998

Daniel H. Raguin, Rochester Photonics
Presider

DMC
1:30pm–3:00pm
Koa Room

Chromatic compensation of free-space light propagation combining diffractive and refractive lenses. Achromatic Fresnel and Fourier applications.

P. Andrés and V. Climent[1]

Departamento de Óptica, Universidad de Valencia, 46100 Burjassot, Spain.
[1] *Departamento de Ciencias Experimentales, Universitat Jaume I, 12080 Castellón, Spain.*

1.- Introduction

It is well-known that the propagation of electromagnetic waves in free space is a physical phenomenon that explicitly depends on the wavelength of the light radiation. This fact results in the chromatic dispersion of the field diffracted by an aperture illuminated with a broadband source. For instance, the Fraunhofer diffraction pattern achieved at the back focal plane of a refractive objective is an example of pure lateral chromatic distortion, whereas axial and transversal chromatic blurring may occur at the Fresnel diffraction region.

In principle, the above fact severely restricts the spectral bandwidth of the light source used in a conventional diffraction-based optical setup. In other words, broadband-dipersion compensation is required, if we are interested in exploiting the whole spectral content of the incoming light [1]. The milestone of the compensation procedure lies in achieving the incoherent superposition of the monochromatic versions of a selected diffraction pattern in a single plane and with the same scale for all the wavelengths of the incident light. Achromatic diffraction systems meet the above requirement in a first-order approximation.

Needless to say that the achromatization of diffraction patterns requires strongly dispersive optical components. The chromatic compensation we propose is carried out taking advantage of the chromatic aberrations associated with diffractive optical elements, by combining diffractive and refractive lenses.

In this paper, we report on a series of new optical setups designed for chromatic-dispersion compensation of light diffraction in the Fraunhofer region and in the Fresnel region as well. These optical devices are constituted by a proper combination of a small number of conventional refractive objectives and diffractive lenses. The residual chromatic aberrations in every case are low even with white light. The unique properties shown by the above achromatic Fourier and Fresnel processors are applied, in a second stage, to develop achromatic diffraction-based applications with color inputs, like wavelength-independent spatial-frequency filtering, parallel color pattern recognition, and white-light array generators.

2.- Achromatic Fourier processors

A few years ago, we demonstrated the achromatic Fourier-transforming ability of an hybrid (diffractive-refractive) lens triplet [2], and more recently of an air-separated diffractive lens doublet [3,4]. Figure 1 shows the schematic diagram corresponding to the latter case, the all-diffractive achromatic Fourier transformer. In this case, DL_1 and DL_2 are the two diffractive lenses and the input transparency is illuminated with a broadband spherical wave front beam converging towards a point source S placed at the optical center of DL_2. The achromatic Fraunhofer diffraction pattern of the diffract-

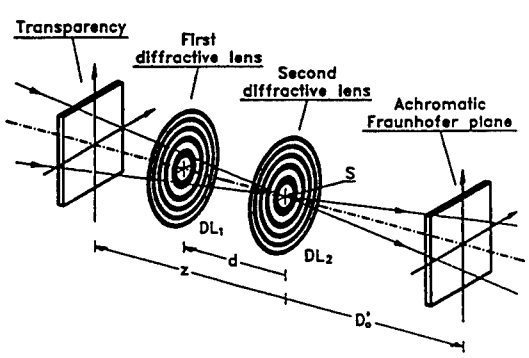

Figure 1. Scale-tunable achromatic Fourier transformer.

ing aperture is achieved when the separation d between both diffractive lenses is

$$d^2 = -Z_0 \, Z'_0 \quad , \qquad (1)$$

where Z_0 and Z'_0 denote the focal length of DL_1 and DL_2 for the reference wave number σ_0, respectively. The above achromatic diffraction field is located at a distance D'_0 from DL_2 such that

$$D'_0 = \frac{d^2}{d - 2Z_0} \quad . \qquad (2)$$

Our optical configuration shows a remarkable feature. The setup displays the achromatized version of the Fraunhofer diffraction pattern of any input transparency with adjustable scale control, i.e., the scale factor of the achromatic Fourier transform can be varied by simply shifting the input along the optical axis of the system, but at the same time the degree of achromatization is preserved.

The above practical achromatic Fourier transformer provides a Fraunhofer diffraction pattern that is achromatic in intensity, i.e., there is a square phase factor that remains chromatically noncorrected. However, by adding properly a refractive objective, L, and a third diffractive lens, DL_3, to the setup in Fig.1, the whole arrangement (see Fig.2) acts as a quasi wavelength-independent imaging configuration [5]. To this end, DL_2 and DL_3 must be conjugated through L. In mathematical terms,

$$\frac{1}{l} + \frac{1}{l'} = \frac{1}{f} \quad , \quad Z'_0 = M^2 \, Z''_0 \quad , \qquad (3)$$

where the distances l and l' are specified in Fig.2. In Eq.(3), f and Z''_0 denote the focal distance of L and DL_3 for σ_0, respectively, and $M = -l'/l$.

This novel optical Fourier processor provides an intermediate achromatic real Fraunhofer plane and a final color image without chromatic distortion. In this way, the same spatial filtering operation can be performed simultaneously, with a single filter, for all the spectral components of the broadband illuminating source.

3.- Achromatic Fresnel processors

An hybrid (diffractive-refractive) doublet [6] or a diffractive singlet [7] can provide an achromatic version of a selected Fresnel diffraction pattern. The single-diffractive-lens achromatic Fresnel transformer is illustrated in Fig.3. Here, the diffracting screen is illuminated by a broadband point source S, located at a normal distance z, and the diffractive lens, DL, is inserted at the virtual source plane. For achieving an achromatic picture of the Fresnel diffraction pattern that appears at a distance R_0 from the diffracting aperture, when it is illuminated with a monochromatic parallel beam of wave number σ_0, the following constraint must be fulfilled

$$z^2 = -Z_0 R_0 \quad , \qquad (4)$$

where Z_0 represents the focal distance of DL for σ_0. The achromatic Frensel diffraction pattern is obtained at a distance D'_0 from DL such that

$$D'_0 = \frac{z^2}{z - 2R_0} \quad . \qquad (5)$$

In contrast to other previously-reported

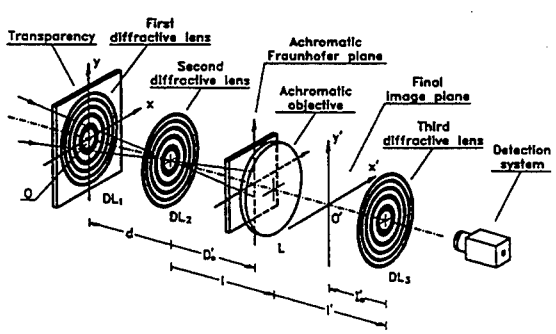

Figure 2. Achromatic Fourier processor.

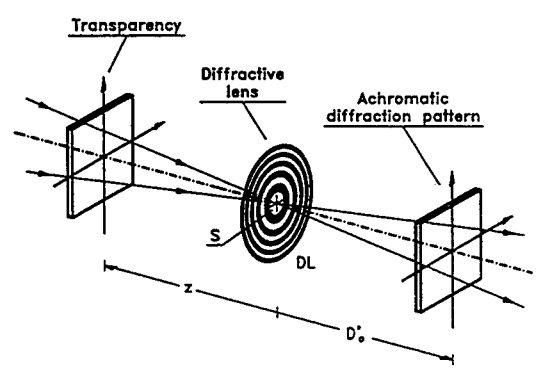

Figure 3. Achromatic Fresnel transformer.

optical setups, now the axial location of the input permits to vary, in a sequential way, the Fresnel diffraction pattern that is achromatized. In this way, by simply shifting the object along the optical axis, we record a continuous range of diffraction patterns with low residual chromatic aberrations.

4.- White-light optical applications with achromatic processors

Generally speaking, spatially coherent but temporally incoherent optical processors offer several main advantages with respect to their coherent counterparts. In particular, they allow to deal with color input signals. Next, the achromatic optical architectures described in the two previous sections are employed to present several white-light diffraction-based applications.

Specifically, the achromatic Fourier transformer in Fig.1 allowed us to obtain the Wigner distribution function of a one-dimensional real signal with white light [8]. Likewise, we have reported a white-light array illuminator based on a single diffractive lenslet array (DLA) [9]. Here, the achromatic superposition of the chromatically-dispersed arrays of monochromatic focal points produced by the DLA under parallel white-light illumination permits to achieve a regularly-spaced set of sharp light spots.

With respect to broadband spatial filtering operations, we carried out a multiple imaging experiment in which we replicate a color input by inserting a diffraction grating in the intermediate achromatic Fraunhofer plane of the optical system in Fig.2 [5]. More recently, we have implemented an achromatic VanderLugt correlator based on the same scheme. Here, a conventional monochromatic complex filter matches all the wavelengths simultaneously. In our unusual parallel multichannel detection technique, a reference pattern is recognized independently of its spectral information. In this way, the position of the color correlation peak at the output plane determines the spatial location of the detecting signal inside a color scene, whereas its chromatic content provides the chromatic composition of the target.

Instead, in the Fresnel region, we have paid attention to obtain achromatic self-images with the optical design described in Fig.3 [6,10]. In a similar fashion, the achromatic record of different fractional Talbot images generated by the focal amplitude distribution of a periodic refractive microlens array allowed us to implement a simple array illuminator with a variable density of white-light spots [11].

All the above techniques have been demonstrated experimentally with conclusive results.

The authors like to thank J. Lancis, E. Tajahuerce, M. Fernández-Alonso, and A. Pons for their direct contribution to the work reported herein.

References

[1] G.M. Morris and D.A. Zweig, in: *Optical Signal Processing*, ed. J.L. Horner (Academic Press, 1987), Ch. 1.2.

[2] P. Andrés, J. Lancis, and W.D. Furlan, Appl. Opt. **31**, 4682 (1992).

[3] J. Lancis, P. Andrés, W.D. Furlan, and A. Pons, Opt. Lett. **19**, 402 (1994).

[4] E. Tajahuerce, V. Climent, J. Lancis, M. Fernández-Alonso, and P. Andrés, Appl. Opt. (submitted).

[5] E. Tajahuerce, J. Lancis, V. Climent, and P. Andrés, Opt. Commun. (in press).

[6] P. Andrés, J. Lancis, E.E. Sicre, and E. Bonet, Opt. Commun. **104**, 39 (1993).

[7] J. Lancis, E. Tajahuerce, P. Andrés, V. Climent, and E. Tepichin, Opt. Commun. **136**, 297 (1997).

[8] J. Lancis, E.E. Sicre, E. Tajahuerce, and P. Andrés, Appl. Opt. **34**, 8209 (1995).

[9] E. Tajahuerce, P. Andrés, J. Lancis, M. Fernández-Alonso, and V. Climent, J. Mod. Opt. (submitted).

[10] J. Lancis, E.E. Sicre, A. Pons, and G. Saavedra, J. Mod. Opt. **42**, 425 (1995).

[11] E. Tajahuerce, E. Bonet, P. Andrés, and V. Climent, Appl. Opt. (submitted).

Multilevel diffraction gratings in the resonance domain: rigorous optimization by simulated annealing

Eero Noponen

Department of Engineering Physics and Mathematics,
Helsinki University of Technology, P.O.Box 2200, FIN-02015 HUT, Finland
Tel: +358 9 451 3157, Fax: +358 9 451 3164
E-mail: eero.noponen@hut.fi

1 Introduction

In the design of diffractive optical elements sophisticated optimization algorithms are required that are capable of finding the optimum structure of the element, described by a set of parameters that define, e.g., the surface profile of one grating period. For binary and multilevel profiles the parameters to be optimized include the profile depth and the positions of the steps or transition points. A wide range of methods exist that are suitable for the solution of this kind of parametric optimization problems, such as direct binary search, conjugate gradient method, steepest-descent method, iterative Fourier-transformation algorithm, simulated annealing, and genetic algorithms.

In this work we consider simulated annealing (SA) [1], which is a stochastic method that closely resembles the Metropolis algorithm used in statistical physics. In contrast to deterministic optimization methods, SA is capable of avoiding stagnation in local minima of the parameter space. SA has been used successfully to solve various optimization problems in optics, e.g., to design paraxial-domain diffractive optical elements by scalar diffraction theory [2, 3]. Recently the use of SA to design gratings with subwavelength features has also been reported [4, 5], in which case rigorous electromagnetic diffraction theory [6] has to be applied.

In this paper we apply SA to the design resonance-domain grating structures with multilevel staircase profiles containing features of the order of the wavelength of light λ. We compare the optimization performance of SA to the results of gradient method.

2 Simulated annealing algorithm

The principles of the SA algorithm are depicted in Fig. 1. During the optimization we wish to minimize the cost function E that, e.g., reflects the difference from the desired diffraction pattern. In SA the cost function is interpreted as the thermodynamic energy, and the algorithm consists of successive thermalization stages at decreasing temperatures T. First a new configuration is generated by introducing a small change to a randomly selected parameter. If the change of the cost function is negative, i.e., $\Delta E < 0$, the new configuration is always accepted. On the other hand, if $\Delta E > 0$, it is accepted with a probability $\exp(-\Delta E/T)$. This procedure is then repeated a number of times at each thermalization stage. In our calculations the number of iterations has been typically 50 to 100 times the number of parameters.

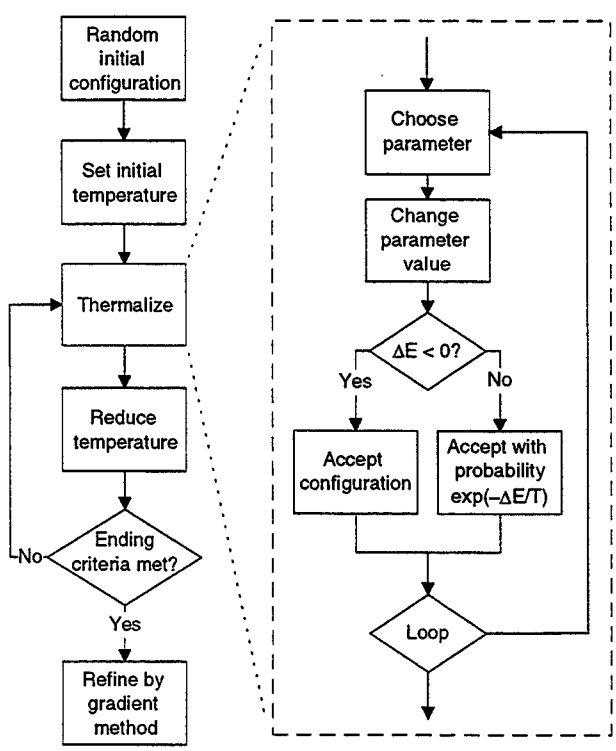

Fig. 1: Simulated annealing algorithm.

At the beginning, with a high initial value of T, nearly all configurations are accepted, but when T is decreased the algorithm begins to seek its way towards a minimum of the cost function. The SA algorithm is terminated when E has been improved less than 1% during the previous 3 to 5 thermalization stages. After that the optimization result has still to be refined, which could be done by direct search by setting $T = 0$, but we have found this method too inefficient. Instead we use the gradient method (steepest descent method), which propagates "downhill" towards the exact minimum of the cost function.

3 Optimization of staircase gratings

To evaluate the power of the SA algorithm, we apply it to the design of multilevel staircase-like grating structures that are supposed to diffract all of the incident light into the first diffraction order. In a previous work we have optimized staircase gratings using gradient method [7], and the method is used also here for comparison. For a grating structure with period 2.5λ consisting of slabs with equal depths, we optimized the transition point inside each slab to maximize the first-order diffraction efficiency by rigorous Fourier-expansion eigenmode method [8]. We assumed TE-polarized illumination normally incident from glass ($n = 1.5$) to air. The resulting optimal grating structures are shown in Fig. 2 for profiles with 4, 8, and 16 evenly spaced surface levels. The profile depths are 1.5λ, 1.75λ, and 1.875λ, respectively. The diffraction efficiencies are 79.5%, 86.1%, 87.9%, and 87.1%, where the last two values correspond to the two slightly different 16-level profiles denoted by A and B in Fig. 2. Note that the optimal profiles for the 8-level and 16-level cases actually have only 5 and 7 separate surface levels, respectively.

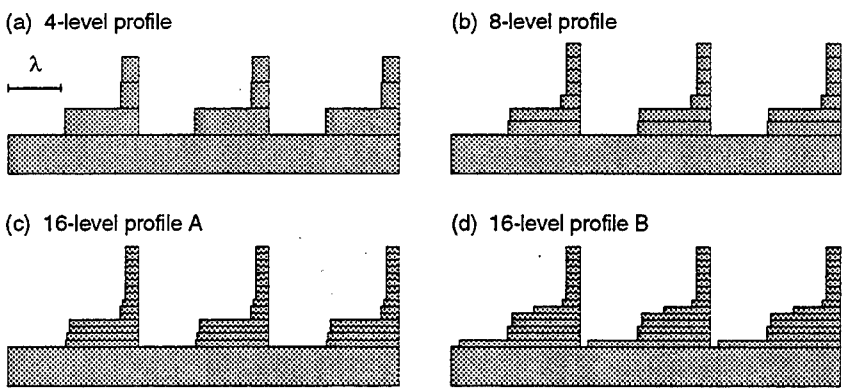

Fig. 2: Optimal staircase grating structures for period 2.5λ: (a) 4-level profile, (b) 8-level profile, and (c)–(d) 16-level profiles.

In general, one run of the optimization process does not always reach a global optimum. Consequently, the process has to be repeated a number of times with random starting configurations to find at least one (nearly) optimal solution. Let us denote by R the number of optimization runs, by N_η the number of runs that yield a solution with diffraction efficiency η, and by T the total number of grating configurations computed during the R optimization runs. With the help of these parameters we define the computational cost $C_\eta = T/N_\eta$ that measures the performance of the optimization method in each optimization case: it gives the average number of computations required to obtain the result with efficiency $\geq \eta$. The values of η, N_η, R, and T, and the estimates of C_η, corresponding to the structures in Fig. 2, are presented in Table 1 for both the SA algorithm and the gradient method. The best 16-level solution [profile A shown in Fig. 2(c)] was found only in a second series of optimizations when the profile was *a priori* assumed to have 9 levels (the last step is from 0.875λ to 1.875λ). This special case is presented in the last two rows of the table.

The results show that the SA algorithm is superior to the gradient method also in rigorous designs, except for the case of 4 levels (only three optimizable parameters), in which case the optimum can be reached in a few runs of the gradient method, each run containing ~ 100 calculations of grating configurations. On the other hand, this number is ~ 1000 for the SA algorithm, the optimum being reached at almost every run, which makes the use of SA inefficient. For the cases with 8 and 16 surface levels (7 and 15 free parameters) the SA algorithm found the global

Table 1: Diffraction efficiencies and optimization characteristics for the staircase grating structures shown in Fig. 2. The last two rows correspond to optimization with 9 levels (8 free parameters).

Nr of levels	η	Simulated annealing N_η	R	T	C_η	Gradient method N_η	R	T	C_η
4	79.5%	9	10	9703	1100	12	50	6314	500
8	86.1%	5	10	29267	6000	1	200	72125	>50000
16 A	87.9%	0	16	129800	$> 10^5$	0	200	135858	—
16 B	87.1%	5	16	129800	26000	1	200	135858	$> 10^5$
16 A (9)	87.9%	3	16	60903	20000				
16 B (9)	87.1%	10	16	60903	5000				

optimum significantly more efficiently, as the gradient method wasted time in the optimization of solutions with lower diffraction efficiencies at local minima of the cost function.

In the 16-level case one run of the SA algorithm contains typically 5000 – 10000 calculations and one run of the gradient method 500 – 1000 calculations of grating configurations. In a DEC AlphaServer 8400 computer one calculation with 4 and 16 levels including 21 diffraction orders requires 0.05 seconds and 0.27 seconds of CPU time, respectively.

4 Conclusions

In this paper we have optimized multilevel diffractive elements with a grating period of 2.5λ by rigorous diffraction theory. We have shown that the simulated annealing algorithm is significantly more powerful than the gradient method when the number of optimizable free parameters is larger than 3 or 4. The gradient method is, however, suitable for refining the optimal solution after the simulated annealing algorithm has reached the vicinity of the optimum.

References

[1] S. Kirkpatrick, C. D. Gelatt, Jr., and M. P. Vecchi, "Optimization by simulated annealing," Science **220,** 671–680 (1983).

[2] J. Turunen, A. Vasara, J. Westerholm, G. Jin, and A. Salin, "Optimisation and fabrication of grating beamsplitters," J. Phys. D: Appl. Phys. **21**, S102–S105 (1988).

[3] J. Turunen, A. Vasara, and J. Westerholm, "Kinoform phase relief synthesis: a stochastic method," Opt. Eng. **28**, 1162–1167 (1989).

[4] Z. Zhou and T. J. Drabik, "Optimized binary, phase-only, diffractive optical element with subwavelength features for 1.55 μm," J. Opt. Soc. Am. A **12**, 1104–1112 (1995).

[5] D. L. Brundrett, E. N. Glytsis, and T. K. Gaylord, "Subwavelength transmission grating retarders for use at 10.6 μm," Appl. Opt. **35**, 6195–6202 (1996).

[6] R. Petit, Ed., *Electromagnetic Theory of Gratings* (Springer, Berlin, 1980).

[7] E. Noponen, J. Turunen, and A. Vasara, "Parametric optimization of multilevel diffractive optical elements by electromagnetic theory," Appl. Opt. **31**, 5910–5912 (1992).

[8] A. Vasara, E. Noponen, J. Turunen, J. M. Miller, M. R. Taghizadeh, and J. Tuovinen, "Rigorous diffraction theory of binary optical interconnects," *Holographic Optics III: Principles and Applications*, G. M. Morris, ed., Proc. SPIE **1507**, 224–238 (1991).

Interference effects in diffractive beam shaping elements

Markus Rossi and Thomas Hessler

CSEM Centre Suisse d'Electronique et de Microtechnique
Badenerstrasse 569, 8048 Zurich, Switzerland
markus.rossi@csemne.ch; phone: +41 1 4971 460; fax: +41 1 4916 323

1. Introduction

An increasing number of commercially available and proprietary design algorithms based on scalar or electromagnetic theory allow the calculation of a large variety of diffractive optical elements (DOEs) with excellent performance and high diffraction efficiencies. However, micro-structuring technologies used for the fabrication of DOEs have tolerances and limitations that reduce the measured diffraction efficiencies to below the theoretical values. For some applications not only the absolute value of the diffraction efficiency is of concern, but at least the same importance has to be paid to the spatial distribution and the optical effects of the stray light. Collimating and beam shaping elements are typical examples for the latter case. Due to interference effects with the "signal beam", very small amounts of stray light can already reduce the optical performance significantly, e.g. characterized by an irradiance uniformity. Especially for applications with beam shaping DOEs in micro-systems these effects get more critical since the short propagation lengths do not allow a complete separation of the desired and the stray light.

In this paper we investigate the spatial distribution and the optical effects of stray light in collimating diffractive elements. A simple model is used to quantify the optical performance. The results can be applied straightforward to beam shaping elements. We also describe possibilities to control and reduce the negative effects of stray light in micro-systems with collimating and beam shaping DOEs.

2. Causes of stray light in diffractive optical elements

Approximations, limitations and tolerances in the fabrication processes of blazed DOEs lead to the diffraction of light in other than the desired orders. In the case a multilevel profile the number of levels N_L determines the maximum diffraction efficiency as well as the spatial distribution of stray light. For a blazed grating with a period Λ designed for the first order the strongest *additional* diffraction orders are $k = 1 \pm N_L$. These orders are caused by the sub-grating with the period Λ/N_L.

Direct write methods allow the fabrication of reliefs with continuous-relief structures without a staircase approximation. However, due to the finite size of the writing tool which can be a laser or an electron beam [1,2] vertical side-walls at the profile steps are difficult to achieve. The resulting profile steps are rounded which lowers the efficiency in the desired diffraction order. For elements designed in the first order, the typical stray light distribution contains energy in the zeroth and negative orders [1]. Additionally, tolerances in the development processes diffract light in neighboring higher or lower orders, depending if the etched depth is too deep or too shallow.

3. Modeling with Gaussian beams

The optical performance of a non-perfect diffractive lens can be approximated by the simultaneous action of a series of lenses with different focal lengths [3]. These focal lengths correspond to higher and lower diffraction orders of the original lens; the energy distribution among them is determined by the nature and amount of profile errors or wavelength deviations. The irradiance distribution I of a diffractive lens in a given plane can therefore be modeled by the coherent superposition of the fields u_k of the different lenses k (cf. Fig. 1):

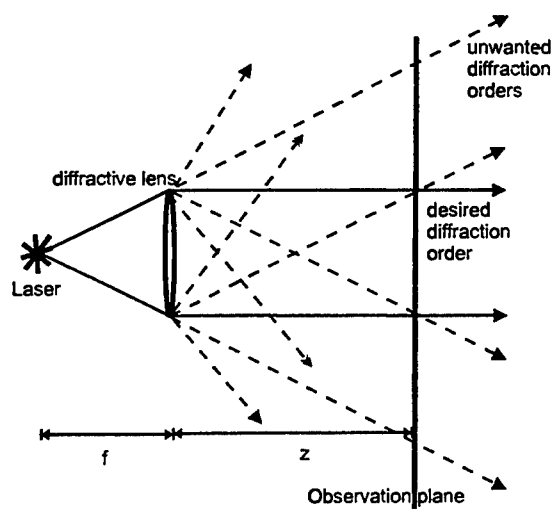

Fig. 1. Desired and unwanted diffraction orders in a collimating diffractive lens.

$$I = \left| \sum_k a_k \, u_k \right|^2 . \qquad (1)$$

The amplitudes a_k are given by the square root of the efficiencies of the diffraction orders k:

$$a_k = \sqrt{\eta_k} \qquad (2)$$

and fulfill the condition:

$$\sum_k \eta_k = 1 . \qquad (3)$$

The set for the parameters η_k is extracted from experimental calibration data [1] and is assumed to be constant over the lens aperture. In order to avoid aperture diffraction effects and to model beam shaping elements such as flat-top generators, Gaussian beams with different divergence angles and waist positions were used instead of spherical waves. The field of the Gaussian resulting from the k-th diffraction order is given by:

$$u_k = \sqrt{\frac{2}{\pi}} \frac{q_{0_k}}{\left(q_{0_k} + z\right) w_0} e^{-i\frac{2\pi}{\lambda}\left(z + \frac{x^2+y^2}{2\left(q_{0_k}+z\right)}\right) + i\varphi_k} \qquad (4)$$

$$\text{with } q_{0_k} = \left(\frac{k-1}{f} - i \frac{\lambda}{\pi \, w_0^2} \right)^{-1} \qquad (5)$$

describing the complex propagation parameter for a collimating diffractive lens (cf. Fig. 1). φ_k is a phase offset, f the focal length of the lens, w_0 the beam waist at the lens aperture of size a and λ the design wavelength. This model was applied to calculate the interference effects between the desired and the stray light.

4. Optical effects in focusing, collimating and beam shaping elements

For a diffractive lens used to focus a point source, fabrication limitations and tolerances lead to a reduced irradiance in the focal spot and a broadly distributed background illumination around it. Since the amplitude of the focused diffraction order is very low outside the Airy disk, the same applies to the interference terms with other diffraction orders. Figure 2 shows the calculated irradiance distribution of a diffractive lens in the focal plane for a perfect profile (η_1 = 100%) and a non-perfect profile (η_1 = 90%). The stray light suppression γ is better than 50 dB. As an upper limit γ can be approximated by:

$$\gamma > \frac{\eta_1}{1-\eta_1} N_F^{\,2} , \qquad (6)$$

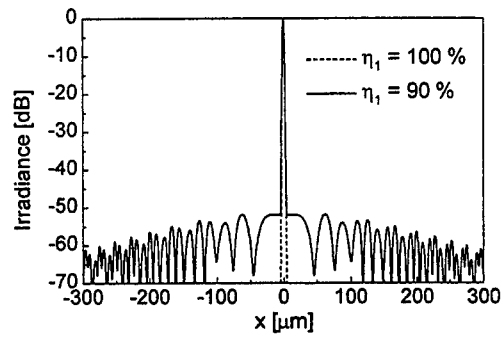

Fig. 2. Calculated irradiance distribution in the focal plane for a focusing diffractive lens with f = 1000 µm, illuminated with a Gaussian beam of λ = 1.0 µm and w_0 = 200 µm.

where the Fresnel number N_F is defined as $N_F = a^2/\lambda f$. The reduced irradiance in the focus and the stray light are tolerable for many applications.

The situation is different for non-focusing elements, especially for diffractive beam shaping elements used in optical micro-systems where only short propagation distances are allowed. The power of the desired diffraction order is distributed over a much larger area and is therefore very sensible to interference with light from unwanted diffraction orders.

Figure 3 shows the calculated irradiance patterns (60 µm × 60 µm) at a distance $z = 2f$ behind a collimating lens (f = 100 µm, w_0 = 50 µm) for various efficiency values η_1. The residual light was assumed to be distributed in the neighboring diffraction orders, mainly the zeroth, the second and the minus first order. It can be seen that already 1% of the light in unwanted orders leads to a relatively strong modulation in the interference pattern. These theoretical calculations match very well with experimental observations.

The spatial frequency of the interference fringes is determined by the number of orders contributing and by the image plane distance z. For larger values of z, the uniformity error σ (defined as contrast of maximum and minimum deviation from the ideal Gaussian distribution) decreases for two reasons:

(i) For first order diffractive collimating lenses at positions $z > f$, all unwanted diffraction orders are divergent. The light of the desired order is concentrated in the area $A_1 = \pi a^2$ for all values of z, whereas the area illuminated by the zeroth order is growing by $A_0 = \pi a^2 z^2 (1/z + 1/f)^2$. For distances $z >> f$ the amplitude for the zeroth order is therefore reduced by (f/z) with the propagation distance z. Thus, the propagation lowers the contrast of the interference pattern significantly.

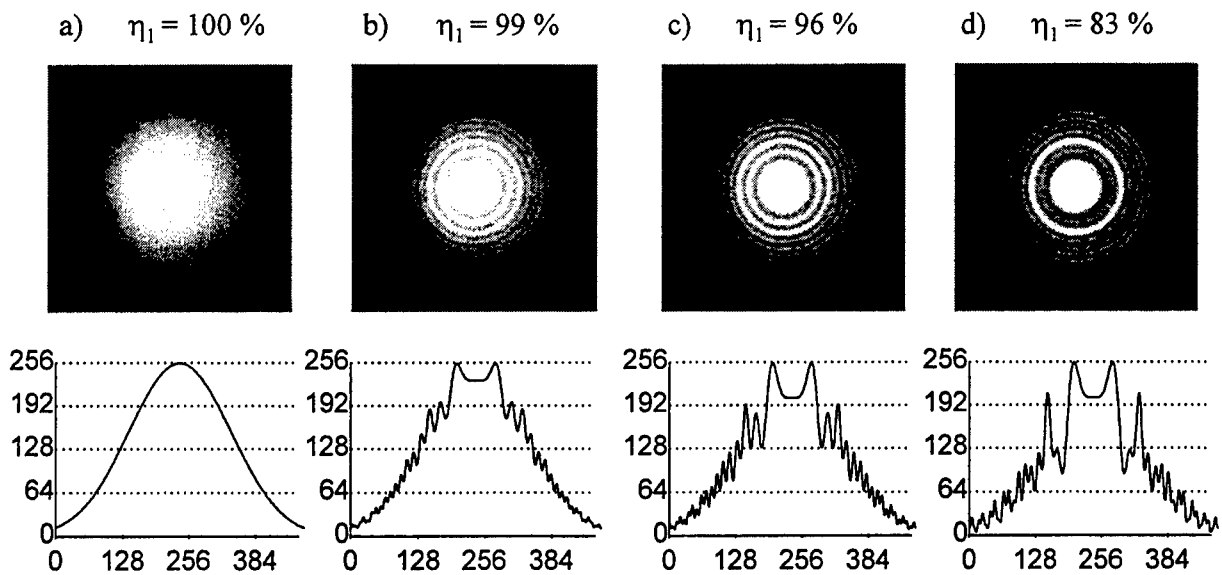

Fig. 3. Normalized gray-scale representation of the irradiance at distance z = 2 f behind the collimating lens for various diffraction efficiencies. The lower row shows a one-dimensional section through the center of the irradiance distribution.

(ii) The radius of curvature of the divergent orders increases with the propagation whereas the radius of curvature of the desired, collimated order remains approximately constant. The spatial frequency of the interference pattern is therefore reduced and the fringes walk out of the region of the collimated beam. This situation is indicated in Fig. 4, showing the irradiance pattern of Fig. 3d) at distances $z = 4f$ and $z = 8f$. Considering only the interference between the zeroth and the first order, the last interference fringe leaves the area of the collimated beam at a distance

$$z = f\,(N_F / 2 - 1). \qquad (7)$$

In many microsystems this distance required for clearing a beam by propagation is often not available and other means are necessary to avoid interference effects. As a first possibility, the phase difference between the first and the zeroth order can be controlled. This allows one to increase the overall uniformity of the beam. We will also present theoretical and experimental results from a novel type of micro-optical element that acts as diffractive lenses but shows less pronounced diffraction orders under typical fabrication conditions. These elements are designed with randomly placed $M2\pi$ phase steps and showed very promising first results.

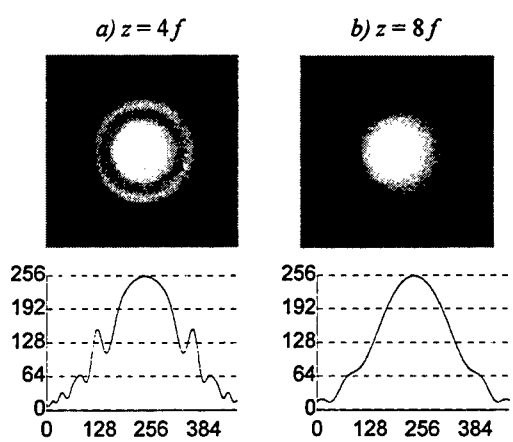

Fig. 4. Irradiance of Fig. 3d) at distance z = 4 f and z = 8 f.

5. Conclusions

The successful implementation of diffractive beam-shaping elements in optical micro-systems depends critically on the limitations of the fabrication technology. Interference effects require special consideration when designing the distances in the optical system. We will demonstrate experimental results for diffractive beam shaping elements fabricated by direct laser beam writing with reduced interference effects.

References

[1] Th. Hessler, M. Rossi, R.E. Kunz, and M.T. Gale, "Analysis and optimization of fabrication of continuous-relief diffractive optical elements," submitted to Applied Optics (1997).

[2] M. Ekberg, F. Nikolajeff, M. Larsson, and S. Hård, "Proximity-compensated blazed transmission grating manufacture with direct-writing, electron-beam lithography," Appl. Opt. **33**, 103-107 (1994).

[3] M. Rossi, R.E. Kunz and H.P. Herzig, "Refractive and diffractive properties of planar micro-optical elements," Appl. Opt. **34**, 5996-6007 (1995).

Stratified diffractive optic approach for creating high efficiency gratings

Diana M. Chambers
Micro Craft, Inc., 620 Discovery Dr., Huntsville, AL 35806
Phone: (205) 971-9356, Fax: (205) 971-9403, e-mail: diana.chambers@msfc.nasa.gov

Gregory P. Nordin
Dept. of Electrical and Computer Engineering and Center for Applied Optics,
The University of Alabama in Huntsville, Huntsville, AL 35899
Phone: (205) 890-6215 x410, Fax: (205) 890-6618, e-mail: nordin@ebs330.eb.uah.edu

1. Introduction

Gratings with high efficiency in a single diffracted order can be realized with both volume holographic and diffractive optical elements. However, each method has limitations that restrict the applications in which they can be used. For example, high efficiency volume holographic gratings require an appropriate combination of thickness and permittivity modulation throughout the bulk of the material. Possible combinations of those two characteristics are limited by properties of currently available materials, thus restricting the range of applications for volume holographic gratings. Efficiency of a diffractive optic grating is dependent on its approximation of an ideal analog profile using discrete features. The size of constituent features and, consequently, the number that can be used within a required grating period restricts the applications in which diffractive optic gratings can be used. These limitations imply that there are applications which cannot be addressed by either technology. In this paper we propose to address a number of applications in this category with a new method of creating high efficiency gratings which we call stratified diffractive optic gratings. In this approach diffractive optic techniques are used to create an optical structure that emulates volume grating behavior.

To illustrate the stratified diffractive optic grating concept we consider a specific application, a scanner for a space-based coherent wind lidar, with requirements that would be difficult to meet by either volume holographic or diffractive optic methods. The lidar instrument design specifies a transmissive scanner element with the input beam *normally* incident and the exiting beam deflected at a fixed angle from the optical axis. The element will be rotated about the optical axis to produce a conical scan pattern. The wavelength of the incident beam is 2.06 μm and the required deflection angle is 30 degrees, implying a grating period of ~4μm. Creating a high efficiency volume grating with these parameters would require a grating thickness that cannot be attained with current photosensitive materials. For a diffractive optic grating, the number of binary steps necessary to produce high efficiency combined with the grating period requires feature sizes and alignment tolerances that are also unattainable with current techniques. Rotation of the grating and integration into a space-based lidar system impose the additional requirements that it be insensitive to polarization orientation, that its mass be minimized and that it be able to withstand launch and space environments.

2. Stratified diffractive optic grating as an alternative

We propose an alternative approach that is inspired in part by previous work on stratified volume holographic optical elements (SVHOE's).[1,2] In that work, diffraction efficiencies comparable to those of a volume grating were achieved by interleaving thin holographic grating layers with homogeneous layers whose thickness was appropriate to ensure phase matching between the zero and first orders. This led to consideration of a similar structure for diffractive optic gratings, *i.e.* stratified diffractive optic gratings.

2.1 Stratified diffractive optic grating structure

In a stratified diffractive optic grating the thin holographic grating layers of SVHOE's are replaced by binary grating layers which are interleaved with homogeneous layers as illustrated in Figure 1. The ridges of the grating layers form surfaces of constant permittivity similar to the

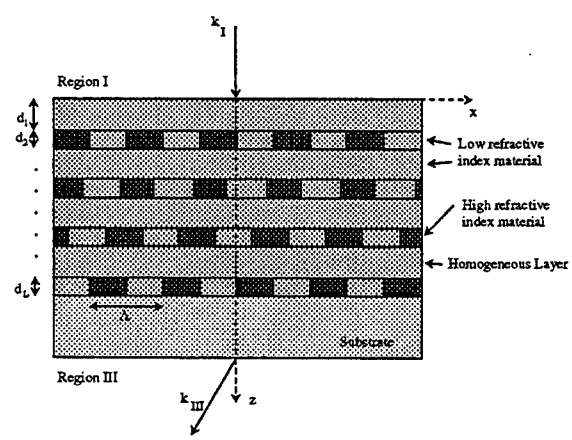

Figure 1: Example stratified diffractive optic grating

fringes in a volume grating. Laterally shifting the binary grating layers creates a stratified diffractive optic structure corresponding to a volume grating with slanted fringes. Refractive index of both the ridges and the grooves of the binary gratings and of the homogeneous layers may be varied as well as layer thickness to enforce phase matching through the structure. The number of layers may also be varied in order to optimize the efficiency of the element.

2.2 Modeling

The grating structure discussed above has an index modulation that is large compared to that of photosensitive materials and, for the example considered here, a small period to wavelength ratio (*e.g.* < 10). Accurate prediction of diffraction efficiency under these conditions requires a rigorous electromagnetic diffraction theory. Rigorous coupled-wave analysis (RCWA) as formulated by Moharam, *et al*[3,4] was chosen as the algorithm to model the behavior of these stratified structures. The implementation encompasses planar diffraction for both TE and TM polarization orientations and conical diffraction. Recent modifications which improve convergence of RCWA for TM polarization and conical diffraction have also been incorporated.[5]

Extension of the published RCWA algorithm to accommodate the unique structure of stratified diffractive optic gratings was necessary. In our version of the algorithm, any number of uniform and grating layers can be sequenced in any order. Binary grating layers can be shifted independently of one another. Refractive index and dispersion can be specified for each uniform layer as well as for both ridges and grooves in each grating layer. These modifications permit examination of general stratified elements.

3. Example design and performance

An initial design process for the lidar scanner element considered stratified diffractive optic grating structures consisting of 2,3,4 and 5 binary grating layers interleaved with homogeneous layers. All homogeneous layers were assumed identical as were all grating layers, with the exception of lateral position. Since the lidar system required normal incidence, the position of the grating layers was shifted such that the fringes they represented were slanted at the Bragg angle. The refractive index of grating ridges was chosen to be 2.0 while the refractive index of grating grooves and uniform layers were both set to 1.5. Iteration of the thickness of grating and homogeneous layers and the associated grating shifts revealed an optimum cumulative grating thickness of 3 μm. Peak diffraction efficiency for the case of two binary grating layers was approximately 70% while the case of three layers increased to 88.5%. Five grating layers yielded a peak efficiency of 90%.

The design with three layers was chosen for further study since it predicted high diffraction efficiency in a relatively simple structure. Figure 2 shows the efficiency of this structure as a function of angle of incidence of the input beam. Note that it maintains greater than 85% efficiency in a region of +/- 1 degree about normal incidence. Figure 3 illustrates that the diffraction efficiency is relatively insensitive to polarization. Figure 4 shows a plot of the electric field as it traverses the stratified binary grating structure. As the wavefronts pass through the first grating layer they are slightly disrupted while passing through the second grating layer causes them to become completely fractured. The third grating layer connects a lagging wavefront with a leading wavefront to effect the redirection of the beam to the desired deflection angle.

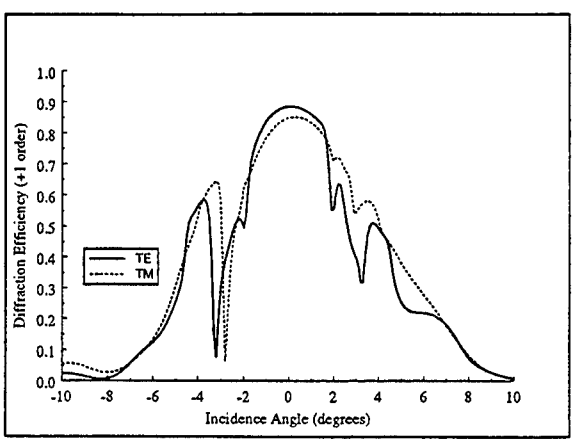

Figure 2: Efficiency vs. Incidence Angle

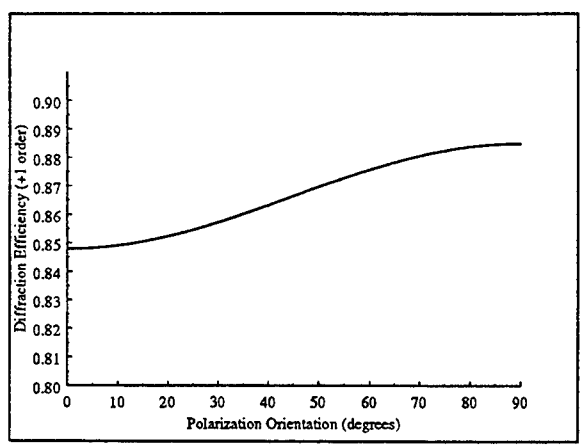

Figure 3: Efficiency vs. Polarization Orientation

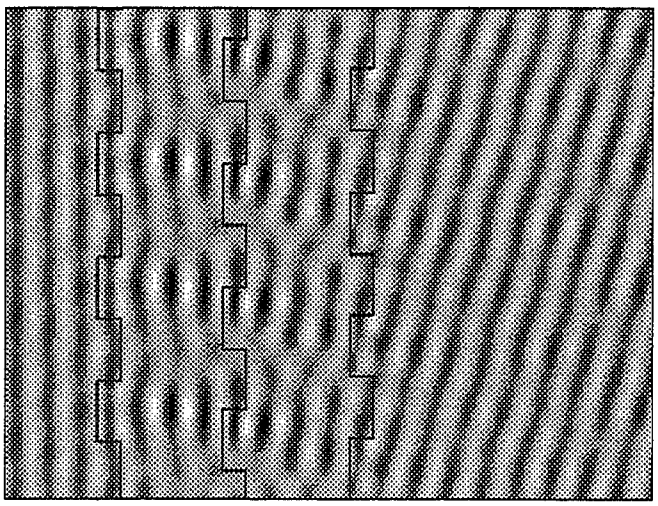

Figure 4: Electric field through stratified diffractive optic grating structure

4. Summary

Stratified diffractive optic gratings have been proposed as a means of producing gratings for applications where the requirements are not suited to traditional volume holographic and diffractive optics techniques. An example application has been studied to illustrate a set of operational and performance requirements that are best met by an approach of using diffractive optic fabrication techniques to emulate volume grating behavior. A modeling algorithm based on RCWA has been described and an example stratified diffractive optic grating structure for the coherent wind lidar application has been discussed. This design yielded a diffraction efficiency of 88.5%.

This work was performed under contract NAS8-40836 in support of NASA/Marshall Space Flight Center with Steve Johnson as task initiator. The authors gratefully acknowledge many helpful discussions with Dr. Farzin Amzajerdian of the Center for Applied Optics at the University of Alabama in Huntsville.

References

1. G.P. Nordin, R.V. Johnson and A.R. Tanguay, Jr., "Diffraction properties of stratified volume holographic optical elements," J. Opt. Soc. Am. A, **9**, 2206-17 (1992).
2. G.P. Nordin and A.R. Tanguay, Jr., "Photopolymer-based stratified volume holographic optical elements," Opt. Lett., **17**, 1709-11 (1992).
3. M.G. Moharam, E.B. Grann, D.A. Pommet and T.K. Gaylord, "Formulation for stable and efficient implementation of the rigorous coupled-wave analysis of binary gratings," J. Opt. Soc. Am. A, **12**, 1068-76 (1995).
4. M.G. Moharam, D.A. Pommet, E.B. Grann and T.K. Gaylord, "Stable implementation of the rigorous coupled-wave analysis for surface-relief gratings: enhanced transmittance matrix approach," J. Opt. Soc. Am. A, **12**, 1077-86 (1995).
5. L. Li, "Use of Fourier series in the analysis of discontinuous periodic structures," J. Opt. Soc. Am. A, **13**, 1870-1876 (1996).

Two-level binary diffractive optical elements for symmetric line-patterns generation from laser diodes

Michael A. Golub,

Holo-Or, Ltd., Kiryat Weizmann, P.O.B. 1051, Rehovot 76114, Israel,
Tel: 972-8-9409687, Fax: 972-8-9409606

Numerous tasks of laser pointing, visual adjustment, targeting and laser radar require shaping of laser diode beam into the line contour patterns. The examples of the line patterns are straight-line segment, cross, contour of rectangle, system of points. One more task is to circularize the elliptical beam that is typical for laser diodes even after passing through standard collimators. The traditional approach is either to use cylindrical lenses[1] or to apply computer-generated phase holograms reconstructing the system of points[2]. The usual problem in computer-generated holograms is the dot-type structure of the image, limited possibilities to achieve uniform intensity distribution along lines. Patterns containing several lines can be formed by faceted diffractive optical elements (DOEs), which use some part of clear aperture for line segment generation. However splitting the aperture adds problems in line uniformity, width, interference between lines. Other way is to use multi-channel DOEs[3] utilizing several diffraction orders of DOE at once. *We propose* a special way to generate symmetrical patterns based on the full use of symmetrical diffraction orders of binary diffraction grating. Full cycle of design, computer simulation, fabrication and experimental investigation of DOEs for laser diodes is described in this report.

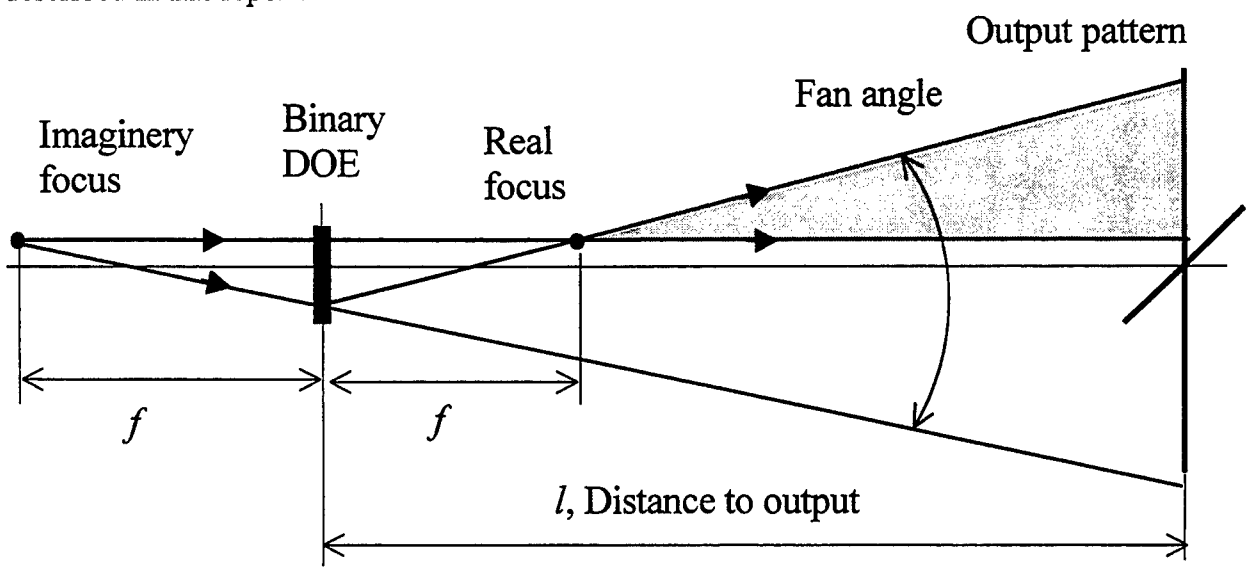

Fig. 1. Pair of spherical beams reconstructed by incident plane wave from binary (two-level phase) DOE

Suggested line-pattern generating DOEs are based on two main ideas. First idea is the gaussian beam shaping to "top-hat" intensity[4] applied in a special 1-D manner along each of the partial lines constituting the pattern. Other idea is a nonlinear transformation of phase function[5] giving two or four symmetrical diffraction orders of binary two-level DOE instead of one diffraction

order characteristic to the blazed DOEs with smooth phase function. Fig. 1 shows two (real and imaginary) point sources reconstructed from two-level DOE illuminated by collimated beam. The axial location of the sources is a bit separated in space, thus giving some asymmetry to the required output pattern, but the impact on the output pattern is negligible. Thus the criteria for the suggested approach is conforming to inequality: $f/l \ll 1$, where f is the focal length of DOE, l - the working distance. Far field operation of laser diodes usually follows this restriction.

It is shown that the phase function $\Phi(\mathbf{u})$ of DOE with symmetrical output pattern can be constructed by special binarization operation $Q[.]$ applied to the weighted mix of two partial phase functions $\Phi_w(\mathbf{u})$, $\Phi_h(\mathbf{u})$ (let say describing half vertical and horizontal line of the cross or rectangular contour). Binarization procedure uses groove-shape functions of couple of diffraction gratings, each giving two diffraction orders (+1) and (-1) with efficiencies C_+^2, C_-^2, c_+^2, c_-^2 respectively (usually $c_+ = C_+$, $c_- = C_-$). The main terms of the complex amplitude just after DOE illuminated by collimated beam can be presented in the form

$$\exp[iQ(\Phi(\mathbf{u}))] = C_+c_+ \exp[i\Phi_w(\mathbf{u})] + C_-c_- \exp[-i\Phi_w(\mathbf{u})] + C_+c_- \exp[i\Phi_h(\mathbf{u})] + C_-c_+ \exp[-i\Phi_h(\mathbf{u})]$$

describing four useful diffraction orders responsible for symmetrical parts of the output pattern. The algorithms for computer-aided design of binary two-level DOEs are implemented in the media of software package DOECAD for Windows developed in Holo-Or. DOECAD is a 32 bit executable program module for Win95 created in object oriented C++ programming language developed with special classes for DOEs. DOECAD for Windows features usual windows menus and parameter dialogue boxes for DOEs, mask-file generation and computer simulation. Figs. 2-4 demonstrate the general view of masks and performance simulation for cross and rectangular-contour generating DOEs for laser diodes of visible region of spectrum (red) with few degrees fan angle. Computer simulation shows that the efficiency of DOEs (defined as the portion of incident light flux directed inside the minimum rectangle including useful contour) is in the range 80-85%.

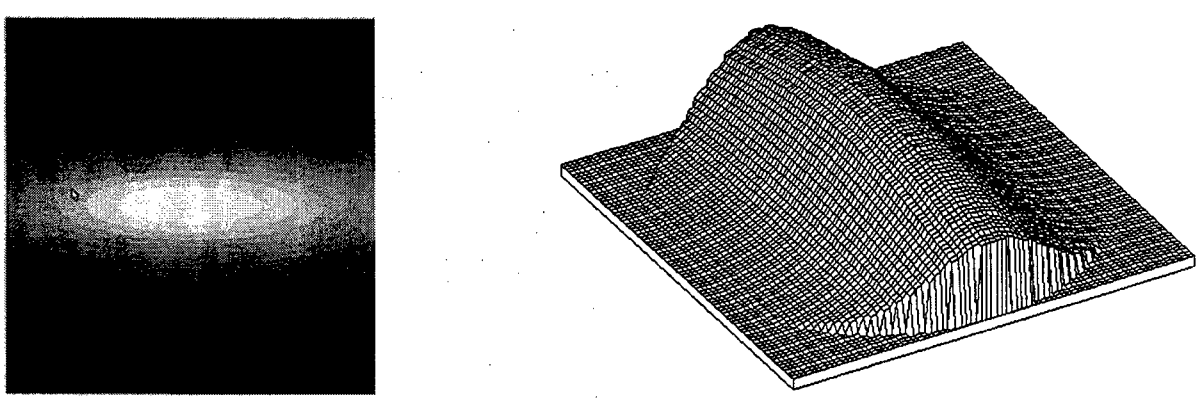

Fig. 2. Gray-level and 3-D presentation of elliptical gaussian beam model of single-modal laser diode

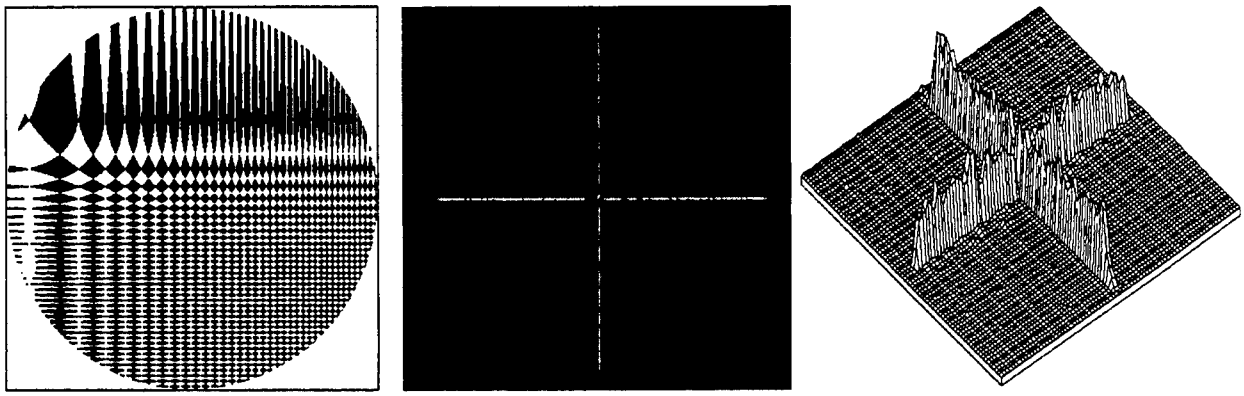

Fig. 3. Zone structure and performance simulation results for cross pattern generator

The masks for cross and rectangular contour DOE were generated by laser writer. The DOEs were fabricated by 1-stage photolithography and reactive ion etching on fused silica. The experimental results with the view of the shaped pattern, presented in the report, demonstrate very good match to simulation results.

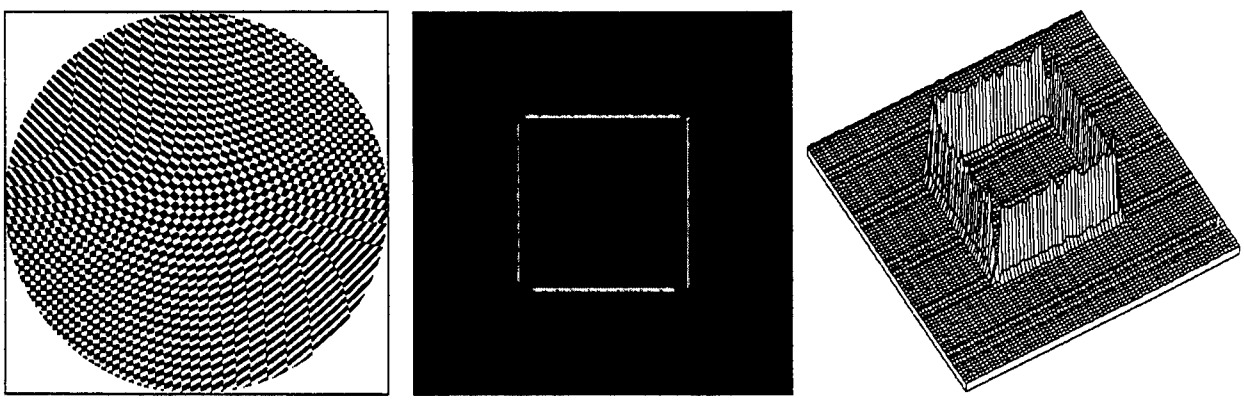

Fig. 4. Zone structure and performance simulation results for rectangular contour generator

The approach is applicable also for getting focal shape patterns for focusing radiation of various types of lasers. For example, focusing of single-modal CO_2 laser beam into focal rectangular frame was achieved by DOE with similar design.

References

1. Casasent D., Yu D, One-dimensional collimating of laser array outputs, *Applied Optics*, **33**(14), 3118, 1994.
2. Dames M.P., Dowling R.J., McKee P., Wood D., Efficient optical elements to generate intensity weighted spot arrays: design and fabrication, *Applied Optics*, **30**(19), 2685, 1991.
3. Soifer V. A., Golub M.A., Laser beam mode selection by computer generated holograms, CRC Press, Boca Raton, 1994.
4. Golub M.A., Sisakyan I.N., Soifer V.A., Infra-red radiation focusators, *Optics and lasers in Engineering*, **15**(5), p. 297, 1991.
5. Golub M.A., Doskolovich L.L., Kazanskiy N.L., Kharitonov S.I., Soifer V.A., Computer generated diffractive multi-focal lens, *J. Modern Optics*, **39**(6), p. 1245, 1992.

Diffractive Optics and Micro-Optics

Optical Interconnects 1

Monday, June 8, 1998

M.G. (Jim) Moharam, University of Central Florida
Presider

DMD
3:30pm–5:00pm
Koa Room

Polarization selective diffractive optical elements and applications

Y. Fainman, F. Xu, R. Tyan, D. Marom, P. Shames, P. C. Sun, J. Ford,+ A. Scherer,* and A. Krishnamoorthy+

Department of Electrical and Computer Engineering, 0407, University of California at San Diego, La Jolla, CA 92093
Tel (619) 534-8909, Fax: (619) 534-1225, fainman@ece.ucsd.edu

+Bell Laboratories, Lucent Technologies, Holmdel, NJ 07733

*Department of Electrical Engineering, Caltech, Pasadena, CA 91125

Computer-generated holograms (CGH) fabricated as phase-only optical elements have proven to be useful for various photonic systems applications. Such elements are normally capable of implementing fixed functionality. However, the performances of packaged photonic systems will be further enhanced with availability of CGH elements with multifunctionality in polarization or color, and programmability. We have constructed polarization selective CGH which apply an independent phase profile during readout by horizontal and vertical light polarizations[1-3]. These elements are composed of two surface relief etched birefringent substrates joined face to face. We describe the design methodology for arbitrary birefringent substrate and gap materials. We show how these holograms are fabricated with standard microelectronics technology, and discuss the effects of etching and alignment errors on performance. We have demonstrated high diffraction efficiency with a polarization contrast ratio of over 100:1, using a multilevel phase hologram made from two birefringent lithium niobate substrates[2].

Our second approach to CGH with multifunctionality in polarization is based on multiple order delay (MOD)[4]. The MOD approach employs deep surface relief structure on a single substrate of a birefringent crystal of yttrium orthovanadate. Rigorous coupled-wave analysis was used to accurately model the diffractive element. The experimentally measured first order showed a close-to-theoretical diffraction efficiency of 39%. The polarization contrast ratio was measured to be 33:1. The MOD approach was also employed to construct a color selective diffractive optical element using the dispersion properties of BK7 glass[5]. We designed and fabricated a color-selective diffractive optical element that separates the standard telecommunication wavelengths, 1.3 and 1.55 micrometers, with 80% efficiency and greater than 30:1 contrast.

Our most recent approach uses artificial dielectric materials for design and fabrication of CGHs with multifunctionality. We designed[6], fabricated and characterized a form birefringent 490-nm-deep nanostructure with a period of 200nm in a GaAs substrate[7]. The numerically

predicted phase retardation was found in good agreement with the experimentally measured results, verifying our rigorous numerical modeling tools. The fabricated nanostructures show extremely large artificial anisotropy compared with that available in naturally birefringent materials and are useful for construction of form-birefringent CGH. We designed, fabricated, and evaluated experimentally a polarization-selective CGH made with form-birefringent nanostructure[8]. The fabricated element showed a large polarization contrast ratio (>250:1) and a high diffraction efficiency (40% for binary phase level element). The experimental evaluation was in good agreement with the design and modeling predictions. Most recently we introduced a novel polarization beam splitter that uses the anisotropic spectral reflectivity (ASR) characteristic of a high-spatial-frequency multilayer binary grating[9]. Such ASR effects allow us to design an optical element that is transparent for TM polarization and reflective for TE polarization. For normally incident light our element acts as a polarization-selective mirror. We fabricated[10] and characterized such devices with ASR characteristics[11]. The design with rigorous coupled-wave analysis was found in very good agreement with the experimentally measured results.

Applications of the multifunctional CGHs for packaging telecommunications and parallel data processing optoelectronic systems will be also presented[12-14]. These include optoelectronic package examples of a compact, folded free-space optical multistage interconnection network utilizing an array of dilated bypass-exchange switches built of our polarization selective CGH combined with an array of polarization modulators. The multistage system is folded using patterned mirrors, increasing SNR and supporting low BERs performance[14]. For the second example, we will describe packaged module incorporating polarization-based beam forming optics implemented with our multifunctional CGH which is integrated with an optoelectronic-VLSI device[15]. The chip has multiple quantum well modulators and detectors flip-chip bonded onto a silicon CMOS integrated circuit. In the assembled module, a polarization-selective CGH converts linearly polarized light to two-dimensional spot array transmitted through a quarter wave plate to illuminate the output modulators. The lenslets do not interfere with input data and the reflected output, which is orthogonally polarized. We demonstrate good spot intensity uniformity and registration with modulators.

References

1. J. E. Ford, F. Xu, K. Urquhurt, and Y. Fainman, "Polarization selective computer generated holograms," *Opt. Lett.*, 18, 456-458, 1993.

2. F. Xu, J. Ford, and Y. Fainman, "Polarization selective computer generated holograms: design, fabrication and applications," *Appl. Opt.*, 34, 256-266, 1995

3. N. Nieuborg, A. Kirk, B. Morlion, H. Thienpont, I. Veretennicoff, "Polarization-selective diffractive optical elements with an index-matching gap material," *Applied Optics*, 36, 4681-4685, 1997.

4. F. Xu, J. Ford, and Y. Fainman, " Single-substrate birefringent computer-generated holograms," *Opt. Lett.*, 21, 516-518, 1996

5. J. Ford, F. Xu and Y. Fainman, " Wavelength-selective planar holograms," *Opt. Lett.*, 21, 80-82, 1996

6. I. Richter, P. C. Sun, F. Xu and Y. Fainman "Design considerations of form birefringent microstructures," *Appl. Opt.*, 34, 2421-2429, 1995

7. F. Xu, R. Tyan, P. C. Sun, C. Cheng, A. Scherer and Y. Fainman, "Fabrication, Modeling and characterization of form birefringent nanostructures," *Opt. Lett.*, 20, 2457-2459, 1995

8. F. Xu, R. Tyan, , P. C. Sun, Y. Fainman, C. Cheng, A. Scherer, "Form-birefringent computer-generated holograms," *Opt. Lett.*, 21, 1513-1515, 1996

9. R. Tyan, P. C. Sun, A. Scherer and Y. Fainman, " Polarizing beam splitter based on the anosotropic spectral reflectivity characteristic of form-birefringent multilayer grating," *Opt. Lett.*, 21, 761-763, 1996

10. C. C. Cheng, A. Scherer, R. C. Tyan, Y. Fainman, C. Witzgall, E. Yablonovitch, "New fabrication techniques for high quality photonic crystals," *J. of Vacuum Technology*, 15, (no.6), 2764-7, 1997.

11. R. Tyan, A. Salvekar, H. Chou, C. Cheng and A. Scherer, F. Xu, P. C. Sun and Y. Fainman, "Design, Fabrication and Characterization of Form-Birefringent Multilayer Polarizing Beam Splitter" *JOSA A,* 14, No 7, 1627-1636, 1997.

12. F. Xu, R. Rao and Y. Fainman. " An intelligent photonic switch using polarization selective birefringent computer generated holograms," Opt. Lett., 20, 336-338, 1995

13. A. Krishnamorthy, F. Xu, J. Ford, Y. Fainman, " Polarization-controlled multistage switch based on birefringent computer generated holograms," *Appl. Opt.*, 36, No. 5, 997-1010, 1997.

14. D. Marom, P. Shames, F. Xu, R. Rao, and Y. Fainman, ":Compact free-space multistage interconnection network demonstration," presented at the *OSA Topical Meeting on Optics in Computing*, Incline Village, Lake Tahoe, Nevada, *Technical Digest*, p. 192-194, March 1997.

15. F. Xu, J. Ford, A. Krishnamoorthy, and Y. Fainman, "A 2-D VLSI/optoelectronic device packaged using a polarization selective computer generated hologram," *Opt. Lett.*, 22, 1095-1097, 1997.

Substrate-mode polarization-controlled optical switch with sandwich reflection holograms

V.Moreau*, S.Habraken+, Y.Renotte* and Y.Lion*

(*) HOLOLAB, Institut de Physique, B5, Université de Liège,
Sart-Tilman, B-4000 Liège, Belgium
Tel: +32 4 366 37 72
Fax: +32 4 366 45 16
E-mail: renotte@gw.unipc.ulg.ac.be
(+) Centre Spatial de Liège, Avenue du Pré-Aily
B-4000, Angleur, Belgium

1. Introduction

The development of optical communication networks has led to a growing need of optical interconnection to route high data-rate signals without optical-to-electrical conversion.[1]

For the last few years, polarization-selective holograms have been proposed for realizing small size, non-blocking and bi-directional optical switches. There are two common ways to obtain gratings polarization sensitivity. The first one involves the etching of anisotropic substrates and permits to take benefits of computational holography.[2] However realization of such gratings remains complex and expensive and their diffraction efficiency are theoretically limited by the number of recorded phase levels.

The second type involves volume holograms. The H.Kogelnik's Coupled Wave Theory[3] predicts that grating with a 90° angle between diffracted and transmitted beams are totally insensitive to TM polarization mode, while a diffraction efficiency close to 100% can be reached for the TE mode.[4]

This type of hologram has shown to be well suited for routing beams inside substrate-mode holographic interconnections where light travels by 45° total internal reflection inside a substrate.[5-6]

We introduce in this paper a new design for 2x2 optical switches based on substrate-mode holography associated with reflective volume polarizing holograms. The use of reflective holograms leads to the possibility of parallel or series associations of switches inside a single substrate, reducing by the way the losses of air-substrate coupling and most alignment problems. Optical path of the signal depends on its polarization state that may be controlled by total internal reflection inside a liquid crystal device.

2. The 2x2 substrate-mode switch

Figure 1 shows the realized switch:

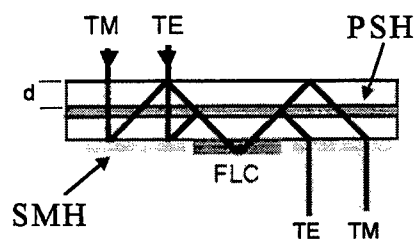

Figure 1: Optical path of the signals in the Substrate-mode 2x2 switch.
SMH: Substrate-Mode Hologram.
PSH: Polarization-Selective Hologram
FLC: Ferroelectric Liquid Crystal device

The manufacturing involves the recording of two different types of holograms. The former is a (0°,45°) mirror called "Substrate-Mode Hologram". Its goal is to couple the wave from the air to the substrate. The second hologram is a (-45°,45°) mirror that only reflects the TE mode in accordance with the Coupled-Wave Theory. The main advantages of associating two reflection elements rather than transmission equivalent ones are a wider angular selectivity, a greater wavelength selectivity and the possibility to reach high diffraction efficiency with the SMH for both polarization modes.

The two incoming beams must be 2d spatially separated (where d is the upper substrate thickness) and are respectively TM and TE polarized. They cross the polarization-selective hologram without being affected because of their inadequate incidence angle. They are coupled in the substrate by the SMH and reflected back under Bragg conditions to the PSH. The latter transmits the TM mode and reflects the TE one in such a way that the two polarization components are superimposed. They are then totally reflected in a FLC device, stuck to the lower substrate face, which permits to invert or not the polarization of both signals. After being switched, signals are spatially separated by the PSH and coupled out of the substrate by the SMH.

3. Recording setup

The holograms are recording in a photopolymer film: Omnidex™ HRF-700 from DuPont de Neumours. The high index modulation amplitude of this photopolymer unables the recording of elements with high performances and permits to take benefit of the dry process in order to save the accurate geometry requested by the desired properties.[7]
The film is a three layers stack: a Mylar® base, the holographic film, and a Mylar® cover sheet. The cover sheet must be removed and the film is laminated on a glass substrate. The material is sensitized for blue and green light and gratings are recorded with an Ar^+ laser (λ=514.5 nm). In order to avoid excessive absorption during read out we adapt recording angles to obtain convenient Bragg conditions for red (He-Ne laser: 632.8 nm) reading wavelength. Both SMH and PSH are recorded, developed and sandwiched with index matching liquid or epoxy. The FLC is stuck to the lower face with index liquid.

4. Experiment and discussion

If we consider that PSH diffraction efficiency is equal to 1 for TE mode and 0 for TM mode, optical attenuation in the switch (insertion loss: η_{switch}) is due to Fresnel reflections from the interfaces (R), SMH diffraction efficiency (η_{SMH}) and to absorption in the photopolymer (α).

$$\eta_{switch} = (R\eta_{SMH})^2 \exp(-\alpha\ell)$$

where ℓ is the absorption thickness, i.e. the photopolymer portion of the signal optical path inside the switch. The worst case is encountered by TM polarization when the switch works in transitive (non-inverting) mode as we can see in table 1.

	TM mode	TE mode
Inverting mode	$\ell=(1+3\sqrt{2})d$	$\ell=(1+3\sqrt{2})d$
Non-inverting mode	$\ell=(1+5\sqrt{2})d$	$\ell=(1+\sqrt{2})d$

Table 1: Total absorption thickness for all optical paths. d is the photopolymer film thickness: d=18µm.

We measured the optical performances of the two holograms before sticking them. Experimental results are summarized in tables 2a and 2b. In respect to our application, depicted PSH performances are high enough. Most losses come from absorption and from SMH TM mode diffraction efficiency, revealing that index modulation is lower than expected.

Polarization-selective hologram	
α	3.43 mm^{-1}
η_{TE}	0.97
η_{TM}	0.02

Substrate-mode hologram	
α	3.52 mm^{-1}
η_{TE}	0.96
η_{TM}	0.89

Table 2a: Measure of optical efficiency of single PSH and SMH.
Recording wavelength = 514.5 nm
Reading wavelength = 632.8 nm

	TM output	TE output
Inverting mode	33.3%	51.3%
Non-inverting	24.8%	33.3%

Table 2b: Transmitted power rate from input to output for each optical path.

5. Planar integration of multistage switch

Waveguide properties of the proposed optical switch lead to the possibility of series and parallel combination of elements for more complex interconnection functions. Figure 2 shows the design of a substrate, 1-D integration of the 4x4 Benes network. Other devices are under study: for instance, substrate-mode demultiplexer and multiplexer.

6. Conclusion

This work introduces the design and proves the feasibility of an original 2x2 polarization-controlled switch based on substrate-mode holography. This component has many advantages: compactness, monolithic structure, easy manufacturing and low cost. Results obtained on DuPont's Omnidex™ films are encouraging ones and open up new horizons towards more complex devices based on the combination of more switches.

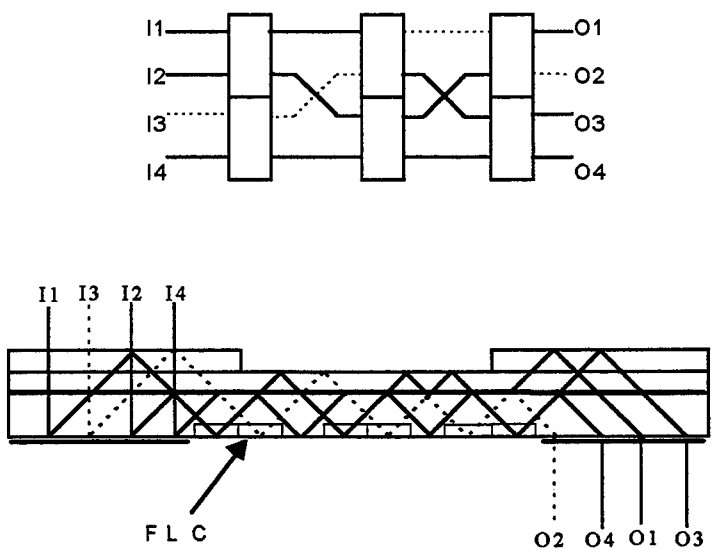

Figure 2: (a) Schematic Benes network for permutative interconnections between 4 inputs and 4 outputs
(b) Planar implementation of 4x4 Benes network with 2x2 substrate-mode switches.
Solid lines show all possible optical paths.
Dotted line shows an example of optical path from input 3 to output 2.

References

1. Photonic Switching - Proceedings of the First Topical Meeting, Incline Village March 18-20, 1987, in Springer Series in Electronics and Photonics, Vol. 25, T.K. Gustafson and P.W. Smith, Springer-Verlag, Berlin 1988

2. A.V. Krishnamoorthy, Fang Xu, J.E. Ford and Y. Fainman, *Polarization-controlled multistage switch based on polarization-selective computer-generated holograms*, Appl. Opt. Vol. 36 (1997), No 5, pp. 997

3. H.Kogelnik, *Coupled Wave Theory for Thick Hologram Grating*, Bell. Syst. Tech. J. 48 (1969), pp.2909

4. S.Habraken, Y. Renotte, St. Roose, E. Stijns and Y. Lion, *Design for polarizing holographic optical element*, Appl. Opt. 34 (1995), pp. 3595

5. R.K. Kostuk, M.Kato and Y-T. Huang, *Polarization properties of substrate-mode holographic interconnects*, Appl. Opt. 29 (1990), No 26, pp. 3848

6. J-H Yeh and R.K. Kostuk, *Design issues for substrate-mode holograms used in optical interconnects*, SPIE 2176 (1994), pp. 207

7. S.Habraken, Y.Renotte, E.Stijns and Y. Lion, *Polarizing optical element in DuPont's Omnidex™ films*, SPIE Symposium, Tech. Paper No 2532-14 (1995)

Novel multichannel WDM-PON demultiplexer using an AWG and diffractive optical elements

E. Pawlowski, M. Ferstl, H. Hellmich, B. Kuhlow, G. Przyrembel, C. Warmuth
Heinrich-Hertz-Institut für Nachrichtentechnik Berlin GmbH
Einsteinufer 37, 10587 Berlin, Germany
Tel: +49 30 31002-429, Fax: -213 , e-mail: pawlowski@hhi.de

J. R. Salgueiro
Universidad de Santiago de Compostela
Campus Sur, 15706 Santiago de Compostela, Spain
Tel: +34 81 5-63100, Fax: -90485, e-mail: fajose@usc.es

Introduction

In order to increase the capacity of optical transmission systems, it is advantageous to use the high-parallel capability of optical wavelength division multiplexing (WDM) [1] techniques. Key devices for WDM-communication systems are optical demultiplexer. A variety of different devices, such as Mach-Zehnder filters [2], diffractive optical elements (DOE) [3], acousto-optical filters [4], transversal filters [5] and arrayed-waveguide gratings (AWG) [6,7] have been already developed. However, to realize a device with a higher functionality it is usefull to integrate waveguide devices with DOEs. As a special case of WDM functionality upgrade, we have considered a 1.55-µm WDM extension of an existing passive optical net (PON). In this paper we report, for the first time to our knowledge, of the fabrication of a fully integrated multichannel WDM-PON demultiplexer. The device is used to distribute 1.3-µm wavelength signals (1/N power) and to multiplex an 8-channel WDM spectrum at 1.55-µm wavelength with 200 Ghz channel spacing. Planar lightwave circuits (PLC), based on silica waveguides, are very attractive devices for these applications [8]. They allow high reliable and low cost production, due to their suitability for integration of optical components. Furthermore, the silica waveguides show low optical losses.

Design and Fabrication

The WDM-PON demultiplexer is a combination of AWG and DOE-coupler. An AWG is an optical high order grating, realized with planar waveguides. It consists of input and output waveguides, two equal focusing slab regions and an arrayed waveguide grating. The arrangement of the demultiplexer is shown in Fig. 1. The arrayed grating is designed based on silica waveguides comprising of 60 regularly arranged waveguides with constant phase difference ($\Delta L = m \cdot \lambda/n$), where λ is the central wavelength , n the effective index of the waveguides and m the order of the grating. The light at the end of the arrayed grating, arranged on a circle with radius f =2.48 mm, is radiated as a 2-D spherical wave into the second slab region. The spherical phase front converges to a focal point, where the outgoing waveguides are located. Single mode waveguides are necessary for exact phase control.

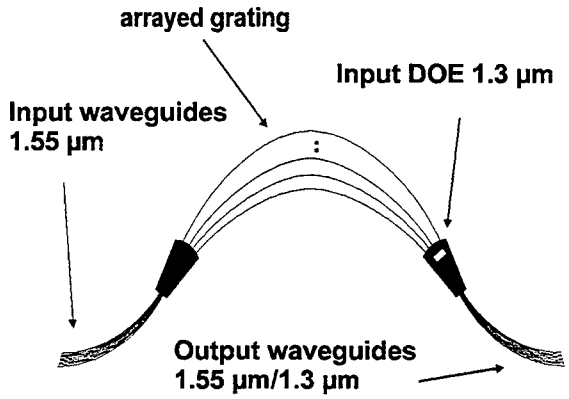

Fig.1 Schematic view of the WDM-PON demultiplexer

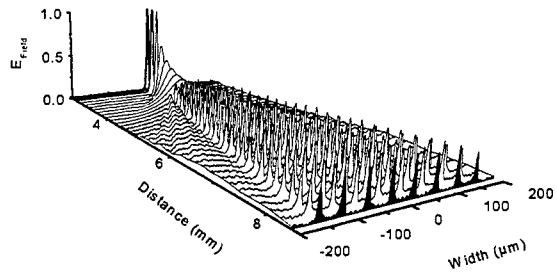

Fig.2 Waveform when light is coupled into output waveguides

To distribute a 1.3-µm signal to all the eight output waveguides, we used a DOE-coupler with rectangular grooves. The DOE design was based on coupled mode equations, which are solved by the transfer matrix method. To obtain the condition that only a single radiation beam into the planar waveguide is coupled, the pitch of the DOE-coupler must satisfy $\Lambda < 2\ \lambda/(n_{eff} + n_{cl})$, where n_{eff} is the effective index of the guided mode and n_{cl} is the index of the cladding. In our design we have chosen a grating period of 760 nm. Fig. 2 shows a BPM-simulation of the electric field waveform, when the light from a fiber is coupled through the DOE into the second AWG-slab and into the eight output waveguides. It can be clearly seen, that nearly all the light is coupled into the waveguides. The radiation efficiency of the DOE can be higher than 80 %, when the coupling angle in the air is about 21°, at 1.3-µm wavelength. The different fabrication processes of the elements are described independently in the following.

Fabrication of the AWG and the waveguides: The AWG was fabricated by flame hydrolysis deposition (FHD) of SiO_2-GeO_2 layers, by optical lithography and reactive ion etching (RIE) with CHF_3-H_2 as etching gas. As etch mask we have used a 3-µm thick resist (AZ5218) postbaked at 120°C for 30 seconds. The SiO_2-buffer layer is about 20 µm and the cladding layer is about 40 µm thick. The core sizes of the waveguides are 6x6 mm^2 and the relative refractive index difference is 0.7 %. The device size dimension is 52x26 mm^2. The fiber to fiber insertion loss, including the intrinsic fiber coupling losses of about 2 dB, is 7 to 8 dB.

Fabrication of the DOE coupler: Conventional UV-contact lithography in combination with an amplitude/phase mask [9] and a subsequent dry etching step is used to fabricate the DOE-coupler. The transfer of the resist patterns into the waveguide material is realized by IBE with Ar^+-ions, accelerated to an energy of 700 eV.

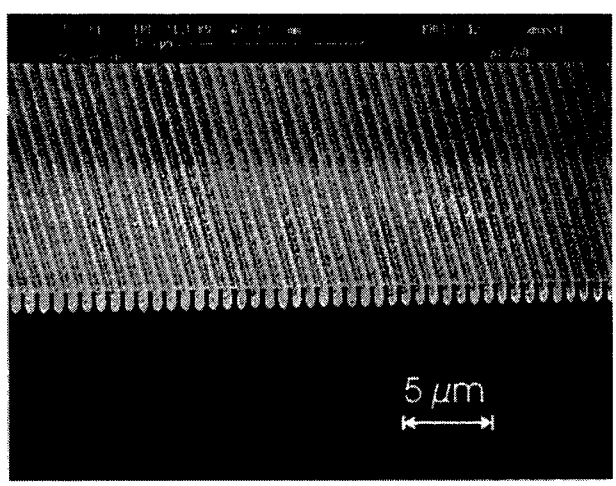

Fig.3 SEM photograph of DOE-coupler, Λ=760 nm, λ= 1.3 µm

The structure depth is defined by the etch selectivity between resist and substrate material and can be monitored by in situ mass spectrometry. Additionally, we have used a combination of ion beam sputtering and lift-off process to realize the coupling element. Fig. 3 shows a SEM photograph of the DOE-coupler with a period of Λ=760 nm, transferred by optical contact lithography at an exposure wavelength of 313 nm into a 1.2-µm thick (AZ 5214) resist. The measured line/space ratio is about 0.5.

Experiment

The transmission spectrum is measured at the eight output ports using an IR-detector (HP 8153A), when light from a tunable laser source (HP 8168B) is coupled to the main input port 5. Fig. 4 shows the mea-sured transmission spectrum of our WDM-PON demultiplexer with 200 GHz (1.6 nm) channel spacing and a central wavelength of 1550 nm. The measured crosstalk is lower than -21 dB. The 3-dB bandwidth was determined to 97 GHz, which is close to the theoretical value of 93 GHz.

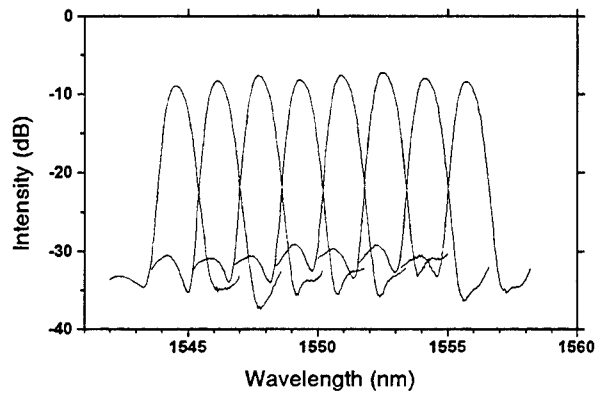

Fig.4 Measured transmission spectrum of the WDM- PON demultiplexer

Conclusions

We have proposed a novel integrated multichannel WDM-PON demultiplexer using an AWG and diffractive optical elements. The basic functions of distributing and multiplexing the light at 1.3-µm and 1.55-µm wavelength have been demonstrated. The device shows high functionality and good optical performances. It is expected, that this new device will find wide applications in WDM systems.

We would like to thank W. Fürst for data generation, R. Steingruber for writing the masks, and G. Urmann for the SEM measurements. This study was financially supported by the Federal Ministry for Education, Science, Research and Technology (BMBF) within the national project 01BS609 and by the city of Berlin.

References

1. W. J. Tomlinson, Appl. Opt., Vol. 16, pp. 2180-2194, 1977.
2. N. Takato et al., IEEE Photonics Techn. Lett., Vol. 2, pp. 441, 1990.
3. E. Pawlowski, The Society of Photo-Optical Instr. Eng., Vol. 2577, No. 28, 1995.
4. K.W. Cheung et al., Electron. Lett. Vol. 25, pp. 375, 1989.
5. E. Pawlowski et al., Electr. Letters, Vol. 32, No. 2, pp. 113-114, 1996.
6. M.K. Smit, Electronic Letters, Vol. 24, No. 7, pp. 385-386, 1988.
7. K. Okamoto et al., Electron. Lett., Vol. 31, pp. 184-185, 1995.
8. M. Kawachi, Opt. Quantum Electron., Vol. 22, pp. 391-416, 1990.
9. E. Pawlowski et al., Pure and Applied Optics, Vol. 6, No. 6, pp. 655-662, 1997.

Grating Coupler utilizing third-order Diffraction

Shogo Ura, Takayoshi Fujii, Toshiaki Suhara and Hiroshi Nishihara

Department of Electronic Engineering, Graduate School of Engineering, Osaka University
2-1 Yamada-Oka, Suita, Osaka 565, Japan
Tel. +81-6-879-7772, Fax. +81-6-877-3544

1. Introduction

A grating coupler [1,2] is useful for exciting a guided wave or taking out a guided wave into the air, and is one of the key components in constructing integrated optic devices [3]. A grating coupler utilizing higher-order diffraction has much longer grating period than that of a 1st-order grating coupler, and is attractive from a view point of fabrication and design flexibility especially for a case using a short wavelength or a high guided-mode index. However, a coupling efficiency of the usual higher-order diffraction is too low to be utilized in practical applications. We reported [4] a proposal and design consideration of a high-efficiency 3rd-order grating coupler for application to a GaAs/AlGaAs waveguide. In this report, an efficiency enhancement technique for 3rd-order grating coupler is demonstrated experimentally for the first time. Wavelength of 0.82μm and a glass waveguide are used for the demonstration.

2. Grating coupler configuration

A vector-diagram of a grating coupler utilizing higher-order diffraction is depicted in Fig. 1. Arrows represent grating vector and wavevectors of an input guided-wave and the diffracted radiation waves. Radii of upper half circle k_0 and lower half circle $n_s k_0$ indicate the wavenumber in the air and in the substrate, respectively. As an input guided wave propagates in the grating region, space-harmonic waves are generated by n-th order diffraction of the grating coupler. Wavevector component along x-direction (guided wave propagation direction) of the harmonic waves are expressed by

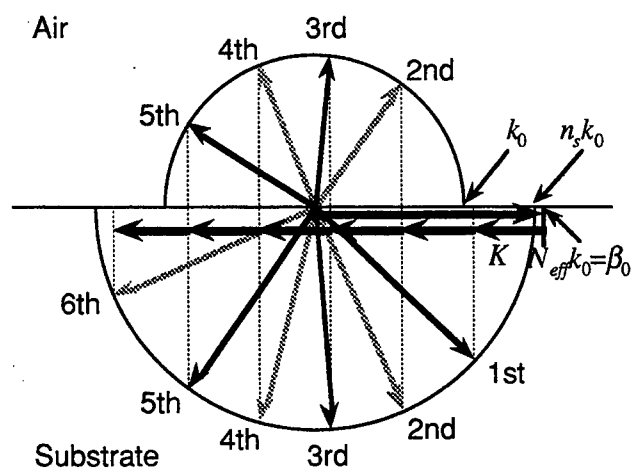

Fig. 1 Vector diagram of grating and waves.

$$\beta_n = \beta_0 - nK\,, \qquad (1)$$

where β_0 and K $(= 2\pi/\Lambda)$ denote the propagation constant of the guided wave and the grating vector size, respectively. The power distribution ratio to lower-order diffraction wave is usually higher. Since the size K in Fig. 1 is designed to be too small to generate the 1st-order air-radiation, most of the guided wave power is coupled to the 1st-order substrate-radiation wave.

We consider here an air-radiation wave generated by the 3rd-order diffraction as an output wave, and discuss how to increase the power distribution ratio to the output wave. A design

concept for the implementation is illustrated in Fig. 2. The substrate-radiation waves are reflected back and eliminated by a reflection metal layer inserted beneath the grating coupler. As to the 1st-order diffraction, another lossy complex waveguide, which is formed by the total internal reflection and the metal layer reflection, appears. Mode indices and the grating period should be designed not to meet a condition that the input guided wave couples to the lossy higher-order guided modes supported by the complex waveguide. For the 2nd-order and 3rd-order diffractions, interferences occur between a wave directly radiated from the grating coupler into the air and a wave radiated once to the substrate and then reflected by the metal layer into the air. A buffer layer thickness is optimized to enhance the 3rd-order air-radiation wave but cancel the 2nd-order air-radiation.

3. Design consideration

Specifications for fabrication are summarized in Table I. A Au film is used as the reflection layer beneath the grating coupler. Calculated dependences of the radiation decay factor α_r and the distribution ratios upon thickness of the optical buffer layer t_b are traced in Fig. 3. The factor α_r has peaks at 1.6μm and 2.0μm of t_b, indicating the coupling of the incident guided mode to the higher-order guided modes. The distribution ratios $\eta_n^{(i)}$ (i=a, s; denoting air- and substrate-radiations, respectively) vary periodically against the t_b with different periods depending on the radiation angles. The thickness t_b was determined to be 1.83μm to give the maximum distribution ratio $\eta_3^{(a)}$ of 60%.

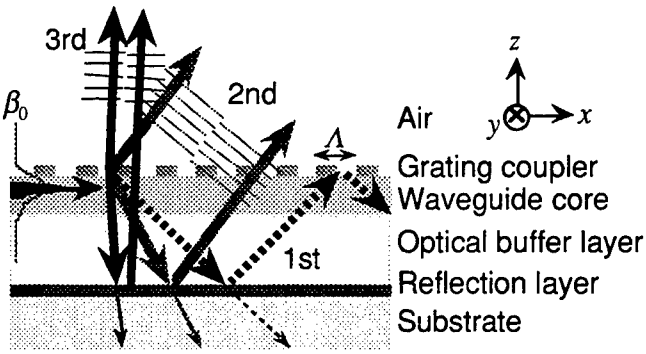

Fig. 2 Cross-sectional structure and effect of reflection layer.

Table I Specifications of the fabricated 3rd-order grating coupler

Light source	Wavelength	0.82μm	
Waveguide	TE_0 Mode index	1.49	
	Material	Index	Thickness
Grating layer	Si-N/Air	1.90/1	0.05μm
Guiding core	#7059 glass	1.54	0.53μm
Optical buffer	SiO_2	1.46	1.83μm
Reflection layer	Au	0.16+j5.06	0.04μm
Substrate	Pyrex glass	1.47	
Grating coupler	Period	1.86μm	
	Line/space	0.5	

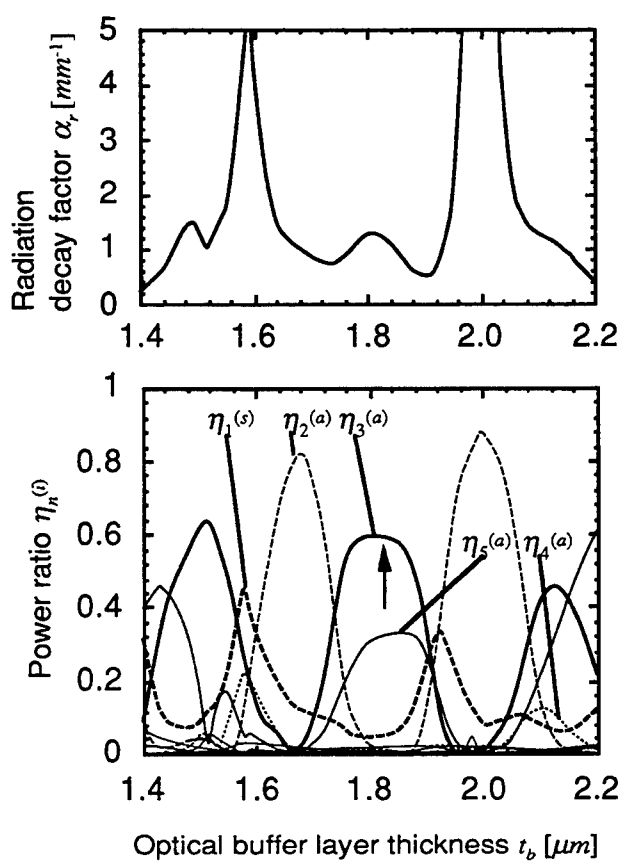

Fig. 3 Calculated dependences of radiation decay factor and power distribution ratios.

4. Experimental results

An SiO_2 buffer layer and a Corning #7059 glass core layer were deposited by RF-sputtering on a Au reflection layer evaporated on a glass substrate. A Si-N grating layer was deposited by plasma enhanced CVD. Grating patterns were written by electron-beam direct scanning in a resist and transferred to the Si-N layer by RIE. Coupling length L of the grating coupler was 2mm. Microphotograph of a part of the fabricated grating coupler is shown in Fig. 4.

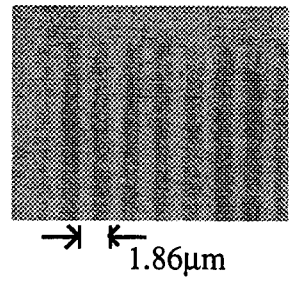

Fig. 4 Microphotogrph of the fabricated grating coupler.

A guided wave was launched by another grating coupler. The radiation decay factor α_r was measured to be 1.9mm^{-1}, by monitoring the radiation wave profile on the grating aperture as shown in Fig. 5. The air-radiation power was measured and compared to the guided-wave power. The guided wave power was estimated by using another pair of input and output grating couplers of 1st order diffraction on the same substrate with no Au reflection layer. The output coupling efficiency $\eta_3^{(a)}$ was 40%. Power distribution to other radiated waves into the air by 2nd-order and 4th-order diffractions were also measured to be 3% ($=\eta_2^{(a)}$) and 40% ($=\eta_4^{(a)}$), respectively. The lower $\eta_3^{(a)}$ and higher $\eta_4^{(a)}$ than the theoretical prediction can be explained to be a fabrication error in a groove-width ratio to grating-period from 0.5, because the $\eta_2^{(a)}$, $\eta_3^{(a)}$ and $\eta_4^{(a)}$ were calculated to be 0%, 40% and 35% for the ratio of 0.57, respectively, showing good agreement with experimental results.

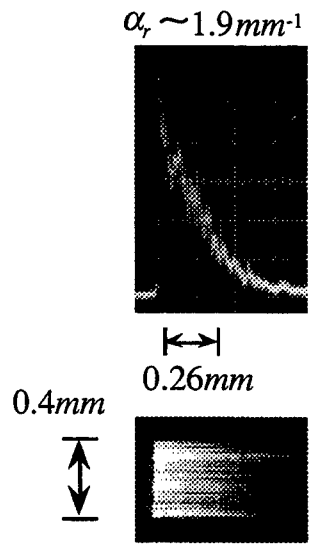

Fig. 5 Radiation decay of the guided wave.

5. Conclusions

A grating coupler utilizing the 3rd-order diffraction was designed and characterized. The grating period was 1.86μm for 0.82μm wavelength. A reflection film was introduced beneath the grating coupler to enhance the air radiation by 3rd-order diffraction as well as to reduce couplings by other diffractions. Output coupling efficiency was measured to be as high as 40%. The proposed configuration and design concept would be useful in constructing future integrated-optic devices using ultraviolet wavelength.

References

[1] M. L. Dakss, L. Kuhn, P. F. Heidrich and B. A. Scott, "Grating coupler for efficient excitation of optical guided waves in thin films", Appl. Phys. Lett., vol. 16, pp. 523-525, 1970.

[2] H. Kogelnik and T. P. Sosnowski, "Holographic thin film couplers", Bell Syst. Tech. J., vol. 49, pp.1602-1608, 1970.

[3] T. Suhara and H. Nishihara, "Integrated optics components and devices using periodic structures", J. Quantum Electron., vol. QE-22, pp.845-867, 1986.

[4] S. Ura, S. Kido, T. Suhara and H. Nishihara, "Design of high efficiency 3rd order grating coupler in semiconductor waveguide", 5th Optoelectron. Conf., 15B4-2, Chiba, July 12-15,1994.

Planar-integrated optical systems for pulse shaping

Markus Testorf
University of Massachusetts-Lowell, Department of Electrical Engineering
One University Ave., Lowell, MA 01854, USA
phone: (508) 934 - 3300; fax: (508) 934 - 3027; e-mail: markus.e.testorf@dartmouth.edu

Ulf Österberg
Thayer School of Engineering, Dartmouth College
8000 Cummings Hall, Hanover, NH 03766, USA

1. Introduction

The ability to influence the temporal shape of short optical pulses[1] provides access to many promising applications. For instance, high capacity optical fiber communication systems based on a wavelet decomposition of the available time-bandwidth product rely on a specific shape of the optical wavelets[2].

An important aspect to make pulse shaping applicable and attractive is the possibility to achieve robust and small scale packaging of the optical setup. In this paper we propose an integrated design based on planar-integrated free space optics[3]. This means, the entire pulse shaper is fabricated as a 2D diffractive optical structure on the surface of a thick transparent substrate. Besides the basic geometry of the integrated system we investigate the principle trade-off between the size of the system and the degrees of freedom to influence the pulse shape. We also discuss modified schemes which provide optimum access to the degrees of freedom planar-integrated optics provides.

2. Planar integration of pulse shaping setups

Fig. 1 shows the conventional scheme of a pulse shaping setup (see e.g. reference 4), which basically consists of a 4-f system. The first 2-f system, in combination with the diffraction grating in the object plane, acts as a spectrometer. In the Fourier plane a spatial filter shapes the spectrum, which corresponds to a modified shape of the optical pulse after all wavelength are recombined by the second 2-f system.

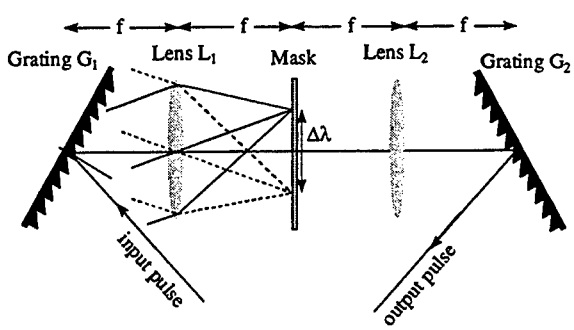

Fig. 1: Scheme of a conventional pulse shaper

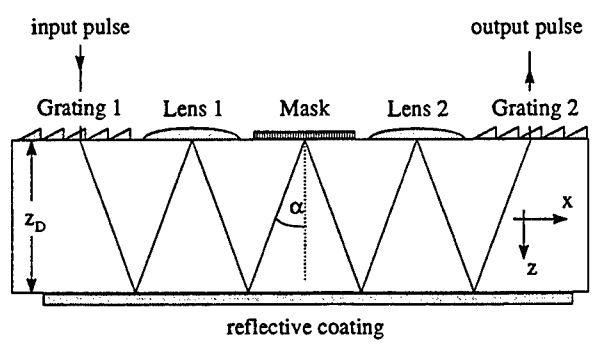

Fig. 2: Schematic planar-integrated system

A planar-integrated version of the setup in Fig. 1 is presented in Fig. 2. All elements are located at the top surface and the optical axis is folded into the plane parallel geometry of the glass substrate. Besides the gratings G_1 and G_2 all elements are working in reflection. The physical parameters of the integrated setup can be estimated from published values of existing configurations. In reference 5 a pulse shaper for picosecond pulses (wavelength λ=1.06μm; spectral width $\Delta\lambda$=4nm) is described. The color separation was performed by diffraction gratings with 1200 lines/mm and the spectrum was dispersed over a range of 7mm in a distance of about 1.5m. The resolution in the filter plane was 300μm, i.e. about 25 features could be accessed.

If this setup is scaled by a factor of 100, preserving wavelength and grating period the planar setup in Fig. 2 can be integrated on a substrate with a thickness of about 5 to 10mm. This matches typical values of planar optics. The grating frequency equals a period of about $d_g = 0.8\mu m$, which can be achieved by photo-lithographic techniques. The spectrum now covers a range of about 70μm. To provide the same number of features as in the large scale setup a resolution of the spectrum of 3μm and thus a Fourier transformation lens with $F_\# = 2.2$ is required. If a diffractive lens is considered the smallest features have to be equal to the resolution in the mask plane and thus can be also fabricated by standard methods.

3. Design considerations on the planar-integrated spectrometer

The key device of the pulse shaping setup is the spectrometer. Its spectral resolution determines the number of accessible features for shaping the optical pulse. The combination of a diffraction grating and a refractive-reflective lens, in Fig. 2, is well suited to obtain the spectrum in the mask plane with good resolution. This is even true if the lens is of cylindrical symmetry in the x-y plane. Astigmatism in the y direction can be tolerated because the optimum spectral resolution must be only achieved in one direction. However, a correcting element in the second spectrometer (Figs. 1 and 2) is necessary if a collimated output beam is desired.

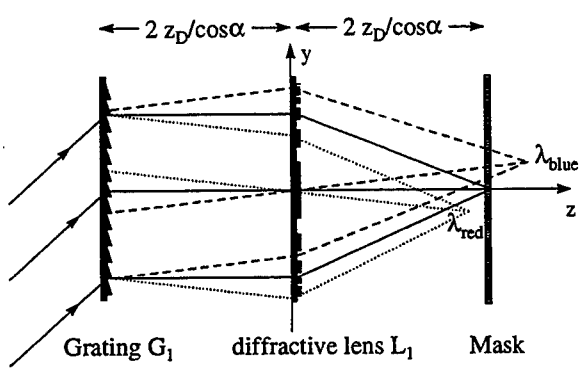

Fig. 3: Unfolded geometry of the spectrometer.

While in principle a planar optical system with both refractive and diffractive elements can be fabricated[6], one of the advantages of planar optics is the fabrication of the entire system as a single diffractive structure. In Fig. 3 the unfolded 2-f setup now contains a diffractive lens and the spectral spread is obtained in the y-direction. In Fig. 2 grating and lens aperture are bounded by the planar geometry, while in Fig. 3 only the lens aperture is limited by the fabrication constraints. This also means, that the resolving power of the spectrometer is determined by the $F_\#$ of the lens rather than by the number of grating lines. The deflection angle α, necessary to separate input and output signal, are now independent from the diffraction angle of G_1 and G_2 and can be e.g. achieved by an oblique incident direction of the signal. The setup in Fig. 3, suffers from chromatic aberrations. The optimum lens shape for this configuration can be obtained as a weighted average of the ideal phase functions for all wavelength[7]. If we assume that the power spectral density S(λ) is a measure for the strength a wavelength contributes to the final pulse shape we can construct the optimum paraxial phase function of the lens:

$$\varphi_{opt} = -\pi \frac{\cos\alpha}{2z_D}\left(x^2\cos^2\alpha + y^2\right)\frac{\int_0^\infty \frac{S(\lambda)}{\lambda}d\lambda}{\int_0^\infty S(\lambda)\,d\lambda} \tag{1}$$

where the local frequency of the corresponding diffractive lens then is proportional to the gradient of the phase. For a rectangular spectral window the ray optical spread of a point in the mask plane depending on the wavelength λ can be estimated from Eq. (1) as

$$\Delta D(\lambda) = \frac{1}{F_\#}\frac{2z_D}{\cos\alpha}\left(\lambda\frac{\ln\lambda_{max} - \ln\lambda_{min}}{\lambda_{max} - \lambda_{min}} - 1\right) \tag{2}$$

where λ_{min} and λ_{max} are minimum and maximum wavelength of the spectrum, respectively. For a $F_\#$=2.2 lens and $2z_D/\cos\alpha$ = 7mm, assuming a center wavelength $\lambda_0 = 1.06\mu m$ and spectral width $\Delta\lambda = \lambda_{max} - \lambda_{min} = 4nm$ we get a maximum value of about $\Delta D = 6\mu m$, i.e. the resolution is limited by the chromatic aberrations of the diffractive lens.

On the one hand, Eq. (2) indicates, that the resolution which can be achieved by an entirely diffractive setup still provides enough resolution for pulse shaping. One the other hand, it shows that further optimization for an diffractive optics design is necessary. Besides the possibility to make use of the entire three dimensional geometry of planar optics, effective optimization can be performed with additional *a priori* knowledge of the input pulse shape. For instance, the lens can be optimized to resolve a limited number of wavelengths tolerating a derogated resolution for any other part of the spectrum. As a third alternative the mask structure can be part of the spectrometer setup. This means, instead of compensating the chromatic aberrations, they can be used to specifically select wavelengths which are focused on an opening in an amplitude mask structure, while all other wavelength are damped. This refers to the concept of matched spectroscopy. A planar-integrated scheme for matched spectroscopy was demonstrated recently[8].

4. Degrees of freedom for shaping optical pulses

From the results of our discussion we now estimate the number of features we can influence in the power spectrum and hence the pulse shape. This number is given as the ratio of the lateral spread Δx in the mask plane and the spot size. As long as the spot size is diffraction limited we get

$$N_d = \frac{\pi}{4 d_g F_\#} \frac{2 z_D}{\cos\alpha} \frac{\Delta\lambda}{\lambda} \tag{3}$$

while assuming the chromatic error to dominate the spot quality Eq. (2) we obtain

$$N_r = \frac{F_\#}{d_g} \frac{\Delta\lambda}{\lambda \frac{\ln\lambda_{max} - \ln\lambda_{min}}{\Delta\lambda} - 1} \tag{4}$$

for a rectangular spectral distribution. Eqs. (3) and (4) formulate a trade-off between diffraction and ray optical performance both dictated by the $F_\#$ of the lens. To decrease the influence of the chromatic aberrations the $F_\#$ has to be increased. For the diffraction limit, this can only be compensated by a larger propagation distance $2z_D/\cos\alpha$, and thus, with some freedom in the design, by a larger size of the system.

5. Conclusion

We have proposed a planar-integrated free-space optics as a possibility to design a compact optical system for pulse shaping applications. While a straightforward extrapolation of published results indicates that the performance of the integrated system is comparable to conventional systems, we encountered the resolution of the spectrometer as the critical parameter. For the integrated setup this resolution is dictated by the $F_\#$ of the lens. In particular an entirely diffractive design suffers from significant chromatic aberrations. It turns out, that for a given light signal this corresponds to a trade-off between the size of the system and the number of features accessible to influence the optical short pulses. Our preliminary considerations illustrate that further optimization of the diffractive optical elements is necessary. For applications like optical communication systems, additional properties have to be investigated, for instance the intensity loss of the signal passing the optical system.

References

1. A. M. Weiner, Prog. Quantum Electron. **19**, 161-237 (1995).
2. T. Olson, D. M. Healy, U. Österberg, R. T. Prosser, Proc. SPIE Vol. 2569, A. F. Laine, M. A. Unser, M. V. Wickerhauser, eds., 576-588 (1995).
3. J. Jahns, A. Huang, Appl. Opt. **28**, 1602-1605 (1989).
4. M. M. Wefers, K. A. Nelson, IEEE J. Quantum Electron. 32, 161-172 (1996).
5. A. M. Weiner, J. P. Heritage, J. A. Salehi, Opt. Lett. 13, 609-611 (1985).
6. Z. Zhou, T. J. Drabik, Appl. Opt. 34, 3048-3054 (1995).
7. J. N. Cederquist, J. R. Fienup, J. Opt. Soc. Am. A **4**, 699-705 (1987).
8. S. Sinzinger, V. Arrizon, J. Jahns, Proc. SPIE Vol. 3002, E. Fred Schubert, ed., 186-189 (1997).

Diffractive Optics and Micro-Optics

Theory 2

Tuesday, June 9, 1998

Lifeng Li, University of Arizona
Presider

DTuA
8:30am–10:00am
Koa Room

Symmetry of the field transmitted by periodic metallic grids

A. Sentenac[#] and D. Maystre[$]

[#]*Laboratoire d'Optique des Surfaces et des Couches Minces,* [$]*Laboratoire d'Optique Electromagnétique,*

Université de St Jérôme, 13 397 Marseille.

E-mail : anne.sentenac@enspm.u-3mrs.fr, *Tel : (33) 4 91 28 87 14. Fax : (33) 4 91 28 80 67*

The symmetry properties of the diffracted orders of gratings in the resonance domain are frequently used in diffractive optics [1]. For example, a beam-splitter element or star coupler (fan-out to N) is obtained with a grating that produces N equal-efficiencies diffraction orders. In general, those gratings are synthesized by using a parametric optimization algorithm combined to rigorous electromagnetic theory. Their shape is then precisely defined. However, in certain cases, the identity of the values of the transmitted efficiencies stems from simple considerations on the symmetry of the field at the bottom of the grid and it does not require drastic specifications on the motif of the grating. It is shown in [2] that lamellar perfectly conducting gratings produce two symmetric transmitted orders with equal amplitude if they are illuminated under -1 Littrow mounting and if the width a of the groove satisfies $\lambda/2<n_g a<\lambda$ in s-polarization and $n_g a < \lambda/2$ in p-polarization, (where λ is the wavelength of the incident beam, n_g is the refractive index of the material filling the groove, n_1 and n_2 are the refractive indices of the superstrate and substrate, respectively, see Fig. 1).

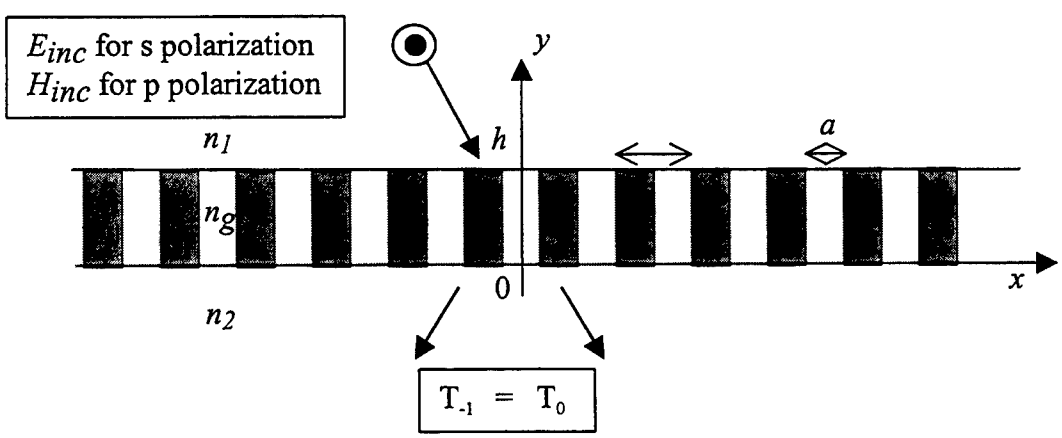

Fig. 1 : Geometry of a one-dimensional grid

Indeed, when the groove width satisfies the conditions written above, the modal expansion of the field inside the through-holes is the sum of a unique symmetric propagative mode and an infinite set of evanescent modes. For example in s-polarization, the field can be written as

$$E(x,y) = \sum_{p=1}^{\infty} [A_p \exp(i\gamma_p y) + B_p \exp(-i\gamma_p y)] \sin[p\frac{\pi}{a}(x + a/2)]$$

with $\gamma_p = \sqrt{(n_g \frac{2\pi}{\lambda})^2 - (p\frac{\pi}{a})^2}$.

It is seen that when $\lambda/2 < n_g\, a < \lambda$, γ_p is real for $p = 1$ and imaginary for $p > 1$. When the height h of the groove is increased, the influence of the exponentially decaying evanescent modes, on the field *at the bottom of the through-hole,* lessens. Thus, the field at $y = 0$ and $-a/2<x<a/2$ can be approximated by the values of the fundamental symmetric propagative mode. The pseudo-periodicity of the problem is then invoked to determine the field throughout the whole plane at $y = 0$. The domination of the symmetric (with respect to 0y) fundamental propagative mode at the bottom of the groove, combined with the symmetry of the incident field (that is obtained when the angle of incidence θ_{inc} corresponds to a N-littrow position, $n_1\ 2\pi/\lambda\ \sin(\theta_{inc})=-N\ \pi/d$ with N integer) yields the symmetry of the transmitted orders. Hence, under –1 Littrow mount, one can obtain two transmitted orders with equal amplitudes if h is important enough.

We have extended this analysis to bi-periodic rectangular perfectly conducting grids (Fig. 2).

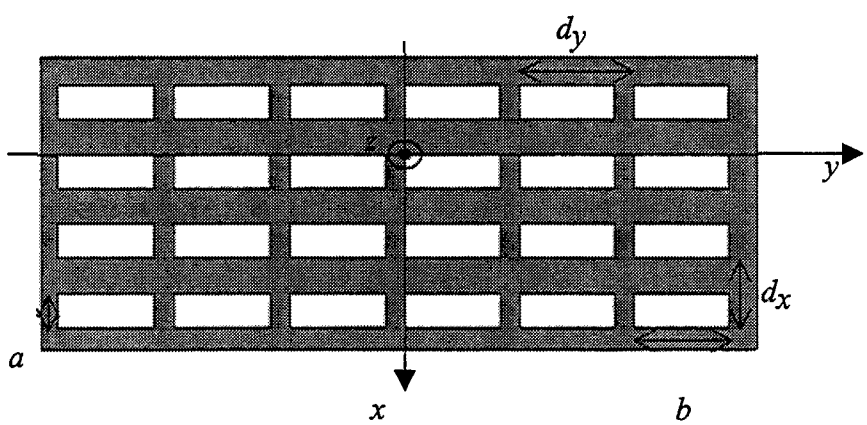

Fig. 2 : Top-view of a bi-periodic rectangular grid

We expand the field inside the through-holes into an infinite series of TE and TM modes and we show that if $n_g b < \lambda < 2n_g b$ and $\lambda > 2n_g a$, (note that $a < b$), there is only one propagative mode, the TE_{01} mode that is written as,

$E_x(x,y,z) = A \sin(y\pi/b) \exp(i\gamma_{01}z)$, $E_y = 0$, $E_z = 0$, with $\gamma_{01} = [\,(2\pi\, n_g/\lambda)^2 - (\pi/b)^2]^{0.5}$.

This mode is symmetric with respect to $0x$ and $0y$. Hence, if the height of the bi-grating is important enough so that the evanescent modes are negligible at the bottom of the grid, and, if the illumination is also symmetric with respect to both axes, the transmitted orders will be symmetric. Under (-1,-1) Littrow mounting, one gets four transmitted orders with equal efficiencies.

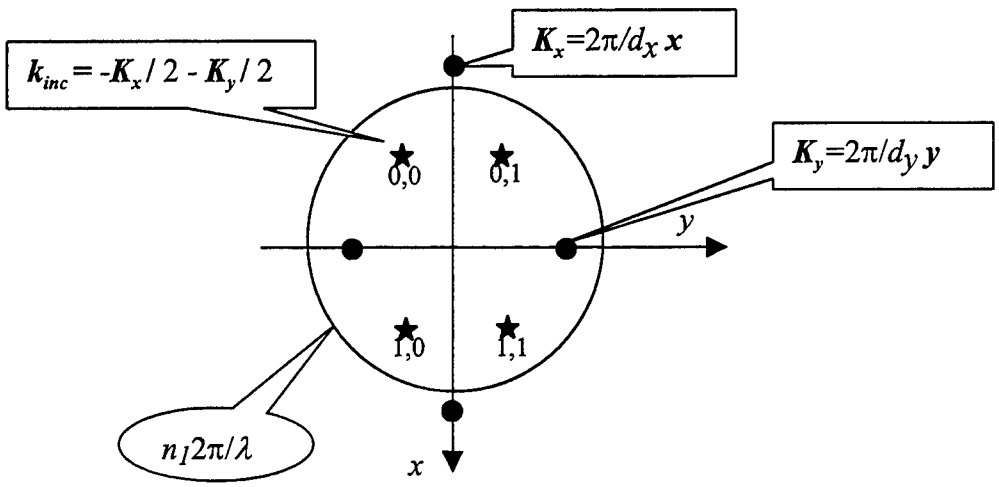

Fig. 3 , Representation in the k-space of the (-1,-1) *Littrow position that leads to 4 symmetric transmitted orders* (★), (0,0), (1,0),(0,1), (1,1).

A study of the coupling between the fundamental mode of the through-holes and the incident field enables to optimize the polarization and the shape of the grid to increase the transmittance of the structure. This model permits also to get a simple analytical expression of the transmitted near field and to calculate the distribution of the electric intensity below the grid. This last point is important if the grid is to be used as a mask in the framework of high-frequency grating duplication by 'photomask self-interference' technique [3].

[1] E. Noponene, A. Vasara, A. Turunen, J. Miller and M. Taghizadeh , J. Opt. Soc. Am. A **9**, 1206-1213 (1992)

[2] A. Sentenac and D. Maystre, to appear in Journal of Modern Optics (1998)

[3] F. Montiel and M. Nevière, J. Opt. Soc. Am. A **13**, 1429-1438 (1996)

Electromagnetic analysis of waveguide Bragg reflectors

Pasi Vahimaa and Jari Turunen

Department of Physics, University of Joensuu, P.O. Box 111, 80101 Joensuu, Finland
Phone +358 13 251 3209; fax +358 13 251 3290; e-mail jari.turunen@joensuu.fi

Bragg gratings are used extensively in fiber and integrated optics as, e.g., input/output couplers and semiconductor-laser mirrors.[1] Typically these devices are analyzed using coupled-mode methods,[2] which are reasonably accurate at least for weakly modulated structures. However, such methods can not model out-of-plane scattering or the effect of grating irregularities. In this paper we model distributed-feedback Bragg reflectors using a rigorous electromagnetic formalism adapted from the theory of conventional gratings much as described in Ref. 3. The method facilitates precise analysis of practically any waveguide grating structure, even in the presence of irregularities introduced, e.g., by fabrication errors.

Figure 1 illustrates the geometry to be considered in this paper. A guided mode is incident on the Bragg grating with N periods (length d) from the left. Here the grating is assumed to be of binary surface-relief type, with modulation depth h, but other surface profiles and index-modulated gratings could be treated as well. In the analysis we replace the true waveguide structure with a periodic structure of period P, which permits us to employ rigorous diffraction theory of multi-level gratings.[4] Rayleigh expansions are used to represent the incident, reflected and transmitted guided modes in the non-modulated waveguide regions, pseudoperiodic Fourier expansions (in the x-direction) are used in the modulated regions, and all expansions are matched at the boundaries in the z-direction. To obtain accurate field representations one must use a sufficiently large period P. This can be checked by comparison of the Rayleigh expansions with the analytic modal-field solutions, and also by observation of the convergence of the results when the period d is increased. To prevent the leakage of the radiation field from neighboring grating periods we assume an artificial absorbing layer (a smoothly varying complex refractive-index distribution) between the periods.

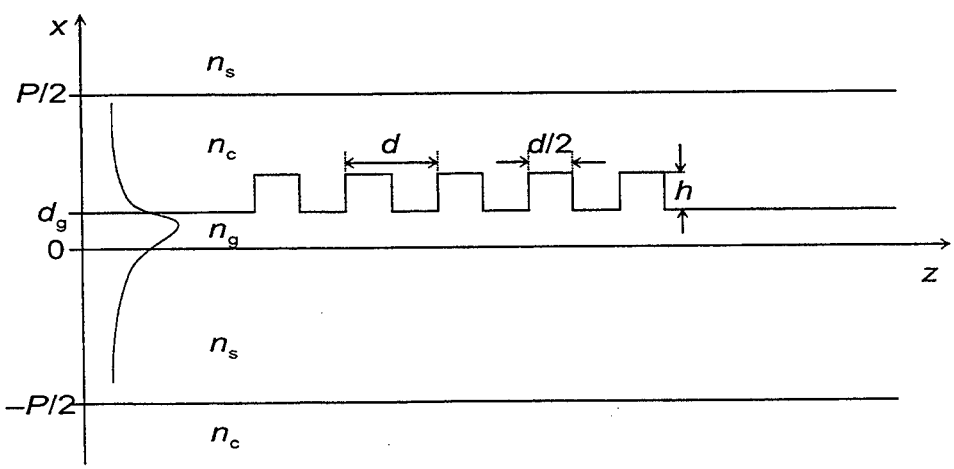

Figure 1: Geometrical configuration: incidence of a guided mode on a surface-relief-type waveguide Bragg grating.

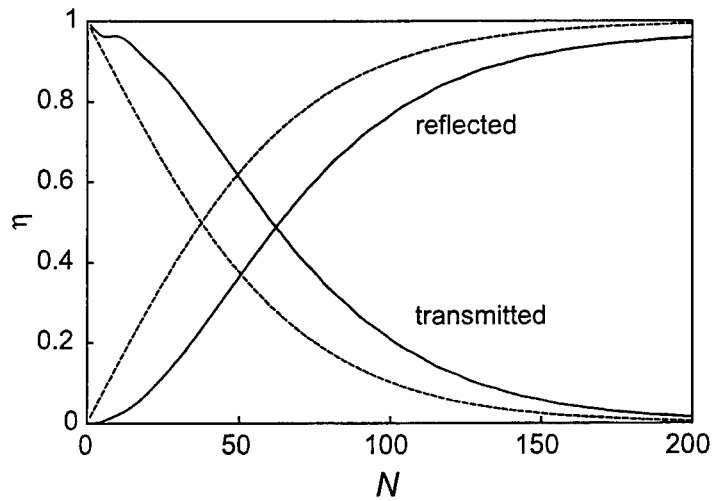

Figure 2: Efficiencies of the reflected and transmitted guided modes as a function of the number of grating period N (solid lines). The dashed lines give the efficiencies of an equivalent film stack.

An example of the results obtained is presented in Fig. 2. Here we consider a regular grating with the following parameters: $d = 0.295\lambda$, $h = 0.1\lambda$, $d_g = 0.5\lambda$, $n_c = 1$, $n_g = 1.8$, $n_s = 1.5$, and $P = 11.5\lambda$, where λ is the optical wavelength in vacuum. The non-modulated waveguide is single-mode and the effective refractive index for the incident mode is $n_{\text{eff}} = 1.683$. The solid lines give the fraction of incident-mode power that appears in the reflected and transmitted guided modes, as a function of the number of grating periods N. As expected, with a sufficiently large N, nearly all of the incident power is reflected. At $N = 200$, the sum of the reflected and transmitted efficiencies is 97.4% — the rest of the incident power is scattered into the radiation field.

The dashed lines in Fig. 2 are predictions of the standard theory of dielectric stratified media[5] for an "equivalent" thin-film stack, which is constructed by assuming that longitudinal refractive-index distribution of the (laterally infinite) thin-film stack is the same as the distribution of effective refractive index of the fundamental mode in the waveguide Bragg grating. This equivalent film stack is illuminated by a normally incident plane wave. It is seen that, although there are clear differences between the exact method and the equivalent-film-stack approximation, the latter gives a good idea of the number of grating period N needed to obtain a high reflection efficiency.

Our approach facilitates straightforward modeling of the effects of fabrication errors in the reflectance of waveguide Bragg gratings. To illustrate this, we model in Fig. 3 the effect of stitching errors in electron beam lithography on the performance of the Bragg grating considered above, with $N = 200$. We model the stitching error by assuming a gap of width w between blocks of 50 grating periods — with $N = 200$ three such gaps are introduced. The size of the block is chosen rather arbitrarily and typically the scan field of electron beam pattern generators is larger than this. However, in the most precise mode of operation of the Leica LION LV1 lithography system available to us at the University of Joensuu the scan field is 23 μm $\times$ 23 μm, which is close to the value assumed here.

The solid curve in Fig. 3 is the result of equivalent-film-stack analysis and the open circles represent results obtained by the exact approach outlined above. It is seen that the equivalent-film-stack model again gives a fairly good idea of the performance that may be expected: the reflectance remains very satisfactory for values smaller than $w \sim 0.25d$, but a catastrophic failure in the form of destructive interference occurs when $w \approx 0.3d$.

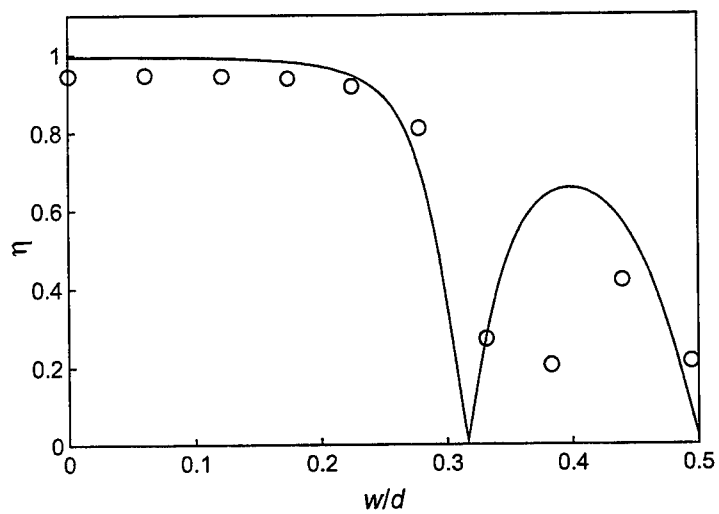

Figure 3: Effect of stitching error in the reflectance of a waveguide Bragg grating with 200 periods. Solid line: equivalent-film-stack method. Circles: exact electromagnetic analysis.

We stress that the method discussed in this paper permits accurate analysis of waveguide Bragg reflectors regardless of the strength of modulation or the number of grating periods since no approximations were made other than the pseudoperiodic representations of continuous field modes. The method also permits the analysis of chirped waveguide gratings, as well as the evaluation of the spectral performance of waveguide gratings. Furthermore, analysis of pulsed fields and therefore studies on pulse compression are possible if a Fourier representation of the pulse[6] is employed.

References

1. S. T. Peng, T. Tamir, H. L. Bertoni, IEEE Trans. Microw. Theory Tech. **MTT-23,** 123 (1975).
2. H. Nishihara, M. Haruna, T. Suhara, *Optical Integrated Circuits* (McGraw-Hill, New York 1985).
3. T. Hosono, T. Hinata, A. Inoue, Radio Science **17,** 75 (1982).
4. J. Turunen, chapter 2 in *Micro-optics* (Taylor & Francis, London, 1997).
5. M. Born and E. Wolf, Principles of Optics (Pergamon, Oxford, 1980).
6. L. Sereda, A. Ferrari, M. Bertolotti, Pure Appl. Opt. **5,** 349 (1996).

Numerical Simulation of Binary Lenses by Direct Solution of the Helmholtz Equation

G. Ronald Hadley
MS 0603
Sandia National Laboratories
Albuquerque, New Mexico 87185-5800
(505)844/4015
(505)844/8985 (FAX)
grhadle@sandia.gov

Binary diffractive optics have become an important class of structures for use in optical interconnects and coupling into fibers[1]. Such structures have been successfully designed in the past using the techniques of Fourier analysis. These techniques are entirely adequate for near-paraxial optics such as occur with high-F-number lenses. The design of fast (F<1.5) lenses such as those required for coupling light into optical fibers, however, requires the use of more accurate techniques, most of which are based upon modal expansions[2,3]. In this paper we describe a new finite-difference method for modeling small-feature-size binary optical structures that involves the direct solution of the scalar Helmholtz Equation in the vicinity of the structure, followed (in the case of lenses) by wide-angle beam propagation to predict the size of the focal spot. In this approach, the structure is described entirely by by its resulting dielectric function, allowing the treatment of aperiodic binary structures of arbitrary complexity. All reflections together with effects due to sub-wavelength feature sizes are automatically included. Polarization effects are treated approximately owing to the use of semivectorial boundary conditions at all dielectric interfaces. This technique has been shown previously[4] to correctly model the behavior of first- and second-order diffraction gratings etched into waveguides. (The present method differs slightly from that described in reference 4 in that the solution method is direct matrix inversion instead of the iterative method described therein.) It involves no expansions or simplifying assumptions (aside from vectorial considerations) and is quite fast, requiring only a few minutes of workstation runtime.

As an illustration of the application of this technique, we model the performance of an 8-level binary focusing lens in GaAs with 80 μm diameter and 110 μm focal length (F1.4) at a wavelength of 980 nm. The cylindrically-symmetric problem geometry (shown in Fig.1) consists of an absorbing region followed by the lens structure and an air diffraction region. An input Gaussian (defined at the bottom boundary) propagates through the absorber towards the

binary lens boundary, and then into the air region. Light reflected from the dielectric-air interface is absorbed during its double pass through the absorber to keep it from further interacting with the lens structure. The top boundary condition is a fourth-order wide-angle BPM to prevent reflections back into the problem region. The air region was kept sufficiently thick so that evanescent fields would not appear at the top boundary. The resulting amplitude contours for the design wavelength (980 nm) are shown in Fig. 2. The standing wave pattern is clearly visible in the dielectric, but otherwise the contours in the air region are complicated, revealing a complex interference between waves scattered from different parts of the lens.

The computed field at the top boundary is finally input into a fourth-order wide-angle BPM calculation to compute the field profile near the focal spot. Repeating the above procedure for a variety of input wavelengths results in the spectral plot (shown in Fig. 3) of the fraction of energy passing through a 20 μm aperture at the focal spot as a function of wavelength. The focal length for these calculations varied with wavelength, but remained within 20% of the design value of 110 μm. As Fig. 3 shows, this structure is predicted to have a broad bandwidth, a desirable feature for a lens intended to operate over a wide range of conditions.

In conclusion, we have described a new technique for the simulation of sub-wavelength binary optical structures. The technique is applicable for fast optics in which shadowing effects may be important, and sufficiently general to allow the modeling of a wide range of aperiodic structures having cylindrical symmetry. Intended future applications include binary reflective and anti-reflective coatings.

1. M. E. Warren, T.C. Du, J. R. Wendt, G. A. Vawter, K. L. Lear, S. P. Kilcoyne, R. F. Carson, P. K. Seigal, M. H. Crawford, H. Hou and R. P. Schneider, "Integration of Diffractive Optical Elements with Vertical-Cavity Surface-Emitting Lasers", Proceedings of Diffractive Optics and Micro-Optics Topical Meeting, April 29-May 2, 1996, Boston, MA, paper DMD2-1.
2. E. Noponen, J. Turunen and A. Vasara, "Electromagnetic theory and design of diffractive-lens arrays", J. Opt. Soc. Am., Vol 10, 434(1993).
3. J. Yamakita, K. Rokushima and S. Mori, "Numerical Analysis of Multistep Dielectric Gratings", Proc. of SPIE Vol. 815 Application and Theory of Periodic Structures, Diffraction Gratings, and Moire Phenomena III, p. 153(1987).
4. G. Ronald Hadley, "Numerical simulation of reflecting structures by solution of the two-dimensional Helholtz equation", Opt. Lett. Vol. 19, 84-86(1993).

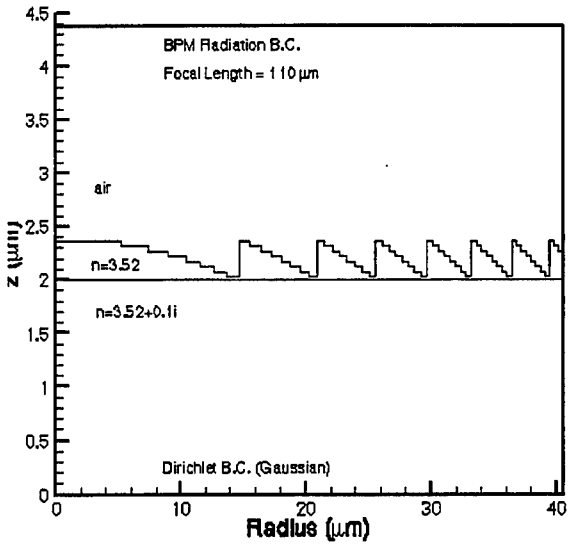

Figure 1. Problem geometry for 8-level lens simulation

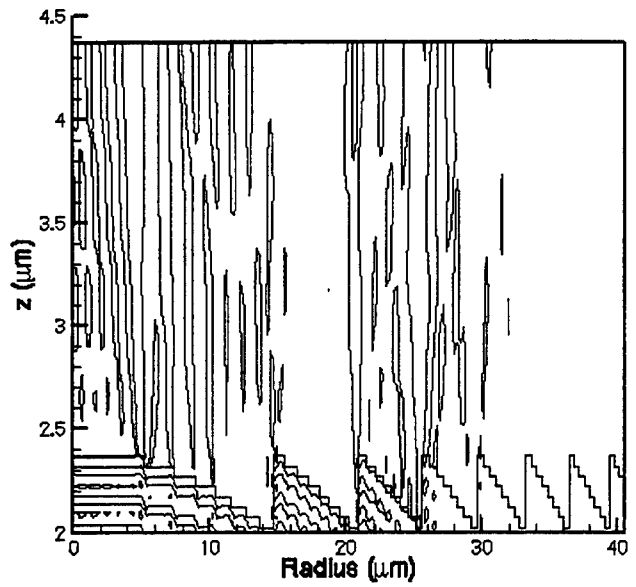

Figure 2. Amplitude contours for solution at the design wavelength (980 nm).

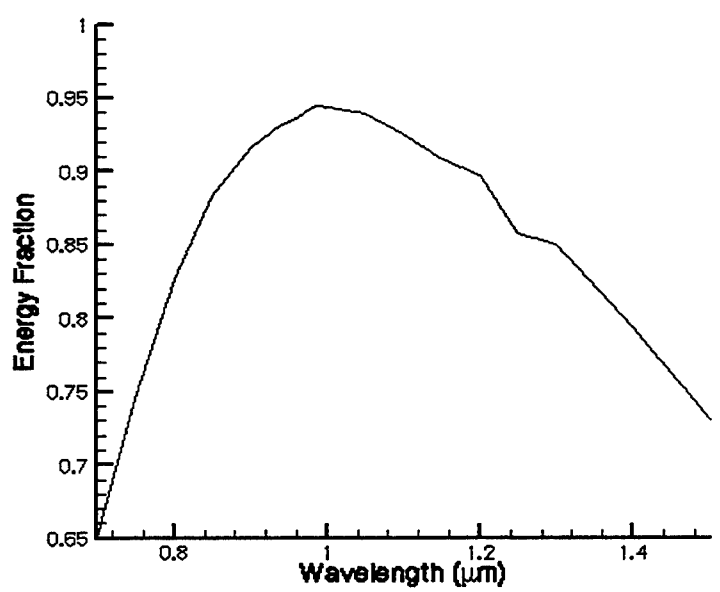

Figure 3. Fraction of light passing through a 20-μm pinhole at the focal plane for the lens structure shown in Fig. 1 as a function of input wavelength.

Analysis and modeling of nonparaxial diffractive optical elements on curvilinear surfaces

Michael A. Golub, Israel Grossinger

(Holo-Or, Ltd., Kiryat Weizmann, P.O.B. 1051, Rehovot 76114, Israel,
tel: 972-8-9409687, fax: 972-8-9409606)

1. Problems with curvilinear-substrate DOEs

Increasing possibilities of precision diamond turning and lithography bring to reality diffractive micro-relief on spherical, aspherical and other curvilinear surfaces. Contact lenses, plastic aspherical, and collimator lenses, aberration correction plates on ZnSe and other materials give the practical examples. Creation of means for design and computer modeling of curvilinear-substrate DOEs are felt essential.

Computer simulation of diffractive optical elements (DOEs) that obey scalar diffraction theory, is traditionally done by Fourier and Fresnel transform under assumption of plane substrate surface[1,2] and paraxial approximation. Nonparaxial Fourier integral[3] on the planar surface is a convolution type integral that still can be brought to a couple of Fourier transforms. However there are interesting cases of DOEs with diffractive microrelief created on the curvilinear surface (Fig.1). In this report we propose "small output spot" approximation approach that brings nonparaxial Kirchhoff integral on steep curved surface to one Fourier transform. *One more problem* is the simultaneous analysis of several diffraction orders created by DOE inside multi-lens optical systems and objectives.

2. Nonparaxial Kirchhoff integral for DOEs on curvilinear substrate surface

We will use Cartesian 3-D coordinate system centered at the vertex O of surface Λ with z-axis along optical axis (Fig. 2). Let's denote $\mathbf{u}=(u,v)$ transverse Cartesian coordinates of the current point $(\mathbf{u},H)$ on the surface Λ where $z=H(\mathbf{u})$ is the equation for surface Λ. Refractive index n_{kirch} of the media after Λ is given. Phase function $\Phi(\mathbf{u})$ of diffractive microrelief is also given on the surface Λ.

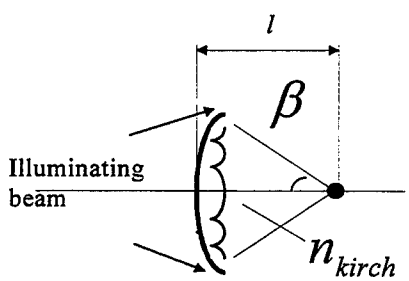

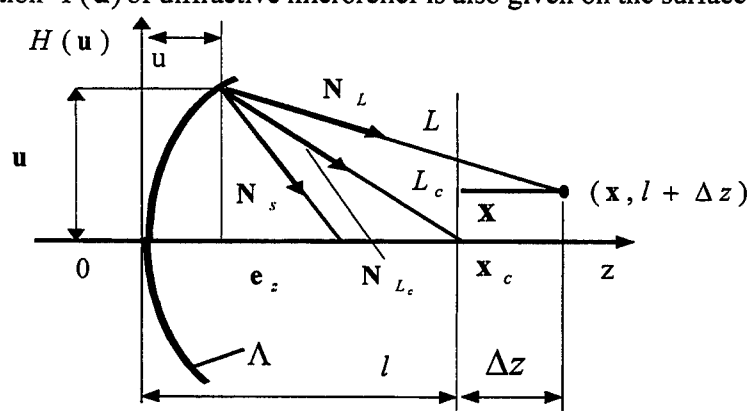

Fig. 1. General scheme for diffraction Fig. 2. Detailed scheme for diffraction on curvilinear surface

We suppose that the light field is concentrated around some center of observation with coordinates $(\mathbf{x}_c,l)$. Thus we have here a small parameter: output spot size is small compared to the focal length. The task is to calculate light field w not only exactly at the point $(\mathbf{x}_c,l)$ but also for the points $(\mathbf{x}_c,l+\Delta z)$ in vicinity of the center $(\mathbf{x}_c,l)$ (See Fig. 2). After a series of transformations with a small-spot approximation for light diffraction on microrelief and substitution of variables we brought the Kirchhoff integral to a single Fourier transform. The substitution is nonlinear, because the distances depend on $\mathbf{u}$. The intensity $I_0(\mathbf{u})$, eikonal $S_0(\mathbf{u})$, and the DOE phase function $\Phi(\mathbf{u})$ can be required

nonsymmetrical functions. Below H' - derivative of H with respect to r, E_{sph} -total power of incident spherical beam converging into the center $\mathbf{x}_c$ of watching points, S_{sph} - square of the sphere with radius l within the optical aperture of base surface, $k = 2\pi / \lambda$, λ wavelength,

$$l_H = l - H + \Delta z\ , \quad L_{c\Delta z} = \sqrt{(l + \Delta z - H(\mathbf{u}))^2 + (\mathbf{x}_c - \mathbf{u})^2} \quad , L_c = \sqrt{[l - H(\mathbf{u}]^2 + (\mathbf{x}_c - \mathbf{u})^2} \qquad (1)$$

Spatial frequencies, coordinates and equivalent focus parameters are defined by the relations:

$$\nu = \frac{n_{kirch}}{\lambda}\frac{\mathbf{u}}{L_{c\Delta z}}; \quad \nu = \frac{n_{kirch}}{\lambda}\frac{r}{\sqrt{l_H^2 + r^2}} \nu = |\nu|, r = |\mathbf{u}| \quad , \quad f_{def} = \frac{(l_H + L_{c\Delta z})(l - H + L_c)}{2\Delta z\left[1 + \frac{l + \Delta z/2 - H}{(L_{c\Delta z} + L_c)/2}\right]} \qquad (2)$$

The Kirchhoff integral takes the form:

$$w(\mathbf{x}, l + \Delta z) = \sqrt{\frac{E_{sph}}{S_{sph}}}\frac{\lambda l \exp(ikn_{kirch}\Delta z)}{n_{kirch} i}\int\sqrt{I_0(\mathbf{u})}\exp[ikS_0(\mathbf{u}) + i\Phi(\mathbf{u})]$$
$$K(\mathbf{u}, 0, \Delta z)\frac{L_{c\Delta z}^3}{L_c l_H}\frac{\sqrt{1 + |(H')|^2}}{|l_H + r\ \ H'|}\exp[-i2\pi\frac{\lambda}{n_{kirch}}\frac{L_{c\Delta z}^2}{2f_{def}(\mathbf{u}, \Delta z)}\nu^2]\exp[i2\pi\nu\mathbf{x}]d^2\nu \qquad (3)$$

Tilt factor is given by rather complicated equation depending on wavelength, spatial frequencies, surface shape and geometry. Equation (3) opened us the possibility of computer simulation in the case of curvilinear nonparaxial surface of DOE. All the algorithms were implemented as the programs written by the author in C++ object-oriented programming language. Some of the results of simulation are presented on the pictures Fig. 3-4. Three foci could be seen at once, with proper scale of intensity for each.

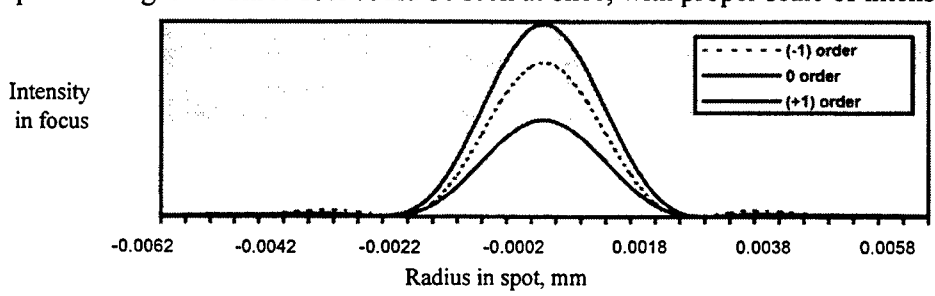

Fig. 3. Simulated focal intensity distribution in multifocal lens

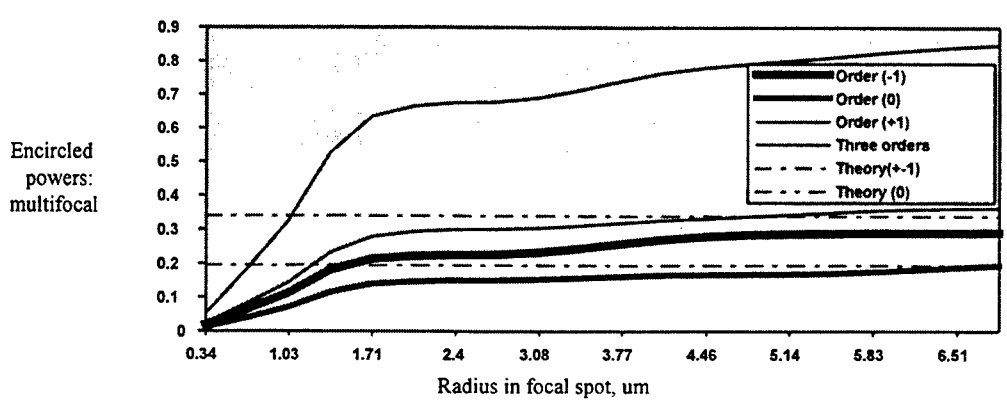

Fig. 4. Encircled powers for multifocal lens simulation in eye model (4 mm diameter)

3. Considering several diffraction orders in multilens optical system

Diffractive microrelief is usually described by its special phase function for each diffractive order. Then each order is treated separately by ray-tracing in routine way [4] without consideration for any interaction between diffraction orders. So far, defocused images of other orders will not be superimposed on the order of interest in the simulation. For proper description of all orders we must really describe diffraction on microrelief. But for this we must interrupt ray tracing on the surface with microrelief. The problem arise: how to know the illuminating beam phase just before the microrelief surface and how to describe multiple beam transformation after its diffraction on microrelief. In other words, the surface with diffractive microrelief is only one of the surfaces in ray-tracing approach, but this particular surface becomes a surface of special attention for all diffractive calculations. We suggest to reduce all the results of long ray tracing to one surface with given phase function on it to get the Kirchhoff diffraction integral applicable. We found the following ***algorithm based on an equivalent scheme of optical system:***

- Ray-trace original optical system (Fig. 5) with diffractive microrelief characterized by phase function in the useful diffraction order (by standard ray-tracing software)
- Find the ***corrective*** polynomial ***aberration*** coefficients on Λ so that ***multi-lens ray-tracing*** in given diffraction order gives ideal imaging from input object (far, middle or near) to the output spot
- In ***equivalent scheme summarize*** the phase on the surface Λ from inverse sign ***corrective*** coefficients with the phase of ***diffractive*** microrelief in given order
- Set distance l of equivalent scheme (Fig.1) so that output numerical aperture β of equivalent system is equal to those of multi-lens system output
- Calculate Kirchhoff integral from surface Λ to the focal domain of interest, at a distance l where the output numerical aperture of equivalent system is equal those of original system (Fig.5).

Thus we are able to deal with equivalent model of diffractive microrelief performance. This means that there is only one surface Λ with diffractive microrelief of variable height h. Contribution of all other optical surfaces is taken into consideration by additional "illuminating" phase jump kS_0 and intensity distribution I_0 on the diffractive surface Λ as was described above.

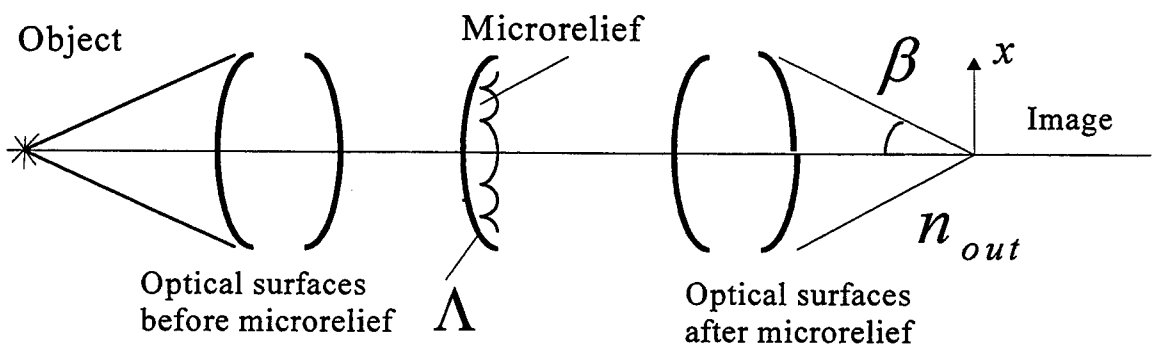

Fig. 5. Original multifocal aberrated optical systems

References

1.M.A.Golub, M.Duparre, E.B. Kley, R. Kowarschik, B. Luedge, W. Rockstroh, H.-J. Fuchs , "Investigation of computer-generated diffractive beam shaper for flattening of single-mode CO_2 -laser beam". *Opt. Eng.* **35**(5), pp.1400-1406, 1996.

2. C. Dahner, M. Larsson, A. Nystrom, S. Hard, "Letter imaging by diffractive, bifocal intraocular lenses: a computer study", *Appl. Opt.* **33**(7), pp. 1135-1140, 1994

3. Born. M., Wolf E., Principles of optics, Pergamon Press, Oxford, 1993

4. L.N. Hazra, Y.Han, C. Delisle, "Curvilinear kinoform lenses for stigmatic imaging of axial objects", *Appl. Opt.* **32**(25), pp. 4775-4784, 1993

Super-resolving filters as diffractive optical elements

CJR Sheppard

Physical Optics Department, School of Physics
University of Sydney, NSW 2006 Australia

and

Australian Key Centre for Microscopy and Microanalysis
Unversity of Sydney, NSW 2006 Australia

Telephone: +61 2 9351 5971
Fax: +61 2 9351 7727
e-mail: colin@physics.usyd.edu.au

Super-resolving filters have potential applications in the areas of optical data storage,[1-3] lithography[4] and microscopy.[5,6] In many applications the behaviour of the filter in the presence of defocus is important. For example, for lithography a large depth of focus is desirable, whereas in microscopy high axial resolution is often required. The effect of particular filters on the three-dimensional focal distribution has therefore been studied.[7-9] It is found that filters which are super-resolving in the transverse direction can be either super-resolving or apodizing in the axial direction. Indeed, a minimum in intensity is often found along the axis at the focal point. For amplitude filters, simple design rules for the three-dimensional focusing properties have been proposed.[7]

Super-resolving filters consisting of arrays of rings can be designed, in which the sign of the transmission of the rings alternates in sign. These are similar in form to a zone plate. They produce two primary foci, in addition to the zero order. When used in the back focal plane of a lens, the zero order results in the focal plane distribution, while the orders of plus and minus one result in additional foci either side of the focal plane. The focal distribution can thus be explained by a zone plate model.

In this way, the filter can be regarded as a diffractive optical element, so that, when used in the back focal plane of a lens the complete system can be regarded as a hybrid system. These functions can also be combined in a single diffractive element which combines the properties of a diffractive focusing device and a super-resolving array, to achieve performance superior to the classical resolution limit.

References

1. IJ Cox, Appl. Opt. **23**, 3260 (1984)
2. Y Yamanaka, Y Hirose, H Fujii and K Kubota, Appl. Opt. **29**, 3046 (1990)
3. TRM Sales and GM Morris, Joint International Symposium on Optical Memory and Optical Data Storage, OSA Tech. Digest Ser. 1996, p.290
4. F Fukuda, T Terasawa and S Okazaki, J. Vac. Sci. Tech. B **9**, 3113 (1991)
5. ZS Hegedus, Opt. Acta **32**, 815 (1985)
6. ZS Hegedus and V Sarafis, J. Opt. Soc. Am. A **3**, 1892 (1986)
7. CJR Sheppard and ZS Hegedus, J. Opt. Soc. Am. A **5**, 145 (1965)
8. CJR Sheppard, J. Mod. Opt. **43**, 525 (1996)
9. CJR Sheppard, G Calvert and M Wheatland, J. Opt. Soc, in press.

Super-resolution in computer-generated holograms

Yasuhiro Takaki

Department of Applied Physics, College of Humanities and Sciences, Nihon University
3-25-40, Sakurajosui, Setagaya-ku, Tokyo 156-8550 JAPAN.
Telephone: +81-3-3329-1151 ext. 5513
Fax: +81-3-5317-9432
E-mail: takaki@chs.nihon-u.ac.jp

Abstract

Resolvable points of the CGH's diffraction image overlap and interfere with one another. By controlling the interference, diffraction intensity distribution can be controlled with high density.

1 Introduction

When a computer-generated hologram (CGH) consists of $N \times N$ sampling cells, the diffraction image also consists of $N \times N$ resolvable points. A number of CGH design techniques have been proposed for controlling the complex amplitude or the intensity of the resolvable points. In this paper, I discuss how the interference between the resolvable points is controlled so that the diffraction intensity distribution can be controlled with higher density than it is by conventional CGHs.

2 Super-resolution

The diffraction image produced by a CGH has both amplitude and phase distributions. Much attention has been paid to controlling the amplitude distribution, especially in kinoform designs; the amplitude distribution is controlled as precisely as possible while the control of the phase distribution is abandoned. However, such design techniques are applicable only to array generation because the resolvable points overlap and interfere with one another on the diffraction plane. In my study such interference phenomenon was positively utilized in order to control the intensity at the intermediate positions between resolvable points.

When the CGH consists of $N \times N$ square cells, each of which has the length of a, the transmittance of the CGH is given by:

$$u(x,y) = [\{f(x,y)comb(x/a,y/a)\} * rect(x/a,y/a)]\, rect(x/Na,y/Na) \tag{1}$$

For simplicity, a Fourier CGH is assumed and the diffraction is given by:

$$U(\nu_x,\nu_y) = N^2a^6\,[\{F(\nu_x,\nu_y) * comb(a\nu_x,a\nu_y)\}\, sinc(a\nu_x,a\nu_y)] * sinc(Na\nu_x,Na\nu_y) \tag{2}$$

Figure 1 illustrates the distribution on the diffraction plane. Each resolvable point has the distribution represented by $sinc(Na\nu_x, Na\nu_y)$.

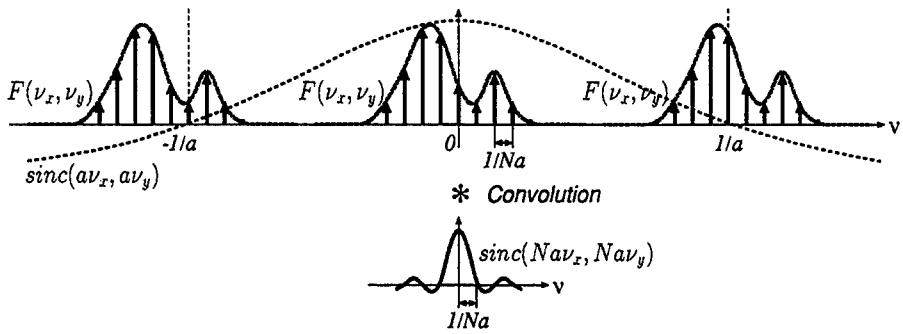

Figure 1. Diffraction of sampled CGH.

Figure 2 shows the super-resolution in CGH. When the resolvable points have the complex amplitude distribution as shown in Fig. 2(a), the resultant intensity distribution becomes that as shown in Fig. 2(b). The intensity drops to zero between resolvable points having complex amplitude of +1 and -1. This figure shows that the intensity distribution can be controlled with density twice as high as the resolvable points in one-dimension, and 4 times as high as those in two-dimension.

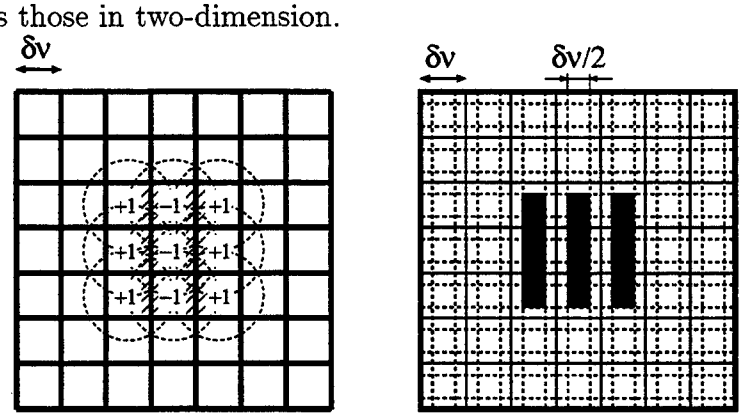

(a) complex amplitude distribution

(b) intensity distribution

Figure 2. Super-resolution in CGH.

3 Experiments

A binary-amplitude CGH was used to demonstrate the super-resolution. The diffraction plane was divided into the signal area and the dummy area. The total number of sampling cells was 64×64 and that of the signal area was 16×16. The binary amplitude distribution of CGHs was optimized by the simulated annealing algorithm.

The target complex amplitude of the resolvable points, the optimized CGH patterns, and the experimental results are shown in Fig. 3. Three different patterns were examined. The conjugate image and zero-order light also appeared in the diffraction image because of the nature of an amplitude hologram. The blooming effect of the CCD element used for image capturing was observed because zero-order light has extremely high intensity.

The binary-amplitude CGHs were used for the demonstration. The use of phase-only CGHs will eliminate the zero-order light and increase the optical efficiency.

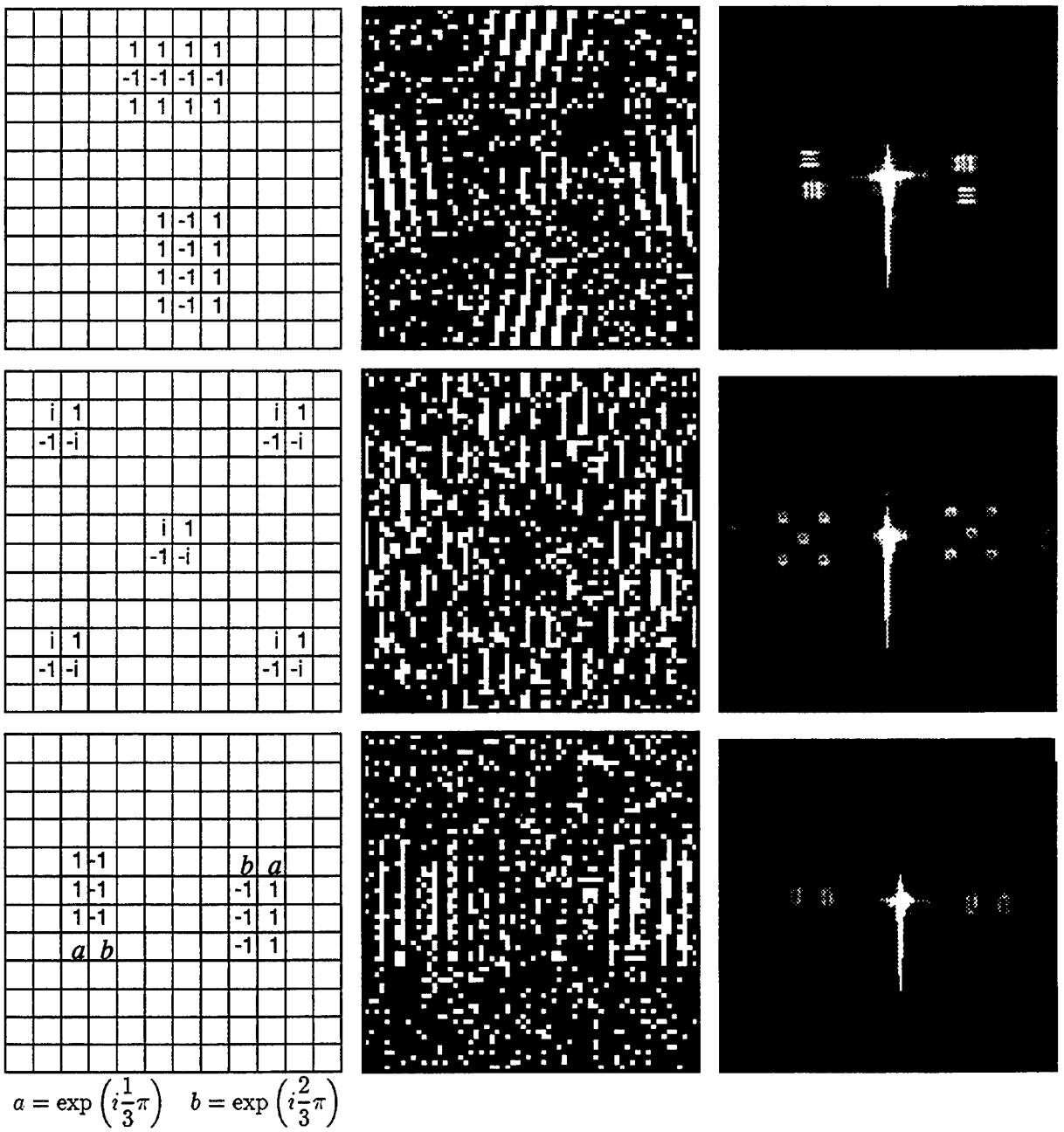

Figure 3. Experimental results of super-resolution CGH.

4 Summary

Super-resolution in CGH was proposed and successful experiments were done. Further study should be done on how arbitrarily the super-resolved intensity distribution can be manipulated and on how to design the target complex amplitude distribution for the super-resolution.

Diffractive Optics and Micro-Optics

Subwavelength Structures 2

Tuesday, June 9, 1998

Robert Magnusson, University of Texas at Arlington
Presider

DTuB
10:30am–12:00m
Koa Room

Abstract for the OSA topical meeting on Diffractive Optics

FABRICATION OF FUNCTIONAL OPTICAL STRUCTURES BASED ON PHOTONIC CRYSTALS

A. Scherer, A. Yariv, Y. Fainman, E. Yablonovitch,
B. D'Urso, O. Painter, C.C. Cheng

Abstract

We have developed techniques to fabricate photonic crystals within functional semiconductor materials to reflect, polarise, and filter light. These manufacturable structures have now allowed us to define high-contrast polarizing beam-splitters and ultra-small optical cavities, and hold the promise of many exciting new applications. Polarizers with over 820:1 TE/TM transmission ratios have been fabricated by microfabricating gratings through a 1-D multilayer Bragg mirror, thereby forming an in-plane 2-D photonic bandgap crystal. Ultra-small optical cavities have also been defined by perforating very thin InGaAsP/InGaAs membranes with 2-D photonic crystals to define in-plane optical resonators. Here, we will describe the fabrication methods and the observed performance of these devices.

Figure 1. Scanning electron micrographs of micro-polarizing beam-splitter and a thin membrane microcavity formed by microfabricated 2-D photonic crystals.

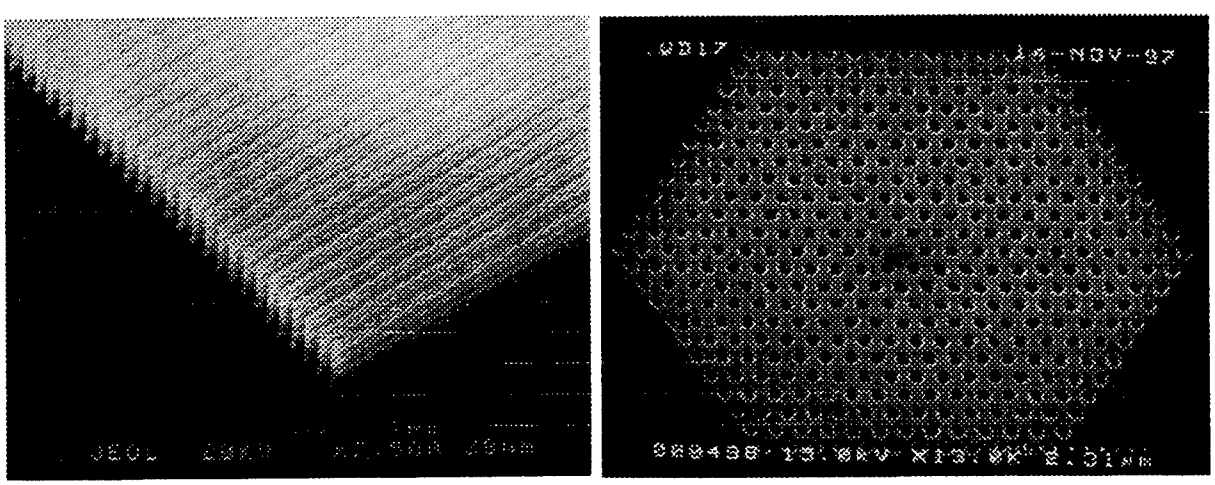

Fabrication and Simulation of Blazed Gratings with Inherent Antireflection Structured Surfaces

Fredrik Nikolajeff
University of Minnesota, Department of Electrical and Computer Engineering, Minneapolis, MN 55455
fredrik@ece.umn.edu

Claus Heine
Balzers Ltd., Thin Films, FL-9496 Balzers, Liechtenstein
hecl@btf.balzers.net

1. Introduction

Subwavelength structured surfaces can be used as very efficient antireflection (AR) coatings, narrowband filters or polarizing elements [1]. In industry, AR coatings and filters are typically produced by using thin-film techniques. Subwavelength structures can avoid many of the problems encountered in thin-film approaches, and be replicated at low cost. Subwavelength structures also have the potential to be combined with micro-optical elements such as lenses, gratings or kinoforms. However, previous studies have either been focused on the analysis of pure subwavelength gratings [2] or micro-optical elements coated with thin films [3].

In this paper, we present a novel scheme for the fabrication of diffractive optical elements (DOEs) with inherent antireflection or polarizing properties. The idea is to fabricate a subwavelength grating directly into the resist material of the DOE. By replicating the diffractive element, the antireflection or polarizing function will be inherent, thus obviating the need of any subsequent processing steps. We give simulated and experimentally measured results from a test structure, based on a subwavelength grating superimposed on a blazed grating. Simulations were performed using a rigorous diffraction theory computer program and test elements were fabricated by direct-write electron-beam lithography.

2. Design and Simulations

In order to investigate the optical properties of a DOE with an embedded subwavelength structured surface, we studied different types of subwavelength gratings superimposed on blazed gratings. More specifically, we wanted to use the subwavelength grating to improve the diffraction efficiency of the blazed grating, by reducing the reflection losses between the substrate and its surrounding medium.

In the theoretical simulations we used the rigorous diffraction theory described in Ref. [4]. One of the elements analyzed was a 6 μm period blazed grating combined with a 1-D 300 nm period binary AR grating. The duty cycle of the AR grating was 0.5. Both diffractive structures were assumed to be made in a medium with refractive index

n = 1.54, surrounded by air (n = 1). The wavelength of the illuminating light was 633 nm. Fig. 1 (a) shows the calculated first order diffraction efficiency (TE-polarization) for a blazed grating with and without the superimposed AR grating, as a function of different relief depths. In the latter fabrication process, we expose both the blazed grating and the AR grating in the same resist, and subsequently develop the combined diffractive structure. This means that as the blaze depth is increased, so is the AR grating depth. In the calculations, we therefore let the depths of the two gratings scale linearly. The proportionality is chosen so that the optimum depth of a bare blazed grating, as given by $d = \lambda/(n - 1)$, coincides with the optimized depth of a bare AR grating.

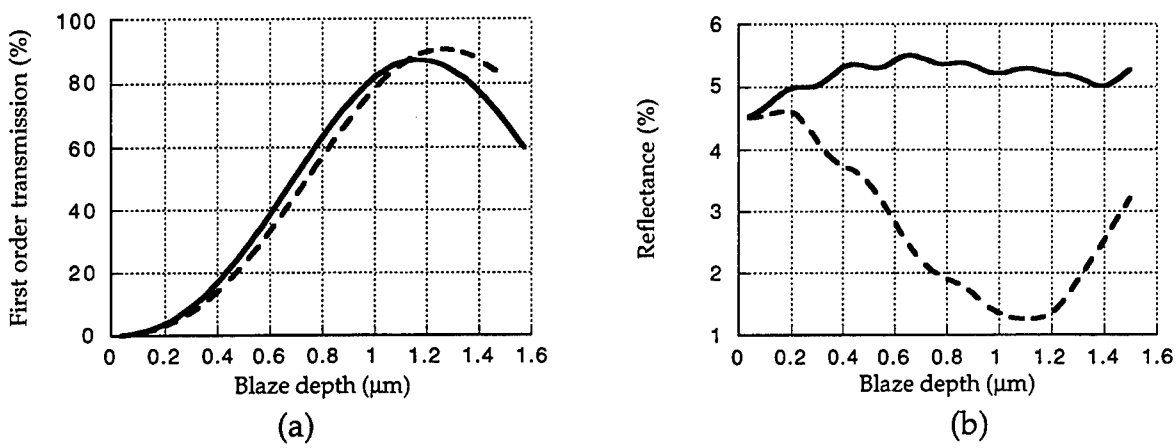

Fig. 1. (a) Calculated first order transmitted intensity (TE-polarization) for a bare blazed grating (solid line) and a blazed grating with a superimposed AR structure (dashed line) as a function of the blaze depth. (b) Calculated total reflectance (TE-polarization) for a blazed grating only (solid line) and a blazed grating with a superimposed AR structure (dashed line) as a function of the blaze depth. In the calculations we used a normally incident plane wave (λ = 633 nm).

The optimum depth of the blazed grating without AR structure is 1.17 μm, yielding a first order diffraction efficiency of 87%. For the combination of a blazed grating and an AR grating, we found that the optimum depth of the blazed grating is shifted to 1.27 μm yielding a diffraction efficiency of 91%. In Fig. 1 (b), we show the reflectance (TE-polarization) for the two elements. Note that the total reflected intensity is close to 5% for all the investigated blaze depths of the bare blazed grating. With a superimposed AR structure the reflectance can be decreased to 1.3% for a blaze depth of 1.11 μm.

3. Fabrication and Experimental Results

We used direct-write electron-beam lithography to fabricate blazed gratings, both with and without superimposed AR gratings. All structures were made in e-beam resist which was spin-coated on quartz substrates. First, we exposed and partially developed the blazed grating, stopping at half the optimum development time for a bare blazed grating . The exposed and developed resist was then subjected to another e-beam

exposure, this time with a subwavelength grating. The subwavelength grating was exposed in a grid pattern, with equidistant e-beam point exposure shots. Finally, we developed the double-exposed resist in a stepwise manner. After each development step we measured the profile depths as well as the reflected and the transmitted diffraction order intensities. One fabricated element consisted of a 16 μm period blazed grating combined with a 2-D 300 nm period AR grating. The optical measurements clearly indicated that, with increasing relief depth, the subwavelength structure starts to reduce the reflection losses of the blazed grating. More specifically, the sum of the measured intensities in all reflected orders minus the zero order value, was found to decrease from a starting value of 3.5% (with no AR structure developed) to 1.7% (after 30 sec. development time). Fig. 3 shows an SEM picture of the fabricated element after the end development time of 60 sec.

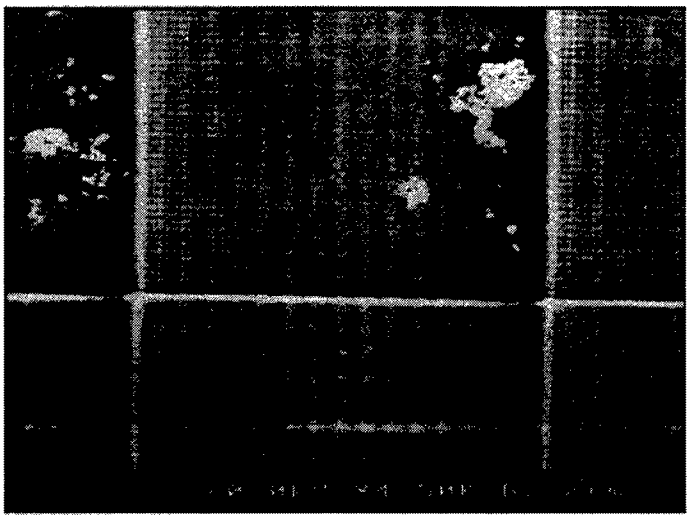

Fig. 3. SEM picture of a blazed grating with a superimposed subwavelength AR grating, manufactured by a two-step e-beam exposure method. The 2-D AR structure is seen in the upper half of the figure as the very fine two-dimensional grid pattern. The lower half of the figure shows the region where we exposed a blazed grating only.

References

[1] D. H. Raguin and G. M. Morris, "Structured surfaces mimic coating performance", *Laser Focus World* **33**, No. 4, 113-117 (1997).

[2] R. C. Enger and S. K. Case, "Optical elements with ultrahigh spatial-frequency surface corrugations", *Appl. Opt.* **22**, 3220-3228 (1983).

[3] E. Pawlowski and B. Kuhlow, "Antireflection-coated diffractive optical elements fabricated by thin-film deposition", *Opt. Eng.* **33**, 3537-3546 (1994).

[4] R. H. Morf, "Exponentially convergent and numerically efficient solution of Maxwell's equations for lamellar gratings", *J. Opt. Soc. Am. A* **12**, 1043-1056 (1995).

Scalar-Based Design of Binary Subwavelength Diffractive Lenses

Joseph N. Mait, Dennis W. Prather,† and Mark S. Mirotznik‡
U.S. Army Research Laboratory
2800 Powder Mill Road
Adelphi, Maryland 20783
phone: (301) 394-2462, fax: (301) 394-5420, e-mail: mait@arl.mil

†University of Delaware
Department of Electrical Engineering
Newark, Delaware 19716

‡The Catholic University of America
Department of Electrical Engineering
Washington, D.C. 20064

Recent research[1–9] has shown that if a binary-phase diffractive optical element (DOE) has features that are on the order of the illuminating wavelength, the performance limits set by scalar-based diffraction theory can be overcome. In fact, diffraction efficiencies in excess of 90% have been predicted for binary gratings that have subwavelength features.[1,4,5] Due primarily to the availability of tools for modeling, the analysis and design of subwavelength DOEs (SWDOEs) has concentrated primarily on gratings.[1–7,10] To overcome this limitation, we have developed numerical routines that use a boundary element method (BEM) to *analyze* diffraction from finite extent, aperiodic DOEs.[11] In this paper we consider diffractive *design*, in particular, the design of diffractive lenses, subject to the constraints of fabrication.

Our technique is based on the combination of two approximate theories of diffraction, scalar diffraction theory and effective medium theory. As a first step in the development of our synthesis procedure we consider the diffractive analysis of a SWDOE $t(x)$ illuminated by TE-polarized light of wavelength λ and fabricated in a substrate with refractive index n_s with etch detph d. We assume that $t(x)$ is binary,

$$t(x) = df(x), \tag{1}$$

with

$$f(x) = \sum_{\substack{k=1 \\ k \text{ odd}}}^{K} \operatorname{rect}\left[\frac{x - (z_{k+1} + z_k)/2}{z_{k+1} - z_k}\right]. \tag{2}$$

By extending effective medium theory for gratings[7,12] to finite aperiodic structures, we can model the relative effective refractive index of $t(x)$ as

$$n^2(x) = \left(n_r^2 - 1\right) g(x) + 1, \; x = [0, W], \tag{3}$$

where $n_r = n_s/n_o$ is the substrate refactive index relative to the index n_o of the external environment and W is the extent of the diffractive element. The index synthesis function $g(x)$,

$$g(x) = f(x) * \frac{1}{\Delta}\operatorname{rect}\left(\frac{x}{\Delta}\right), \tag{4}$$

accounts for the effective medium averaging within each subwavelength region Δ of $t(x)$,[8] where $\Delta \leq s_\lambda = \lambda/2n_s$.[1]

Effective medium theory provides a link between the effective refractive index $n(x)$ of the SWDOE $t(x)$ and its structure $f(x)$. Scalar diffraction provides the link between $n(x)$ and the phase transformation $\theta(x)$,

$$\theta(x) = \theta_0 \frac{n(x) - 1}{n_r - 1}, \tag{5}$$

where $\theta_0 = 2\pi d n_o (n_r - 1)/\lambda$.

Equations (3) and (5) allow one to predict the phase transformation $\theta(x)$ given a particular index synthesis $g(x)$. To determine a $g(x)$ that realizes a desired phase transformation $\theta(x)$ one must invert these equations and combine them,

$$g(x) = \frac{\{(n_r - 1)\,[\theta(x)/\theta_0] + 1\}^2 - 1}{n_r^2 - 1}. \tag{6}$$

As an example, we consider the design of a 20-μm focal length lens with a 22.72-μm diameter ($f/\# = 0.88$) for operation at $\lambda = 1$ μm. The lens functions in free space and has a refractive index of 9. Because our intent is to highlight the design method and not the design of a particular lens, the artificially high refractive index keeps the computational costs of analyzing the lens low. In addition, we assume that fabrication technology limits the etch depth to 62.5 nm and the minimum feature δ_{min} to 0.1 μm.

Figure 1(a) represents the substrate profile that corresponds to a continuous 2π-phase diffractive lens (125 nm maximum etch depth). However, the desired phase $\theta(x)$ must be quantized to a phase range θ_0 dictated by d. Figure 1(b) is the profile that minimizes the quantization error of the 2π phase lens given a 62.5-nm etch depth (π phase). Figure 1(c) is the index synthesis function that corresponds to the phase represented by Fig. 1(b).

To determine $f(x)$ given $g(x)$ (Eq. (6)) one must invert Eq. (4). Because $g(x)$ is a low pass filtered version of the binary $f(x)$, the low pass spectra of the two functions must match. The problem of determining a binary structure $f(x)$ whose low pass structure matches that of the continuous function $g(x)$ is similar to the design of a (0,1)-binary amplitude computer-generated hologram. The distinction is, however, that the function $g(x)$ is related to the desired phase transmission, not to the total complex-wave amplitude transmission. We can therfore rely upon the wealth of techniques in the literature, both optimal and suboptimal, to perform the inversion. As a simple example, we use pulse-width encoding to generate $f(x)$ from $g(x)$:

$$f(x) = \sum_{m=0}^{M-1} \mathrm{rect}\left(\frac{x - m\Delta - g_m\Delta/2}{g_m\Delta}\right), \tag{7}$$

where $g_m = g(m\Delta)$, $m = [0, M-1]$, $M = \mathrm{ceil}\,[D/s_\lambda]$, and $\Delta = D/M$. The binary structure $f(x)$ is shown in Fig. 1(d).

The smallest feature δ in the structure represented in Fig. 1(d) is 4.8 nm, which insures that the smallest change in g_m can be resolved between adjacent subperiods Δ. However, because $\delta < \delta_{min}$, $f(x)$ must be spatially quantized before it can be fabricated. Spatial quantization of the binary profile in Fig. 1(d) to 0.1 μm yields the profile represented in Fig. 1(e).

This final profile can be used as input to a vector-based optimization algorithm.[13] In some instances we found that the subsequent optimization was capable of recovering all the losses in efficiency that occur from this technique. Thus, this procedure in combination with optimization offers a simple but effective technique for the design of SWDOEs constrained by fabrication.

REFERENCES

[1] M. W. Farn, Appl. Opt. **31**, 4453–4458 (1992).

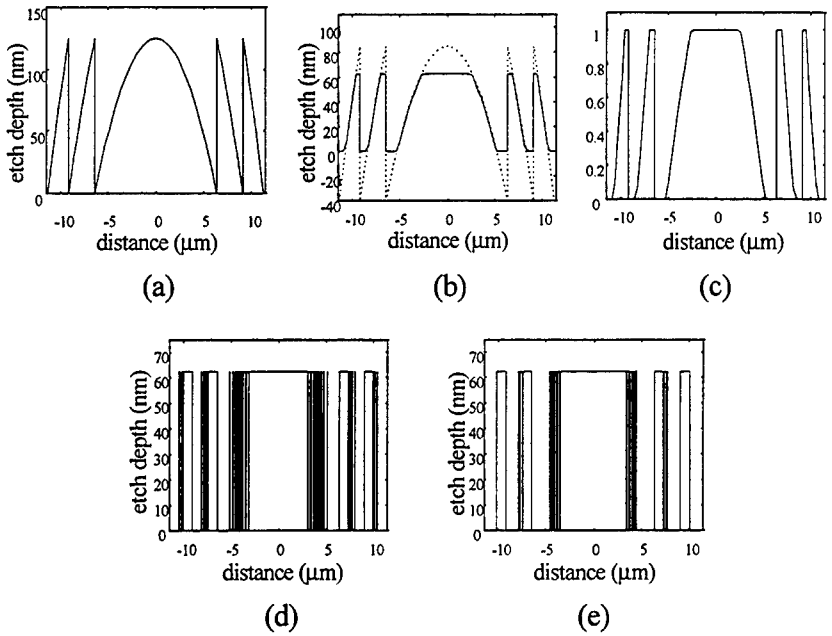

Figure 1: Binary subwavelength lens design. (a) Continuous 2π-phase lens profile. (b) Continuous π-phase quantized lens profile. (c) Index synthesis function. (d) $(0,\pi)$-Binary phase subwavelength lens profile. (e) Spatially quantized $(0,\pi)$-binary phase subwavelength lens profile.

[2] H. Haidner, J. T. Sheridan, J. Schwider, and N. Streibl, Opt. Commun. **98**, 5–10 (1993).

[3] D. H. Ranguin, *Subwavelength Structured Surfaces: Theory and Application*, Ph.D. thesis, University of Rochester, 1993.

[4] Z. Zhou and T. J. Drabik, J. Opt. Soc. Am. A **12**, 1104–1112 (1995).

[5] E. Noponen, J. Turunen, and F. Wyrowski, J. Opt. Soc. Am. A **12**, 1128–1133 (1995).

[6] M. Schmitz, R. Bräuer and O. Bryngdahl, J. Opt. Soc. Am. A **12**, 2458–2462 (1995).

[7] P. Lalanne and D. Lamercier-Lalanne, J. Mod. Opt. **43**, 2063–2085 (1996).

[8] P. Kipfer, M. Collischon, H. Haidner, J. Schwider, Opt. Eng. **35**, 726–731 (1996).

[9] M. Schmitz and O. Bryngdahl, J. Opt. Soc. Am. A **14**, 901–906 (1997).

[10] T. K. Gaylord and M. G. Moharam, Proc. IEEE **73**, 894–937 (1985).

[11] D. W. Prather, M. S. Mirtoznik, and J. N. Mait, J. Opt. Soc. Am. A **14**, 34–43 (1997).

[12] M. Born and E. Wolf, *Principles of Optics* (New York, NY, Pergamon Press, 1980).

[13] D. W. Prather, J. N. Mait, M. S. Mirotznik, and J. P. Collins, "Vector-based synthesis of finite, aperiodic subwavelength diffractive optical elements," J. Opt. Soc. Am. A, submitted for review.

Three Dimensional Vector-based Analysis of Subwavelength Diffractive Optical Elements using the Finite-Difference-Time-Domain (FDTD) Method

Mark S. Mirotznik, Joseph N. Mait,* Dennis W. Prather,+ and William A. Beck*

Dept. of Electrical Engineering
The Catholic University of America
Washington, D.C. 20064

*U.S. Army Research Laboratory
2800 Powder Mill Road
Adelphi, Maryland 20783

+ Dept. of Electrical Engineering
University of Delaware
Newark, Delaware

Introduction

Diffractive optical elements (DOEs) whose features are smaller than the wavelength of illumination are referred to as subwavelength diffractive optical elements (SWDOEs). Subwavelength features provide SWDOEs with an added degree of flexibility over their superwavelength counterparts. For example, in the case of binary structures, SWDOEs have been shown to achieve diffraction efficiencies in excess of 90%[1]. This added flexibility, however, results in a significant cost. Namely, the analysis and subsequent design of SWDOEs require the use of rigorous electromagnetic (EM) models. These models, which incorporate the full vector nature of electromagnetic fields, can be theoretically challenging to construct and often demand considerable computational resources.

While the microwave community has put forth considerable effort to develop computationally efficient EM algorithms, little of this work has been applied to optical devices such as SWDOEs. One exception to this is the large body of work on the analysis and design of infinitely periodic gratings with subwavelength features using rigorous coupled wave theory [2]. However, only a handful of articles address finite aperiodic SWDOEs [3,4,5] and these only analyze one-dimensional elements. To the best of the authors knowledge ours is the first application of a rigorous EM model to two-dimensional (2D) finite aperiodic SWDOEs.

Here we present the use of the finite-difference-time-domain (FDTD) method for the analysis of 2D SWDOEs. FDTD is a computationally practical method for performing 3D analysis on both infinitely periodic and finite aperiodic SWDOEs. A specific example is given of a binary subwavelength lens.

FDTD Method

The FDTD was first introduced by Yee in his 1966 seminal paper [6]. The method was later refined by Taflove and others [7] and is now one of the most widely used numerical techniques for solving EM problems. The method derives its name from a direct finite difference approximation to Maxwell's time-dependent curl equations. This approximation results in a set of six time dependent algebraic equations for all electric and magnetic field components.

The unknown field distribution over a finite space is calculated by applying the FDTD equations to a volumetrically sampled grid of cells called Yee cells. Each edge of the Yee cells may be assigned independent electrical properties allowing one to model complex objects consisting of lossy, inhomogenous or anisotropic materials.

After incorporating a time-dependent incident field, a time-marching algorithm is employed to calculate the unknown field distribution. To determine a steady state solution for time-harmonic

fields one would simply time march a plane wave incident field with sinusoidal time dependancy until all transients have adequately decayed. Alternatively, non-sinusoidal incident fields that contain an entire band of frequencies (e.g., Gaussian-modulated sinusoids) can be applied. Since the FDTD method (and all of our materials) are linear, the various frequencies in the incident field propagate independently through the time stepping. Therefore, Fourier analysis of the time-dependent fields at each point in the solution space yields the steady-state field solution throughout the entire frequency spectrum of the incident field. In other words, we can obtain DOE performance over an entire spectrum of wavelengths in a single FDTD run.

Custom FDTD code was written in Fortran 90 and run on a SUN Ultra Sparc II workstation. The code implements a full 3D scattered field formulation of the FDTD method [see Taflove] and incorporates a variety of boundary conditions. These include: 1) Liao's absorbing boundaries (to simulate open surfaces), 2) perfect electrical conductors, 3) periodic boundaries and 4) one and two fold mirror symmetry planes. We can therefore analyze both finite aperiodic and infinitely periodic 2D SWDOEs using the same FDTD code.

Example

To illustrate the FDTD method on a SWDOE, we analyzed the diffraction from a binary subwavelength diffractive lens. The lens was designed using a technique we developed that combines scalar diffraction and effective medium theory [8]. For this example, we extended our one-dimensional technique to two dimensions. The lens was designed with a 5μm focal length and a 10 x 10 μm^2 aperture. Its minimum feature size was 0.1μm. The wavelength of illumination in free-space was 1μm and the index of refraction of the lens was 1.50. The lens was analyzed using a finite difference grid of cubical cells 0.05μm on a side. The entire mesh consisted of 9 million cells and required over 400 MBytes of computer memory to solve. The entire computation was completed on a 250 MHz Sun Ultra Sparc Workstation in approximately 8 hours. The results of the analysis are represented in Fig. 1.

Conclusion

We have presented the analysis of a 2D binary subwavelength lens using the FDTD method. Our Fortran 90 code permits the analysis of both finite aperiodic and infinite periodic elements. Future work will concentrate on validating the code for a wide variety of DOEs as well as on improving the computational efficiency of the method.

References

1. M.W. Farn, *Appl. Opt.* 31, 4453-4458 (1992).
2. T.K. Gaylord and M.G. Moharam, *Proc. IEEE.* 73, 894-937 (1985).
3. M. S. Mirotznik, D. W. Prather and J. N. Mait, *J. Mod. Opt.* 43, 1309-1321 (1996).
4. D.W. Prather, M.S. Mirotznik and J.N. Mait, *J. Opt. Soc. Am. A* 14, 34-43 (1997).
5. K. Hirayama, E. N. Glytsis, T.K. Gaylord and D.W. Wilson, *J. Opt. Soc. Am. A* 13, 2219-2231 (1996).
6. K.S. Yee, *IEEE Trans. Ant. Prop.* 14, 302 (1966).
7. A. Taflove, *Computational Electrodynamics: The Finite-Difference Time-Domain Method* (CRC Press, Boca Raton, 1993).
8. J. N. Mait, D. W. Prather, and M. S. Mirotznik, "Scalar-based design of subwavelength, finite extent, aperiodic diffractive elements," OSA Annual Meeting 1997.

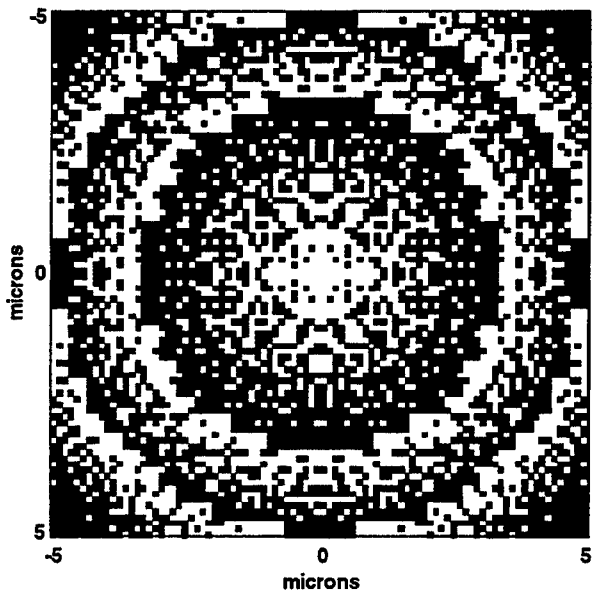

Figure 1(a)

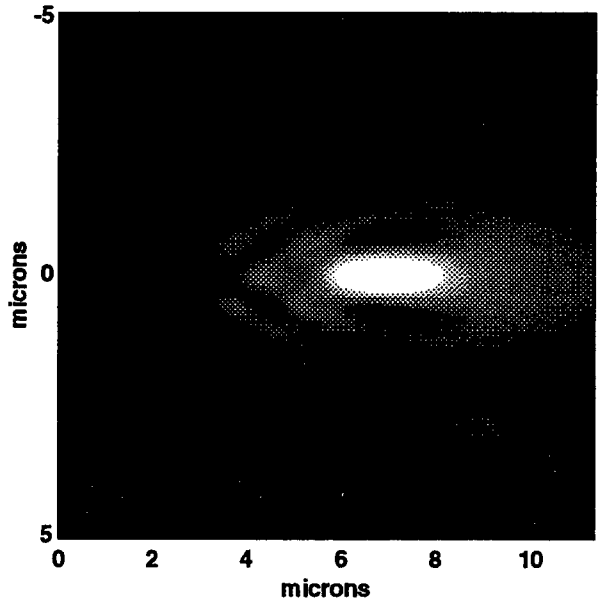

Figure 1(b)

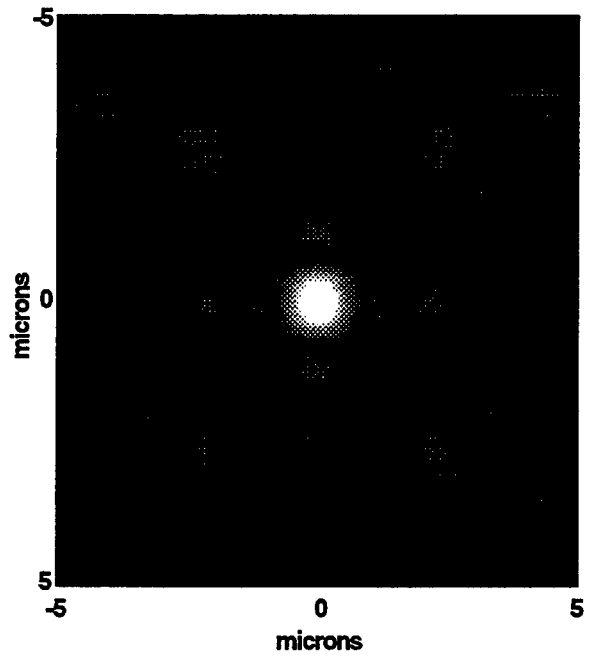

Figure 1(c)

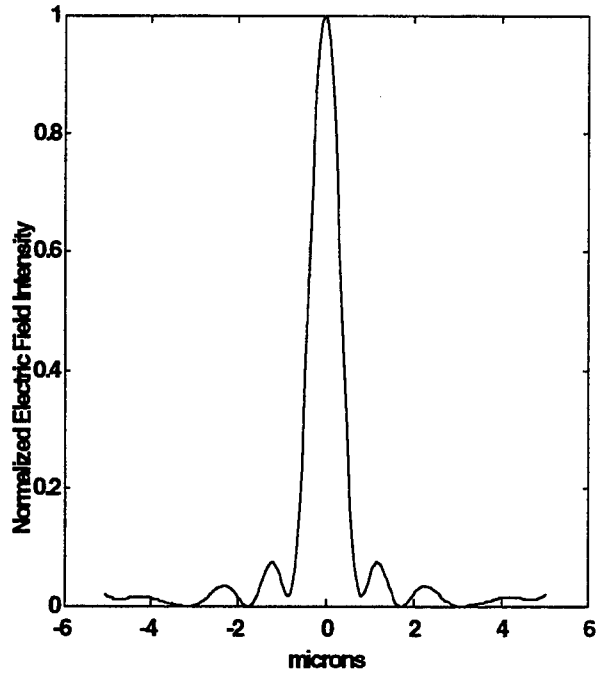

Figure 1(d)

Figure 1. Diffractive analysis of a two-dimensional binary subwavelength lens. a) Cross sectional view of lens. b) Electric field intensity in plane of propagation. c) Electric field intensity in focal plane. d) Line scan of normalized electric field intensity in focal plane.

Vector-Based Analysis of Axially Symmetric and Conducting Diffractive Lenses

Dennis W. Prather,[1] Shouyuan Shi,[1] Mark S. Mirotznik,[2] and Joseph N. Mait[3]

[1]University of Delaware
Department of Electrical and Computer Engineering
140 Evans Hall
Newark, DE 19716
phone: (302)-831-8170, fax: (302)-831-4316, email: *dprather@ee.udel.edu*

[2]The Catholic University of America
Department of Electrical Engineering
Washington, DC 20064

[3]U.S. Army Research Laboratory
2800 Powder Mill Road
Adelphi, MD 20783

The analysis of diffractive lenses that have feature sizes comparable to the illumination wavelength require a rigorous, or vector-based, model of diffraction. However, most techniques presented in the literature for the vector-based analysis of such elements are limited to two-dimensional (2D), or cylindrical, lenses. In this paper we present a vector-based technique for the analysis of three-dimensional (3D), or spherical, diffractive lenses that are perfect electrical conductors (PEC).

Our technique uses the method of moments to solve the 3D electric field (*surface*) integral equation (EFIE) for the induced current distribution over the surface of an axially symmetric PEC diffractive lens. Once determined the surface current distribution is used to calculate the diffracted fields in the focal plane of the lens. This approach has several advantages over alternate techniques in that once the current distribution is known it can be used to determine the complex vector field amplitudes anywhere in space, it is applicable to 3D finite aperiodic lenses, and by exploiting axial symmetry the computational domain is reduced to the contour of the cross section of the lens, i.e., its generating arc.

Our description of the technique begins with the EFIE and the PEC boundary condition on the total electric field, i.e., $\mathbf{E}^{tot} = 0 = \mathbf{E}^{inc} + \mathbf{E}^{sc}$, where $\mathbf{E}^{tot}$, $\mathbf{E}^{inc}$ and $\mathbf{E}^{sc}$ are the total, incident, and scattered electric field vectors, respectively. As a result the EFIE can be written as,

$$\hat{n} \times \mathbf{E}^{inc}(\mathbf{r}) = \hat{n} \times \left[\frac{j\omega\mu}{4\pi} \iint_{\Gamma} \mathbf{J}(\mathbf{r}')\, G(\mathbf{r},\mathbf{r}')\, d\Gamma + \frac{j}{4\pi\omega\epsilon} \nabla \iint_{\Gamma} (\nabla_{\Gamma} \cdot \mathbf{J}(\mathbf{r}'))\, G(\mathbf{r},\mathbf{r}')\, d\Gamma \right], \quad (1)$$

where $\hat{n}$ is the outward unit normal vector, $\mathbf{J}$ is the induced surface current vector, G is the free space scalar Green's function, $\mathbf{r}'$ and $\mathbf{r}$ are vectors from the origin to the source and observation points, respectively, and Γ is the surface of integration, see Fig. 1. It should be noted that this form of the EFIE restricts the observation vector, $\mathbf{r}$, to the surface of the lens. The general application of Eq. (1) to 3D structures requires extensive computational resources, however, by defining a local coordinate

system along the lens contour which consists of the tangential, $\hat{t}$, and azimuthal, $\hat{\phi}$, unit vectors we can reduce computational costs. This is achieved by noting that the induced surface current in the $\hat{\phi}$ direction, for an axially symmetric lens, is periodic. Consequently, we can expand it, the incident electric field, and the free space Green's function into Fourier series representations,

$$\mathbf{J}(\mathbf{r}) = \mathbf{J}_t(t) + \mathbf{J}_\phi(t) = \sum_{m=-\infty}^{\infty} J_{t,m}(t)\, e^{jm\phi}\, \hat{t} + \sum_{m=-\infty}^{\infty} J_{\phi,m}\, e^{jm\phi}\, \hat{\phi} \tag{2}$$

$$\mathbf{E}^{inc}(\mathbf{r}) = \mathbf{E}_t^{inc}(t) + \mathbf{E}_\phi^{inc}(t) = \sum_{m=-\infty}^{\infty} E_{t,m}^{inc}(t)\, e^{jm\phi}\, \hat{t} + \sum_{m=-\infty}^{\infty} E_{\phi,m}^{inc}\, e^{jm\phi}\, \hat{\phi} \tag{3}$$

$$G(\mathbf{r},\mathbf{r}') = G(t,t',\phi-\phi') = \frac{1}{2\pi} \sum_{m=-\infty}^{\infty} G_m(t,t')\, e^{jm(\phi-\phi')}, \tag{4}$$

where

$$G_m(t,t') = \int_0^{2\pi} G(t,t',\alpha)\, e^{-jm\alpha}\, d\alpha.$$

The advantage of the Fourier series expansions is that each Fourier mode, or coefficient, is decoupled from every other Fourier mode. Thus, one can therefore determine each mode independently by forming a separate system of equations,

$$\begin{bmatrix} E_{t,m}^{inc} \\ E_{\phi,m}^{inc} \end{bmatrix} = \begin{bmatrix} Z_{11,m} & Z_{12,m} \\ Z_{21,m} & Z_{22,m} \end{bmatrix} \begin{bmatrix} J_{t,m} \\ J_{\phi,m} \end{bmatrix}, \tag{5}$$

where $Z_{ij,m}$ are the integro-differential operators operating on the mth mode of the surface current distribution in Eq. (1). Equation (5) is solved by using the method of moments.[1,2] Once determined $\mathbf{J}(\mathbf{r}')$ is used to calculate the diffracted field anywhere in space using,

$$\mathbf{E}^{sc}(\mathbf{r}) = \frac{-j\omega\mu}{4\pi} \iint_\Gamma \mathbf{J}(\mathbf{r}')\, G(\mathbf{r},\mathbf{r}')\, d\Gamma - \frac{j}{4\pi\omega\epsilon} \nabla \iint_\Gamma (\nabla_\Gamma \cdot \mathbf{J}(\mathbf{r}'))\, G(\mathbf{r},\mathbf{r}')\, d\Gamma. \tag{6}$$

We validated our implementation of Eqs. (5) and (6) by first determining the induced surface currents for a normally incident plane wave, with $\mathbf{E}_x^{inc}$ polarization, on a PEC sphere of 1.0λ in diameter and by calculating the forward scattered fields, produced by the surface current, in a plane 4.0λ from the sphere. Both agreed with analytic solutions. Once confident our model was working we used it to the analyze binary and 8-level diffractive lenses as shown in Figs. 2 (a) and (c). The f/numbers and minimum feature sizes for the binary and 8-level lens are: $f/1.0$, 0.93μm and $f/0.75$, 0.4μm, respectively. Both lenses had a focal length of 30μm and a wavelength 1.0μm. Figures 2 (b) and (d) illustrate the electric field magnitude in the focal plane of each lens.

1 REFERENCES

[1] A. W. Glisson and D. R. Wilton, IEEE Trans. Antennas Propag. **AP-28** (1980), 593-603.

[2] S. D. Gedney and R. Mittra, IEEE Trans. Antennas Propag. **AP-38** (1990), 313-322.

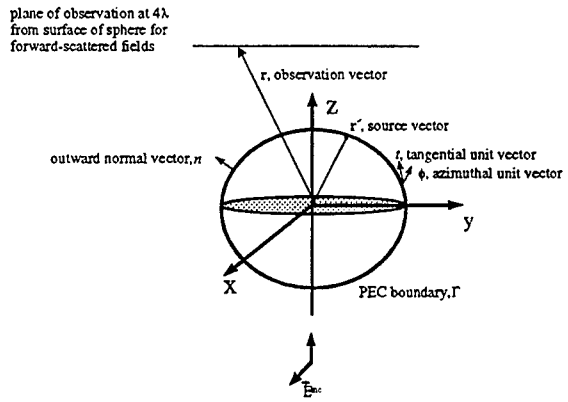

Figure 1: Geometry used for implementing the axi-symmetric electric field integral equation.

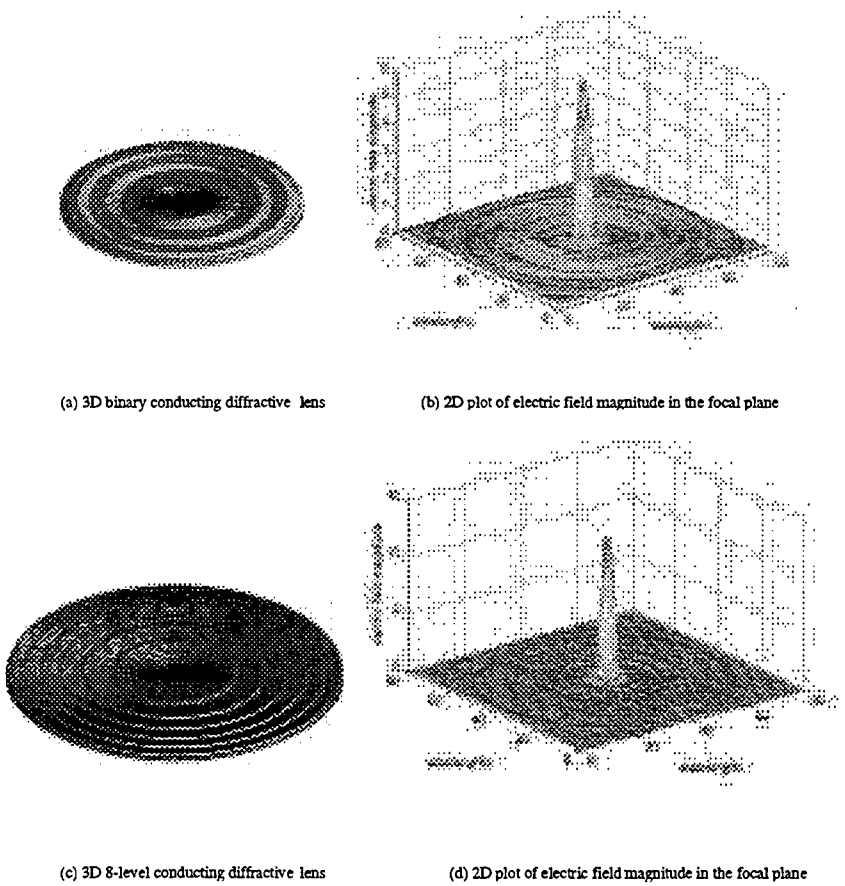

Figure 2: Analysis of PEC diffractive lenses, (a) binary lens, (b) electric field magnitude in focal plane of (a), (c) 8-level lens, and (d) electric field magnitude in focal plane of (c).

Diffractive Optics and Micro-Optics

Optical Interconnects 2

Tuesday, June 9, 1998

James R. Leger, University of Minnesota
Presider

DTuC
1:30pm–3:00pm
Koa Room

Diffractive optics for optical interconnects

Hudson Welch, Eric Johnson, Michael Feldman
Digital Optics Corp.

Summary not available.

Two dimensional microoptical interconnects for a multiprocessor system

U. Danzer, J. Schwider
Universität Erlangen-Nürnberg, Lehrstuhl für Optik, Staudtstr. 7, D-91058 Erlangen, Germany
Phone: ++49-9131-858396, Fax: ++49-9131-13508

The trend of modern high-performance computer systems is directed towards parallel processing /1/,/2/. That results from the high complexity of physical, technical and administrative problems that must be solved. To avoid or to minimize the reduction of these multi-dimensional equation systems to computer compatible serial data streams, a parallel data processing is proposed. One major problem of that highly parallel multiprocessor systems is to handle the enormous data flow through the system. In that systems the data transfer and the communication protocols will be subdivided in hierarchical planes and the communication system is split into several independent interconnection networks. A common practice realizing short and medium distance bus systems is to use copper based communication media. The disadvantages of that solution are the fundamental electromagnetic properties of electrical interconnections at high frequencies. If the wavelength of the electrical signals and the transmission line have similar order of magnitude, a multitude of problems is arising. Screening of all transmission lines is necessary to prevent crosstalk through electromagnetic radiation. Termination of the lines is required to suppress reflections and standing waves and impedance matching is essential for splitting and joining signal lines.

Optoelectronic interconnection concepts for local area and short distance applications are frequently discussed /3/, to avoid the above mentioned problems. Large bandwidth, galvanic decoupling, flexible coupling structures, small size and easy signal splitting are significant advantages of optoelectronical interconnection systems. Hence we designed and realized for two interconnection networks optoelectronical prototypes.
The first massively parallel point to point interconnection system is designed for board-to-board or chip-to-chip communication and the second diffractive optical star network is used for global data exchange and process synchronisation in a multiprocessor system.

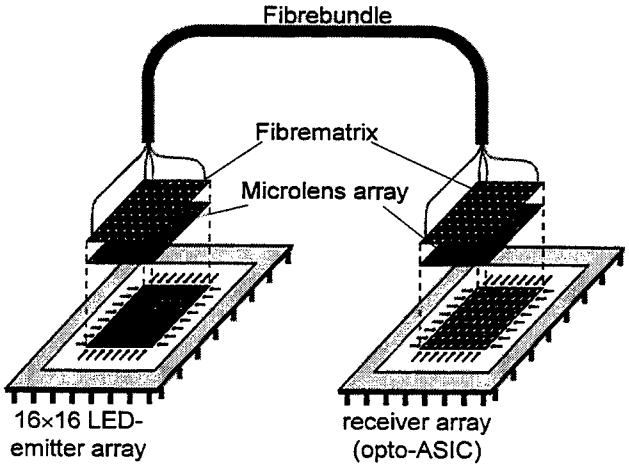

fig. 1) Schematic set-up for a 2D-opto-electronical interconnection system

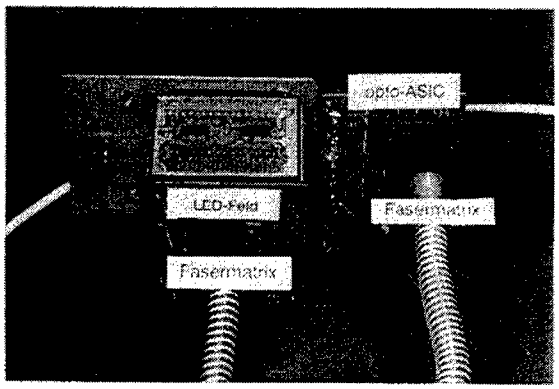

fig. 2) Realised system

For the highly parallel point to point interconnection system a 2-dim. optical coupling structure is used /4/. In fig. 1) and fig. 2) the principle of the set-up and the realized prototype are shown. A single addressable 16 by 16 LED array with a pitch of 420 µm and a light emitting area of 100 x 100 µm² is applied as transmitter module. The LED's radiate at a centre wavelength of 850 nm with a 30 nm 3 dB halfwidth. At a working current of 10 mA the LED's emit 50 µW of optical power with a Lambertian intensity distribution. To overcome crosstalk problems, caused by the Lambertian light sources, the data transmission is performed in a differential way: two physical channels are used to encode one logical channel, which leads to a parallelism of 128 logical channels. 16 by 16 photodiodes with current amplifiers and the comparator modules for the differential coded signals are integrated into a monolithic opto-ASIC /5/. The 150 x 150 µm² PN-photodiodes also have a pitch of 420 µm and a responsitivity of 0.4 A/W. At 10 fJ/Bit optical energy at a data rate of 10 Mbit/channel one receiver unit have a bit error rate of less than 10^{-11}. The data transmission between emitter- and receiver array occurs by a fibre bundle with 256 100/140 µm multimode step-index fibres with a numerical aperture of NA = 0.21. Two fibre arrays with a pitch of 420 µm constitute the end planes of the fibre bundle. Microlens arrays /6/, in front of the LED array and the opto-ASIC are used for optimizing the coupling efficiency of the optical transmission path. Each microlens has a focal length of 350 µm and a diameter of 400 µm. To optimize the coupling efficiency and to reduce optical crosstalk a 1 : 4 imaging set-up between LED- and fibrearray is used. The demonstration system is designed for direct communication between processor and memory with a data rate of 10 MHz, which causes a transmission rate of above 1Gbit/s for the whole system.

The second interconnection system designed for a modular expandable multiprocessor system, has to ensure a direct link between all multiprocessor nodes. For synchronisation purposes or clock distribution the signal delay from one transmitter to all receivers should be the same. A fibre optical star network ensures a data distribution from all emitters to all receivers without delay, assuming equal fibre lengths.
We developed a star-topology bus system (STBS) for the above mentioned application. Using a free space optical set-up yields a rather flexible architecture of the interconnection system /7/, /8/. Especially a space invariant arrangement enables a direct coupling of independent bus systems, a serial or parallel interconnection structure and a high output uniformity.

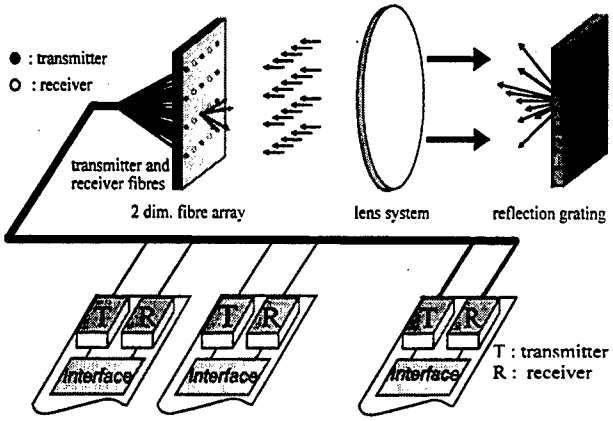

fig. 3) 2-dim. space invariant star network

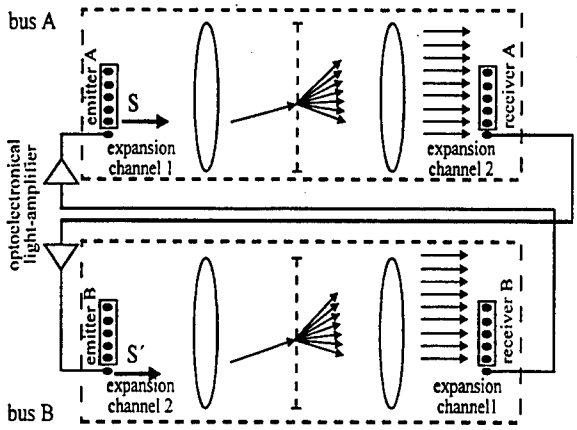

fig. 4) Direct expansion of space invariant bus systems

The basic structure of the STBS is an optical "wired-or" interconnection. It is realized by a 2-dim. space-invariant optical set-up with one fibre array and a reflective binary phase grating (Dammann grating with a 150 nm Ti Au coating) as beam splitting module (see fig. 3). Multimode fibres are attached to all transmitters (LD) and all receivers. Both, the transmitter and receiver fibres are joined in the 2 dim. fibre array. The optical setup is a folded 4f system. The 2-dim beam splitting module enables a serial bus design with N x M participants (N rows, M columns) and causes a splitting loss of 1/(4(N*M)). Using a 1-dim. grating, a parallel interconnection with N participants and M parallel channels (splitting loss 1/2N) can also be realized. The space-invariant optical set-up enables a direct coupling of independent bus systems (see fig. 3). To avoid feedback it is necessary to use separate expansion channels. The signal S (bus A) reaches all receivers, however the amplified signal S′ cannot couple back to bus A.

The realized prototype for a parallel optoelectronic bus-type interconnection network was developed for a modular expandable multiprocessor system with 20 participants. A silicon V-groove technology was applied to produce the two dimensional (10 rows x 5 columns) fibre array with 50/125 µm (transmitter) and 100/140 µm (receiver) multimode fibres. Due to a self adjusting and sandwiching method, alignment tolerances of less than 10 µm were achieved. The transmitter (driver and laser diodes) and receiver modules are designed for data-rates from DC up to 100 Mbit/s. This causes a theoretical insertion loss of 24 dB. An insertion loss (splitting- & excess loss) of 27 dB with an output uniformity of < 4 dB was measured. The variation of the output power is mainly caused by the alignment tolerances of the fibres in the array.

To avoid the wavelenght dependend signal splitting of the grating a quasi achromatic system /9/ was designed. The realized system works in a wavelenght range of 840 nm ± 10 nm. Especial for synchronisation tasks an active system set-up was developed and realized.

References

/1/ Ph. Lalanne, P. Chavel (Eds.), "Perspectives for Parallel Optical Interconnects", Springer-Verlag, Berlin Heidelberg New York, 1991

/2/ Arndt Bode, Mario Dal Cin (Eds.), " Parallel Computer Architectures", Springer-Verlag, Berlin Heidelberg New York, 1993

/3/ Christopher Tocci, H. John Caulfield (Eds), " Optical Interconnection, Foundations and Applications", Artech House, Boston, London, 1994

/4/ K.Zürl, " 2-D parallel optoelectronic interconnect using highly light sensitive monolithic receiver array",WOIT, Workshop on Optoelectronic Interconnect, Edinburgh, 1991

/5/ K. Zürl, E. Gluch, N. Streibl, "A high sensitive monolithic opto-asic for 128 channels", LEOS 1992, Summer Topical Meeting Digest on Smart Pixels, IEEE Lasers and Electro-Optics Society, Santa Barbara, California,1992

/6/ S.Haselbeck, H.Schreiber, J. Schwider, N. Streibl, " Microlenses fabricated by melting a photoresist on a base layer", Opt. Eng. 6, 1322-1324, 1993

/7/ U. Krackhardt et al., " Concept for an Optical Bus-type Interconnection Network", Appl. Opt., 1991

/8 / U.Danzer, J. Schwider, "Two dimensional optical star network", CLEO, Hamburg, Germany, 1996

/9/ M. Schwab et al., " Compensation of the wavelenght dependence in diffractive star couplers", JOSA A12,1994

Hybridization of Fresnel diffractive microlenses and VCSELs arrays for free space optical interconnections

Michel FRACES
Tel : (33) 562 25 26 04
Fax : (33) 562 25 25 88
E-mail : Michel.Fraces@onecert.fr

Pascal CHUROUX
Tel : (33) 562 25 26 03
Fax : (33) 562 25 25 88
E-mail : Pascal.Churoux@onecert.fr

Jean-Pierre BOUZINAC
Tel : (33) 562 25 26 24
Fax : (33) 562 25 25 88
E-mail : Jean-Pierre.Bouzinac@onecert.fr

common mail address : ONERA / CERT / DOTA
Unité Lasers et Optoélectronique
2 avenue Edouard Belin
31055 TOULOUSE CEDEX 4 (France)

1. Introduction

Multi-level electronic integration of massively parallel computers leads to latency effects and I/O bottlenecks. Free space optical interconnections might be a good alternative to interconnect processors located on face to face PC boards.
When the processors are integrated in MultiChip Modules, an obvious improvement to the latency problem can be making the MCMs to communicate from board to board.
We present here part of a project which was led in collaboration with the CEA / LETI / DEIN (Commissariat à l'Energie Atomique) in Saclay (France).

The LETI DEIN was in charge of the conception of the parallel architecture, of the design of the MCMs and of the electrical architecture. The Optics Department of ONERA CERT has to make the choice of the optoelectronic components, their caracterization and hybridization.

2. The SYNOPTIQUE architecture

SYNOPTIQUE is the optical version of the previous SIMD massively parallel calculators developped by CEA/LETI /DEIN [1,2].
The processing units are constituted by ASICs including 4 PEs each. Then four ASICs are integrated in a ceramic MCM providing by this way more communication efficiency between the ASICs. One can find more rough information about the MCMs in ref. [3,4]. The last level of integration is constituted by the electronics boards where four MCMs are integrated. We can have untill 16 different boards connected on a common backplane..
All the MCMs of the architecture are linked by a ring network through the BUS backplane of the different boards. Free space optical links may allow MCMs on face to face PC boards to communicate. (figure 1)
For connecting the MCMs on two different boards, a linear Fresnel microlenses array is stuck onto a corresponding VCSEL array mounted in a DIP package (figure 2).
The choice of the focal length is very critical. We have developped a theory which allows to determine the best value of the focal length by using the diffraction Fresnel theory.

With the caracteristics of figure 2, we found the best focal length value f_{OP} :

$$\frac{1}{f_{OP}} = \frac{1}{R(z)} + \frac{1}{e/n + d}$$

where n is the refractive index of the Fresnel lens array and R(z) is the radius of curvature of the Gaussian beam in the Fresnel lenses plane.

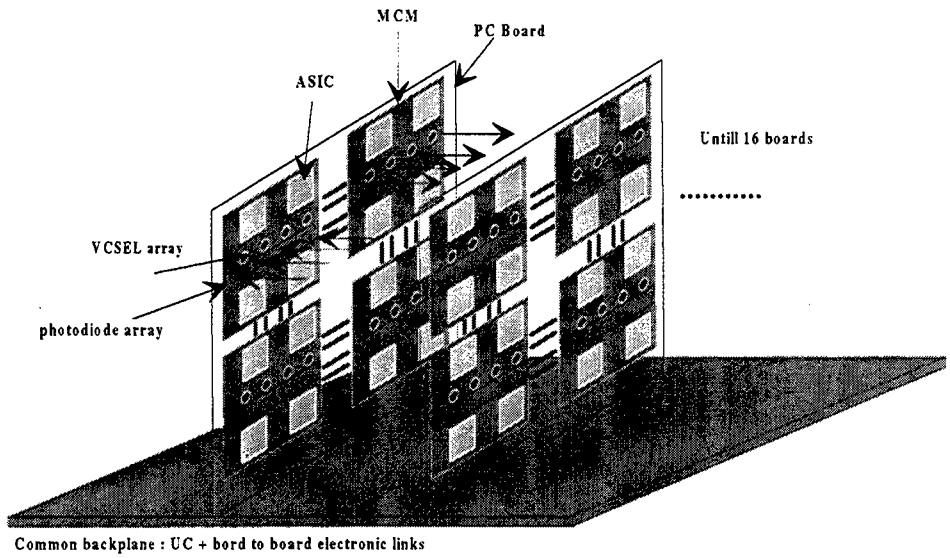

Figure 1 : Massively parallel Optoelectronic SYNOPTIQUE architecture

The radius of the beam waist in the detection plane is then given by : $W' = \frac{\lambda(e/n + d)}{\pi W(Z)}$

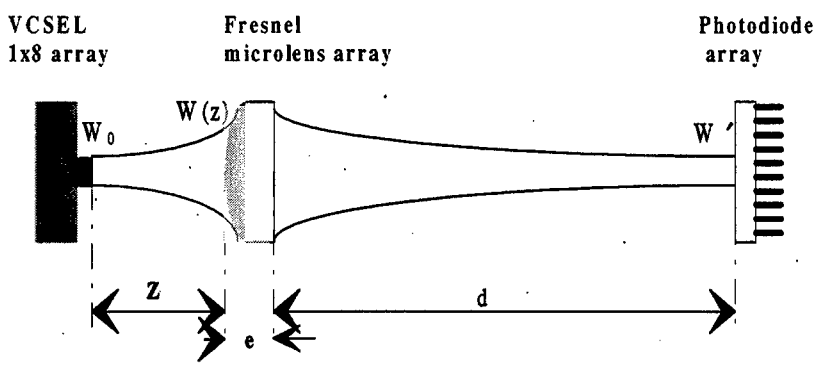

Figure 2 : Geometrical caracteristics of the free space optical link
Another calculation might allow us to take account of the truncature of the lenses.

3. Hybridization

We have developped an original method to hybridize the Fresnel lens array onto the VCSEL one. We first used a 1x16 linear VCSEL array from VIXEL corp where only one VCSEL over 2 is connected. The resulting pitch is 250 µm. The sources were GaAs / Ga Al As microlasers emitting at a central wavelength slightly above 854 nm. The microlenses and the laser package were positionned at a micronic precision with a microscope modified on purpose.
Figure 3 shows the superposition of the lasers and the microlenses plane with a reference grid centered on the lasers.

Figure 3 : Superposition of the VCSEL and Fresnel microlenses

Figure 4 shows the spots of 3 lasers in the detection plane and figure 5 the vertical profile of a particular spot.

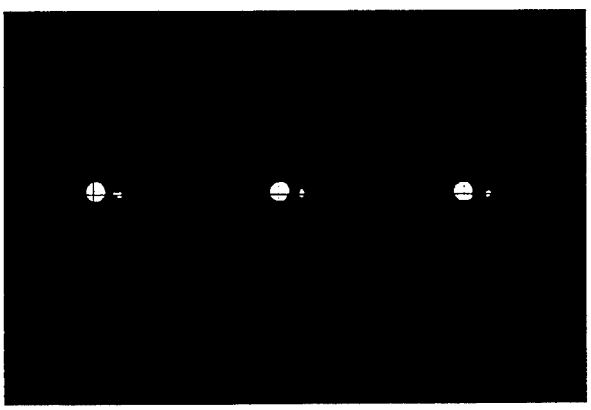

Figure 4

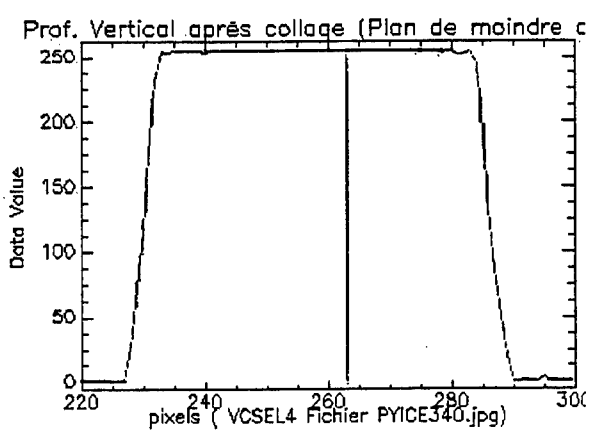

Figure 5 : Spot profil in the detection plane
1 pixel camera = 0,408 µm
Spot diameter = 26 µm

We are now doing the same work for a 1 X 10 VCSEL linear array manufactured by MOTOROLA Inc., which has a lower threshold current (2.2 mA instead of 5.8 mA for the previous device).

4. Conclusion

An original method to hybridize microlenses ans VCSELs was presented. The choice of the diffractive technology for focusing the VCSELs beams at a distance of several millimeters (untill 20 mm), was imposed by :
- the necessity to fix the focal length at the calculated f_{OP} best value
- the monochromatic radiation of the micrlasers

The spots diameter represents no more than 1/ 10 of the arrays pitch and its value at $1 / e^2$ is well predicted by the truncated gaussian beam theory.

References

[1] D.Juvin et al., Sympathi2, a 1.5 D processor array for image Applications. *Signal Processing IV : Theory and Applications*, Elsevier Science Publishers B.V., North Holland , 1988.

[2] T. Collette et al., Symphonie, calculateur massivement parallèle : modelisation et réalisation. proceedings of Journées Adequation Algorithme Architecture an Traitement du signal et images, Toulouse (France), pp.279-286, January 1996.

[3] P. Scheer, T.Colette, D.Juvin, A. Chenevas-Paule, J.P. Bouzinac, P.Churoux, M.Fracès, " A Massively parallel SIMD muti-processor using Optical interconnects : SYNOPTIQUE ", OC 96, Tech. Digest, Vol1, p 120

[4] P. Scheer, T.Colette (CEA/LETI/DEIN), P. Churoux (ONERA / CERT /DOTA) " Free space Optical Interconnections within Massively Parallel Computers ", MPPOI 1997, pp 167-177, june 22-24 1997 Montreal (Canada)

Reconfigurable optical interconnects in free-space optical processing modules based on polarization-selective diffractive optical elements

H Thienpont[1], N Nieuborg[1], A Goulet[1], A Kirk[3], P Koczyk[1], P Heremans[4], M Kuijk[4], C De Tandt[2], W Ranson[2], R Vounckx[2] and I Veretennicoff[1]

[1] Laboratory for Photonic Computing and Perception, [2] Laboratory for Microelectronics and Technology, Department of Applied Physics (TW-TONA), Vrije Universiteit Brussel, B-1050, Brussel, BELGIUM
Tel. +32 2 629 3451 Fax +32 2 629 3450 e-mail nnieubor@vub.ac.be

[3] Photonic Systems Group, Department of Electrical Engineering, McGill University, 3840 University Street, Montreal, Quebec, H3A 2A7, CANADA

[4] IMEC, Kapeldreef 75, B-3001 Leuven, BELGIUM

1. Introduction

Free-space optical interconnects have been widely used in parallel optical information processing systems [1]. The growing complexity of the desired routing configurations has created an urgent need for data transparent, reconfigurable and flexible interconnections. Polarization has always played an important role in the realization of such interconnects, because of the possibility to route the optical data via an electro-optic control of its state of polarization.

In this paper we demonstrate the use of polarization-selective diffractive optical elements for the realization of reconfigurable optical interconnects in parallel free-space optical information processing modules. In these modules a liquid crystal variable retarder is used as a polarization controller and arrays of differential pairs of optical thyristors [2] serve as optoelectronic processing planes. These differential pairs of optical thyristors may be used as dual-rail optoelectronic transceivers in digital information and image processing systems [3, 4]. Differential competition ensures that if a voltage above the break-over voltage (V_{BR} = 5V) is applied after illumination, that side which received the greatest optical energy will emit light while the other will remain switched off. The emitted light is of a Lambertian nature and has a spectral full width half maximum of 45nm centred around 860nm.

Recently we have demonstrated array-to-array data transcription with a static fanout of 3 [3]. Therefore we built a compact and modular free-space imaging system (fig. 1). Light emitted from the transmitter plane was collimated through a 0.2 pitch GRIN-lens. The collimated beam was then diffracted into 3 beams by a diffractive optical element and focussed onto the receiver plane by a second identical GRIN lens [5]. The advantage of this optical system is that its Fourier plane is situated between the two GRIN lenses, allowing us to insert shift invariant diffraction based fanin and fanout elements.

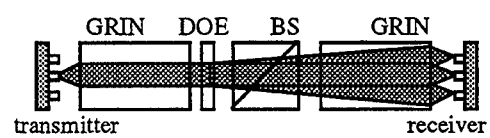

Figure 1. Optical system used for the data transcription between planes of optical thyristors; BS – beam-splitter.

In this paper we will show that it is possible to increase the functionality of this interconnection system by replacing the diffractive optical element with a polarization-selective diffractive optical element [6,7] in combination with a polarizer and a polarization controller.

Polarization-selective diffractive optical elements are elements that can fulfil two different functions dependent on the polarization of the incident beam. For the fabrication of such elements we use two wet etched calcite ($CaCO_3$) plates, which we align orthogonal to one another and join together using an index-matching thermoplastic (Cargille Meltmount 1.662) (see fig. 2). For such a structure a TM polarized beam will only see the phase pattern etched in the first substrate, whereas a TE polarized beam will only see the pattern in the second substrate. Typical first order diffraction efficiencies of these binary elements are 30-40%, and polarization contrast ratios up to 1000:1 have been demonstrated.

As examples of how to implement these ADOEs for reconfigurable interconnects we will bring forward two demonstrators. A first makes use of an on/off switchable binary grating that performs the logical NOT operation. The other allows establishing a reconfigurable 1 to 4 / 1 to 5 / 1 to 9 interconnection pattern between the emitting and the receiving plane.

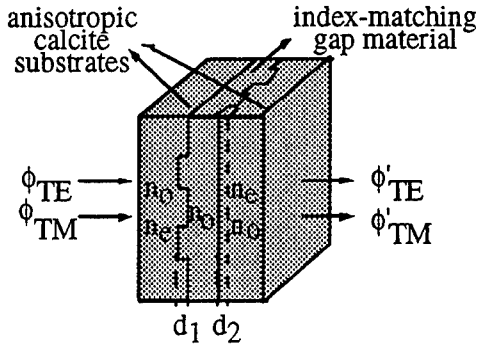

Figure 2. Polarization-selective diffractive optical elements consisting of two etched anisotropic substrates, joined together by an index-matching polymer.

2. Switchable digital optical logical inverter

Differential pairs of optical thyristors can be used as optical logic gates, by using the convention that a logical 1 corresponds to an emitting left hand thyristor, whereas a logical 0 corresponds to an emitting right hand thyristor [4]. Hence to perform a NOT operation within a dual-rail logic system it is necessary to interchange the signals of the left and right channels. Such a cross-over can be achieved through the use of a diffraction grating. By the choice of a suitable grating pitch the +1 diffracted beam from the left-hand transmitter channel can be made coincident with the right-hand receiver channel while the -1 diffracted beam from the right-hand transmitter can be coincident with the left-hand receiver. The gratings are designed such that the other orders fall outside the active area of the receivers. Fig. 3 shows the setup that was used to perform the reconfigurable inversion.

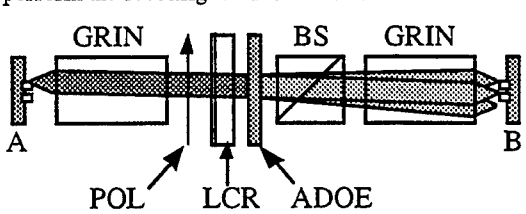

Figure 3. Integration of a switchable digital logical inverter between planes of optical thyristors; POL – polarizer; LCR – liquid crystal retarder; ADOE – anisotropic diffractive optical element.

The spacing between two thyristors in the receiver plane is 45μm, resulting in a grating period of 304μm. An individually electrically addressable pair of optical thyristors in the transmitter plane can be switched such that either the left or right hand side of the pair will emit light. A polarizer is used to polarize the light vertically (TE) (see fig. 3).

An electrically controllable liquid crystal retarder (LCR) is used to switch the polarization state between TE and TM. The polarization-selective grating was designed such as to simply transmit the light for TE polarization (yielding transcription without inversion), and to diffract it for TM polarization (yielding transcription with inversion). Fig. 4 shows the results of the switchable inversion.

The first two traces show the voltage applied to the left and the right transmitter elements. The third trace shows the output of the left thyristor of the receiver differential pair. The results show that dependent on the voltage applied on the LCR transcription with or without inversion is realized. The reconfiguration rate of this system is limited by the switching speed of the LCR, which is 20Hz in the case of a nematic liquid crystal retarder. In the case of a ferroelectric LCR this can be increased up to 20kHz.

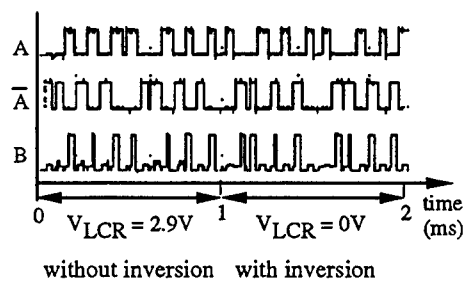

Figure 4. Demonstration of the NOT operation

3. Reconfigurable fanout element

The same principle of combining ADOEs together with liquid crystal polarization controllers can be used to realize more complicated reconfigurable interconnection schemes. In this paragraph we present a reconfigurable fanout element that, dependent on the polarization of the incident beam, connects either to 4, to 5 or to 9 nearest-neighbours in the receiver plane (see fig. 5).

In order to achieve this functionality we have designed two crossed gratings for the 1 to 4 and the 1 to 5 interconnect respectively. The spacing between the differential pairs in the receiver plane was 96μm in the horizontal direction and 100μm in the vertical direction, resulting in grating periods of 144μm and 137μm respectively. These resulting grating patterns are combined in one polarization-

selective diffractive optical element, that can realize the 1 to 4 interconnect for horizontally, and the 1 to 5 interconnect for vertically polarized light. For circularly polarized light a combination of the two functionalities is obtained and so a 1 to 9 interconnection will be established.

Fig. 5b shows the response of ADOE and fig. 6 shows the corresponding response of the receiver plane for the three different polarization states when the left-hand (a) and the right-hand (b) transmitter element were switched on. When the left-hand transmitter element is switched on the left-hand thyristors of the addressed differential pairs in the receiver plane will switch on (i.e. emit light), whereas the other elements of the receiver plane will not be addressed optically, and will therefore switch at random. We can see that the fanout is correctly realized. We should however note here that the higher the fanout the lower the intensity of the individual optical channels, resulting in a trade-off between the fanout of the grating and the switching speed of the thyristors in the receiver plane.

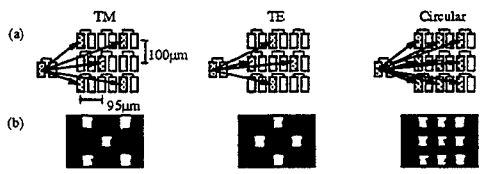

Figure 5. Desired interconnection scheme (a) and experimentally obtained output (b) for the reconfigurable polarization-based fanout-element when the polarization of the incident beam is vertical, horizontal or circular.

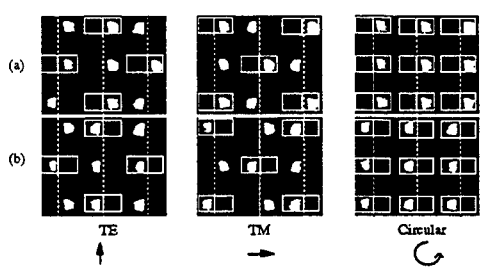

Figure 6. Output from differential pair receiver for input to the left (a) and to the right (b) for the different possible polarization states.

4. Conclusion

We have shown that we can increase the functionality of a free-space digital parallel optoelectronic data transcription system based on differential pairs of optical thyristors by use of polarization-selective diffractive optical elements and polarization controllers. We have demonstrated the application of a switchable diffractive grating as a logical inverter, and we have demonstrated that it is possible to realize reconfigurable 1 to 4, 1 to 5 and 1 to 9 fanout operations. Finally it is important to notice that we can easily change the functionality of the ADOE by altering its design or by replacing it with a polarization-selective computer-generated hologram [8], and that the techniques that have been presented here are also generally applicable to other types of opto-electronic transceiver elements.

References

[1] H. S. Hinton, An introduction to photonic switching fabrics, Plenum Press, New York, 1993.

[2] M. Kuijk, B. Knüpfer, P. Heremans, R. Vounckx, G. Borghs, "Down-scaling differential pairs of depleted optical thyristors," *IEEE Photon. Technol. Lett.*, vol. 7, no. 6, pp.646-648, 1995.

[3] A.G. Kirk, H. Thienpont, A. Goulet, P. Heremans, G. Borghs, R. Vounckx, M. Kuijk, I. Veretennicoff, "Parallel Optoelectronic Data Transcription with Fan-Out Between Planes of PnpN Optical Thyristors," *IEEE Phot. Techn. Lett.*, vol. 8, no. 3, pp.464-466, 1996.

[4] A.G. Kirk, H. Thienpont, A. Goulet, P. Heremans, G. Borghs, R. Vounckx, M. Kuijk, I. Veretennicoff, "Demonstration of Optoelectronic Logic Operations with Differential Pairs of Optical Thyristors," *IEEE Phot. Techn. Lett.*, vol. 8, no. 3, pp.467-469, 1996.

[5] A.G. Kirk, A. Goulet, H. Thienpont, N. McArdle, K.-H. Brenner, M. Kuijk, P. Heremans, I. Veretennicoff, "Compact optical imaging system for arrays of optical thyristors," *Applied Optics*, vol. 36, no. 14, pp. 3070 - 3078, 1997.

[6] N. Nieuborg, A. Kirk, B. Morlion, H. Thienpont, I. Veretennicoff, "Polarization-selective diffractive optical elements with an index-matching gap material," *Applied Optics*, vol. 36 (20), pp. 4681-4685, 1997.

[7] A. Goulet, N. Nieuborg, H. Thienpont, A. Kirk, P. Koczyk, P. Heremans, M. Kuijk, C. De Tandt, W. Ranson, R. Vounckx, I. Veretennicoff, "Polarization-based reconfigurable optical interconnects in free-space optical processing modules," *IEEE Phot. Techn. Lett.*, accepted.

[8] F. Xu, Y. Fainman, J.E. Ford, A.V. Krishnamoorthy, "Optoelectronic-VLSI packaging with polarization-selective computer-generated holograms," *Optics Letters*, vol. 22, no. 14, pp.1095-1097, 1997.

Demonstration of a Monolithic Micro-Optical Bridge for Free-Space Intrachip Interconnects

H.Thienpont, G. Verschaffelt, R. Buczynski, P.Tuteleers, P.Vynck, V.Baukens, S.Kufner, M.Kufner, A.Hermanne*, J.Genoe**, D. Coppée**, R. Vounckx**, P. Heremans*** and I.Veretennicoff

Department of Applied Physics and Photonics, Faculty of Applied Sciences, Vrije Universiteit Brussel, B-1050, Brussel, Belgium, Tel. 32 2 629 35 69, Fax. 32 2 629 34 50, Email hthienpo@vub.ac.be

*Cyclotron Department, Vrije Universiteit Brussel, Laarbeeklaan 103, B-1090 Brussel, Belgium

**Laboratory for Microelectronics, Faculty of Applied Sciences, Vrije Universiteit Brussel, B-1050, Brussel, Belgium

***IMEC, Kapeldreef 75, B-3001 Leuven, Belgium

Summary

Future advances in the application of photonic interconnects will involve the insertion of parallel-channel links into Multi-Chip Modules (MCMs) [1]. These will make use of new device-level components such as arrays of Vertical Cavity Surface Emitting Lasers (VCSEL's) [2] or arrays of Micro Cavity Light-Emitting Diodes (MCLED's) [3] and low power photoreceiver circuits [4]. One of the challenges associated with the development of free-space intra- and inter-MCM optoelectronic interconnects is the fabrication of manufacturable, chip-compatible, and high precision monolithic micro-optical pathway blocks. These three-dimensional modules should integrate micro-optical components to optically interconnect surface-normal transmitters and receivers.

In this paper we first report on the fabrication of such a refractive micro-optical bridge by deep proton lithography [5]. Next we use this component to demonstrate the proof-of-principle of optical intra-chip interconnects by establishing a digital data link between optoelectronic transceivers positioned on the same chip. Finally we project future performances of this approach by extrapolating present-day results in the light of improved lens and emitter characteristics.

Deep proton irradiation of Poly Methyl MethAcrylate (PMMA) is a deep etch lithographic technique that allows the fabrication of monolithic structures integrating refractive microlenses, microprisms, fiber positioning holes, stand-offs and alignment features [5] [6]. The technique works as follows: a proton beam in the energy range between 5 and 10 MeV, passing through a metal mask, impinges on a high molecular weight PMMA substrate. The protons break the polymer chains and decrease the material's molecular weight. Using a specific developer the irradiated zone can then be selectively removed, making it possible to structure the sample to depths of several hundreds of microns with an optical surface quality of better than 20 nm. To demonstrate an intra-chip optical interconnect between two opto-electronic transceiver elements, we have applied this deep proton lithography to fabricate a monolithic micro-optical bridge consisting of two micromirrors and two cylindrical microlenses (see Fig. 1 and Fig. 2).

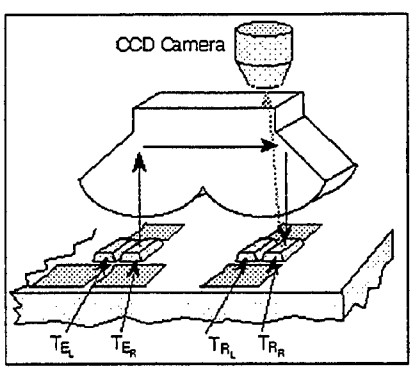

Figure 1 Setup for intra-chip data transcription

Figure 2 Photograph of the micro-optical bridge used to realize the optical pathway represented in fig. 1

As opto-electronic transceiver elements we have used optical thyristors [7]. These emitter-receiver devices are fabricated as a double heterojunction PnpN structure in the GaAs/AlGaAs material system. They are bistable

elements and have an S-shaped quasi-static I-V curve. Thyristors can be operated both in a light emitting (850 nm) and a light detecting mode depending on the control voltage.

For a voltage below the breakover voltage V_{BR} the thyristors are said to be in their 'off' state and they have a high impedance. When a voltage greater than V_{BR} is placed across them, this impedance falls dramatically and they emit light as a LED. External illumination reduces V_{BR} and they are thus optically sensitive. This optical sensitivity can be greatly increased by connecting two devices together with a common resistance in a differential pair configuration. When an optical input is applied to one of the elements photo-induced electron-hole pairs are generated. Placing a voltage across the pair causes a differential competition to take place between the elements. The one which has the lowest break-over voltage (caused by precharging due to the optical input) will begin to switch on first, drawing charge carriers from the other and preventing it from switching on. The energy required to switch such a differential pair is 15 aJ μm^{-2} optical window area. After emission the devices are reset in less than 5 ns by applying a negative voltage pulse (-8V). The devices used at present have an active window of 16 μm x 19 μm. The center separation of each element in the pair is 26 μm (see Fig. 3).

In our experiments we used two kinds of thyristor configurations: a thyristor pair where both thyristors are electronically and individually addressable (see Fig. 3a) and a differential pair configuration that is optically addressable (see Fig. 3b). An optical signal sent from the right handside thyristor emitter T_{ER} is routed by the optical bridge to the right handside receiver T_{RR}, and the left handside thyristor emitter T_{EL} signal is routed to the left handside receiver T_{RL}, respectively. Because of the differential nature of the receiving thyristors, it is only the difference in energy received by T_{RR} and T_{RL} that will determine which one of the receiving thyristors will switch on. Therefore data transcription will not be disturbed if some of the light is falling on the wrong receiving thyristor, e.g. if light is going from T_{EL} to T_{RR}.

The distance between the center of the lenses is choosen to match the pitch of the two thyristor pairs (844 μm). The lenses have apertures of 844 μm and focal lengths of 1044 μm. Microlens M_1, positioned above the individually addressable thyristors T_{EL} and T_{ER} acts as a beam collimator, while microlens M_2 collects incoming light on the optical window of thyristors T_{RL} and T_{RR} respectively, both working in receiver mode. Each micromirror surface makes an angle of 45° with respect to the optical axes of the lenses in order to deflect the collimated beam by 90°. The optical bridge was designed such that the mirrors cover only half of the lens aperture such that a part of the light can escape from the top of the bridge, which allowed us to monitor the optical bitstreams (see Fig. 1).

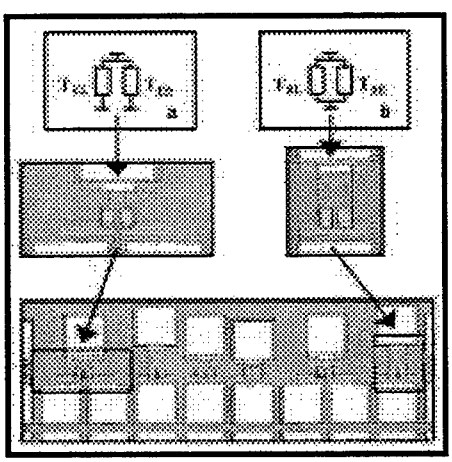

Figure 3 Photograph of the thyristor chip used to realize the optical pathway represented in Fig 1

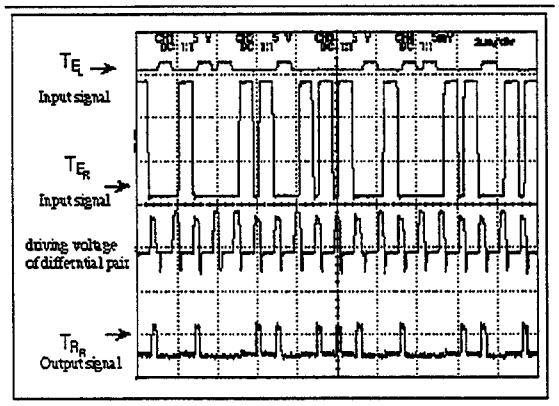

Figure 4 Driving waveforms for emitter (T_E) and receiver (T_R) and the optical output

To perform the experiment the optoelectronic chip was mounted on a probe station. An electrical waveform was applied to the emitting optical thyristor T_{ER} (see trace T_{ER} in Fig. 4) such that a regular optical bitstream was produced and sent to the receiving element T_{RR} (see trace T_{RR} in Fig. 4). In case of a correct data transcription, T_{RR} should switch on and start to emit light only when a logic one (corresponding to a high optical input) was sent by T_{ER}. As can be seen in Fig. 4, the binary input data from T_{ER} are perfectly reproduced by T_{RR}. In order to determine the maximum transmission rate, the duration of the input signals was reduced until reliable transcription was just

obtained. The minimum bit length achieved was 1 μs (consisting of 800 ns for the receiving phase and 200 ns for the reset and emission phase of the differential pair) when an input driving voltage of 14 V was used. This is equivalent to a bit rate of more than 1 Mbs^{-1}.

Using a Monte-Carlo based radiometric simulation we found an optical efficiency η_0 of 0.06% for the photonic data transmission system described above. Together with the switching energy E_s of the differential pair and the power P_e emitted by the individual thyristors, we can determine the minimum duration τ_e^{min} of the receiving face of the differential pair in order to obtain correct data transcription.

$$\tau_e^{min} = \frac{E_s}{P_e \eta_0}$$

Using 6 fJ for E_s and 35 μW for P_e, we found a value of 0.3 μs for τ_e^{min}, which is in good agreement with the experimental value of around 0.8 μs. The difference between the experimental and the expected value can be attributed to misalignment errors.

From the expression for τ_e^{min} we can see that there are different ways to improve the performance of the interconnection. First it is possible to improve the efficiency of the optical system by replacing the cylindrical lenses with spherical lenses, which can also be fabricated by deep proton lithography [5]. Next, we can replace the thyristors, which are Lambertian sources, by transceivers with better output characteristics and a higher emission efficiency, such as MCLED's and VCSEL's. Table 1 gives an overview of the calculated optical efficiencies for different configurations. Note that all of these efficiencies can be multiplied with a factor of two by making the micro-mirrors longer, such that the mirrors cover the complete lens aperture. In the case of the MC-LED and the VCSEL based system, the overall system performance will not only increase due to a higher optical efficiency of the optical pathway block, but also because these sources have a higher emission efficiency [3].

Configuration	**Optical efficiency** (mirrors cover half of the lens aperture)
Cylindrical lenses, LED (div. Angle 180°)	0.06 %
Spherical lenses, LED (div. Angle 180°)	0.9 %
Spherical lenses, MC-LED (div. Angle 100°)	1.5 %
Spherical lenses, VCSEL (div. Angle 12°)	46 %

Table 1

In this paper we have demonstrated a single channel monolithic free-space micro-optical intra-chip interconnect. The optical bridge was fabricated by deep proton lithography. The concept of this approach can be extended to manufacturable massively parallel optical intra- and inter-chip interconnects. Although we reported on moderate bandwidths only, it can be stated that this technology holds all the potentialities for very large bandwidths and huge aggregate bitrates. At the conference we will report on more advanced multi channel optical bridges with spherical microlenses which we are currently characterizing for cross-talk and optical efficiency.

References

[1] R.F.Carson et al., "Low-power approaches for parallel free-space photonic interconnects", SPIE CR 62, Eds. R.T.Chen and P.S.Guilfoyle, pp. 35-63, 1996.

[2] K.H. Gulden, D. Ruffieux, K. Thelen, M. Moser, D. Leipold, J. Epler, H.P. Schweizer, E. Greger and P. Riel, "16*16 Individually Addressable Top Emitting VCSEL Array with High Uniformity and Low Threshold Voltages", Proc. E.O.S., Conf. On Optics and Information, pp. 6.1, Mulhouse, France, 1995.

[3] H. De Neve, J. Blondelle, P. van Daele, P.M.A. Demeester, R.G. Baets, G. Borghs, "Planar substrate-emitting microcavity light-emitting diodes with 20% external QE", Proc. of SPIE, vol. 3002, pp. 74-84, SPIE Photonics West, San Jose, California, 1997.

[4] T.K. Woodward, A.V. Krishnamoorthy, A.L. Lentine, L.M.F. Chirovsky, "Optical receivers for optoelectronic VLSI", IEEE Journal of Selected Topics in Quantum Electronics, vol. 2, pp. 106-116, 1996.

[5] M. Kufner and S. Kufner, "Micro-optics and Lithography", VUB Press, Brussels, 1997.

[6] M. Kufner, S. Kufner, "Fabrication of monolithic integrated fiber-lens connector arrays by deep proton irradiation", Microsystem Technologies, pp. 114-118, 1996.

[7] B Knupfer, M Kuijk, R Vounckx, P Heremans, G Borghs, "Cascadable differential PnpN optoelectronic switch operating at 50 Mbit/s with ultrahigh optical input sensitivity", Electr. Letts. 31 pp 485-486, 1995.

Diffractive Optics and Micro-Optics

Poster Preview

Tuesday, June 9, 1998

G. Michael Morris, University of Rochester
Presider

DTuD
3:30pm–4:30pm
Koa Room

Optical Elements for Elimination of On-Axis Visible Transmission

Luzhong Cai, Chunfei Li, Jianhua Zhao, and Hua-Kuang Liu
Department of Electrical and Computer Engineering
University of South Alabama
Mobile, Alabama 36688-0002
(Voice) 334-460-7516
(Fax) 334-414-8272
E-mail: liuhk@aol.com

We have analyzed the transmitted spectra of optical elements including the phase gratings and Fabry-Perot (FP) and found design parameters of these elements for the elimination/reduction of on-axis transmission of broadband of visible light.In this paper, we will present a detailed theoretical analysis on the design and performance of the optical elements that will greatly reduce the transmittance of the beam in its original path of propagation. We will give the numerical computation results derived from the formula showing the spectral dependence of the direct intensity transmittance for different optical elements.

Recently, it has been noticed that optical elements enabling the reduction of zero order transmittance are needed for the applications in optical limiting. For this reason, we have systematically analyzed with numerical computations the transmission properties of a variety of diffractive optical elements. These elements include the rectangular phase grating, the blazed (or triangular) phase grating, the sinusoidal phase grating, and the FP, which are illustrated in Fig.1. The analyses include the zero order intensity transmittances with respect to the variation of the depth of modulation, and the spectral response of transmittance functions in the visible band (400 to 700 *nm*). The effects of the errors in the fabrication of the depth of the groves of the phase gratings and the spacing between of the two mirrors of a FP on the element's zero order transmittance have also been analyzed. With regard to the spectral response of the zero order(on-axis) intensity transmittance of these elements, we have reached the following conclusions.

1. All the optical elements we analyzed can provide zero direct transmittance for a certain wavelength if their shape and depth are specially designed.

2. It is not possible to totally extinguish the directly transmitted light over a wide range of wavelength. Nevertheless, a specifically designed optical element such as a diffraction grating can provide a very low direct light transmittance over quite a broad range of wavelength. The zero order transmittance function depends on a parameter m, which defines the grating modulation depth or the separation of the two mirrors in a FP, h. For example, the light intensity transmittance, T, of the visible band is less than 0.2 for a rectangular grating (m=0), less than 0.1 for a blazed grating (m=1,2,3) and a sinusoidal grating (m=2,3,4, ...), and less than 0.02 for a blazed grating ($m\geq3$, see Fig.2 as an example), a sinusoidal grating ($m\geq10$) and FP (m=0, R≥0.8).

3. The bandwidth of the spectral response of each optical element also varies with the parameter *m*. For the rectangular grating a lower *m* yields a wider spectral response. For the blazed and sinusoidal gratings a higher *m* gives a low zero order transmittance over a broader spectral band. The lowest order (m=0) provides the lowest T and broadest spectral band for the FP.

4. In practice, it is nearly impossible to fabricate a grating exactly according to the design specifications. We have paid special attention to this point and evaluated its effects. (We have found that there is a difference in the intensity transmittance for different optical elements that have different grating depth deviation, Δh, which is due to the inaccuracy in the fabrication of the gratings) The theoretical analyses show that the error of h, Δh, due to the inaccuracy in the fabrication of elements, will generally increase the zero order transmittance and reduce the spectral bandwidth of low transmittance. However, the effects of Δh on the transmittance are different for different elements. The blazed grating gives the greatest allowance for this fabrication error. Specifically, in Fig. 3, it can be seen that T<0.02 for m=3 and T<0.004 for $m \geq 5$ over the visible wavelength (between 400 and 700 *nm)* and for Δh = -100 to 100 *nm*.

The results of our analyses should be useful for the design of a variety of optical elements of low zero order transmittance which can serve as foundations in the creation of a new and important class of optical limiting devices.

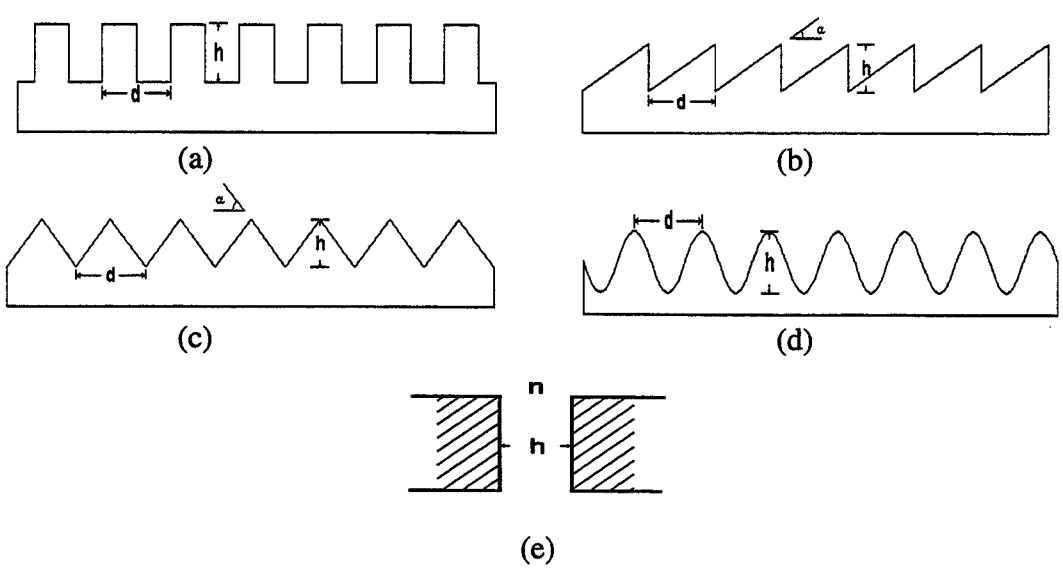

Figure 1. The phase structure of the (a) rectangular grating, (b) and (c) blazed gratings, (d) sinusoidal grating, and (e) FP.

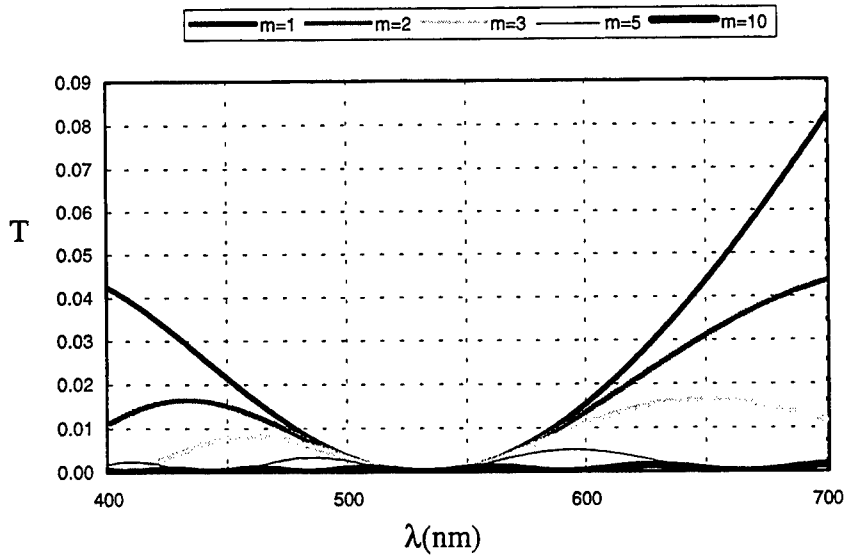

Figure 2. Zero order intensity transmittance spectra, T, of the blazed grating for different *m*.

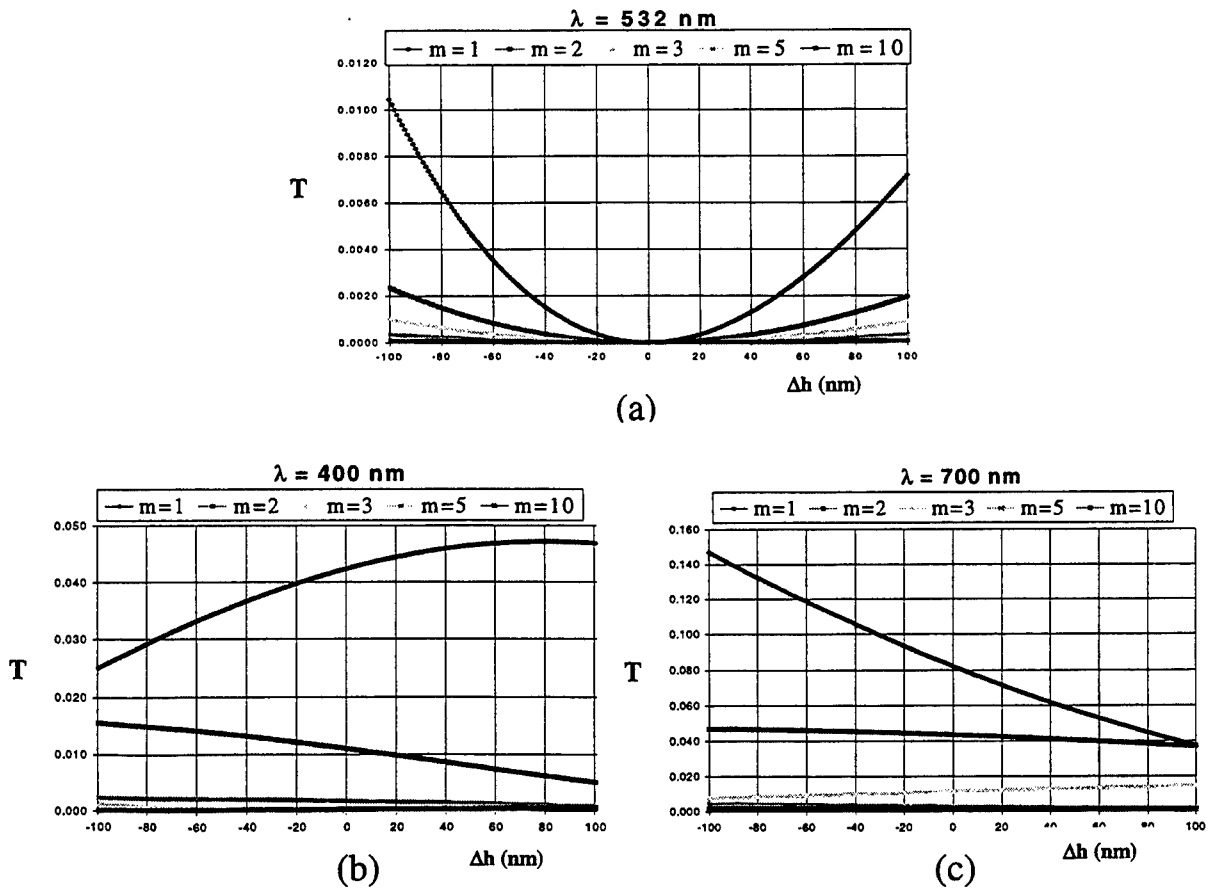

Figure 3. The zero order intensity transmittance, T, of a blazed grating versus the depth deviation Δh for different values of *m* at three different wavelengths.

Generic approach to relate surface-relief profile height and the phase function of diffractive optical element

Michael A. Golub,

(Holo-Or, Ltd., Kiryat Weizmann, P.O.B. 1051, Rehovot 76114, Israel,
tel: 972-8-9409687, fax: 972-8-9409606)

1. Problem of diffractive microrelief characterization

Phase transfer function Φ of thin surface-microrelief diffractive optical element (DOE) is usually considered proportional to its microrelief height h in accordance with relation $\Phi = k\mu h$, where $k = 2\pi/\lambda$, λ is the wavelength, μ is the scaling factor. Conventional approximate equations[1] are $\mu = n-1$ for transmitting and $\mu = 2\cos\theta_0$ for reflective elements, where n is the refractive index of the microrelief material and θ_0 is the angle of incidence. This relations are approximate even within scalar diffraction approach because they do not take into consideration the local slopes of the incident and the output beam as well as the curvature of the substrate surface, orientation of microrelief with respect to incident beam. Solutions of rigorous diffraction theory[2] are much more precise, but limited to the cases of regular diffraction gratings, while most of DOEs and computer generated holograms feature more complicated spatial structure. Piecewise-smooth surface considerations[3,4] are related to the definite type of DOE and require numerical solutions even for simple phase functions.

The necessity for getting more exact equations for "height and phase " relations is felt strongly for DOEs with relatively low F# and also for diamond-turned DOEs based on curvilinear substrate surface. Fig. 1 illustrates how phase mismatch got by the use of equation $\mu = n-1$ gives the reduction of diffraction efficiency ε of DOE, depending on F# parameter.

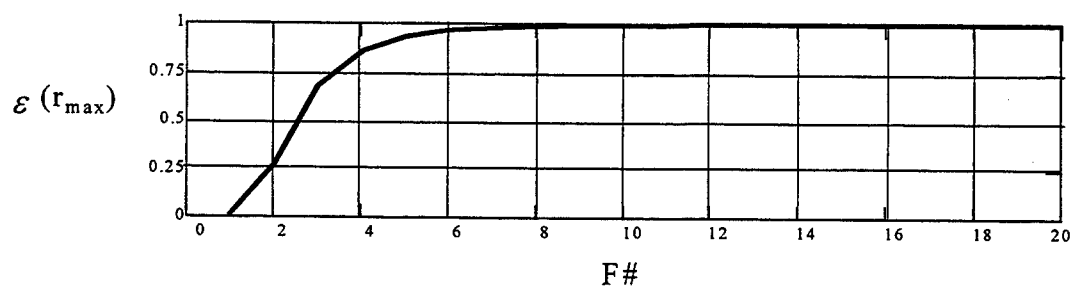

Fig. 1. Efficiency fall on the edge of lenses with various F-numbers (transmitting microrelief on the surface on the side of focus, height measured along the optical z-axis)

1. Generalized equations for microrelief height

In this report we offer general method for getting analytical microrelief equations that relate DOE phase transfer and microrelief height with specially modulated μ factor that we will call now "modulation factor". Our approach gives maximum accuracy possible for thin-element approximations in scalar description of the light. The equations for μ factor are derived by local plane wave approach, that is similar to the ray-tracing but more suitable for this task. The proposed general way to get new equations for modulation factor μ and microrelief height h in the following. We apply ray tracing eikonal equations within the microrelief thickness and proceed with diffraction just after microrelief. The substantiation for the use of the geometrical optics is the small height of microrelief in thin optical elements. Thus we reduce actual beam propagation inside diffractive microrelief pattern to the phase

jump on the substrate surface. Cases of reflecting and transmitting DOEs with microrelief located on (or opposite to) the side of incident beam are under consideration. Fig. 2 shows as an example the geometry for reflective microrelief and introduces proper notations. The microrelief shape on any surface can be presented in the form $\mathbf{r}_R = \mathbf{r} + h(\mathbf{r})\mathbf{N}_S$, where $\mathbf{r}$ - point on thin microrelief surface, $h(\mathbf{r})$ – microrelief height along the vector $\mathbf{N}_S$ that can be either unit normal vector of the surface or the ort of the optical axis z. Local plane-wave approximation of incident-beam, output beam eikonals and eikonal inside microrelief can be applied in the vicinity of the point $\mathbf{r}$ ($\mathbf{N}_0, \mathbf{N}, \mathbf{N}_M$ -unit vectors of incident, output beam and beam inside the material of microrelief respectively, the last vector used for transmitting case only)

$$kS_0(\mathbf{r}) = kn_0\mathbf{N}_0\mathbf{r}; \quad kS(\mathbf{r}_R) = kS(\mathbf{r}) + kn\mathbf{N}(\mathbf{r}_R - \mathbf{r}); \quad kS_M(\mathbf{r}_R) = kS_M(\mathbf{r}) + kn_M\mathbf{N}_M(\mathbf{r}_R - \mathbf{r}) \qquad (1)$$

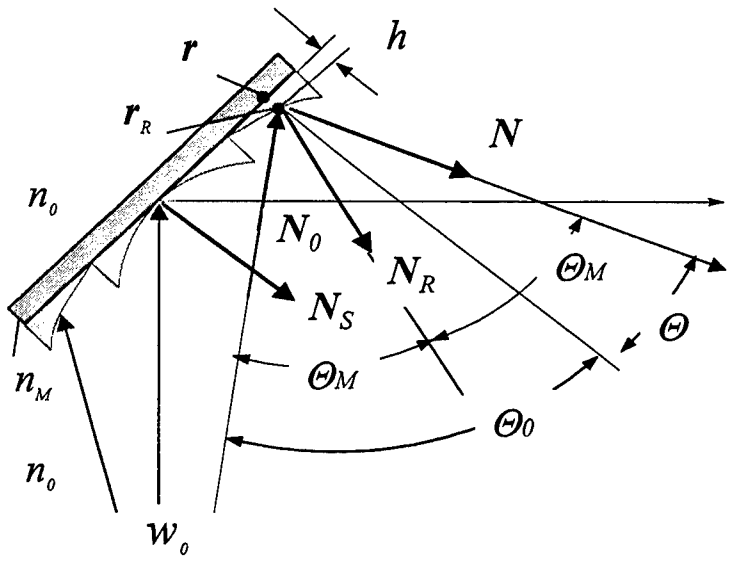

Fig. 2. Light beam interaction with reflective-type diffractive microrelief

Continuity equations $S(\mathbf{r}_R) = S_M(\mathbf{r}_R)$, $S_M(\mathbf{r}) = S_0(\mathbf{r})$ give us proper presentation for the phase function of DOE for transmitting case and general expression for the height modulation factor for transmitting microrelief located on the substrate on the side of focus:

$$\Phi(\mathbf{r}) = k[S(\mathbf{r}) - S_0(\mathbf{r})] = k\mu(\mathbf{r})h \qquad \mu(\mathbf{r}) = k(n_M\mathbf{N}_M\mathbf{N}_S - n\mathbf{N}\mathbf{N}_S)h \qquad (2)$$

It is shown that the basic equation like Eq.(6) can brought to the form depending directly on the local angles of incident beam and output beam. For reflective microrelief derived equation takes form

$$\mu = n_0\cos\Theta_0 + n\cos\Theta, \qquad \text{generalizing} \qquad \mu = 2n_0\cos\Theta_0 \qquad (3)$$

where Θ_0- angle of incidence (input), Θ - angle of final refraction (output). For transmittance-type microrelief derived equation takes form

$$\mu = \sqrt{n_1^2 - n_0^2\sin\Theta_0} - n\cos\Theta, \text{ generalizing } \mu = n_1 - n_0 \qquad (4)$$

The important result is that $h_{\max}$ depends on the local angle of arrival and the angle of deflection of the ray in each point of diffractive element. So the phase-matching conditions are varying from point to

point. Exact expression (4) for μ -factor presented is applicable to both the ray-traced beams and to "complex-eikonal" beams such as the Gaussian ones[5].

3. Examples for microrelief height correction

Microrelief equation we proposed gave us possibility to enhance the design of several optical elements. As an example Figs 3 show the μ -factor dependence for diffractive lens with plane substrate. The impact of the modulation factor on the diffractive microrelief height on aspherical surface is illustrated in Figs. 4,5 where microrelief height is calculated along the optical z-axis.

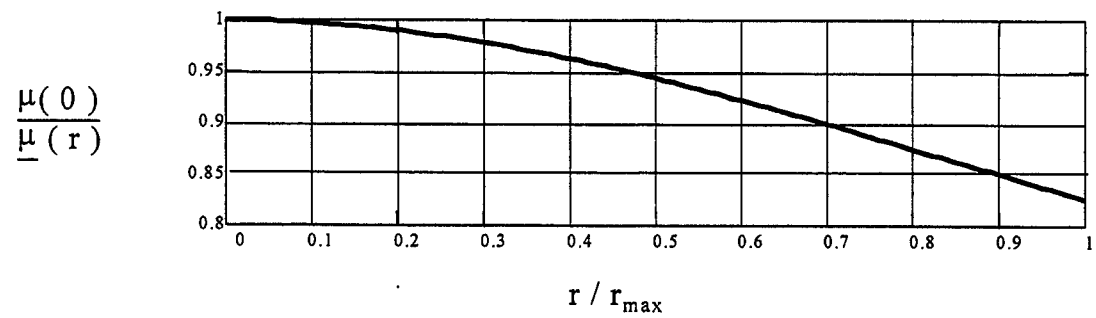

Fig. 3. Modulation curve for microrelief within the aperture of the lens with f-number 4 (transmitting microrelief, on the surface on the side of focus, height measured along the optical z-axis)

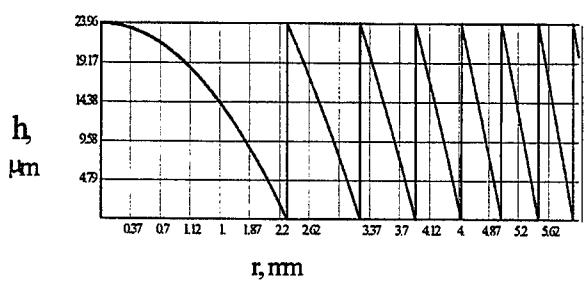

Fig. 4. Example of regular diffractive microrelief profile within traditional approach

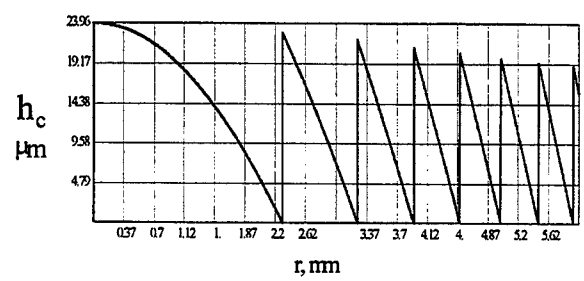

Fig. 5. Example of corrected diffractive microrelief profile, calculated with modulation factor

Conclusions

- Microrelief height nonlinearly depends on phase function, its gradient in each point and orientation of the diffractive microrelief pattern with respect to the incident beam
- Maximum height (depth) of diffractive microrelief depends on the local angles of incident and "diffracted" ray and varies from zone to zone while phase jumps are constant and equal to 2π.
- Microrelief equations we proposed gave us possibility to enhance the performance of wide class of diffractive optical elements

References

1. Francon M., Holographie, Masson et Cje, Paris, 1969
2. Pommet D.A., Moharam M.G., Grann E.B., Limits of scalar diffraction theory for diffractive phase elements, *J.Opt.Soc.Am,* **A 11(6)**, 1827, 1994.
3. Hazra L.N., Han Y., Delisle C.A., Curved kinoform lenses for stigmatic imaging of axial objects, *Applied Optics*, 32(**25**), p. 4775, 1993.
4. Han Y., Hazra L.N., Delisle C.A. , Exact surface-relief profile of a kinoform lens from its phase function, *J.Opt.Soc.Am,* **A 12**(3), p. 524, 1995.
5. Soifer V. A., Golub M.A., Laser beam mode selection by computer generated holograms, CRC Press, Boca Raton, 1994.

NEW THEORETICAL METHOD FOR NONUNIFORM GRATINGS INVESTIGATION

G.G.Karapetyan

Fiber Optics Communication Laboratory,State Engineering University of Armenia
105 Terian str.,Yerevan 375009, Armenia,E-mail:hovik@seua.am

Uniform Fiber Bragg Gratings are wavelength selective reflectors obtained by a periodic modulation of core refractive index along the fiber. They have many applications as narrow-band elements in optical fiber systems. Recently the NG are used for many purposes [1]. For their investigations the numerical solutions of coupled mode equations are used traditionally. This appoach requires a much machine time, and is not convenient for NG design. Therefore the analytical formulaes for characteristics of NG will be of benefit in NG design, syntezing, and optimization. The first step in solving this problem has been undertake in [2] where the WKB- approximation for solving coupled mode equations has been used. The drawback of this approximation is that it is not uniform in all frequency interval and is not valid near so called turning points. Then, an unknown phase shift occurs in formulaes which can not be determined within the WKB- approximation, and one needs to evaluate this unknown parameter from qualitative estimations. To avoide these drawbacks of WKB- approximation we elaborated another more suitable method which is valid uniformely in all frequency interval. This method, called R-approximation is the generalization of asymptotic solution of second order differential equation having one turning point [3] for the case when there are two or more turning points. In the result the analitical formulaes for characteristics of arbitrary NG obtained. R-approximtion is more exact and common than WKB-approximation. The last come to R-approximation by removal from turning points. As an uniform asymtotic formulaes R-approximation has a relative error ~ O(1/H) in all frequency interval, where $H=\pi\mu N$ describes the gratings strength, μ-is the depth of effective permittivity modulation, N-is the number of grating periods (for uniform grating the maximum reflectivity is $|R|^2=th^2(H/4)$). On the basis of obtained common formulaes a special case of linearly chirped gratings (LCG) is investigated in detail and a designing software "LCG" is created. This software provides all characteristics of LCG versus strength, detuning, and chirping rate, and is a powerfull and convinient tool for designers.

In Fig.1 the reflectivity and relative delay is presented. Here $x=(n\omega\Lambda(0)/\pi c-1)/\mu$ -is dimensionless detuning, $r=(\Lambda(0)/\Lambda(L)-1)/\mu$ -is chirping rate ,$\Lambda(0)$ and $\Lambda(L)$-are local periods in the beginning and the end of LCG, n -is the average refractive index, ω -is the frequency, c -is the speed of light *in vacuo*. Note that in these units unchirped strong grating has a bandwidth x=(-1/4,1/4).One can see that the bandwidth of LCG increases linearly by increasing $|r|$, exceed in ~2 times the bandwidth of unchirped grating when $|r|\cong 1/2$. Relative delay is an oscillative function from frequency which middle value is about linear function in grating bandwidth and is constant out of bandwidth.

REFERENCES

[1] Special issue on fiber gratings, photosensivity, and poling, IEEE J. Lightwave Technol. vol. 15, No 8, 1997.

[2] L.Poladian,"Graphical and WKB analysis of nonuniform Bragg Gratings", Phys.Rev.E. vol.48,No 6,pp.4758-4767, 1993.

[3] H.Jeffreys, B.Swirles," Methods of mathematical physics", Cambridge University Press, Cambridge, 1966.

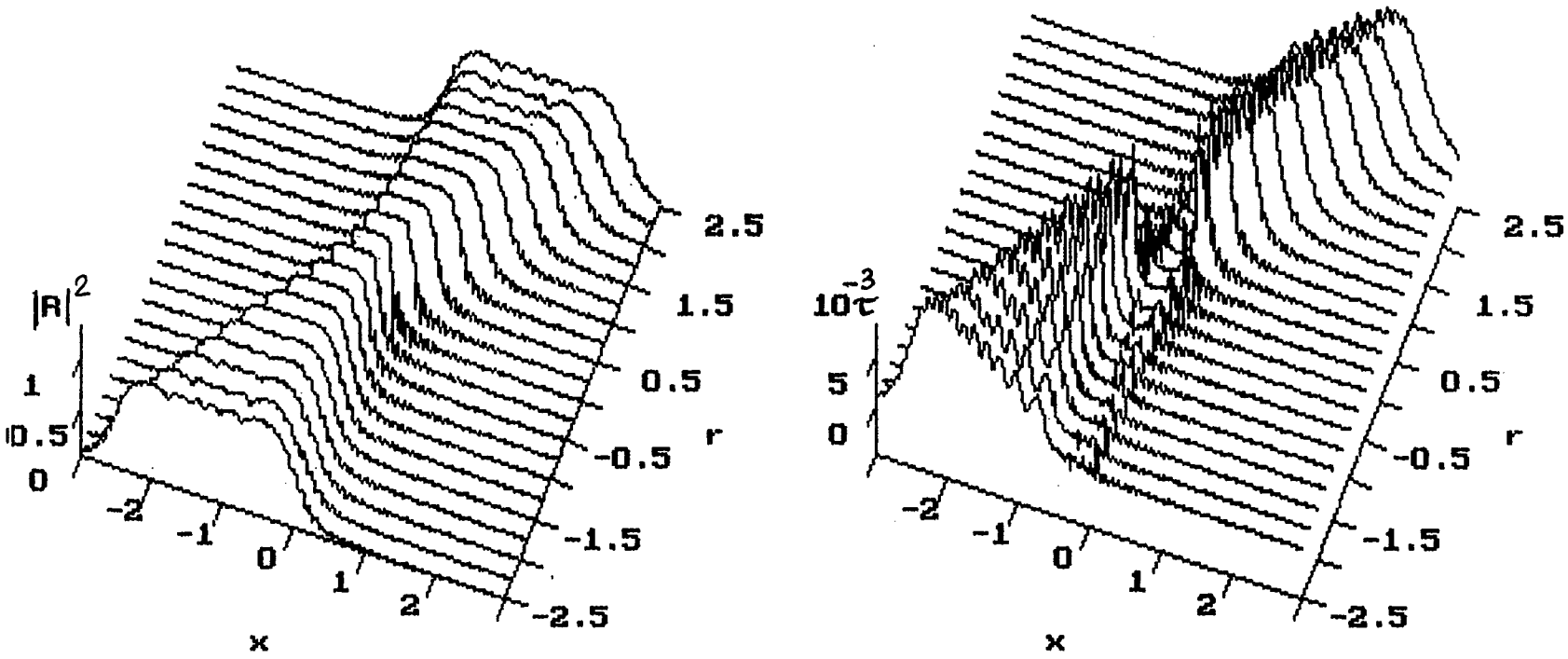

Fig.1 Reflectivity and relative delay of linearly chirped grating. $H=10\pi$.

A Contribution to the Analysis of Relief Diffraction Gratings

I. Richter, Z. Ryzí, and P. Fiala

Czech Technical University in Prague, Faculty of Nuclear Sciences and Physical Engineering

Department of Physical Electronics, Břehová 7, 115 19 PRAGUE 1, Czech Republic

Phone: (4202) 2191 2285, Fax: (4202) 688 4818, e-mail: richter@troja.fjfi.cvut.cz

In the last years, modeling in diffractive optics have been of great interest due to increasing amount of applications of diffractive optical elements in many different optical areas [1]. As far as the analysis problem is of interest, originally-used scalar methods became inapplicable, and more complicated (i.e. rigorous) treatments had to be developed. Among several rigorous methods (integral, modal) for the analysis of diffraction characteristics of dielectric gratings proposed, the rigorous coupled-wave analysis (RCWA) has been employed the most since it is a deterministic, noniterative, relatively straightforward technique for obtaining the exact solution from the exact electromagnetic formulation [2].

The goal of this paper is to compare different methods describing the diffraction from periodic diffractive structures. Diffraction characteristics of relief gratings with various relief profiles (as the binary grating shown in Fig.1) for both TE and TM polarizations are studied using several different theoretical approaches: RCWA, Kogelnik's two-wave method, the scalar method of transmittance, and combined method based on optical path, amplitude transmittance and coupling effects. Typical relief profiles are compared and analyzed, and some general conclusions are made. For comparison

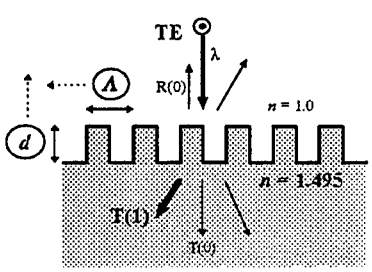

Fig. 1 Diffraction from a surface-relief grating.

purposes, gratings made from an isotropic nonabsorbing substrate in the planar diffraction regime, and both TE (electric field *parallel* with grating grooves) and TM (magnetic field *parallel* with grating grooves) polarised incident waves, are considered. The diffraction efficiency of such gratings is calculated with respect to the relative grating profile depth (d/λ) and relative period (Λ/λ) in order to describe and explain the behavior of diffraction efficiency, i.e. to identify the regions with typical diffraction regimes, of all gratings of a chosen kind given by a grating profile. The whole kind of gratings with a given grating profile can thus be analyzed simultaneously provided that the angle of incidence and refractive index of the grating material are given (see, e.g. Fig.2 for the case of a binary grating). In that way, it is possible to choose the most efficient grating, and also to better understand the synchronism and coupling processes leading to a specific diffraction efficiency functioning in the whole (Λ/λ, d/λ) plane.

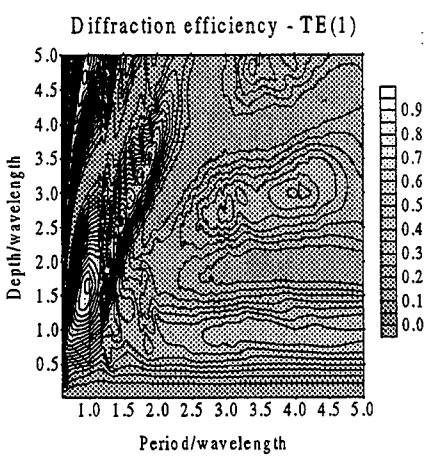

Fig. 2 Diffraction efficiency of the transmission binary grating in the first transmission order and TE polarization, 30 deg. angle of incidence, refractive index n=1.495.

The method of transmittance formulates transmittance amplitude function which directly gives the diffraction efficiencies in particular diffraction orders for *thin gratings*. Such theory is especially valuable if the ratio of the grating period over wavelength is much larger than one. Both the classical and modified methods of transmittance, as defined in Ref. 3, are treated in this paper. In contrast to the classical method, the modified approach incorporates in its transmittance function the changes of the volume phase synchronism with respect to the relative grating period [4]. It is based on a different approach in defining the transmittance function by calculating the optical path difference between real and reference rays,

i.e. on incorporating the propagation process of diffracted waves within a grating into the transmittance function. It will be also shown how the transmittance method can be combined with optical path method including coupling effects during the propagation through the grating depth in order to properly describe the volume phase synchronism (the combined method). The volume phase synchronism will be compared with that obtained by the RCWA technique.

By analyzing the diffraction efficiency pattern, regions with typical diffraction regimes can be found: 1) High spatial frequency region, 2) Volume grating region 3) Intermediate region, 4) Thin grating region, and 5) Resonant regions [4]. Here, we discuss how these regions vary for different grating profiles and for the two incident polarisations (TE and TM). In detail, we discuss particularly the properties of resonant regions, i.e. such areas where diffraction orders (not only transmission but also reflection) are generated, i.e. just when they start to become propagating.

In conclusion, a comparison of different methods for calculating the diffraction efficiency of relief gratings was made for different relief profiles and the two incident polarisations, and the properties of diffraction regimes were discussed.

REFERENCES

[1] H. P. Herzig, Ed., 1997, *Micro-optics: elements, systems and applications*, (Taylor & Francis, London).

[2] Moharam, M. G. and Gaylord, T. K., 1982, Diffraction analysis of dielectric surface-relief gratings. *J. Opt. Soc. Am.*, **72**, 1385.

[3] Richter, I., Ryzí, Z., and Fiala, P., 1997, Analysis of diffraction gratings: comparison of different approaches, *Proceedings of EOS Topical Meetings Digest Series*, **12**, 140-141.

[4] Richter, I., Ryzí, Z., and Fiala, P., 1997, Analysis of diffraction gratings: comparison of different approaches, submitted to *Journal of Modern Optics*.

Rigorous coupled-wave diffraction analysis of stratified volume photopolymer holograms

Yukihiro Ishii
Department of Electronics, University of Industrial Technology, Sagamihara
4-1-1 Hashimotodai, Sagamihara, Kanagawa 229-11, Japan
Phone:+81-427-63-9161 Fax: +81-427-63-9168 e-mail: yukidai@uitec.ac.jp

Toshihiro Kubota
Department of Electronics and Information Science, Kyoto Institute of Technology
Matsugasaki, Sakyo-ku, Kyoto 606, Japan
Phone:+81-75-724-7443 Fax: +81-75-724-7400 e-mail: kubota@dj.kit.ac.jp

1. INTRODUCTION

Stratified volume holograms (SVHs) have been studied[1,2] in the layered structures of holograms that are useful for several applications in optical communication such as an optical wavelength-selective filter. The hitherto investigation was performed by using the beam propagation method (BPM) to emulate the SVH with thin (Raman-Nath) gratings, taking into no account the reflection at the boundaries. Here we develop a rigorous coupled-wave model to analyze the TE-polarized diffraction properties of stratified volume photopolymer holograms. The numerical and experimental angular selectivities of stratified holograms are shown.

2. RIGOROUS ANALYSIS OF STRATIFIED HOLOGRAM

Stratified hologram consists of a succession of thin holographic layers interleaved with homogenous buffer layers. As shown in Fig. 1, the stratified element consists of a succession of N_m thick grating layers with the thickness D_m and (N_m-1) intermediate buffer layers with the thickness D_b. The unslanted dielectric grating layers (region II) are divided into N_d thin planar grating slabs perpendicular to the z axis. Then the rigorous coupled-wave analysis[3] is applied to each slab grating. The electric fields used in the analysis are included forward and backward waves at the boundaries. The numerical procedure is shown to obtain the desired ith diffracted wave amplitude $S_{i,N,M}(z)$ in the Mth thin slab of Nth holographic modulation layer. The electric fields are substituted into the TE wave equation with dielectric sinusoidal gratings those corresponding index of refraction is

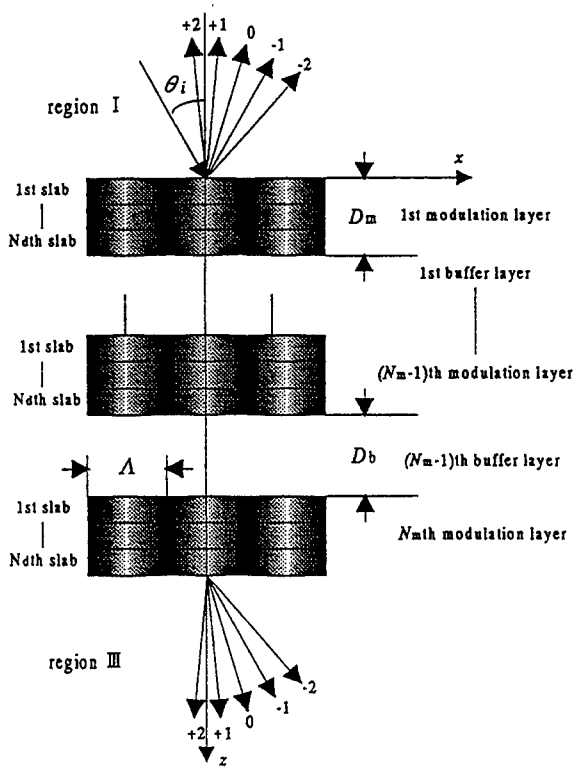

Fig. 1. SVH model to calculate it.

$$n(x) = n_0 + \Delta n \cos(Kx), \qquad (1)$$

where n_0 is the average index in the grating region, Δn is the modulation index of refraction and $K=2\pi/\Lambda$, where Λ is the grating period.

After performing the 2nd-order differentiation in the wave equation, the rigorous coupled wave equation for Mth thin slab inside Nth thick hologram is produced. The solutions in the diffracted field S_i can be changed from the original solutions[3] to

$$S_{i,N,M}(z) = \sum_{q=1}^{2s} C'_{q,N,M}\omega_{i,q,N,M} \exp\left[\lambda_{q,N,M} \cdot \left(z - \left((N-1)(D_m + D_b) + (M-1)\frac{D_m}{N_d}\right)\right)\right], \qquad (2)$$

where the quantities λ and ω are the eigenvalues and eigenvectors of the matrix showing the coupled wave equation, s is the number of the diffraction orders retained in the analysis, and the quantities C' are unknown constants to be determined by the boundary condition. For the computation in Eq. (2), the exponential term $\exp(\lambda_{q,N,M} \cdot z)$ increases as the waves propagate along z direction in the thick hologram layer and/or the diffraction order s increases. It causes the unwanted numerical overflow. The calculation in Eq. (2) can be virtually performed such that the thick hologram layer D_m is regarded as stacking the thin layer D_m/N_d inside the thick hologram layer. It can be exempted from the numerical overflow as the number N_d of stacked thin slabs increases as many as possible.

The numerical stabilities are retained from the boundary condition for the tangential electric field as well as the magnetic field between Mth and $(M+1)$th thin slabs. Finally the forward diffracted amplitudes can be solved by using the large system of equations derived from the boundary conditions with the use of the Gauss elimination with maximum pivot.[4]

3. SVH Angular Selectivity

A. Numerical

Numerical results obtained from the present coupled-wave model are given for two-layer (N_m=2) and eleven-layer (N_m=11) SVHs. SVHs are emulated to use the transmission photopolymer holographic material. The readout wavelength is chosen as 0.68 μm. The refractive indices of the glass buffer and the photopolymer modulation layers are n_b=1.51, and n_0=1.55 and Δn =0.01 those thickness are D_b=170 μm and D_m=10μm, respectively. The grating period is Λ =3.9 μm such that the Bragg angle is 5° in a region I or III. Figure 2 shows the angular selectivities as a function of readout incident angle. The computation has numerical stability for the divided number N_d=5 of one thick hologram layer. The 82-% diffraction efficiency for an 11-layer SVH is shown

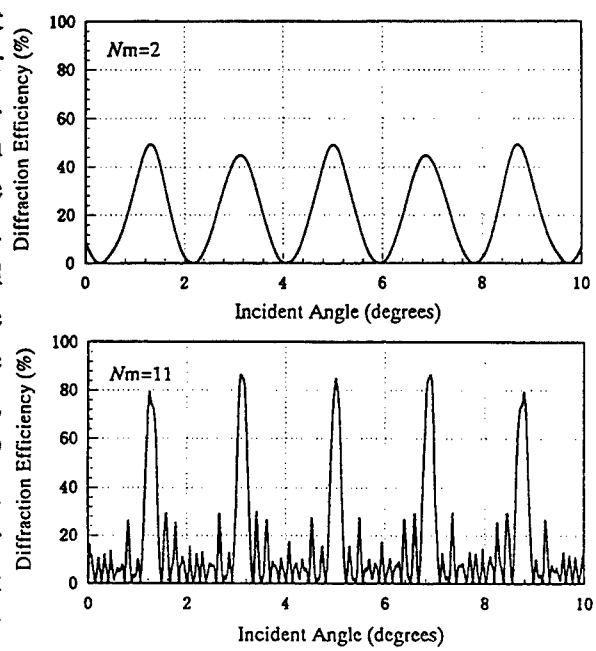

Fig. 2. Numerical angular selectivities versus incident angle for the 2- and 11-layer SVHs.

to simulate the diffraction property of deep volume hologram. The high diffraction efficiency is attributed to the high index modulation Δn. The sidelobes structure exhibits N_m-2 sidelobes between adjacent diffraction peaks and a larger sidelobe amplitude than the simulation result with the optical BPM.[5]

B. Experimental

Experimental results are given in Fig. 3 for two-layer (N_m=2) and eleven-layer (N_m=11) SVHs. The interference patterns produced by two collimated beams with an interbeam angle $2\theta_i=2\times9.1°$ are recorded on assembly-structured photopolymer SVHs. The modulation layer of D_m=10 μm was coated from a finite volumetric photopolymer solution onto a glass slide whose thickness D_b is ranged from 120 to 170 μm. The recording and readout wavelengths are 0.633 μm of a He-Ne laser. The grating period is Λ =2 μm such that the Bragg angle is 9.1°. The 25-% diffraction efficiency for an 11-layer SVH is demonstrated in Fig. 3, and is much less than that in the numerical result in Fig. 2. The agreement between them would be anticipated such that the overestimated index modulation Δn must be changed to that derived from the well-approximated expression for the diffraction efficiency. Nevertheless the high angular selectivity is exhibited that is available for an optical angular filter.

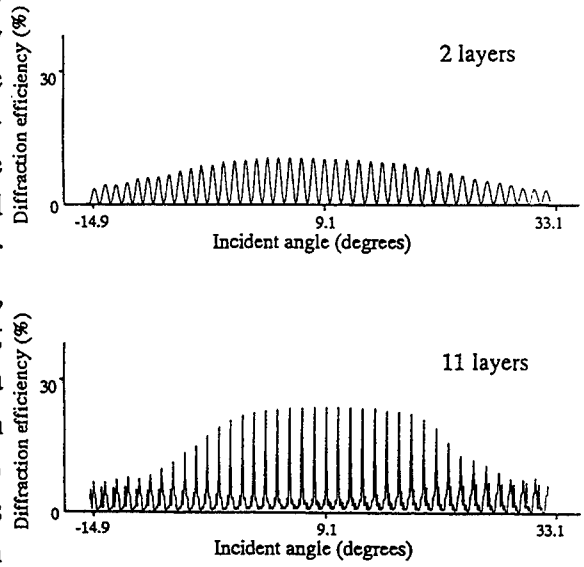

Fig. 3. Experimental angular selectivities vs. incident angle for the 2- and 11-layer SVHs.

4. CONCLUSION

SVH angular selectivity has been demonstrated by using a rigorous coupled-wave analysis, taking into account the reflection at the boundaries. This approach can be applied to arbitrary number of hologram layers with any thickness. Finally, the performance of an eleven-layer photopolymer hologram, an optical multiple-angular selective filter is analyzed with a coupled-wave model to avoid an exponential increase of deep hologram layer.

The authors gratefully thank Mr. Y. Ohyagi, Enplas Inc. for the numerical help, and Drs. H. Tanigawa and T. Ichihashi, Osaka Nat'l Res. Inst. for supplying the photopolymer.

REFERENCES

1. R. V. Johnson and A. R. Tanguary, Jr., Opt. Lett., **13**, 189(1988).
2. G. P. Nordin, R. V. Johnson and A. R. Tanguary, J. Opt. Soc. Am. A, **9**, 2206(1992).
3. T. K. Gaylord and M. G. Moharam, Proc. IEEE, **73**, 894 (1985).
4. M. Schmitz, R. Bräuser, O. Bryngdahl, Opt. Commun., **124**, 1(1996).
5. G. P. Nordin and A. R. Tanguary, Jr., Opt. Lett., **17**, 1709(1992).

Binary high-efficiency single order gratings for beam switching

Hartmut Bartelt, Tilman Glaser, Siegmund Schroeter
Institut fuer Physikalische Hochtechnologie, Helmholtzweg 4, 07743 Jena, Germany,
Tel: +49-3641-302800, Fax: +49-3641-302850

1. Introduction

Grating structures with a grating period in the range of the illumination wavelength differ in their diffraction properties considerably from conventional diffraction structures. In this case diffraction properties are sensitive in a complex manner to illumination direction, structure thickness, illumination wavelength or polarization. For modeling of the diffraction properties rigorous solutions of the wave equation have to be used [1]. Specific examples of the properties of such gratings include highly efficient single order gratings or polarization dependent beam splitting structures [2]. Although theoretical modeling of such gratings is known for a long time, practical realization of such gratings was limited until recently by the structuring technology. After first investigations based on an interferometric technique now also more flexible techniques based on direct e-beam writing in the submicrometer range become available [3]. In the following we want to describe at first results for the design of an efficient single order binary phase grating structure. Then the combination of two single order gratings for achieving beam switching properties with small mechanical shifts in the sub micrometer range will be discussed.

2. Binary high efficiency grating

Binary phase gratings may achieve diffraction efficiencies close to 100 % in the case of high spatial frequencies. For a design of such a high efficiency binary phase grating we have analyzed gratings in Littrow mount. In Littrow mount configuration the first reflected order is diffracted in the direction of the illumination light. The design of the grating is based on a rigorous coupled wave analysis. In order to allow later fabrication of the structures, assumptions have been made concerning wavelength (λ=543nm), duty cycle (f=0.5), refractive index of the wafer material (n=1.474) and thickness of the wafer (infinite thickness). The numerical simulation (grating period 580nm, structure depth 1.1µm) resulted in an optimized diffraction efficiency of 95.9% for the first transmitted diffraction order in TM-polarization mode (fig. 1a). This grating structure was realized using e-beam lithography in photoresist and reactive ion beam etching in a Borofloat glass wafer. The structures achieved the required depth of 1.1µm at the grating period of 580nm. The experimental diffraction results showed efficiencies of 94% and proved the possibility to achieve in practice the predicted high diffraction efficiencies for a binary phase grating (fig. 1b). In general, diffraction efficiencies may differ considerably for different polarizations. In the specific case of the grating analyzed in fig. 1 also TE-mode gave high efficiencies of about 85 %. Other designs result in large differences of diffraction efficiency, which can be useful as polarization element or as polarization beam splitting element.

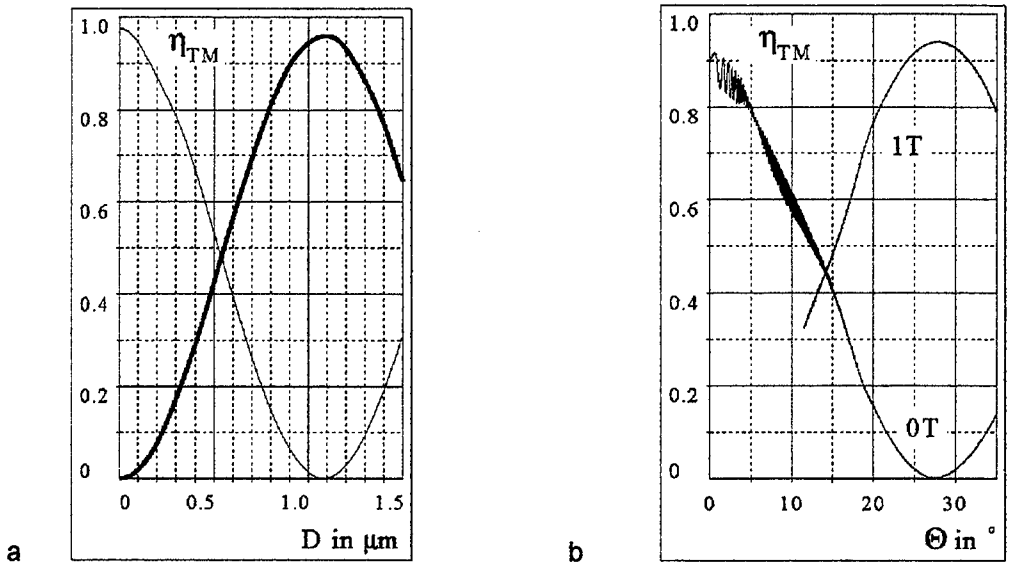

Fig. 1 Theoretical (a) and experimental (b) diffraction efficiency for TM-polarized light for a single order grating showing zeroth (thin line) and first (thick line) diffracted order.

3. Combination of two gratings for beam switching

The concept of our diffractive beam switch is based on two grating structures which can be shifted relative to each other (fig. 2). This principle is also known from conventional grating structures for switching or sensor applications [4]. In comparison to conventional phase grating structures with larger grating period, the high frequency grating structures allow high efficiencies with binary structures, may include polarization sensitive properties and require only very small mechanical shifts in the subwavelength range. This offers the chance of increased switching speeds. In fig. 2 two switching states for the grating switch are indicated in principle. Both gratings are assumed to be identical. In case of no relative shift between the gratings, the structure corresponds to a diffraction grating with twice the thickness of the single gratings and may diffract light with high efficiency. In case of a relative shift between the gratings of half a period the system corresponds to an unstructured plate with no diffraction in transmission at all.

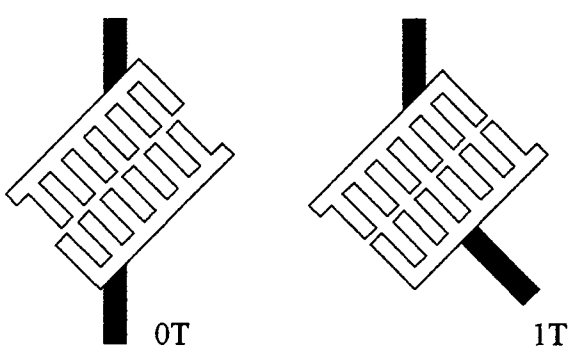

Fig. 2 Principle setup of switching element in two switching states (transmission and diffraction)

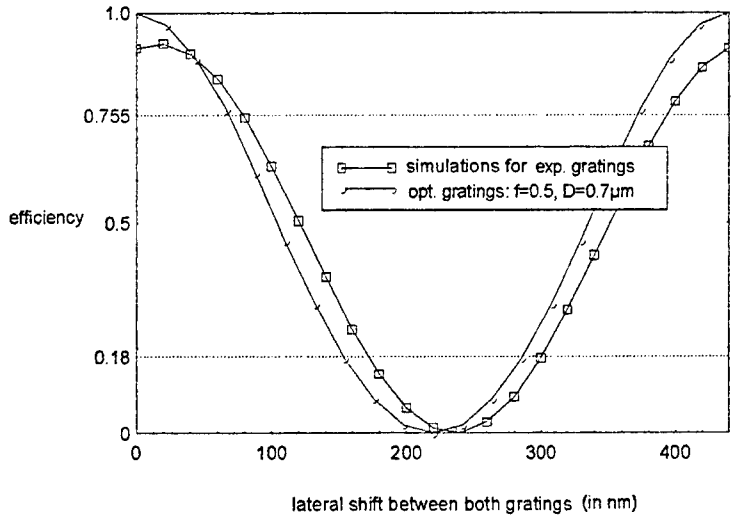

Fig. 3 Simulation of first order diffraction efficiency (TM-mode) in dependence on lateral shift between gratings for optimized and experimental single order gratings.

Using again rigorous coupled wave theory a grating design was obtained for TM-polarized light at 543nm resulting in the following parameters: grating period 440nm, structure depth of single grating 700nm. In fig. 3 the simulation of the switching properties in dependence on relative shift is shown. For the optimized grating diffraction efficiencies of the switched states for TE- and TM-polarization are >93% and >97%, respectively. The parameters of the realized gratings deviated from the optimum design (duty cycle f=0.61 and f=0.54, structure depth 730nm and 750nm). With these parameters lower switching efficiencies are expected (fig. 3). In the experimental measurements similar results with diffraction efficiency in the upper switching states of 75% were achieved. It can be therefore expected that a careful realization of the optimized gratings would allow switching with higher efficiency. For the lower switching state a diffraction efficiency of 18% was measured.
It also possible to design the grating structures in such a way that a strong difference in efficiency between TE- and TM-mode is achieved. The switch can be then used as a polarization switching element.

4. Acknowledgment

The authors would like to acknowledge the technological expertise of E.B. Kley and his team at the University of Jena. The work was funded by the German Science foundation (DFG) under grant INK/A1.

5. References

[1] E. N. Glytsis, T.K. Gaylord, D.L. Brundrett, Rigorous coupled-wave analysis and applications of grating diffraction, in: Diffractive Optics and Miniaturized Optics (S.H. Lee, editor), SPIE Critical Reviews of Optical Science and Technology 1993, Vol. CR 49, p. 3-31

[2] M.W. Farn, Binary gratings with increased efficiency, Appl. Opt. 31, 4453-4458 (1992)

[3] R.C. Enger, S.K. Case, High-frequenc holographic transmission gratings in photoresist, JOSA 73, 1113-1118 (1983)

[4] W.B. Spillman, Multimode grating sensors, in: Fiber Optic Sensors (E. Udd, editor), John Wiley & Sons, New York 1991

A WEDGE MADE IN AN ARTIFICIAL DIELECTRIC

C.Giaconia*, R.Torrini*, S. Murad and C.D.W.Wilkinson
Department of Electronics and Electrical Engineering, Glasgow University
Oakfield Avenue G12 8LT Glasgow, Scotland - UK
*on leave from the Dipartimento di Ingegneria Elettrica, University of Palermo - Italy

Conventional diffractive optical components require fabrication of an approximation to a surface shape and to achieve high efficiency, it is necessary to use multiple levels to build up the desired shape. For say 16 steps, four masking steps are required and each has to be accurately aligned. The overall process is time-consuming and does not have good yield. However the phase of the light can be controlled locally by using a series of slots of different widths provided these slots are narrow enough to avoid diffraction - thus forming an artificial dielectric. The key point is that the slots all have same depth and so only a single lithographic step is required.

We have designed artificial dielectric components using a hybrid technique that combines Rigorous Coupled Wave Theory (RCWA) and Effective Medium Theory (EMT). The model allows for the constraints imposed by fabrication (minimum linewidth and maximum aspect ratio of features) to be included automatically in the optimisation of the design. The first design is for a wedge, to be built in Gallium Arsenide for operation at a wavelength of 1.15 μm. The design has a theoretically diffraction efficiency greater than 90%.

The designed pattern is written in electron beam resist (PMMA) using a Leica Beamwriter. After development the pattern is transferred into an 100 nm thick layer of silicon oxide deposited by plasma enhanced chemical vapour deposition. This is then used as the masking layer in the transfer of the pattern into an epitaxial GaAs film on a GaAs substrate. The oxide layer is removed by wet etching prior to testing.

The wedge has an overall period of 2.3 μm and is divided into seven slots with a minimum linewidth of 70 nm. The etch depth is 740 nm. Initial devices gave a diffraction efficiency of greater than 80% - further details of the device performance will be given.

Key words: DOE, Artificial Dielectric, RCWA, EMT, Gratings, nanolithography, e-beam lithography, dry etching.

HIGH EFFICIENCY BINARY BLAZED GRATING WAVEGUIDE COUPLERS

Michael D. Watson

NASA Marshall Space Flight Center
Optics Branch (MS EB52)
MSFC, Alabama 35812
(205)544-3186
(205)544-2659 fax

Mustafa A.G. Abushagur

University of Alabama in Huntsville
Electrical and Computer Engineering Department
Huntsville, Alabama 35899
(205)890-6215 x408
(205)890-6618 fax

Paul R. Ashley

U.S. Army Missile Command
Weapons Sciences Directorate Research, Development, and Engineering Center
Redstone Arsenal, Alabama 39898
(205)876-7484
(205)842-2507 fax

Helen Cole

NASA Marshall Space Flight Center
Electro-Optics Branch (MS EB53)
MSFC, Alabama 35812
(205)544-6790
(205)544-2659 fax

Blazed grating features result in a modification to the Bragg Equation which yields only a single output radiation mode (either substrate or cladding). [1]. Since blazing requires a triangular grating line shape, fabrication can be difficult. As a simplification, a discrete step approximation is often used to approximate a blazed structure. However, the discrete approximation requires multiple exposure steps making the fabrication process complex. The fabrication process can greatly simplified by approximating the blazed grating line shape by a periodic rectangular grating with a varying duty cycle [2]. Thus, the process used to fabricate periodic rectangular gratings can be used to fabricate the binary approximation of a blazed grating. Dividing the blazed grating structure into several (I) substructures, results in a substructure (i), each having a different discrete refractive index based on their location along the slope as shown in Figure 1.

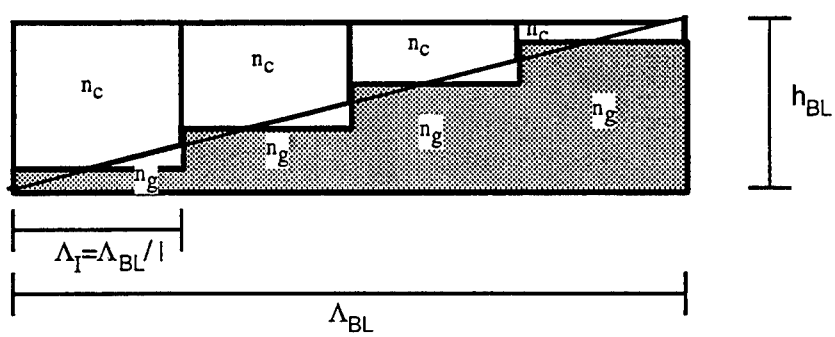

Figure 1: Discrete Approximation of Blazed Grating Structure

The phase delay of this discrete approximation of the blazed grating substructure can be defined as:

$$\Phi_{BL} = h_{BL}k_oN_i = h_{BL}k_o\left[\frac{2i-1}{2I}n_g + \left(1-\frac{2i-1}{2I}\right)n_C\right],$$

where,

Φ_{BL} is the phase delay of the Blazed grating structure, and
h_{BL} is the height of the Blazed grating structure.

The height, h_{BL}, of the blazed grating can be found from the geometry of the grating (shown in Figure 1) as:

$$h_{BL} = \Lambda_{BL}\tan\theta_{BL}.$$

Now, a binary approximation should generate the same phase delay as the discrete approximation in order to output the same radiation mode. A binary structure with variable duty cycle can be used to create a varying phase delay for such a grating [3]. The phase delay of a binary structure can be found through the use of the Theory of Form Birefringence. This theory states that light propagating through thin regions (satisfying the Small Period Approximation) of different refractive index will see an effective refractive index for the region. Defining t_m as the duty cycle within a periodic structure, the effective index of refraction may be written as [4]:

$$n_{Gc} = \sqrt{n_g^2t_m - n_c^2(t_m-1)}.$$

The phase delay of a structure of refractive index n_{Gc} can then be written as:

$$\Phi_{BA} = h_{BA}k_on_{Gc} = h_{BA}k_o\sqrt{n_g^2t_m - n_c^2(t_m-1)},$$

where,

Φ_{BA} is the phase delay of the Binary Approximation structure
h_{BA} is the height of the Binary Approximation structure.

Equating the phase delay of the Binary Approximation with the Discrete Approximation of the blazed grating yields the phase relationship:

$$\Phi_{BA} = h_{BA}k_o\sqrt{n_g^2t_m - n_c^2(t_m-1)} = \Phi_{BL} = h_{BL}k_o\left[\frac{2i-1}{2I}n_g + \left(1-\frac{2i-1}{2I}\right)n_C\right].$$

Solving this relationship for t_m, results in:

$$t_m = \left(\frac{N_i^2\Lambda_{BL}^2\tan^2\theta_{BL}}{h_{BA}^2(n_g^2-n_c^2)}\right) - \left(\frac{n_c^2}{n_g^2-n_c^2}\right).$$

h_{BA} can be found by noting that, t_m, representing the duty cycle must vary between 0 and 1. Thus, using these values as limiting conditions, the maximum and minimum values of h_{BA} can be found as:

$$h_{BA} = \frac{N_i\Lambda_{BL}\tan\theta_{BL}}{n_c}; \qquad t_m = 0,$$

and,

$$h_{BA} = \frac{N_i\Lambda_{BL}\tan\theta_{BL}}{n_g}; \qquad t_m = 1.$$

Finally, each line of the grating will then have a width defined by:

$$w_m = t_m \Lambda_i .$$

The resulting binary blazed grating coupler is shown in Figure 2.

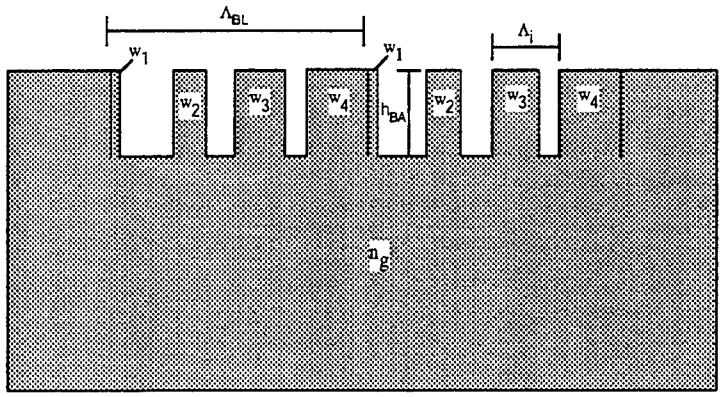

Figure 2: Binary Blazed Grating Coupler

The efficiency of the Binary Blazed Grating Coupler may now be calculated using the basic efficiency equations for a rectangular relief grating structure. Using this approach , efficiencies of 80% of the total incident energy can be output through first order cladding mode for single mode waveguides.

Given a desired output angle and waveguide structure, a coupler may designed by solving for t_m. In evaluating the minimum and maximum values of h_{BA}, a range of common values can be found for all discrete elements (i). In examining this range, the minimum depth is found to occur when t_m=1 for the highest index region. Thus, this region will not have a gap and will directly join the first step of the next region as illustrated in Figure 2. This has the dual benefit of providing the smallest depth (and therefore smallest aspect ratio) and adjoining the smallest step with the largest step (which essentially eliminates the small step from the fabrication process). Using this approach, a binary blazed grating with an 80 degree output coupling angle can be designed with the features sized shown in Table 1. This design is for a waveguide made from AMOCO Ultradel 9020D Polyimide.

Table 1: Binary Blazed Grating Design Parameters

Λ_{BL}	Λ_i	w_1	w_2	w_3	w_4	h	L
2.4316μm	.6079 μm	.1086 μm	.2633 μm	.4207 μm	.6079 μm	.8545 μm	5mm
Mode	λ	N_0	N_1	$\theta_{-1}^{(c)}$	T	α_{bl}^{-1}	η_{-1}
TE	1.3μm	1.519	1.494	80.00_	2.99μm	1281.54	99.9997
TM	1.3μm	1.497	-	80.00_	2.99μm	843.22	99.9782

Currently, fabrication methods are being defined to fabricate these grating couplers. These couplers provide great utility by providing highly efficient, high output angle coupling.

REFERENCES

[1] Chang, K. C., Tamir, T., Simplified Approach to Surface-Wave Scattering by Blazed Dielectric Gratings, *Applied Optics*, Vol 19, No 2, 15 Jan 1980, pp 282-288.

[2]Haidner, H., Sheridan, J. T., Streibl, N., Dielectric Binary Blazed Gratings, *Applied Optics*, Vol. 32, No. 22, 1 August 1993, pp 4276-4278.

[3] Farn, Ibid.

[4] Born, Ibid.

Arrays of infrared micropolarizers

Gregory P. Nordin, Jeffrey T. Meier, Panfilo Deguzman
The University of Alabama in Huntsville
Electrical & Computer Engineering Department, Huntsville, Alabama 35899
Ph. 205-890-6214 ext. 410, Fax 205-890-6618, nordin@ece.uah.edu

Blair Barbour and Michael W. Jones
Nichols Research Corporation
Systems Development and Evaluation Center
P.O. Box 400002, Huntsville, AL 35815
Ph. 205-885-7290, Fax 205-885-7900, barbourb@nichols.com

1. Introduction

High spatial frequency metal gratings have long been recognized as an effective polarizer option for the infrared portion of the spectrum.[1] Numerous applications can benefit from the development of arrays of such wire-grid polarizers in which subsets of the polarizers have arbitrary angular orientations. In this paper we describe the design and fabrication of an array of small aperture polarizers (i.e., micropolarizers) for the 3-5 μm wavelength range.

2. Design

Our particular application requires an array of micropolarizers with three distinct angular orientations. The array itself consists of a 128 x 128 grid of unit cells, with each unit cell composed of a 2 x 2 array of micropolarizers. As illustrated in Fig. 2(a), each micropolarizer has a 16

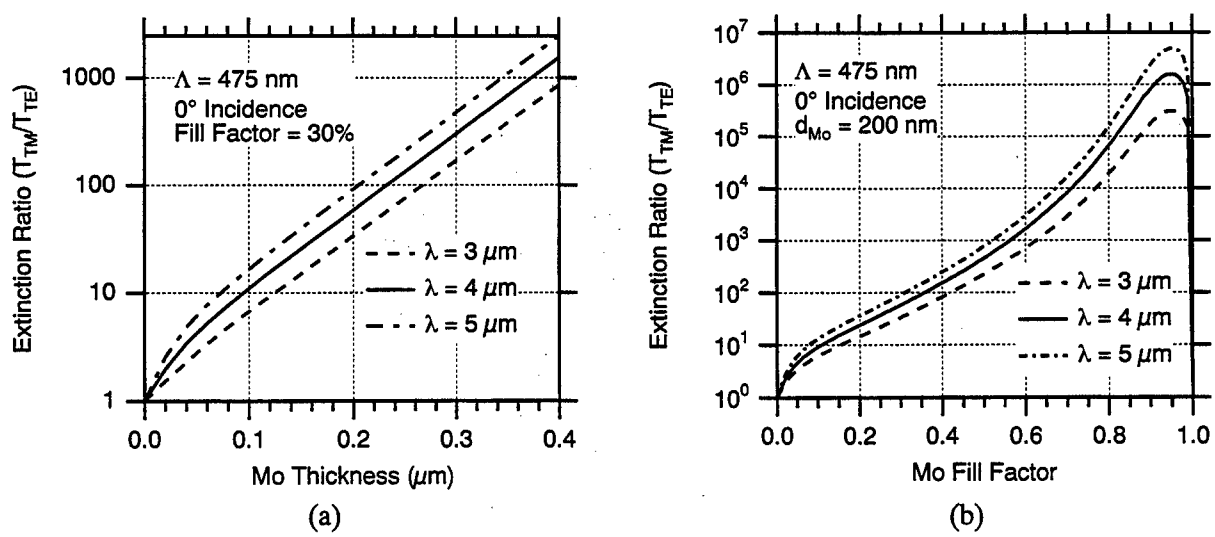

Figure 1. Extinction ratio of a Mo grating on Si as a function of (a) Mo thickness and (b) Mo fill factor.

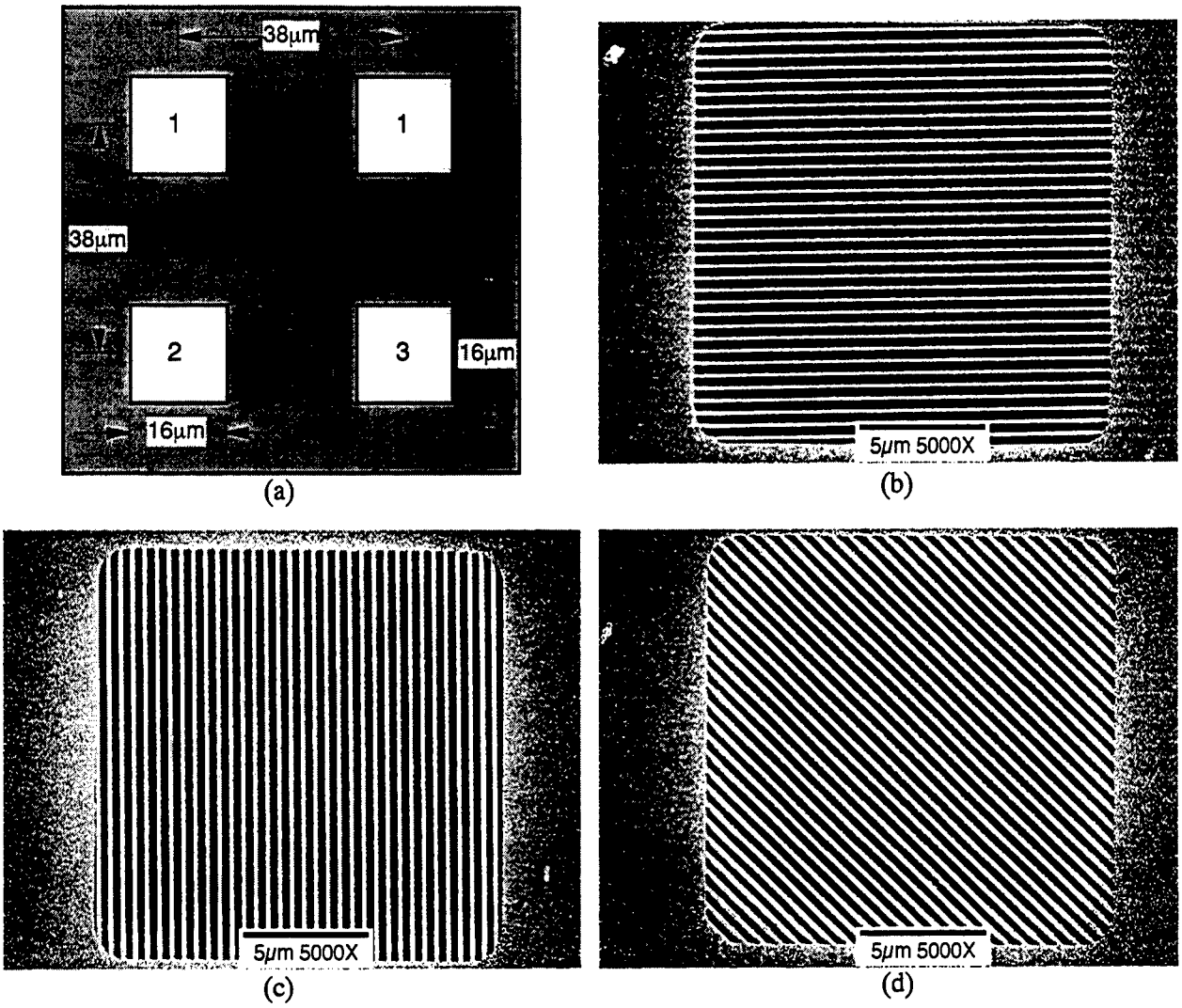

Figure 2. (a) Schematic diagram of 2 x 2 unit cell. (b)-(d) SEM images of 475 nm gratings found in the squares labeled 1-3, respectively, in (a).

μm square aperture and is centered on a 38 μm square grid. Each unit cell is 76 μm x 76 μm. Two of the micropolarizers in each unit cell have grating ridges oriented horizontally, while the other two micropolarizers have ridges oriented vertically and at 45° ccw from vertical, respectively.

Rigorous coupled wave analysis[2,3] was used to design the polarizers to achieve an extinction ratio of ≥30 across the 3-5 μm wavelength region for a molybdenum wire grid polarizer on a silicon substrate. Illustrative simulation results for a 475 nm period grating are shown in Fig. 1.

3. Fabrication

The micropolarizer array is fabricated from a 200 nm thick Mo film RF sputtered onto a 3" Si wafer. Our fabrication process involves sequentially forming the three sets of differently ori-

ented micropolarizers in the array. In each case, a SiO_2 masking layer is first deposited on the Mo film and then an array of 16 μm square holes is etched in the SiO_2 layer. Next, a bottom-layer anti-reflection coating (ARC) is applied followed by photoresist. A 475 nm period grating pattern is then holographically formed in the photoresist with 442 nm illumination from a HeCd laser. After dry etching the ARC, the Mo is reactive ion etched (RIE) with a fluorine-based etch chemistry to form the Mo grating. A two-stage Mo etch is used to minimize undercutting of the underlying Si. After stripping the photoresist, ARC, and SiO_2, this same sequence of steps is used to form the other two sets of micropolarizers.

4. Results

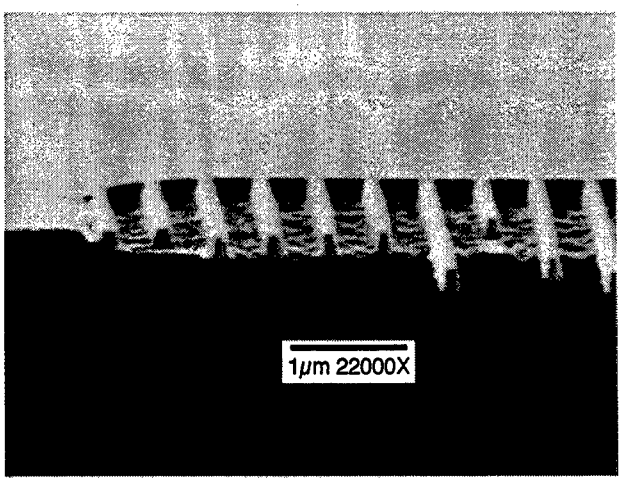

Figure 3. SEM image of grating cross-section.

A number of micropolarizer arrays have been fabricated. In Figs. 2(b)-(d), top view SEM images of representative micropolarizers at each of the three angular orientations are shown. These images are from a single sample. Note the uniform line widths and spacings across each of the apertures, and the well-defined edges.

A cross-sectional view of a vertically oriented grating is shown in Fig. 3. The Mo grating fill factor is approximately 25%, and the side-wall angles are ~84°. Undercutting of the Si substrate has clearly been avoided, although the Si revealed in the grating troughs has been roughened by the Mo etch. Since the roughness is on a scale of 100 nm or less, this is not expected to degrade device performance.

Extinction ratio measurements in the 3-5 μm wavelength range will be performed in the near future and compared with predicted performance. Qualitative examination of the micropolarizers at 1 μm shows excellent polarization characteristics.

References

1. G. R. Bird and M. Parrish, Jr., "The wire grid as a near-infrared polarizer," J. Opt. Soc. Am. **50**, p. 886-891 (1960).

2. M. G. Moharam, E .B. Grann, D. A. Pommet and T. K. Gaylord, "Stable implementation of the rigorous coupled-wave analysis for surface-relief gratings: enhanced transmittance matrix approach," J. Opt. Soc. Am. A, **12**, p. 1077-1086 (1995).

3. L. Li, " Use of Fourier series in the analysis of discontinuous periodic structures," J. Opt. Soc. Am. A, **13**, p. 1870-1876 (1996).

Novel Polarizers Using 2D Photonic Band Gap Structures

T. Hamano*, † and M. Izutsu†

* Telecommunications Advancement Organization of Japan (TAO)
† Communications Research Laboratory (CRL),
4-2-1 Nukui-kita, Koganei, Tokyo 184 JAPAN
Voice #: +81 423 27 5418 Facsimile #: +81 423 27 6106
Email: tetze@crlsv.crl.go.jp

Photonic band gap (PBG) structures have been studied due to interests in the control of spontaneous emission as well as due to their applications in optical devices. Some applications of PBG structures have been proposed, such as reflectors [1], cavities [2], waveguides [3] etc. In order to utilize them in these applications, 2-dimensional (2D) PBG structures are required to producing 'complete' band gaps. Thus, their necessary band gaps must be wide in any direction on plane and must operate in two orthogonal polarization states which are parallel and perpendicular to the pillars (or holes) of the structures.

Since any photonic band distribution of 2D PBG structures provides directional dependence as well as polarization dependence, the exploitation of other devices or components are expected to make the better use of those dependence characteristics. For example, their directional dependence may be applied in WDM system. In this paper, we propose a 2D PBG structure-based polarizer in which we use the polarization dependence of a 2D PBG structure. We calculated numerically the transmission coefficient of a 2D PBG structure using finite differential time domain (FDTD) method [4], and then obtained the extinction ratio of two orthogonal polarized waves.

We assumed a lower-symmetric model of a 2D PBG structure as shown in Fig. 1. It consisted of square pillars of GaAs arranged in square lattice in the air. The number of the lattice elements in y-direction was finite, 20, while the number in x-direction was taken to be infinite so that the numerical calculation can be simplified. The lattice constant a was fixed to be half of wavelength λ, and the pillar size r was taken a variable parameter.

In the FDTD method, the lattice space increments Δ for both x- and y-directions were 0.02 μm, and the time increment $c\Delta t$ ($=\Delta\tau$) was half of Δ where c is the velocity of light in the air. Periodic boundary condition was taken in the x-direction since we assumed an infinite number of lattice elements in this direction. Furthermore, we assumed the absorbing walls were located at the edges of the crystal in y-direction. Thus Mur's absorption boundary condition [5] could be applied. The

input plane wave, whose intensity was normalized to 1.0, was incident into input plane E_{in} as indicated in Fig. 1. In order to examine the transmission coefficient, the output intensity was obtained at the output plane E_{out}. The transmission direction in this calculation was corresponding to the Γ-X direction of the square lattice.

The theoretical band distribution in the normalized frequency (wavelength) against the normalized pillar size where an infinite size of crystal in both of x- and y-directions was assumed, as shown in Fig. 2. At r=0.52a whose structure can be expected to have a photonic band gap only in H-polarized wave, the output intensities of two orthogonal polarized waves were compared. Here, we considered the electric fields parallel and perpendicular to the pillars to be the E-polarized wave E(E-pol.)=(0, 0, E_z) and H-polarized wave E(H-pol.)= (E_x, 0, 0), respectively. The output intensity of H-polarized wave decreased to less than 1 % of the input intensity, while the output intensity of E-polarized wave was nearly 1.0. In Fig. 3, the output intensities of both polarized waves E_{out}(H-pol.) and E_{out}(E-pol.) are shown against the normalized pillar size. The smaller output intensities in Fig. 3 correspond to the calculated existence of band gaps at a=λ/2 as indicated in Fig. 2.

The extinction ratio of transmission coefficient of two polarized waves, E_{out}(H-pol.)/E_{out}(E-pol.), is graphed against the normalized pillar sizes in Fig 4. The positive value of the ratio represents the suppression of the transmission of the E-polarized wave against H-polarized wave, while the negative value gives the opposite meaning. The maximum calculated ratios in the positive and negative values are +28 dB and –40 dB, respectively.

This result suggests that the polarization dependence of a 2D PBG structure can be utilized in order to construct a novel variable polarizer. We expect this polarizer to find many useful applications since the required polarization can be designed by properly choosing the particular lattice constant or pillar size against wavelength. Lastly, by optimizing the design of structures, a 60 dB or higher extinction ratio is obtainable.

Reference: [1] J. O'Brien, O. Painter and A. Scherer, Electron. Lett. **32**, 2243 (1996). [2] H. Hirayama, T. Hamano and Y. Aoyagi, Appl. Phys. Lett. **6**, 791 (1996). [3] A. Mekis, J. C. Chen, I. Kurland, S. Fan P. R. Villeneuve and J. D. Joanopoulos, Phys. Rev. Lett. **77**, 3787 (1996). [4] K. S. Yee, IEEE Trans. Ant. Propag. **Ap-14**, 302 (1966). [5] G. Mur, IEEE Trans. Electromag. Comp., **EMC-23**, 377 (1981).

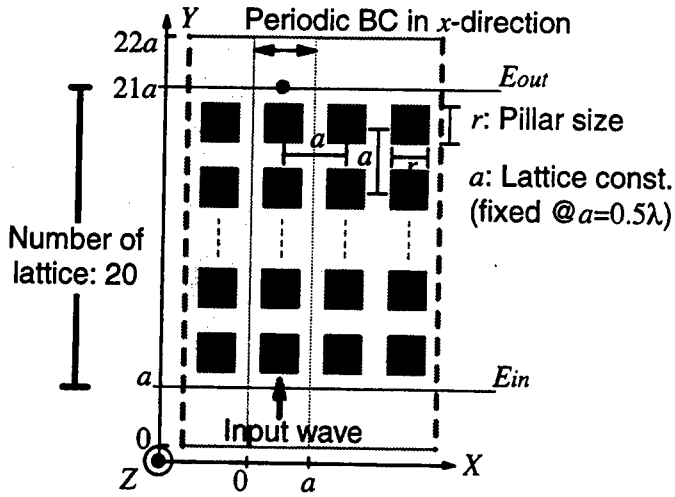

Fig.1 Model of a 2D PBG structure

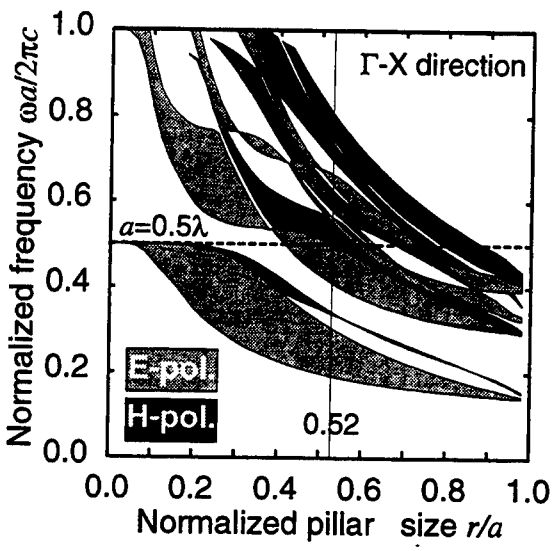

Fig.2 Band gap distribution in frequency range against normalized wave

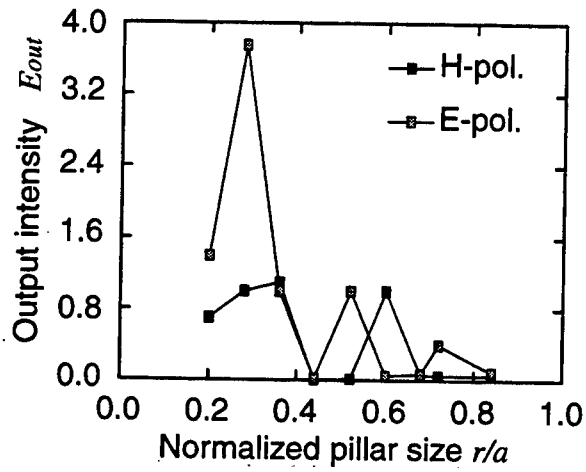

Fig. 3 Output intensities in a PBG structure of two orthogonal polarized waves

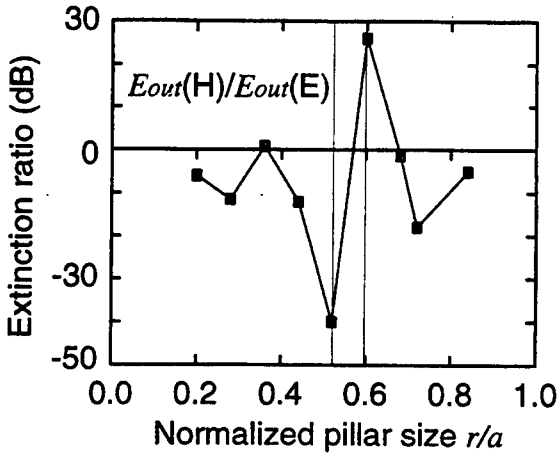

Fig. 3 Extinction ratio of a 2D PBG structure polarizer

Color pseudo-nondiffracting beams generated by diffractive phase elements

Bi–Zhen Dong, Rong Liu, Ben–Yuan Gu,* and Guo–Zhen Yang

Institute of Physics, Academia Sinica, P. O. Box 603, Beijing 100080, China

Tel: +86–10–62559131 ext. 229; Fax: +86–10–62562605

* E–Mail : guby@aphy01.iphy.ac.cn

Nondiffracting beam has extensive applications such as optical alignment, surveying, industrial inspection, and optical interconnection. Recently, pseudo-nondiffracting beam (PNDB) has been proposed. All the PNDB's, a single and two segments, are almost generated in the monochromatic light illuminating system.[1–2]

In this presentation we present for the first time design of diffractive phase elements (DPE's) that generate color PNDB's in a polychromatic light illuminating system. The color PNDB's are characterized by dividing the axial–intensity distribution into several segments with high transverse resolution within a given axial region. Each segment exhibits only one color with a special wavelength component, and different segments contain different wavelength components. We carry out the relevant design in the polychromatic light illuminating system based on the conjugate gradient method.[3]

Consider a rotationally symmetric optical system. Assume that the incident light consists of several components with different wavelengths incoherently. Diffractive phase element is placed on the input plane of the system. The incident light passes through the DPE and then propagates in free space, and finally arriving at the output plane. In the Fresnel approximation, the wave distribution on the output plane which is located at an axial distance z_β from the DPE is expressed

$$U_2(\lambda_\alpha, z_\beta) = \frac{2\pi}{i\lambda_\alpha z_\beta} \exp(i2\pi z_\beta/\lambda_\alpha)$$

$$\times \int_0^{R_{1m}} \rho_1(r_1, \lambda_\alpha) \exp[i\frac{2\pi}{\lambda_\alpha}(n(\lambda_\alpha) - 1)h(r_1)] \times \exp(i\pi r_1^2/\lambda_\alpha z_\beta) r_1 dr_1, \quad (1)$$

where r_1 and R_{1m} denote the radial coordinate and the maximum radius of the DPE, respectively; $\rho_1(r_1, \lambda_\alpha)$ stands for the amplitude distribution of the incident light at the wavelength component λ_α; $h(r_1)$ represents the distribution of surface–relief depth of the designed DPE.

In general, the synthesis of the color PNDB's can be stated as follows: From a given amplitude distribution of the incident wave, how can we determine the profile of the surface-relief DPE so that the axial–intensity distribution approaches the preset one with a high accuracy ? An error

function used for appraising the performance of the designed DPE is defined by

$$E = \sum_{\alpha=1}^{N_\lambda} \sum_{\beta=1}^{N_z} W(\lambda_\alpha, z_\beta) \left\{ [\tilde{\rho}_2(\lambda_\alpha, z_\beta) - \mid U_2(\lambda_\alpha, z_\beta) \mid]^2 \right\}, \tag{2}$$

where $\tilde{\rho}_2(\lambda_\alpha, z_\beta)$ describes the preset axial–amplitude distribution, and $W(\lambda_\alpha, z_\beta)$ is a weighting factor which satisfies normalization condition $\sum_{\beta=1}^{N_z} W(\lambda_\alpha, z_\beta) = 1$ for each wavelength. It is clearly seen from Eqs. (1) and (2) that the problem of the design of the DPE's can be regarded as an optimization problem: Minimizing the error function with respect to the distribution of surface–relief depth, $h(r_1)$.

We now carry out the design of a DPE that generates dual–chromatic PNDB's with two segments; each of them retains a desired monochromatic wavelength component, such as $\lambda_1 = 514.5nm$ for the first segment, and $\lambda_2 = 632.8nm$ for the second segment. Assume that an incident wave with uniform profile, consisting of two wavelength components, illuminates the DPE. We employ 256 radial–sampling points within the aperture radius $4.0mm$ of the DPE. The axial spacing between adjacent sampling planes is $5.0mm$.

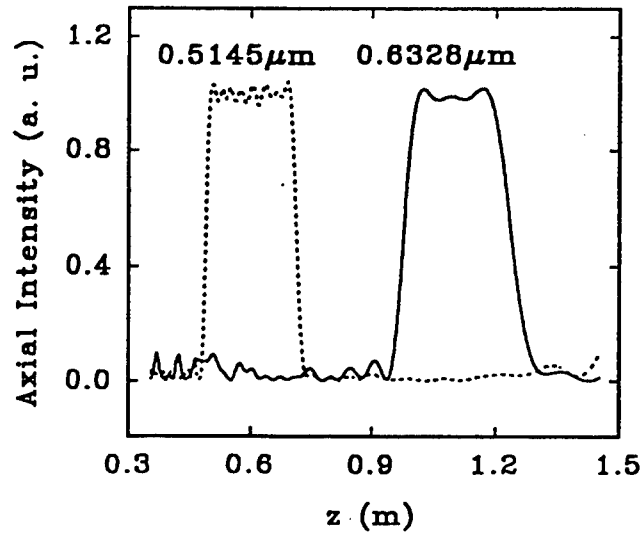

Fig. 1. Axial–intensity distribution of the dual–chromatic PNDB with two segments.

The axial–intensity distribution generated by the designed DPE is shown in Fig. 1. Dashed curve corresponds to the axial–intensity distribution for the wavelength $\lambda_1 = 514.5nm$, while solid one to that of $\lambda_2 = 632.8nm$. It is worthy to pointing out that the color of each segment can be arbitrarily preset. To show the characteristics of the beamlike shape of the dual color PNDB's clearly, we display the transverse–intensity distribution in a three-dimensional (3D) plot in Fig. 2. It corresponds to the second segm-

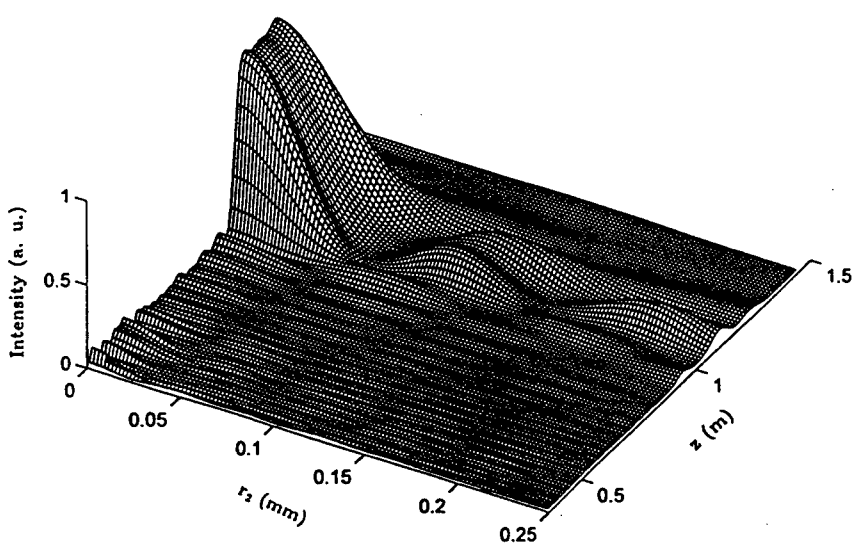

Fig. 2. Three dimensional plot of axial–intensity distribution of the dual–chromatic PNDB. Here we display only the second segment with $\lambda_2 = 632.8nm$ for clarity.

ent with λ_2 of Fig. 1. It brings us a good view of both the axial–intensity uniformity and the transverse–intensity resolution. It is clearly seen that this dual–chromatic PNDB exhibits well beamlike shape.

To further demonstrate different fashions of the PNDB's, we present a synthesis of four–segment PNDB with dual wavelength components; the color of these four segments is alternately changed by taking one of values, i.e., λ_1 or λ_2. Figure 3 displays the axial–intensity distribution of four segment PNDB with the preset segment color, generated by the designed DPE. Dashed curve and solid curve correspond to the wavelength component of $514.5nm$ and $632.8nm$, respectively. The length of individual segment sets to $0.15m$. Note that the present method is also appropriate to achieving the synthesis of dual–color PNDB with unequal–length segments.

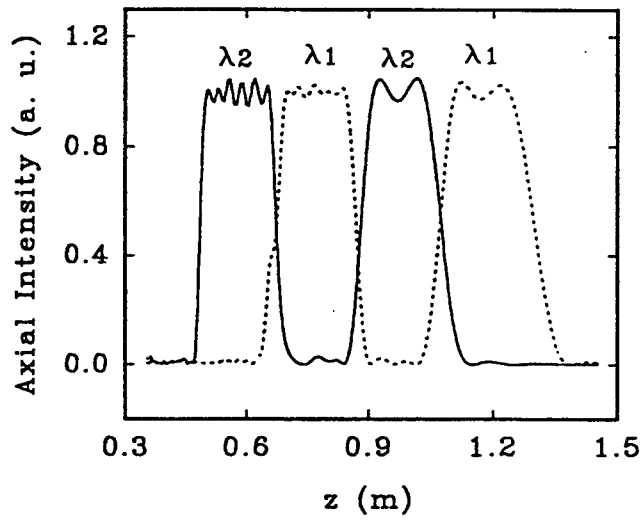

Fig. 3. Axial–intensity distribution of four segment PNDB with dual chromatic.

In summary, we have proposed for the first time the design of the DPE's that produce the color PNDB's in the polychromatic illuminating system. Several model designs were carried out by using the conjugate gradient method. Satisfactory results were obtained. It is expected that the favorable feature of the color PNDB's may be desirable in some practical applications.

One of the authors (B. Z. Dong) gratefully acknowledges the support of K. C. Wong Education Foundation, Hong Kong, China.

References

1. J. Rosen, B. Salik, and A. Yariv, J. Opt. Soc. Am. A **12**, 2446 (1995).

2. B. Salik, J. Rosen, and A. Yariv, J. Opt. Soc. Am. A **12**, 1702 (1995).

3. M. Avriel, *Nonlinear Programming : analysis and methods*, 1st ed. (Englewood Cliffs, New Jersey, 1976), Chap. 10, p. 299.

Optical Wavelet Transform with Use of A Computer–Generated Hologram

Guo–Zhen Yang, Yan Zhang, Ben–Yuan Gu, and Bi–Zhen Dong

Institute of Physics, Academia Sinica, P. O. Box 603, Beijing 100080, China
Phone: +86-10-62559131 ext. 229; Fax: +86-10-62562605; E-mail: guby@aphy01.iphy.ac.cn

The wavelet transform (WT) is a relatively useful and powerful technique in many applications, such as signal processing, pattern recognition, data compression, and so on.[1–3] It overcomes the disadvantages of the Fourier transform and the Gabor transform, and provides an explicit representation of a signal in both space and frequency domains. Many configurations have been proposed to implement the wavelet transform, however, most of them are based on optical correlator. In this presentation, we present a new scheme to achieve the WT by a computer–generated hologram (CGH) based on the general theory of optical transform.[4–6] The equation for determining the CGH is derived and a computer simulation is presented.

The WT definition is based on a set of daughter wavelets $h_{a,b}(x)$, which are generated form the mother wavelet $h(x)$ by dilation and shift operations, as

$$h_{a,b}(x) = \frac{1}{\sqrt{a}} h\left(\frac{x-b}{a}\right), \qquad (1)$$

where b is the shift, a is the scale, and $\sqrt{a}$ is the normalization factor. Then the WT of a one–dimensional (1D) signal $f(x)$ is defined by

$$W(a,b) = \int f(x) h^*_{a,b}(x) dx. \qquad (2)$$

In practical applications, it is reasonable to consider the signals are band–limited in both space and frequency domains, thus only finite discrete dilation and shift factors are involved. Consequently, a two–dimensional (2D) output signal can be expressed in the form of 1D distribution. Assuming that the band width of b is b_m and only two dilation factors are employed, then Eq. (2) can be rewritten

$$W(x_2) = \begin{cases} \int f(x) h^*_{a_1, x_2 - b_m/2}(x) dx, \\ \quad \text{for } b_m/2 \geq x_2 > 0, \\ \int f(x) h^*_{a_2, x_2 + b_m/2}(x) dx, \\ \quad \text{for } -b_m/2 \leq x_2 < 0. \end{cases} \qquad (3)$$

For a discrete sample, the continuous signal is represented by its value at a set of sampling points. If the numbers of the sampling points are N_1 and N_2 for the input and output planes, respectively, thus we have

$$W_l = \sum_j^{N_1} T_{lj} f_j,$$

$$l = 1, 2, 3, ..., N_2 \ and \ j = 1, 2, 3, ..., N_1, \qquad (4)$$

where T is a matrix to be the combination of two integral operators in Eq. (3).

The schematic diagram of an optical system for achieving the wavelet transform is shown in Fig. 1, where x_{m1}, x_m, and x_{m2} are the sizes of apertures; N_1, N, and N_2 are the numbers of sampling points in the input, the CGH, and the output planes, respectively. G_1 and G_2 denote the relevant transforms which can be easily implemented in optics, such as the Fourier transform, the Fresnel transform, and so on. H indicates the amplitude phase distribution of the CGH. The output wave function U_2 is related to the input one U_1 as follows:

$$U_2 = G_2 H G_1 U_1. \qquad (5)$$

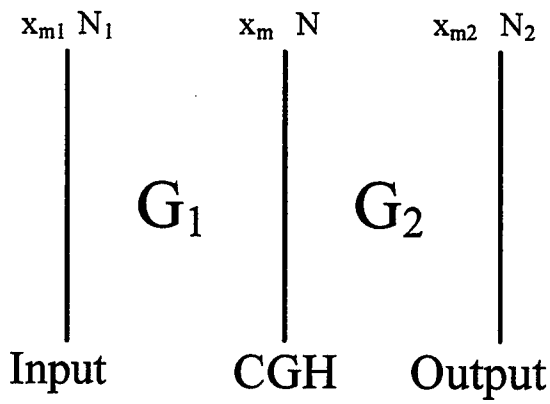

Figure 1. Schematic diagram of a single CGH system for achieving the WT.

The question of implementing the wavelet transform by the configuration shown in Fig. 1 is: How can we design the CGH so that the following equation is satisfied to a high accuracy?

$$T = G_2 H G_1. \tag{6}$$

If we find this CGH, the optical system with use this CGH can then achieve the wavelet transform accurately. Eq. (6) includes $N_2 \times N_1$ simultaneous equations and N unknown variables for H. In order to solve it, we prefer to introduce the following matrices: $A = G_2^+ G_2$, $B = G_1 G_1^+$, and $C = G_2^+ T G_1^+$, where "+" indicates a Hermitian conjugation operation. Then Eq. (6) is reformed

$$ABH = C. \tag{7}$$

Eq. (7) is completely equivalent to Eq. (6), but Eq. (7) is a set of linearly simultaneous equations including N equations and N unknown variables of the H, so we can solve them by standard procedure and obtain the desired solutions. Finally, the CGH can be determined completely. If we consider the Fourier transform, Eq. (7) can be substantially simplified by choosing the appropriate parameters under the following conditions:

$$\begin{cases} x_{m1} x_m / \lambda f = 1/N, \\ x_m x_{m2} / \lambda f = 1/N_2, \\ N = N_1 \times N_2, \end{cases}$$

or

$$\begin{cases} x_{m1} x_m / \lambda f = 1/N_1, \\ x_m x_{m2} / \lambda f = 1/N, \\ N = N_1 \times N_2, \end{cases} \tag{8}$$

where f is the focal length of the Fourier lens, and λ is the wavelength of the illuminating light. Thus we have

$$AB = kI, \tag{9}$$

where k is a complex constant and I is an $N \times N$ unit matrix. Substituting Eq. (9) into Eq. (7), finally, we obtain

$$H = C/k. \tag{10}$$

Considering only the planar CGH, the matrix of the amplitude–phase distribution of the CGH becomes diagonal. The equation which determines the amplitude–phase distribution of the CGH reduces to

$$H_{nn} = C_{nn}/k, \quad n = 1, 2, 3, ..., N. \tag{11}$$

Form the above derivation, it clearly shows possibility by using a single CGH optical system to achieve the WT at a high accuracy.

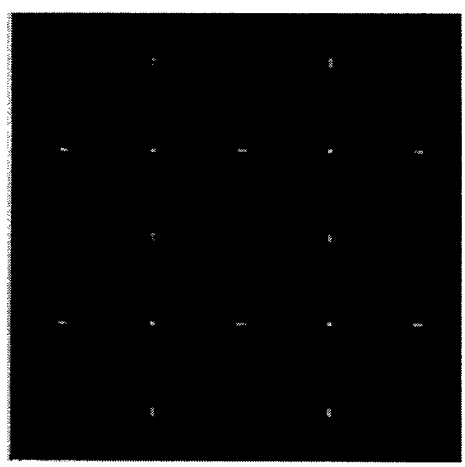

Figure 2. Partial amplitude distribution of the designed CGH.

To demonstrate our method, we present a computer simulation of 2D WT. The parameters are chosen as follows: N_1 =

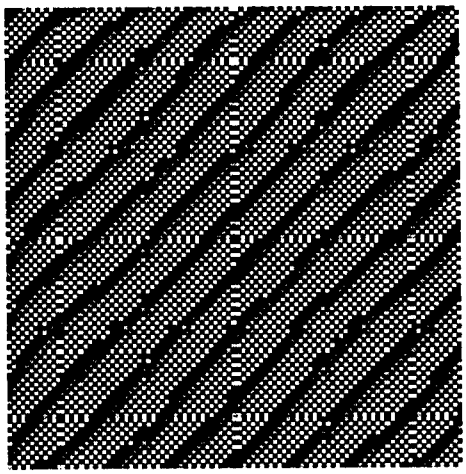

Figure 3. Partial phase distribution of the designed CGH.

$20, N_2 = 40, N = N_1 \times N_2 = 800$, $x_{m1} = 6.328mm, x_{m2} = 0.316mm$, and $x_m = 32mm$. The wavelet considered is the form

$$H(x) = -x\exp(-\frac{x^2}{2}), \qquad (12)$$

which is usually used to extract the edges of the images. When $x_2 < 0$ and $y_2 > 0$, the original input image is needed; when $x_2 > 0$ and $y_2 > 0$ ($x_2 < 0$ and $y_2 < 0$), the X-(Y-)direction WT is performed, while $x_2 > 0$ and $y_2 < 0$ both X- and Y-direction WTs are performed. Fig.2 displays the partial amplitude distribution and Fig. 3 shows partial phase distribution of the designed CGH. The input image is shown in Fig. 4, and the output result is shown in Fig. 5. It is clearly seen from Fig. 5 that the edges and corners of the input image have been satisfactorily extracted. It follows that the WT can be successfully implemented by a CGH based on the present approach.

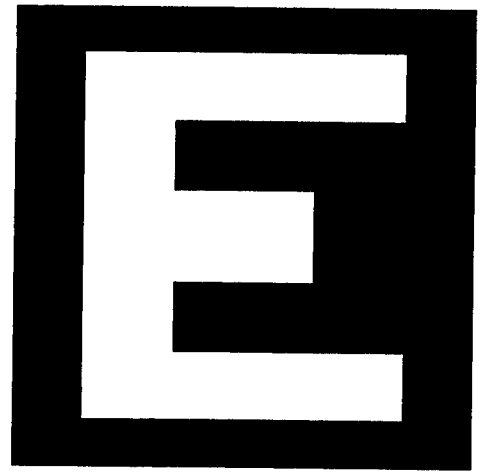

Figure 4. Input image

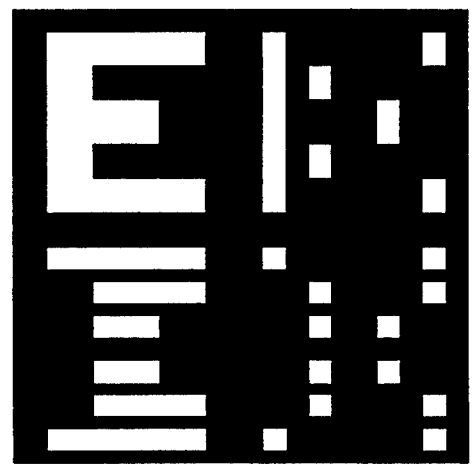

Figure 5. Output result of the computer simulation

REFERENCES

1. H. Szu, Y. Sheng, and J. Chen, *Appl. Opt.* **31** 3267–3277 (1992).
2. Y. Sheng, D. Roberge, and H. Szu, *Appl. Opt.* **31**, 1840–1845 (1992).
3. Y. Sheng, D. Roberge, H. Szu, and T. Lu, *Opt. Lett.* **18**, 299–301 (1993).
4. G. Yang, *Acta. Phys. Sin.* **30**, 1340–1350 (1980).
5. B. Gu, G. Yang, and B. Dong, *Appl. Opt.* **25**, 3197–3205 (1986).
6. B. Dong and B. Gu, *Acta. Phys. Sin.* **35**, 235–242 (1986).

Locating Rotation–Invariant Optical Correlation

Yan Zhang, Ben–Yuan Gu, Bi–Zhen Dong, and Guo–Zhen Yang

Institute of Physics, Academia Sinica, P. O. Box 603, Beijing 100080, China
Phone: +86-10-62559131 ext. 229; Fax: +86-10-62562605; E-mail: guby@aphy01.iphy.ac.cn

Optical correlation is one of important operations for many applications, for example, pattern recognition, feature extraction, and so on. With the development of optical information processing, many techniques have been applied to the optical correlation to meet different requirements. The conventional correlation is based on the Fourier transform,[1,2] therefore, it is space–invariant. However, when one pays attention to the correct location of the object and does not care for whether it has been rotated at some angle. In this case, not only the space–variant but also rotation–invariant correlation is needed. In this presentation, we combine the fractional correlation with the method of the circular harmonics decomposition, and present a method to achieve the locating rotation–invariant correlation.

The fractional Fourier transform, which is the generation of the conventional Fourier transform, was introduced to optics by Mendlovic *et al.*[3,4] Its mathematical definition is

$$U_2(x_2) = F^P\{U_2(x_2)\} = \sqrt{1 - i\cot\alpha}\int U_1(x_1)$$

$$\times \exp[i\pi(x_1^2+x_2^2)\cot\alpha - i2\pi x_1 x_2 \csc\alpha]dx_1, \quad (1)$$

where $U_1(x_1)$ and $U_2(x_2)$ denote the input and output objects; x_1, x_2 are the coordinates in the input and output planes, respectively. P is a fractional order and $\alpha = P\pi/2$. The parameter P determines the space–variant property of the transform. When $P = 0$, the FRFT domain is equivalent to the original input domain, thus the transform is completely space–variant. However, for $P = 1$, the FRFT reduces to the conventional Fourier transform, which is space–invariant. For any other fractional order, the FRFT is partially space–variant. Based on the FRFT, the partially space–variant correlation was proposed.[5,6] It is defined by

$$C_{1,2}^{P_1,P_2,P_3}(x) = F^{P_3}\{F^{P_1}\{t_1(x_1)\}F^{P_2*}\{t_2(x_1)\}\}, \quad (2)$$

where $C_{1,2}^{P_1,P_2,P_3}$ denotes the fractional correlation of two objects $t_1(x_1)$ and $t_2(x_1)$, and the star relevant * represents the complex conjugate. For obtaining the strong correlation peak, the fractional orders should satisfy the following condition

$$\frac{1}{\tan(P_1\pi/2)} - \frac{1}{\tan(P_2\pi/2)} + \frac{1}{\tan(P_3\pi/2)} = 0. \quad (3)$$

For simplicity, we concern only with a special case: $P_1 = P_2 = P, P_3 = -1$ in all the demonstration examples.

Circular–harmonic decomposition is usually used for rotation–invariant pattern recognition. It projects the object $f(r,\theta)$ into a set of orthogonal functions $\{\exp(iN\theta)\}$ [7,8]

$$f(r,\theta) = \sum_{N=-\infty}^{\infty} f_N(r)\exp(iN\theta), \quad (4)$$

where $f_n(r)$ is radial function and defined by

$$f_M(r) = \frac{1}{2\pi}\int_0^{2\pi} f(r,\theta)\exp(-iM\theta)d\theta. \quad (5)$$

For obtain locating rotation–invariant correlation, we decompose the reference object $g(r,\theta)$ into the circular harmonics and choose only one harmonic which contains the maximum energy of the object, then this harmonic is regarded as the representative of the reference object in the fractional correlation. Assume that the M–th

order harmonic $g_M(r)\exp(iM\theta)$ is selected, the filter is

$$\exp(-iM\phi)H_M^{\alpha *}\{g_M(r)\}, \tag{6}$$

where

$$H_M^{\alpha}\{g_M(r)\} = 2\pi\int_0^{2\pi} g_M(r)J_M(2\pi r\rho\csc\alpha)rdr. \tag{7}$$

For any input object $f(r,\theta)$, it can be decomposed into circular harmonics. Its FRFT for order P is given by

$$F^P\{f(r,\theta)\} = \sum_N(-i)^N\exp(iN\phi)H_N^{\alpha}\{f_N(r)\}. \tag{8}$$

So, on the plane just behind the filter, the amplitude–phase distribution is

$$D(\rho,\phi) = \sum_N(-i)^N\exp(iN\phi)\exp(-iM\phi) \times H_N^{\alpha}\{f_N(r)\}H_N^{\alpha *}\{g_M(r)\}. \tag{9}$$

The correlation peak value of E_M corresponds to the intensity at the origin point $(x=0, y=0)$ on the output plane,[8] by using the Perseval law, it reads

$$E_M = \int_0^{\infty}\int_0^{2\pi} D(\rho,\phi)\rho d\rho d\phi. \tag{10}$$

Because the circular harmonics are orthogonal each other, only one term with $N = M$ in the summation of Eq. (9) persists nonzero, thus one obtains

$$E_M = 2\pi(-i)^M\int H_M^{\alpha}\{f_M(r)\}H_M^{\alpha *}\{g_M(r)\}\rho d\rho. \tag{11}$$

If the input object has a rotational pattern similar to the reference one, and locates at the correct position, thus $H_M^{\alpha}\{f_M(r)\} = H_M^{\alpha}\{g_M(r)\}$, high correlation peak can be observed, otherwise, the intensity of correlation peak drops rapidly.

To demonstrate the capability of the new approach, we present some computer simulations. The fractional order $P = 0.8$ is selected for all cases. The binary image of the letter "E", as

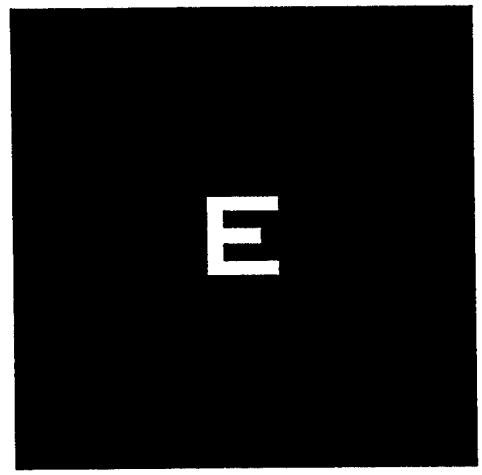

Figure 1. Reference object.

shown in Fig. 1, is employed as a reference object. This image is expressed by a matrix of 64×64 pixels around the center of the input plane. This object is decomposed into circular harmonics and the harmonic of order $M = 0$ is served as the representative of the original reference object. First, we place the reference object and one of its different rotational versions at the center of the input plane, and perform the corresponding correlation one by one. The intensities of the corresponding correlation peaks are displayed in table 1. They vary within a small rang of 7.8×10^{-2} to 8.4×10^{-2}, which show that the suggesting method can provide rotation–invariant recognition. Then, a false–alarm object "P" is placed at the center of the input plane, we find that the corresponding correlation peak is 3.6×10^{-2}, which manifests that our approach has good discriminability. In contrast, when moving all the objects toward upper–right position and performing the correlation again, the intensities of correlation peaks take the value between 3.3×10^{-3} to 9.2×10^{-3}, as shown in table 1. They are one order of magnitude smaller than that of unmoving input object. These results denominate that this kind of correlator is quit sensitive to the variation of the object's position. At last, we employ a mixing input object, as shown in Fig. 2. It is the superposition of a letter "E" rotated by 90° at

the center of the input plane and an unrotated "E" at the upper side of the input plane. Fig. 3 displays the intensity distribution on the output plane for this special input object. At the center of the output plane, the correlation peak is sharp and strong, however, the peak intensity appearing at the upper side is quite low. It shows that our method can provide locating rotation–invariant correlation correctly.

Table 1 Intensities of the correlation peaks for $P = 0.8$

Input objects	Case A ($\times 10^{-2}$)	Case B ($\times 10^{-3}$)
Letter "E"	8.4	9.2
"E" rotated by 45°	8.0	7.4
"E" rotated by 90°	8.4	3.9
"E" rotated by 135°	7.9	3.3
"E" rotated by 180°	8.3	4.3
Letter "P"	3.06	4.3

Case A: The intensity of the correlation peak for object was located at the center of the input plane. Case B: The intensity of the correlation peak for object was moved to the upper–right position on the input plane.

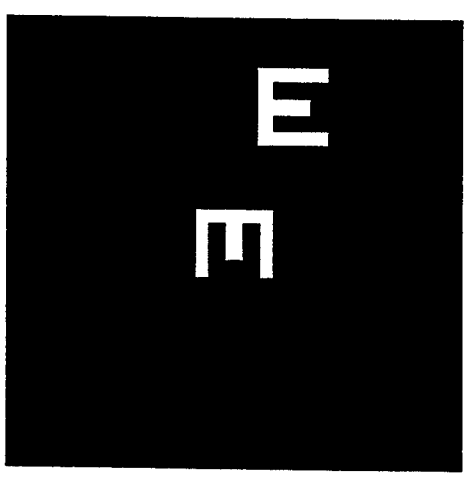

Figure 2. Mixing input object.

For $P = 0.3$, the above simulations are repeated with use of the same reference. Similar results were obtained. It is worthy to point out

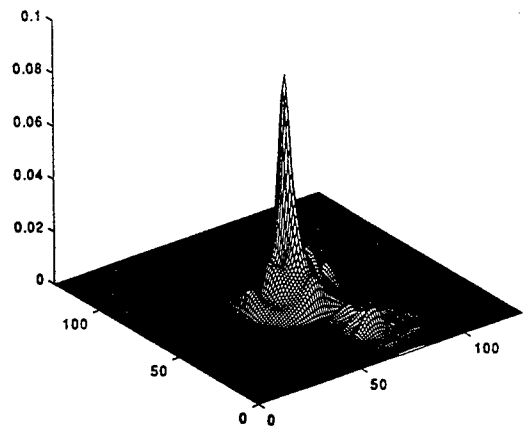

Figure 3. Intensity distribution on the output plane with use of the object as shown in Fig. 2 as the input image.

that the fact the energy of the correlation peak and the discriminability may be degraded because only one harmonic of the reference object is considered. However, one may employ the wavelength multiplying method, as is suggested in Ref. 9, to solve this problem.

REFERENCES

1. A. Vander Lugt, *IEEE Trans. Inf. Theory* **IT-10**, 139–140 (1964).
2. C. S. Weaver and J. W. Goodman, *Appl. Opt.* **5**, 1248–1249 (1966).
3. D. Mendlovic and H. M. Ozaktas, *J. Opt. Soc. Am. A* **10**, 1875–1881 (1993).
4. . W. Lohmann, *J. Opt. Soc. Am. A* **10** 2181–2186 (1993).
5. D. Mendlovic, H. M. Ozaktas, and A. W. Lohmann, *Appl. Opt.* **34**, 303–309 (1995).
6. S. Granieri, R. Arizaga, and E. E. Sicre, *Appl. Opt.* **36**, 6636–6645 (1997).
7. Y. Sheng and H. H. Arsenault, *J. Opt. Soc. Am. A* **4**, 1793–1799 (1987).
8. Z. Zalevsky, I. Ouzieli, and D. Mendlovic, *Appl. Opt.* **35**, 3141–3147 (1996).
9. Z. Zalevsky, D. Mendlovic, and J. Garcia, *Appl. Opt.* **36** 1059–1063 (1997).

Character display unit using a binary phase hologram array and a LC-SLM

Bong-Gyun Kang*, Nam Kim*, Ho-Hyung Suh**, Duck-Hee Lee**

* Department of Computer & Communication Engineering, Chungbuk National University, Cheongju, South Korea

** Research Department, Electronics and Telecommunications Research Institute, Taejon, South Korea

We have demonstrated the character display unit that combines the dynamic property of the LC-SLM with the high efficiency property of the phase hologram fabricated by photolithography.

Recently, phase holograms with high diffraction efficiency are used in photo-logic devices, optical information processing, and free-space optical interconnection systems etc.[1-4] In this paper, we proposed new method of optical information processing using a phase hologram array and a LC-SLM, and implemented the optical system to display various characters.

Assume that $g(x, y)$ is a binary phase hologram array with $N \times M$ sub-holograms, then it is expressed as follows:

$$g(x,y) = \sum_{m=1}^{M}\sum_{n=1}^{N} H_{m,n} rect\left[\frac{x-mR}{D_x}, \frac{y-nC}{D_y}\right] \tag{1}$$

where $H_{m,n}$ is the phase transmission function of n row and m column hologram out of $N \times M$ sub-holograms, D_x and D_y are hologram periods in the direction of x and y, respectively, and R and C are intervals between adjacent two hologram centers in the direction of x and y, respectively.

Sub-holograms are designed to get output images at the specific position according to their rows. As shown in figure 1, each row is made up of holograms for the characters of the same position out of N positions at the output plane. Therefore, from the holograms in all M columns of each row, output characters are displayed in the same position.

As an example, in order to display the character SUN, the light has to pass through holograms in 1 row and 1 column, and 2 row and 1 column, and 3 row and 1 column. If the light passes through more than two holograms in the same row at the same time, the overlapping characters are obtained at the output plane. Using the same manner, various characters are reconstructed according to the different input patterns.

The size of each cell is 1μm×1μm, and one period of a hologram is 128μm×128μm. The total size of sub-holograms replicated 16×26 (row×column) times is 2.048mm×3.328mm, and the spacing between adjacent different sub-holograms is 0.384mm. These amplitude patterns on the *e*-beam mask were transferred into optical surface-relief patterns by contact micro-lithography techniques.

To transmit the laser beam selectively, we use a LC-SLM placed in the only front of the hologram array. Figure 2 shows the setup for the character display using a phase hologram array and a LC-SLM. Figure 3 shows examples of input patterns transmitting a LC-SLM before passing through a hologram array. Figure 4 is the experimental results of images appearing on the output plane, after transmitting each input pattern of figure 3 in the LC-SLM and the phase hologram array by using the experiment unit of figure 2. The reason why the image is symmetrical to the origin is that the phase of holograms is binary (0 or π).

In conclusion, we proposed and optically implemented the unit that can display various characters in real time using a binary phase hologram array and a LC-SLM. It combines the dynamic property of the LC-SLM with the high efficiency property of the phase hologram fabricated by photolithography. It is very different from existing electronic display units in points that all input and output units use the light and the parallel processing for displaying the image. Therefore, there is the significance in the following respects, the high-speed display and the capability of 3-dimensional image generation using holograms. As the result, the character display unit proposed in this paper has a fundamental and important meaning as new method displaying images by using only light and will be used in optical information processing and optical communications fields.

References

[1] S. H. Song et al., "Beam-array combination with planar integrated optics for three-dimensional multistage interconnection networks," Appl. Opt., Vol. 36, No. 23, Aug. 10, 1997.

[2] D. J. Lee et al., "Dynamic optical interconnection in free-space switching system," Opt. Rev., Vol. 3, No. 6B, pp. 475-477, 1996.

[3] H. H. Suh et al., "Combined binary-phase holograms for free-space optical interconnection," Opt. Lett. Vol. 20, No. 20, pp. 2131-2133, 1995.

[4] J. E. Morris and M. R. Feldman, "Reconfigurable optical interconnects by a combined computer-generated hologram and spatial light modulator method," Appl. Opt., Vol. 33, No. 17, pp. 3683-3694, 1994.

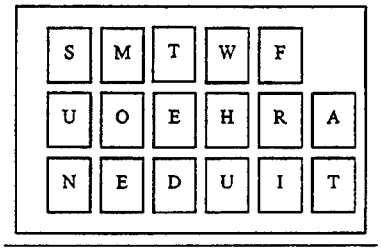

Figure 1. Arrangement scheme of a hologram array

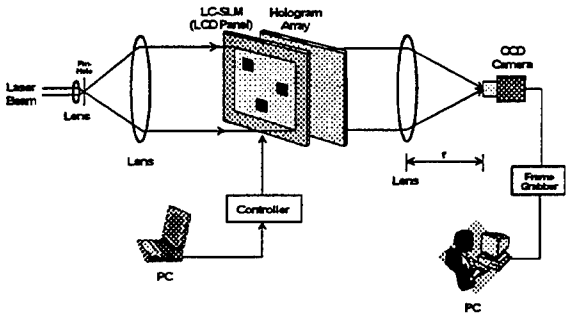

Figure 2. Character display unit using a hologram array and a LC-SLM

Figure 3. Input patterns modulated in a LC-SLM

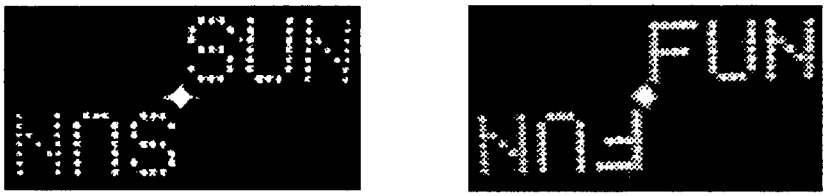

Figure 4. Experimental results

Beam-Steering in the Spectrum of a Liquid Crystal Spatial Light Modulator.

Peder Rodhe, Centre for Computer Systems Architecture, Halmstad University, Box 823, SE-30118 Halmstad, Sweden
Tel. +46 31 274110, Fax +46 31 274120

In this report we take up some new aspects of optical beam-steering by means of liquid crystal spatial light modulators (SLM's). Our starting-point is that any form of modulation should modify the spectrum of an applied "carrier" [1]. To this end, we devote our interest to diffraction in the spectrum established by these SLM's [2], focussing on applications of smectics (either A* or C* [3]), because these materials have shown their potential, e.g., for rapid switching and small pixel size.

Since the amplitude and phase control of individual pixels should be of key importance [4], we first need to derive these characteristics for a single cell element. A simple model will suffice (figure 1), whereby details of the optical propagation in cell substrates and buffer layers may be neglected. By assuming a "bookshelf orientation" of the smectic layers [3], molecules would align parallel to the substrate boundaries. Due to their polar and chiral properties, molecules still may be tilted about an average direction normal to the layer boundaries, by applying an electric field between the substrates. Very generally, the tilt angle can be said to depend on the sign, amplitude and frequency of the field.

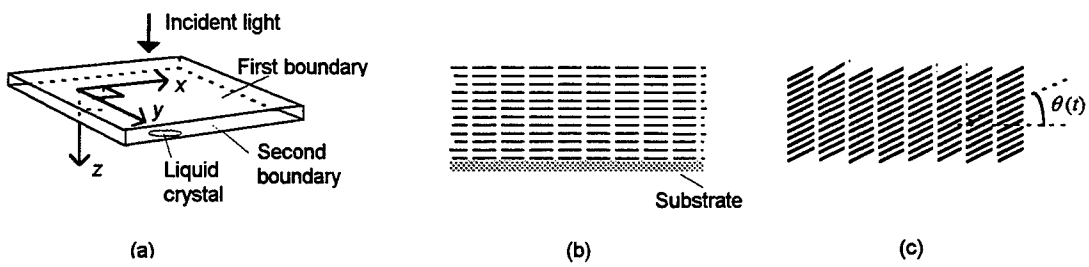

Figure 1. Single cell: (a) geometry, (b) book-shelf layers from the edge of and (c) from above one of the substrates.

On assigning an optic axis parallel to the molecular direction, we may show that a monochromatic, linearly polarized lightwave, after passing through the cell, separates into orthogonal wave components with distinct characteristics. We illustrate this for a cell satifying the half wave-plate condition. By a proper choice of x and y axes, the wave components (their electric fields) may then be derived as

$$E_x = E_{in} \sin\left[2\theta(t)\right] \sin\omega t \tag{1}$$

and

$$E_y = E_{in} \cos\left[2\theta(t)\right] \sin\omega t\,, \tag{2}$$

where E_{in} is the amplitude of the incident wave, $\theta(t)$ is the time-dependent optic axis tilt imposed by some, yet unspecified change of the applied electric field, and ω is the optical frequency. At any rate, this signifies an amplitude modulation [1]. The baseband spectra of the modulation factors $\sin[2\theta(t)]$ and $\cos[2\theta(t)]$ will thus be frequency translated into the optical domain, locating themselves around a "carrier frequency," ω.

A numerically calculated baseband spectrum is shown in figure 2 (a) involving a simple cosine tilt function,

$$\theta(t) = \theta_0 \cos\left(\omega_m t - \phi_m\right), \tag{3}$$

where θ_0 and ϕ_m are amplitude and phase constants, respectively, and ω_m is the modulation frequency (here normalized to 1 radian/s). In this particular case, our result can be checked by expanding the modulation factors into well-known series of Bessel functions. Figure 2 (b) shows another example, where the tilt function is a square-wave, approximated by ten terms of its series expansion.

Now consider a linear SLM array of pixels arranged as a finger structure (figure 3). A typical array may consist of up to several hundred parallel fingers, 10-50 μm wide and up to a few millimetres high, and with a

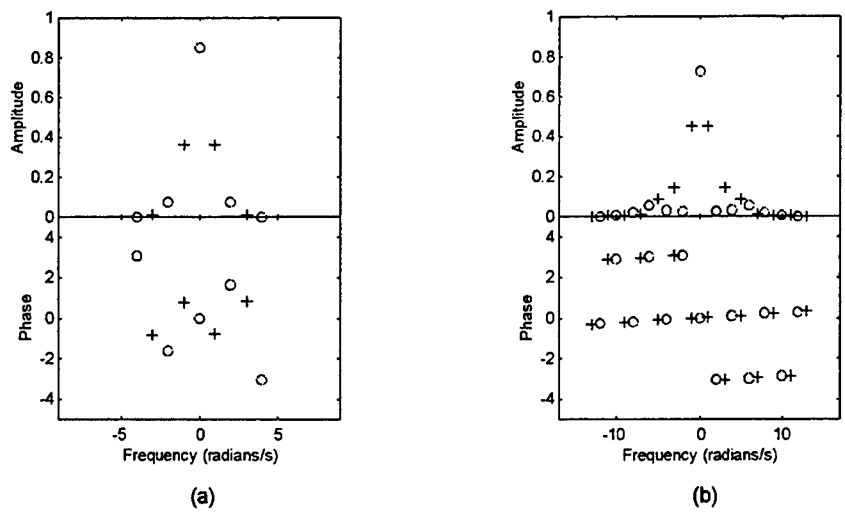

Figure 2. Baseband amplitude and phase spectrum (half wave-plate condition). (a) for a director tilt according to equation (3), $\omega_m = 1$ radians/s, $\phi_m = \pi/4$, $\theta_0 = \pi/8$. (b) for a director tilt described by a square wave of frequency 1 radians/s, amplitude $\pi/8$ and zero phase, approximated by 10 terms of its series expansion. Crosses are the amplitude components of the sine factor of equation (1), and rings the components of the cosine factor of equation (2).

maximum dead-space between pixels of 5 to 10 μm. Normally, the half wave-plate condition holds somewhere in the visual region, say, at a wavelength around 600 nm.

We may apply a tilt function for each pixel of the array according to equation (3), keeping the θ_0 and the ω_m, fixed, but considering a sequence of individual pixel phases, $\phi_{m,n}$, (ordering the pixels by $n = 1, 2, 3, \ldots N$). Evidently, the translated baseband spectrum obtains a form, whereby the optical phase-shifts between neighboring pixels (intra-pixel phase-shifts) become equal to those appearing at baseband.

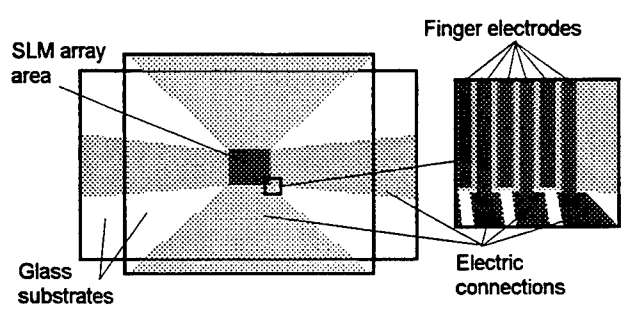

Figure 3. Outline of a linear SLM array.

A particularly interesting case of focussed beam-steering has been simulated, as shown in figure 4. Here we consider the x component of the transmitted wave, according to equation (1), together with the pair of first frequency components of the sine modulating factor (represented by crosses in figure 2 (a) at ± 1 radians/s). By adopting a phase sequence that has a quadratic variation, with a minimum at the centre pixel of the array, we thus established a step-approximation for a sinusoidal zone-plate [5]. From calculations of the Fresnel diffraction we see that the component of positive frequency at baseband yields a wave converging towards the real focus of the zone-plate (complying with a sequence of decreasing phase away from the array centre), while the component of negative frequency (i.e., an increasing phase) is associated with a diverging wave coming from the virtual focus. Moreover, by adding a constant intra-pixel phase-shift (ϕ_0 in figure 4), we may realize a tilting zone-plate. Figure 4 (a-c) shows the power density of the beam for three different values of ϕ_0. A maximum tilt of about 1 degree may be achieved for $\phi_0 = \pi$ with the parameters used in this example.

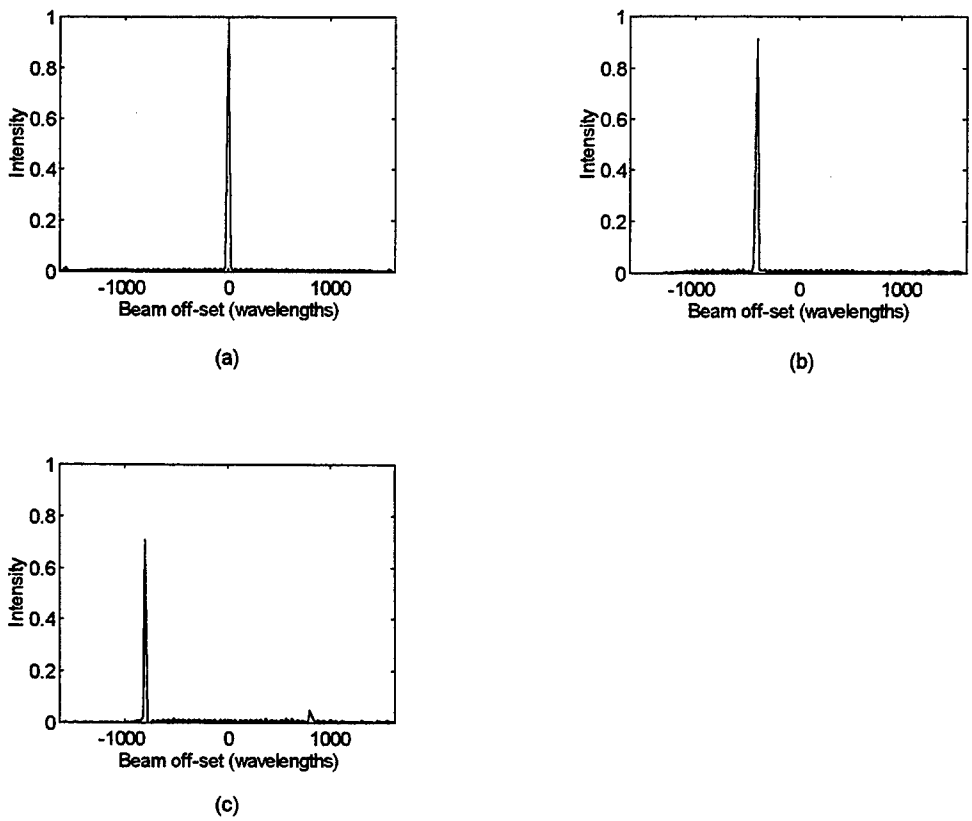

Figure 4. Simulated beam off-sets (optical power density) at the real focus of a one-dimensional, step-approximated, sinusoidal zone-plate using a fixed, quadratic phase-shift with respect to the centre pixel of the array, and adding a constant intra-pixel phase-shift ϕ_0 (i.e., $\phi_{n+1} - \phi_n = \phi_0$), yielding a corresponding wave-front tilt. (a) $\phi_0 = 0$, (b) $\phi_0 = \pi/2$, and (c) $\phi_0 = \pi$. Number of pixels $N = 64$, pixel distance = 25 λ, dead-space = 7,5 λ, focal distance = $4 \cdot 10^4 \lambda$.

Figure 2 (a) suggests there might even be some contributions from the third harmonics of the spectrum. However, by choosing a small θ_0 these may become so small that we could neglect them in our simulation. Also the interference between the converging and diverging waves has been neglected as a first approximation. To some extent such issues are connected with the coherence of the light source. Diffraction effects of "dead-spaces" between pixels are minimized here, by assuming these narrow regions as continuously changing, at each instant adapting themselves to an average of the phase-shifts of the two nearby pixels.

A host of additional questions are yet to be discussed in the practical application of these arrays. The main point remains, however, that there should be a direct and simple way of influencing the spectral characteristics of beam diffraction with a liquid crystal SLM, by changing the amplitude and phase spectra at baseband.

References.

1. A. B. Carlson, *Communication Systems* (McGraw-Hill, New York, 1986), Ch. 6.
2. Somewhat related concepts may be found in doppler velocimetry, see, e.g., S. Hård, Y. Hamnerius, O. Nilsson, Laser heterodyne apparatus for measurements of liquid surface properties - Theory and experiments, J. Appl. Phys. **47**, 2433-2442 (1976), and in integrated optics, see, e.g., L. Thylen, L. Stensland, Electrooptic approach to an integrated optics spectrum analyzer, Appl. Opt. **20**, 1825-1832 (1981).
3. J. W. Goodby, R. Blinc, N. A. Clark, S.T. Lagerwall, M. A. Osipov, S. A. Pikin, T. Sakurai, K. Yoshino, B. Zeks, *Ferroelectric Liquid Crystals, Principles, Properties and Applications* (Gordon and Breach, Philadelphia, 1991).
4. P. F. McManamon, T. A. Dorschner, D. L. Corkum, L. J. Friedman, D. S. Hobbs, M. Holz, S. Liberman, H. Q. Nguyen, D. P. Resler, R. C. Sharp, and E. A. Watson, Optical phased array technology, Proc. IEEE **84**, 268-298 (1996).
5. M. V. Klein, *Optics* (Wiley, New York, 1970), Ch. 8.

Paper withdrawn.

Binary Zone Plate Array for Parallel Joint Transform Correlator System:Design and Evaluation

Asako HASHIMOTO, Kyoko KODA and Kashiko KODATE
Japan Women's University, Dept. of Mathematical and Material Structure Science
2-8-1 Mejirodai, Bunkyo-ku, Tokyo-112, Japan
tel: +81-3-3942-6126 fax: +81-3-3942-6126
e-mail: asako@fourier.jwu.ac.jp
Roshan THAPLIYA and Takeshi KAMIYA
University of Tokyo, Dept. of Electronic Eng., 7-3-1 Hongo, Bunkyo-ku, Tokyo-113, Japan

1. Introduction

Optical information processing systems based on Fourier transformation, such as the matched filtering correlation or the joint transform correlation, offer advantages such as parallel processing capability, direct input of signal images, freedom from electronic noise, and so on[1,2]. The key components of these systems are micro-optic components for generating efficient multiple image and spatial light modulators for real-time optical filtering . Binary zone plate array (BZPA), one of the diffractive optical elements, is especially attractive in the fields of optical computing and interconnection, where use of free space optics offer flexibility in designing a system of massive parallelism[3,4].

we have reported new attempts of BZPAs, such as 2D uniform intensity focusing spots array generators and many kinds of Talbot array illuminators[5,6]. we have also applied BZPA to the facial recognition system based on parallel joint transform correlation[7,8].

The present work describes a design procedure to optimize the performance of BZPA as the input image duplicator and Fourier transform lens. The design is implemented by 8 level binary optics technology, yielding high efficiency. The evaluation is done by measuring the signal quality of facial recognition system.

2. Design of BZPA for Parallel joint transform correlator

The architecture which we investigate is based on a combination of an optical joint transform correlator (JTC)and a personal computer (PC) as shown in Fig.1. Optical Fourier transform provides the instantaneous correlation and spatial parallelism accelerates the processing speed. The unknown input image is pre-processed by PC and is duplicated by BZPA1, stored in optically addressed spatial light modulator (PAL-SLM1). The reference data base is provided from PC2 and is transferred to the electrically addressed SLM(TNL-SLM). Reference images and signal images are jointly transformed by BZPA2 and the resulting intensity holograms are recorded at PAL-SLM2. The inverse Fourier transform of them by BZPA3 give the correlation signals. The discrimination is made at PC3.

There is a fundamental trade-off relationship between signal quality and channel number. For given number of pixels in spatial light modulator, the increase in channel number results in the reduced pixel number per unit image, degrading the image quality. The numerical aperture (NA) of BZPA raises the other trade-off; namely smaller NA provides more tolerant fabrication conditions, while it lowers the spatial cut-off frequency.

Therefore the optimizing design should be such that the cut-off spatial frequency as defined by NA of BZPA should match the pixel number of SLMs. Our design procedures include the following design parameters and/or design conditions: (a) focal length, (b) aperture size, (c) number of parallel channels, (d) geometrical arrangements of BZPs, (e) diffraction angle due to lattice of SLM pixellation. With given sizes of spatial light modulators (640 x 239 pixels; 21.1x15.9 mm^2), we determined the aperture size for

facial recognition to be 5.0 mm and that for character recognition to be 2.6 mm.

Fig.2 shows the designed BZPAs of 5 channels for the former specification and of 20 channels for the letter. It should be noticed that an irregular geometrical arrangement was introduced to avoid the overlap of signal patterns with pixel lattice diffraction. The design parameters are given in Table 1.

The BZPAs were fabricated by e-beam mask pattern generation, followed by optical lithography and dry etching. We attempted to measure the actual errors by observing the surface profiles with an AFM.

In Table 2, the experimental results for optical performance are summarized. With 8 level binary optics, spot sizes of 40.2 ± 2.6 μ m, resolution ability of 11.9 ± 0.8 lp/mm, and focusing efficiencies of 88.0 ± 2.1% were reached. These values close agreement with the theoretical calculation values using the equation of Fresnel-Kirchhoff's approximation.

3 Evaluation of Parallel Facial Recognition System

We applied the fabricated 5 channel BZPAs to the recognition of unknown face in comparison with the registered 100 faces. Using the experimental setup of Fig.1, the correlation signals are monitored by CCD. Typical results are shown in Fig.3, where significant peak height difference between auto-correlation and cross-correlation appears. A systematic study of all 100 faces as input signal resulted in perfect discrimination. Also we could demonstrate the separation of unregistered faces from registered faces. As the supplementary tests, we also checked the degradation of the correlation signal when the spatial cut-off frequency was gradually lowered.

The recognition of font characters should be easier than that of faces, because of the relative simplicity of the patterns[9]. We estimate 20 channel parallel processing is feasible for the recognition of alpha-numeric characters or Devanagari script, a representative script of south Asia. Potential of further throughput acceleration by increasing parallelism and corresponding optimum design of diffractive optical elements will also be discussed.

4. Conclusion

A new design procedure of binary zone plate array dedicated to parallel optical pattern recognition was introduced. Using 8 level binary optics, 5 and 20 channel BZPAs were fabricated with efficiency of 88%. Five channel parallel joint transform correlation system was assembled for facial recognition. For a 100 person data base, processing speed on the order of 1.8 s/face was achieved with satisfactory discrimination yield. Furthermore, application to character recognition, throughput improvement and data base size up-grade are discussed.

The authors wish to thanks Mr. N. Hori of Topcon Co., Ltd. for his help in processing BZPA. This work was supported by a Grant-in aid for scientific research from the Ministry of Science, Education and Culture, Japan.

References

1) David L. Flannery and Joseph L. Horner: Proc. IEEE, **77**, 1511 (1989).
2) C. S. Weaver and J. W. Goodman,: Appl. Opt. **5**, 1248 (1966).
3) Veldkamp WB, Leger JR and Swanson GL: Opt. Lett. **11**, 303 (1986).
4) M. Schmitz and O. Bryngdahl: J. Opt. Soc. Am. A, **14**, 901 (1997).
5) K. Kodate, E. Tokunaga, Y. Chen JL and T. Kamiya: Appl. Opt. **29**, 5115 (1990)
6) W. Klaus, Y. Arimoto and K.Kodate: J. Opt. Soc. Am. A **14**, 1092 (1997).
7) K. Kodate, Y. Ohya, R. Thapliya, T. Tsuchiya and T. Kamiya,: Optical Review **3**, 400 (1996).
8) K. Kodate, A. Hashimoto, Y. Takahashi, R. Thapliya and T. Kamiya,: Tech. Dig. CLEO/Pacific Rim '97, 276 (1997).
9) R. Thapliya, A. Hashimoto, K. Kodate, M. Tsuchiya and T. Kamiya,: Tech. Dig. CLEO/Pacific Rim '97, 310 (1997).

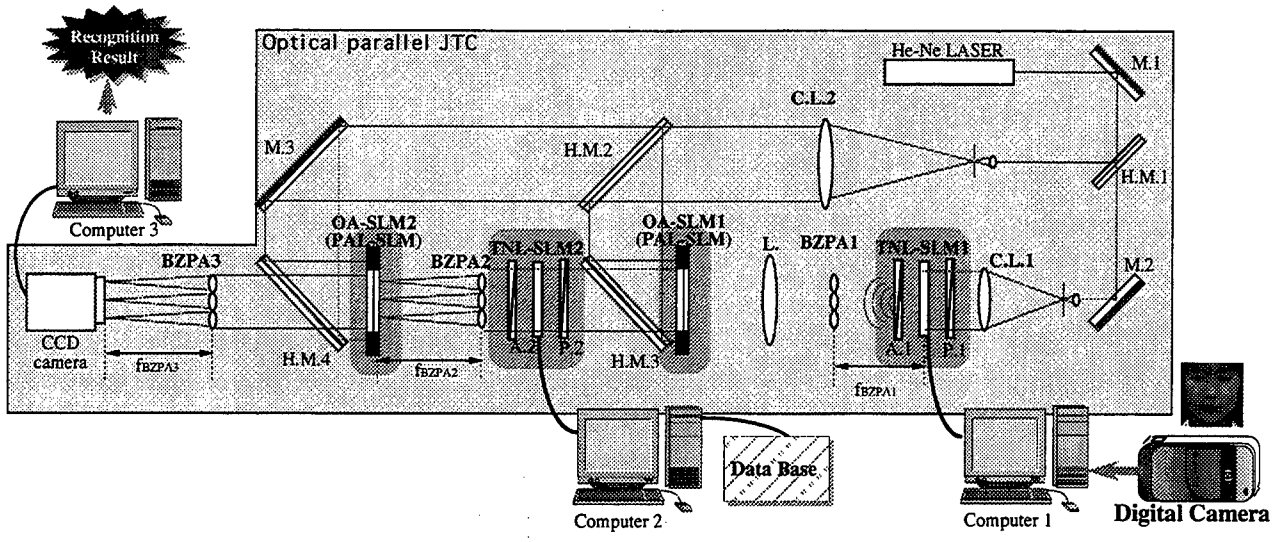

Fig.1 The experiment setup of Parallel Joint Transform Correlator with 5-channel BZPAs for a duplicator and Fourier trnsform lens.

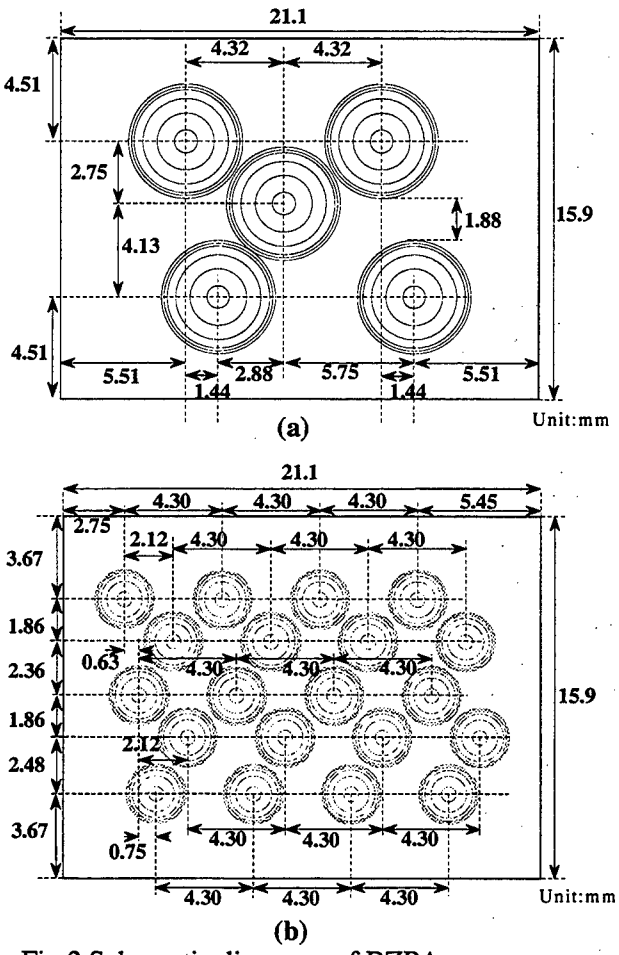

Fig.2 Schamatic diagrams of BZPAs irregular channel arrangements
(a) 5-channel BZPA for facial images.
(b) 20-channel BZPA for character images.

Table 1 Design parameters of two kinds of BZPA.

	5-channel	20-channel
focal length	*300 mm*	*300 mm*
N.A.	*0.00833*	*0.00433*
aparture size	*5.0 mm*	*2.6 mm*
number of level	*8 level*	*8 level*
line number	*131 line*	*35 line*
minimum line width	*9.5 μm*	*18 μm*

Table 2 Optical performance of 5 channel BZPA.

efficiency	*88.0±2.1 %*
spot size	*40.2 ±2.6 μm*
resolution	*11.9±0.8 lp/mm*

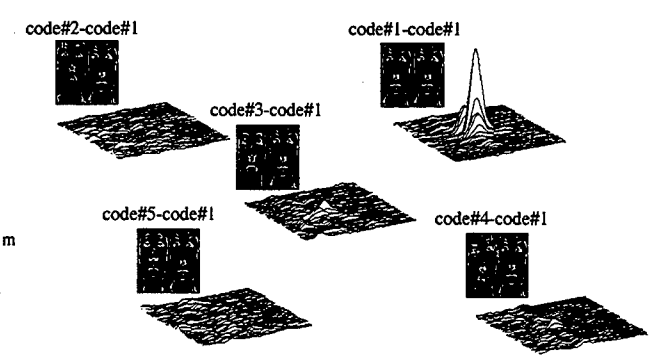

Fig.3 Experimental results formed 5-channel of correlation signals.

Polarization analysis for detection of molecular reactions

E.-B. Kley, B. Schnabel,
Friedrich Schiller University Jena, Institute of Applied Physics
Max-Wien-Platz 1, 07743 Jena, Germany
Tel.: +49-3641-657647, Fax: +49-3641-657680

U. Riß
DRE-Dr. Riss Ellipsometerbau GmbH
Feldstrasse 14, 23909 Ratzeburg, Germany

1. INTRODUCTION

The direct measurement of molecular reactions is interesting for a lot of applications, for example for medical diagnostics, DNA, smell or taste-analysis. We have focussed on medical diagnostics. An improvement of the conventional analysis methods is possible by a direct optical measurement of the biochemical reaction. For this purpose we developed a microoptical device based on subwavelength period metal stripe gratings.

2. BIOMEDICAL BACKGROUND

The measurement of antigen-antibody reactions is an essential part of medical *in vitro* diagnostics. At the moment mainly immuno assays like ELISA, RIA and FIA [1] are used for this. All tests are based on a similar principle; for example an ELISA test works like this: antigens are bound to a solid phase. Afterwards the prepared substrate is exposed to human or animal serum, which has to be tested. If there are antibodies in the serum, they will react with the immobilized antigens bound to the solid phase. The number of bound antibodies is the relevant information for medical diagnosis. But a conventional ELISA, RIA or FIA-test can not measure the binding rate directly. For the analysis, secondary or tertiary antibodies with markers are needed which is usually a time consuming procedure. For a long time a method which works without synthetic produced secondary and tertiary antibodies is looked for. The new technique we developed shows a way to realize this.

Just as conventional immuno assays the new technique uses antigens, which are bound to a solid phase. In the next step the number of antibodies which are binding to the antigens can be measured directly without having the need of secondary and tertiary antibodies with markers by use of polarized light [2]. The technique is called A.N.D.R.E.A.-technique which stands for: anisotropy considering, not contacting, direct measuring, partial resonance using, eigen-polarization amplifying analysis. This new technique requires a polarized light source, a surface which binds only special types of molecules and a polarization-changing and detecting module. Measurements which are done with different allergy-antigens and blood serum, in which IGE-

which IGE-antibodies are, have shown that the sensitivity of the A.N.D.R.E.A.-technique is sufficient for medical diagnostics. We think the A.N.D.R.E.A.-technique can be used also for DNA, smell and taste analysis. The contamination of a surface with DNA can be measured directly, the measurement of DNA-hybridization is under development. Smell and taste analysis will work on the same basis. If the bound molecules have a different refractive index from the surface the A.N.D.R.E.A. principle must work also for smell and taste analysis. The tests for medical diagnostics are done with a relatively big built up. For a small sensor one very important component is a small polarization detecting unit. In this paper we present a microoptical solution.

3. POLARIZING ELEMENTS

The basic optical property needed for our polarimeter is the ability of polarizing light. For this purpose we used metal stripe subwavelength gratings. Polarization effects on such gratings were calculated and shown by Stenkamp et al. [3] before.
We investigated gratings with different periods of about 200nm to 400nm written by the e-beam writer LION LV1. For the fabrication of metallic grating lines we used layers of chromium with a thickness of 35nm. This enables the systematic study of the polarization effect depending on grating period and duty cycle. The best polarization ratios measured are in the range of 5. An increase of the polarization effect may be achieved by using thicker layers but even a low polarization effect is sufficient for a polarization analysis. For the application in the polarimeter circular subwavelength gratings with concentric grating lines were used. For writing such gratings the "continuous path control" writing modus (CPC) of the LION LV1 e-beam writer is an ideal one. The characteristics of this mode is working with a fixed e-beam and a moving x/y stage. That means, in the writing process the x/y stage drives the lines or curves to write. The illumination of such a grating results in an angular intensity distribution of the transmitted light due to the polarizing properties of the circular metal stripe subwavelength grating, which is usable for determining the polarization plane of the illuminating light (figure 1). This is the basic effect of the polarimeter devices [4].

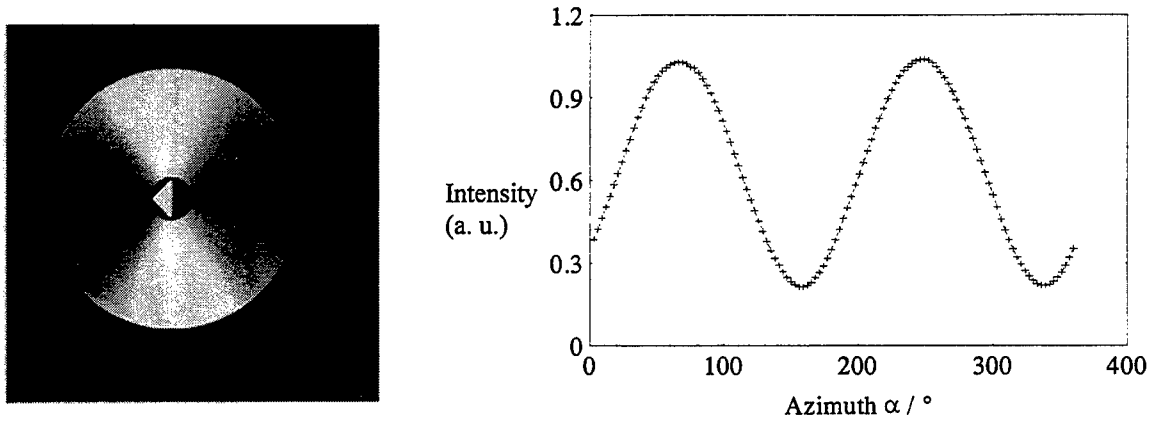

Figure 1: Intensity behind the circular polarizing grating, left CCD camera image, right intensity measured

4. POLARIMETER DEVICE

Due to the usage of microoptical components (current diameter of analyzing element and lens about 500µm), the whole optical set-up is very small, a volume of much less than 1 cm^3 is required.
Basically, for the polarimeter device only an analyzing element with laterally different polarizing properties (grating with different grating directions) and a detector array (CCD camera or specially adapted photodiode array) are necessary. Due to the different grating directions, no more mechanical movement of the analyzing element is necessary. The polarization direction may be determined directly from the intensity distribution. When drawing up the light intensity versus the angle, a sinusoidal dependence is obtained. From this the direction of the polarization may be derived directly whereas the degree of polarization may be obtained by calibrating the sensor.

5. RESULTS AND OUTLOOK

The biochemical reaction described in section 2 causes a change of the polarization direction of about 0.1° and a change of ellipticity of about 1° in case of elliptically polarized illumination of the sample surface. We realized a laboratory setup of a polarimeter described above. The polarizing grating and the photo diode array were arranged in a TO9 mounting. Based on first results achieved we expect the sensor to be applicable for detecting the antibody reaction. On this basis it will be possible to create a sensor for medical diagnostics, DNA, smell and taste-analysis which has a size of 5mmx5mmx10mm.

[1] R.H. Burdon, P.H. vam Knippenberg, eds., “Laboratory techniques in Biochemistry and Molecular Biology”, Vol. 15 Elsevier Science Publishers B.V., Amsterdam, New York, Oxford 1988

[2] U. Riß, “Neuer immunologischer Test mit Laserlicht”, Biospectrum 6/1997, Berlin

[3] B. Stenkamp, M. Abraham, W. Ehrfeld, E. Knapek, M. Hintermaier, M.T. Gale, R. Morf, "Grid polarizer for the visible spectral region", SPIE Proceedings Vol. 2213

[4] Kley E.-B., Schnabel B., Hübner H. und Zeitner U.D.: "Application of metallic subwavelength gratings for polarization devices", SPIE 2863, 166 (1996)

A confocal profilometer using microlens arrays

M. Eisner, N. Lindlein, J. Schwider
Physikalisches Institut, University of Erlangen-Nürnberg,
Lehrstuhl für Optik, Staudtstr.7/B2, D-91058 Erlangen
phone: ++49/9131/858395
fax: ++49/9131/13 508
email: schwider@move.physik.uni-erlangen.de

Confocal reflected light microscopy provides a very high depth resolution if the numerical aperture of the micro-objective is on the order of 1. The most common confocal microscopes rely on scanning the field of view by means of a Nipkow-disc or simply by mechanical scanning the object in a raster scan /1,2,3/. The basic idea of confocal imaging is spatial filtering on the way to and from the object through a small pinhole. This means that only the light from the immediate neighborhood of the image plane is allowed to pass the optical channel which means a very strong suppression of light coming from other than the plane the microscope is focused on. In a reflected light microscope the pinhole of the illuminating light path is imaged sharply onto the surface to be measured and is reflected back and has to pass the same pinhole again. Only if the pinhole is sharp on the surface to be measured the pinhole is imaged on itself and light can get through this pinhole. Unsharp imaging causes the image of the pinhole to be spread out over a considerable area which means that the total light flux is very low.
If the object is scanned by a piezo-transducer along the optical axis different lateral regions will pass through the plane of best focus and become bright if the object is scanned by means of a Nipkow-disc one after the other. Also the use of microlens arrays in front of the measured object has been proposed /4/, but in this case the depth resolution is rather poor. Another approach used the combination of a Nipkow disc scanning with a matching microlens array /5/.
What is proposed here is the use of multiple pinholes simultaneously together with a two-dimensional CCD-array for the detection of light. To enhance the efficiency of the optical channel we propose the use of a microlens array having the same pitch and being centered on the respective pinhole axis. One main issue is the production of such an aligned pinhole/microlens array for doing confocal microscopy without the need to scan the field of view mechanically. The scheme of our experimental setup is shown in Fig.1.

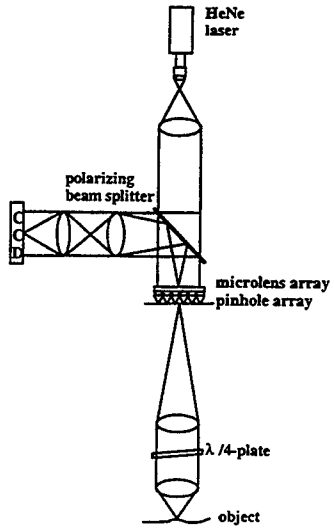

Fig.1: setup of the confocal microscope with one combined microlens/pinhole array

The light from an intensive light source is focused onto a stop of suitable diameter and afterwards collimated and polarized by means of a polarizer. This collimated beam enters a polarizing beam splitter which lets the light pass on to the microlens/pinhole array. The microlenses split the beam into N^2 sub-beams each of them being focused onto the pinhole of the subaperture. The stop array is positioned in the intermediate image plane of the microscopic objective which images the back-illuminated stop array onto the object surface reduced in size by the scaling factor of the microscope. A quarter-wave-plate suitably oriented will change the polarization plane in double pass geometry from TE to TM polarisation. Together with the polarizing beam splitter reflections from surfaces in front of the quarterwave plate are heavily suppressed. The image of the stop array illuminates the object surfaces and the reflected light is imaged onto the intermediate image plane. Only the surface regions being in focus will produce a sufficiently small light spot in order to allow a great part of this light to pass the stop again. The polarizing beam splitter will only direct this light to a CCD-array where the bright spots are detected. Through scanning of the object along the optical z-axis each spot image of the array will go through a maximum value of the intensity which can be used as an „in-focus" criterion. If the axial position is measured in addition the profile z(x,y) of the surface is known form the in-focus indication for the lateral surface area. To improve the sensitivity for the in-focus position at least five neighboring intensity values are stored and used for a parabolic maximum finding calculation.

Microlens/pinhole arrays with a pitch of 50-100µm over an area of several cm´s in the intermediate image plane of the microscope seem to be possible. High aperture microscopes have scaling factors on the order of 100 which means that the image of the stop area samples the surface under test with a pitch of 0.5 to 1 µm which should be good enough for a sufficient data density even for such complex elements as diffractive optical elements. The intermediate plane has also to be scaled down by a factor 3-4 at the detector end of the optical channel to match the image to the pitch of the CCD-camera. Since the CCD-arrays become more and more HDTV-compatible the full extend of the space bandwidth product of the optical channel will in future be accessible.

In a first demonstration we used a refractive microlens/pinhole array with a pitch of 250µm and a micro-objective 50x/0.85 . One pseudo-3D-plot of a refractive microlens is shown in Fig. 2 as a preliminary result for such a two-dimensional confocal profile. The pinholes had a diameter of 50 µm. The microlens/pinhole array worked with a Fresnel number of 8.

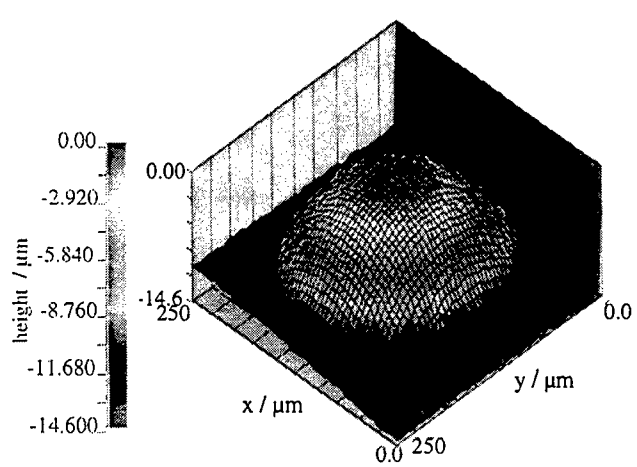

Fig. 2 : pseudo -3D- plot of a refractive silicon microlens measured with the help of a setup due to Fig. 1

References:

/1/ S. Inoue, K. R. Spring; „Video microscopy"; 2-nd ed. Plenum Press, 1997, New York, London.

/2/ Wilson /Sheppard: „Theory and Practice of Scanning Optical Microscopy", Academic Press Inc. 1984, London

/3/ G. S. Kino in „Handbook of biological confocal microscopy", Plenum Press, 1990, New York

/4/ H. Tiziani, H.-M. Uhde; „Three-dimensional analysis by a microlens-array confocal arrangement"; Appl. Opt. **33,** (1993) 567-572

/5/ A. Ichihara et al.; „High-speed confocal flourescence microscopy using a Nipkow scanner with microlenses for 3-D imaging of single flourescent molecule in real-time"; Bioimages **4,** (1996) 57-62.

Spectral calibration of MODIS bands using the SRCA

Harry Montgomery
Goddard Space Flight Center, Greenbelt, MD 20721, (301)286-7087, FAX:(301)286-0213, hmontgom@ltpmail.gsfc.nasa.gov
Nianzeng Che
Swales Aerospace, Beltsville, MD 20705, (301)902-4350, FAX:(301)902-4114, nche@swales.com
Jeff Bowser
Hughes STX, Greenbelt, MD 20721, (301)286-7088, FAX:(301)286-0373, Jeff.Bowser@gsfc.nasa.gov

SRCA layout in spectral calibration

The Spectro-Radiometric Calibration Assembly (SRCA) is one of the on-board calibrators of MODerate resolution Imaging Spectrometer (MODIS), designed and manufactured by Hughes Santa Barbara Remote Sensing (SBRS). The SRCA has three calibration functions: radiometric, spectral, and spatial.

Spectral characterization for MODIS is needed because of the spectral shifts observed in the solar reflective band filters during ground testing of MODIS precursor instruments, and because some on-orbit measurements from precursor instruments have been interpreted as showing evidence of on-orbit spectral shift.

When the SRCA is in spectral mode, it is operated as a monochromator. The unique feature of the SRCA lies in its capability of wavelength self-calibration [1]. Hence, the MODIS band/channel center wavelength shift can be determined when a set of monochromatic beams from the SRCA illuminates the MODIS detectors. The spectral mode provides calibration for the Visible (VIS), Near Infrared (NIR), and Short wavelength IR (SWIR) bands.

The SRCA consists of three sub-assemblies: a light source, a monochromator/relay collimator, and a folded collimator (Figure 1) [2]. In the spectral mode the light from the Integration Sphere (IS) is from each of two lamp configurations, 1-10W and 3-10W. The filter wheel, located in front of the SRCA IS, is placed at one of the four positions: an open hole and three diffraction order sorting filters to isolate the diffraction orders. Meanwhile, the grating motor places a grating in position and the slit/reticle motor places the entrance and exit slits at the foci of the collimating mirror and focusing mirror, respectively. When the grating is rotating, narrow spectral beams exit from two slits: main exit slit and a secondary slit.

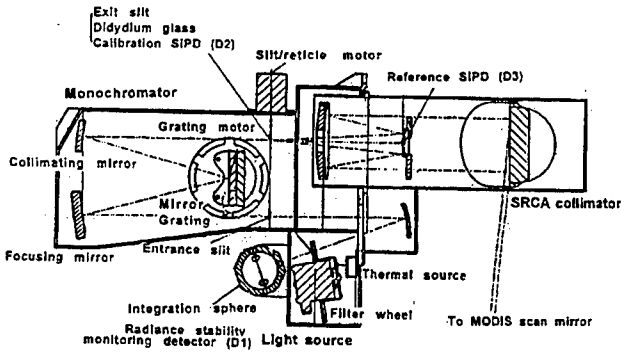

Figure 1. The SRCA layout

Located at the secondary slit, in parallel with the main exit slit, is a piece of didymium glass with a calibration Silicon Photo-Diode (SiPD) behind it. The slits are separated by six millimeters. The spectral beam from the secondary slit passes through the didymium glass and is detected by the calibration SiPD while the beam from the main slit is sampled by a reference SiPD, with the same characteristics as the calibration SiPD and located at the center of the secondary mirror of the Cassegrain telescope to provide a normalizing signal. The main portion of the beam is further collimated by the Cassegrain telescope to form a collimated beam and folded towards the MODIS scan mirror by a plain mirror. The two sets of SiPD signals form the data base for wavelength self-calibration.

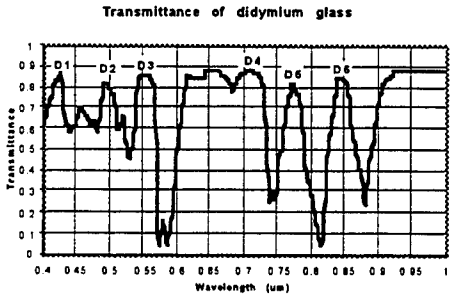

Figure 2. Didymium transmittance profile [3]

The wavelength self-calibration capability depends upon the optical properties of the didymium glass (Figure 2). The signals from the calibration SiPD behind the didymium glass are what we call the spectrum modified by the didymium transmission curve while the signals

from the reference SiPD are the spectrum itself. The calibration SiPD signal shape, after dividing by the reference SiPD signals, will be the same as the didymium transmission curve. However, the location difference of the two SiPDs complicates the signal processing.

Methodology of the wavelength self-calibration

When the grating rotates an angle θ_m with an initial offset angle θ_{off}, the wavelength of the exit beam from the main exit slit can be written as (only in the diffraction plane for simplicity)

$$\lambda = \frac{2A}{m} sin(\theta_m + \theta_{off}) \cdot cos\beta \qquad (1)$$

if we select negative diffraction order m. In Eq. (1) β is the half angle between the incident and diffracted beams and A is the grating spacing.

The wavelength self-calibration is to determine two monochromator parameters: β and θ_{off} because the two parameters may change under different environments. When the monochromatic beam exits from the didymium slit, an angular distance Δ from the main slit, The grating equation takes the form:

$$\lambda = \frac{2A}{m} sin(\theta'_M + \theta_{off} + \frac{\Delta}{2}) \cdot cos(\beta + \frac{\Delta}{2}) \qquad (2)$$

As mentioned, the signal from the calibration SiPD, DN_{CDS}, must be normalized by the signal from the reference SiPD, DN_{SDS}, to calculate the didymium peak profiles. For the normalization the numerator and the denominator of the ratio should be evaluated at the same wavelength values. The θ'_M corresponding to each θ_M is calculated by setting Eq.(1) equal to Eq.(2) [4]:

$$\theta'_M = sin^{-1}(sin(\theta_M + \theta_{off}) \frac{cos\beta}{cos(\beta + \frac{\Delta}{2})}) - [\theta_{off} + \frac{\Delta}{2}] \qquad (3)$$

The normalized calibration signal is

$$CDS_{Norm}(\theta'_M, m) = \frac{DN_{CDS}(\theta'_M, m) - DN_{Dark}}{DN_{SDS}(\theta_M, m) - DN_{Dark}} \qquad (4)$$

where DN_{Dark} is the dark readings. The normalized calibration signals are shown in Figure 3 where two didymium peak wavelengths and three peak positions are utilized: one is at 0.496μm (D2) with diffraction order of -3 (named D32), the other is at 0.551μm with diffraction order of -2 and -3 (named D23 and D33).

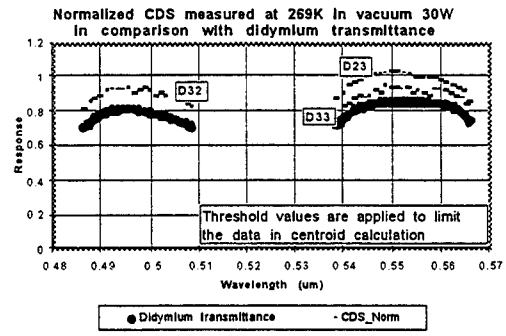

Figure 3. CDS_{Norm} matches didymium peaks

The centroid of CDS_{Norm} with respect to grating angle, over the didymium peak regions from θ'_{M1} to θ'_{M2}, is $\Omega_{CDS,m}$ and given by:

$$\Omega_{CDS,m} = \frac{\sum_{\theta'_{M1}}^{\theta'_{M2}} CDS_{norm}(\theta'_M, m) \cdot \theta'_M}{\sum_{\theta'_{M1}}^{\theta'_{M2}} CDS_{norm}(\theta'_M, m)} \qquad (5)$$

With the same sample points as CDS_{Norm}, the centroid wavelength of the didymium peak is:

$$\lambda_{didymium} = \frac{\sum_{\lambda_1}^{\lambda_2} \tau_{didymium}(\lambda) \cdot \lambda}{\sum_{\lambda_1}^{\lambda_2} \tau_{didymium}(\lambda)} \qquad (6)$$

where λ_1 and λ_2 are calculated at the range limits θ'_{M1} and θ'_{M2} by Eq.(2) using design values of β, θ_{off}, and Δ. The use of exactly the same data samples in Eqs. (5) and (6), instead of integrating uniformly over the $\tau_{didymium}(\lambda)$ profile over the peak region, avoids bias in wavelength calibration since limited samples can cause different calculated values of $\lambda_{didymium}$. The wavelength bias can be as high as 1.1 nm.

Eq.(5) is expressed in terms of grating angle and Eq.(6) is in terms of wavelength. Both equations give three values, respectively. Least-square fit technique [4-6] is applied to adjust β and θ_{off} in Eq.(2) along with replacing θ'_M with $\Omega_{CDS,m}$ to obtain the best match of the three $\lambda_{didymium}$ wavelengths (Figure 3). The result of the least-square fit gives the β and θ_{off} of current monochromator parameters. Therefore, the wavelength scale has been established for a monochromatic beam illuminating MODIS channels/bands in terms of grating step number.

Determination of MODIS band center wavelength shifts

The radiance of the monochromatic beam illuminating the MODIS detectors is spectral-

dependent. The beam is spectrally dependent on the SRCA IS light source, the grating efficiency, the SRCA transmittance, and the reflectivity of the mirror. For accurately determining the center wavelength shift, the MODIS detector signals need to be normalized by the spectral-dependent signals from the SRCA. The reference SiPD provides the normalization signal except that the reference SiPD signal includes the modification by the SiPD spectral response. Hence, the band/channel $DN(\theta_m,m)$ must be normalized by $DN_{SDS}(\theta_m,m)$ and multiplied by the SiPD response at the wavelength that θ_m corresponds.

Due to the limitation of the reference SiPD response, the normalization can only be performed for wavelengths less than 1μm. For the bands with wavelength greater than 1μm the MODIS detector signals are not normalized and the spectral calibration accuracy is not addressed in the MODIS specification.

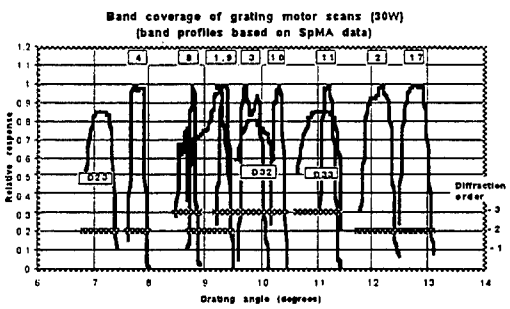

Figure 4. SRCA band coverage for 3-10W lamp configuration

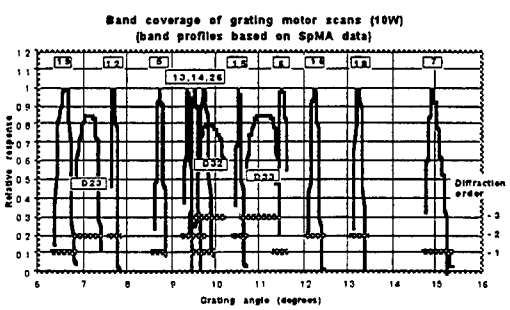

Figure 5. SRCA band coverage for 1-10W lamp configuration

The spectral beam output from the SRCA performs wavelength self-calibration while providing a monochromatic beam to measure MODIS band response. Within two unidirectional grating rotations for 1-10W and 3- 10W lamp configurations, respectively, the SRCA covers the didymium peaks and all MODIS bands for VIS, NIR, and SWIR. The SRCA measured band coverage is illustrated in Figures 4 and 5. The band numbers and the diffraction orders are marked accordingly.

The centroid wavelength calculated by the SRCA differs from the centroid wavelength of data measured by a ground-based double-monochromator named Spectral Measurement Apparatus (SpMA) because the SRCA slit has about 1/3 of the bandwidth of MODIS bands to increase signal intensity. In addition to the SRCA partial aperture filling effect, the SRCA measured MODIS band responses differ from those measured by the SpMA due to different slit width. However, the centroid band shift measured by the SRCA reflects the MODIS band shift. The difference between the centroid wavelength measured by the SRCA and by SpMA serves as correction values (Figure 6). These correction values will be applied on-orbit to correct the calculated band centroid wavelength assuming that the correction values do not change in operation.

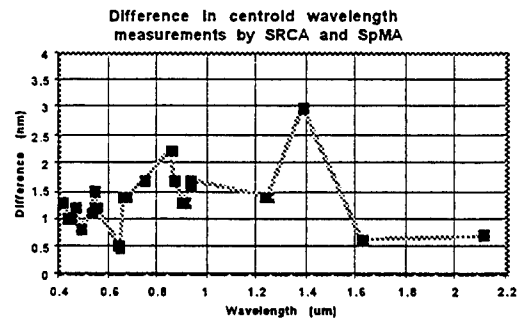

Figure 6. SRCA centroid wavelength correction value

From the calibration results, the SRCA has high repeatability. It can meet the specification that the spectral calibration uncertainty is within (Center wavelength/0.412μm)nm [7].

References

[1] "MODIS-N SRCA baseline design", SBRS Internal Memorandum, PL3095-Q01118, by E. Johnson, May, 1992.
[2] MODIS calibration presentation, SBRS, Sep. 1993.
[3] Measured by SBRS.
[4] "The Spectro-Radiometric Calibration Assembly (SRCA) of MODIS, Detailed support document to ATBD 1996", MCM-SSATBD-01-U-R0C0", MODIS characterization support team, Apr.25, 1997.
[5] "SRCA spectral calibration methodology", SBRS Internal Memorandum, PL3095-N04744, by J. young, Mar. 1995.
[6] "SRCA spectral calibration algorithm", SBRS Internal Memorandum, PL3095-Q05661, by R. Osgood, March. 1996.
[7] "Specification for the Moderate-Resolution Imaging Spectrometer", GSFC 422-20-02 Dec. 1994.

Reactive ion etching: a versatile fabrication technique for micro-optical elements

Margit Ferstl

Heinrich-Hertz-Institut für Nachrichtentechnik Berlin GmbH
Einsteinufer 37; D-10587 Berlin; Germany
Phone: + 49/ 30/ 31002 430; fax: + 49/ 30/ 31002 213;
E-mail: ferstl@mails.hhi.de

Introduction

Reactive ion etching (RIE), a well established technology in semiconductor industries, has proven to be also a versatile tool for the fabrication of optical components. Using fluor based processes, we fabricated refractive spherical and cylindrical microlenses as well as various diffractive optical elements (DOEs) e.g. Fresnel zone lenses (FZLs), linear binary gratings, triangular gratings etc., in quartz glass and in silicon. Furthermore we realized waveguide components, above all arrayed waveguide gratings (AWGs) in silica on silicon for WDM applications. To meet the specific demands of these various optical structures (differing in shape, feature size, resolution, etch depth, etc.) appropriate structuring methods, mask materials and etching parameters had to be chosen.

Fabrication techniques

Two methods were employed for structuring the DOEs: binary optics technology which uses multiple steps of repeated pattern transfer by photolithography and successive RIE (Fig. 1a), and, analog etching of a polymer mask which has been preshaped by direct electron-beam writing (Fig. 1b).

The refractive lenses were fabricated by heating the patterned photoresist above the melting point (Fig. 1c). During thermal reflow the resist is forming a nearly spherical surface which was transfered into the substrate by RIE.

The anisotropic etching required for all of these optical components was performed in a conventional parallel plate reactor operated at radio frequency.

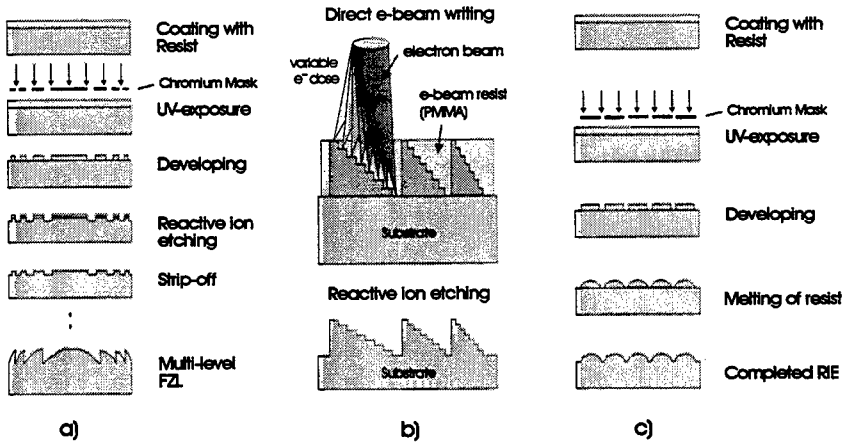

Fig.1: Fabrication methods

For etching of quartz glass and SiO_2-layers a CHF_3/H_2 gas composition was used whereas the silicon was etched in a CF_4 plasma. Chromium, amorphous silicon (α-Si), PMMA, and various positive photoresists served as mask materials. Employing suitable etching parameters selectivities from 1 to 40, etch depths of up to 10 µm, and etching rates of up to 70 nm/min could be achieved.

Diffractive optical elements

- Fresnel zone lenses

A great number of various FZLs with different focal lengths (400 µm to 22.8 mm) and of different apertures (200 µm to 2 mm) was fabricated in quartz glass. The on-axis and off-axis FZLs designated for collimating, focusing and deflecting purposes were realized for the wavelengths of 633 nm and 1.5 µm [1]. These lenses whose smallest feature size was about 0.8 µm were approximated by up to 16 levels using multiple steps of mask transfer and high anisotropic and high selective RIE. Thus diffraction efficiencies of about 94 % could be achieved. The optical structures were of high quality showing steep sidewalls, sharp etch edges and smooth surfaces. The overlay accuracy we reached was about 0.2 µm. One possibility to avoid alignment errors which result in a decrease of the diffraction efficiency [2], is to directly write the appropriate structure into resist and to analog transfer this polymer mask into the substrate. Thus FZLs of 150 µm in diameter and a F-number of about F = 0.4 were realized in silicon for 1.5 µm wavelength (Fig. 2). The lenses whose profile was approximated by 8 levels were created in PMMA by direct e-beam writing. The successive transfer of this structure into the Si-substrate required a soft etch process of high anisotropy (i.e. no lateral etch component), and a well known selectivity between mask and substrate to meet the desired level heights. The total etch depth of this analog transfered FZL is about 610 nm which corresponds very well with the calculated phase height of 606 nm.

- Linear Gratings

Various linear binary gratings with feature sizes down to the sub-micron range were structured in SiO_2 and Si. The SiO_2-gratings were realized by using chromium as mask material. Thus selectivities of 40:1 were achieved. Figure 3 shows a linear grating with a grating period of 2 µm and a line width of about 200 nm, etched in quartz glass. The etch depth is about 1 µm which results in an aspect ratio of about 5. The SEM picture reveals that we get steep sidewalls and smooth surfaces; the roughness determined with a Tencor P1 surface profiler was below 2 nm.

The binary gratings fabricated in Silicon had periods of down to 200 nm with feature sizes of down to 100 nm. In order to get such a high resolution these small structures were first written in PMMA. The etch depths of these high frequency gratings were 100 nm and 500 nm respectively.

Additional sinusoidal and trapezoidal gratings with periods down to 2 µm were produced by variable dose e-beam writing. In order to get surfaces of acceptable roughness (in the nm-range) the subsequent direct transfer of the analog resist masters into the Si-substrate demanded a soft etching process (RF-power about 80 W) of low selectivity (about 1:1).

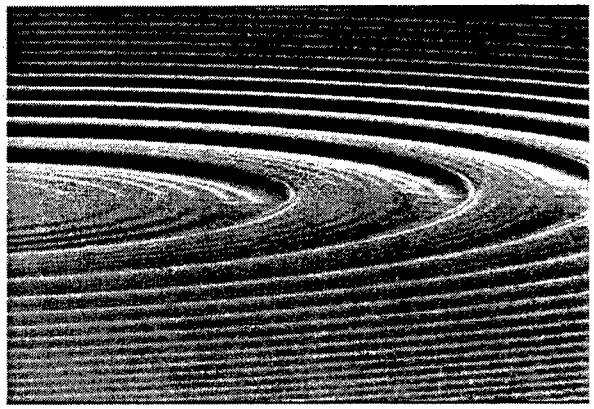

Fig. 2: SEM picture of an 8-level FZL directly etched in Si; etch depth: 610 nm

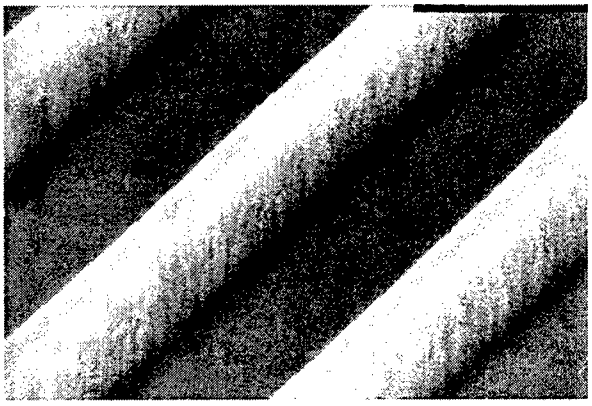

Fig. 3: Binary grating in quartz glass; etch depth: 1 µm; feature size: 200 nm.

- Arrayed Waveguide Gratings

Furthermore we fabricated waveguide components designed for the wavelength of 1.5 µm in silica on silicon, mainly AWGs for wavelength division multiplexing applications. The structuring of the ridge waveguides (WGs) with lateral and vertical dimensions of 6-7 µm required high etching rates. For masking a thick positive resist (3 µm - 6 µm) as well as amorphous Si was used. By employing a HF-power of 200W etch rates of about 70 nm/min were achieved. The selectivities were between 2:1 and 3:1. The SEM micrograph in Fig. 4 shows a section of an AWG where the grating WGs lead into the slab region.

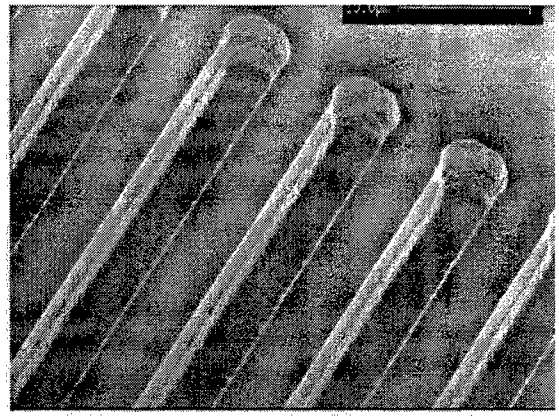

Fig. 4: Section of an arrayed waveguide grating

Refractive optical elements

Refractive spherical and cylindrical lenses were realized by melting photoresist cylinders and bars, respectively. The resulting resist lenses were transfered into quartz glass and silicon by RIE.

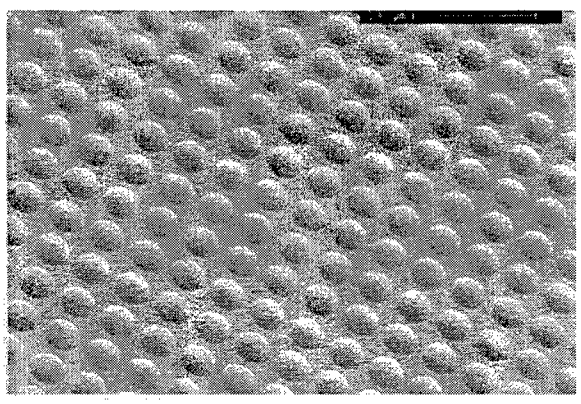

Fig.5: SEM view of a F/3, 30 µm diameter microlens array fabricated in quartz glass

To achieve a good transfer of the lens shape, that means to etch the resist and the substrate at the same rate, we added oxygen to our fluor-based etching gases, and balanced the gas mixtures to result in an 1:1 etch ratio.

Microlens arrays of more than 32,000 spherical lenslets with circular and square apertures of 30 µm and 34 µm in diameter (36 µm pitch) and cylindrical lenses of 50 µm width (200 µm pitch) were fabricated. The focal lengths of our lenses typically were in the range of 80 µm - 100 µm and 150 µm - 300 µm for the cylindrical lenses. In figure 5 an array of close spaced spherical microlenses with speed of F/3 and 30 µm diameter is depicted.

Conclusions

Various optical components were fabricated in quartz glass, Silica and Silicon by reactive ion etching combined with lithographic pattern transfer and direct e-beam writing. Proper usage of materials and processes enabled us to successfully exploit RIE -a mature VLSI technology- for the manufacturing of refractive and diffractive optical elements. The variety and high quality of the realized elements show that RIE is an important and versatile tool for the fabrication of optical components.

This work was financially supported by the German „Bundesminister für Bildung, Wissenschaft, Forschung und Technologie“, and the City of Berlin.

References

[1] Ferstl M., Frisch A.-M., J. Mod. Optics, **43**, pp.1451-1462, 1996.
[2] Ferstl M., Kuhlow B., Pawlowski E., SPIE **1992**, pp. 90-101, 1993.

Diffractive focusing elements for signal purposes produced by e-beam lithography

Z. Ryzi, F. Matejka
Czech Holography s.r.o., Rez u Prahy 199, 250 68, Czech Republic
phone: +420-2-6858236, fax: +420-2-6858427
e-mail: ryzi@troja.fjfi.cvut.cz or *czholo@holo.cz*

There is a great number of applications of signal lights in many areas of people's lives, for instance in industry, traffic, households, etc. All these signal lights contain, in addition to the light source, a focusing element. Such an element has several characteristics: it converts the light intensity distribution of a light source to another distribution; enlarges radiation area; and is usually specified by the major narrow angle intensity distribution, which contains most of the light energy, and the minor intensity distribution which should direct radiation to the rest of the solid angle. These focusing elements are usually produced as reflectors or refractors, and there are advanced technologies developed for their production. However, focusing elements for signal lights can also be a field for the application of diffractive optical elements.

We designed and are producing a diffractive focusing element for small signal lights which redistributes radiation of a light-emitting diode. The size of the element is 16 mm in diameter, the focal length is 8 mm and the light-emitting diode has a wavelength of 617 nm. As a focusing diffractive structure we chose a binary relief Fresnel zone plate. The minus first diffraction order can play the role of the narrow angle intensity distributor, and the first and residual zeroth orders radiate to the rest of the solid angle. The whole focusing element was fabricated by an e-beam lithograph with a resolution limit of positioning of 100 nm. This resolution is not high enough to precisely position each Fresnel zone; nevertheless, since the focusing element does not necessarily need to be without aberrations, the lithograph resolution is for this application sufficient.

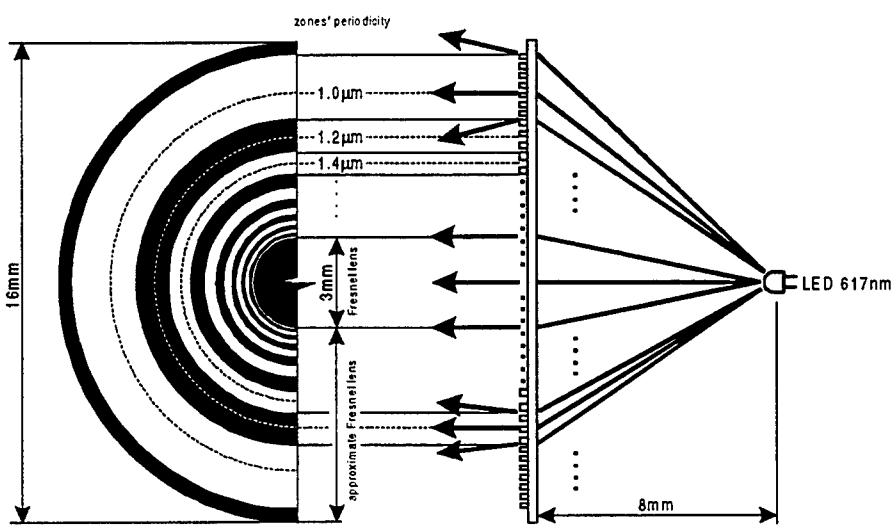

Figure 1: Composition of focusing element for a signal light - central Fresnel lens surrounded by circular zones appromating Fresnel lens of up to 16 mm (left), and its main focusing function (right)

The focusing element consists of a 3 mm central Fresnel lens surrounded by circular zones with constant periodicity (due to lithograph resolution limitation) which represent an approximation of a Fresnel lens of up to 16 mm diameter (see Figure 1). The depth of relief is about 600 nm.

Figure 2 shows the angle intensity distribution of the light-emitting diode (thin solid line), the desired redistribution (dashed line), and the resulting redistribution reached by our focusing element (thick solid line).

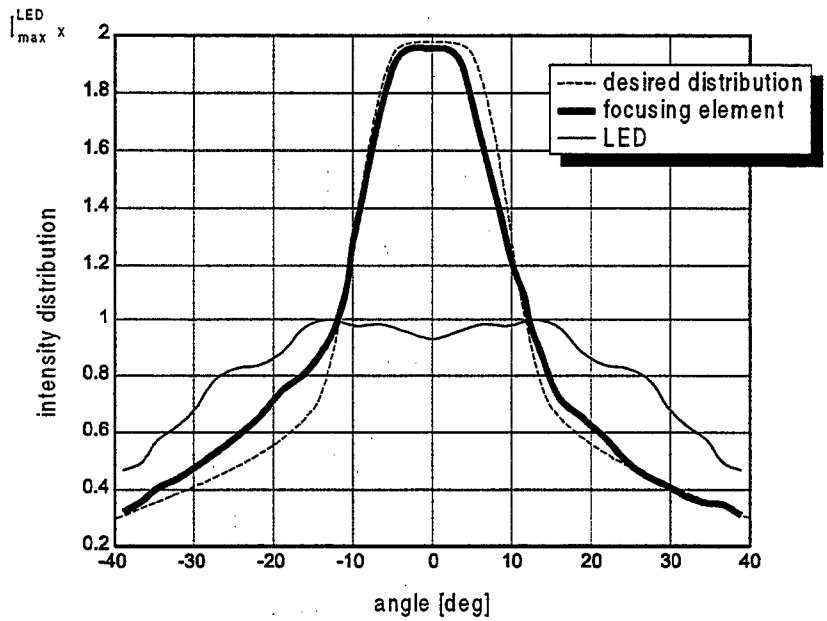

Figure 2: Measured intensity disributions of light-emitting diode (thin solid line), our focusing element (thick solid line), and desired intensity distribution of the focusing element (dashed line)

Photodeposition technique for restoring holographic films of polydiacetylene

Hossin Abdeldayem, Mark S. Paley, William Witherow, and Donald O. Frazier
ES 76, Building 4481, Space Science Laboratory, NASA-Marshall Space Flight Center, Huntsville, AL 35812
Phone (205)544-3494, Fax (205)544-2102
E-mail: hossin.abdeldayem@msfc.nasa.gov

Summary

Polydiacetylenes are a very promising class of polymers for both photonic and electronic applications[1-3] because of their highly conjugated structures. We, recently, have discovered the possibility of depositing a permanent holographic grating of information, made of polydiacetylene on a glass substrate. A novel technique for obtaining high quality thin films of a polydiacetylene derivative of 2-methyl-4-nitroaniline (PDAMNA) using photodeposition from monomer solutions onto UV transparent substrates was discovered by members of our group a few years back[4]. This compound was one of several asymmetric diacetylenes that were first studied extensively for their optical and electronic properties by Garito and co-workers in the late 1970s; however, their investigations did not include behavior in solutions[5,6]. PDAMNA films can be obtained readily from solutions of DAMNA in 1,2 -dichloroethane by irradiation with UV light through a quartz or glass window, which serves as the substrate. This simple straightforward process yields transparent films with thickness on the order of 1μm[7]. To obtain PDAMNA thin films, a solution of DAMNA in 1,2-dichloroethane is placed inside a chamber shown in figure 1. DAMNA monomer exhibits strong absorption at 366nm. A hand-held 15W UV lamp placed directly in front of the substrate (approximate radiation intensity of 800 $\mu W/cm^2$ at 6 in.), a film of approximately 0.6 μm thickness is obtained after 24 hours of exposure.

Initially, we realized that any substrate which is sufficiently transparent to UV light can be used; thus far we have grown PDAMNA films onto glass, quartz, mica, indium tin oxide coated glass, polyethylene teraphthalate , KBr, and NaCl. In the deposition process, we have conducted masking experiments in which a portion of the substrate is blocked from exposure to the UV light during film deposition. The mask is placed on the exterior surface of the substrate (opposite to the side on which the film is grown) and thus is not in contact with the solution ; it serves merely to protect part of the substrate from the light. Interestingly, the result is that film deposition occurs only where the substrate is directly exposed to the light (figure 2).

Photodeposition was also achieved using a UV-Argon ion laser at 364m. The chamber was mounted onto a computer-controlled translation stage, which had been programmed to trace out a desired pattern. The laser was then focused onto the substrate as the translation stage traced out the test pattern shown in figure 3. The line thickness in the pattern is controlled by the intensity of the laser, the translation rate, and the number of times the pattern is traced. The width of the line is determined by the focal width of the laser beam.

Most recently, a holographic grating of information made of PDAMNA was constructed on a glass substrate. This holographic recording on the polydiacetylene film was an analogue recording, which is necessary for a number of vital application, such as

associative memory, pattern recognition, holographic optical elements, holographic interconnection for neural networks, etc.. In the process, two coherent beams of UV at 364nm from an Ar^+ laser were made to interfere at the substrate which is an optical window of the monomer solution in figure 1. One of the beams was carrying certain information. The interference of the two beams at the substrate induces an interference grating which carries the same information that was carried by one of the beams. The information on the grating was later retrieved by a cw a He-Ne laser at 633nm as shown in figure 4 (23X magnification). The intensity of the interference pattern formed by the grating induces changes in the property of the recording medium through polymerization. Consequently the polymer will be deposited on the substrate according to the grating intensity pattern. The complex index of refraction n of the deposited polymer film will be given by :

$$n = n_0 - i\kappa \qquad (2)$$

where n_0 is the real index of refraction and κ is the imaginary index of refraction which depends on the absorption coefficient of the solution to the UV light. The hologram obtained by PDA is a combination of both amplitude and phase gratings.

The hologram was distinguished as an intermediate grating between a thick (3-D) or thin (2-D). This was determined by the Q-parameter criterion given by Klein as

$$Q = 2\pi\lambda d / n\Lambda^2 \qquad (3)$$

where λ is the wavelength of the illumination reference beam (366nm), n is the refractive index of the recording medium(1.7) and Λ is the grating period of the holographic grating, which is ~364nm, where the angle of incidence is ~ 30^0. More investigations are under way to estimate the maximum resolution possible of these holograms, and consequently the maximum storage density.

References:

1. Polydiacetylenes; Bloor, D., Chance, R. R. , Eds.; Martinus Nijhoff Publishers: Dordrecht, The Netherlands, 1985.
2. Nonlinear Optical Properties of Organic Molecules and Crystals ;Chemla, D. S. , Zyss, J. Eds; Academic Press: Orlando, FL , 1987; vol. 2.
3. Introduction to Nonlinear Optical Effects in Molecules and Polymers; Prasad, P. N., Williams, D. J., Eds..; John wiley and Sons, Inc. : New York, 1991.
4. Paley, M. S. ; Frazier, D.O.; Abdeldayem, H. ; McManus, S. P. Chem. Mater. 1994, 6(12), 2213.
5. Horner, C. J.; Garito, A. F. Makromol. Chem. 1981, 182, 19.
6. Garito, A. F. ; Singer, K. D. ; Teng, C. C. In Nonlinear Optical Properties of Organic and Polymeric Materials ; Williams, d. J. , Ed.: ACS Symposium Series, vol. 233; American Chemical Society: Washington, DC. 1983; pp.1-26.
7. Paley, M. S. ; Frazier, D.O.; Abdeldayem, H. ; Armstrong, S.; and McManus, S. P., J. Am. Chem. Soc. Vol. 117, No. 17, pp. 4775-4780, 1995.

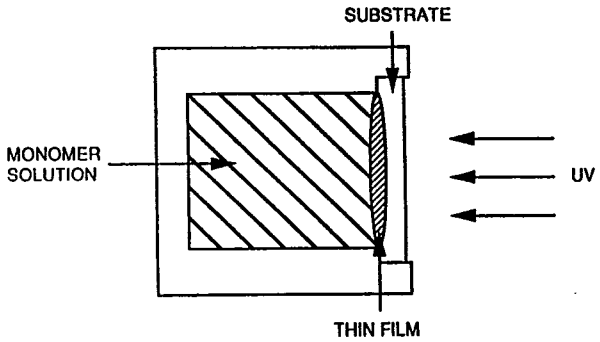

Figure 1. Diagram of the apparatus used for the photodeposition of PDAMNA thin films from solution substrate.

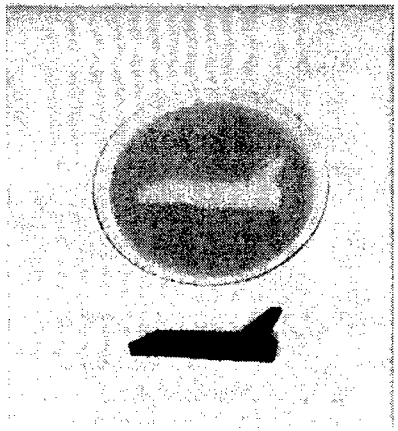

Figure 2. PDAMNA film formed by photodeposition from solution onto a thin glass. A portion of the substrate was blocked from exposure to the UV light by the mask shown below the film.

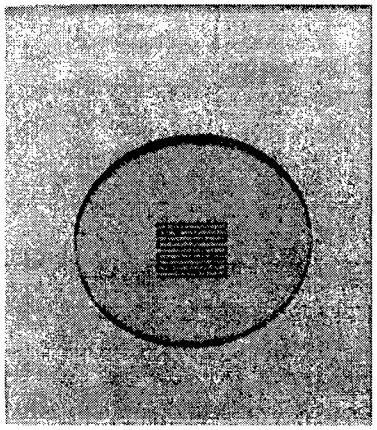

Figure 3. PDAMNA circuit photodeposited onoto quartz using the UV laser.

Figure 4. Retrieved information from the holographic grating of PDAMNA.

Fabrication of microprisms for planar-optical interconnections using analog gray-scale lithography with high energy beam sensitive glass

Ch. Gimkiewicz[1], D. Hagedorn[1], J. Jahns[1], E. B. Kley[2], and F. Thoma[2]

[1] Fernuniversität Hagen, Optische Nachrichtentechnik
Feithstrasse 140, D-58084 Hagen, Germany

[2] Friedrich-Schiller-Universität Jena, Institut für Angewandte Physik
Max-Wien-Platz 1, D-07743 Jena, Germany

Integrated planar free-space optics is a viable concept for building compact systems for interconnection and sensor applications. Micro-optical elements are integrated on a single substrate to guide the light signals traveling inside the substrate [1]. Optoelectronic devices are bonded on the substrate by hybrid integration techniques such as flip-chip bonding. For interconnection applications, vertical-cavity surface emitting laser diodes (VCSELs) are of particular interest as fast 2-D input arrays.

The optical design of an interconnection system requires the fabrication of microoptic elements for coupling and imaging. These can be implemented either as diffractive or refractive elements. With the use of conventional "binary optics" technology, practical difficulties arise since it is hard to achieve high diffraction efficiency and large coupling angles at the same time. Losses in the optical system, however, require higher optical power of the VCSELs and therefore result in more dissipated heat and a lower system bandwidth. Therefore, it is desirable to design and implement the optics in such a way that losses are minimized. The issue of light efficiency is related to the implementation of the optical elements, where the critical part is the coupling of the light into and out of the substrate.

Here, we suggest to use microprisms that are directly etched on the bottom surface of the VCSEL chip (Fig. 1). The integration of refractive microlenses with VCSELs using a reflow technique was demonstrated recently [2]. Here, we demonstrate arrays of microprisms (Fig. 2). The prisms shown in Fig. 2 are fabricated in photoresist. The size of each prism is 100µm x 100 µm. A sag of 10-20 µm can be achieved. If etched into the GaAs, this allows one to couple the light into the glass substrate under angles of up to 27°.

The microprisms were fabricated by means of analog optical contact lithography using gray scale masks as demonstrated before for diffractive elements [3]. The dissolution rate of the photoresist during development is determined by the light exposure. For the fabrication of the gray scale mask, we use HEBS (high energy beam sensitive) glass [4] which is a special ion-exchanged glass. The patterning of the mask with a continuous gray scale pattern is achieved by electron beam writing at a variable dose. The glass was tested and used for the fabrication of various micro-optic elements [5]. For a given photolithographic process, the resulting resist profile depth depends on the electron dose. Starting with a resist layer of approximately 21µm thickness (AZ 4562), a profile depth of over 20µm was obtained. Other values for the resist thickness, development time, etc. result in different depth profiles.

References:

1. J. Jahns, "Planar packaging of free-space optical interconnections," Proc. IEEE 82 (1994) 1623-1631.
2. E. M. Strzelecka, G. D. Robinson, M. G. Peters, F. H. Peters, and L. A. Coldren, "Monolithic integration of vertical-cavity laser diodes with refractive GaAs microlenses," El. Lett. 31 (1995) 724-725.
3. W. Däschner, Pin Long, R. Stein, Ch. Wu, and S. H. Lee, "Cost-effective mass fabrication of multilevel diffractive optical elements by use of a single optical exposure with a gray-scale mask on high-energy beam-sensitive glass," Appl. Opt. 36 (1997) 4675-4680.
4. "HEBS glass photomask blanks," Product information 96-01, Canyon Materials Inc., 6665 Nancy Ridge Drive, San Diego California, 92121 (USA).
5. E. Kley, F. Thoma, U. D. Zeitner, and L. Wittig, "Fabrication of micro-optical surface profiles by using gray scale masks," Proc. SPIE, vol. 3276 (1998).

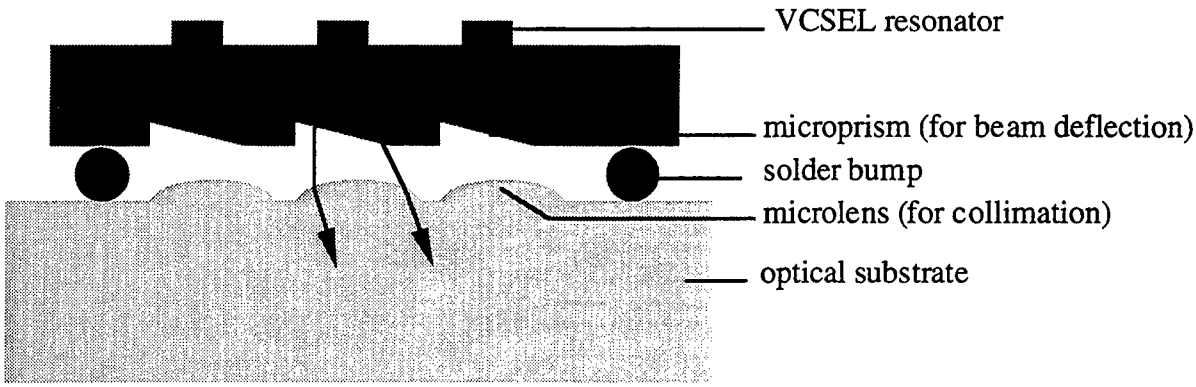

Figure 1: Use of microoptical elements in the planar-optical interconnect. Microprisms for beam deflection are integrated directly on the bottom surface of the VCSEL chip. Microlenses are used to collimate the beam.

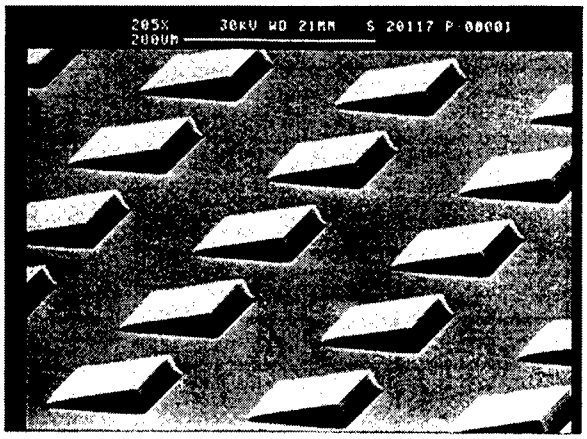

Figure 2: Array of microprisms fabricated in photoresist by analog gray-level lithography.

GRIN-lens based optical interconnection systems for planes of micro emitters and detectors: Microlens arrays improve transmission efficiency.

V. Baukens, A. Goulet, H. Thienpont, I. Veretennicoff, W.R. Cox[1] and C. Guan[1].
Vrije Universiteit Brussel, Applied Physics Department (TW-TONA), Pleinlaan 2,B-1050 Brussel, Belgium,
Tel. +32 2 629 3451, Fax. +32 2 629 3450, vbaukens@vub.ac.be
[1]MicroFab Technologies, Inc. 1104 Summit Avenue, Suite 110, Plano, Texas 75074

1. Introduction

There has recently been significant progress in the development of arrays of fast and sensitive optoelectronic emitters, detectors and transceiver devices. If arrays of these devices are to be successfully incorporated into switching fabrics, data communication or information processing systems, then highly efficient optical systems must be developed to interconnect them. It is indeed important to minimise transmission losses, because the bandwidth of such data channels strongly depend on the amount of optical power impinging on the receivers. The highly divergent nature of some of these sources, such as Lambertian emitters and microcavity LEDs, does not facilitate this task, because of the high insertion losses at the input of the optical system. Moreover we want these systems to be compact, low cost, robust and easily assembled. In this paper we present a novel, hybrid and compact optical system, based on large diameter radial gradient refractive index (GRIN) lenses and microlenses that fulfills these requirements. We also model this system with raytracing software and evaluate its performances experimentally.

2. An optical imaging system based on large diameter GRIN lenses

In imaging between arrays of devices, a distortion-free system is critical and therefore a telecentric system is chosen in order to minimize distortion and coma [1]. Because the input and output arrays consist of emitter-receiver optoelectronic elements a beam-splitter is required in the system. This acts both as a port for optical communication with successive device planes and for observing the state of both planes. By placing the beam-splitter at the center of the telecentric system any spherical aberration introduced is minimized. In the future, emitter and detector arrays of up to 2.5 x 2.5 mm side length are expected. This requires a circular field of view (FOV) with a diameter of 3.5 mm. The system that was chosen is shown in Fig. 1. GRIN lenses (with a 5 mm diameter and a length Z of 31.9 mm) were used to image between two device arrays. GRIN lenses were chosen for their ease of alignment and relatively low cost. The lenses were placed in V- grooves, ensuring that their optical axes were in line. Fig. 2 shows a photograph of this system. Focusing was achieved by sliding the lenses in the V-grooves. In the application described here, lenses with a pitch of slightly less than 0.25 were used, so that rays entering the lens from a point source located at a working distance L from the front face of the lens, are collimated on emerging from the back face of the lens. A working distance of several millimetres was required to allow space for the wire bonds used to contact the active devices. The parameters of these lenses at 860 nm were given by the manufacturers as $n_{00}=1.631$, $n_{10}=-1.32 \times 10^{-3}$ mm^{-2}, $n_{20}=0$ mm^{-4}. This gives a value for $\sqrt{A}$ of 0.0402. The pitch of the lenses used here were 0.204. The working distance L is given by (1) and was found to be 4.52 mm. The numerical aperture NA is obtained by (2) where r_0 is the lens radius, r is the distance of the ray from the centre axis, $R=r/r_0$ is the normalised distance from the centre axis and φ is the angular distance of the ray from the y-axis. The numerical aperture was found to be 0.16 on axis. The effective focal length f_{eff} for the lens in air is given by (3) and is 15.9 mm. The transmission efficiency of the system was assessed experimentally. The measured on-axis transmittance was found to be 0.27% for an 860 nm Lambertian source. A test grid has been imaged through the system to study the FOV and to measure the distortion. With the exception of some distortion at the edge of the FOV, no measurable aberration was found.

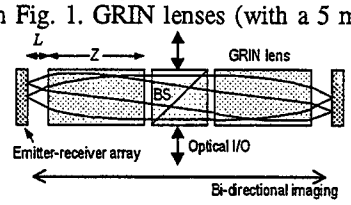

Fig. 1. Optical plane to plane imaging system (BS – beam-splitter)

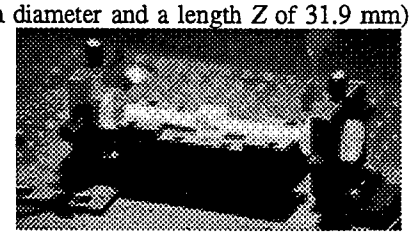

Fig. 2. Photograph of the optical system.

$$L=\frac{1}{n_{00}\sqrt{A}\tan(\sqrt{A}Z)} \quad (1)$$

$$N_A=n_{00}r_0\left(1-\frac{Ar_0^2}{2}\right)\left(\frac{A(1-R^2)}{1-R^2\sin\varphi}\right)^{1/2} \quad (2)$$

$$f_{eff}=\frac{1}{n_{00}\sqrt{A}\sin(Z\sqrt{A})} \quad (3)$$

3. System improvements

From these results it is apparent that the main disadvantage of this system is the high insertion loss caused by the combination of the highly divergent nature of the sources and the relatively low numerical aperture of the GRIN lenses. A solution is required which will both increase the speed of the optical system and reduce the size of the received spots at the image plane without reducing the field of view. This may be achieved by developing a hybrid system in which an array of microlenses is used to collimate the light. This will have the effect of both reducing beam divergence at the entrance plane of the GRIN lens imaging system and allowing more light throughput. Placing an identical microlens array at the receiver plane concentrates the light into the detector windows. This hybrid system is shown in Fig. 3. The microlenses can be put either on the optoelectronic devices or on the flat surface of the GRIN lens.

To manufacture these spherical microlens arrays a special fabrication technique, called "Drop-on-demand microjet printing" will be used [2]. With this technique microdroplets of optical polymeric materials of 25-50 µm in diameter, can be dispensed at temperatures up to 220°C onto optical substrates and components, in order to create precisely placed and formed micro-optical elements 40-1,000 µm in size. The printed microlenses are nearly-diffraction-limited and have a speed range of f/0.7 to f/6 and substrate surface contact angles up to 145°.

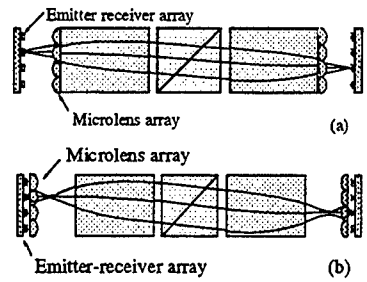

Fig. 3. Hybrid system: (a) µlens on GRIN, (b) µlens on transceivers

4. Design of the hybrid system

As described above, there are two approaches to incorporate microlenses in the optical interconnection system. The design of these two systems is somewhat different. In case the microlenses are put directly on the optoelectronic emitter-receiver devices, a pedestal should be incorporated between the microlenses and the devices. This is needed to bring the microlens at the correct distance from the source, to collimate the light. Here the optical GRIN-BS-GRIN imaging system does not change. In case the microlenses are put on the flat surface of the GRINs, the distance from the source to the microlens should be small enough, such that the microlens can collect enough light to improve the transmission efficiency considerably. This means that the working distances from the GRIN to the optoelectronic emitter-receiver devices are in the order of 100 µm. Therefore we need GRINs with a quarter pitch.

The array of optoelectronic devices under study consists of a pair of transceiver devices with a Lambertian emission pattern. One pair of these devices forms a single data channel. The dimensions of the optical windows of devices (emitter or detector area) and their separation are shown in fig. 4. The pitch of these pairs within the array is 96 µm. In our study we have looked at systems where the microlens area covers a pair of these devices (fig. 4). This means that the emitter and detector are positioned off-axis with respect to the microlens. If we want to perform an array-to-array transcription, the microlens may not have a diameter larger than the array pitch. To prove theoretically that in this way we can enhance the transmission efficiency, we compared the modeling results for a single data channel with and without microlens. In this case the diameter of the microlens is not limited to the array pitch.

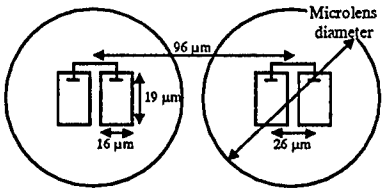

Fig. 4. Dimensions of the devices

In a first step we did a paraxial study to see what diameters and focal numbers (f#) for the microlens are necessary to collimate the off-axis source, such that the direction angle of the collimated beam was within the acceptance cone of the GRIN lens. From this simplified study of the system we could already conclude that the microlens should have a large diameter and a large focal number. Next we have looked at the angular field of view of the lens. Here again we can conclude that a large diameter for the microlens results in a larger angular field of view, while a smaller distance between the source and the lens results in a better collection of the light. The need for a small working distance imposed by the second conclusion and a large focal number as put forward by the first conclusion are in clear contradiction. Hence, trading-off both parameters must yield an optimum f# for every lens diameter.

These trends have been used to choose the parameters for the microlenses studied in our radiometric calculations, performed with the commercial raytracing software OptikWerks. Both systems (microlens on GRIN, microlens on optoelectronic devices) have been simulated with a plano-convex microlens with a refractive index of 1.6. In our radiometric analysis, we have modelled the source as a grid of point sources. Each point source emits a number of rays within an emission cone, both specified by the user. The receiving element is modelled as a two dimensional rectangular grid. Every point of this rectangular grid is in fact a small detector. The rays that hit such a small detector are counted and give us a measure for the transmission efficiency of the optical system. To speed up the

radiometric calculations, the emitting element was not modelled as a Lambertian source, but with a uniform angular intensity distribution featuring an emission cone of 45°. We can justify this simplification, since we were only interested in the relative improvement of the system and not in the absolute value of the transmission efficiency of the system.

We will focus in this paper on the optical system where the microlenses are printed on the flat surface of the GRIN lens. This approach is easier to realize with the "drop-on-demand microjet printing" than the hybrid system with the microlenses on the optoelectronic devices. In case of the latter approach, pedestals have to be inserted between the microlens and the devices and the lenses have to be printed on a structured chip surface.

We have simulated the optical system for different diameters of the microlenses. For each lens diameter we have calculated the transmission efficiency for several values of the focal number. The curves shown in fig. 5 are the results for different lenses (determined by their diameter and f#), when the lenses are positioned at the working distance that results in the highest transmission efficiency. For small diameter microlenses we need a large f# and, as the diameter increases, the required f# decreases. The dashed horizontal line in fig. 5 is the transmission efficiency of the optical system without microlenses. The transmission efficiency for this hybrid system is maximum when a microlens with a diameter of 175 µm and a f# = 1 is used, and for a working distance of 120 µm. The efficiency has a value of 9.47% and represents an improvement over the system without microlenses of almost 5. We have also studied the cross-talk in the optical data transfer when using this interconnection system. A source of cross-talk could be the Lambertian emission pattern of the source, which will also illuminate the microlenses of the neighboring data channels. The light collected by the neighboring microlenses will result in an input beam for the GRIN lens with an angle larger than its NA. Therefore the GRIN lens will not at all accept it. Another possible reason for cross-talk is that the spot size is so large or so deformed that it affects the other element within the pair. But as can be seen in fig. 6, the optical power that is impinging on the correct element in the pair is much larger than the power on the neighboring element.

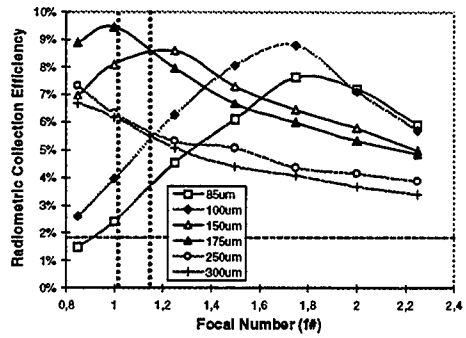

Fig. 5. collection efficiency of the hybrid system versus the simple GRIN system

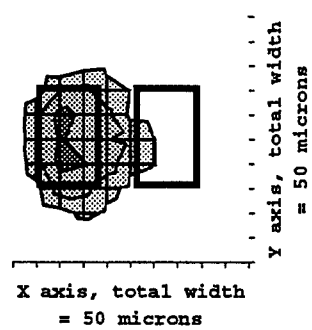

Fig. 6. Intensity plot on the detector pair

5. Parameters of the printed microlenses

Working towards a practical realization of the system, we have printed these microlenses on the GRIN surface, using a material had an index of refraction of 1.53 at 850nm. Microlenses with focal numbers in the range of 1.2 to 1.3 were achieved. Taking into account that the simulations were performed with an index of refraction of 1.6, the best lens within this f# domain (see fig. 5, f# domain between the dotted lines) has a diameter of 175 µm and a focal number of 1.2 when the index of refraction is 1.53. Microlens arrays with a pitch of twice the device pitch (192µm) and a lens diameter of 150 µm were printed, as well as arrays with three times the device pitch (288µm) and a lens diameter of 200 µm. To obtain the highest collection efficiency, the smallest possible focal number, i.e. f# = 1.2 was chosen.

6. Conclusions

We have modelled, designed and constructed a compact hybrid optical system, integrating large diameter GRIN lenses with arrays of microlenses to interconnect large arrays of microemitters and detectors with a high transmission efficiency. At the conference we will discuss our findings in detail and we will also report on the experimental characterisation and demonstration of this hybrid system for LED-type microemitter arrays.

References

[1] A. Kirk, H. Thienpont, N. McArdle, K.H. Brenner, M. Kuijk, P. Heremans, I. Veretennicoff, "A compact optical imaging system for arrays of optical thyristors", *Applied Optics*, Vol. **36**, No. **14**, pp 3070-3078, 1997.

[2] W.R. Cox, D.J. Hayes, T. Chen, H.J. Trost, M.E. Grove, R.F. Hoenigman, "Low cost optical interconnects by microjet printing", *Journal of Microcircuits & Elect. Pack.*, Vol. **20**, No 2, pp 89-95, 1997.

See also W.R. Cox et al, **invited paper** at this conference.

Visible testbed projector with replicated DOE

C. Bill Chen, Ronald G. Hegg, Todd Johnson, Bill King, David F. Rock
Raytheon Sensors and Electronic Systems
El Segundo, California

Robert Spande
U.S. Army CECOM NVESD
Ft. Belvoir, Virginia

This paper focuses on the need and proper application of DOE's invisible systems and on the nature and performance of the projector optical design and test results.

Micro Optics

Wednesday, June 10, 1998

Madeleine B. Fleming, 3M Company
Hudson Welch, Digital Optics Corp.
Presiders

DWA
8:30am–10:00am
Koa Room

Micromachining for micro-optics

Ming C. Wu
University of California at Los Angeles
66-1470 Engr. 4
Los Angeles, California 90095-1594

We report on the application of the emerging micromachining technology for fabrication of micro-optics as well as its integration with microactuators for adaptive control and dynamic alignment.

Integrated micro-optical systems fabricated by replication technology

M.T. Gale and M. Rossi

CSEM Centre Suisse d'Electronique et de Microtechnique
Badenerstrasse 569, CH-8048 Zurich, Switzerland
Tel. +41 1 4971 440, Fax. +41 1 4916 323, e-mail michael.gale@csemne.ch

L. Stauffer, M. Scheidt and J.R. Rogers*

Leica Geosystems AG, CH-9435 Heerbrugg, Switzerland
Tel. +41 71 727 3550, Fax. +41 71 727 4685, e-mail laurent.stauffer@email.leica.com

* Present address: Optical Research Associates, 320 East Foothill Blvd., Pasadena CA 91107
Tel. 818 795 9101, Fax. 818 795 9102, e-mail jrogers@opticalres.com

1. Introduction : Integrated micro-optical systems

Optical microsystems formed by the planar integration of micro-optical elements on a transparent slab are of considerable interest as compact, robust microsystems for applications in sensors and optical instruments. In a typical such microsystem [1], a sequence of micro-optical elements are arranged on one surface of a slab substrate which folds the optical paths between the elements by reflection at the opposite surface (Fig. 1). A major advantage of this approach is the ability to fabricate all micro-optical elements as one block, thus avoiding subsequent positioning and alignment steps. This can readily be achieved by the use of 'planar' (micrometer relief) micro-optical elements. Most commonly they are fabricated in a fused silica slab either as binary optical elements, by conventional multiple resist lithography and etching steps [1], or as continuous-relief elements, by techniques such as direct laser or e-beam writing or halftone lithography followed by transfer into the slab material by proportional etching [2].

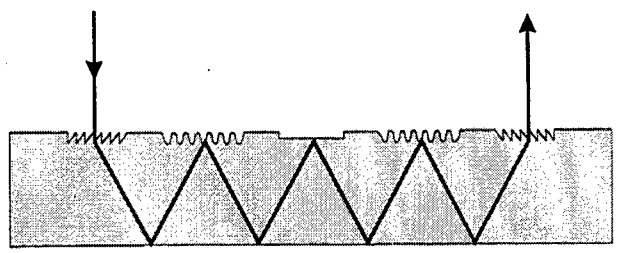

Fig. 1. Basic configuration of a slab optical microsystem.

An alternative approach which promises a low-cost, mass-production process is the use of replication technology to reproduce the surface-relief microstructure [2,3]. In this paper we describe progress in work aimed at investigating the potential and limitations of this approach. In this work Diffractive Optical Elements (DOEs) are fabricated together with other micro-optical elements as a single continuous-relief microstructure in a single laser writing step. The replication technology, however, applies equally to binary optical DOEs or any other elements with similar surface relief microstructure of profile depth in the micrometer range.

The replication work is currently concentrated on developing the technology for replicating the micro-optical elements into a thin film of uv-curable polymer on one surface of a glass slab (uv-embossing [3]). The thermal and mechanical properties are then dominated by those of the glass slab. Work is also underway to investigate the performance and properties of the alternative approach of injection moulding the complete slab microsystem in a polymer such as polycarbonate.

2. Fabrication: Concept and results

Replicated slab microsystems are being investigated for a variety of sensor applications. Fig. 2 shows an example of a design containing a number of reflective micro-optical elements, including a computer generated hologram (CGH), reflective lenses and plane mirrors (other

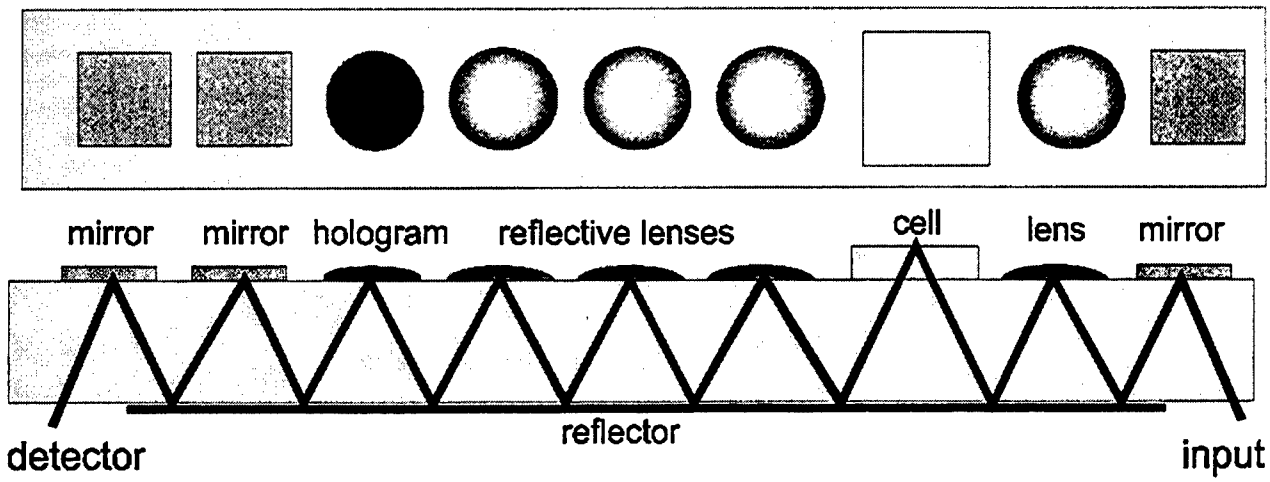

Fig. 2 Slab optical microsystem under investigation. The optics includes a continuous-relief hologram and reflective lens elements.

designs which are being investigated include diffractive lenses for higher NA micro-optical elements). The custom cell in this example contains a reference surface for application as an inclination sensor. The optical microsystem is completed by light source (diode laser) and detector (CCD imager) components hybridly attached to the slab as separate modules.

The fabrication of the slab microsystem shown in Fig. 2 involves 3 basic steps:

- ***Origination*** Direct laser writing of the micro-optical elements as an array in photoresist. The size and alignment of all the elements are determined in this step.
- ***Electroforming*** Fabrication of a nickel shim electroformed from the microstructured resist surface.
- ***Replication*** Replication from the Ni shim into a thin film of uv-curable polymer on the surface of the glass slab.

2.1 Origination by direct laser writing

An original of the micro-optical elements is fabricated using the CSEM LaserWriter III direct laser writing system which has been described in detail in previous publications [2,4]. A photoresist coated substrate is raster scanned under a focused HeCd laser beam (wavelength λ= 442 nm) whose intensity can be synchronously modulated to 256 discrete levels. In the LaserWriter III system, the raster scan is performed by a high precision (25 nm) roller-bearing stage and the focused laser writing spot is generated by a modified CD autofocus optic. Continuous-relief diffractive, refractive and reflective micro-optical elements such as CGHs, microlenses, and Fresnel elements can be routinely fabricated with a minimum lateral feature size of about 5 µm and a maximum relief height (sag) in excess of 10 µm. The reflective lens elements shown in Fig. 2 have a typical diameter of 1.5 mm and a sag of about 6 µm. By writing all micro-optical elements in a single step, the position and alignment of all elements can be realised to sub-micrometer tolerances.

2.2 Electroforming

The photoresist original is converted to a Ni shim by electroforming [3]. The flatness of this shim over the area of the micro-optical elements, typically about 3x8 mm, is critical for the quality and performance of the replicated micro-optical system and has been the subject of considerable work and improvement. Initial 'standard' shims of about 100 µm thickness fabricated by electroplating in a low stress Ni bath showed a flatness error (peak-to-valley) in

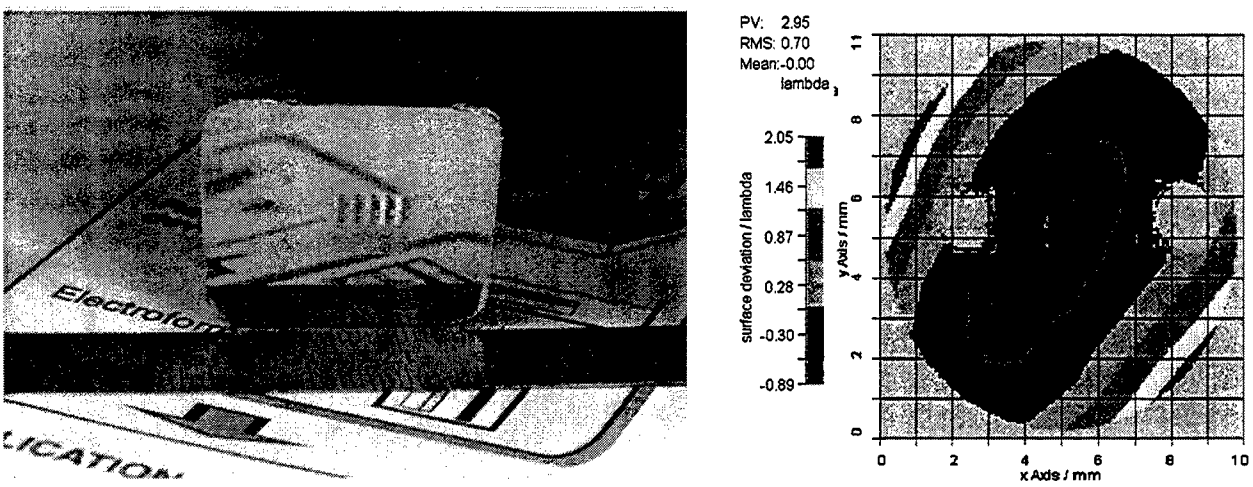

Fig. 3 Replication shim for the micro-optical components of the slab optical microsystem (left) and interferometer measurement (FISBA μPhase) of the flatness error.

excess of 9λ over this area. Improvements in the technology, in particular by reducing the Ni thickness and cementing a backing plate to the shim before separation from the resist original, enabled this error to be reduced to less than 3λ. Fig. 3 shows a photograph of such a shim and the interferometer measurement of the flatness.

2.3 Replication by uv-embossing

The micro-optic structure is replicated into a thin film of NOA 61 uv-curable polymer coated onto a blank glass slab, a process referred to as uv-embossing [2,3]. The Ni shim is pressed onto the film in a specially designed jig and cured by exposure through the glass to radiation from a high pressure Hg lamp. Typical film thicknesses of the cured polymer are in the 10-30 μm range. Separation of the shim from the cured polymer is facilitated by sputter coating the shim with a thin (~5 nm) film of PTFE-like material. Following the curing, the micro-optical elements are metallised where required by the evaporation of Al through a suitable mask.

3. Conclusions

Slab optical microsystem prototypes for a variety of applications have been fabricated using the uv-embossing replication approach described above. Other replication technologies are under investigation. The use of direct laser writing and replication technology will enable a low-cost production process to be established which is economically interesting also for low volume applications.

The authors gratefully acknowledge the contributions of H. Schütz, J. Pedersen and R. Stutz of CSEM Zurich. This work was supported in part by the Swiss Priority Program OPTIQUE.

References

[1] J. Jahns and A. Huang, "Planar integration of Free-Space Optical Components", Appl. Opt. **28**, 1602 (1989).

[2] M.T. Gale and M. Rossi, "Continuous-relief diffractive lenses and microlens arrays", Ch. 4 in *Diffractive Optics for Industrial and Commercial Applications*, J. Turunen and F. Wyrowski (Eds.), Akademie Verlag, Berlin (1997).

[3] M.T. Gale, "Replication", Ch. 6 in *Micro-Optics : Elements, systems and applications*, H.P. Herzig (Ed.), Taylor and Francis, London (1997).

[4] M.T. Gale et al., "Fabrication of continuous-relief micro-optics: progress in laser writing and replication technology", OSA Technical Digest Series **5**, 335 (1996).

Mass-transport gallium-phosphide refractive micro-lenses for diode array reconfiguration

T.A. Ballen, J.R. Leger

Department of Electrical and Computer Engineering, University of Minnesota
200 Union St. SE, Minneapolis, MN 55455
phone (612) 624-8848, fax (612) 625-4583, tballen@ece.umn.edu

Laser diode arrays are useful for pumping of fiber and solid-state lasers due to their high power and narrow linewidth. In addition, multi-mode fibers offer a convenient method of transporting light for applications such as illumination and materials processing. However, the pumping geometry of end-pumped lasers or the waveguide shape of multi-mode fibers often does not match the diode array illumination pattern (approximately a line source). More efficient light-coupling is possible through a geometric transformation of the individual diode sources to more closely match the desired geometry[1]. In this paper mass-transport smoothing is used to fabricate arrays of off-axis aspheric refractive collimating lenses and prisms for efficient reconfiguration of a linear laser diode. The modeling and design of the aspheric lenses is described and the performance characteristics of a fabricated prism demonstrated.

Recent development of mass-transport fabrication of optical elements allows the generation of highly-efficient micro-optics[2-5]. The use of high-index materials results in low f/# lenses with reduced sag compared to traditional lens materials. Furthermore, aspheric surfaces can be easily generated, allowing diffraction-limited performance. While previous efforts have concentrated on rotationally-symmetric lenses, this technique is well-suited for the fabrication of arbitrary surfaces, including the off-axis aspheric and prismatic elements described below.

The diode transformation system (Fig. 1) consists of a linear array of aspheric lenses that provide collimation both perpendicular and parallel to the diode junction in addition to off-axis steering, followed by a 2-D array of prisms to correct the tilt of each collimated beam at the desired

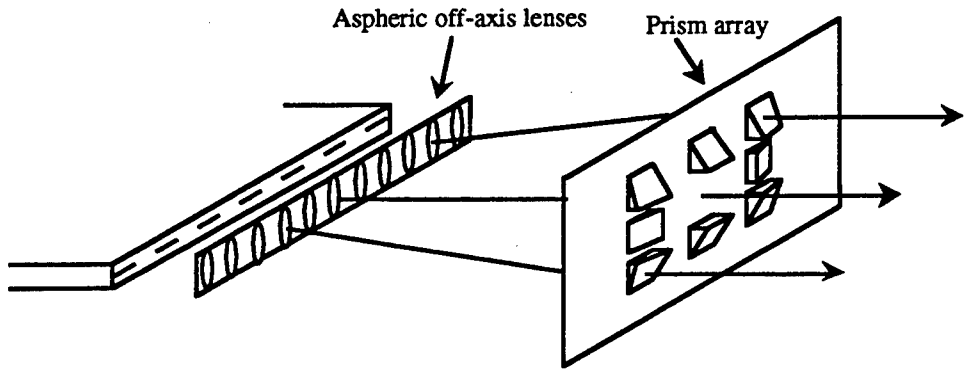

Figure 1. Diagram of diode array transformation system

plane. Both arrays are made by mass-transport smoothing of gallium phosphide (GaP) pre-forms.

The mass-transport process involves high temperature diffusion where atoms move from convex to concave regions driven by surface-energy minimization[4]. A single step broadens with the fourth root of time, while the amplitude of a sinusoidal profile decreases with the fourth power of the spatial period of the structure. Initial structures are formed using either a binary etching technique[3], where the local spatial fill-factor is determined by the local profile height after mass-transport, or a multi-step method[2], where the local curvature of the final surface is controlled by the pre-form step height. Practical fabrication of efficient micro-optics is possible because sharp edges created in fabrication smooth away quickly, while the overall lens shape changes very slowly.

The aspheric surfaces used for collimation and steering are 10th-order x-y polynomials optimized by a lens design code to direct light from each diode emitter into a particular direction. The necessary pre-forms to produce these surfaces are generated by the solution of diffusion equations. Simulated smoothing of a binary pre-form to generate an f/1.5, 200 μm-diameter lens to collimate and steer 2.9° is shown in Fig. 2. The etched pre-form is shown as a solid curve, the smoothed profile as a dashed line. The final profile deviates from the desired optical surface across 80% of the lens by ~0.05λ (rms.), corresponding to a Strehl ratio of ~90%.

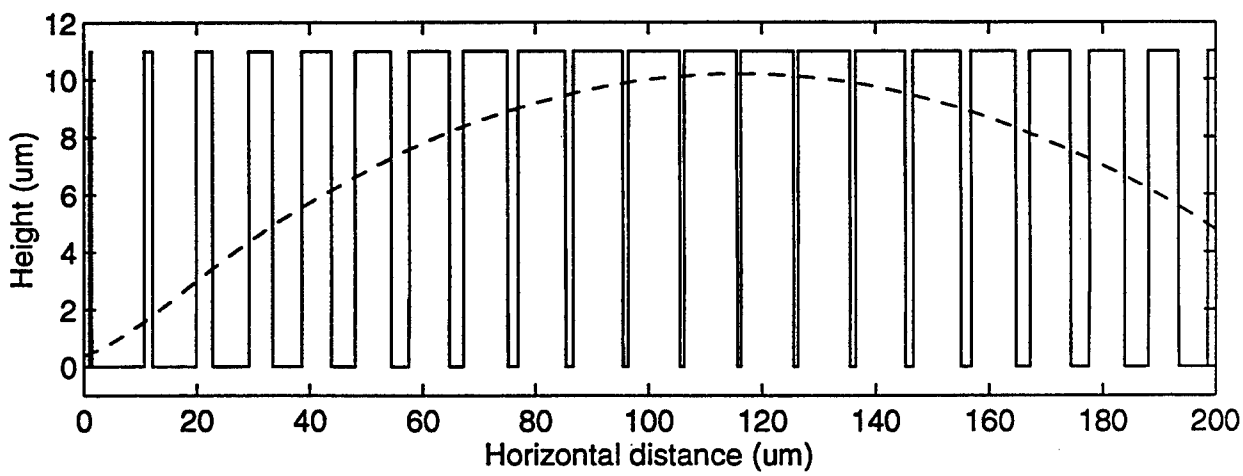

Figure 2. Simulation of smoothing of mass-transport pre-form.
Solid line corresponds to etched pre-form; dashed line shows final lens surface.

An efficient optical element for performing the prismatic tilts in the second plane of Fig. 1 has been realized by the fabrication of a GaP biprism using the multi-step, rather than the binary, technique. Steps were formed in GaP using photolithographic methods and chemically-assisted ion-beam etching (CAIBE). Repetition led to a 1-D pyramidal structure with five steps of equal height and width. Using a sealed-ampoule technique[5], the GaP was heated in a furnace at 1100 °C

for 34 hours in a phosphorous overpressure to maintain stoichiometric composition. This process smoothed the etched steps into the biprism structure shown by interferometric data in Fig. 3. Following application of an AR coating, the beam-steering properties of the biprism were investigated by illumination with a normally-incident He-Ne beam reduced to a 35 μm-diameter spot. Translation of the biprism resulted in steering of the beam in three directions (deflection angle ~12°), corresponding to the two faces of the prism and a flat section of the substrate. Far-field intensity data for these three positions demonstrate the quality of the prism surface by the resulting diffraction-limited spots produced at each beam location. Power measurements yield an efficiency of >94% (including all absorption and scattering loses) for steering in either direction.

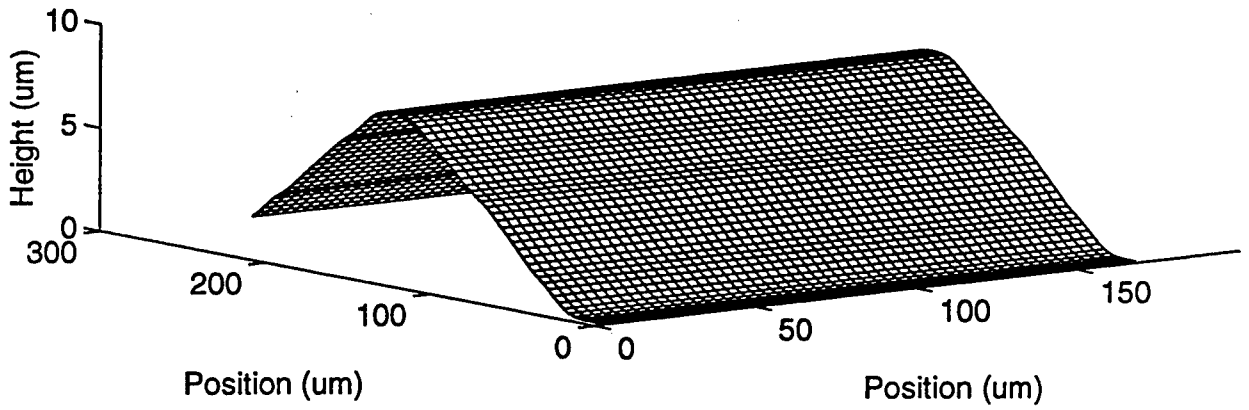

Figure 3. Interferometric surface profile of GaP biprism

In conclusion, the use of mass-transport fabrication techniques to generate arrays of GaP off-axis aspheric collimating lenses and prisms for the geometric transformation of a linear laser diode bar has been described. A biprism has been fabricated and tested, yielding high steering efficiency. Combination of the proposed elements will result in efficient light-coupling techniques.

This work is supported by the Army Research Office, the Army Research Laboratory, the Night Vision and Electrooptic Sensors Directorate, and Cynosure, Inc.

References

1. J.R. Leger, and W.C. Goltsos, IEEE J. Quant. Elec. **28** (4), 1088 (1992).
2. Z.L. Liau, et al., Appl. Phys. Lett. **55** (2), 97 (1989).
3. Z.L. Liau, et al., Appl. Phys. Lett. **64** (12), 1484 (1994).
4. Z.L. Liau, and H.J. Zeiger, J. Appl. Phys. **67** (5), 2434 (1990).
5. J.S. Swenson, et al., Appl. Phys. Lett. **66** (11), 1304 (1995).

Vector Radiation Coupling Method for High Efficiency and High Uniformity Lightguide

Masayuki Shinohara, Masataka Tei, Shigeru Aoyama and Masashi Takeuchi
Omron Corporation, Central R&D Laboratory
20 Igadera, Shimokaiinji, Nagaokakyo City, Kyoto 617, Japan
Telephon:+81-75-957-9819
Fax: +81-75-953-7604

1.Introduction

Lightguides with LED light sources are becoming important components in the application of LCDs for mobile use, because of their thin structures and light weight. Unfortunately, conventional lightguides suffer from poor performance, such as a non-uniform brightness , and this results in poor image and a low efficiency which leads to high power consumption.

In this paper, we propose a novel method for vector radiation coupling using a concentric chirped microlens array to achieve high efficiency and high uniformity . We also present the experimental result of the fabricated device.

2.Principle

Vector radiation coupling method allows only a single direction of light path at any position of the lightguide by arranging the light source at single localized spot and a concentric chirped microlens array. This makes it possible to estimate analytically a certain transfer function, and leads to uniform brightness.

A schematic view of the proposed lightguide is shown in Fig.1. The cylindrical microlenses which cause light to radiate from the surface of the lightguide, are arranged concentrically around the light source, and this produces radially expanding straight light paths as shown in Fig.2 (a). In the conventional method, the light is split and deflected in many directions in a sequence due to the scattering dot patterns as shown in Fig.2 (b). These complex light paths have been known to cause difficulty in analytically estimating the distribution of brightness. As a result, only empirical optimization has been applicable in the design.

A major advantage of the vector radiation coupling method is that each light path is independent of the others due to straight paths. This enables an analytical design with a transfer function. When light propagates along a straight light path, a transfer function can be expressed by a radiation decay factor[1)] which is the ratio of the amount of light being propagated to the radiation loss . This radiation decay factor is controlled by the density of the microlenses as shown in Fig.3. Uniform brightness is achieved by optimizing the radiation decay factor along each light path.

3.Experimental results

Photographs of the concentric chirped microlens array of the fabricated lightguide are shown in Figs.4 (a) and 4(b). The size of each microlens is 10 μm wide and 2.5μm high

and the periods between patterns are 11.5-200 μm. The effective illumination area of the lightguide is 22×38 mm^2, and the thickness of the lightguide is 0.8 mm.

The fabrication process for the concentric chirped microlens array is as follows.

1. A master pattern for the microlens array is fabricated by electron beam lithography.[2)]
2. The master pattern is transformed by electroplating in the form of a stamper made of Nickel.
3. Using this stamper, the pattern is replicated on a plastic lightguide by molding.[3)]

The efficiency defined by the ratio of the power of coupled light to the emitted light, was measured as high as 70% which is four times higher than that of the conventional method. Figure.5. shows the experimental results on the uniformity of distribution. The vertical axis represents normalized brightness. Note That maximum to minimum ratio of brightness was reduced to 1.5 from 3 with the proposed method.

4.Conclusion

We have proposed the vector radiation coupling method which use a concentric chirped microlens array. The efficiency as high as 70% was achieved ,which is 4 times higher than with the conventional method. The maximum to minimum ratio of brightness was reduced to 1.5 from 3. Future study will focus on larger area illumination for broader range of applications.

5.References

1. H.Nishihara,M.Haruna and T.Suhara;"Optical Integrated Circuits",McGraw-Hill,New York(1985)
2. S.Aoyama, N.Horie, and T.Yamashita;"Micro Fresnel lens fabricated by electron-beam lithography",Proc.SPIE 1211, 175-183(1990).
3. H.Hosokawa, N.Horie, T.Yamashita;"Mass-producible Optical Guidedwave Devices Fabricated by Photopolymerization",Photopolymer Device Physics, Chemistry,and Applications,Proc.SPIE 1559,229-237(1991).

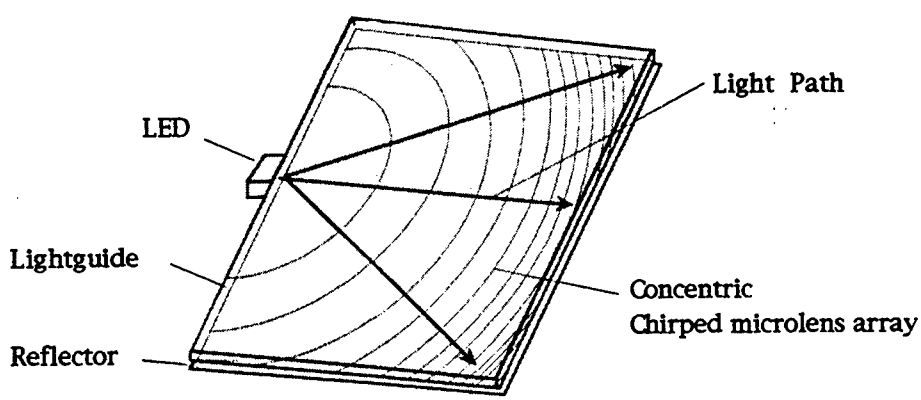

Fig. 1. Schematic illustration of a lightguide based on the proposed vector radiation coupling method

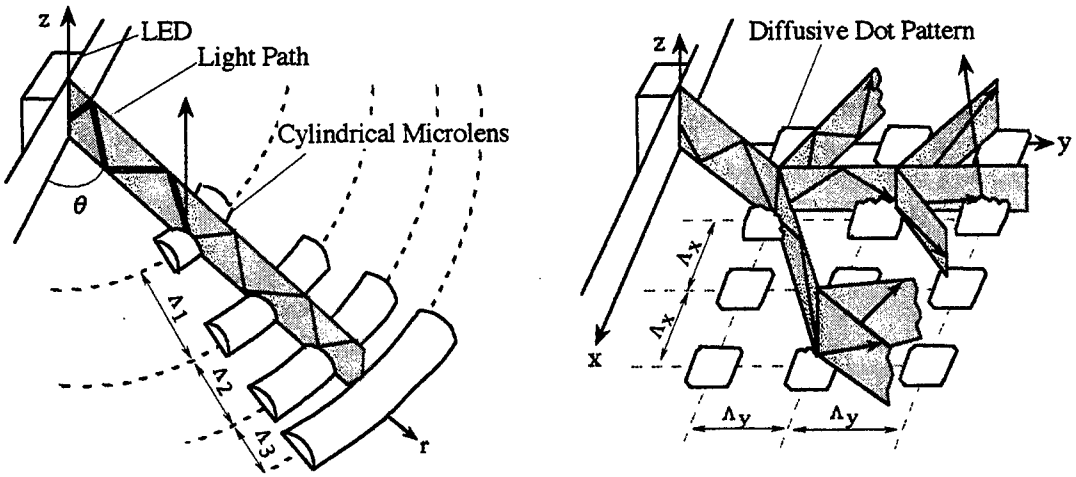

(a) Vector radiation coupling method (b) Conventional method

Fig. 2. Schematic illustrations showing propagations of light

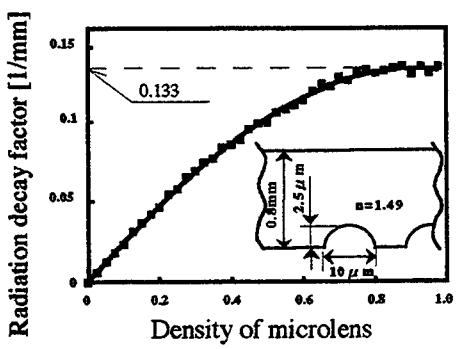

Fig. 3 . Simulation results of radiation decay factor versus density of microlens

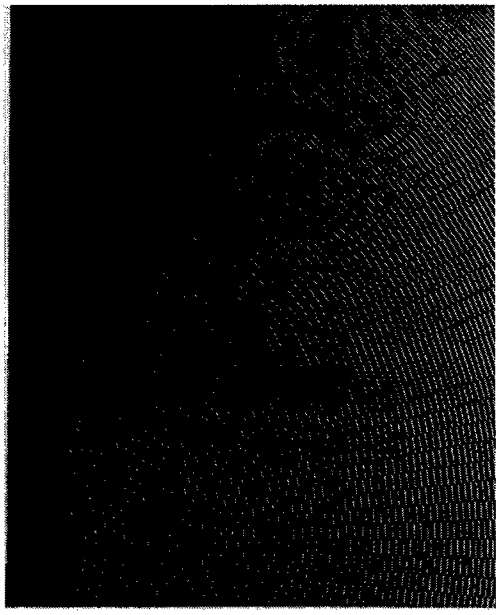

(a) Top view

(b) SEM photograph of a cylindrical microlens

Fig.4. Photographs of a concentric chirped microlens array

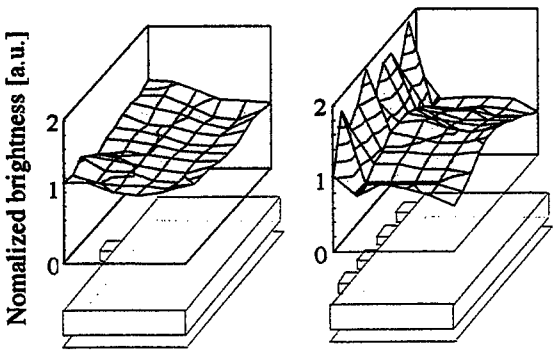

(a) Vector radiation coupling method (b) Conventional method

Fig. 5. Uniformity of brightness

Diode laser illuminated automotive brake lamp using a linear fanout diffractive optical element

J.T. Remillard
Ford Motor Company, Ford Research Laboratory - MD 3028
20000 Rotunda Dr. Dearborn, MI 48121
Telephone: 313-323-9840 Fax: 313-322-7044
Email: jremilla@ford.com

M.A. Marinelli
Visteon, Exterior Systems Engineering
24300 Glendale, Detroit MI 48239
Telephone: 313-592-2897 Fax: 313-592-2911
Email: mmarinel@ford.com

T. Fohl
Technology Integration Group
681 South St., Carlisle, MA 01741
Telephone: 508-369-5649 Fax: 508-287-4207
Email: tfohl@world.std.com

D.A. O'Neil
O'Neil Engineering
Unit 130 C, 500 East Lancaster Ave., Wayne, PA 19087
Telephone: 610-964-8989 Fax: 610-964-1779
Email: dao1@cornell.edu

Marinelli and Remillard discussed the design and fabrication of diode laser illuminated automotive signal lamps.[1] The optics are made from thin (~5 mm) plastic sheets that manipulate light using reflection and refraction from edges, surfaces, and shaped cut-outs. The resulting lamps can be well under 1 inch in thickness providing functional and styling advantages not attainable with conventional automotive lighting systems. Functionally, the sheet optic consists of a section that receives, divides, and expands the laser light (the manifold), and a section that directs it out of the lamp into the appropriate beam pattern (the kicker). The kicker is the visible part of the lamp optic, and the most efficient use of space is realized by maximizing the ratio of kicker to manifold area. Here we describe the design and fabrication of a thin, laser illuminated brake lamp that uses a diffractive optical element (DOE) at the entrance of the manifold. The DOE provides a compact way of uniformly spreading the light exiting the fiber, and allows for smaller manifolds than those discussed in the previous work.

The prototype lighting system consists of a remotely located diode laser (a proprietary, high power device emitting at 650 nm obtained from SDL Inc., of San Jose CA) and a 1 mm diameter glass optical fiber which couples light into the manifold of a thin sheet, acrylic lamp optic. The sheet optic must reduce the brightness of the light exiting the optical fiber by a factor of $\sim 10^4$ to meet the Society of Automotive Engineers (SAE) photometric requirements. Using a DOE, a compact laser illuminated optic has been designed for use in a current production model Ford Escort station wagon signal lamp.

Fig. 1 shows the fabricated sheet optic design which uses a linear fanout DOE (manufactured by Teledyne Brown Engineering) at the manifold entrance. This DOE splits collimated incident light into six beams and is optimized for use at a wavelength of 632.8 nm. The beams propagate in the same plane and are separated by a nominal angle of 4.8°. Approximately 80% of the input power is contained in the six beams, with an intensity variation between them of ±10%. The remaining power is distributed in secondary orders and reflections.

In our application, however, the DOE is illuminated by diverging light. Specifically, light exiting the fiber has an included spread angle of ~15°. Instead of forming six well defined beams, the DOE spreads the light into a horizontal band. Figure 2 shows contour plots of the light distribution exiting the fiber and after passing

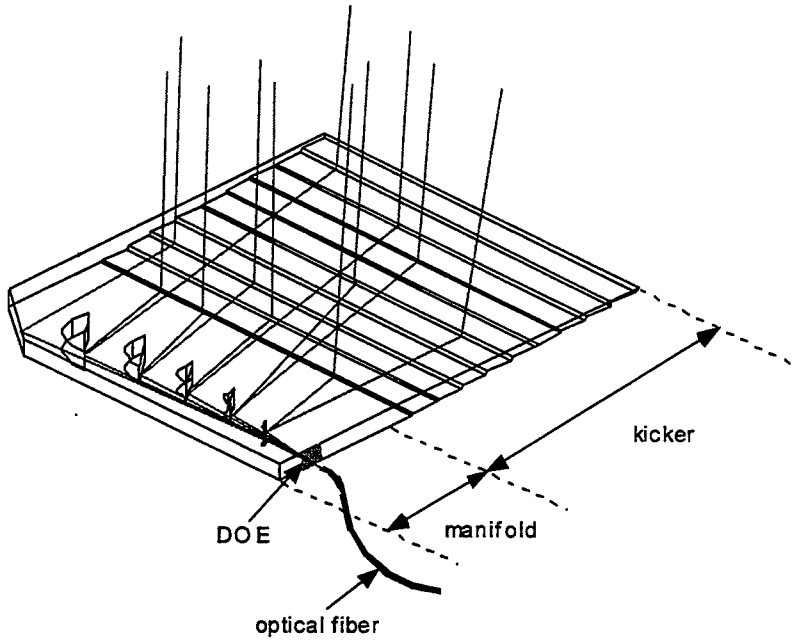

Figure 1: Optical schematic of thin sheet optic used in laser illuminated brake lamp. A diode laser (not shown) coupled to a ~1 mm diameter optical fiber feeds light into a ~5 mm thick acrylic sheet. The DOE spreads the light exiting the fiber into a horizontal band.

through the DOE where θ_H and θ_V are the deflection angles from the fiber optic axis. These data were acquired using an imaging photometry system developed by the Technology Integration Group, of Carlisle MA.

As the light spreads within the manifold, it is intercepted by an array of six mirrors. Five of these mirrors are formed by cut-outs that completely penetrate the thickness of the sheet, and a sixth mirror is formed by the diagonal outer edge of the manifold. The amount of light received by each mirror can be altered by changing its size and position, allowing a simple way of adjusting the luminance distribution across the lamp surface.

Light is reflected by the mirrors into the kicker section. The reflecting surfaces have a slight convexity to cause spreading of the light in the plane of the optic. The tapered kicker section has an area of ~90×70 mm^2 and consists of 35 facets (0.128 mm in height, separated by 2 mm) that reflect light out of the device. By adjusting the mirror curvature and kicker facet angles, a beam pattern can be formed that meets SAE photometric requirements.

The device of Fig. 1 was fabricated from a ~5 mm thick sheet of optical grade acrylic and its efficiency (power exiting the kicker/power exiting the optical fiber) was measured to be ~47% using the imaging photometry system discussed above. Accounting for Fresnel losses due to reflections at various air/dielectric interfaces within the system (a prism assembly used to couple light into the optic is not shown in Fig. 1) the efficiency of the optics alone is ~60%. This compares to an efficiency of ~80% estimated by ASAP, a non-sequential ray tracing package developed by Breault Research Organization of Tucson, AZ used to model the performance of the optic. The discrepancy between the measured and predicted efficiency is most likely due to scattering caused by imperfections in the device shape and surface finish caused by the machining process. Devices made using injection or compression molding techniques should have improved efficiencies. These methods result in precise smooth surfaces, and permit the fabrication of features considerably finer than those used in the present optic.

Figure 3 shows a comparison between the existing Escort lamp package and one that incorporates the thin sheet optic of Fig. 1. As can be seen, the laser illuminated lamp (right) is significantly thinner than its conventional counterpart (left). Besides reduced lamp depth, these optics can be used to make lamps with a variety of lit and unlit appearances. Because the optics are made from transparent acrylic, the lamps can take on the color of the underlying sheet metal. When lit, the illuminated facet surfaces result in a striped appearance that give the illusion

of considerable lamp depth. A more uniform surface luminance can be produced by using closely spaced facets. An extremely uniform lit appearance can be obtained by using a holographic diffuser on the outer surface of the optic to spread the light into the appropriate beam pattern. In these designs, flat mirrors and facets angled at 45° are used to extract collimated light from the sheet optic. Alternatively, the beam pattern can be formed by pillow optics placed on the outer surface of the sheet optic.

In summary, a novel laser illuminated lamp has been designed and fabricated using a DOE and thin sheet optics. DOE sheet optic hybrids allow for the design of compact, uniformly illuminated lamps.

REFERENCE

1. M.A. Marinelli and J.T. Remillard, "Diode-laser illuminated automotive lamp systems," Proc. Laser Diode Applications IV, SPIE Optoelectronics and High-Power Lasers and Applications Conference, Paper #3285B-30, 1998.

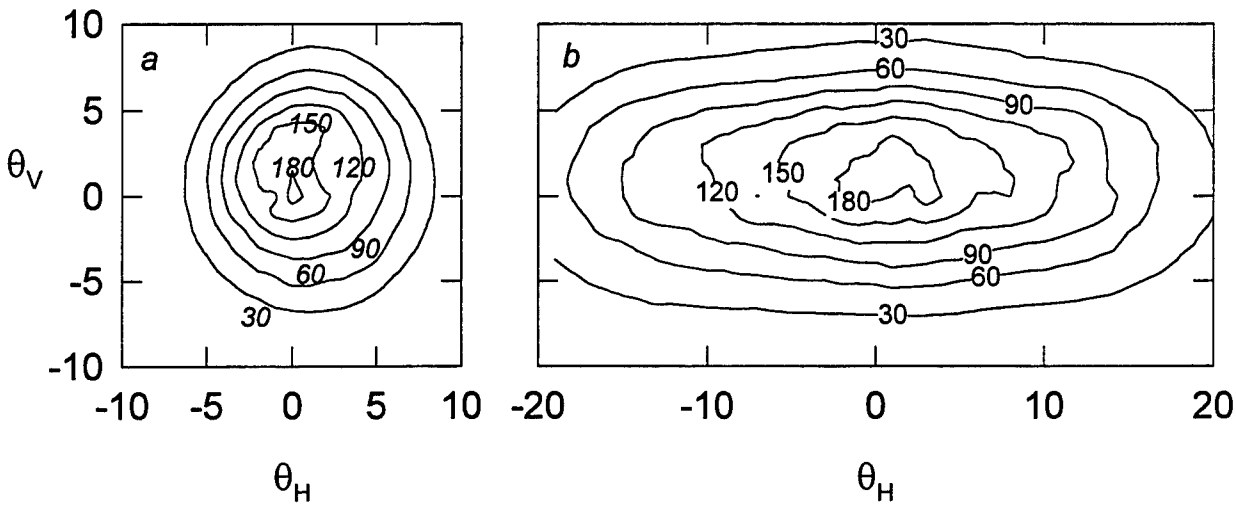

Figure 2: Contour plot of light (a) exiting optical fiber, and (b) after passing through DOE. θ_H and θ_V are the horizontal and vertical deflections angles from the optical fiber axis respectively.

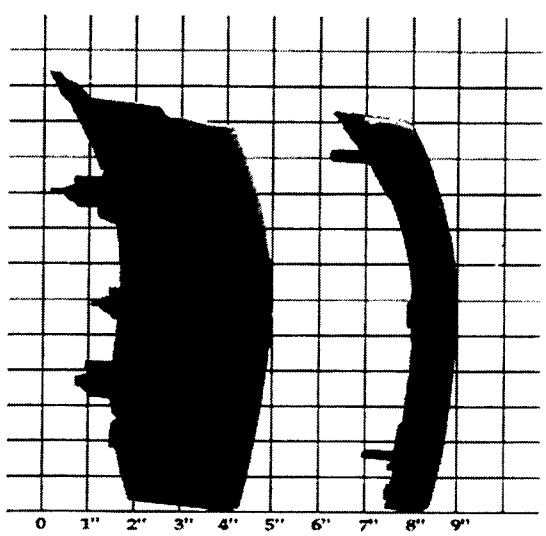

Figure 3: Left: Conventional Escort wagon signal lamp. Right: Prototype laser illuminated lamp.

Diffractive Optics and Micro-Optics

Applications 1

Wednesday, June 10, 1998

Michael T. Gale, CSEM Centre Suisse d'Electronique et de Microtechnique, Switzerland
Presider

DWB
10:30am–12:00m
Koa Room

HOLOGRAPHIC OPTICAL ELEMENT FOR A DUAL FOCUS OPTICAL HEAD

Yoshiaki Komma[1], Shin-ichi Kuwamoto[2], Hideki Aikou[1], Kenichiro Urairi[3], Michihiro Yamagata[4] and Yasuhiro Tanaka[4]
[1]Optical Disk Systems Development Center, Matsushita Electric Industrial Co. Ltd., 1006 Kadoma, Kadoma-shi, Osaka 571 Japan
Telephone:+81-6-906-4396 Facsimile:+81-6-906-5693.
[2]AVC Device Division,
[3]Optical Disk Systems Division,
[4]AVC Products Development Laboratory.

1. Introduction

A high density optical disk format named DVD adopts a 0.6 mm disk to simultaneously use a high numerical aperture (NA) lens and gain tolerance of disk tilt.[1] Because of the immense popularity of the CD format, it is important to playback the current widely used Compact Discs (CDs) on DVD format players. This requires an optical head that can read both conventional 1.2 mm disks and the new 0.6 mm disk. To read both disks with the same optical head, it is necessary to overcome spherical aberration caused by the difference in disk thickness.

2. Dual focus optical head

We have proposed a dual focus optical head that utilizes a hologram (holographic optical element: HOE) to compensate for spherical aberration, thus allowing the reading of both 0.6 mm disks and 1.2 mm disks.[2-7] The thin disk is read by the HOE's transmitted zero-order diffracted light. The thick disk is read by +1st-order diffracted light (Fig. 1). The HOE is blazed to increase light power efficiency. This element is designed as a concave lens so that the +1st-order diffracted light focuses on a point farther from the objective lens than does the zero-order diffracted light. Accordingly, there is no cross-talk between the two focused beams on a disk. Furthermore, this configuration needs only a HOE, which is a small, light and inexpensive element.

3. Unnecessary stray diffracted light

The +1st-order diffracted light is utilized in both a forward path (from a laser diode (LD) to the disk) and a backward path (from the disk to photodetector(PD)) for reading 1.2 mm disks. Therefore, the light beam produces a double-lens effect and the reflected light beams are parallel (Fig. 2) after focusing on the 1.2 mm disk. Zero-order diffracted light is not focused on the 1.2 mm disk, but when the reflected beam is diffracted to the 2nd-order, the light also produces a double-lens effect and becomes nearly parallel. Then the 0th-2nd and 2nd-0th diffracted lights in the forward and backwards path, respectively, become stray lights because they are focused on a PD plane to be almost as small as 1st-1st signal light. They move on the PD plane when the disk tilts because their focused points are not on the disk plane. This movement of the stray light changes the focusing servo characteristics. In conventional configurations, the grating profile of a blazed HOE is a sawtooth shape. Its depth is designed to be $\lambda/2(n-1)$ to obtain a 1:1 ratio between zero-order and +1st-order diffraction efficiency, where λ is wavelength and n is refractive index of the HOE. The 2nd-order

diffraction efficiency is 4.5% of incident light power. Figure 3 shows the measured focusing-error (FE) signal of a 1.2 mm disk. When the disk tilt is 0° the sensitivity of the FE signal decreased because the stray lights are in almost the same position.

4. Grating profile of HOE

We optimized the grating profile to suppress the 2nd-order diffraction efficiency. We started from a conventional sawtooth shape. One period of the sawtooth shape is represented as

$$y = a\,x \quad , \qquad (1)$$

where x is position and y is optical phase difference given by the HOE. By adding higher order polynominals, we use Eq. 2 as a model of phase profile.

$$y = a_1\,x + a_2\,x^2 + \cdot\cdot\cdot + a_n\,x^n \quad . \qquad (2)$$

Each coefficient is changed in turn to minimize the 2nd-order diffraction efficiency with the restriction that both the zero- and the +1st-order diffraction efficiencies should be more than 38%. This process was repeated until all coefficients converged. The 'n' was chosen to be 20. We obtained the profile as shown in Fig. 4. The zero-, +1st- and 2nd-order diffraction efficiencies were 38.0%, 38.0% and 2.6%, respectively. This profile was observed to have a double peak feature. For convenience in manufacturing, the profile was simplified as shown in Fig. 5. The zero-, 1st- and 2nd-order diffraction efficiencies were calculated to be 38.6%, 38.1% and 1.1%, respectively.

5. Experimental results

An HOE with the grating profile shown in Fig. 5 was fabricated on an objective lens surface.[8-11] The 2nd-order diffraction efficiency was actually suppressed to as small a level as expected from our calculations. Figure 6 shows measured FE signals of a 1.2 mm disk. Disk tilt did not change FE signal characteristics because the 2nd-order diffraction efficiency was successfully suppressed.

6. Conclusions

The grating profile of an HOE used for a dual focus optical head was optimized to suppress 2nd-order diffraction efficiency. The HOE was fabricated on an objective lens surface. Stable FE signal characteristics for a 1.2 mm disk were achieved by suppressing the 2nd-order diffraction efficiency.

References

1. T. Ohta, K. Inoue, T. Ishida, Y. Gotoh and I. Satoh: Jpn. J. Appl. Phys. **32**, 5214 (1993).
2. Y. Komma, S. Nishino and S. Mizuno: Optical Review **1**, 27 (1995).
3. Y. Komma, K. Kasazumi, S. Nishino, S. Mizuno, Y. Kanda and H. Hayashi: Proc. SPIE. Vol. 2338, pp. 282 (1994).
4. K. Urairi, Y. Komma, Y. Shibata, S. Mizuno, H. Hayashi and K. Wakabayashi: Extended Abstracts of The Japan Society of Applied Physics, Nagoya, Vol. 3, pp. 918 (1994) [in Japanese].
5. Y. Komma, N. Ito, M. Yamagata, K. Urairi, S. Nishino and S. Mizuno: Extended Abstracts of The Japan Society of Applied Physics, Nagoya, Vol. 3, pp. 917 (1994) [in Japanese].

6. Y. Komma, Y. Tanaka, K. Urairi, S. Nishino and S. Mizuno: Jpn. J. Appl. Phys. **32**, 5214 (1993).
7. Y. Komma, S. Kuwamoto, H. Aikou, K. Urairi, M. Yamagata and Y. Tanaka: Extended Abstracts of The Japan Society of Applied Physics and Related Societies, Funabashi, Vol. 3, pp. 1073 (1997) [in Japanese].
8. Y. Tanaka, Y. Nagaoka and M. Ueda: Jpn. J. Appl. Phys. **26** (1987) 121.
9. Y. Komma, K. Urairi, Y. Shibata, S. Mizuno, M. Yamagata and Y. Tanaka: Extended Abstracts of The Japan Society of Applied Physics, Kanazawa, Vol. 3, pp. 956 (1995) [in Japanese].
10. Y. Tanaka, M. Yamagata, Y. Komma, S. Mizuno and M. Sunohara: Post-deadline Papers Technical Digest of ISOM '95, P-38, pp. 15 (1995).
11. K. Goto, K. Mori, G. Hatakoshi and S. Takahashi: Proc. Int. Symp. on Optical Memory, 1987, Jpn. J. Appl. Phys. **26** (1987) Suppl. 26-4, p. 135.

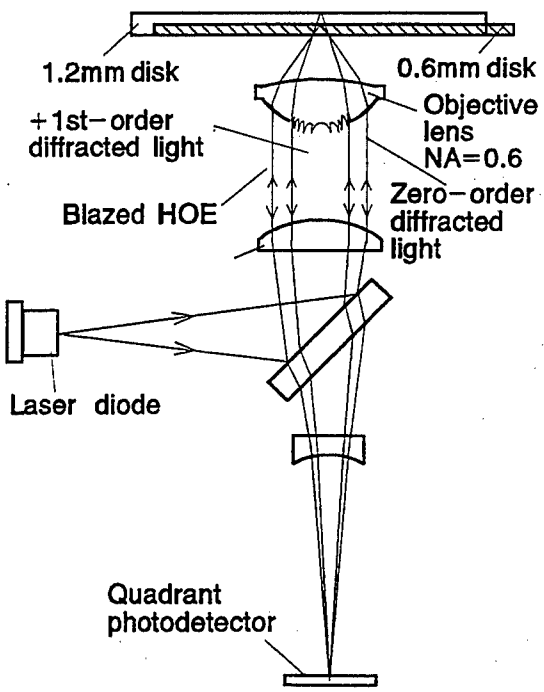

Fig.1. Optical configuration of dual focus optical head.

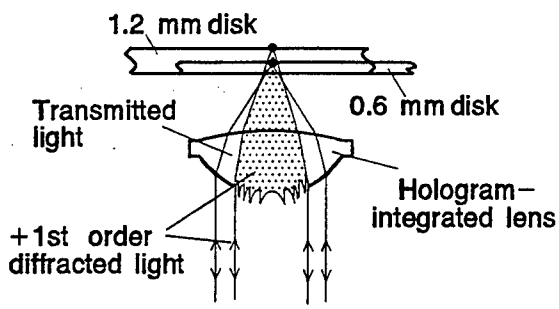

Fig. 2. Function of HOE in dual focus optical head.
For 0.6 mm disk, zero-order diffraction is utilized on both forward and backward paths.
For 1.2 mm disk, +1st-order diffraction is utilized on both forward and backward paths.

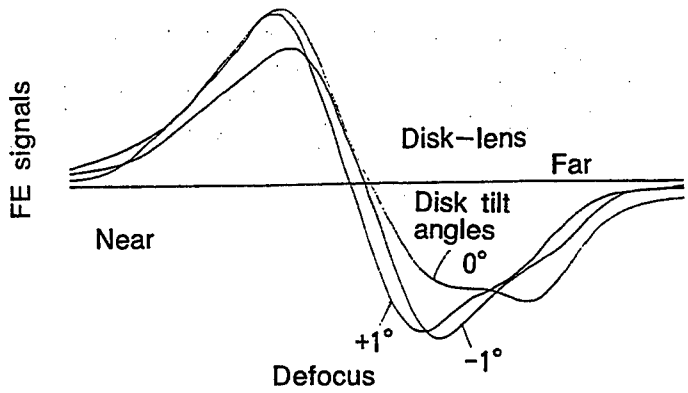

Fig. 3. FE signals for a 1.2 mm disk using HOE with sawtooth grating profiles.

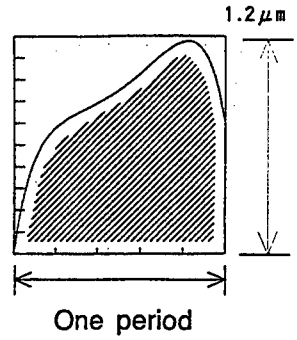

Fig. 4. Grating profile improved to suppress 2nd−order diffraction efficiency.

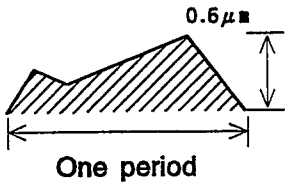

Fig. 5. Simplified gating profile.

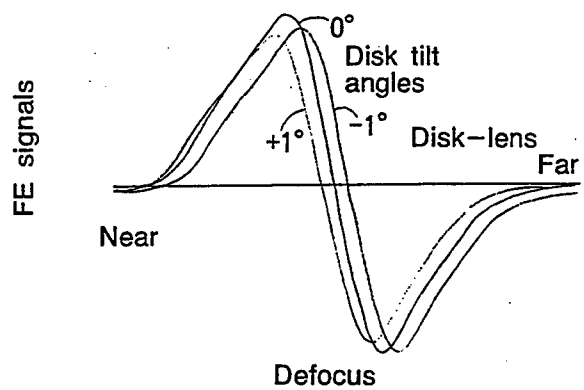

Fig. 6. FE signals for a 1.2 mm disk using HOE with optimized grating profiles.
Each curves are drawn with a shift for every disk tilt angle in horizontal axis for clear indication.

Counterfeit-Deterrents for Surface-Relief Diffractive Optical Elements

Daniel H. Raguin, Robert McGuire, Geoffrey Gretton
Rochester Photonics Corporation, 330 Clay Road, Rochester, NY 14623
P: (716) 272-3010, F: (716) 272-9374

Introduction

Surface-relief diffractive optical elements (DOEs) have a wide range of applications in present-day optical systems. DOEs have been used for the achromatization, color-correction, and athermalization of imaging systems. Diffractive phase plates are used as fanout gratings in optical interconnect and laser machining applications. Phase plates are also prevalent in display and alignment applications whereby they are used to generate arrows, company logos, and grids and lines, respectively. The ability to design and fabricate high-quality, precision, surface-relief, DOE masters requires a high level of intellectual property in addition to sophisticated manufacturing infrastructure. However, once a high-quality DOE is produced, it is an easier task to produce polymer replicas of the surface using technologies such as cast-and-cure, embossing, and injection molding.[1] The technology to perform high-quality replicas of DOE surfaces is becoming more prevalent globally. As the volume of surface-relief DOEs inserted into the marketplace increases, one must consider measures to deter unauthorized reproductions of one's intellectual property. Counterfeiting is a $50 billion dollar a year business,[2] and although most of the items counterfeited include computer hardware and software, clothing, and perfume, DOEs, as their market-presence increases, will attract counterfeiters.

Although diffraction gratings have been used to prevent counterfeiting of numerous non-optical products,[3] in this paper we present several counterfeit-deterrent measures for optical diffraction gratings themselves. The technology illustrated does not prevent or make replicating a particular DOE surface more difficult. It does, however, allow one to determine with certainty which company fabricated the original master. From this information, one can determine whether or not the replica is an authorized reproduction or not, and the appropriate actions can be taken.

Counterfeit-Deterrent Schemes for DOEs

The first counterfeit-deterrent scheme to pursue is patent or trademark protection. This can be applied to novel optical system designs as well as to phase plates that project a company logo or other trademarked image. However, most DOEs, due to prior art, cannot be protected using such legal means. One may mark a DOE by creating a surface-relief structure in the image of the company name or serial number at the edge of the diffractive clear aperture. Although a useful practice, it will not deter counterfeiters since the trademarked area of the DOE can easily be masked and the subsequent element replicated.

The solution to counterfeit deterrence is to embed a pattern into the clear aperture of a DOE so that it cannot be masked. These identification markings must be designed so that there is little interference with the function of the DOE. The identification markings proposed can be divided into two categories based upon the inspection scheme used to identify the source of the original DOE master.

1. Microscopic inspection of the DOE surface
2. Optically probing the DOE surface

In Option 1, one adds surface-relief identification marks to a DOE that represent serial numbers or the company logo. These DOE marks can be inspected underneath a high-power microscope for identifications purposes. Through the use of laser pattern generation, contact, or projection lithography one can pattern such identification marks. To help minimize any interference with the DOE's function, the company logo or identification mark can be written using one-micron lithography, and the identification mark need only take up a 10 μm by 30 μm area. This marking can be repeated across the clear aperture of

the diffractive element. Since most DOEs operate with beams of radiation at least 1 mm in diameter, one can repeat the identification mark every 500 μm or so, see Fig. 1(a). If tiled in a 2-D grid, then the identification marks encompass a mere 0.12% of the area of the DOE, and therefore have negligible effects on the DOE's performance. If larger identification marks are required, and if one wants to tile the marks with a smaller separation distance, one can pattern the surface such that phase depth of the marks, see Fig. 1(b) are 2^1 for the design wavelength. In this manner, for monochromatic applications, one can tile a DOE with identification markings that reach a density of 100% without affecting the fundamental operation of the DOE.

In Option 2, one adds identification marks to a DOE master that do not require a high-power microscope for inspection. Instead one adds high-frequency gratings, see Figs. 2 and 3, to the surface such that an optical probe beam can be used to detect the presence of the added structures. To ensure that the high-frequency gratings do not interfere with the intended operation of the DOE, one uses the grating equation to choose a grating period fine enough that for the DOE's operating spectral range and field-of-view, no diffracted order other than the zeroth propagates. The high-frequency grating can be added holographically, through e-beam lithography, or through optical lithography, depending upon the grating frequency chosen. During the fabrication process of the high-frequency grating, one masks the clear aperture of the high-frequency grating such that it outlines a company logo or similarly appropriate identification mark. When the DOE master or subsequent replicas are illuminated with the appropriate wavelength of light at oblique angles of incidence, the diffracted light outlines identifying letters, numbers, or images, see Fig. 2(b). It should be noted that the diffraction efficiency of the high-frequency grating can be well below 1% and still be detectable using a bright light source. In this manner, the effect of the high-frequency grating upon the phase of the transmitted radiation during normal operation of the DOE can be minimized by fabricating very shallow (<100 nm) surface-relief structures.

For machined DOEs (e.g., single-point diamond turned diffractive lenses), one can add a high-frequency grating to the surface directly, see Fig. 3. Although the high-frequency grating will not diffract radiation in the shape of an identifying mark, one can control the feed rate of the machine to create a grating period that varies with zone position. In this manner, a unique high-frequency pattern can be transcribed to the surface, that can be detected at large angles of incidence by a probe beam. By measuring the scattering angles for different zonal positions, a company can determine whether or not a particular DOE can be traced back to one of their DOE masters.

Summary

As the ability to replicate and reproduce diffractive optical elements becomes more prevalent globally, one must begin to think of measures for protecting one's technological ability to fabricate a DOE master. We have presented several options for placing identification marks on surface-relief DOE elements. Although these markings do not make the DOE more difficult to copy, they do serve to deter would-be counterfeiters. The markings allow one to identify the master from which a particular replica was fabricated. By then tracing the sales for that particular product, one can determine whether or not the DOE in question is an authorized replica, and if not, the appropriate legal action can be taken.

At the conference, we will illustrate experimental results of the counterfeit deterrent schemes presented.

References

[1] See, for example, M. T. Gale, *et al*, "Fabrication of continuous-relief micro-optical elements by direct laser writing in photoresist," Opt. Eng. **33** (1994), pp. 3556-3566.

[2] Product Counterfeiting (and Diversion) Protection Conference, PIRA, 17-18 NOV 97, Orlando, FL.

[3] See, for example, M. T. Gale, "Buried dielectric gratings: a new class of security features," SPIE Proc., **1210** (1990), p. 83, and Chock E., "Holographic bank draft," U.S. Patent 5,267,753, Dec. 7, 1993.

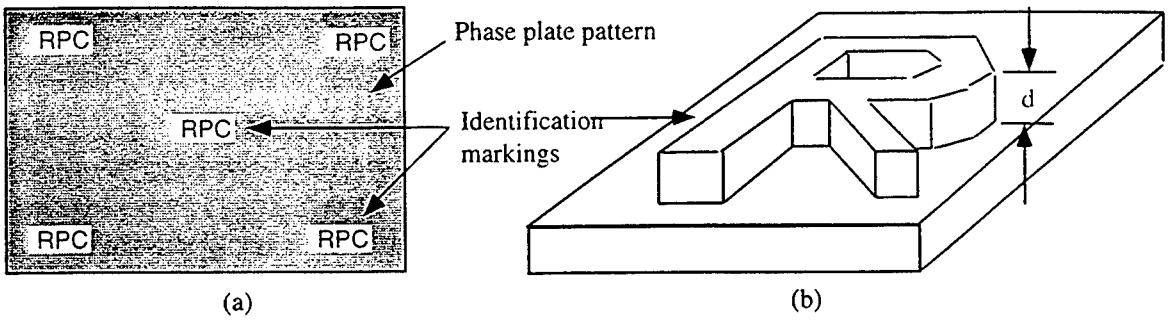

Fig. 1. Counterfeit deterrent marks for DOEs. (a) Phase plate pattern with identifying marks. Fraction of area taken up by security marks can be less than 1% of total area or (b) height d of surface-relief marks can correspond to a phase height of 2^1 at the operating wavelength, to minimize the effect on the optical performance of element.

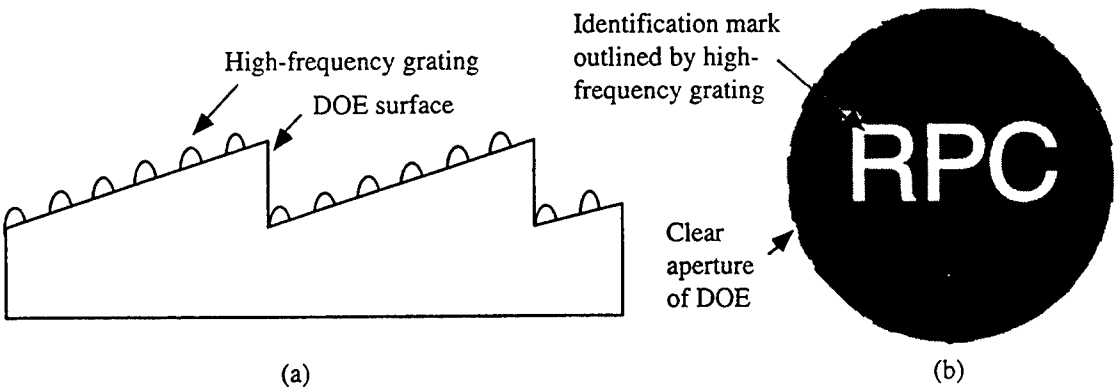

Fig. 2. (a) High-frequency grating added to DOE for identification purposes. (b) When DOE element is illuminated at grazing incidence one can detects markings on the surface due to high-frequency grating areas in the shape of letters that diffract light. Under normal operation, the high-frequency grating is too fine to diffract light and does not interfere with the desired operation of the DOE.

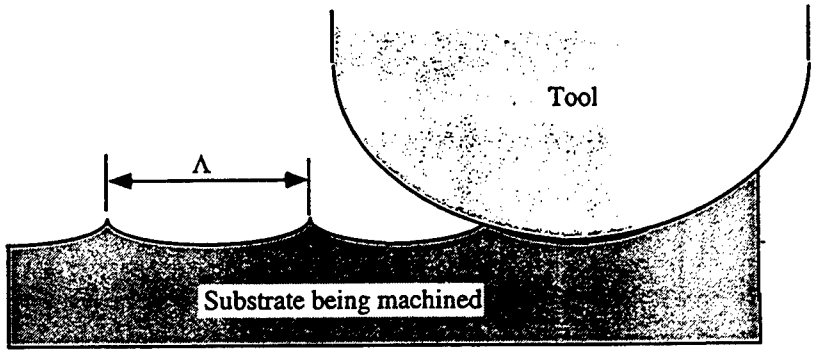

Fig. 3. In machined gratings (e.g., single-point diamond turning), by controlling the feed rate of the tool, one can create a high-frequency grating superimposed upon the diffractive lens being cut. The resulting grating spacing Λ can be varied with radius position to create a unique optical signature when probed by laser beam at oblique angles of incidence.

Dual Element Diffractive Element Algorithm for Beam Shaping and Phase Encryption

Eric G. Johnson and Adam Fedor
Digital Optics Corporation
5900 Northwoods Parkway, Suite J
Charlotte, NC 28269
(704)599-9191 eric@doc.com

ABSTRACT

This paper illustrates a technique for phase encryption and beam shaping using two diffractive elements in a cascaded optical system. The method is based on the method of projections and can be used to form both intensity and phase distributions in the output plane.

SUMMARY

Phase encryption is the art of encoding information into a phase function for security and/or information storage. Refregier and Javidi (1995) introduced a cascaded phase element system using a random encoding process. Figure 1 illustrates the optical setup. In their system, the image was encoded into a white stationary sequence. This method has advantages in terms of its security, but the phase masks are difficult to fabricate. In this paper, an alternative phase encryption methodology is explored for cascaded diffractive elements. Additional examples will also be presented for phase and amplitude mappings for beam shaping applications.

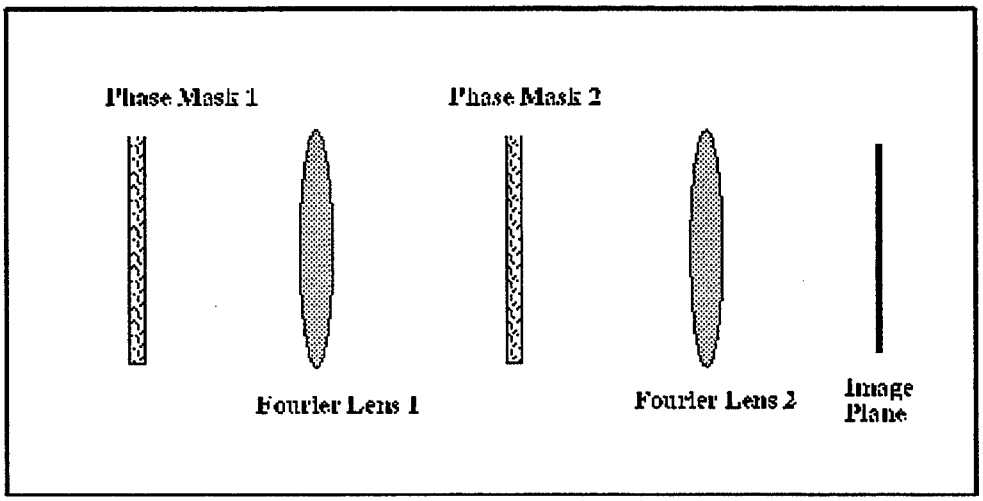

Figure 1. Optical implementation of a phase encoded image using random phase masks as proposed by Refregier and Javidi (1995).

In the 4f correlator design, two diffractive phase elements are cascaded in a coherent optical correlator architecture. The first phase element, $\phi_1(x,y)$, lies in the front focal plane of the first lens, f_1, this phase function is then Fourier transformed through propagation. At the Fourier plane of the first lens system, a second phase function, $\phi_2(x,y)$, is used to phase filter the output of the Fourier transformer. Studying this process, it is easily concluded that the design follows that of the cascaded Method of Projections as illustrated in Figure 2 (Johnson and Brasher 1996).

$$
\begin{array}{ccccccc}
(f_1) \Rightarrow & [L_1] & \Rightarrow (f_2) \Rightarrow & \{C_2\} & \Rightarrow (f_3) \Rightarrow & [L_2] & \Rightarrow (f_4) \\
\Uparrow & & & & & & \Downarrow \\
\{C_1\} & & & & & & \{C_3\} \\
\Uparrow & & & & & & \Downarrow \\
(f_8) \Leftarrow & [L_1^{-1}] & \Leftarrow (f_7) \Leftarrow & \{C_4\} & \Leftarrow (f_6) \Leftarrow & [L_2^{-1}] & \Leftarrow (f_5)
\end{array}
$$

Figure 2. Dual Element Method of Projections Algorithm.

As an example of this 4*f* encryption method, a sample function was selected for encryption. The input function for the cascaded element was a collimated wave in a 64 by 64 array padded with a 32 pixel border of zero intensity. This border was incorporated to minimize the aliasing effects associated with the Fourier Transforms. The phase functions ϕ_1 and ϕ_2 were intialized with a random number $r \in [-\pi/2, \pi/2]$. The desired signal was a binary image of the letter E. After 100 iterations through the dual element algorithm, the resulting phase functions $\phi_1[n,m]$ and $\phi_2[n,m]$ are illustrated in Figures 3 (a) and (b). The resulting image intensity and phase are given in Figures 4 (a) and (b). As can be observed, the resulting image is very defined; however, the phase in the image plane is somewhat arbitrary. This is due to the signal constraints on the image intensity and not any placed on the phase. However, phase constraints could be placed on the image, if so desired. The residual degradation around the edges of the resulting intensity are due to the bandpass filtering of the hard aperture located around the second phase element.

REFERENCES

E.G.Johnson and J.D. Brasher, Opt. Lett. **21**, 1271-1273 (1996).

P. Refregier and B. Javidi, Opt. Lett. **20**, 767-769 (1995).

H. Stark, ed., *Image Recovery: Theory and Application*, (Academic Press, Inc., 1987).

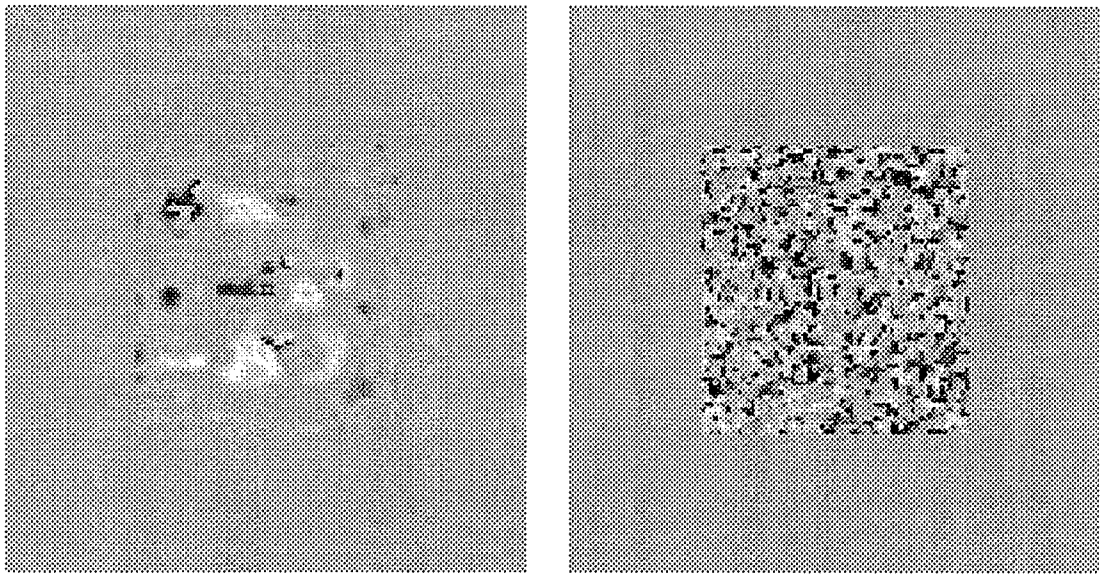

(a) (b)

Figure 3. Resulting phase functions for dual element optimization algorithm using the Method of Projections: (a) $\phi_1[m,n]$ and (b) $\phi_2[m,n]$.

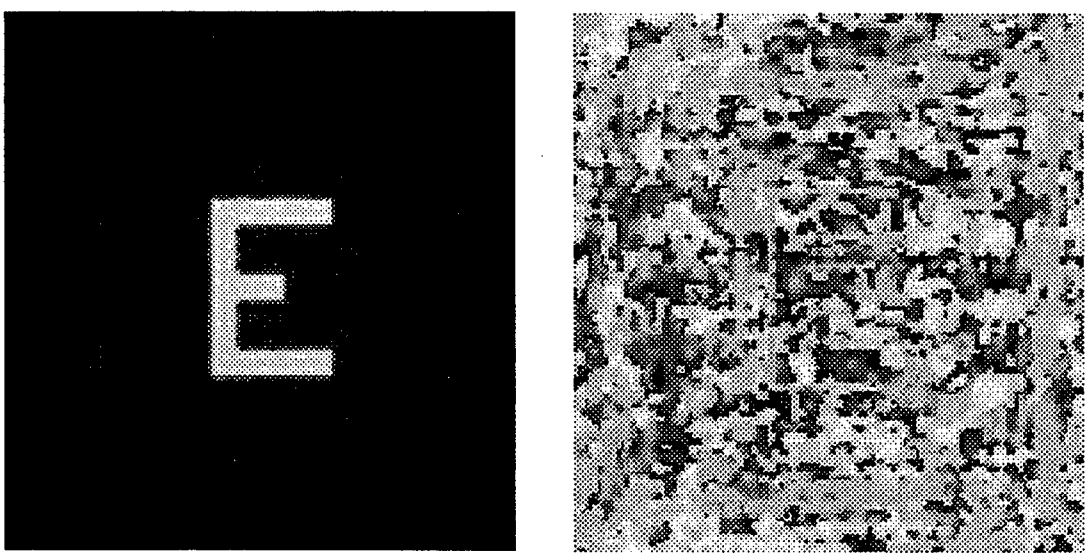

(a) (b)

Figure 4. Resulting image for dual element optimization algorithm using the Method of Projections : (a) image $f[m,n]$, and its corresponding phase $\vartheta[m,n]$.

Diffractive optic power monitor for use with a VCSEL source

B.Fritz, J.A Cox, T.Werner, and J. Gieske

Honeywell

Honeywell Technology Center
3660 Technology Dr.
Minneapolis, MN 55418

612.951.7711
612.951.7438 Fax

fritz_bernie@htc.honeywell.com

Diffractive optical elements (DOE's) were designed and fabricated to provide a means both for monitoring vertical-cavity-surface-emitting-laser(VCSEL) output power and for coupling the VCSEL output onto a fiber. The design put two DOE's on opposite sides of a glass cover positioned over the VCSEL header/can. The power monitor DOE, located on the inner surface of the cover glass, operates in reflection and focuses ~2% of the emitted radiation into an annular ring centered on the VCSEL. Approximately 88% of the transmitted light is in the zero order and is available for focusing on to a fiber by a second DOE located on the back (outer) surface of the cans cover glass.

From considerations of both eye safety and minimum feature size in the DOE's, the final design specified a blaze of three phase levels in the reflective DOE (power monitor) and four phase levels in the transmissive DOE (fiber coupler), giving theoretical diffraction efficiencies of 68% and 81%, respectively. Because the minimum Fresnel zone width in both DOE's is ~2.5 microns, direct-write electron-beam lithography has to be used in order to fabricate the phase profiles with minimum loss in efficiency from process errors.

In designing the power monitoring element various approaches were evaluated. The VCSEL was to sit on a silicon detector that would monitor the VCSEL's output power. The power monitoring element would sample the VCSEL's wavefront and redirect it onto the power monitor detector. A major issue was that the VCSEL's wavefront be completely sampled and not partially sampled. Complete sampling of the VCSEL's wavefront would eliminate VCSEL spatial moding issues. The solution was a diffractive structure used in reflection which mapped the VCSEL source onto an annulus on the power monitor detector. Figure 1 shows the VCSEL module with the diffractive optic window used to sample the VCSEL's wavefront and image onto the detector power monitor.

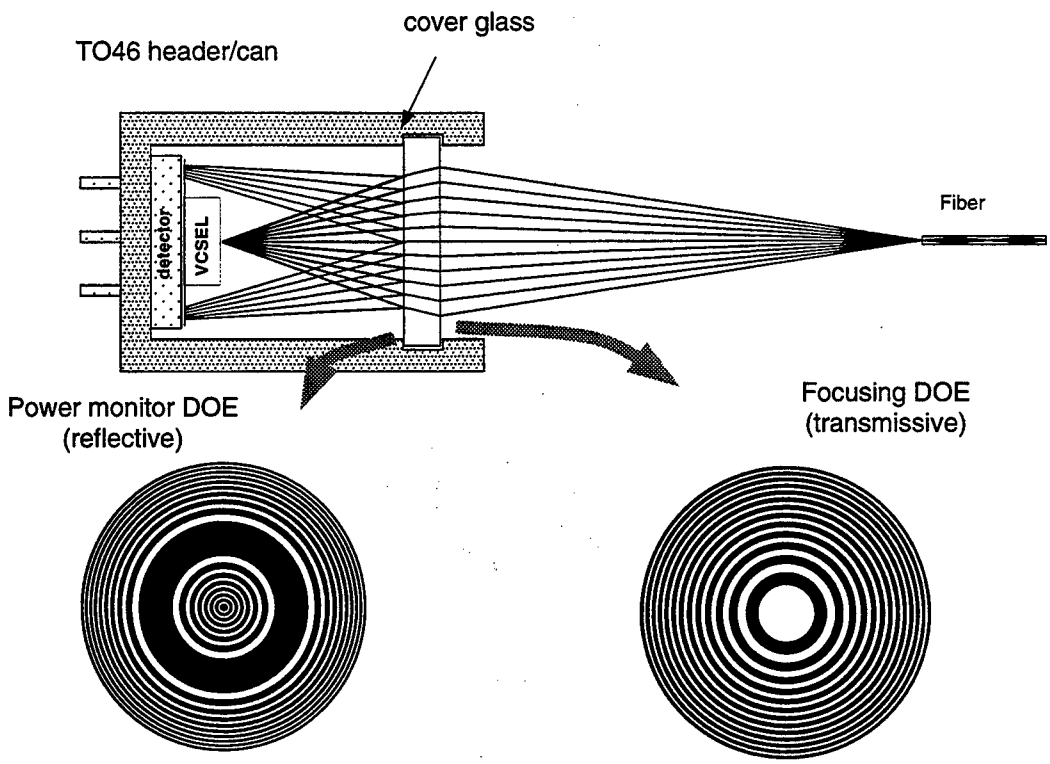

Figure 1. VCSEL module with diffractive optics

On the second side of the window a positive power transmissive difffractive lens is placed to couple the VCSEL output onto a fiber. Shown also in Figure 1 is the representative diffractive element structure.

To verify the power monitor concept, a lower efficiency, one sided, two-level DOE's were fabricated using standard contact lithography of the reflective and transmissive power monitor elements. This was feasible since ~1.25 micron linewidths are attainable with contact lithography and no mask alignment is required for two phase levels. Although both the reflective and transmission DOE's have only ~40% diffraction efficiency, we were able to test several design variations.

Preliminary examination of the transmissive elements indicated that the spot size was ~30 microns (as designed) and at approximately the correct distance from the DOE. More precise measurements will be done later.

Numerous reflective power monitor elements were examined closely. The source consisted of a 15 micron pinhole at the focus of a 10x microscope objective illuminated by collimated light at 850.0 nm. The wafer containing the DOE's was positioned over the source with a three-axis

micrometer stage, and the ring image of the source was observed with a microscope looking through the backside of the wafer. A DOE under evaluation was centered over the source and the source-to-DOE separation adjusted to bring the ring sharply into focus in the plane of the source. According to design, this separation should be 1.746 mm. The actual source-to-DOE separation was measured with a micrometer drive on the microscope, as was the ring diameter. The quality of the ring was noted qualitatively, and an electronic image was captured with a CCD camera a stored. The performance of the reflective power monitor DOE's showed a well defined ring with uniform brightness and ring diameters consistent with the design. The average source-to-DOE separation was 1.760 mm.

Waveguides and Diffractive Elements for Non-contact Sensors: Analysis

Palle G. Dinesen, Lars Lading, and Jens-Peter Lynov,
Optics and Fluid Dynamics Department
Risø National Laboratory
P.O. Box 49
DK-4000 Roskilde, Denmark

E-mail: lars.lading@risoe.dk
Phone: +45 4677 4501

Jan S. Hesthaven
Div. of Applied Mathematics
Brown University
Providence, RI, USA

Summary

A number of optical techniques for measuring the dynamic motions of fluids and solids are based on quasielastic light scattering and detection by light beating (dynamic interferometry). Most of the methods are used for scientific investigations. The set-ups are generally bulky and delicate to operate. A considerable reduction in size can be obtained by applying diffractive (or holographic) elements.[1,2,3]

Sensors: An example of a sensor for non-contact measurement of visco-elastic properties (viscosity and surface tension) of liquids is shown in Figure 1. Implementations both in glass, III-V, and polymers are considered. The diffractive structures serve to couple light out of the planar waveguide in two single mode beams with slightly different directions of propagation, but intersecting at the locations of their beam waists on the surface. The power of the first beam should be as high as possible, whereas the power of the second beam should only be about one percent of the power of the first beam. Light from the first beam diffracted by thermally excited capillary waves on the surface in a well defined direction is collected by a third diffractive structure on the planar waveguide. This light interferes with surface reflected light from the weak beam on the photodetector. The dynamics of the capillary waves are reflected in the spectrum of the photodetector from which the viscoelastic properties can be inferred.

A second example is shown in Figure 2 showing an integrated lay-out of a laser time-of-flight velocimeter. An essential feature is that the transmitter structure consists of partly multiplexed diffractive lenses. A well-defined displacement of the two lenses smaller than the lens diameters is necessary in order to obtain a calibration of the sensor that is independent of the distance between sensor and target.

Analysis and design: A key-element is to design the diffractive structure(s) so that the desired coupling is obtained, which implies well defined beam properties and a high overall efficiency. Our approach is as follows:

1. The desired field distribution on the target is established on the basis of the physical principles of the measurement.
2. The corresponding field distribution right outside the planar waveguide is found by simple paraxial free-space propagation.
3. The surface diffractive pattern is established on the basis of simple non-paraxial diffraction theory.
4. The diffractive structure is analyzed numerically by a new pseudospectral time-domain method. A variation of key-parameters provides the basis for obtaining an actual field distribution close to the desired distribution and also a high coupling efficinecy.

The numerical method is based on a so-called pseudo-spectral solution of Maxwell's equations in the time-domain. Pseudo-spectral methods are well-known within the field of fluid dynamics and have recently been employed on electromagnetic scattering problems[4]. In brief, such methods are superior to e.g. finite difference methods due to the low number of points needed to accurately resolve the electromagnetic wave. Typically, 7-10 points per wavelength is sufficient, whereas the Finite Difference Time-Domain methods (FDTD) requires 40 or more points per wavelength.

In the time-domain, Maxwell's equations form a set of hyperbolic differential equations which facilitates the decomposition of the full computation domain into sub-domains through the use of characteristic variables. Each sub-domain can be arbitrarily shaped and using transfinite blending functions[5], the sub-domain is mapped to the unit square. A Chebyshev collocation scheme is then employed to solve the Maxwell's equations. In such a scheme, the equations are satisfied at certain points, the collocation points, and the differential operators are replaced by matrix operators. Unlike the FDTD, where the derivatives are estimated only from neighbor points, in this pseudo-spectral scheme, the derivatives are calculated using information from the entire sub-domain. Hence, the increased accuracy.

When the solution in each sub-domain has been found, the global solution is found by patching the local solutions employing the characteristic variables of the equations. Between sub-domains of different refractive indices, the physical boundary conditions are enforced strongly.

The system is advanced in time using a fourth-order Runge-Kutta scheme.

Figure 3 shows an example of wave propagation in a thin film waveguide where the surface of the top cladding layer is modulated. The structure is excited at $z=0$ with the TE_0-mode of the un-perturbed waveguide. Shown is the E_y-component at t=300 periods.

Writing of structures: The actual writing of the surface structures is done with a novel high performance laser plotter with gray-scales (8 bits). However, the resolution of the current plotter is not adequate for the structures necessary in the cases discussed here. A new plotter with adequate resolution and repeatability is currently under construction.

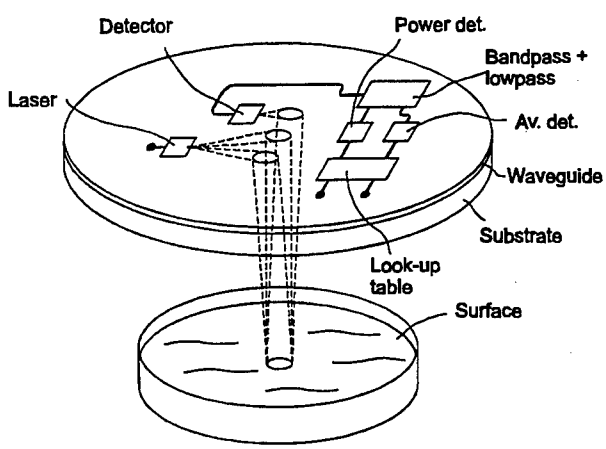

Figure 1. A completely integrated system for measuring visco-elastic properties of liquids. The system is based on a planar waveguide, surface diffractive structures, an embedded distributed-feedback laser and an embedded detector.

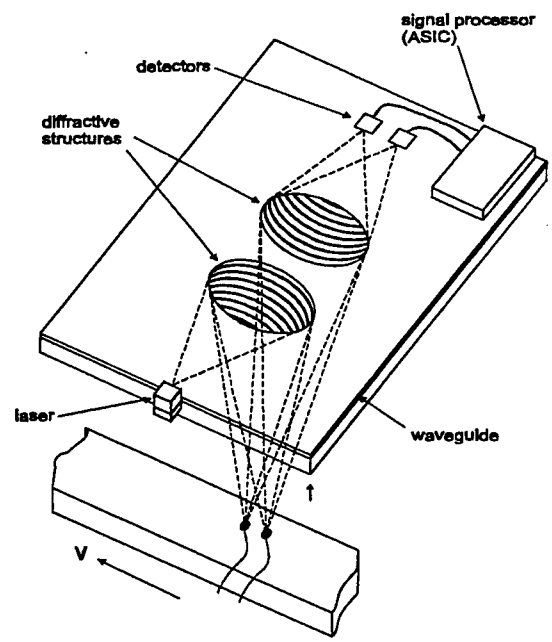

Figure 2. A velocimeter based on measuring the time of flight between two focal spots.

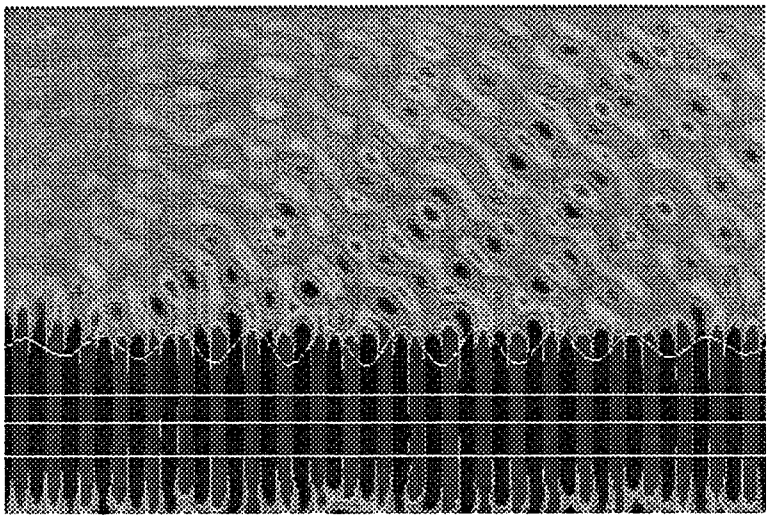

Figure 3. Snapshot of the E_y-component of a TE mode propagating in an out-of plane DOE. Boundaries between layers of different dielectric constants are indicated by white lines.

[1] S. Ura, Y. Furrukawa, T. Suhara and H. Nishihara, "Linearly focusing grating coupler for integrated-optic parallel pickup," J. Opt. Soc. Am. A **7**, 1759 - 1763 (1990).

[2] Steen G. Hanson, Lars R. Lindvold and Lars Lading, "A surface velocimeter based on a holographic optical element and semiconductor components", *Meas. Sci. Technol.* **7**, 69-78, (1996).

[3] Lars Lading, Carsten Dam-Hansen, and Erling Rasmussen, "Surface light scattering: integrated technology and signal processing", Appl. Opt. **36**, 7593-7600 (1997).

[4] B. Yang, D. Gottlieb, and J. S. Hesthaven, "Spectral Simulation of Electromagnetic Wave Scattering", *J. Comput. Phys.* **134**, 216-230 (1997).

[5] W. J. Gordon and C. A. Hall, "Transfinite Element Methods: Blending-Function Interpolation over Arbitrary Curved Element Domains", *Numer. Math.* **21**, 109-129 (1973).

Diffractive Optics and Micro-Optics

Joint Session with International Optical Design Conference

Wednesday, June 10, 1998

J. Allen Cox, Honeywell, Inc.
Presider

JWC
1:30pm–3:00pm
Koa Room

Diffractive Optics in the Thomson Group

J. Rollin
Thomson CSF Optronique
Rue Guynemer, BP55
78283 Guyancourt Cedex
France

C. Puech
Angenieux
42570 St Heand
France

P. J. Rogers
Pilkington Optronics
Glascoed Road, St Asaph
Denbighshire LL17 0LL
U.K.

Summary

1. Introduction

Two parameters govern the performance of a surface-relief diffractive:-
- the phase function, given by the radial positions of the diffractive steps, which provides a means for counterbalancing both chromatic aberration and spherochromatism;
- the diffractive step heights, and the zone shapes between these steps, dictate the grating efficiency within a selected diffractive order.

Due to the anomalous dispersion of a diffractive profile, a hybrid lens employing such a surface on a refractive substrate can achieve color correction without requiring the optical material pairing used in conventional refractive designs. Furthermore, while most conventional designs for far infrared applications are made of germanium because of its high refractive index and low dispersion, a diffractive surface allows the use of materials not normally considered.

An example of the above is the replacement of germanium in a system where high temperatures are encountered. Germanium suffers from increased bulk absorption and a large change in refractive index as the temperature rises, resulting in low transmission and thermal defocus respectively. Higher dispersion materials do not show these drawbacks and can be achromatized by the use of a diffractive surface, the change of grating power with temperature is quite insignificant since it is only related to the expansion coefficient of the substrate material.

The zone transition (step) heights are formulated such that a 2π phase delay is introduced at each zone boundary and, therefore, energy from all zones is in phase at one diffractive order for a specific combination of wavelength and incidence angle. Away from the latter, diffraction efficiency calculations need to be made over the extended scalar regime.

A number of widely-ranging hybrid optic examples have been manufactured within the Thomson Group and the paper will highlight a number of these. Topics such as the effect on MTF of diffractive efficiencies (including those from unwanted orders), obscuration & stray light, and the specification of a diffractive surface will be addressed.

Many specifications relevant to manufacturing issues - such as roughness, step height tolerance, radius of the diamond tool in single-point turning - can be defined at the very start of a project : these aspects will be outlined in examples. The diamond turning means, and the associated metrology, available within the Thomson Group will also be described.

2. Example in the 8-12μm waveband.

The first example deals with a far infrared telephoto lens having a focal length of 440mm, an aperture of F/4.4, and comprising only two lenses. The conventional all-refractive solution is fabricated from germanium, while its diffractive counterpart uses two ZnSe aspheric lenses, the first of which is diffractive with 39 diffractive zones over a clear diameter of 100mm.

Once manufactured, the hybrid objective was tested : both MTF and diffractive efficiencies within useful and neighboring regions were measured. The final paper provides a more detailed account of these procedures. Figure 1 shows the diffractive design and demonstrates the benefits by comparison with the original conventional design.

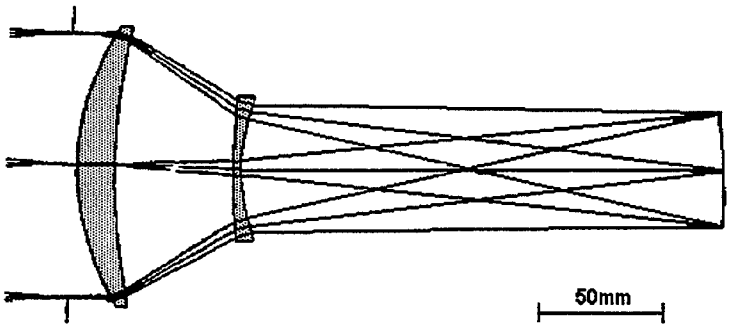

Temperature	Ge system	ZnSe system
20°	0.94	0.92
85°	0.65	0.92

Thermal	Ge system	ZnSe system
Defocus	24.4mm	9.8mm

Figure 1: ZnSe diffractive telephoto lens and its advantages compared with a conventional design

3. Examples in the 3-5μm waveband

The 3-5μm waveband is a fruitful region of the spectrum for the use of a diffractive surface due of the lack of an optical material that has very low chromatic dispersion. Two examples below illustrate the range of applications:- a diffractive singlet that uniquely satisfies both the requirements of achromatism and athermalism; and a compact low-mass zoom lens only made possible by the use of two diffractive surfaces.

A 13-zone arsenic trisulfide hybrid optic of 150mm focal length and F/2 aperture has been designed to be of zero coma shape in order to cover a small field-of-view of about 1 degree. An arsenic trisulfide lens is almost athermal when housed in an aluminum body but has significant chromatic dispersion which can be removed by the use of the diffractive surface. The theoretical polychromatic MTF of the lens, which is currently under test, shows almost no change over a range of 110° in temperature - Figure 2.

A 220-88mm focal length zoom lens operating over fields-of-view of 5° to 12.5° at a high aperture of F/1.5 has been designed and fabricated. The fundamental requirements of achromatism in the fixed front lens and both zoom groups would have been very difficult in a conventional system of similar length due to high optical powers which would also have led to high mass. The latter have been avoided by the use of diffractive surfaces on both front lens and first zoom group - Figure 3. The use of silicon for the front lens means that the overall zoom lens is of low mass.

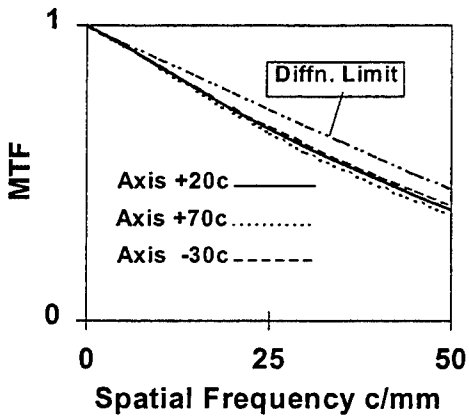

Fig 2: MTF for an As_2S_3 diffractive

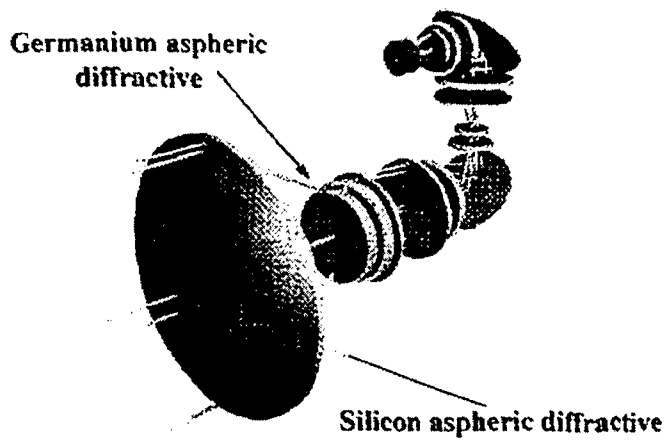

Fig 3: Compact, low-mass diffractive zoom lens

4. Manufacture

Many infrared optical materials - germanium, silicon, zinc sulfide (FLIR & multispectral), zinc selenide, arsenic trisulfide, KRS 5, and AMTIR-1 - have been diamond-turned successfully by the Thomson Group. Experience has shown that optimum feed rates and other parameters need to be determined for each material

Measurement of surface profile is one of the limitations in the manufacture of larger diffractive lenses : this will be alleviated by the special Form Talysurf that is being acquired in order to accommodate lenses larger than 300mm in diameter.

Surface statistics such as step profile & surface roughness are measured very accurately using a Zygo NewView - a scanning white light interferometer. Measurements have shown that step heights can be within 20nm of the typical required height of 1.60μm. Finite tool size leads to some non-verticality of the step and causes a small loss in transmission due to shadowing.

5. Conclusions

The experience resulting from the design and fabrication of diffractive optics in both thermal infrared wavebands is enabling the Thomson Group to formulate theoretical guidelines for their design, and also to define the optimum manufacturing tolerances.

6. Bibliography

"Using hybrid refractive-diffractive elements in IR Petzval objectives", A.P.Wood, SPIE Vol.1354 (1990)

"Predesign of diamond turned refractive/diffractive elements", M.J.Riedl, Conference on Binary Optics (1993)

"Use of hybrid optics in the 3-5μ infrared band", P.J.Rogers, SPIE Vol. 2540/13 (1995).

"Diamond turning of silicon optics", P.M.Parr-Burman, SPIE 2775/575 (1996)

"High aperture zoom optics, employing diffractive surfaces, in the 3-5 micron infrared waveband", M.Roberts, SPIE Vol.3129/120 (1997)

Ring toric optics for optical data-storage applications

Michael R. Descour and Daniel I. Simon
Optical Sciences Center
University of Arizona
Tucson, AZ 85721
(520) 626 5086
(520) 621 3389 FAX
michael.descour@opt-sci.arizona.edu

Ring-toric lenses are optical elements of use in optical data storage as focus-error and track-error sensing elements.[1,2]

We have designed and fabricated a set of diffractive ring-toric lenses of varying focus-ring radius. The ring radii varied from 80 μm to 500 μm. The lenses were designed and fabricated for operation at 635 nm. In all cases, the lens aperture measured 4 mm on a side and the focal length was 20 mm. Fabrication of a ring toric lens as a diffractive optical element (DOE) affords us accurate control over the ring radius (see Figures 1 and 2) and the lens's focal length. The next challenge is to increase the diffraction efficiency of the lens.

We are developing the capability to fabricate diffractive elements using grayscale photomasks.[3-6] This type of photomask offers the potential of a significant increase in diffraction efficiency. The increase in diffraction efficiency is achieved without the added complexity of fabrication with multiple binary photomasks. DOEs with useful functionality and practical diffraction efficiency can be fabricated with a single photomask. We plan to use an ion-milling machine as well as a reactive-ion etching system to fabricate DOEs with grayscale masks.

We plan to characterize the sensitivity of the DOE ring-toric lens to defocus. The experimental measurements will be related to predictions obtained from a lens design program.

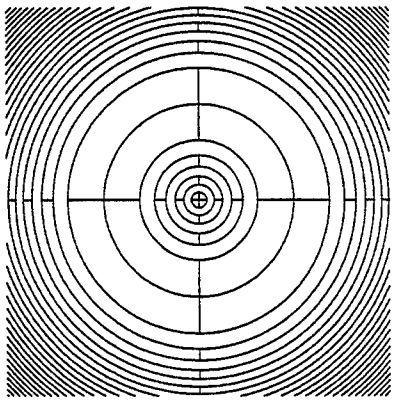

Figure 1. Center detail of ring-toric lens photomask. The depicted ring toric lens was designed for a ring radius of 300 μm and a focal length of 20 mm.

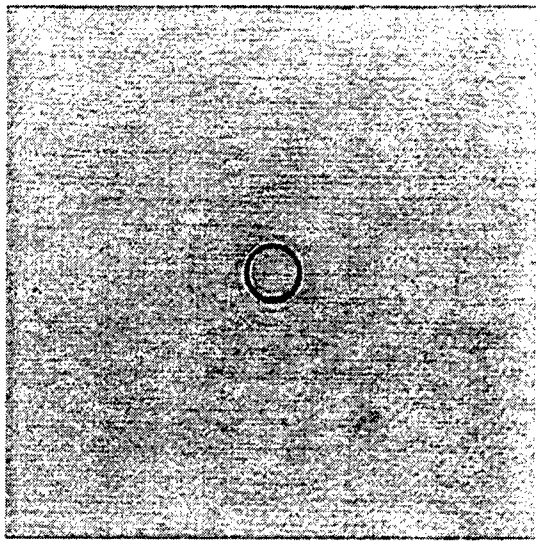

Figure 2. Ring focus, radius of 80 μm. The width of the ring is approximately 17 μm. The image is shown in negative contrast.

References:

1. M. Mansuripur, "Certain computational aspects of vector diffraction problems," *J. Opt. Soc. Am.*, **6**, No. 5, pp. 786-805 (June 1989).
2. M. Mansuripur, *The Physical Principles of Magneto-optical Recording*, Ch. 8 (Cambridge University Press, 1995).
3. W. Daeschner, *et al.*, *App. Opt.*, **36**, No. 20, 4675 (1997).
4. W. Daeschner, *et al.*, *J. Vac. Sci. Technol. B*, **14**, 3730 (Nov/Dec 1996).
5. T.J. Suleski and D.C. O'Shea, *App. Opt.*, **34**, No. 32, 7507 (1995).
6. D.C. O'Shea and W.S. Rockward, *App. Opt.*, **34**, No. 32, 7518 (1995).

Talbot array illuminators for high intensity compression ratios

Werner Klaus
Space Communications Division, Communications Research Laboratory
Ministry of Posts and Telecommunications
4 - 2 - 1 Nukui-kita, Koganei, Tokyo 184-8795, Japan
tel : +81 - 423 - 27 - 5769
fax : +81 - 423 - 27 - 6699
e-mail : klaus@crl.go.jp

Kashiko Kodate
Department of Mathematical and Physical Science, Japan Women's University, Tokyo 112, Japan

1. Introduction

The Talbot array illuminator (TAIL) is well known as an efficient diffractive optical element that transforms, in the near field, a spatially coherent monochromatic wave into a large number of bright spots. Its performance is generally measured in terms of the highest achievable intensity compression ratio, i.e., the maximum achievable ratio of the array illuminators grating cell area to the area of the bright spot (or spots) formed within the cell area.

Previous publications [1,2] have shown that a higher intensity compression requires a more complex surface profile of the grating, and hence a higher expenditure in fabrication, i.e., a larger number of binary masks when fabricated, e.g., by lithographic means. Due to the apparent huge variety of phase gratings providing a proper wavefront transformation in the near field, it seems furthermore difficult to theoretically determine the absolute minimum of phase levels required for a certain compression ratio, underlining the importance of looking constantly for new grating profiles with better performance.

In one of our recent publications [3], we discussed the one-dimensional (1D) phase profiles of a new family of TAIL's with features that make them very attractive to be used as high compression ratio array illuminators. In this paper, we take a more detailed look on the corresponding two-dimensional profiles, discuss briefly their theoretical diffraction efficiencies and present some experimental results.

2. Array illuminators providing high compression

The complete set of 1D profiles of the new TAIL's is described by the following two simple equations:

$$\phi(k,N_{1D}) = \pi(k-1)(N_{1D}-k)/N_{1D} \quad , \tag{1a}$$

$$\phi(k+N_{1D},N_{1D}) = \pi + \phi(k,N_{1D}) = \pi\, k(N_{1D}-k+1)/N_{1D} \quad , \tag{1b}$$

with $k = 1,2,\ldots,N_{1D}$ where N_{1D} denotes the 1D compression ratio. The 2D profile is obtained by simply superimposing orthogonally two 1D profiles. For simplicity, we consider here only quadratic elementary cells, hence $N_{2D} = N_{1D}^2$. The 2D profile for $N_{2D} > 4$ consists of $4N_{2D}$ [= $(2\ N_{1D})^2$] features

where the term feature refers to the smallest grating substructure of uniform phase. Note that the feature area equals the area of the spots to be generated.

The distances of maximum contrast and highest compression (mchc) are given by

$$z_{mchc} = z_t / (8N_{1D}) \quad , \tag{2}$$

with the Talbot distance $z_t = 2d^2/\lambda$ where d is the grating period and λ denotes the wavelength of the illumination. The 2D surface profile of an elementary cell for $N_{2D} = 16$ and the calculated intensity distribution at the closest mchc-distance is shown in Fig. 1(a) and 1(b), respectively. The new TAIL's provide four spots within the elementary cell area at the mchc-distance.

Of particular interest are the profiles designed for 1D compression ratios described by a power of two, i.e. 2^m. In these cases, the number of required masks equals the exponent m (similar to the case of binary Fresnel lenses) and, in addition, all masks that have been used to obtain the compression ratio 2^m can be reused to obtain the next higher compression ratio 2^{m+1}, as illustrated in Figs. 2(a) and 2(b) for the cases $m = 2$ and 3. Note however that the latter feature requires the spot size to remain constant but the grating cell area (or the spot period) to increase with increasing compression ratio.

3. Array illuminator efficiency

The efficiency of a diffractive optical element fabricated by using binary optics technology is mainly determined by two types of errors: (a) the etching depth error, and (b) the alignment error. To estimate the upper limit of the new TAIL's efficiency under the presence of such fabrication errors, we calculated the intensity distributions at the mchc distances using the non-paraxial scalar theory and assumed the grating feature size to be larger than about 15 wavelengths. Figure 3 shows for example the decrease in efficiency due to etching errors. We assumed that the relative etching depth error equally occurs for each new mask (i.e., for each new etching process). The numerical evaluations show that efficient high-compression array illumination (i.e., within 95% of the predicted non-paraxial values) requires the etching depth errors to stay below 10% and the alignment errors to remain below 3% of the feature size. With common error tolerances of nowadays binary optics technology of about 10% for the etching depth error and about 1 μm for the alignment error we conclude that nearly ideal illumination performance is obtained for spot sizes (feature sizes) at least down to 30 μm at $\lambda = 0.633$ μm.

4. Experimental evaluations

To confirm the theoretical results mentioned above we fabricated two quartz-glass phase gratings designed for the compression ratio $N_{2D} = 16$ and 1024, respectively. The former grating's elementary cell is shown in Fig. 1(a) with 4 phase levels requiring two lithographic masks. The latter is given in Fig. 4 with 32 phase levels fabricated by 5 masks. The feature size of the former TAIL amounts to 50 μm and of the latter TAIL to 30 μm. The measured intensity and phase distributions

observed behind both TAIL's will be presented.

References

1. P. Szwaykowski and V. Arrizón, Appl. Opt. 32, 1109 (1993)
2. C. Zhou and L. Liu, Opt. Commun. 115, 40 (1995)
3. W. Klaus, K. Kodate, and Y. Arimoto, J. Opt. Soc. Am. A 14, 1092 (1997)

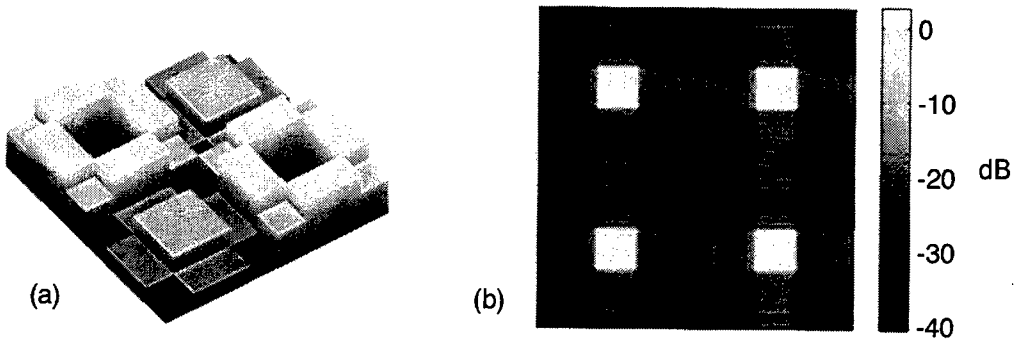

Fig. 1 (a) Surface profile of a TAIL designed for $N_{2D} = 16$, (b) intensity distribution at $z = z_t/32$

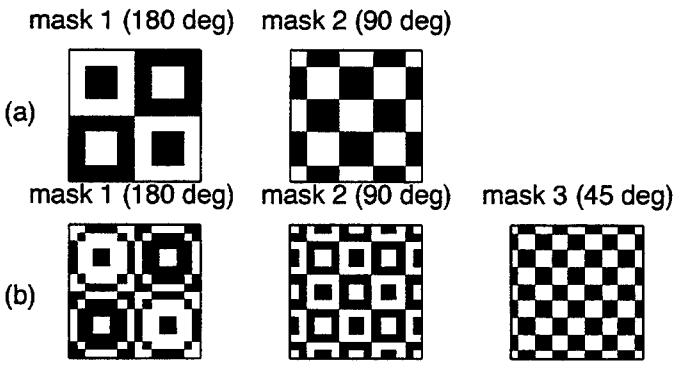

Fig.2 Mask pattern and etching depth for (a) m = 2 and (b) m = 3

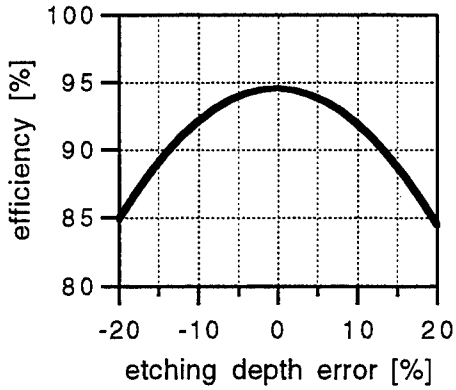

Fig.3 Efficiency vs. etching depth error

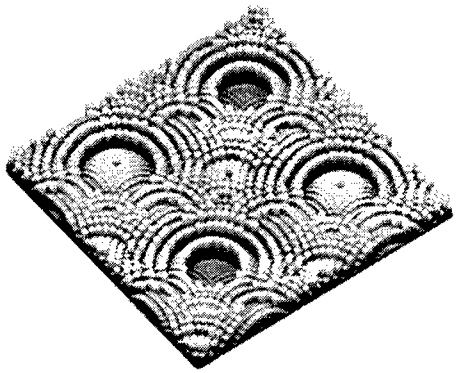

Fig.4 Surface profile of a TAIL designed for $N_{2D} = 1024$

Super resolution and Dammann gratings

Adolf W. Lohmann, David Mendlovic, and Zeev Zalevsky

Tel-Aviv University, Faculty of Engineering, 69978 Tel-Aviv, Israel
Email: mend@eng.tau.ac.il, Tel: 972-3-6408245, Fax: 972-3-6423508

The resolution of a system is defined as the finest detail that can pass through the system without being distorted. The motivation of the super resolution field is to handle the non resolved details using a given apriori information about the input signal [1], e.g. apriori knowledge on: object shape, temporal behavior, wavelength behavior, dimensions and polarization. The super resolution effect is achieved by exchange of degrees of freedom. For instance, let us assume that the spatial aperture of a system is small and some of the signal's information is lost due to this fact. If it is also apriori known that the signal's information is monochromatic, one may convert part of the spatial information into wavelength information, in such a way that the aperture of the system is synthetically expanded. Based on the distinction between the signal information and system's capabilities one may adapt the space bandwidth function (SW) of the signal to the SW function of the system using the Wigner chart [1].

One of the most brilliant approaches for resolving powers exceeding the classical limits is related to temporally restricted objects and based on two moving gratings [2]. In this optical setup, two synchronized moving gratings are attached to the input and output planes. Under the assumption of a stationary scene, the moving gratings generate replica of the scene spectrum, each encoded by different temporal dependence. Using an appropriate demodulation technique (second grating movement and integration along many cycles), this approach provides a synthetic aperture 3-5 times larger than the physical aperture of the system.

This interesting approach suffers from two disadvantages: The synchronization task between the two gratings and a distortion of the synthetic aperture due to the nonuniform intensity of grating diffraction orders.

The second problem has been solved [3] by using Dammann gratings instead of Ronchi ones [3]. In order to perform an experimental demonstration of this approach, a folded setup was used. Fig. 1 shows schematically the construction of this system.

An input beam hits the input mask that is assumed to be approximately independent of the time ("temporal restricted"). While saying "temporal restricted" we mean that the temporal spectral contributions are not allowed to overlap. Otherwise, de-multiplexing by the second grating and the integrator is not possible uniquely. Hence the object is sufficiently "temporally restricted" if its temporal bandwidth is less than the temporal carrier frequency caused by the moving grating. Close to the input mask, there is a rotating Dammann grating. This grating was drown as a ring structure, which provides one-dimensional movement with a velocity V. Due to the folding, the output is obtained at the same lateral plane as the input, thus the same Dammann grating can be used. This solves the synchronization problem. It was shown experimentally [3] that this configuration is able to increase significantly the effective aperture of the system.

Recently, a similar setup was used for experimental demonstration of a two dimensional super resolution performance [4]. Here, the simple Dammann grating has been replaced by a two dimensional grating, plotted in a spiral structure. When rotation is applied, two dimensional movement is achieved.

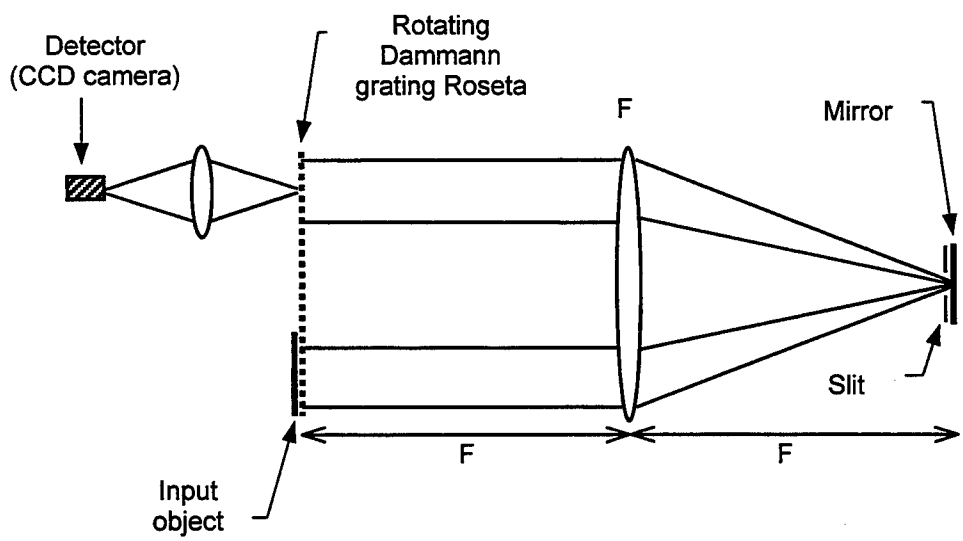

Fig. 1 Schematic illustration of the optical setup used for system experimental demonstration.

Other approaches for achieving super resolution are based on static gratings. These approaches are sometimes more attractive since they avoid the synchronization problem. Moreover, they may work also with non-stationary scenes. However, in these approaches one gains spatial resolution by paying with a smaller object field (either 1-D or 2-D). The first proposal along this line was performed by Grimm and Lohmann [5]. They have illustrated a technique for achieving a super resolution of 1-D object by placing a rotated grating. By attaching the grating to the sample one

observes Moire effect, i.e. demodulation of the high frequencies existing in the input. A second proposal was presented again by Lukosz. This time the two gratings are static and should be placed carefully in order to achieve the super resolution effect [6]. Here, a major problem is that one of the two gratings should be placed outside the imaging system (either before or after). This problem has been solved recently by adding a third grating to the system [7].

In all of these systems, the use of diffraction phenomena is the basis for achieving synthetic aperture. The grating creates the synthetic aperture and we claim that by replacing the Ronchi grating by a Dammann one, these three system types provide better performances.

References:

[1] D. Mendlovic and A. W. Lohmann, ""SW - adaptation" and its application for super resolution - Fundamentals," JOSA **A14**, 558-562 (1997), and D. Mendlovic, A. W. Lohmann and Z. Zalevsky, "SW- adaptation and its application for super resolution - Examples," JOSA **A14**, 563-567 (1997)

[2] W. Lukosz, "Optical systems with resolving powers exceeding the classical limit," JOSA **56**, 1463-1472 (1966).

[3] D. Mendlovic, A. W. Lohmann, N. Konforti, I. Kiryuschev and Z. Zalevsky, "One dimensional super resolution optical system for temporally restricted objects," Appl. Opt. **36**, 2353-2359 (1997).

[4] Mendlovic, I. Kiryuschev, Z. Zalevsky, A. Lohmann and D. Farkas, "Two dimensional super resolution optical system for temporally restricted objects," Appl. Opt. (to be published)

[5] M. A. Grimm and A. W. Lohmann, "Super resolution image for 1-D objects," JOSA **56**, 1151-1156 (1966).

[6] A. Bachl and W. Lukosz, "Experiments on superresolution imaging of a reduced object field," JOSA **57**, 163 (1967).

[7] Z. Zalevsky, D. Mendlovic and A. W. Lohmann, "Super resolution optical systems using static gratings," Appl. Opt. (submitted).

Design of holographic optical beam splitters based on thin grating sequential diffraction technique

Michael R. Wang
Dept. of Electrical and Computer Engineering
University of Miami
Coral Gables, FL
Tel. (305) 284-4041
Fax. (305) 284-4044

Bragg diffractions by superimposed transmission phase gratings are important schemes for the realization of optical beam splitters for optical fanout interconnection, neural network implementation, data storage, and parallel optical processing and computing. The theory of optical beam diffractions by superimposed transmission phase gratings have been developed by several authors [1-13]. However, the existing techniques are limited to 2-D diffraction geometry, suffering from numerical problems when the superimposed grating number increases, and/or restricted to small-angle diffractions. For 3-D diffractions by superimposed transmission phase gratings, required for holographic beam splitting applications, there is no simple theoretical model to treat such problem. Complete modal analysis [6,7] already yields complicated results for single-grating diffraction, because the grating vector can have an arbitrary orientation with respect to the plane of incidence. As a consequence the s- and p-polarized field components become coupled inside the grating region and can no longer be treated separately by conventional coupled-wave theory [14]. The coupled 3-D diffraction is much more complicated than the single-grating case. It is, so far, hard for a design engineer to determine suitable grating index combinations prior to device implementation. As a result, superimposed gratings are often recorded through trial and error in hoping on getting a desired energy distributions for splitted beams.

We report on a simple numerical computation method, namely thin grating sequential diffraction technique, for analyzing Bragg diffractions by superimposed transmission phase gratings in 3-D geometry. Superimposed planar phase gratings are partitioned into grating subsections with each grating subsection still consisting of superimposed planar phase gratings. The Bragg diffraction of an incoming coherent collimated light beam in the grating subsection is calculated sequentially by each grating using the 3-D coupled-wave theory [9]. In other words, we calculate the Bragg diffraction of both s- and p-polarizations by one grating of the subsection length. The results of this grating subsection diffraction is used as incident beams to calculate diffraction by another superimposed grating in the same grating subsection, and so on. After all superimposed gratings have been considered for diffractions in the same grating subsection, the overall results are used as incident beams for the next grating subsection diffractions. Again the diffraction calculation is performed sequentially for all superimposed gratings in the subsection. The calculations go on until all grating subsections have been considered.

Because the grating subsection length is small, the sequence of grating diffraction by the superimposed gratings in each subsection is no longer important. Thus, the technique shows validity on analyzing both direct coupled and cross coupled diffraction cases.

To examine the validity of using the thin grating sequential diffraction technique for analyzing the Bragg diffractions by superimposed transmission phase gratings, we computed the diffractions by two superimposed transmission phase gratings under the same diffraction parameters of Ref. 2 for direct coupling case. The incident angle (reference to the incident surface normal in the direction pointing toward the grating plane) for s- polarized beam was set at -2° and the laser wavelength was 0.488 μm. The bulk index was 1.52 and the total grating interaction length was 15.9 μm. The diffraction angles α_d (reference to the output surface normal) for the first and second gratings were 19.6° and -18.6°, respectively. The grating index modulation Δn_1 for the first grating was set at 0.01489 which is required to achieve 100% efficiency for its single grating diffraction case. The grating index modulation Δn_2 for the second grating were set at $\Delta n_2 = 0.5\ \Delta n_1$ to produce the angular selectivity curves plotted in Fig. 1. Our results match well to those calculated using thin-grating decomposition technique [2]. The validity of our technique for analyzing Bragg diffractions by three or more superimposed transmission phase gratings with well separated Bragg angles is expected although the result comparison has not yet been performed due to the lack of published selectivity curves by other techniques.

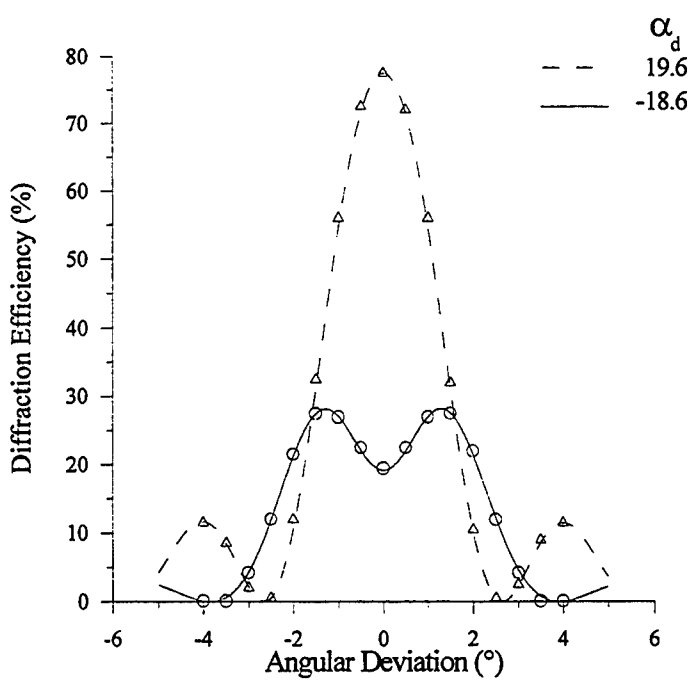

Figure 1

Calculated angular selectivity curves for direct-coupled superimposed two-grating diffraction case of Ref. 2. The data points designated by (Δ) and (O) were taken from the corresponding plots of Ref. 2 for comparison.

The calculation technique can be used to adjust the superimposed grating index combination to control the splitted beam intensity distributions. Table 1 shows a calculation example with incident beam wavelength of 632.8 nm, s-polarized incident beam, bulk grating index of 1.5, incident angle of 0°, total grating thickness of 50 μm,

and 10000 partitioned grating subsections. The diffraction efficiencies are not uniformly distributed with the identical index modulation of 0.003. After the grating index adjustment all four diffracted beams approach the expected average efficiency of 25%. Both index modulations for gratings 1 and 2 are increased since the original efficiencies were lower than the expected average. The index modulation for grating 4 is decreased since the original efficiency was higher than the expected average. The efficiency for grating 3 was most closed to the expected efficiency. Its index adjustment is based on the outcome of other grating index adjustments that affect its efficiency. In theory, we can achieve exactly 25% for all diffracted beams of the present example by index adjustment. Further index adjustment was not attempted owing to the practical concern on the significant digits of the grating index modulation. Establishing correct combinations of grating index modulations can make device implementation a lot easier.

Table 1 Example of grating index adjustment for better efficiency uniformity.

Grating #	Diff. Angle	Before Index Adjustment		After Index Adjustment	
		Index Mod.	Efficiency %	Index Mod.	Efficiency %
1	20°	0.003	20.70959	0.00342	24.29295
2	30°	0.003	22.46939	0.00327	24.09536
3	40°	0.003	25.39970	0.00308	24.16410
4	50°	0.003	30.26699	0.00283	24.30990

Calculations for efficiency and angular/wavelength selectivity curves for superimposed grating Bragg diffractions in both 2-D and 3-D geometries have been performed. The results will be presented. In general, the selectivity curves appear to depart significantly from the $(\text{sinc})^2$ functional dependence of the single grating 2-D diffraction case. The efficiency adjustment for each diffracted beam should consider other grating diffraction and other diffracted and undiffracted beam polarization statuses.

References

1. R. Alferness, Appl. Phys. 7, 29 (1975).
2. R. Alferness and S. K. Case, J. Opt. Soc. Am. 65, 730 (1975).
3. S. K. Case, J. Opt. Soc. Am. 65, 724 (1975).
4. V. Minier, A. Kevorkian, and J. M. Xu, IEEE Photonics Technology Letters, 4, 1115 (1992).
5. R. Kowarschik, Optica Acta, 25, 67 (1978).
6. E. N. Glytsis and T. K. Gaylord, Appl. Opt. 28, 2401 (1989).
7. R. Magnusson and T. K. Gaylord, J. Opt. Soc. Am. 67, 1165 (1977).
8. M. G. Moharam and T. K. Gaylord, J. Opt. Soc. Am. 73, 1105 (1983).
9. M. R. Wang, G. J. Sonek, R. T. Chen, and T. Jannson, Appl. Opt. 31, 236 (1992).
10. K. Y. Tu and T. Tamir, Appl. Opt. 32, 3654 (1993).
11. K. Y. Tu, T. Tamir, and H. Lee, J. Opt. Soc. Am. A, 7, 1421 (1990).
12. S. Ahmed and E. N. Glytsis, Appl. Opt. 35, 4426 (1996).
13. P. Asthana, G. P. Nordin, A. R. Tanguay, Jr. And B. K. Jenkins, Appl. Opt. 32, 1441 (1993).
14. H. Kogelnik, Bell Syst. Tech. J. 48, 2909 (1969).

Diffractive Optics and Micro-Optics

Fabrication 1

Wednesday, June 10, 1998

Shigeru Aohama, Omron Corporation, Japan
Presider

DWD
3:30pm–5:00pm
Koa Room

Paper withdrawn.

Fabrication of large circular diffractive optics

J. H. Burge

Steward Observatory and Optical Sciences Center
University of Arizona, Tucson, AZ 85721
phone: 520-621-8182, fax: 520-621-1578
jburge@as.arizona.edu

Equipment and techniques were developed at the University of Arizona for fabricating large computer-generated holograms (CGH's) for measuring aspheric telescope mirrors. A large laser writing machine was built to fabricate binary zone plates onto spherical surfaces up to 1.8 meters in diameter and with focal ratios as fast as $f/1$. This machine writes 6-μm to 150-μm features with radial position accuracy better than 1 μm rms over the full diameter. The problems of applying and processing photoresist are avoided by writing the patterns using a simple thermochemical technique. Numerous holograms up to 1.2 m across have been successfully written and tested.

Convex secondary mirrors for University of Arizona telescopes are interferometrically measured using concave spherical test plates with circular CGH's fabricated onto the curved surfaces.[1] Diffraction from the holograms compensates for the aspheric departure of the secondary mirrors. The accuracy of the measurements relies on the ability to fabricate binary circular patterns with thousands of rings to micron accuracy. The development of the equipment and techniques for making these patterns was motivated by the requirement to measure these optical surfaces.

Circular patterns are optimally fabricated using polar coordinate machines that expose rings by rotating the substrate under a fixed writing beam. The hologram accuracy depends on the quality of the rotation bearing, the ability to control the radial position of the writing beam, and the ability to locate the center of rotation. This geometry has been used by several groups for writing accurate zone plates onto small, flat substrates.[2,3,4,5] Also, diffractive optics for infrared applications have been turned using precision lathes with diamond tools.

Large circular hologram writer

A large circular hologram writer was designed and built for fabricating the patterns required for measuring the convex telescope mirrors. The holograms used for optical testing must diffract light with an accurate phase distribution, but the amplitude (or diffraction efficiency) is not so important. This translates into a tighter specification of line position than line size. The machine was designed to write lines with radial position accuracy of 1 μm and with line widths accurate to 5%. We have demonstrated that the writer meets these requirements for large patterns on steeply curved surfaces.

The writer uses cylindrical r, θ, and z coordinates, where a write head that controls and focuses the laser beam is moved in the r and z directions with horizontal and vertical linear stages. The substrate is rotated face up about a vertical axis on a precise air spindle. The laser itself is mounted to the frame and the collimated beam is directed to the optics head using mirrors and prisms. The beam is shaped, measured, modulated and brought to focus at $f/6$ onto the hologram substrate. Machine specifications are summarized in Table 1.

The accuracy of the radial position is achieved using laser interferometers, active control for laser beam drift, a rigid athermal support frame, and a temperature controlled enclosure. Two interferometers are used to measure the radial position and tilt of the write head. The interferometers are mounted to minimize sensitivity to changes in temperature.

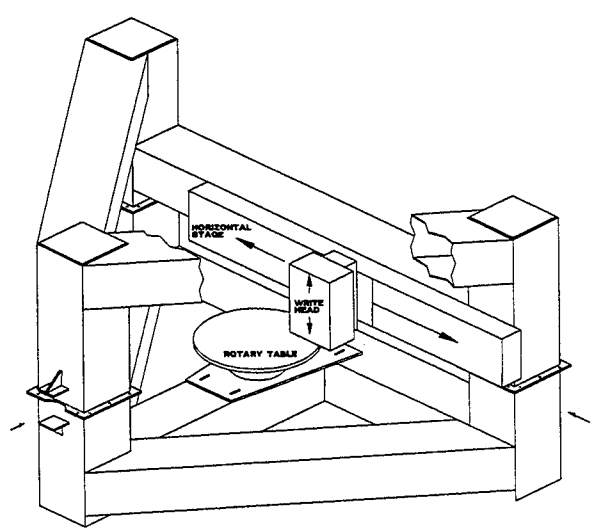

Figure 1. Large circular hologram writer support frame.

The write head is a 16 x 16 x 32 cm box that is crammed full of optics and electronics for beam measurement and control. The writing power, scanning, and fine steering of the beam are controlled using an acousto-optic modulator (AOM). The amplitude of the RF driving signal is varied to adjust the diffraction efficiency, thus the power of the writing beam. The frequency of the RF signal is varied to change the diffracted angle, which translates the focused spot over a ±80 μm region. The AOM and drive electronics allow 300 kHz bandwidth for both the power and position control, although we run them much slower. Rings with different widths are written by scanning the 6-μm spot radially with the AOM. A 5 to 70 kHz sawtooth-type signal is fed to a voltage controlled oscillator, which frequency-modulates the RF signal with the scanning function. Intensity variations can be programmed into the scanning beam to allow writing of blazed patterns.

Table 1. Specifications for the large circular hologram writer.

Diameter of hologram	25 – 1850 mm
Maximum weight of substrate	1000 kg
Laser source	1 W Argon laser at 488 nm
Line width per rotation	6 - 150 μm wide exposures
Pattern types	binary or blazed
Radial travel	r from -40 mm to 1860 mm
Resolution of stage radial position	0.1 μm
Resolution of writing spot position	0.5 μm
Absolute accuracy of radial position	1 μm rms
Accuracy of line width	5% of value
Angular accuracy of linear motions	100 μrad P-V
Axial travel	100 mm
Axial position resolution	1 μm
Absolute accuracy of axial position	5 μm rms
Rotation rate	1 - 15 rpm
Rotary bearing error	< 0.25 μm at optical surface
Temperature control	±0.2 °C

The light passes through the AOM and a filter (to isolate the correct order of diffraction), and then a beamsplitter which taps off 3% of the power for measurement. Half of this light is sent to a photodiode for measuring the writing power. The writing power is stabilized with an analog servo that uses feedback from the photodiode and amplitude control with the AOM. The rest of the split-off light is projected onto a CCD array to form a magnified image of the writing spot. Since the scan frequency is many times faster than the video rate, the image is blurred out to appear as a continuous line. The CCD image is digitized and processed real time to measure the center position and the width of the scan. This information is coupled with the position data from the interferometers and fed back to the AOM control to adjust the center position and width of the scan.

The writer has a microscope mode that uses a fold mirror to focus light reflected from the substrate onto the CCD camera to give an image of the surface with sub-micron resolution. This is used for setting focus and finding center. The focus is set with 5 μm resolution by using the microscope to visually inspect the image of the writing spot. Since the depth of focus is large, we do not require an auto-focus system. The center of rotation is found by burning a small ring, 20 - 60 μm in diameter and finding its center. This is easily done with 1 μm resolution.

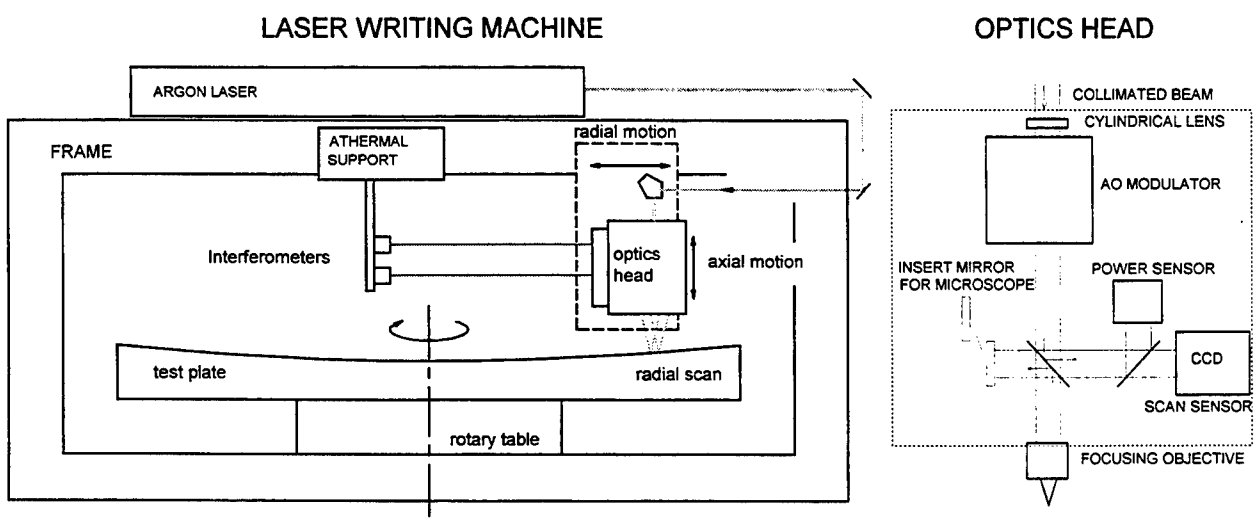

Figure 2. Schematic drawings of writing machine and optics head.

Pattern fabrication using oxidation of chrome coating

Computer-generated holograms are commonly manufactured by exposing thin layers of photoresist with near-UV light. This technology is mature for small flat substrates, but it is difficult to apply and develop resist on large, curved substrates. These difficulties are avoided by using a different fabrication method -- thermochemical writing.[6] This technique avoids the use of photoresist by writing the image directly onto a chrome film with a laser beam using a thermochemical effect. The laser exposes the chrome by heating it, which causes an oxidation layer at the surface. After writing the complete pattern and creating this oxide latent image, the optic is immersed into a caustic bath of NaOH and $K_3Fe(CN)_6$ that dissolves the bare chrome much more quickly than the chrome oxide. So after developing, a pattern of chrome remains where the laser had exposed the surface and created the oxide layer.

The amount of power required to create an optimal oxide layer depends on the scanning velocity, the overlap between scans, the writing spot shape, the line width, and the chrome coating. We typically write onto 50 nm thick chrome with a 6 x 18 μm spot moving with instantaneous scan velocity 1 m/s and with a 6 μm scan period. This requires writing power around 200 mW for writing lines 20 - 150 μm wide.

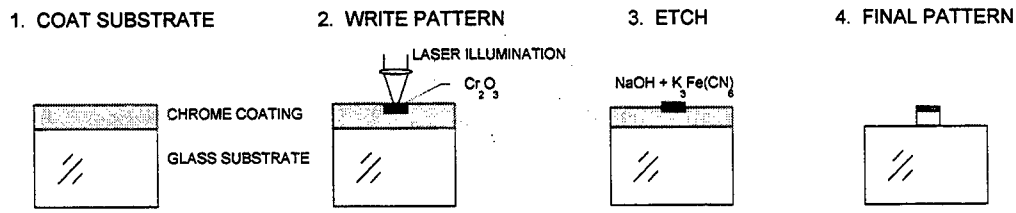

Figure 3. Pattern generation using laser induced oxidation.

Verification of writer performance

Several large tests have verified the accuracy of the hologram writer. A holographic measurement of a 38-cm aspheric mirror was compared to a classical interferometric measurement of the same mirror.[7] These agreed to 0.01 λ, which was the limitation of the interferometric test. For another verification, an 84-cm diameter pattern that produces a spherical wavefront was written onto a concave sphere. The hologram was designed to diffract light to simulate a perfect spherical surface with radius of curvature slightly longer than the substrate radius. The pattern with 1694 rings was written in 5 hours on the large hologram writer. The hologram accuracy was measured using an interferometer with a HeNe source. The measurements of the reflected and diffracted wavefronts show the surface figure to be 0.076 waves rms. The difference between these measurements shows hologram errors of only 0.0074 λ rms. Writer errors would cause mostly axisymmetric errors, which were only 0.0016 λ rms. This confirms the writer accuracy of < 0.7 μm rms for radial positioning.

Conclusions

Unique capabilities for fabricating large circular CGH's onto curved surfaces have been developed at the University of Arizona. The equipment and techniques are optimized for writing 30 cm to 1.8 m binary zone plates with rings 15 to 150 μm wide that are accurately positioned to 1 μm. With some hardware and software modifications we believe we could write 2 to 30 cm diameter patterns with lines 2 to 30 μm width, accurate in position to 0.25μm. The writer is also capable of exposing blazed patterns into resist. The machine specifications were driven by the need to fabricate the holographic test plates, but we hope to use the machine for more diverse research in the field of diffractive optics fabrication.

References

1 J. H. Burge, "Measurement of large convex aspheres," Proc. SPIE **2871**, 362-373 (1996).

2 V. P. Koronkevich, *et al.*, "Fabrication of kinoform optical elements," Optik **67**, No. 3, 257-266 (1984).

3 W. Goltsos and S. Liu, "Polar coordinate laser writer for binary optics fabrication," Proc. SPIE **1211**, 137-147 (1990).

4 T. Nomura, *et al.*, "An instrument for manufacturing zone-plates by using a lathe," Prec Eng **16**, 290-295 (1994).

5 J. P. Bowen, *et al.*, "Generation of large-diameter diffractive elements with laser pattern generation," Applied Optics **36**, 8970-8975 (1997)

6 V. Cherkashin, J. H. Burge, *et al.*, "Processing parameter optimization for thermochemical writing of DOEs on chromium films," Proc. SPIE **3010**, 168-179 (1997).

7 J. H. Burge, M. J. Fehniger, and G. C. Cole, "Demonstration of accuracy and flexibility of using CGH test plates for measuring aspheric surfaces," Proc. SPIE **3134**, 379-389 (1997).

New Convex Grating Types Manufactured by Electron Beam Lithography

Paul. D. Maker, Richard E. Muller, Daniel W. Wilson, and Pantazis Mouroulis

Jet Propulsion Laboratory
California Institute of Technology
MS 302-231, 4800 Oak Grove Drive, Pasadena, CA 91109
Tel. 818-354-2118
Fax 818-393-3548
E-mail: maker@vaxeb.jpl.nasa.gov

The advantages of spectrometer forms utilizing concentric surfaces have been recognized for some time.[1,2] In order to realize these advantages in practice, a reliable and flexible method of generating gratings on curved substrates is needed. Concave gratings are commonly manufactured using both ruling and holographic techniques. However, it is difficult to produce well-blazed curved gratings.[3,4,5] These difficulties are exacerbated in concentric spectrometer designs in which the grating must typically cover an arc that is greater than the blaze angle itself.

Using electron-beam (E-beam) lithography techniques[6,7,8] it has been possible to manufacture a variety of convex gratings that are admirably suited to the requirements of concentric spectrometers and in fact enable the practical realization of these designs. The motivation for this work was provided by the New Millennium Earth Orbiting 1 mission, which is scheduled to test a grating-based imaging spectrometer from low Earth orbit. One of the gratings described here has been selected for the above mission. The gratings were meant to cover simultaneously two wavelength regions, 1-2.5 μm in the first order, and 0.4-1 μm in the second order.

The grating designs that have been produced and tested are the following:

1) true blazed gratings, in which the blaze angle remains constant relative to the local surface normal
2) dual-panel blazed gratings, which split the total grating area into two (concentric) regions with different blaze angles, thus providing a broader wavelength band, and
3) dual-angle blazed gratings, which incorporate a groove with a compound profile having two segments with different slopes. This also has the effect of broadening the wavelength response band, especially in the second order.

The E-beam method provides great flexibility in designing the groove shape and blaze angle, including any desirable variations (or lack thereof) across the grating. In addition, it permits arbitrary panel shape for a multi-panel grating as well as control of the average diffracted phase from each panel. All these characteristics are important in determining the image quality of an imaging spectrometer.

The method involves first coating the flat or low sphericity substrate with a thin (2 – 3 μm) film of polymethyl methacrylate (PMMA, Plexiglas) using a standard semiconductor fabrication spin-coater. The grating pattern is written by an electron beam lithography tool using, typically, a 50 kV, 2 mA, 0.5 μm waist beam. In order to produce flat, blazed surfaces, it is necessary to compensate for both (a) the nonlinear response of the PMMA and (b) the E-beam 'proximity effect', exposure produced by electrons that are back-scattered from deep within the substrate. This is accomplished by (a) careful calibration and (b) deconvolution of the experimentally determined, delta plus Gaussian instrument function. The exposed patterns are developed in pure acetone for roughly 10 seconds. Final groove depth is adjusted to the design value using incremental development steps interspersed with physical depth measurements. When working with curved substrates, the pattern is subdivided into narrow annular regions that can be exposed adequately at fixed E-beam focal distance. Coincident with changing the focal distance, the E-beam electronic deflector circuits must be adjusted both for scale and rotation. Again careful calibration is necessary. It is found that adequate precision can be realized over a region that varies ±25 μm in height. Fig. 1 illustrates the quality of gratings that have been produced using these techniques. It shows atomic force microscope (AFM) data that includes the boundary between zones having different blaze angles. A fine (sub micron) 'picket fence' of residual PMMA separates the regions. It is the result of imperfect pattern matching and/or exposure. Fig. 2 illustrates an actual part.

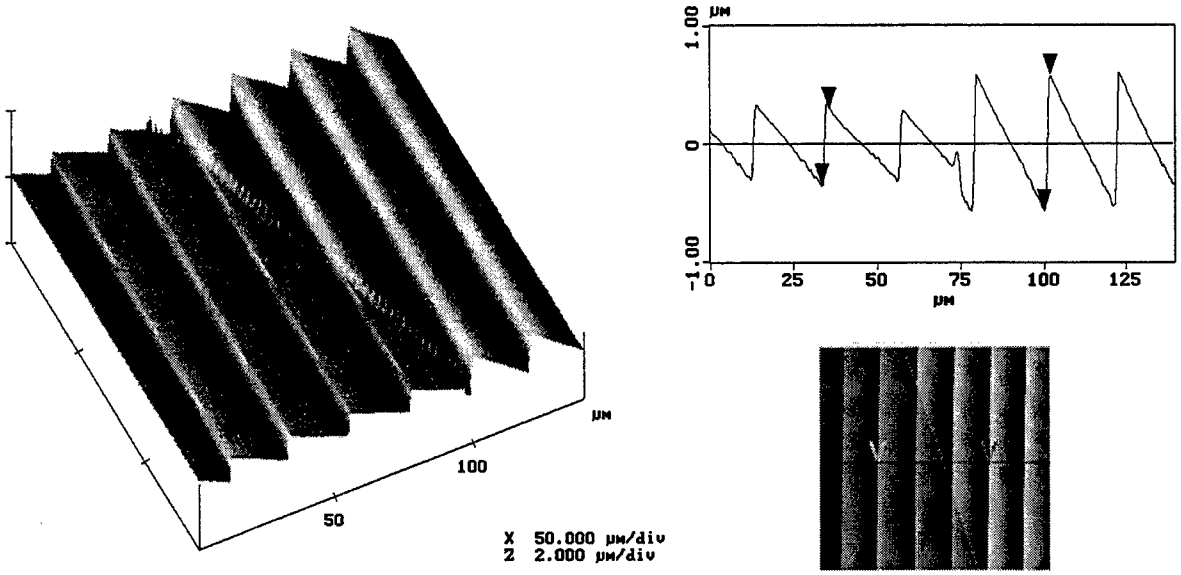

Figure 1. Atomic force microscope surface profile of a dual-blaze grating on a convex substrate.

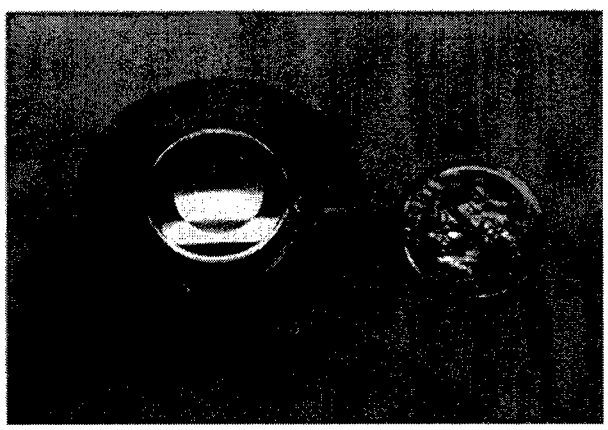

Figure 2. Photograph of a single-blaze convex grating on a flight substrate. Note the shift of the diffracted image due to the high visible-wavelength efficiency of the second order.

Fig. 3 shows the relative diffraction efficiency of four different gratings with similar specifications, all produced on the same convex substrate. The efficiency up to 1 µm is that of the second order; above, that of the first order. It can be seen that the highest peak efficiency is provided by the dual-angle blazed grating, while the dual-blaze grating gives the best overall efficiency within the bands of interest. A similar broadband response is obtained by the ruled grating (which was a 3-panel design), due to the variation in blaze angle that is inevitable with this type. The holographic grating was not an enhanced (ion-etched) type and had limited maximum attainable efficiency.

Compared to the ruled and holographic gratings, E-beam gratings exhibited extremely low scatter. Using a HeNe laser and a 100 µm slit in front of a photodetector, scatter from the E-beam grating was not measurable while that from both the ruled and the holographic gratings was clearly measurable. Regular ghosts at ¼ of the spacing between orders were observed, with a maximum intensity of 0.2% relative to the second order at 632.8nm. However, even this value compared favorably with the satellites or scatter generated by the conventional gratings.

The wavefront quality of the E-beam gratings was also superior. For the single blaze or dual-angle blaze gratings, a p-v wavefront error of 0.2λ was observed at 632.8nm. This was comparable with the wavefront quality

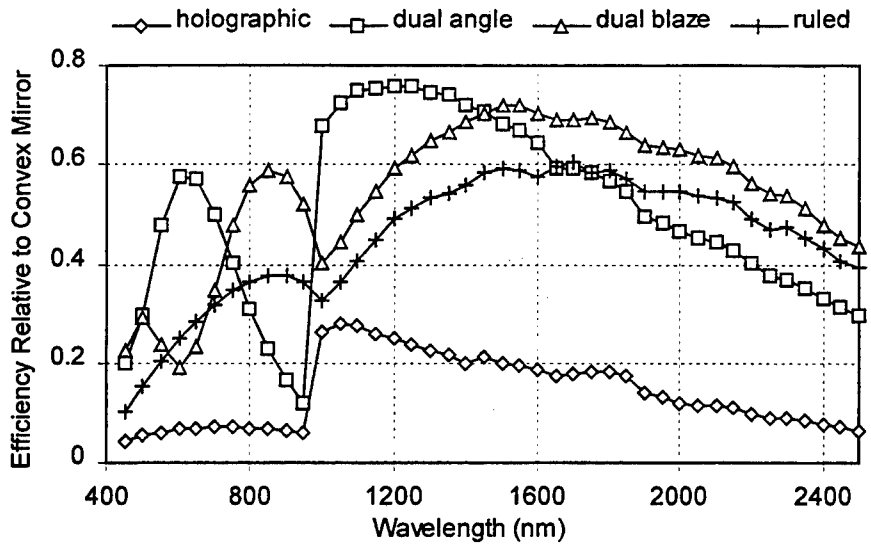

Figure 3. Efficiencies of two E-beam fabricated gratings (dual angle and dual blaze), a holographic grating, and a ruled grating. 400-1000 nm: second order efficiency, 1000-2500 nm: first order efficiency

of the holographic grating. The dual blaze gratings presented a discontinuity at the blaze boundary, which was due to experimental error in matching the average heights of the two blaze areas (a maximum of $\lambda/5$ at 632.8nm). However this was only half the value obtained for the ruled grating. A second dual blaze grating showed a better match between blaze areas ($\lambda/10$).

The flight candidate gratings were subjected to environmental tests, including thermal cycling (-50 to +50° C), vibration, out-gassing, and tape-test adhesion on witness samples. All tests were successful and no variation in optical properties was detected.

In conclusion, electron-beam lithography has been shown to be capable of producing high-quality gratings on convex substrates that compare favorably with gratings produced through conventional techniques. The method allows great flexibility in grating design and thus enables the practical realization of new spectrometer design forms.

The research described in this paper was performed by the Jet Propulsion Laboratory, in part by the Center for Space Microelectronics Technology, California Institute of Technology, and was sponsored by the National Aeronautics and Space Administration.

References

1. L. Mertz, "Concentric spectrographs," *Opt. Eng.* **14**, 130-132 (1975).
2. D. R. Lobb, "Theory of concentric designs for grating spectrometers," *Appl. Opt.* **33**, 2648-2658 (1994).
3. M. Neviere and W. R. Hunter, "Analysis of the changes in efficiency across the ruled area of a concave diffraction grating," *Appl. Opt.* **19**, 2059-2065 (1980).
4. E. G. Loewen, E. K. Popov, L. V. Tsonev, and J. Hoose, "Experimental study of local and integral efficiency behavior of a concave holographic diffraction grating," *J. Opt. Soc. Am. A* 7, 1764-1769 (1990).
5. M. C. Hutley, *Diffraction Gratings*, Academic Press (1982).
6. P. D. Maker and R. E. Muller, "Phase holograms in polymethyl methacrylate," *J. Vac. Sci. Technol.*, **10**, pp. 2516-2519, Nov-Dec. 1992.
7. P. D. Maker and R. E. Muller, "Continuous phase and amplitude holographic elements," U.S. Patent No. 5,393,634, assigned to NASA, issued Feb. 28, 1995.
8. P. D. Maker, D. W. Wilson, and R. E. Muller, "Fabrication and performance of optical interconnect analog phase holograms made be E-beam lithography," in *Optoelectronic Interconnects and Packaging*, R. T. Chen and P. S. Guilfoyle, eds., SPIE Vol. **CR62**, pp. 415-430, Jan. 1996.

Fabrication of blazed holographic optical elements on oxygen free copper by ultrahigh precision cutting

Shin-ya MORITA[1,2,3], Yutaka YAMAGATA[2,3], Toshiro HIGUCHI[2,4],

1 Graduate School, University of Tokyo
Higuchi-Kurosawa Lab., Dept. of Precision Engineering, Hongo 7-3-1, Bunkyo, Tokyo, Japan 113-0033
Tel: +81-3-3812-2111(ex. 6466), Fax: +81-3-5800-6968, E-mail: morishin@intellect. pe. u-tokyo. ac. jp
2 Kanagawa Academy of Science and Technology (KAST)
3 Materials Fabrication Lab., The Institute of Physical and Chemical Research (RIKEN)
4 Dept. of Precision Engineering, University of Tokyo

1.Introduction

A holographic optical element (HOE) is a kind of diffractive optical element. An HOE can substitute an optical system with multiple optical components like lenses, mirrors, beam-splitters, prisms and so on. So it is expected to reduce the number of its optical parts, improve a performance of various optical systems, such as optical storage systems[1] like CD or DVD systems, optical instrumentations, fiber optics and etc., and make an optical system simple, small and light weighted.

Though it has a number of advantages, its fabrication process faces many difficulties because of its size and complicated shape. An HOE is a kind of diffraction grating which consists of curved grooves of altered width and depth with the position. The cross section of the grooves is usually saw-tooth shape to obtain higher diffraction efficiency. The fabrication process of an HOE should meet those requirements: (1) Fabrication of curved grooves (2)Saw-tooth cross section with varying width (3)Optical quality surface finish. The fabrication technology of integrated circuits using photolithography and etching is a usual method for fabricating HOEs. Certainly it is an effective and widely used way to fabricate micro and complicated structures like that. But it is difficult to make saw-tooth slopes with different width and surface finish tends to be insufficient by photolithography technology. The ultrahigh precision cutting method the authors propose in this paper solves those problems. Using a single crystalline diamond cutting tool with four degree-of-freedom motion control, it is possible to satisfy the requirements stated above.

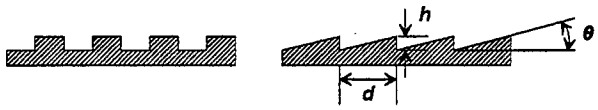

(a) Rectangular profile (b) Saw-tooth profile (Blazed HOE)

Fig.1 Cross-sectional view of surface-relief HOE

2.Fabricating Method of HOEs

Fig.1 (b) shows the schematic view of the cross section of an HOE. Its grooves form free curves and the cross section is saw-tooth. The inclination angle of the slope varies according to the groove width. Concerning the cutting tool motion, two degree-of-freedom (DOF) is required for groove shapes, one for cutting depth control, and one for controlling slope inclination. Consequently, four DOF motion of the cutting tool is required for fabrication of an HOE. Fig. 2 denotes the principle of varying slope inclination angle by giving twist angle to the cutting tool. Fig. 2 (a) shows the cutting with twist angel of 0 to form smallest slope inclination angle, while (b) shows the cutting operation

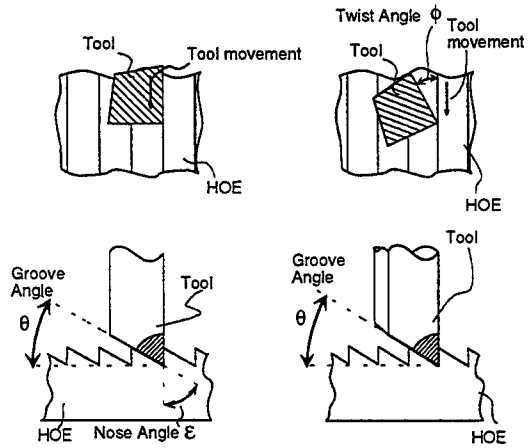

(a) $\phi=0$ (b) $\phi\neq0$

Fig.2 Fabricating method for different groove width by twisting cutting tool

with a certain twist angle ϕ given to the cutting tool to form larger slope inclination angle. The relationship between slope inclination angle θ, tool nose angle ε, and the twist angle ϕ can be described as follows:

$$\tan(\frac{\pi}{2} - \theta) = \tan\varepsilon\cos\phi$$

Thus, controlling twist angle ϕ, the inclination angle of the groove can be varied. The nose angle of the cutting tool have to be designed to give smallest slope inclination angle when ϕ=0.

Fig. 3 shows the schematic view of the cutting tool and machine tool configuration for HOE fabrication. The work piece is attached on the C spindle and the cutting tool on the Y column facing the work piece. The twist angle ϕ is given by the rotation of C spindle, groove curves are controlled by X and Y axes motion, and the depth of cut is controlled by Z axis motion.

Table 1 Machine specification

Linear Axis (Special Roller Guide)
Stroke x:200mm,y:150mm,z:220mm
Scale Resolution: 1nm,Straightness:0.1 μm
Max. Speed: 1000mm/min
C Spindle (Precision Air Bearing)
Rotary Encoder:1/10000°,Max. Speed:3000rpm
Rotation Precision:0.05 μm
Grinding Spindle (Precision Air Bearing)
Max. Speed:40,000rpm
Rotation Precision0.05 μm
Controllable Axis
Four(X,Y,Z, and C)

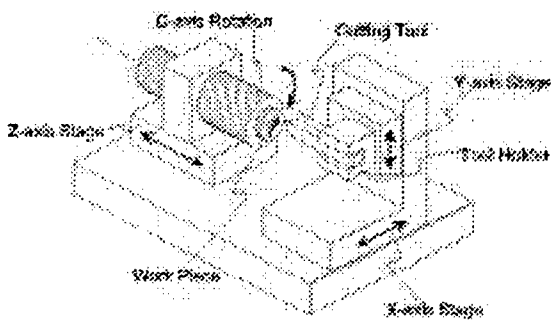

Fig.3 Configuration of machine tool

3.Fabrication of HOEs

We actually fabricated HOEs by the method mentioned above using four axis ultra-precision machine tool and single crystalline diamond cutting tool. The specification of the machine tool is summed up in Table 1[2][3]. Fig. 4 illustrates the optical configuration of the fabricated HOE. It was designed as a convergence reflector, where wave length of laser is 780nm. The number of grooves was 906, the blaze angle adjusted from 10.5 to 12.3deg., the depth was 0.44 μm.

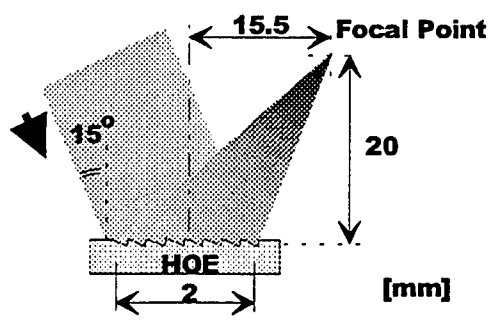

Fig.4 Optical configuration of fabricated HOE

Cutting condition was specified by our previous study[4][5]. Oxygen free copper (OFC) was used, considering machinability and life-time of the cutting tool. A single crystalline diamond tool which nose angle is 80 degree was used for machining. Cutting speed was 50 mm/min, cutting depth 2μm. It took 50 min to fabricate the HOE. Fig.5 are images of fabricated HOE magnified by SEM. These photographs show that grooves was sharp and well-formed in most areas. However, burrs appears on the edge of saw-tooth in some regions (Fig.5(b)). This is presumably due to the difference of crystal orientation of OFC grains.

The laser beam reflected by the HOE made a focus as desired.

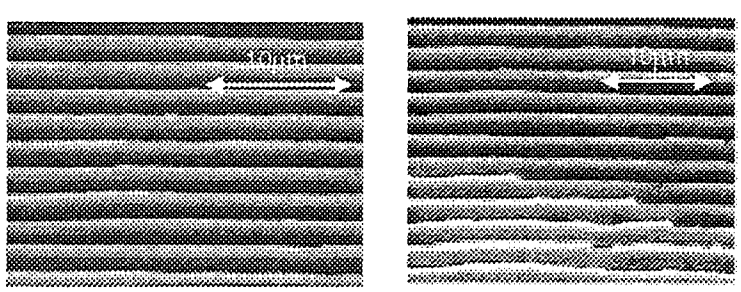

(a)Fabricated HOE (b)Fabricated HOE (Appearance of Burrs)

Fig.5 SEM images of fabricated HOE

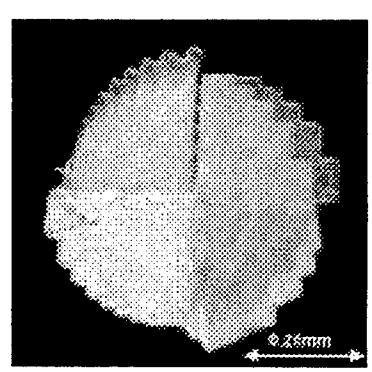

Fig. 6 HOE divided into four sections

The diffraction efficiency was 51%. But there was some unnecessary diffracted light observed. Radiation of the unwanted light is presumably due to the damage of groove shapes and burrs.

Fig. 6 is an example of multiple-segmented HOEs. It is divided into four sections and each section functions as a convergence reflector that has a different focal point from the others. At least four lenses and a prism are necessary in order to replace this HOE. The use of multiple-segmented HOE makes possible to reduce the number of components in the micro optical system.

4.Fabricating test on single crystalline copper

In order to confirm the relationship between quality of groove shape and crystal orientation of material, a fabricating experiment was made on single crystalline copper(Cu(111)). Fig. 7(a) and Fig. 7(b) were cross-sectional views of fabricated grooves under the same condition except for cutting direction. The images are measured by AFM. They show obvious gap of shape quality. The result means that the difference of crystal orientation of material affects fabricated grooves in the quality of their cross-sectional shape certainly.

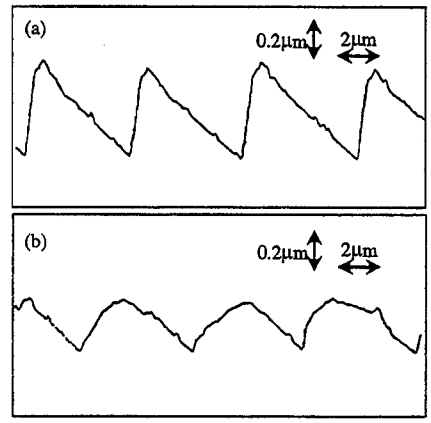

Fig. 7 Fabricating test on single crystalline copper (measured by AFM)

5.Conclusion

A novel fabrication method of an HOE is proposed, using a single crystalline diamond cutting tool with four axis ultra-precision machine tool. A reflective HOE functioned as convergence reflector was fabricated by it. And its optical property was verified through experiments. The diffraction efficiency was 51%. A multiple-segmented HOE was also fabricated. In addition, the difference of crystal orientation of material affects fabricated grooves in the quality of their cross-sectional shape .

Evaluating from those experimental results, the method proposed has proved to be effective for fabricating HOEs. The authors would like to optimize cutting conditions or work piece materials for better optical quality, and develop a variety of applications of HOEs about optical instrumentation, optical storage system and so on.

References

[1] Y.Kimura, S.Sugama and Y.Ono; High Performance Optical Head using Optimized Holographic Optical Element, *Jpn. J. Appl. Phys., 26, Supple. 26-4, p.131 (1987)*

[2] Y.Yamagata, T.Higuchi, S.Mihara; Fabrication of micro parts by precision cutting, *Proceedings of the Spring annual meeting (1994) of the Japan Society of Precision Engineering, p.653*

[3] Y.Yamagata and T.Higuchi; Four Axis Ultra Precision Cutting Technique, *Proceedings of the 8th International Precision Engineering Seminar (1995), p.467*

[4] Y.Yamagata, T.Higuchi, Y.Takashima, and K.Ueda; Fabrication of micro mechanical and optical components by ultra-precision cutting, *Proceedings of SPIE's MM96 Symposium (1996) on Microelectronic Structures and MEMS for Optical Processing II, SPIE Vol.2881, p.148*

[5] Y.Yamagata, S.Morita, T.Higuchi, Y.Takashima, and K.Ueda; Fabrication of Holographic Optical Elements by Ultra Precision Cutting, *Proceedings of 9-IPES/UME4 (1997), p.588*

Single-step etching fabrication of diffractive microlens on high-energy-beam sensitive glass

Michael R. Wang and Heng Su
Department of Electrical and Computer Engineering
University of Miami
Coral Gables, FL 33124
Telephone: (305)284-4041
Fax: (305)284-4044

Diffractive microlens has a variety of applications including spot array generation, optical or hybrid opto-electronic interconnections, Fourier transformation, imaging, focusing, collimating, coupling, and beam shaping.[1-4] Diffractive microlens is also important for printing, optical data storage, and display applications. High lens efficiency is often required to minimize unwanted zero-order non-diffracted light beams that are responsible for optical crosstalks and background noises. High diffraction efficiency can be achieved by increasing number of phase levels of surface relief diffractive microlens structures.

We present a new technique of fabricating multi-phase-level diffractive microlenses using an in-house generated gray-level glass mask and chemical direct etching on such glass[5, 6]. The technique eliminates photolithographic processing steps required by conventional diffractive optics fabrication. Laser direct-writing on a pre-darkened ion-exchanged high-energy-beam sensitive (HEBS) glass generates gray-level transmittance distribution on the glass. Direct etching the gray-level glass mask using a diluted hydrofluoric acid results in the desired surface relief patterns owing to the gray-level transmittance dependent different etching rate on the glass mask surface. The etching is followed by a low-temperature baking to yield a transparent phase-modulation only microlens. The process with no photolithographic processing is attractive and can be compared to laser-assisted chemical etching on and through photoresist or polymer layers. Our technique offers excellent stability on the gray-level glass mask and also on the surface etched microlenses. The excellent transmittance of the glass allows the fabricated microlenses to be used in visible and some infrared wavelengths. Based on fabrication calibration, a sixteen-phase-level diffractive microlens at 640 nm operation wavelength has been realized. Focusing efficiency has been measured to be about 94% compared with the theoretical limit of 99%.

High-energy-beam sensitive glass[5, 6] is the base recording media for gray-level glass mask and for the microlens substrate. Non-saturation laser direct-writing can result in the gray-transmittance-level distribution on the darkened ion-exchanged layer of the HEBS glass. The laser writing calibration is given in Figure 1. For laser writing calibration, a focused diode laser write beam at 640 nm wavelength was used while the focusing spot size was 0.8 μm. The pre-darkened glass with 3 μm thick ion-exchanged layer was place at the laser focal plane. The laser writing speed was fixed at 30 μm/sec. Fig. 1 calibration curve was achieved by four repeated writings to yield a reasonably large gray transmittance range.

From our experimental observations, the etching rate of the ion-exchanged HEBS glass under diluted hydrofluoric acid depends on the optical transmission property of the ion-exchanged layer. This is the basis of this study since controlled etching of multi-phase-level diffractive

optical element is possible through controlled laser writing of gray transmittance levels on the glass.

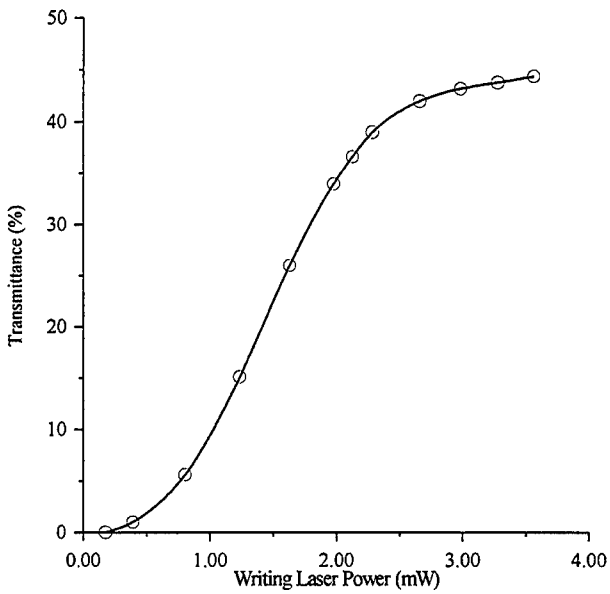

Fig. 1 Non-saturation written transmittance as a function of focused laser writing power at a constant writing speed of 30 μm/s, and a writing spot size of 0.8 μm.

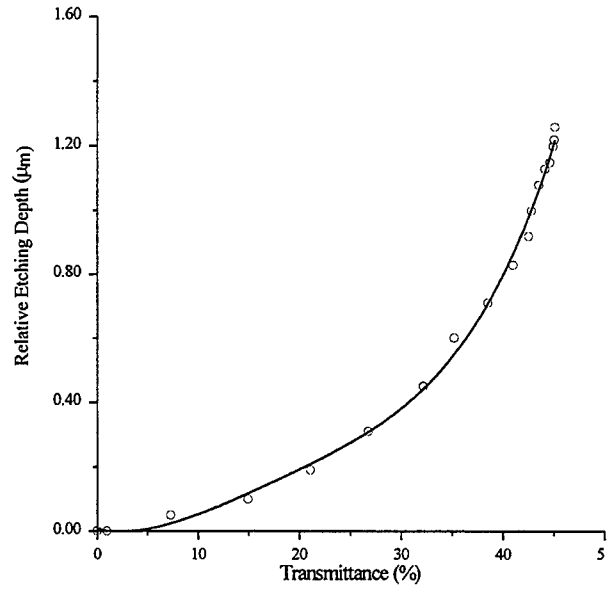

Fig. 2 The relationship between the etching depth and the regional transmittance at 640 nm after 1740s etching in a 3.3% diluted hydrofluoric acid at room temperature (20°C).

To control the etching depth of the multi-phase-level structures, calibration experiment has been performed to quantify the relationship between the etching depth and the laser written transmittance distribution. For the calibration, a diluted 3.3% hydrofluoric acid solution was used for glass surface etching while the etching time was fixed at 1740 seconds. The environmental temperature was 20 °C. The resulted surface relief structures were measured by an Alpha-Step 100 surface profiler. The etching calibration curve is shown in Figure 2. A 1.22 μm maximum relative etching depth corresponds to about 45% transmittance level on the ion-exchanged HEBS glass.

The multi-phase-level Fresnel lens with discrete phase levels has been designed based on the well-known Fresnel diffraction theory and the above calibration curves. A sixteen-phase-level microlens with twelve total zones have been designed and fabricated for focusing plane incident laser beam at 640 nm wavelength and with a focal length of 10 mm. Each zone introduces a maximum 2π phase change. Based on the analysis and the known glass refractive index of 1.549, the maximum relative etching depth was determined to be 1.166 μm, other relative etching depths, gray transmittance levels, and corresponding laser power values for the sixteen-level structure were also determined. Fig. 3 (a) shows the picture of the laser written sixteen-phase-level microlens glass mask prior to the chemical etching. Fig. 3 (b) shows the etched sixteen-phase-level microlens. The diffraction efficiencies of the fabricated sixteen-phase-level diffractive microlenses were measured to be varying from 93.5% to 95.5%, and the average effciency was determined to be 94%. The focused beam spot size was measured to be about 10 μm.

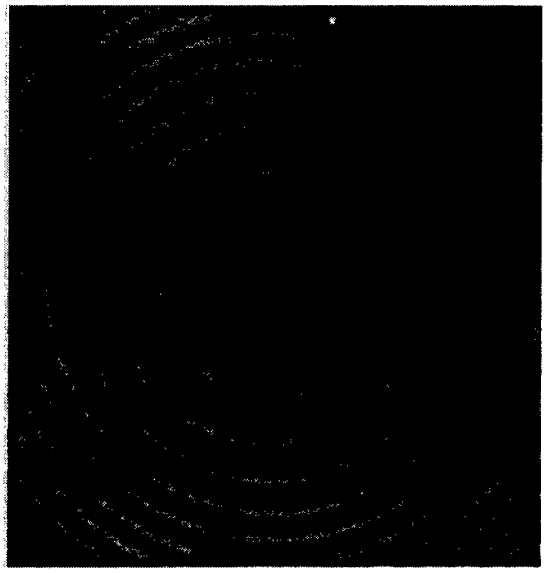

50 μm

(a) Gray level microlens mask before etching processing.

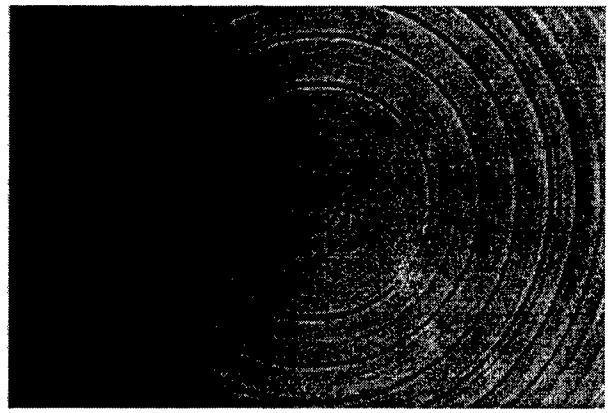

50 μm

(b) The microphotograph of the etched multi-phase structures of the diffractive microlens.

Fig. 3 Pictures of the diffractive microlens mask and etching result

The demonstrated one-step maskless fabrication technique should prove valuable for efficient production of diffractive optical elements including diffractive microlenses. The fabrication process is simple and independent of the number of phase levels required.

References

1. L. A. Hornak, "Fresnel phase plate lenses for through-wafer optical interconnections," Appl. Opt. **26**, 3649-3654 (1987).
2. R. L. Morrison, S. L. Walker, and T. J. Cloonan, "Beam array generation and holographic interconnections in a free-space optical switching network," Appl. Opt. **32**, 2512-2518 (1993).
3. D. Prongue, H. P. Herzig, R. Dandiker, and M. T. Gale, "Optimized Kinoform structures for highly efficient fan-out elements," Appl. Opt. **31**, 5706-5711 (1992).
4. W. Daschner, M. Larsson, and S. H. Lee, "Fabrication of monolithic diffractive optical elements by the use of e-beam direct write on the analog resist and a single chemically assisted ion-beam-etching step," Appl. Opt. **34**, 2534-2539 (1995).
5. W. Daschner, P. Long, R. Stein, C. Wu, and S. H. Lee, "Cost-effective mass fabrication of multilevel Gluch diffractive optical elements by use of single optical exposure with a gray-scale mask on high-energy beam-sensitive glass," Appl. Opt. **36**, 4675-4680 (1997).
6. H. Su and M. R. Wang, "Laser direct-write optical grating lenses and lenslet arrays on glass for optical interconnect applications," Proc. SPIE **2891**, 82-87 (1996).

Diffractive Optics and Micro-Optics

Metrology and Testing

Thursday, June 11, 1998

Hans Peter Herzig, University of Neuchatel, Switzerland
Presider

DThA
8:30am–10:00am
Koa Room

Diffraction efficiency limitations on visually coupled hybrid optics

Brian H. Tsou
Air Force Research Laboratory
AFRL/HECV, 2255 H Street, WPAFB, OH 45433-7022
Voice: (937) 255-8896
Fax: (937) 255-8366
Email: btsou@al.wpafb.af.mil

Carl R. Ingling, Jr., and Julie Beegan
Ohio State University
Zoology and Biophysics, 1314 Kinnear Road, Columbus, OH 54321

Abstract

This is a report on the development of a psychophysical scale for measuring the image quality of photographic and video images. We found subjects can consistently use the method of direct magnitude estimation to judge the quality of images degraded by noise. An example of how this scale is used to assess the image quality produced by various optical elements will be presented.

Introduction

The diffractive optical element (DOE) has come a long way since its first introduction into the Air Force/Navy Interim-Night Integrated Goggle and Head Tracking System (INIGHTS) program in the early 1990's [1]. Recently, DARPA, the Army and their industrial partners successfully led a research program to evaluate the usefulness of DOE for helmet-mounted displays, anticipating weight-saving, cost-reduction and performance-enhancement [2]. The potential for commercial application of this technology has also been documented [3]. Experts in the field seem to agree, however, that the difficulty in manufacturing DOE is currently limiting its full potential for visual displays in general. More importantly, they also agree that there is a need for clear and specific performance criteria to guide development. This presentation describes our approach to the problem of relating subjective impressions of image quality to physically quantifiable measures of DOE performance.

Background

A visually coupled system is defined, following Cox [4], as an image (generally a virtual image) formed by an optical system viewed by a human observer. Therefore, the observer's impression of the image determines the quality, reliability and usefulness of the visually coupled system. Because displays of images from which information is to be extracted by an observer are fundamental in visual communication, there has always been wide interest in methods for characterizing the quality of images. Because of the multi-dimensional factors involved, little progress has been made in developing satisfactory measures of image quality. Although, optical engineers have used point spread function or modulation transfer function (MTF) to characterize the spatial-frequency response of optical elements, it is not clear exactly which features of the MTF correlate with subjective image quality.

Approach

Our proposed solution is to treat image quality as a psychophysical variable, analogous to other psychophysical variables such as luminance or loudness. Psychophysical variables have been used to relate subjective magnitude to quantifiable physical measures by employing conventional magnitude estimation. Stevens and collaborators, and now many others [5], have shown that prothetic continua scale as power laws; subjectively experienced magnitudes are proportional to the *n*th power of the physical stimulus. For example, the subjective intensity of a sound is measured in sones based on loudness scaling, which is related to a psychophysical quantity (phons) derived from loudness level matching to a standard 1 kHz pure tone, which is in turn related to decibels of sound pressure level. By internationally agreement, one sone corresponds to a loudness of 40 phons. A 50-phon tone sounds on average twice as loud as a 40-phon sound and, therefore, has a sone value of 2. The 50-phon is 10

decibels above 40-phon sounds in intensity [6]. Thus, by developing a psychophysical scale for sound, the subjective magnitude of a sound loudness (measured in sones) can be related to a physically measured quantity, namely decibels. Similarly, we apply Stevens' procedures to derive scales which relate specific physical aspects of pictures (direct or imaged) to perceived quality. Pilot experiments carried out by Ingling in 1990 demonstrated the feasibility of adding noise to images of various quality to match defocus and relating it to a scale of image quality derived by magnitude estimation. The present question is whether this approach can be generalized to other image degradations, in particular, those peculiar to hybrid optics.

This approach requires that the proposed perceived image quality scale derived by direct magnitude estimation can be related to any arbitrary image degradation process. A scale relating perceived image quality to noise can be derived by having observers make direct estimates of the quality of reproduction to which various amounts of noise has been added. Pilot experiments indicate that indeed perceived quality is a power-law function of noise. The underlying premise is that, given a scale as described, any image-degrading process can be quantified by its noise equivalence. Determining the relationship between an image degradation process and noise yields immediately the perceived image quality on an absolute (physically quantified) scale. Knowing the noise equivalence of a particular degradation, such as stray light, ghost images, chromatic aberration, etc., observed with DOE, provides a real criterion for optimizing visually coupled designs.

Stimuli

To create the test stimuli for scaling, we physically degraded images by adding noise. The measure of noise is objective and specifiable using standard parameters. Various amounts of noise were added to a range of test stimuli. Human observers rated a series of such test stimuli to obtain the subjective image quality scale. A set of ecologically relevant test images (faces, natural or computer-generated scenes, scenes containing sharp edges, etc.) were investigated. Figure 1(a) shows an example of the pictures used in the study with no noise added; Figure 1(b) shows the picture with 50% noise added. Pictures were displayed on a high-resolution monitor and relayed by a Nikkor 60-mm f/2.8 photographic lens to form an aerial image. Observers viewed and then rated the images alternatively with hybrid optics and conventional eyepieces.

Fig. 1(a) no-noise

Fig. 1(b) 50%-noise

Procedure

To find the relationship between subjective image quality and the objective physical amount of noise in the test stimuli, subjects were asked to assign a number that reflected his/her internal quality scale for each test stimulus viewed. There was no limit to the range of numbers subjects could use to estimate image quality. Subjects knew various amounts of noise had been added to some test stimuli. The experimental session was self-paced by the observer. Each observer rated each test stimuli 20 times. Test stimuli were presented in random order. Observers

were given rests between sessions. In the second half of the experiment, observers compared, or more precisely, matched pictures imaged by hybrid optics and pictures imaged by conventional eyepieces. Observers were instructed to "dial-in" noise to the picture viewed through the conventional eyepiece to match the picture imaged by hybrid optics in order to find the noise equivalence of the image degradation caused by hybrid optics.

Result

Figure 2 shows the power-law relationship (n= -1.14, averaged exponent across three observers) of subjective quality assigned by each subject to proportions of noise added to the picture shown in Figure 1. It is similar to the psychometric functions found for a number of sensory modalities including loudness, brightness, touch, taste and smell [5]. The collection of matching data to compare the image quality of hybrid optics and conventional eyepieces are proceeding and will be presented at the Diffractive Optics and Micro-Optics Conference.

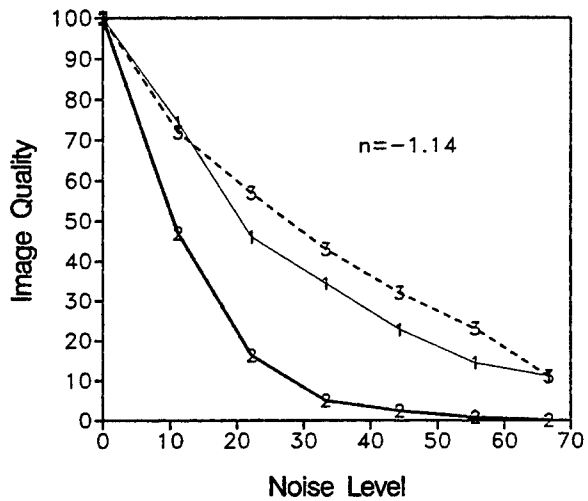

Fig. 2 Image quality assigned by each observer to a range of noise levels

Summary

Our preliminary results demonstrate that human observers could reliably extract subjective image quality from pictures to which various proportions of noise had been added. Its applicability to evaluating various optical degradations especially related to diffractive optics will be discussed. Future studies have also been planned to systematically sort out the possible dependency of this image quality scale on spatial content, dynamic range, luminance and contrast level. Such studies will be necessary in order to establish its generality for efforts related to the specification of image quality with visually coupled displays such as helmet-mounted displays and night vision viewers. These displays are essential in improving pilot performance and mission success.

References

1. J. A. Cox, T. A. Fritz, T. Werner, "Application and demonstration of diffractive optics for head-mounted displays," *Proc. SPIE* **2218**, pp. 32-40, 1994.
2. C. B. Chen, R. G. Hegg, T. Johnson, B. King, D. F. Rock, R. Spande, "Visible testbed projector with replicated DOE," *1998 Diffractive Optics and Micro-Optics Technical Digest*, Kailua-Kona, HI, 8-12 June 1998.
3. D. Stephenson, "Diffraction gratings: The clear choice," Photonics Spectra, PP. 94-98, April 1996.
4. J. A. Cox, Application of diffractive optics to visual imaging systems, In P. Mouroulis (Ed.), *Optical design for visual instrumentation*, McGraw-Hill, NY (in press).
5. G. A. Gescheider, *Psychophysics: Methods, Theory, and Application*, pp. 217-236, 2nd ed., Lawrence Erlbaum and Associates, Hillsdale, NJ 1985.
6. E. F. Evans, Basic physics and psychophysics of sound, In H.B. Barlow and J.D. Mollon (Eds.), *The senses*, Cambridge University Press, 1982.

Optical measurement of the global and local geometry of grating structures

P. Blattner, S. Traut, H. P. Herzig
Institute of Microtechnology, University of Neuchâtel,
rue A.-L. Breguet 2, 2000 Neuchâtel,
Switzerland
Phone : +41 32 718 32 67 , Fax : +41 32 718 32 01
E-mail: peter.blattner@imt.unine.ch

1 Introduction

Advancement in the areas of lithography and holography have enabled the realization of very fine surface-relief grating structures in the nanometer to micrometer range. The characterization of such structures is of obvious importance. Different methods exist to determine the optical properties of gratings. The dispersion properties are typically analysed by spectrometers. The wavefront quality is measured by commercially available interferometers. The diffraction efficiency can be determined by scanning the far-field intensity distribution.

If the grating structures are used as test elements for process monitoring, the geometrical parameters are very important. Current techniques for measuring the grating relief are scanning electron microscopy and atomic force microscopy. None of these techniques, however, is capable of providing rapid accurate submicrometer information over larger areas. Therefore, optical testing methods have been applied also here. Optics allows nondestructive testing and can measure large-aspect-ratio submicrometer features. In the following, we highlight two approaches to determine the global and local geometric parameters of gratings. The average grating period can easily be determined knowing the diffraction angle. Based on this principle, we built a highly accurate laser diffractometer (see Sec.2). For local parameter estimation, we introduced the scanning spot metrology. The method is presented in Sec. 3.

2 Laser diffractometer

The laser diffractometer is a well-known method to determine the grating period by measuring the diffraction angles. We will show that this method is highly accurate. The basic principle is illustrated in Fig. 1. A grating structure splits an incoming beam into different

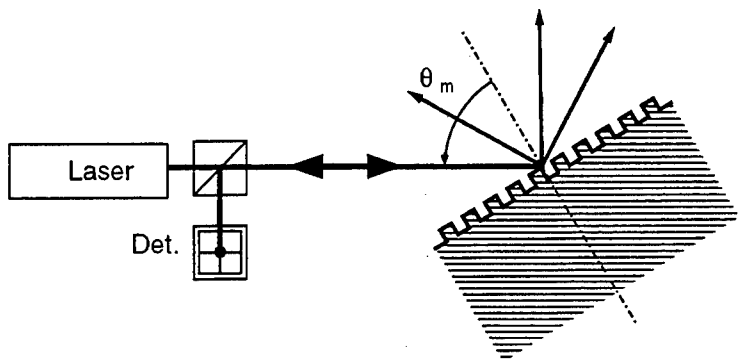

Figure 1: Littrow diffraction angle measurement system

diffraction orders. The direction of the diffraction orders is related to the grating period by the grating equation in Littrow mount

$$n_{\text{air}} \sin \theta_m = m\lambda/2\Lambda \quad , \tag{1}$$

where n_{air} is the refractive index of the air, m is the diffraction order, λ is the wavelength and Λ the grating period. Measuring the Littrow diffraction angles enables the determination of the mean grating period with only one rotating stage.

If the laser diffractometer is placed in a temperature and humidity controlled environment, high accuracy can be achieved. The index of the air has to be taken into account to the same precision than the measurement accuracy ($|\Delta\Lambda/\Lambda| = |\Delta n_{\text{air}}/n_{\text{air}}|$).

Based on this principle a laser diffractometer has been built and characterized. The angular precision of the rotary stage is in the order of $0.1''$. This instrument allows the rapid and precise determination of the grating period of reflection gratings (period $\Lambda = 400nm \ldots 10\mu m$) with an accuracy better than 1E-5. Hence, it is possible to determine the mean grating period of a $1\mu m$ grating to of better than 10 picometer!

3 Scanning spot metrology

Additional parameters (depth and width) of a grating test structure, can be determined by scattering an incident laser beam at the structure and measuring the far-field intensity distribution [1]. The main drawback is that this technique only determines the average parameters, and doesn't allow to determine local errors, such as single line defects. Therefore, we investigated a metrology which provides accurate information about surface-relief grating structures. The method involves illuminating the structure with a small spot size focused laser beam and evaluating the diffraction pattern as the structure is scanned. It has been applied to amplitude gratings, realized typically by opaque and transparent line structures on chrome masks.

The total transmitted power gives information about the edge locations of the lines [2]. In the case of phase gratings a different approach is used. The focused laser beam

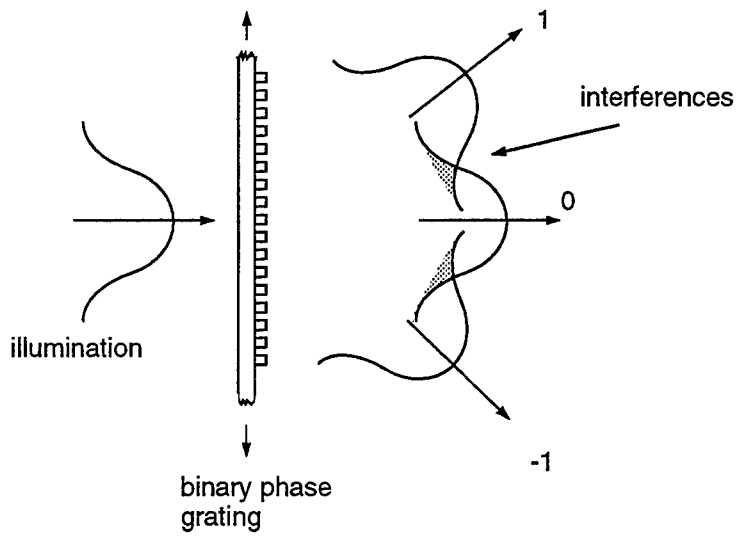

Figure 2: Principle of the scanning spot metrology

generates enlarged diffraction orders. If the beam size is sufficiently small, i.e. has a large angular spectrum, the diffraction pattern of the diffracted orders overlap and interfere (Fig.2). Scanning the mask introduces a (linear) phase change of the higher diffraction orders. The resulting interference modulation depends on the ratio between the grating period and the focus spot size. This modulation can be used to extract the edge locations with high accuracy [3]. A drawback of the method is that for high accurate edge location determination, the light interaction has to be calculated by a time consuming rigorous diffraction theory, such as the rigorous eigenmode method [4].

Based on this principle, we were able to determine local linewidth of $1\mu m$ gratings with a precision of $10nm$.

References

[1] Naqvi, S. S. H. and R. H. Krukar, "Etch depth estimation of large-period silicon gratings with multivariate calibration of rigorously simulated diffraction profiles". J. Opt. Soc. Am. A,**11**(9), 2485-2493 (1994).

[2] P. Blattner, H. P. Herzig, and S. S. H. Naqvi, "Scanning spot metrology for testing of photolithographic masks". Opt. Eng., **34**(8), 2425-2427 (1995).

[3] P. Blattner, H. P. Herzig, "Optical testing of fine grating structure", Proc. SPIE Vol. **2782**, 628-634 (1996).

[4] J. Turunen, "Diffraction theory of microrelief gratings", in *Micro-optics*, H. P. Herzig ed. (Taylor & Francis, Inc,1997), pp 31-52.

Optical Testing of Technical Surfaces with Diffractive Optical Elements

Sven Brinkmann, Thomas Dresel, Roland Schreiner, Johannes Schwider,
Universität Erlangen-Nürnberg, Lehrstuhl für Optik, Staudtstr. 7, D-91058 Erlangen, Germany
Phone: ++49-9131-858396, Fax: ++49-9131-13508

Optical techniques which are well established for the testing of optical surfaces usually suffer from speckle noise caused by the roughness of technical surfaces. For this reason the shape control of technical workpieces is commonly carried out by tactile profilometers. An optical and much faster alternative to mechanical profilometry is grazing incidence interferometry. It suppresses speckle noise by increasing the effective test wavelength from λ to $\lambda/\cos\vartheta$, where ϑ is the angle of incidence [1-3]. Diffractive optical elements, containing the shape information of an ideal object in their surface relief, are used as references for the workpiece enabling a null test of the entire mantle surface in a single step. The period p of the diffractive optical elements determines the diffraction angle $\alpha=\arcsin(\lambda/p)$ and hereby the angle of incidence $\vartheta=\pi-\alpha$, the effective wavelength $\lambda_{eff}=p$ and the sensitivity $\lambda_{eff}/2$ of the interferometer.

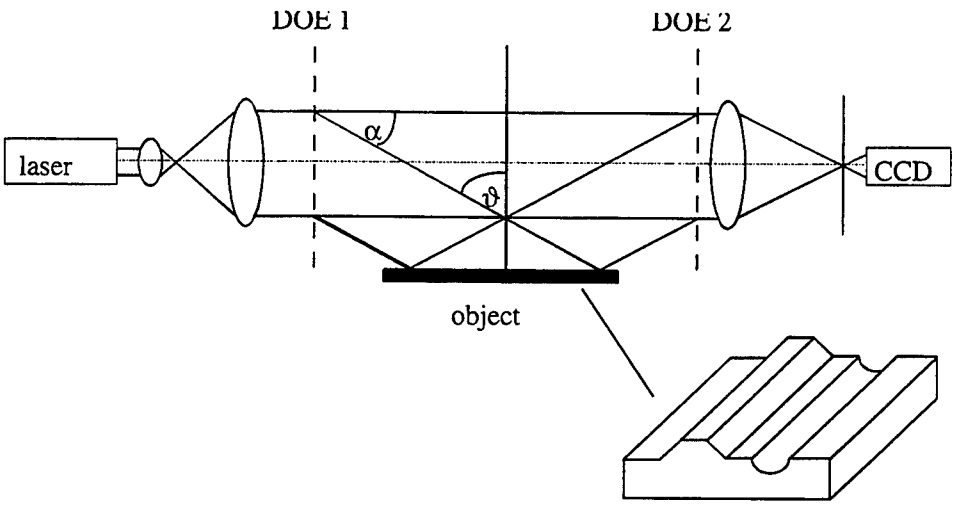

Fig. 1: Setup of the grazing incidence interferometer.

The principle of the interferometer is shown in fig. 1. Well collimated laser light impinges onto a first diffractive optical element, realized as a computer generated phase-only hologram, which acts as a beam splitter. The zero diffraction order passes through a second, well adjusted diffractive optical element and is used as the reference wave in the interferometer. The first diffraction order illuminates the workpiece and serves as an object wave. It is reflected at the mantle surface of the workpiece and is recombined with the reference wave into an interference pattern at the second diffractive optical element. The necessary phase shifts for the evaluation of the interference pattern with phase stepping software are realized by varying the distance between the diffractive optical elements [4].

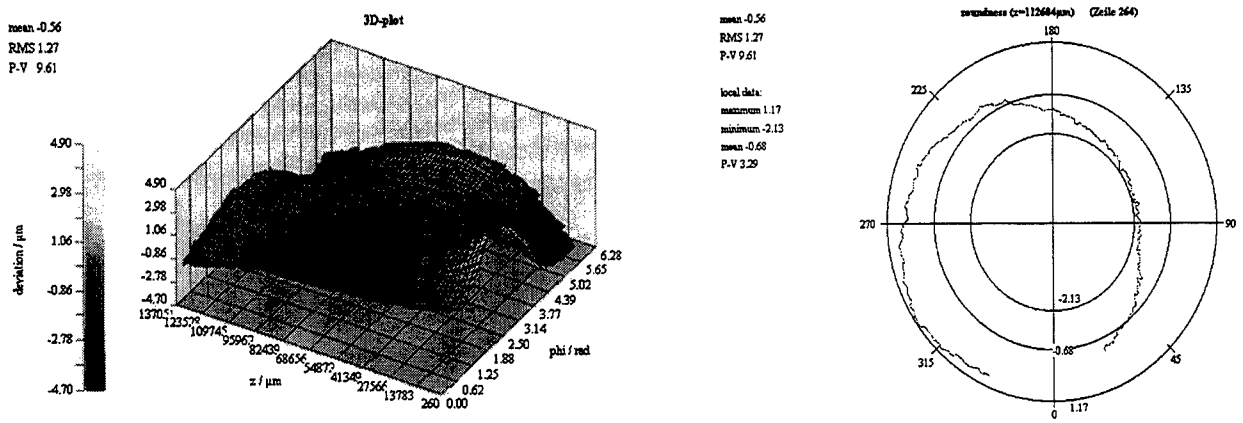

Fig. 2: Deviations from cylindricity and roundness of a slightly bent cylinder.

Each class of workpieces requires specific computer generated holograms for the wavefront adaption, so that an ideally shaped workpiece will result in a zero fringe field. The appropriate object wave for testing plane surfaces is a plane wave generated by linear phase gratings. For testing cylindrical (see fig.2) and conical surfaces the required conical wave is generated by diffractive axicons [5-7]. A method of how to encode the shape information of more complicated objects having a constant cross-section in the (x,y)-plane along the z-axis is described in [8].

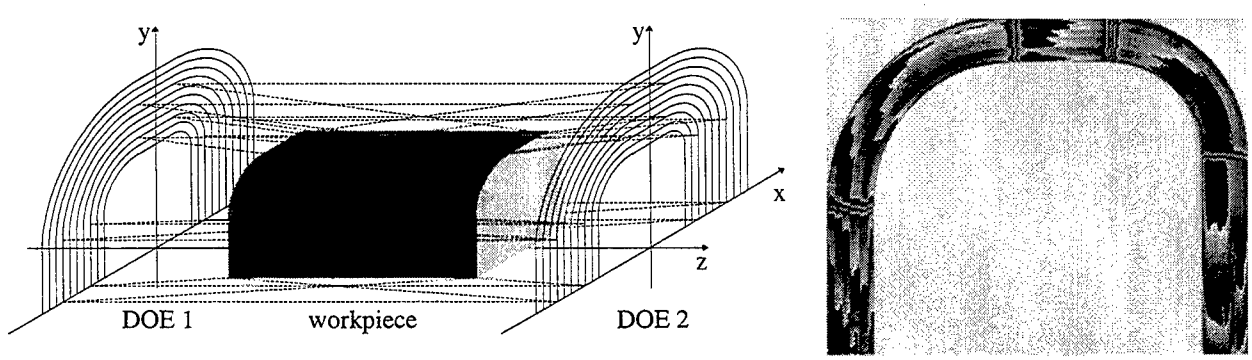

Fig. 3: Workpiece of konvex profile and affiliated wrapped phases.

Both surface deviations of the workpiece from the ideal shape and misadjustments of the workpiece in the interferometric setup are indicated by characteristic interference fringes. As the adjustment aberrations can be described mathematically with sufficient accuracy [9], they can be determined by a least square fit and separated from the genuine surface deviations [6-8]. Measurements up to an accuracy of $\lambda_{eff}/100$ should be achievable with a grazing incidence interferometer. Our system needs 10s for the measurement of plane workpieces, 15s for cylindrical ones and 25s for a workpiece which mantle surface consists of three plane and two cylindrical segments. This time includes phase stepping, LSQ-fit, elimination of adjustment aberrations and visualization of the results.

REFERENCES

[1] N. Abramson, "The Interferoscope, a new type of interferometer with variable fringe separation," *Optik* **30**, pp. 56-71 (1969).
[2] K.G. Birch, F.J. Green, "Oblique incidence interferometry applied to non-optical surfaces," *J. Phys. E (GB)* **6**(10), pp. 1045-1048 (1973).
[3] L. Denes, J. Salsbury, "Flatness, parallelism and other novel uses of grazing-incidence interferometry in precision engineering," Topical Conference on Microscopic Inspection of Macroscopic Structures, American Society of Precision Engineering, pp. 20-23 (1995).
[4] T. Dresel, J. Schwider, A. Wehrhahn, S. Babin, "Grazing incidence interferometry applied to the measurement of cylindrical surfaces," *Opt. Eng.* **34**(12), pp. 3531-3535 (1995).
[5] J. Schwider, "Verfahren zur Prüfung technischer Oberflächen mit Hilfe von computer-erzeugten Hologrammen," GDR Pat. Appl. No. WP 106769, (04.01.1972).
[6] S. Brinkmann, T. Dresel, R. Schreiner, J. Schwider, "Axicon-type test interferometer for cylindrical surfaces," *Optik* **102**(3), pp. 106-110 (1996).
[7] S. Brinkmann, T. Dresel, R. Schreiner, J. Schwider, "Grazing incidence interferometer for plane and cylindrical surfaces," submitted to *Opt. Eng.*
[8] T. Dresel, S. Brinkmann, R. Schreiner, J. Schwider, "Testing of rod objects by grazing incidence interferometry: theory," submitted to *Appl. Opt.*
[9] N. Lindlein, R. Schreiner, S. Brinkmann, T. Dresel, J. Schwider, "Axicon-type test interferometer for cylindrical surfaces: systematic error assessment," *Appl. Opt.* **36**(13), pp. 2971-2795 (1997).

Neural networks as a statistical model for optical scatterometry

Ilkka Kallioniemi and Jyrki Saarinen
Department of Engineering Physics and Mathematics, Helsinki University of Technology,
FIN-02015 HUT, Espoo, Finland,
Tel.: +358 9 451 3155 or 3157, Fax: +358 9 451 3164,
e-mail: Ilkka.Kallioniemi@hut.fi or Jyrki.Saarinen@hut.fi

Erkki Oja
Department of Computer Science and Engineering, Helsinki University of Technology,
FIN-02015 HUT, Espoo, Finland,
Tel.: +358 9 451 3265, Fax: +358 9 451 3277,
e-mail: Erkki.Oja@hut.fi

1 Introduction

The advancement of new lithography techniques, such as electron-beam lithography and x-ray lithography, has enabled the fabrication of diffractive optical elements (DOEs) with feature sizes of the order of hundreds of nanometers and even less. There is also a continuous trend towards smaller line widths and higher packaging densities in memory cells and other semiconductor devices. Most of the elements are still done successfully by UV lithography which is still in the development stage in the deep UV region.

One of the major bottlenecks in the progress of all the techniques mentioned above is the lack of suitable methods for inspecting the quality of the smallest features. Both mechanical and optical profilometry as well as optical microscopy are limited in resolution when the smallest feature sizes are below 1 μm. It is possible to use Scanning Electron Microscopy, Near Field Microscopy, or Atomic Force Microscopy to view the topological image of the sample but they are slow and expensive methods, and require preprocessing of the sample.

Optical scatterometry is not an imaging method but it determines the sample topology by solving the inverse scattering problem [1]. The sample is first probed with a coherent laser beam, and the light scattered from the sample is measured by a photodetector. The spatial distribution of the scattered light can be used as an optical fingerprint for identification. However, because several different topologies correspond to the same spatial distribution, it is always necessary to measure more data from each sample. This is realised by varying the measuring set up, e.g., the wavelength and the state of polarization of the laser beam, as well as the angle of incidence of the laser beam.

2 Data analysis

A mathematical model has to be utilized to determine the unknown sample topology from the scattering data. The simplest approach uses lookup tables where the data is compared to that which has been previously collected by measurements or calculated numerically from a number of different topologies. The best matching topology is chosen.

The more analytic methods use linear regression models to form a statistical mapping between the scattering data and the parameterized sample topology. It is then possible to interpolate to the unknown topology by means of the model. Several methods, such as the Partial Least Squares method (PLS) [2, 3] and the Principal Component Analysis (PCA) [4] have been developed and optimized for the purpose. The major limitations emerge from the linearity of the methods.

Neural networks offer the possibility to model arbitrary nonlinear mappings between the scattering data and the sample topology when the neural network is properly implemented. Prior to usage of neural networks a learning stage has to be performed. In the learning stage the neural network is taught by providing it with examples of input-output, i.e., scattering-topology, pairs from the range of interest of sample parameters [Fig. 1(a)]. For periodic DOEs the examples are easily generated by either scalar diffraction theory or rigorous diffraction theory [5] depending on the scale of the features.

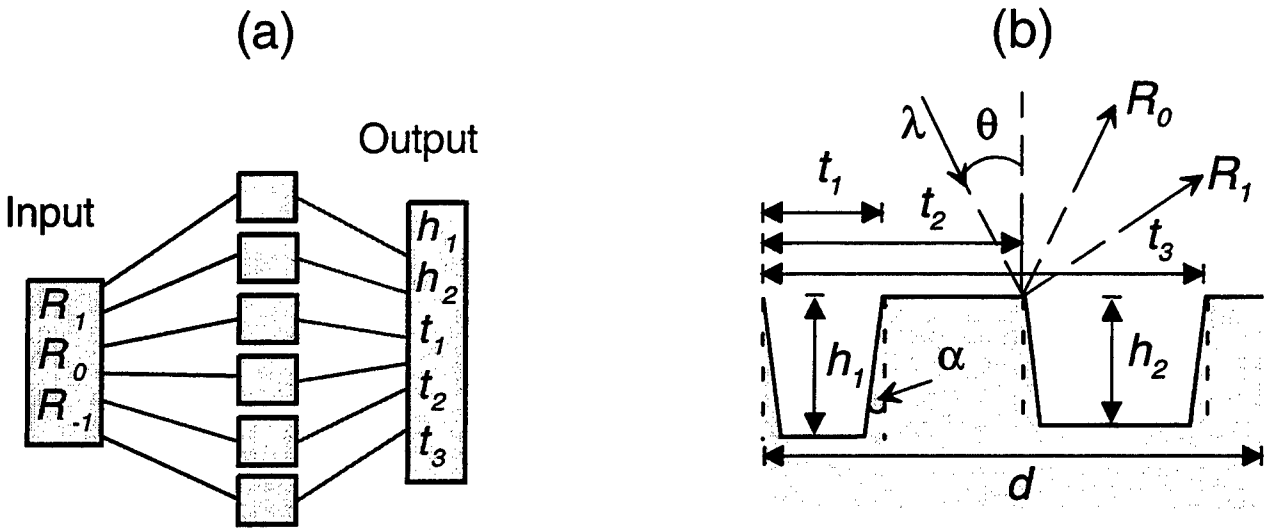

Figure 1: (a) Feedforward (without feedback) neural network with one hidden layer between the input and the output layers. The input consists of the intensities of scattered diffraction orders, such as the reflected orders R_{-1}, R_0, and R_1. The output consists of the prediction of the grating topology. Only a few of the weights between the layers are shown. (b) The topology of a doubly-grooved binary diffraction grating with period d is determined by six independent parameters: h_1, h_2, t_1, t_2, t_3, and α. The incident light (with wavelength λ) hits the grating at the angle θ. Two of the reflected diffraction orders, namely R_0 and R_1 are illustrated.

3 Results

We consider a binary DOE that is designed to deflect as much as possible of the incident light (at wavelength λ = 632.8 nm) asymmetrically into the 1st reflected order [6]. The doubly-grooved element topology is shown in Fig. 1(b). The scattering data has to be calculated by means of the rigorous diffraction theory because the smallest feature sizes are well below the wavelength of light.

We choose five independent parameters to characterize the topology, namely the depths of the grooves and the positions of the groove walls [Fig. 1(b)]; the groove walls are here assumed to be vertical, namely $\alpha = 0°$. The optimum values for the parameters are $h_1 = h_2 = 61$ nm, $t_1 = 68$ nm, $t_2 = 270$ nm, and $t_3 = 517$ nm with period $d = 613$ nm. The refractive index of the gold grating is $n_g = 0.12 + 3.29\,i$ and the incident light comes from glass with refractive index $n_1 = 1.46$. When the ideal grating is illuminated with TM polarized light in the zero angle of incidence, it deflects 70.5% of the light into the 1st reflected diffraction order.

We teach a neural network with one hidden layer of 18 neurons by means of the Levenberg-Marquedt technique which considerably fastens the convergence of the learning stage [7]. The network is taught to work over a range of parameters: $h_1, h_2 \in$ [49 nm...73 nm], $t_1 \in$ [29 nm...107 nm], $t_2 \in$ [231 nm...309 nm], and $t_3 \in$ [478 nm...556 nm]. Although small, the range is realistic considering the accuracy of the electron-beam lithography. The weight coefficients between the input and the hidden layer as well as between the hidden layer and the output [Fig. 1(a)] are iteratively adjusted until a suitable error criteria is met. In order to obtain a reasonable level of uniqueness for the optical identification, the calculations are made with two wavelengths $\lambda_1 = 632.8$ nm and $\lambda_2 = 442$ nm in three different angles of incidence, namely $\theta = 0°, 20°$, and $40°$.

The neural network is subsequently tested by providing it with scattering data calculated theoretically from randomly chosen sample topologies. Gaussian noise, in maximum 4% of the intensity of the reflected diffraction orders, is added to the scattering data to make the simulation more realistic. The root-mean-square (rms) errors for the simultaneous prediction of the five parameters are $\mathrm{rms}_{h_1} = 5.8$ nm, $\mathrm{rms}_{h_2} = 1.5$ nm, $\mathrm{rms}_{t_1} = 6.8$ nm, $\mathrm{rms}_{t_2} = 9.7$ nm, and $\mathrm{rms}_{t_3} = 7.5$ nm. The effect of errors of this size to the functionality of the element is illustrated in Table 1. where the intensity of the 1st reflected diffraction order is seen to deviate only little from the optimal value. The accuracy of the neural network is therefore adequate for this application. The learning stage takes only a few CPU hours in this case.

As another application we consider a subwavelength binary diffraction grating with period $d = 300$ nm with only one groove within the period and the operation equivalent to a thin-film antireflection coating [8]. The structure is characterized by the depth of the single groove h, the linewidth w, and the deviation α of the groove walls from vertical [c.f. Fig. 1(b)]. The element enables over 99% of the incoming light with wavelength $\lambda = 632.8$ nm to be

Topology	h_1(nm)	h_2(nm)	t_1(nm)	t_2(nm)	t_3(nm)	R_1(%)
I	55.2	61	68	270	517	69.6
II	61	59.5	68	270	517	70.4
III	61	61	61.2	270	517	70.4
IV	61	61	68	260.3	517	69.8
V	61	61	68	270	509.5	68.8
VI	55.2	59.5	61.2	260.3	509.5	69.1

Table 1: Intensity of the 1st reflected diffraction order, R_1, for several erraneous grating topologies. In topologies I-V one of the parameters is deviated by the amount of the corresponding rms error while keeping the others fixed, and in topology VI all the five parameters are deviated simultaneously.

transmitted into the zeroth order when the substrate is glass (refractive index $n = 1.5$) and the following optimal values of the parameters are used: $h = 129$ nm, $w = 120$ nm, and $\alpha = 0°$. A neural network is taught to work over a range of parameters: $h \in [89 \text{ nm} \ldots 169 \text{ nm}]$, $w \in [69 \text{ nm} \ldots 165 \text{ nm}]$, and $\alpha \in [0° \ldots 20°]$.

The performance of the taught network is again tested with intensities of diffracted orders that are calculated from randomly chosen topologies. The rms errors of prediction for the three parameters are $\text{rms}_h = 1.0$ nm, $\text{rms}_w = 0.7$ nm, and $\text{rms}_\alpha = 1.9°$ when no noise is added to the scattering data. Adding Gaussian noise, in maximum 4% of the intensity of the diffraction orders, to the scattering data worsens the rms errors only little, i.e., $\text{rms}_h = 2.5$ nm, $\text{rms}_w = 5.8$ nm, and $\text{rms}_\alpha = 3.1°$.

4 Conclusion

We have demonstrated successfully, first time to our knowledge, that it is possible to use optical scatterometry in connection with neural networks to predict simultaneously several parameters that characterize the topology of a diffraction grating. Currently we use five parameters and we are now proceeding to verify our method experimentally, as well as expanding the range of parameters. As the number of predicted topological parameters increases, the multidimensional mapping between the scattering data and the topology becomes more complex. Neural networks have an advantage here because of their nonlinear nature.

It is possible to make the predictions more accurate by using a smaller step size in the range of interest of topological parameters when generating the learning data. This leads to longer calculation times; thus certain amount of trade-off is necessary. As a rule of thumb, the error of prediction should be in consistency with the sensitivity of the element to fabrication errors [c.f. Table 1].

References

[1] J. R. McNeil, S. S. H. Naqvi, S. M. Gaspar, K. C. Hickman, K. P. Bishop, L. M. Milner, R. H. Krukar, and G. A. Petersen, Solid State Tech. **36**, 29 (1993).

[2] S. S. H. Naqvi, R. H. Krukar, J. R. McNeil, J. E. Franke, T. M. Niemczyk, D. M. Haaland, R. A. Gottscho, and A. Kornblit, J. Opt. Soc. Am. A **11**, 2485 (1994).

[3] J. Bischoff, J. W. Baumgart, H. Truckenbrodt, and J. J. Bauer, Proc. SPIE **2725**, 678 (1996).

[4] K. P. Giapis, R. A. Gottscho, L. A. Clark, J. B. Kruskal, D. Lambert, A. Kornblit, and D. Sinatore, J. Vac. Sci. Tech. A **9**, 664 (1991).

[5] M. G. Moharam and T. K. Gaylord, J. Opt. Soc. Am. **71**, 811 (1981).

[6] J. Saarinen, E. Noponen, J. Turunen, T. Suhara, and H. Nishihara, Appl. Opt. **33**, 2401–2405 (1995).

[7] C. M. Bishop, *Neural Networks for Pattern Recognition* (Oxford University Press, New York, 1995).

[8] T. K. Gaylord, W. E. Baird, and M. G. Moharam, Appl. Opt. **25**, 4562 (1986).

Evaluation of a diamond-cut large-groove grating for near infrared spectroscopy

Miwa Goto, Masatoshi Imanishi, Fumihide Iwamuro, Toshinori Maihara

Department of Physics, Kyoto University,
Kitashirakawa-Oiwake-Cho, Sakyo, Kyoto, 606-01, JAPAN
Electronic mail: mgoto@cr.scphys.kyoto-u.ac.jp
imanishi@cr.scphys.kyoto-u.ac.jp
iwamuro@cr.scphys.kyoto-u.ac.jp
maihara@cr.scphys.kyoto-u.ac.jp
Telephone number: JAPAN(81)-75-753-3857
FAX number: JAPAN(81)-75-701-5377

1. Fabrication of large-groove grating

The rapid progress of large format infrared detector arrays enables us to take a fairly wide spectrum with a medium resolution by a single exposure, if a coarsely grooved echelle-type grating can be used. To produce such a spectrum onto a square detector array, it is necessary to fabricate a grating with much larger groove separation than those used in visible spectroscopy, which has so far not been available. For instance, if we envision a spectrograph which produces an echelle spectrogram in the 3 to 4 microns, a realistic solution of spectrograph design would be to employ a large-groove grating usable in the orders ranging from 20-th to 30-th, or even higher. Of course, the width of such grooves is beyond the limit of the usual ruling method. We therefore attempted to produce a grating with a 125 μm groove scale by the high precision cutting of an Aluminum alloy directly with a diamond bite. In this report, we present the test result of the machine-cut grating, and make evaluation of the diffraction efficiency by referring to the result of a numerical simulation software. The grating is now incorporated in an astronomical spectrograph which works mainly in 3 μm region (Imanishi et al 1996).

		specification	results
groove period	[μm]	125±1	124.99±0.01
blaze angle	[°]	26.75±0.75	26.53
roughness	[μm]	<0.5	<0.15
size	[mm]	50×50×10	

Table 1:

2. Measurement of grating shape

The two most important features of a grating are the smoothness of the reflective surface and the precision of groove period. The former was measured by a scanning needle and is shown in figure 1. The scan direction is vertical to a groove. The peak-to-peak roughness along the 106 μm trace is 0.136 $\pm$0.005 μm. To estimate the groove period we measured the width of 100, 200, 300, and 400 grooves by an optical microscope. The average groove separation is found to be 124.99 μm without any accumulation of errors in all the measurements.

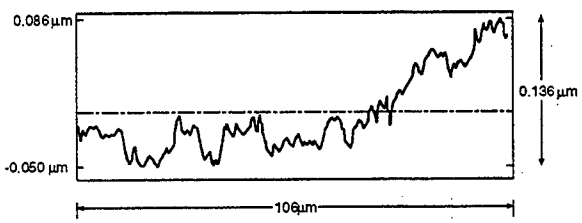

Figure 1:

3. Diffraction efficiency

The diffraction profiles of the grating were measured with a scanning spectral photometer, which is equipped with a nearly monochromatic beam and a PbS detector mounted on a moving arm. The result is shown by dots in figure 2. The test wavelength is 2.156 μm. The order of the central peak is 48-th. The diffraction efficiency was obtained by integrating the central peak profile after deconvolving the overlapped profiles. The theoretical diffraction efficiency was calculated by a grating simulator, GSOLVER, developed by Grating Solver Development Co. (Gaylord et al. 1985, Moharam et al. 1986). The simulated diffraction efficiencies are represented by solid bars in figure 2. There is remarkable agreement between the actual diffrac-

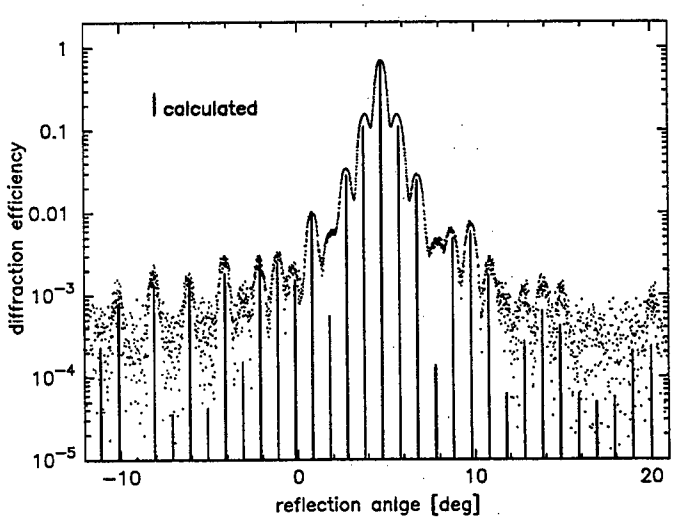

Figure 2:

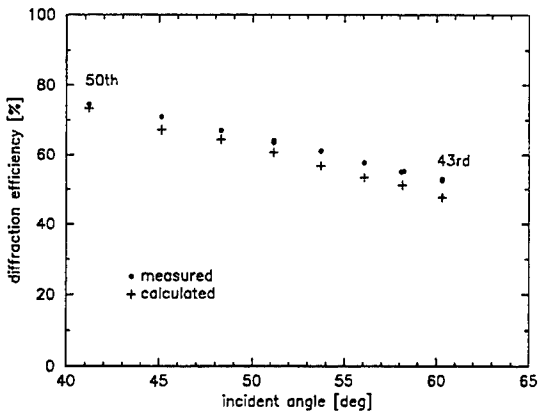

Figure 3:

tion profile and the pattern of simulated diffraction efficiencies. The diffracted energy concentrated in the central peak decreases when the incident angle increases as displayed by filled circles in figure 3. On the other hand the simulated diffraction efficiency exhibits almost identical behavior as shown by crosses in figure 3. Consequently, our conclusion is that the fabricated grating is nearly ideal with an unprecedentedly large groove.

Reference

1. Gaylord, T. K., Moharam, M.G. 1985, Proceedings of the IEEE, vol.73, No. 5, pp. 894

2. Imanishi, M. Terada, H., Sugiyama, K., Tomita, K., Goto, M., and Maihara, T.,1996, PASP, 108, 1129

3. Moharam, M. G., Gaylord, T. K. 1986, J. Opt. Soc. Am. A, vol. 3, No. 11, pp. 1780

4. Grating Solver Development Co., http://www.gsolver.com

Diffractive Optics and Micro-Optics

Joint Session with International Optical Design Conference

Thursday, June 11, 1998

Michael Missig, Opkor Inc.
Presider

JThB
10:30am–12:00m
Koa Room

DIFFRACTIVE OPTICS: From Basic Research to Practical Applications

Prof. G. Michael Morris

The Institute of Optics
University of Rochester
Rochester, New York 14627

Phone: 716-275-5140
Fax: 716-271-1027
e-mail: morris@optics.rochester.edu

Rochester Photonics Corporation
330 Clay Road
Rochester, New York 14623

Phone: 716-272-3010
Fax: 716-272-9374
e-mail: morris@Rphotonics.com

1. Introduction

A diffractive optical element is an optical device that utilizes interference and diffraction, rather than refraction or reflection, to shape an emerging wavefront. In this talk we will concentrate on the image-forming capabilities of diffractive optics. Traditional Fresnel zone plates are characterized by low efficiency as a result of their construction with alternating clear and opaque regions and do not find wide application. Volume holography has distinct advantages for certain applications; however, environmental and material issues preclude its use in many applications. The majority of applications today utilize surface-relief diffractive optical elements. Surface-relief diffractive optics make use of precision-engineered surface structures to provide wavefront transformations in optical phase and can be highly efficient. In the past few years, diffractive optics has received overwhelming attention and numerous commercial and government applications of the technology are being developed. A key factor for this transition from the research laboratories to practical applications is the improvements in the manufacturing processes that provide high quality (high diffraction efficiency/low scatter) diffractive optical elements.

A typical surface-relief diffractive lens consists of concentric annular zones. It is often useful to think of a diffractive lens as a "modulo 2π" lens, i.e., all integral multiples of 2π in the phase have been removed. The radius of the *m*-th zone boundary, r_m, is determined by the following relation: $\phi(r_m) = 2\pi m$, where $\phi(r)$ is the desired phase profile for the lens; these are called full-period zones. In general, the phase function associated with a symmetric lens operating at wavelength λ_o is given by $\phi(r) = Ar^2 + Gr^4 + Hr^6 + \ldots$ where $A = \pi/(\lambda_o F)$, G and H are associated with aspheric coefficients of the emerging wavefront, and F is the principal focal length of the lens. The important parameters of the element to control are the zone spacing, the step height at each zone boundary, the surface profile within each zone, and the alignment of the diffractive element with respect to other elements in the system. Diffractive optics offers an optical designer new degrees of freedom that can be used to optimize system performance and design novel optical components and systems.. Using diffractive optics one can:

- Create arbitrary phase functions needed to optimize optical system performance;
- Correct chromatic aberrations using a single optical material;
- Eliminate the need for exotic materials;
- Fabricate diffractive elements directly on the surface of conventional optical elements for aberration control and thereby eliminate the need for additional optical elements;
- Fabricate microlens arrays and micro-optic components for a wide variety of applications, including laser

diode collimation, wavefront sensing, detector enhancement, and optical interconnections for optoelectronic integrated circuits.

These features enable the design and fabrication of high performance, lightweight and low-cost optical components and subsystems, which are applicable in numerous commercial and government systems.

In this presentation, we will review the various fabrication techniques that are used to produce surface-relief diffractive optical elements and discuss the features and limitations of each method. We will then describe the design, features and performance of diffractive optics in several different applications, including head-mounted displays, laser printing systems, and laser projection displays.

2. Fabrication Methods

Previously, wide-spread applications of diffractive optics have been limited because of the effects associated with scattered light. There are two sources of scattered light associated with diffractive optical elements. We will refer to these as "structured scattering" and "statistical scattering." Structured scattering is associated with light that is distributed into unwanted diffraction orders, and statistical scattering is associated with the surface roughness (or finish).

To produce high quality diffractive optical elements, one must shape, or "micro-machine," the required surface profile. To achieve high diffraction efficiency, the edge step at each zone boundary must be extremely sharp and the surface-profile within each zone must be shaped (or blazed) and smooth to avoid "statistical" scattering. This requirement for sharp edges and smooth blazed surfaces places stringent, and somewhat incompatible, requirements on the fabrication process used to make the surface-relief master.

The basic approach to produce a surface-relief DOE is to fabricate a precision surface-relief master element that can be used as a tool for making a large number of replicas from the master or sub-master elements. The tooling costs for surface-relief DOEs are similar to those realized with plastic-injection molding processes. The cost savings is achieved through replication or molding. With a suitable replication (or molding) process, one can fabricate tens of thousands of elements using a single tool.

There are several methods available for the fabrication of surface-relief diffractive master elements –optical and electron-beam lithography (mask-and-etch), single-point diamond turning, and single-point laser pattern generation methods. To my knowledge the first report of fabrication of diffractive lenses using the (mask-and-etch method) was made by d'Auria et al.[1] in 1972. In their work three successive masks were used to expose a photoresist-coated silica substrate, which was etched to the desired step depths by controlling the etching time. The resulting silica master was then used as a mold to make a plastic copy, which to my knowledge was the first experimental demonstration of a plastic-molded diffractive lens. The mask-and-etch lithographic was later investigated in detail by Veldkamp[2] and co-workers at the MIT/Lincoln Laboratory in the 1980's, who coined the term "Binary Optics" to describe the mask-and-etch process. The primary difficulty in achieving high quality diffractive optical elements with the binary-optics approach is the precision of mask alignment required to build up the approximate "stair-case" approximation to the desired blaze (or surface-relief) profile. Mask alignment errors have a profound effect on diffraction efficiency and the amount of structured scattering.

By the late 1980's and early 1990's several groups were investigating the use of single-point diamond turning (SPDT) for both visible[3] and infrared applications[4]. In the visible-light applications, SPDT was used to fabricate a metal master, which was subsequently used to mold diffractive optical elements in plastic. To my knowledge the first commercial application involving molded diffractive lenses was the "Posterior

Chamber Ultraviolet Light Absorbing Intraocular Lens with Multifocal Optic" introduced by 3M Company in May 1989, which consisted of a lens optic made of molded polymethylmethacrylate (PMMA) with an ultraviolet absorbing agent added. Quoting from the 3M product description insert, "The multifocal optic is designed to provide the patient with an enhanced near vision accommodation. The optic consists of a concentric diffractive microstructure superimposed upon the posterior surface of a conventional lens which diffracts light to create 2 foci." Rochester Photonics Corporation (RPC) has recently set a new performance standard for diffractive lenses operating in the visible wavelength range.[5] We have been able to reduce significantly the deleterious effects associated with scattered light from surface-relief diffractive optical elements. The diffraction efficiency of replicated (and injection molded) diffractive lenses now consistently ranges between 97% to 99% at the design wavelength, and the measured rms-surface roughness within each zone is approximately 40 angstroms; this is the highest diffraction efficiency that has been produced for visible-light diffractive elements. Figure 1 shows a typical diffractive surface-relief profile produced in a molded element. Sharp edge transitions at the zone boundaries and smooth surface-relief (or blaze) profiles within each zone are the key features required to produce high quality diffractive elements.

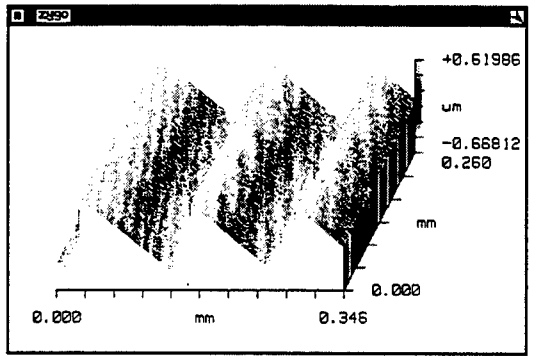

Fig. 1. Surface-relief profile of a molded diffractive optical element produced using a SPDT master.

Single-point laser pattern generation offers a combination of the virtues of single-point diamond turning (i.e. continuous blaze profile) and laser-based photolithographic fabrication[6]. RPC currently operates two laser pattern generation systems. In one machine the surface-relief pattern is produced using a Cartesian, (x,y), scan format. The other machine uses a r-theta scan geometry, in which the substrate is spun on an air-bearing spindle.

In these systems the substrate (coated with a photosensitive material) is scanned by a focused laser beam, typically from an argon-ion or helium-cadmium laser. As the beam is scanned, the laser intensity is modulated and the beam exposes the photosensitive layer, which upon development produces a continuous surface-relief pattern. The resulting surface can then be used to produce a tool suitable for replication or molding, or etched directly into the underlying substrate using a chemically-assisted etch process, such as reactive-ion etching.

A key feature of single-point laser pattern generation is that one can produce arbitrary surface-relief structures, such as diffractive and refractive microlens arrays, anamorphic optics for laser-diode systems, and complicated grating-like structures for fan-out arrays. A continuous-blaze, diffractive microlens array produced using the x-y laser pattern generator is shown in Fig. 2. Other applications include structured light

Low-Distortion Imaging Spectrometer Designs utilizing Convex Gratings

Pantazis Mouroulis
Jet Propulsion Laboratory
California Institute of Technology
MS 306-336, 4800 Oak Grove Drive, Pasadena, CA 91109
Tel. (818) 393-2599
Fax (818) 393-9567
email: pantazis.mouroulis@jpl.nasa.gov

The requirement for very low distortion in pushbroom imaging spectrometers has been recently recognized. It has been shown that the spectral response function of a pixel must be known with great accuracy.[1] A small uncertainty in the location of the peak of this function can lead to significant error in the calculated pixel radiance. A maximum shift of less than 1% of the spectral response function (e.g. 0.1nm in 10nm halfwidth) has been identified as desirable in order to produce data that are free of significant spectral calibration errors.

Although elaborate calibration methods can conceivably reduce the effect of such errors, it is nevertheless desirable to start with a design that lessens the need for and dependence on such methods. The 1% maximum shift translates to a distortion value of 1/100th of a pixel, a value that is well outside the range of familiar optical designs. The designer was thus requested to investigate novel spectrometer forms that are capable of such low distortion both in theory and in practice.

The spectrometer designs that were found capable of such performance were based on the Offner reflective relay.[2] Concentric spectrometer forms have been recognized for their potential of providing good optical correction and compact size.[3,4] However, the requirement for submicron distortion has not been explicitly stated or evaluated previously. In addition, lack of an appropriate technology for grating fabrication has limited the practical realization of these designs.

Progress in electron-beam lithography techniques has permitted the fabrication of high-performance convex gratings that are a perfect solution to the above problems. Specifically, such gratings can be produced with the required substrate convexity, while providing flexibility in the following grating parameters: variation of the blaze angle (or lack thereof) across the grating, control of the shape of different blaze areas, control of the average diffracted phase difference between different blaze areas, control of the groove shape (beyond sawtooth or sinusoidal), and precise control of the grating pitch including any desirable variation. All these grating properties impact the distortion characteristics of the spectrometer.

An example of a low-distortion design is shown in figure 1. The input slit is perpendicular to the plane of the paper at the top left of the figure. The grating is formed on the convex mirror which is also the stop location. The design is telecentric, with a magnification of -1. Other characteristics of this design are: all spherical concentric surfaces, f/2.8, 18mm slit length,

spectral range 1-2.5μm, greater than 82% diffraction ensquared energy within a 27μm square pixel across field and wavelength, spectral resolution of 10nm, and total volume of 14x13x6cm (including slit and image). There is practically zero distortion. The optical design program gives a maximum distortion value of 0.00012% (~10^{-6}). However, the percent distortion as commonly understood in optical design is not an adequate measure. The spectrometer distortion requirement involves a spectral as well as a spatial dimension.

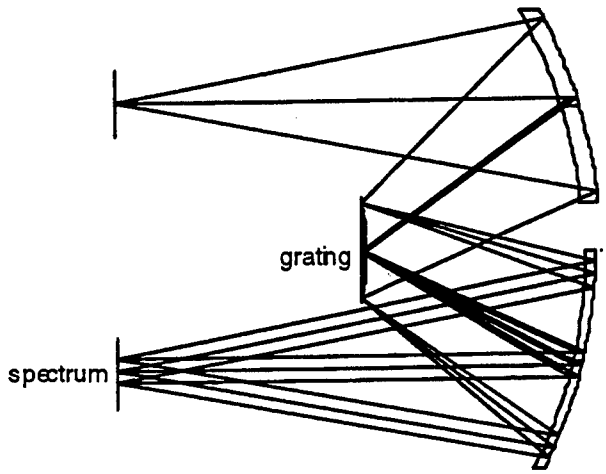

Figure 1. Schematic of a typical low-distortion Offner spectrometer design

Thus the first distortion requirement is that the monochromatic image of the slit remain straight to within a small fraction of a pixel for all wavelengths. A traditional way of relaxing this requirement is through the use of curved slits, but a straight slit is preferable in terms of ease of fabrication and alignment. On the assumption then that the monochromatic slit images are aligned with the columns of the detector array, the second distortion requirement is that the spectrum of any point along the slit be straight and parallel to a row. These two requirements have been called spectral and spatial distortion, but the names are not intuitively obvious since both can apply equally to either type of distortion; hence they are avoided here.

The design optimization utilizes a merit function in which appropriate rays are used, whose image plane intersections are representative of the centroid locations for the corresponding image points. The difference between the x or y coordinates of these locations is then set to zero to within a desired accuracy by assigning appropriate weighting factors in the corresponding operands. The remainder of the merit function is concerned with optimizing the spot size (or rms wavefront error) as usual.

Tolerance analysis performed on a sample design indicated that two of the three mirrors could be fitted to manufacturer's testplates, while the radius of the third had to be controlled to within 0.1%. The system is sufficiently tolerant of tilts, decenters, or random wavefront error.

A system optimized in this fashion rests on the assumption that the grating has no imperfections in wavefront quality, and that the diffraction efficiency is uniform across its entire extent for all wavelengths. These requirements are in fact not normally satisfied, and must be addressed if the system is to approximate its design performance. Normally, the grating must be blazed for high efficiency. The electron-beam technique allows the fabrication of gratings in which the blaze angle remains constant with respect to the local grating normal. This cannot be done with ruling techniques unless the tool were made to change angle continuously for every groove. Ruled gratings will also suffer from wavefront irregularities, which will in general affect the centroid location and hence the distortion. Electron-beam gratings can approximate the true blaze profile without variation even over a curved surface, thus providing good wavefront quality and uniform pupil transmittance.

In some designs it has been found necessary to use two different blaze areas in order to obtain moderately high efficiency over a wider band than would be possible with a single blaze. The resulting wavelength-dependent apodization and phase difference between the two blaze areas can affect adversely the distortion as calculated on the assumption of a uniform grating. However, the electron-beam technique allows the production of concentric blaze areas, which, when coupled with lack of coma in the design, reduce the effect of the apodization to almost undetectable levels. In addition, the technique permits the control of the average relative depth of the two blaze areas. Specifically, the average depth difference can be made to be zero (within experimental error), which is also impossible with ruling techniques.

Low distortion designs have been produced over various bands within the range 0.2-12μm, with slit lengths up to 27mm, f-numbers down to 2.2, and all centered spherical optics, with sizes never exceeding 14x14x7cm. Electron-beam lithography allows the production of gratings that can satisfy the stringent distortion tolerances imposed by the spectrometer spectral calibration requirements.

The research described in this paper was carried out by the Jet Propulsion Laboratory, California Institute of Technology, under a contract with the National Aeronautics and Space Administration.

References

1. R. O. Green, "Spectral calibration requirement for Earth-looking imaging spectrometers in the solar-reflected spectrum", Appl. Opt. (1998) in print.

2. A. Offner: "Unit power imaging catoptric anastigmat", U.S. Patent No. 3,748,015 (1973)

3. L. Mertz: "Concentric spectrographs", Appl. Opt. **16**, 3122-3124 (1977)

4. D. R. Lobb: "Theory of concentric designs for grating spectrometers", Appl. Opt. **33**, 2648-2658 (1994).

Laser printer scan lens with diffractive optics

Kevin J. McIntyre and G. Michael Morris, Institute of Optics
University of Rochester, Rochester, NY 14627
(716) 275-2322, (716) 275-1027 (FAX)
kmci@optics.rochester.edu, morris@optics.rochester.edu

Susan Dunn, Karen Rumsey, and Ken Ossman, Xerox Corporation
800 Phillips Road, Webster, NY 14580
karen_rumsey@wb.xerox.com, ken_ossman@wb.xerox.com

Introduction

A scan lens for a laser printer system consists of an F-θ lens and a scanning element, typically a polygon mirror. Due to mechanical wobble and facet-to-facet misalignment, a polygon mirror tends to steer the focused beam out of the intended scan line and therefore requires some form of optical compensation. The most common method[1] makes use of anamorphic optical elements. Traditionally, lenses based on this approach contain either a toroidal surface or a reflective cylindrical field lens, both of which are relatively expensive. *It is possible to use a diffractive surface to replace the need for either of these surface types.* Non-toroidal hybrid scan lenses have been discussed previously[2,3]. These designs were limited to rotationally-symmetric geometries and therefore could not be used with polygon mirrors. This paper discusses the design, fabrication, and testing of a prototype diffractive scan lens for a 600 dpi laser printer system.

F-Θ Design

The basic layout is depicted in Figure 1. The system contains a diode laser, collimator, plano-cylindrical lens, polygon mirror, and two post-polygon lenses, both of which are cylindrical-spherical elements. The collimator produces a collimated, elliptical beam from the diode source. A rectangular stop is located after this lens. The plano-cylindrical lens focuses in the sagittal plane and forms a line image at the polygon. This line image is re-imaged by the post-polygon lenses to form a focused spot at the photoreceptor plane. As the polygon rotates, the spot image will not shift appreciably in the sagittal direction due to the conjugate relationship between the mirror facet and the photoreceptor in the sagittal plane.

Rotationally-symmetric diffractive surfaces are located on the spherical surfaces of the collimator lens and the first F-θ lens element. The diffractive surface on the collimator lens helps correct spherical aberration, coma, and chromatic aberration. The minimum zone width is 67 microns. The diffractive surface on the first F-θ lens element helps correct field-curvature, chromatic aberration, and distortion. The post-polygon refractive lens layout was chosen to minimize Petzval curvature and axial astigmatism, while the diffractive surface was designed to minimize the residual off-axis astigmatism. The minimum zone width for this diffractive surface is 34 microns. The diffractive surfaces were created using a polymer replication technique performed directly on the glass lens substrates. Tooling for the replication process was produced by single-point diamond turning. Diffractive surface fabrication was performed by Rochester Photonics Corporation[4].

Basic Design Specifications

The prototype was designed for a 600 dpi laser printing system with a 12" scan line (305 mm). This implies a pixel (writing) width of about 42.3 microns. Some basic design specifications are given below:

Focal length	323.389 mm
Beam scan angle	+/- 27 deg
Scan length	305 mm

Spot size (FWHM)	27 um (tan) x 38 (sag)
Wavelength	670 nm (+/- 5 nm)
Diode diverg. (FWHM):	9 x 30 deg
# Polygon facets	8
Inscribed polygon diam	58 mm
Feed angle	42 deg
Wobble - spot shift*	< 1 um
Scan linearity	< 100 um

* spot shift in sagittal direction for 25 arcsecond mechanical tilt of facet mirror in sagittal plane

Feed angle is the angle between the optical axes of the pre-polygon and post-polygon lenses, and scan linearity is defined as the deviation from the distortion relation, $y = f \cdot \theta$, where y is the tangential image position, f is the scan lens focal length, and θ is the optical scan angle. The design bandwidth of 10 nm is provided to allow for wavelength variation as a function of temperature. The focused spot should not shift (along the scan line) more than 10% of the pixel width (42.3 um) when the laser mode hops ($\Delta\lambda \sim 1$ nm).

Design Performance

The important theoretical design results are shown in Figure 2. The spot sizes have a uniformity of better than +/- 10 % of nominal across the entire scan line. The nominal spot size can be altered by adjusting the size of the limiting aperture. The maximum scan linearity error is 26 microns, less than a pixel width. The maximum lateral color for a 10 nm bandwidth is approximately 25 microns. For a mode hop of 1 nm, this corresponds to a spot shift of 2.5 microns. The sagittal spot shift due to polygon wobble is less than 1 micron across the entire scan line.

A prototype lens based on this design has been fabricated. At the time of this writing, the lens was being tested for all of the performance specifications described above. So far, the measured results have been in very good agreement with theory. A discussion of test results will be presented at the meeting.

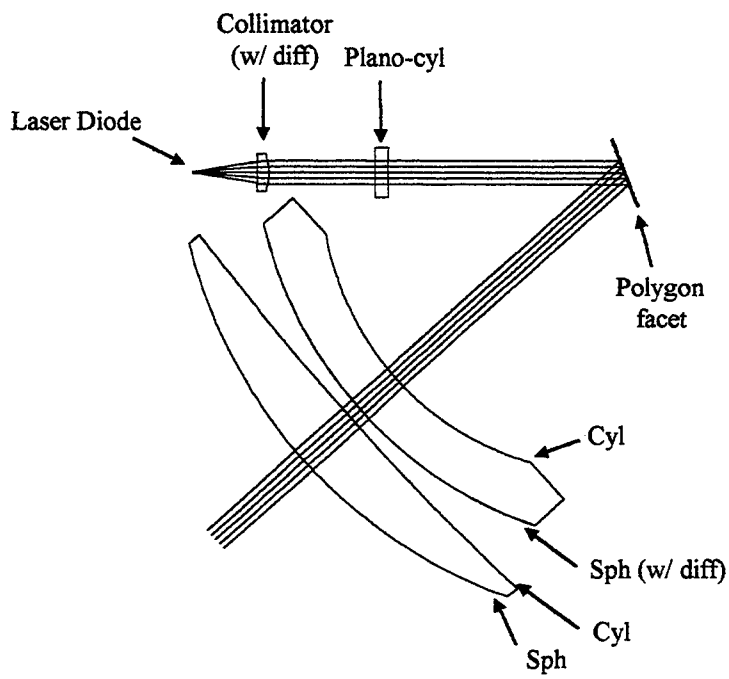

Figure 1. Layout of diffractive scan lens.

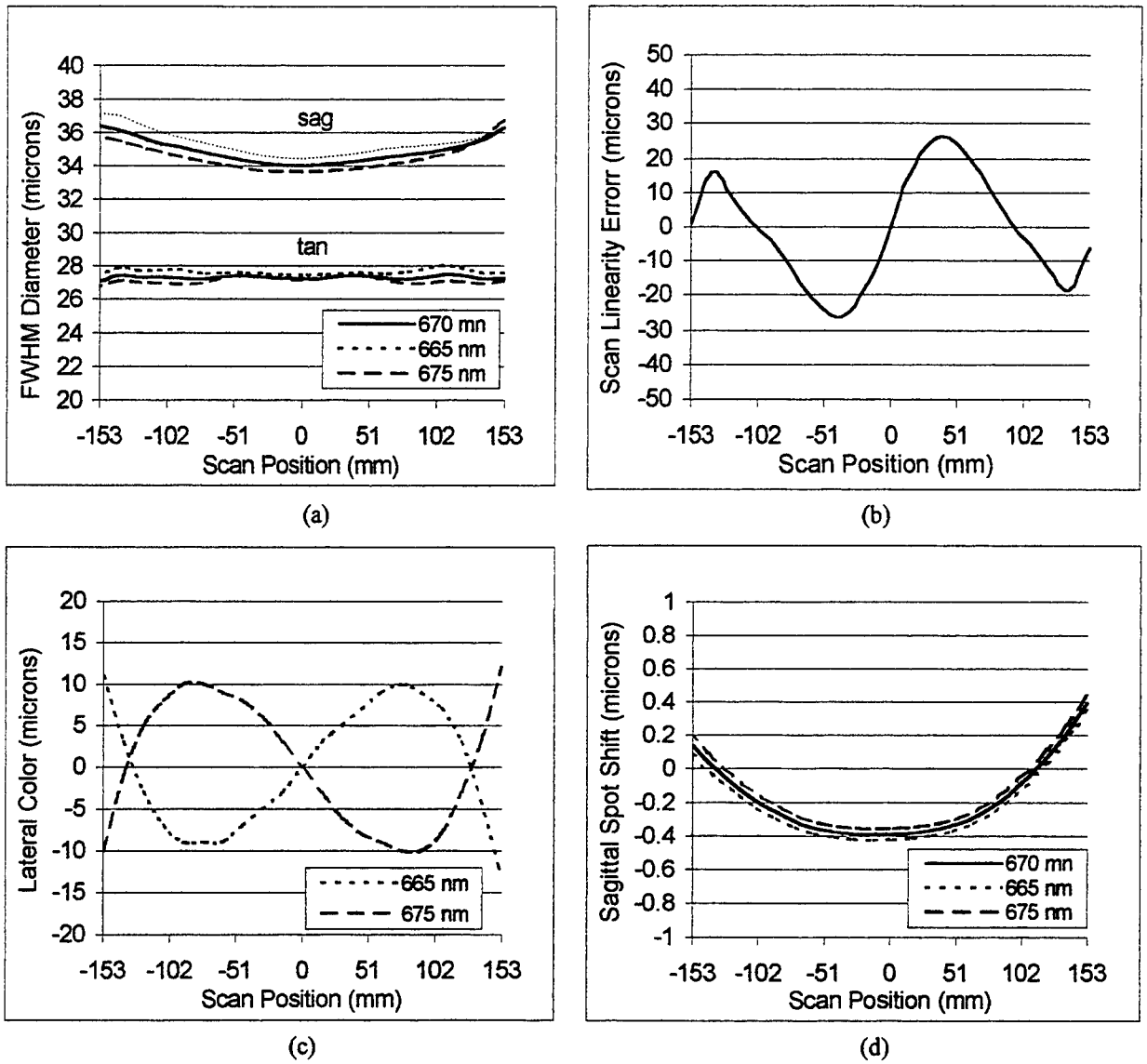

Figure 2. Theoretical performance curves. Negative scan position corresponds to the feed (diode) side. (a) FWHM spot diameters along tangential and sagittal directions, (b) Scan linearity error for $\lambda = 670$ nm, (c) Lateral color relative to $\lambda = 670$ nm, (d) Sagittal spot shift due to 25 arcsecond mechanical tilt of facet mirror in sagittal plane.

Acknowledgement: This work supported in part by the Center for Electronic Imaging Systems.

References

[1] Fleischer, J. M., "Light Scanning and Printing System," U.S. Patent No. 3,750,189 (1973).

[2] Stephenson, D., "Diffractive Optical Elements Simplify Scanning Systems," Laser Focus World, pp 75-80, (June 1995).

[3] McIntyre, K. J. and Morris, G. M., "Diffractive Optics Technolgy for F-θ Scan Lenses," *in Diffractive Optics and Micro-Optics*, Vol. 5 of 1996 OSA Technical Digest Series (Optical Society of America, Washington, D.C., 1996), pp 94-97.

[4] Rochester Photonics Corporation, 330 Clay Road, Rochester, NY, 14623, USA.

Hybrid optics in dual waveband infrared systems

A. P. Wood and P. J. Rogers

Pilkington Optronics
Glascoed Road, St. Asaph, Denbighshire, LL17 0LL, U.K.
Tel. (01745) 588402
Fax. (01745) 588356

P. B. Conway and P. A. Manning

Defence Research Agency
St. Andrews Road, Gt. Malvern, Worcestershire, WR14 3PS, U.K.
Tel. (01684) 895846
Fax. (01684) 896530

1. INTRODUCTION

Diffractive optics in the form of hybrid elements manufactured by single point diamond turning are now well-established and widely used in both mid-wave and long-wave infrared optical systems. The fundamental advantages, based on the reduced element-count, can have a significant impact on cost, mass and overall complexity

The problems associated with chromatic correction of infrared systems are particularly acute in dual waveband applications [1, 2]. Achromatisation using diffractive optics is therefore potentially of great interest and it has been shown that improvement of multi-waveband infrared systems is, in principle, possible [3]. However, useful performance requires that different diffraction orders are used in each band. It is essential in the design of these systems to take full account of the effects of reduced diffraction efficiency which limits the useful wavelength range in both bands.

This paper examines the fundamental diffraction-based performance limitations of dual waveband systems which incorporate hybrid lenses. These limitations must be understood in order to identify the key trade-offs and optimise the design of the diffractive element. With the basic performance limitations established, the correction of chromatic aberration is considered.

A dual waveband objective lens for an uncooled staring array camera has been designed and manufactured .

2. DIFFRACTION-LIMITED PERFORMANCE

The additional parameter of diffraction efficiency associated with hybrid optics modifies the aberration-free performance which applies to conventional lenses. The effects become more significant as the diffraction order which is used in a given waveband increases. It is insufficient to simply identify solutions for which good aberration correction may be achieved in determining the key trade-offs, particularly when making comparisons with conventional solutions. The main issues have been addressed by considering fundamental results from a scalar diffraction model and by examining a range of aberration-free hybrid lens systems.

As an example, figure 1 shows the polychromatic MTF for a 100 mm, f/1, diffraction-limited hybrid lens, analysed over the 8-12 μm band. Figure 2 shows the polychromatic MTF of such a lens in the 3-5 μm band. In each case, the top solid curve represents a diffraction-limited conventional solution with no diffractive surface. The other curves result from diffractive surfaces in the hybrid lens with different first-order peak wavelengths.

Clearly, even with a second-order peak near the centre of the lower band (first-order peak at 8 μm), a substantial compromise in performance is seen. This suggests that the chromatic aberration correction of an equivalent conventional solution may be relaxed which must play a crucial role in any trade-off considerations.

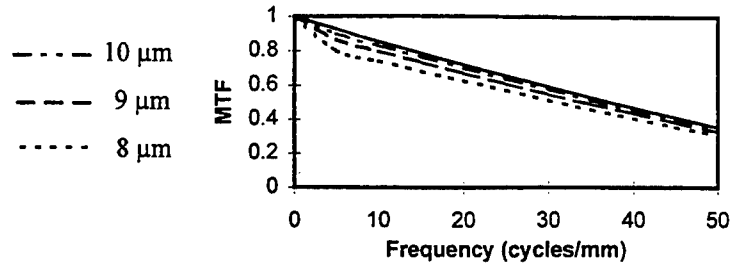

Figure 1 : Upper band MTF

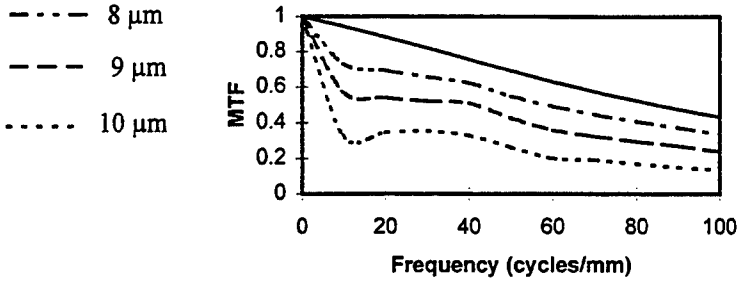

Figure 2 : Lower band MTF

3. CHROMATIC CORRECTION

A comprehensive analysis aimed at identifying useful combinations of elements to correct chromatic aberration over both bands has been undertaken. Software is employed to find all potential 2-material, 3-material and 4-material thin lens achromatic combinations from an exhaustive list of candidate materials; a diffractive surface is included as an additional "material". The option exists to allow a difference in focal lengths between the two wavebands. Output includes a calculation of the element powers for unity focal length, RMS focus excursion, thermal defocus and a risk factor based on material properties. Results may be sorted using a range of criteria. Table 1 illustrates the output; in this typical example, the best four solutions are ranked in order of RMS focus error.

BEST SOLUTIONS IN FOCUS EXCURSION ORDER (UNITY FOCAL LENGTH AT 4.0, 7.0 & 10.5µm))

MATERIALS			POWERS			RMS FOCUS ERROR	TEMP. DEFOCUS	RISK
GE	KRS5	NACL	-0.586	1.787	-0.200	0.80E-05	0.43E-03	4.3
GE	ZNSE	KRS5	-0.695	-0.878	2.573	0.10E-03	0.67E-03	4.7
GAAS	AMTIR-1	NACL	-1.606	2.802	-0.195	0.13E-03	-0.22E-04	3.8
GAAS	KRS5	NACL	-1.643	2.663	-0.020	0.16E-03	0.70E-03	7.4

Table 1 : A sample of 3-material solutions

In addition, a graphical approach which displays the change in power as a function of wavelength has been adopted and allows optimum thin lens solutions to be designed rapidly with an interactive approach. Figure 3 shows the variation of power, for unit power lens, across both wavebands for three promising simple hybrid lenses designed to be achromatic at 8 µm and 12 µm. Aberrations are shown in the first and second diffracted order for the upper and lower bands respectively.

This shows that hybrid optics offer the possibility of extremely simple solutions, provided that a shift in focus is permissible between bands. If a common focal plane is required in the two bands, then it is shown that the benefits gained from the use of a diffractive element are limited.

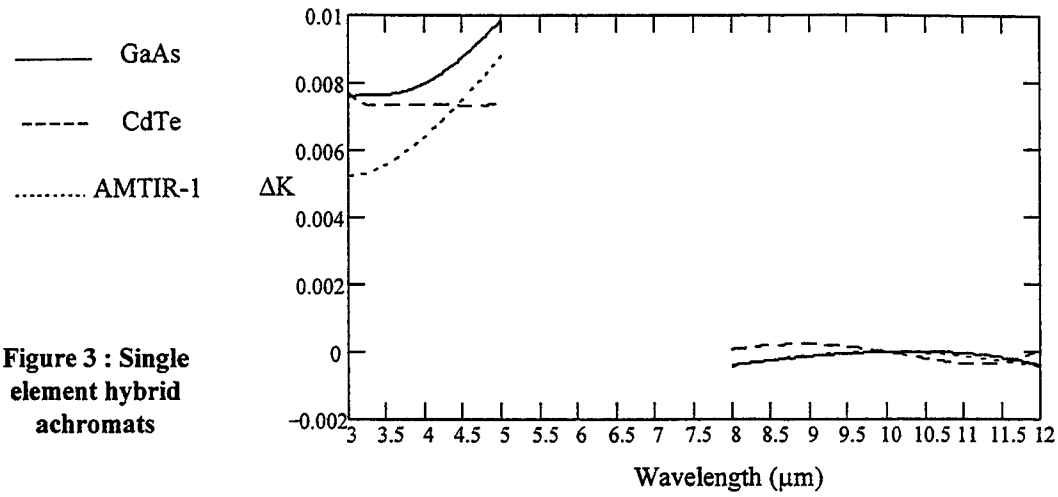

Figure 3 : Single element hybrid achromats

4. A DESIGN EXAMPLE

Figure 4 shows a dual waveband objective lens which has been designed for use with an uncooled focal plane array. This 75 mm, f/1, lens has a diagonal field-of-view of ±6°. The key component is a gallium arsenide hybrid lens using a diffractive element designed with a first-order efficiency peak at 9 μm.

The polychromatic MTF, calculated using software developed in order to take full account of light scattered into unwanted orders, is shown in table 2 using the wavelengths and weights given. The figures in parentheses ignore the effects of this scattered energy, and assume 100% efficiency in the first and second orders for the upper and lower bands respectively. The diffraction limited MTF at 9 cycles/mm, which represents the Nyquist frequency of the detector array, is 88% (long-wave) and 95% (mid-wave).

Two prototype lenses have been manufactured and evaluated.

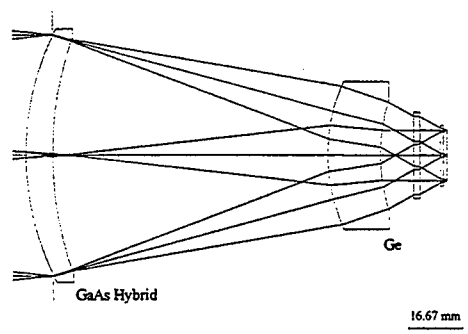

Figure 4: Dual band objective

Field Angle	Upper Band MTF (%)		Lower Band MTF (%)	
	Sagittal	Tangential	Sagittal	Tangential
0.0°	81.3 (86.9)	81.3 (86.9)	82.5 (93.0)	82.5 (93.0)
4.2°	77.6 (83.1)	79.7 (85.1)	79.1 (89.7)	79.1 (88.9)
6.0°	73.2 (77.8)	69.1 (73.0)	74.2 (84.2)	64.9 (71.8)

Wavelengths (Weights)

Upper Band
9.0 μm (1), 10.5 μm (2), 12.0 μm (1)

Lower Band
3.8 μm (1), 4.3 μm(2), 4.8 μm (1)

Table 2 : Polychromatic MTF

5. REFERENCES

1. M. O. Lidwell, "Achromatisation of lenses for thermal IR", Proc. SPIE, Vol. 518, pp 73-80 (1984).
2. M. Roberts and P. J. Rogers, "Wide waveband infrared optics", Proc. SPIE, Vol. 1013, pp 84-91 (1988).
3. M. O. Lidwell, "Diffractive lenses for dual waveband IR", Proc. SPIE, Vol. 2774, pp 352-362 (1996).

A new approach to correct chromatic aberrations utilizing a hybrid surface

C. Gary Blough
Melles Griot, 55 Science Parkway, Rochester, NY 14620
Phone (716) 241-2298, Fax (716) 244-6292
E-mail: blough@rochester.mellesgriot.com

Introduction

A diffractive surface provides a unique method of achromatizing an optical system. Conventional techniques of achromatization with refractive elements utilize the balancing of optical powers and lens material properties to provide a corrected system.[1] This requires the introduction of more refractive power than necessary in the system to satisfy the first-order requirements. The addition of more optical power typically requires steeper surface radii and the general correction of the system performance becomes more difficult. A diffractive surface provides a more natural method of achromatizing a system because refractive and diffractive surfaces of the same sign of optical power provide an achromatic solution.[2] Hence, the need to introduce excess amounts of optical power to satisfy the first-order properties is eliminated. The diffractive surface can also be utilized to provide aspheric correction, although the wavelength range must be limited to reduce the effects of spherochromatism. In addition, the potential operating wavelength range is limited because of loss in diffraction efficiency introduced from wavelength detuning.

The new approach to chromatic correction utilizing a hybrid surface involves the introduction of an optical element that has no optical power at the design wavelength. Hence, the amount of refractive and diffractive power is equal and opposite at the design wavelength. However, as the wavelength varies, the more dispersive diffractive surface results in the introduction of optical power, which is approximately linear with the change in wavelength. The change in refractive power with wavelength reduces the linearity of the hybrid surface power variation. A unique characteristic of such a surface is that when a continuous phase relief diffractive surface and refractive surface of identical but opposite focal length are combined, the resulting surface has a staircase type form that is reminiscent of a binary optic.

A brief discussion of the basic operation and design approach to utilizing the new method is presented. In addition, a simple laser diode collimator design is presented as an example.

Theory of Operation

A refractive surface has optical power that can be given by

$$\Phi_R(\lambda) = \frac{n(\lambda)-1}{R}\ , \tag{1}$$

where R is the radius of curvature, $n(\lambda)$ is the index of refraction, and $\Phi_R = 1/F_R$, where F_R is the focal length. The phase of a rotationally symmetric diffractive surface can be written as

$$\phi(r) = \frac{2\pi}{\lambda_o}(c_1 r^2 + c_2 r^4 + c_3 r^6 + ..)\ , \tag{2}$$

where λ_o is the design wavelength, c_1 is related to the diffractive surface focal length by $F_D = -\frac{1}{2c_1}$, and $c_{2..n}$ coefficients represent the aspheric terms of the phase. If a refractive optical system is not achromatized, the system is said to be under-corrected; shorter wavelengths focus closer to the lens than longer wavelengths. Hence, the hybrid element must have a positive focal length (i.e. c_1 is < 0 for first-order diffraction) to provide chromatic correction for an under-corrected refractive optical system.

The optical power of a diffractive surface as a function of wavelength can be written as

$$\Phi_D(\lambda) = \frac{\Phi_D \lambda}{\lambda_o} , \tag{3}$$

where $\Phi_D = 1/F_D$. The power of the hybrid surface can be calculated by adding Eq. (1) and Eq. (3)

$$\Phi_H(\lambda) = \frac{\Phi_D \lambda}{\lambda_o} + \Phi_R(\lambda) , \tag{4}$$

where $\Phi_H(\lambda_o)=0$ or $\Phi_D = -\Phi_R(\lambda_o)$. For narrow wavelength applications, such as those containing laser diodes, $n(\lambda)$ is typically constant such that Eq. (4) represents a line with slope Φ_D/λ_o. The power of the hybrid surface can be represented as

$$\Phi_H(\lambda) \approx \Phi_D \frac{\lambda - \lambda_o}{\lambda_o} . \tag{5}$$

The ray deviation provided by the hybrid surface has a paraxial representation given by

$$nu'(\lambda) = nu(\lambda) - y\Phi_H(\lambda) , \tag{6}$$

where $nu(\lambda)$ is the incident angle, $nu'(\lambda)$ is the deviated output angle, and y is the ray height on the hybrid surface. To design the required hybrid surface, the ray deviations resulting from the refractive optical system are equal and opposite to those generated by the hybrid surface.

Design of a Diode Collimator

Consider a laser diode operating at a wavelength of 635 nm that is perfectly collimated with a 10 mm focal length f/2 lens manufactured from SFL6. From thin lens equations, the amount of axial color from a collimating lens is given by the ratio of the focal length and Abbe ν-number.[3] However, for the case presented here, the object is a point source and the axial color results in the output beam being deviated from collimation. If the wavelength range is 635 nm±5 nm, the maximum beam deviations are calculated using thin lens equations to be -0.0002 rad for 630 nm and 0.0002 rad for 640 nm, where the negative angle implies the beam is converging. The thin lens equation used to calculate the beam deviations can be written as

$$\Delta nu(\lambda) = \frac{-y\Delta n(\lambda)}{efl_R \cdot (n(\lambda) - 1)} , \tag{7}$$

where $\Delta n(\lambda)$ is the change in index of refraction from the design wavelength value (i.e. $n(\lambda)$-$n(\lambda_o)$) and efl_R is the focal length of the collimating lens. Equation (6) illustrates the potential correction from the hybrid surface, while Eq. (7) represents the errors introduced by a thin refractive lens. To collimate the diode assembly over the wavelength range, Eq. (6) must be satisfied to provide $nu'(\lambda)=0$. Hence, the incident angles of Eq. (6) are actually generated from Eq. (7). Setting $nu'(\lambda)$ to zero and substituting Eq. (7) into Eq. (6) yields

$$\Phi_H(\lambda) = \frac{-\Delta n(\lambda)}{efl_R \cdot (n(\lambda) - 1)} . \tag{8}$$

Further substituting Eqs. (3) and (5) into Eq. (8) provides an expression for the required diffractive surface focal length

$$F_D = \frac{-efl_R \cdot (n(\lambda) - 1)(\lambda - \lambda_o)}{\Delta n(\lambda) \cdot \lambda_o} . \tag{9}$$

By using Eq. (9), the focal length for the diffractive surface is calculated to be 104.9 mm. The surface consists of 46.9 zones across the 5 mm clear aperture. If the substrate material is BK7, the index of refraction at 635 nm is 1.5150. Using Eq. (1), the refractive surface radius of curvature is -54.0235 mm. The diffractive surface zone height is 1.233 μm. The hybrid element can be constructed on a plano-plano substrate, where the hybrid surface has a concave surface profile, which is illustrated in Fig. 1. Note that even though the diffractive surface is designed to be a continuous surface relief, the zone structure has no

surface curvature. This effect results from matching the refractive and diffractive focal lengths at the design wavelength.

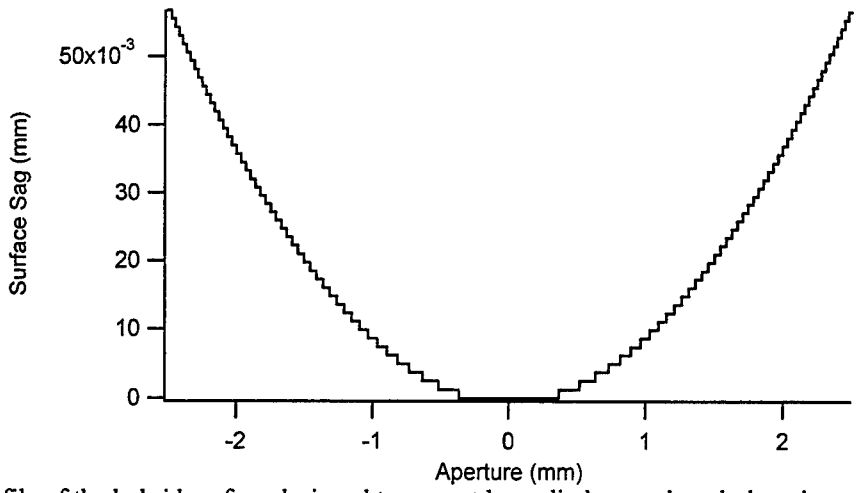

Fig. 1. Profile of the hybrid surface designed to correct laser diode wavelength detuning.

Another interesting application area for the hybrid element is in providing a predetermined amount of beam divergence from an achromatic collimated beam. An example of this application includes laser scan lenses, which typically are not well-corrected for chromatic aberrations.[4] Hence, the hybrid element can be utilized to provide the input ray angles that compensate the axial color present in the system. This technique could easily be implemented by inserting the element between the collimated input beam, which typically is a laser diode, and the scan mechanism. Such a system has been designed and provides excellent axial color correction for a laser-diode-based f-theta scan lens system. A potential shortcoming of the approach is that the lateral color from the scan lens is not corrected by this technique.

Conclusions

A new technique for chromatic correction utilizing a hybrid "no power" surface has been outlined. The resulting surface profile from the element has a unique characteristic in that a continuous phase relief diffractive surface and opposite power refractive surface yield a staircase type surface, which appears much like a binary optic surface. It is important to note that the diffraction efficiency of the hybrid surface can be determined using scalar diffraction theory. The theoretical efficiency is 100% in contrast to 40% for a binary phase profile. The implementation of such an element may provide a cost-effective approach for chromatic correction of optical systems. In addition, the technique provides the ability to utilize low cost glass aspheric collimating lenses in laser-diode-based systems that provide a well-corrected beam over an extended wavelength range.

References

[1] W. J. Smith, "Modern Optical Engineering," Second Edition McGraw-Hill, pg. 375, (1990).
[2] T. Stone and N. George, "Hybrid diffractive-refractive lenses and achromats," Appl. Opt. **27**, pg. 2960, (1988).
[3] R. Kingslake, "Lens Design Fundamentals," Academic Press, pg. 79, (1978)
[4] G. F. Marshall, "Optical Scanning," Marcel Dekker, pg. 27, (1991).

Diffractive Optics and Micro-Optics

Fabrication 2

Thursday, June 11, 1998

Fina R. Kritchevsky, Donnelly Corporation
Presider

DThC
1:30pm–3:00pm
Koa Room

Micro-jet Printing of Refractive Microlenses

W. Royall Cox, Ting Chen, Chi Guan, Donald J. Hayes and Rick E. Hoenigman
MicroFab Technologies, Inc., 1104 Summit Ave., Suite 110, Plano, TX 75074
ph: (972) 578-8076 / fax: (972) 423-2438 / email: mfab@metronet.com
Brian T. Teipen and Duncan L. MacFarlane
The University of Texas at Dallas, P.O. Box 830688, EC33, Richardson, TX 75083
ph: (972) 883-2165 / fax: (972) 883-6839 / email: dlm@utdallas.edu

1. Introduction

The technology for fabricating micro-optical elements for low cost optical interconnects by micro-jet (ink-jet) printing has been under development for over two years [1,2]. This data-driven method of micro-optics fabrication offers the benefits of low cost, flexibility and *in-situ*, non-contact processing. These features can be used to advantage in applications where increasing the efficiency of optical power coupling as a value-added step is a goal, and they provide unique capabilities for rapid prototyping and customization of microlens arrays. Here we present our latest results in developing this Optics-Jet technology for applications such as collimation of the outputs of LEDs and diode lasers, as well as for increasing the efficiency of focusing of GRIN lenses [3]. Data on printed microlens optical characteristics will be shown, as well as their performance in collimation and astigmatism reduction of optical sources.

Figure 1. *Generation of 50μm droplets at 2 kHz.*

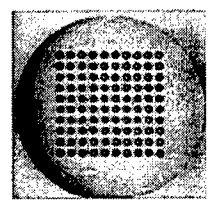

Figure 2. *10x10 array of 220μm diameter micro-lenses printed onto 5mm GRIN lens.*

2. Microlens Printing Method

In "drop-on-demand" microjet printing a single droplet is ejected from the print head every time its piezoelectric actuator is pulsed, producing droplets with precise volumetric control at rates up to 5 kHz, as illustrated in the photograph of Figure 1. To fabricate a microlens by this method, a print head with 30-60 μm orifice diameter is used to deposit at 165°C similarly sized droplets of UV-curing optical material onto the target site which is typically held at 40°C. An example of microlenses formed in this way is the array pictured in Figure 2 of 220 μm diameter lenslets printed directly onto one end of a 5 mm diameter GRIN lens for reduction of optical insertion loss. For a given optical material, device orifice size and substrate, the diameter and focal length of a printed lenslet are logarithmic functions of the number of deposited droplets, as seen in the data of Figure 3. The speed of a printed microlens for a given mass of deposited material is a function of the degree of spreading which occurs on the substrate prior to solidification which, in turn, is controlled by the viscosity level of the material and the degree to which it wets the substrate surface. For polymeric optical materials deposited onto a silanized glass substrate, microlens speed remains relatively constant over a wide range of diameters.

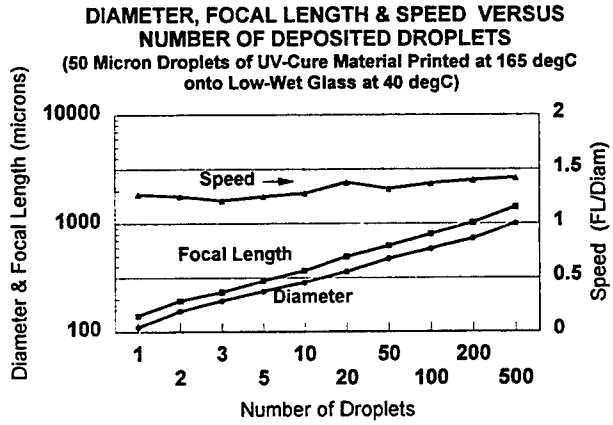

Figure 3. *Variation of printed hemispherical microlens geometry with number of deposited droplets.*

3. Printed Microlens Optical Characteristics and Reproducibility

The optical imaging quality of printed hemispherical microlenses was assessed by measuring the Modulation Transfer Function (MTF). The measurement system, which utilizes a virtual point source of 665 nm to illuminate the convex surface of the lenslet under test and a 100x microscope objective to project the focused light

onto a CCD camera, is capable of measuring microlenses with diameters in the 100 μm - 50 mm range. Measured MTF data for a printed 110 μm diameter microlens with speed of f/1.25, given in Figure 4 along with the those for an ideal (diffraction-limited) lenslet of the same speed, show an identical cutoff spatial frequency (1,200 lp/mm). The Strehl Ratio, obtained from the ratio of integrated areas under the measured and theoretical curves, is 0.71, indicating that the printed microlens produces relatively little spherical aberration in this measurement configuration. To determine the reproducibility of printing a microlens, a microscope system is used to measure diameters and focal lengths of individual microlenses within variously configured arrays. Focal length data for a 10 x 10 array of 495 μm diameter microlenses printed onto low-wet-coated glass on 750 μm centers are given in Figure 5. The standard deviations from the average values of focal length and diameter within such arrays are on the order of 1.5% and 1%, respectively, which are within the measurement errors and sufficient for many array optical

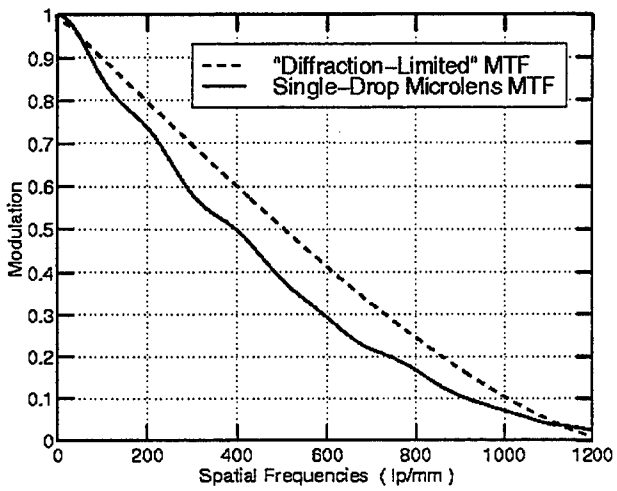

Figure 4. *Modulation transfer function for an f/1.25 microlens printed with one 50μm drop of UV-curing optical material (solid curve), compared to ideal, diffraction-limited case (dashed curve) at same f/#.*

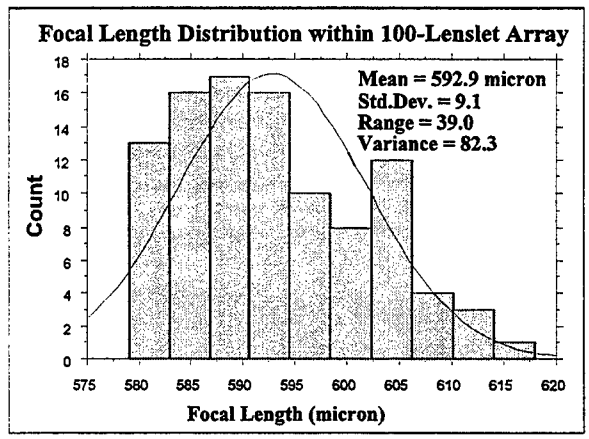

Figure 5. *Distribution of focal lengths of 100 each 0.5 μm diameter microlenses printed in 10x10 array on 750 μm centers, showing a typical standard deviation from the average value of 1.5%.*

interconnect applications. Microlens placement accuracy depends primarily on the accuracy of the substrate stages and the distance between print head orifice and substrate surface. At a typical printing distance of 1 mm, our R&D system can place microlenses with an accuracy ≤ 2 μm.

4. Microlens Printing for LED and Diode Laser Collimation

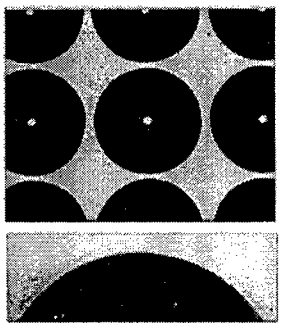

Figure 7. *Array of 355 μm diameter microlenses printed on 375 μm centers, shown in substrate plane (top) and in profile (bottom).*

The printing of plano/convex microlenses for source collimation is currently being explored in several areas, including hemispherical microlenses for LED and VCSEL (smart pixel) arrays and hemi-elliptical lenslets for edge-emitting diode laser arrays. For the LED array case, a microlens is printed directly above each emitter with back focal length adjusted to be at the effective emitting point, as indicated in Figure 6. Here the lenslets are printed either onto a thin glass substrate positioned above the emitters or onto a flat surface established by dispensing and curing of the same or similar material on and around the emitters to the requisite height. A typical configuration suitable for display light sourcing, and for which collimation performance data will be presented, is an array of 15 x 15 each 250 μm square LEDs on 375 μm pitch, with an array of 355 μm diameter, f/1.22 microlenses printed at the same pitch as shown in the photos of Figure 7. Data illustrating the use of printed microlenses for VCSEL array collimation will also be

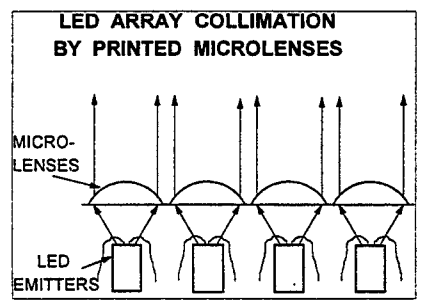

Figure 6. *Geometry for LED array collimation by printed microlenses.*

presented, with emitter/lenslet pitches down to 250 μm.

The objective of our work with high power edge-emitting diode laser arrays is to increase efficiency of coupling into optical fibers. The suitability of our printed microlenses for high power applications has been demonstrated by post-cure baking experiments where no measurable change in focal length occurred after exposure to temperatures up to 200°C. Collimation of an edge-emitting diode laser emitter by a printed microlens requires a slight ellipticity in lenslet shape, in order to correct for astigmatism and bring the rapidly (~40°) and more slowly (~10°) diverging planes of light into collimation at the same z-axis plane. These hemi-elliptical microlenses are printed along the bar direction by depositing a line of droplets of optical material, which join by cohesion prior to curing, and adjusting the number and spacing of the droplets to control lenslet size and ellipticity. An example of a series of microlenses of differing degrees of ellipticity is given in Figure 8, where six 60 μm droplets were printed at adjacent sites to form each lenslet, with increasing site spacing for successive lenslets. The variations with deposition site spacing of the major and minor axis lengths and corresponding "slow" and "fast" focal lengths of the microlenses pictured in Figure 8 are plotted in Figure 9. Increasing site spacing effectively increase the ratios of both major/minor axes and slow/fast focal lengths, providing the capability for tuning printed microlens properties for a wide range of diode laser configurations. In practice, the degree of ellipticity required may be quite small, e.g., on the order of 1.001 to correct an astigmatism of 5 μm.

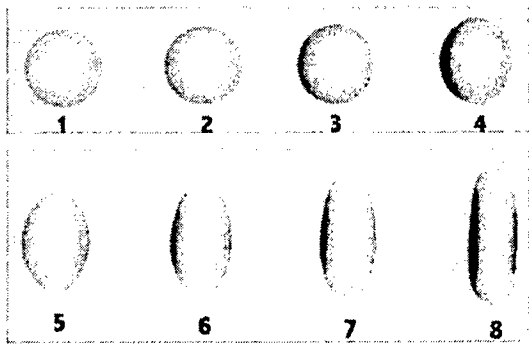

Figure 8. *Hemi-elliptical microlenses printed with 6 each 60 μm droplets on site spacings increasing by 10 μm from #1 to #8 (100X mag).*

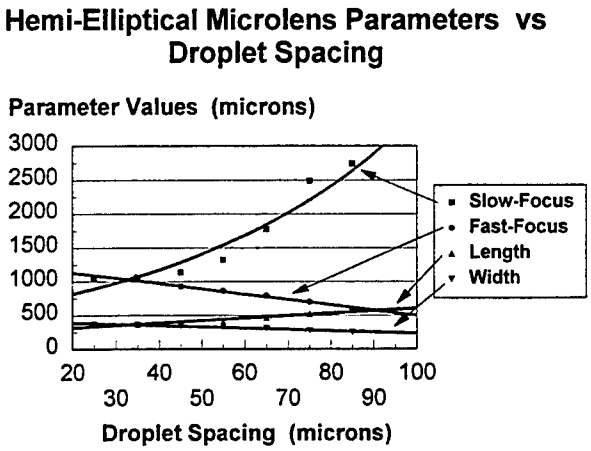

Figure 9. *Variation with droplet spacing of focal lengths and dimensions of hemi-elliptical microlenses of Fig. 8.*

5. Conclusions

Practical applications of this micro-optics printing technology are rapidly emerging in diverse and important areas of optoelectronics manufacturing where the associated benefits of cost reduction and flexibility can provide a competitive edge. As capabilities continue to develop for both improving further the accuracies of the processes for micro-optics printing and reducing the element sizes which can be fabricated, the potential application areas will be expected to expand from LED and diode laser beam shaping to new arenas such as display and sensor manufacturing.

Acknowledgments

This work has been supported in part by the U.S. Air Force Phillips Laboratory and the U.S. Army Research Office.

References

[1] W.R. Cox, T. Chen, D.W. Ussery, D.J. Hayes, and, R.F. Hoenigman, "Microjet printing of anamorphic microlens arrays," *SPIE Proceedings*, Vol. 2687, pp.89-98, 1996.

[2] W.R. Cox, D.J. Hayes, T. Chen, H-J Trost, M.E. Grove, R.F. Hoenigman and D.L. MacFarlane, "Low cost optical interconnects by microjet printing," *IMAPS International Journal of Microcircuits & Electronic Packaging*, Vol. 20, No. 2, pp.89-95, 1997.

[3] V. Baukens, A. Goulet, H. Thienpont, I. Veretennicoff, W.R. Cox and C. Guan, "GRIN-lens based optical interconnection systems for planes of micro-emitters and detectors: microlens arrays improve transmission efficiency," *OSA Diffractive Optics and Micro Optics Topical Meeting*, Kailua-Kona, Hawaii, June, 1998.

Different concepts for the fabrication of hybrid (refractive/diffractive) elements

H. P. Herzig, Ph. Nussbaum, A. Schilling, S. Traut, I. Philipoussis, C. Ossmann, R. Völkel, M. Rossi*, H. Schift**

Institute of Microtechnology, University of Neuchâtel, Rue A.-L. Breguet 2, CH-2000 Neuchâtel, Switzerland
Phone: +41 32 718 3270, Fax: +41 32 718 3201, E-mail: hanspeter.herzig@imt.unine.ch

*CSEM Centre Suisse d'Electronique et de Microtechnique, Badenerstrasse 569, CH-8048 Zurich, Switzerland

**Paul Scherrer Institut, CH-5232 Villigen, Switzerland

Introduction

Various fabrication methods have been investigated to manufacture refractive and diffractive micro-optical elements [1]. The structure of the elements is generated by holographic recording, optical lithography and direct writing (e-beam, laser beam). The pattern is then transferred into quartz by reactive ion etching (RIE), or replicated into plastic for low-cost mass production. Of special interest is the fabrication of hybrid elements, which combine the unique properties of diffractive optics (fan-out, high dispersion) with those of refractive optics (high numerical aperture, low dispersion). Therefore, we have studied different concepts for the manufacturing of hybrid (refractive/diffractive) elements and we present here some first results.

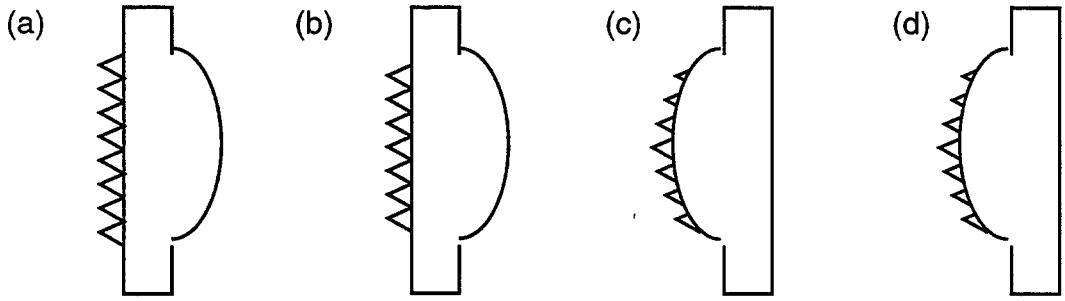

Figure 1 Hybrid elements fabricated by (a) lithography and etching (refractive lens and Dammann grating), (b) injection molding (refractive lens and Dammann grating), (c) direct laser writing (refractive lens + fan-out element), (d) holographic recording (refractive lens and grating).

The diffractive elements are gratings or fan-out elements which are realized on the planar and on the curved surface of plano-convex microlenses (see Fig. 1). This combination is attractive for applications in optical interconnects (fan-out elements), wavelength demultiplexing (gratings) and in analytical chemistry (arrays of mini-spectrometers). In all cases described in this paper, we have realized the refractive lenses by melting resist technique, where photoresist cylinders are fabricated

by lithography and are melted in a subsequent process step. The plano-convex spherical lenses are formed by surface tension [2]. Single elements and arrays of elements have been fabricated.

Lithography and etching

A diffractive and a refractive element have to be combined into one monolithic component. In this case, we fabricate the diffractive element directly on the backside of a refractive lens by photolithography and subsequent etching into quartz. The alignment between the structures is done with a mask aligner (better than 1 μm). The diffractive element is a Dammann grating which generates a fan-out of 4x4 beams with a theoretical diffraction efficiency of 76%. The period of the 2-dimensional fan-out grating is 64 μm. The refractive element is a plano-convex lens with a diameter of 610 μm and an f-number of 1.5. The refractive lens has been fabricated first in photoresist. We measured the deviation from an ideal spherical surface with a Twyman-Green interferometer. The deviation of the lens is 0.12 λ (rms) and 0.5 λ (p/v). A challenge is the transfer of the resist lenses into quartz by reactive ion etching (RIE). Up to now, we have etched lenses with a depth of 20 μm with good quality, i.e. 0.5 λ (p/v). Our final lenses will have a depth of about 60 μm in quartz.

Injection moulding

Dammann grating and refractive lens have been fabricated separately in photoresist with the same dimensions as described above. Afterwards, the elements have been combined in a mould in order to replicate single hybrid elements in polycarbonate by injection moulding. The replication process has been executed at the IMM in Mainz. This technique is suitable for low-cost mass production. A problem is the alignment between the refractive and the diffractive surface. The alignment accuracy is in the order of 20 μm. This accuracy is enough for periodic structures as our fan-out element. However, for a diffractive aspheric correction of the micro-lenses, the alignment accuracy will become critical. Another critical parameter is the efficiency and the uniformity error of the Dammann grating. The efficiency was measured to be 73% for the original grating in photoresist and 62% for the replicated element in polycarbonate. An uniformity error of ±2.6% was measured for the original and ±20% for the replication.

Direct laser beam writing on a curved surface

The diffractive grating can also be written directly on top of a microlens, as shown in Fig. 1(c). In that case, the refractive and the diffractive function are combined in one surface. Such elements have been fabricated at CSEM Zurich [3]. The autofocus system of the laser writing system enables a depth variation of ±0.5 mm of the writing spot. Thus, the writing spot can scan on a curved surface of a microlens. A continuous-relief 5x5 fan-out element has been written into a resist layer of 3 μm thickness. The scan speed of the laser writer was reduced down to 10 mm/sec. The period of the fan-out grating is 51 μm.

Holographic recording

Holography is a powerful method to realize fine grating structures. Therefore, it is attractive to combine holographic recording with the manufacturing technology of micro-optics. The first step is the fabrication of the microlens array by melting resist technique. The lenses have here a diameter of 100 μm and a height of 6 μm. The array is then spin coated with a resist layer of 2 μm thickness. We investigated the coating properties of the lens array. The photoresist partially fills the gaps between the lenses and therewith smoothens the sharp transitions between lens and substrate. To gain more information on the change of surface properties, we measured the standard deviation from an ideal spherical surface with a Twyman-Green interferometer. Before deposition of the photoresist layer, the standard deviation was measured to be 0.15 λ (rms). These values did not increase for the same lenses measured after coating.

We recorded gratings interferometrically using a Krypton ion laser at a wavelength of 413.1 nm. We were able to record uniform gratings with depths up to 2 μm on the curved surface of microlenses. The period of the gratings is 1 μm and the profile nearly binary. Figure 2 shows an example of such a grating on a microlens. The method can also be extended to record fan-out elements [4].

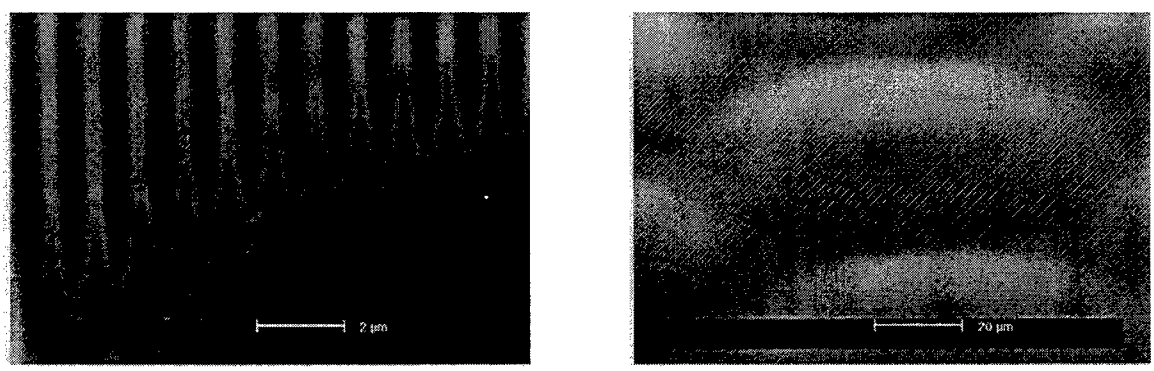

(a) (b)

Figure 2 (a) cross section and (b) top view of a grating (period 1 μm, depth 2 μm) fabricated on a microlens array.

References

[1] H. P. Herzig, ed., *Micro-Optics: Elements, Systems, and Applications*, (Taylor & Francis, London, 1997), ISBN: 0 7484 0481 3 HB.

[2] M. C. Hutley, "Refractive Lenslet Arrays", in Ref. 1, pp. 127-151.

[3] M. T. Gale, M. Rossi, H. Schütz, P. Ehbets, H. P. Herzig, D. Prongué, "Continous-relief diffractive optical elements for two-dimensional array generation," Appl. Opt. **32**, 2526-2533 (1993).

[4] H. P. Herzig, P. Ehbets, "From holography to micro-optics," J. Imaging Science & Techn. **41**(5), 488-496 (1997.

Diffraction characteristics of thick phase volume hologram recorded in photo-thermo-refractive glasses

S. Dunn, M. G. Moharam, L. Glebov, and K. R. Richardson
Center for Research and Education in Optics and Lasers, University of Central Florida
Orlando, Florida 32816-2700
(407) 823-6833, Fax (407) 823-6810, email: moharam@creol.ucf.edu

Introduction:

Volume holographic optical elements have numerous applications in beam shaping, spectral filters, optical display systems, optical interconnects, and data storage. One of the primary challenges facing the development of applications involving volume holographic optics is the recording media. It must meet a number of requirements including phase volume recording with high efficiency, low scattering, large dynamic range, and high resolution, while exhibiting good thermal, chemical, and mechanical durability, as well as environmental stability. Current recording media include photographic films, dichromated gelatin, photoresists, photopolymers, photochromics, photo-organics, and photorefractive media. These media meet only a few of the desired requirements.

Photo-thermo-refractive (PTR) glasses:

Photo-thermo-refractive (PTR) glass is a silicate glass (SiO_2, Al_2O_3, ZnO, Na_2O with Ag_2O, CeO_2, and floride doping). This material can undergo photo-induced nucleation and crystallization to induce a permanent volume refractive index change in the bulk glass. These glasses appear to be an excellent candidate for holographic recording media [1,2,3]. Exposure to the UV interference and thermal treatment will result in the formation of permanent volume phase grating. The process of inducing the refractive index changes in silicate PTR glass involves two distinct processes: 1), exposure to UV illumination (CW milliwatts at 300-350 nm for few seconds), to creat colloidal nucleating sites through electron ionization from a dopant (Ce^{3+}) and subsequent retrapping at acceptor sites (Ag^{+}) and 2) thermal (crystallization) treatment to produce crystalline particles (NaF) of differing refractive index thus resulting in an index modulation in the bulk glass. The refractive index of the micro-crystals (~1.32), nanometers in size which is different from the surrounding glass matrix (~1.5) results in refractive index modulation (up to ~0.0001) without modification of the material's macroscopic optical properties.

PTR glass has many properties that are essential for successful volume holographic recording media. They include: 1) thick (up to tens of millimeters) volume holographic elements, 2) high spatial frequency and high diffraction efficiency, 3) permanent index change; insensitive to visible radiation and thermal effects, 4) high homogeneity and reproducibility in large volume low cost production, 5) durable, environmentally stable media with good thermal, mechanical, and chemical properties, and 7) machineable into arbitrary shapes (prizms, lenses, etc) for hybrid holographic/refractive optical elements.

Volume holographic grating recording:

Photo-thermo-refrective (PTR) glass used was melted and processed at CREOL. The glass composition contains SiO_2, Al_2O_3, ZnO, and Na_2O. The glass samples were cut and polished to 2 mm thick samples. Thick volume phase holographic gratings were recorded in the glass samples using the typical holographic recording experimental arrangement. A He-Cd single longitudinal mode UV laser (325 nm), a spatial filter, a beam collimator, and a beam splitter are used to interfere two beams on a 0.1 cm^2 square area on the 2 mm thick PTR glass samples. The sample was exposed to UV interference pattern with periodicity of 1 micron and with more than 95% modulation in the transmission grating geometry. The

combined power of the two beams was about 100 mW/cm^2. The exposure time ranged from 1 to 12 seconds. The samples were then heated at 520 °C in steps of 15 minutes. The diffraction efficiency and the angular selectivity of the induced volume phased gratings were measured at each heating step using a He-Ne laser (632.8 nm) of about 2 mm beam diameter. Minimal light scattering (less than 1%) was observed in all measurements. The measured diffraction efficiency is defined as the ratio of the diffracted beam intensity to that of the sum of the transmitted and diffracted beams. A computer controlled rotation stage/data acquisition system is used to measure the angular selectivity characteristics of the recorded gratings.

Experimental Results:

Figure 1 shows the on-Bragg diffraction efficiency as a function of the thermal development (crystallization) duration for different UV exposure (with 100 mW/cm^2 total power). As shown in fig. 1, longer exposure results in higher diffraction efficiency with shorter thermal treatment. This appears to be consistent with the understanding that the exposure level determines the number of nucleation centers and the duration of the thermal treatment determine the size of the microcrystals, longer exposure and shorter thermal crystallization duration appears to result in more, but smaller microcrystals. For this particular sample composition, diffraction efficiency of 45% was achieved at 1.2 J/cm^2 UV exposure and 120 minutes thermal development duration. This diffraction efficiency indicates a refractive index sinusoidal modulation of about 0.75 10^{-5}. Higher efficiency is achieved by increasing the thermal development duration but with observable second Bragg angle diffraction.

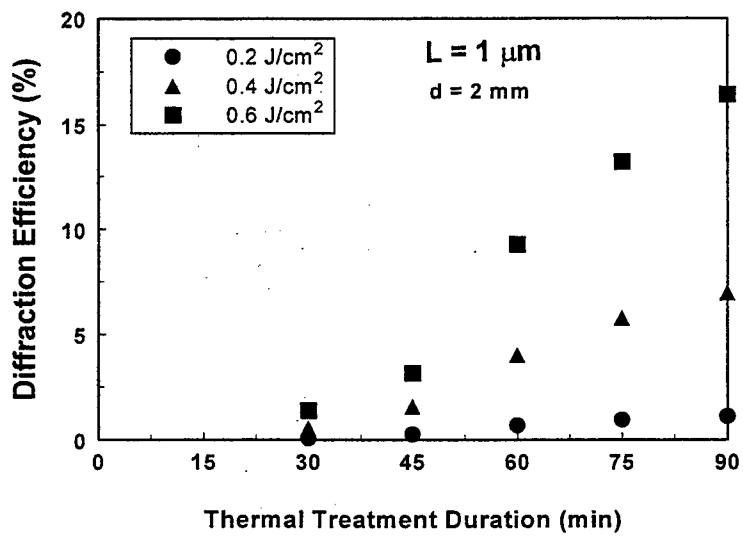

Figure 1. Diffraction efficiency vs. thermal treatment duration and UV exposure

Figure 2 shows the angular dependence of the diffraction efficiency of gratings recorded in a 2 mm PTR glass sample for several values of the diffraction efficiency. The measured angular selectivity (FWHM) is 0.045 degree (0.785 mrad) in air for all values of the maximum diffraction efficiency which is consistent with the theoretical value of 0.65 mrad predicted by Kogelnik's coupled wave theory for thick holographic gratings [4]. That is

$$\Delta\theta_{air}(rad) \cong Fn\frac{L}{d}$$

where L is the grating period, d is the grating thickness, n is the refractive index of the media, and F is an index modulation dependent quantity that ranges from 0.8 (for 100% efficiency) to 1.0 (for 1% efficiency or less). It is also observed that side lobes are suppressed where the theory predicts about 5%

relative maximum intensity in the side lobes. This is the result of the Gaussian nature and beam divergence of the reading beams.

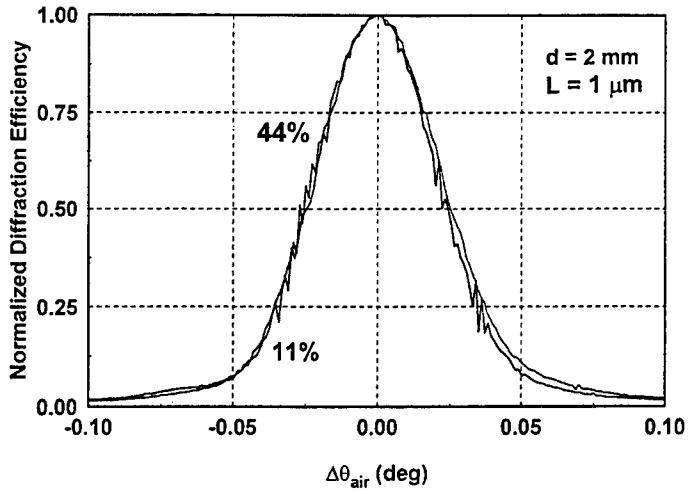

Figure 2. Angular selectivity of gratings recorded in PTRG

Conclusions:

High diffraction efficiency high-resolution low scattering thick volume phase holographic gratings recorded in bulk PTR glasses are characterized. Angular selectivity approaching the theoretical limit is observed. PTR glasses have very promising potential as an efficient durable and stable holographic recording media. The ability to machine PTR glass into arbitrary shapes offers the potential for exciting novel applications in hybrid phase holographic/refractive optical elements, such as combined optical filter-focusing elements, combined optical filter-beam direction (prism) elements, and for data storage.

References:

1. Glebov, L. B., Nikonorov, N. V., Panysheva, E. I., Petrovskii, G. T., Savvin, V. V., and Tunimanova, I. V., "Photochromatic glasses- a new materials for recording volume phase holograms," Sov. Phys. Dokl., 35, 878 (1990)
2. Glebov, L. B., Nikonorov, N. V., Panysheva, E. I., Petrovskii, G. T., Savvin, V. V., and Tunimanova, I. V., "New ways to use photosensitive glasses for recording volume phase holograms," Opt. Spectrosc., 73, 237 (1992)
3. N. V. Nikonorov, M. G. Moharam, K. A. Richardson, "Volume phase hologram recording in photo-thermo-refractive glasses", Technical Digest, the Conference on Lasers and Electro-Optics (CLEO), Baltimore, MD, May 1995.
4. H. Kogelnik, "Coupled wave theory for thick hologram gratings", Bell Sys. Tech. J., vol. 48, pp. 2909-2947 (November 1969).

Acknowledgments

This work has been supported by BMDO/NCCOSC contract #N66001-97-C6008 and by BMDO/ARO contract # DAAG55-97-1-0294. The authors wish to acknowledge L. Glebova for PTR glass melting and sample preparing.

One-Step fabrication of a high-efficiency flat-top beam shaper

Xu Guang Huang and Michael R. Wang
Department of Electrical and Computer Engineering
University of Miami
Coral Gables, FL 33124
Tel.: (305) 284-4041
Fax: (305) 284-4044

A compact beam shaper is required to efficiently convert coherent Gaussian beam into a flat-top beam for applications such as optical processing, laser radar, laser microfabrication, and laser scanning. A number of techniques for laser beam shaping have been developed so far [1-3]. Directly truncating the Gaussian beam with an aperture and weighting the Gaussian beam with a neutral density filter of proper amplitude transmittance profile have very poor energy efficiency. Binary shaper based on interlaced diffraction gratings suffers from its limited diffraction efficiency. Diffractive optics beam shaper fabricated by computer-generated hologram technique, by only changing the propagation phase patterns prior to diffraction focusing, is an effective beam shaper method.

We report herein the realization of a diffractive optics beam shaper on an ion-exchanged high-energy-beam sensitive (HEBS) glass using laser-assisted chemical etching technique. Laser direct-write technique is applied to generate a 120-level transmittance distribution on the glass. Etching the written glass with a diluted hydrofluoric acid achieves a quasi-continuous thickness distribution. After etching, the sample is thermally bleached and forms a transparent phase-modulation-only beam shaper element. With this technique, a compact flat-top beam shaper combining with a focal lens has been fabricated. High energy conversion can be achieved. The maskless fabrication is attractive in the sense of easy process and is independent of the number of phase levels required.

The design of the diffractive optics beam shaper is based on the well-known Fresnel diffraction theory. To obtain the special phase distribution function $\psi(\xi)$ to satisfy the diffraction transformation equation and to realize the desired focal flat-top beam, the stationary phase method is used. It gives the phase function

$$\psi(\xi) = \sqrt{\pi}/2\xi erf(\xi) + \exp(-\xi^2)/2 - \frac{\pi\omega_0^2}{\lambda f}\xi^2,$$

where $\xi = r/\omega_0$. r is the radial coordinate. ω_0, λ are the beam waist and the wavelength of the input beam. f is the focal length.

To fabricate this phase-only beam shaper, the silver ion-exchanged layer of the HEBS glass is used as the base media of multi-level transmittance writing and of laser assisted chemical etching. Upon exposure to electron beam, the ion-exchanged layer of the glass

is pre-darkened in the visible wavelengths by converting silver ions to sliver particles. The darkened layer can be changed back to transparent by heat at the temperature above 140 °C, through heat oxidation of silver metal particles. Our experiment shows that the optical transmission level of the HEBS glass can also be changed with different laser writing intensity in visible wavelengths, and the etching rate of the ion-exchanged HEBS glass in a diluted hydrofluoric acid depends on the transmittance of the ion-exchanged layer. Therefore, any surface profile and phase distribution can be easily realized by controlling laser writing intensity level on the glass and by follow-up one-step etching in a diluted acid solution. A D/A converter is used to control laser intensity by a computer program. There is a linear relationship between the D/A setting and the laser writing beam power. At D/A setting of 255 the corresponding laser writing power is 5 mW while at D/A setting of 0 the focused laser power is 1 mW. Fig. 1 is the calibration curve of writing intensity level (D/A setting) vs. the relative etched depth. Writing laser wavelength, spot size and writing speed are 640 nm, 1 μm and 30 μm/s, respectively. Etching time is 29 minute with 3.3% diluted hydrofluoric acid at room temperature (20°C). The etched profile was measured with an Alpha-Step 100 surface profiler. For the refractive index 1.549 of the glass, 1.166 μm etched depth corresponds to a 2π phase change.

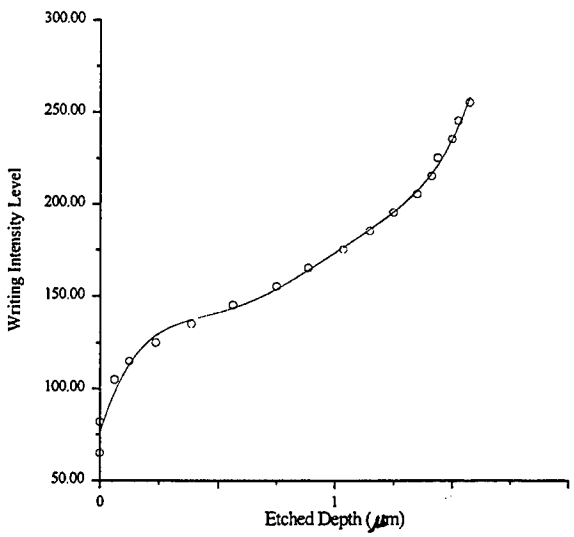

Fig.1 The calibration curve of writing intensity level (D/A setting for laser intensity control) vs. relative etched depth.

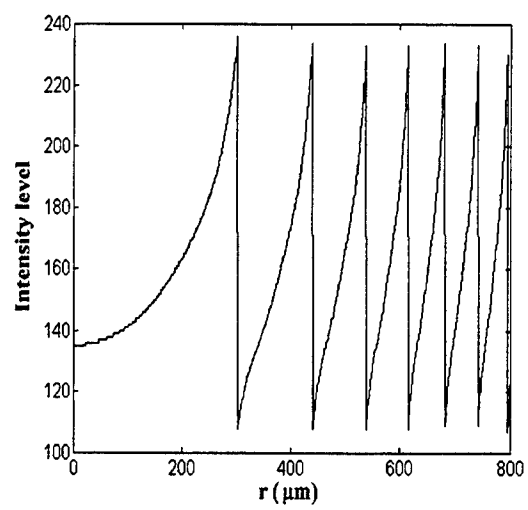

Fig. 2 120-level (D/A setting level) laser writing intensity curve along the radius direction.

Combining the special phase distribution of the beam shaper, the refractive index of the HEBS glass, and its etching calibration curve, the 120-level (D/A control level) laser writing intensity curve along the radial direction is given in Fig. 2. The diffractive optics beam shaper with quasi-continuous phase distribution was written according to this curve and fabricated by the chemical etching process. Fig. 3 is the reflective micrograph of the etched beam shaper after heat bleaching. To measure the conversion efficiency, an incident Gaussian beam from a He-Ne laser with 632.8 nm wavelength and with the

beam waist of 400 μm was used. A CCD camera on its focal plane collected intensity profile information of the output shaped beam. The energy conversion efficiency of the beam shaper is more than 70%. Near 90% conversion efficiency can be possibly achieved with further improvement of the fabrication process.

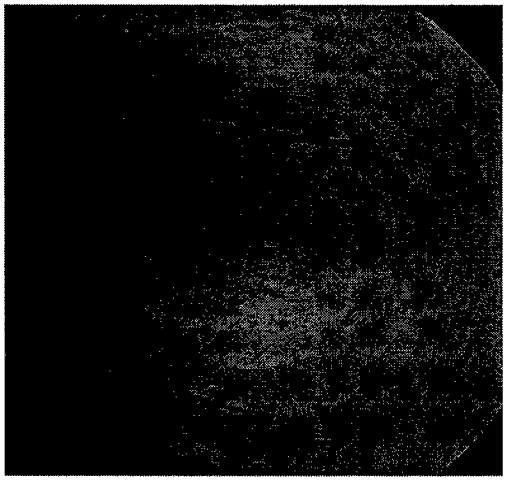

Fig. 3 The reflective micrograph of the etched sample after heat bleaching.

References:

1. M. Quintanilla and A. M. deFrutos, Appl.. Opt., 20, 879 (1981).
2. M. T. Eismann, A. M. Tai, and J. N. Cederquist, Appl. Opt., 28, 2641 (1989).
3. L. A. Romero and F. M. Dickey, J. Opt. Soc. Am. A 13, 751 (1996).

Effects of fabrication errors on Talbot array illuminators

Thomas J. Suleski
Digital Optics Corporation
5900 Northwoods Business Parkway, Suite J
Charlotte, NC 28269
Tel: 704-599-9191 Fax: 704-599-4997 E-mail: tom@doc.com

Introduction

Talbot array illuminators (TAI's) were first proposed by Lohmann as a means of creating optical interconnections.[1] TAI's are phase gratings that, under coherent, plane wave illumination, give rise to 100% modulated, square wave field and irradiance patterns. These patterns bear a strong resemblance to the spatial structure of the phase grating itself (Figure 1). Such patterns are referred to as Lohmann images[2] to distinguish them from Talbot images. Talbot images are replicas of the complex field distribution immediately behind a periodic structure. Talbot images occur at integer multiples of the Talbot distance $Z_T = 2d^2/\lambda$, where d is the grating period and λ is the wavelength of the illuminating radiation. By comparison, only a limited number of combinations of grating duty cycle w/d, phase depth ϕ, and propagation distance z will generate Lohmann images.

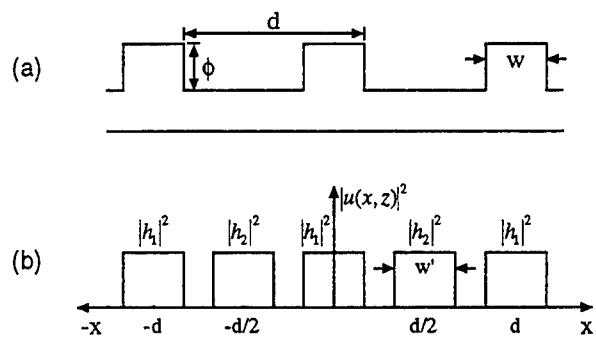

Fig. 1: (a) A simple, binary phase grating and (b) the Lohmann image that can result from it.

Researchers have proposed applications that require two TAI's in cascade[3] and TAI's used in conjunction with spatial light modulators (SLM's) to create reconfigurable diffractive optical elements.[4,5] Both types of applications are highly dependent on the TAI creating an electric field distribution of well-defined amplitude and phase. However, differences in grating duty cycle or phase depth from the design value can have unusual effects on the output field pattern from the first TAI. In this paper, we consider the effects of fabrication errors on the performance of binary phase TAI's. For the purposes of this discussion, we will consider the TAI with duty cycle $w/d = 1/3$ and phase step $\phi = 2\pi/3$ that generates a single Lohmann image at $z = Z_T/3$ and a double Lohmann image at $z = Z_T/12$. A more detailed discussion of the possible Lohmann images from binary phase gratings is presented in Ref. 2.

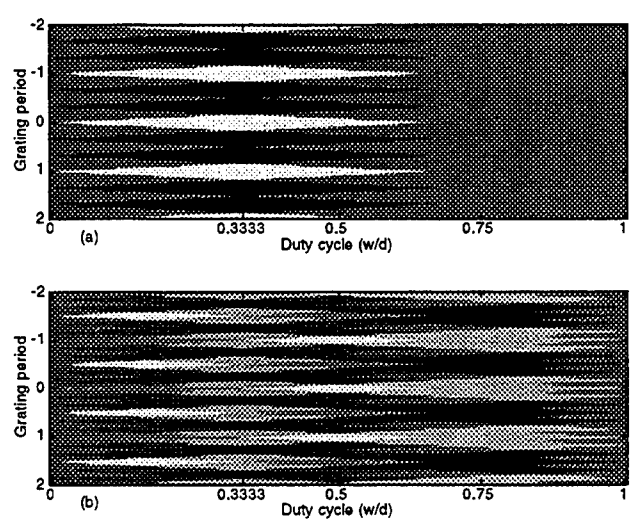

Figure 2: Transverse irradiance profiles as a function of duty cycle for a grating with $\phi = 2\pi/3$ at (a) $z = Z_T/3$ and (b) $z = Z_T/12$.

Transition Errors

One key factor in the generation of diffractive optical elements is the fidelity with which features in the component can be created. Deviations from the proper size can occur if the technique used to generate the mask or exposure pattern does not have adequate resolution. This problem is reduced if high-resolution methods such as electron-

beam lithography is used. However, even with a "perfect" mask, improperly sized features can still occur if the component is over-exposed or over-developed during the lithographic process.

In order to help visualize the effects of transition errors on the Lohmann images, a series of computer simulations was performed. In these simulations, the duty cycle of the TAI was varied from 0 to 1 in 0.01 increments. The phase step and propagation distance remained fixed as the duty cycle was varied. The transverse irradiance distributions as a function of duty cycle are shown in Fig. 2.

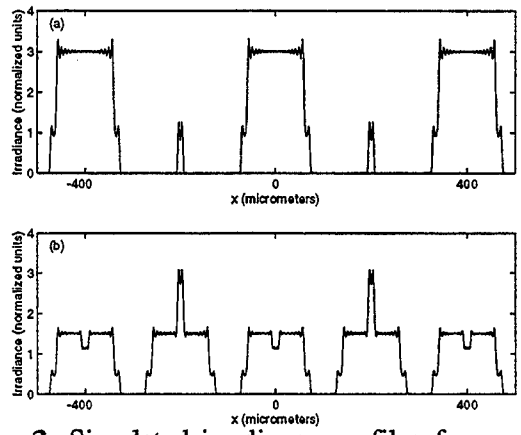

Fig. 3: Simulated irradiance profiles from a 400 micron period binary phase TAI with transition errors. (a) single image at $z = Z_T/3$, and (b) double image at $z = Z_T/12$.

The most striking effect of transition errors on the performance of binary phase TAI's is the formation of undesirable spikes or valleys in the centers of irradiance features. These undesirable features become larger as the error increases. The formation of these features is best understood using the weighted superposition model of periodic structures.[6,7] Multiple copies of the field distribution immediately behind the grating, appropriately shifted and weighted, form the Lohmann image in a given fractional Talbot plane. When the opening ratio and phase depth of the grating are "correct," these multiple copies fit together perfectly, forming uniform, square wave distributions. Any deviation in the widths of features in these multiple copies results in an imperfect fit: overlaps or gaps occur that give rise to unwanted features. In the case of overlapping images, the features can be sharp spikes or valleys, depending on the relative phases of the copies and the resulting constructive or destructive interference. Some irradiance profiles illustrating these sharp features are shown in Fig. 3. These profiles are generated from a grating with a duty cycle of 0.30, rather than the design value of 0.333. This type of error is consistent with overexposure or over-development during fabrication.

Etching Errors

With modern mask-fabrication technologies such as electron-beam lithography, it is relatively easy to avoid the problems with transition errors discussed above. Unless grating features are very small, transition errors due to the device resolution are usually negligible. It is more difficult to precisely control the etching processes used to create the phase step of the grating. Depth errors of ~5% are common with both reactive ion etching and wet chemical etching techniques. We now consider the effects of these depth errors on the performance of binary phase TAI's.

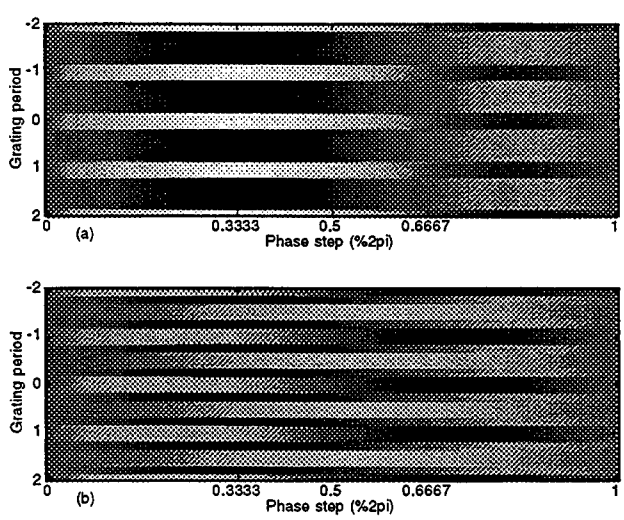

Fig. 4: Transverse irradiance distributions as a function of phase depth for a binary phase TAI with duty cycle of 1/3. (a) Single Lohmann image at $z = Z_T/3$, and (b) doubled Lohmann image at $z = Z_T/12$.

The image formation process discussed previously is also useful in considering the effects of phase-depth errors on the performance of binary

phase TAI's. If the feature sizes are correct, the multiple images will still fit together properly. The locations of features and transitions in the field and irradiance patterns will not change, and no new features are generated. However, deviations from the proper phase depth will result in changes in the way power is apportioned between the various windows, because of changes in the amount of constructive or destructive interference in a given subinterval.

A series of computer simulations was performed to explore the effects of phase-depth errors on the Lohmann images. In these simulations, the phase step was varied from 0 to 2π while the duty cycle and propagation distance remained constant. Transverse irradiance distributions as a function of phase depth are shown in Fig. 4. We observe that the contrast of the single Lohmann image decreases as the phase error increases. It is also noteworthy that alternating peak heights change in opposite directions for doubled Lohmann images as the phase step is varied. This behavior has been observed experimentally as well (Fig. 5). The grating that generated this irradiance pattern was designed for a phase step of $\phi = 2\pi/3$, but in reality the step height was $0.977(2\pi/3)$.

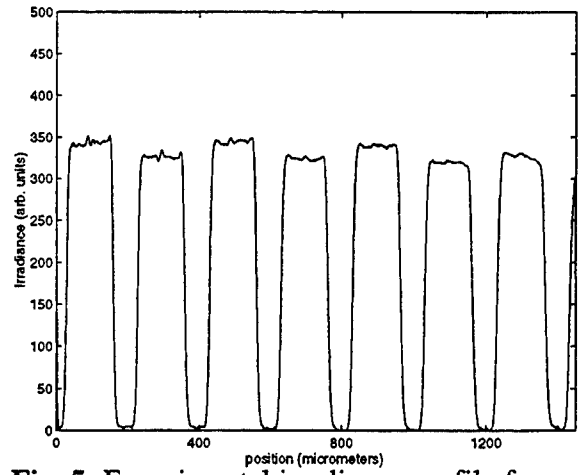

Fig. 5: Experimental irradiance profile from a 400 micron period binary phase TAI with $w/d = 1/3$ at $z = Z_T/12$. The differences in the alternating peak heights arise from a small phase depth error.

Conclusions

In conclusion, the effects of common fabrication errors on the performance of binary phase TAI's has been examined. Transition errors can introduce new, undesirable features in the output pattern of the TAI. Phase depth errors reduce the contrast and efficiency of a TAI, and, in the case of doubled Lohmann images, reduce the uniformity as well. In practice, phase depth errors are a more likely occurrence than transition errors. It is necessary to be aware of the effects of fabrication errors on the performance of TAI's, particularly when they are to be used in cascade with another grating or an SLM for reconfigurable diffractive optical systems.

References

[1]A.W. Lohmann, "An array illuminator based on the Talbot-effect," Optik **79**, 41-45 (1988).

[2]T.J. Suleski, "Generation of Lohmann images from binary-phase Talbot array illuminators," Appl. Opt. **36**, 4686-4691 (1997).

[3]V. Arrizón,"Array illuminator with arrangement of binary phase gratings," Opt. Lett. **18**, 1205-7 (1993).

[4]J. Turunen, "Fractional Talbot imaging setup for high-efficiency real-time diffractive optics," Pure Appl. Opt. **2**, 243-250 (1993).

[5]H. Hamam and J. L. De Bougrenet de la Tocnaye, "Programmable joint fractional Talbot computer-generated holograms," J. Opt. Soc. Am. A **12** (2), 314-24 (1995).

[6]J.T. Winthrop and C.R. Worthington, "Theory of Fresnel images. I. Plane periodic objects in monochromatic light," J. Opt. Soc. Amer. **55**, 373-381 (1965).

[7]J.T. Thomas, "Binary-phase elements in photoresist," Diplom Thesis, Physikalisches Institut der Universität, Erlangen-Nürnberg, 1989.

Diffractive Optics and Micro-Optics

Applications 2

Thursday, June 11, 1998

Shogo Ura, Osaka University, Japan
Presider

DThD
3:30pm–5:00pm
Koa Room

Diffractive and micro-optics at Centro Ricerche Fiat: implemented technologies and applications in the transport industry and general lighting

P. Perlo, P.M. Repetto, S. Sinesi, V. Lambertini, C. Bigliati
Centro Ricerche
Fiat, Italy

Emphasis on the design methodologies and on the technologies implemented to rapidly manufacture large nonrepeated cluster is given. The development of systems based on diffractive and micro-optics for the motorcycle, automotive and general lighting industries is presented. Considerations on their use over the more conventional approaches conclude the paper.

High efficiency transmission diffractive grating and grating lens of the Megajoule laser final optic assembly

Alain Adolf, Arnaud Dulac and Eric Journot

CEA/LV-DLP/SCSL
94195 Villeneuve St Georges CEDEX

e-mail : journot@aol.com

Introduction

The French Megajoule laser facility (LMJ) is designed to provide 1,8MJ/600TW of UV light on an X-ray drive target. This performance requirements are given by inertial confinement fusion ignition mission. The LMJ laser will have 30 bundles of 4x2 IR phosphate-glass amplifier chains of 40 cm square aperture. In the target area this bundles are split into 2x2 bundles which are called « quads ». These quads are directed around the target chamber, converted into UV light and focused on the target. The final optics assembly is a critical element in the LMJ design providing multiple important functions :

- Convert the 1ω (1.053μm) incident IR beam into 3ω (0.351μm) UV beam using KDP crystals,
- Focus the 40 cm aperture UV beam within a near 500 μm diameter optically smoothed spot,
- Eliminate the residual unconverted 1ω and 2ω light,
- Provide a high quality 3ω sample for 3ω beam diagnostics,
- Protect the KDP crystals from neutron irradiation.

The final optics require also a high UV damage threshold of 12 J/cm^2 with 3ns pulse duration. Finally, to avoid non linear effects in optical materials, optical components have to be as thin as possible.
To fulfill this functions, we have designed a new class of final optics assembly based on the use of a pair of high efficiency diffractive components.

The LMJ final optics assembly

The LMJ final optics assembly (FOA) is shown below :

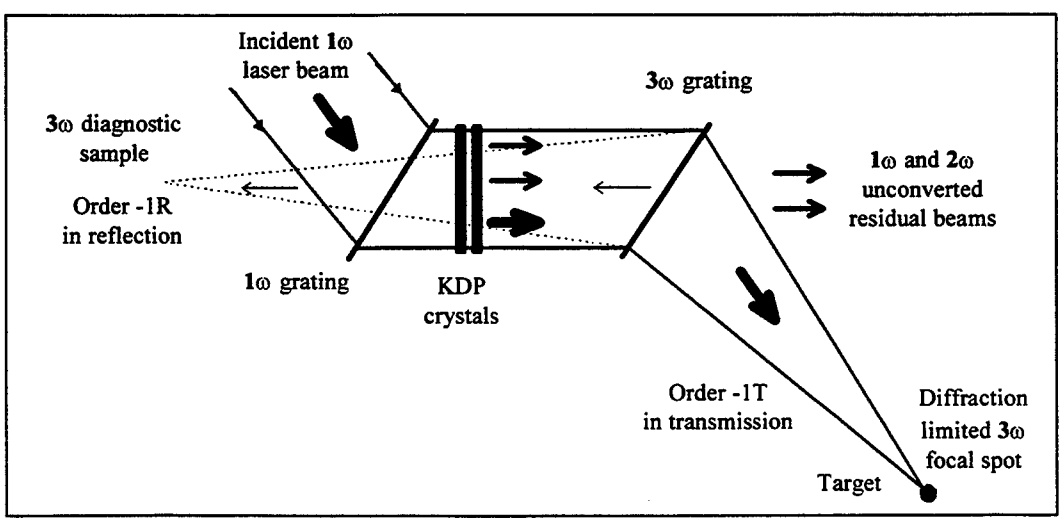

Two diffractive components are used in this system : one « 1ω grating » which diffracts the 1ω beam (IR) and one « 3ω focusing grating » which diffracts the 3ω beam (UV).
The 3ω focusing grating ensures most important functions : beam deviation, residual 1ω and 2ω beam elimination, 3ω beam focusing without creating ghost beams, and it provides a high quality sample for 3ω diagnostics containing exactly the same phase information as the target focused beam.
The 1ω grating is necessary to get the same propagation length for all parts of the deviated beam. But it also plays a leading role for beam smoothing : for TM polarization and a type1-type2 conversion scheme, the angular dispersion created by the 1ω grating leads to a higher spectral acceptance of the tripling crystal, and thus to much better efficiency of the frequency converter when laser beams with spectral bandwidth up to 5 Å are used.

Design of the 1ω grating and the 3ω grating lens

From precedent studies on transmission gratings /1/ /2/ , one knows that to obtain high diffraction efficiency, one needs to use the grating approximately on a Bragg condition given by :

$$\sin\theta = -p\,\lambda/2\Lambda$$

θ : incident and diffracted angle *p : order of diffraction*
λ : wavelength *Λ : local spatial period of the grating*

By properly choosing θ and Λ, we can limit the number of diffracted order to two : the zero and the first one. The zero order is not affected by the grating. By optimizing the grating relief profile we can maximize the diffraction efficiency (η_{-1T}) of the first order for the TM polarization.

Major Characteristics of the 1ω grating :

$\lambda = 1.053\mu m$
$\Lambda = 1.2458\mu m$
$\eta_{-1T} = 96\%$ (fused silica), $\eta_{-1T} = 97.3\%$ (photopolymer)

If the grating lens f-number is not to small, that is about 8, one can verify that everywhere on the grating lens, one is not very far from the Bragg condition which is only rigorously respected at the center of the component.

Major Characteristics of the 3ω grating lens :

$\lambda = 0.351\mu m$
$\Lambda = 0.395$-$0.435\ \mu m$ (0.415μm at the center of the component)
$\eta_{-1T} = 95\%$ (at the center of the component)

Fabrication process

The gratings are holographically recorded on photoresin from the interference pattern of two plane waves for the classical grating and between a 3ω plane wave and a 3ω spherical wave for the grating lens. The photoresin pattern is then transferred into fused silica by ion etching process.
At 1ω, we can use special photopolymer which have very high damage threshold to record the interference pattern.

Experimental results

For the fabrication of the gratings, we are collaborating with the French venders ISA Jobin Yvon and Thomson. Different 1ω and 3ω gratings of diameter 50 mm and 150 have been realized. We have obtain, for TM polarization, diffraction efficiencies up to 95% at 1ω and 3ω. The 3ω focal spot is nearly diffraction limited for both -1T order focused on target and -1R sampling order. The grating are characterized by MEB microscopy and the real profiles are simulated. The agreement between experimental and theoretical diffraction efficiencies are very good.

The 1ω and 3ω damage threshold measurements made on 1ω and 3ω gratings show that the the diffractive structure threshold is the same as the bare material threshold.

We show the diffractive profile of a fused silica 3ω focusing grating. Note the aspect ratio of the structure.

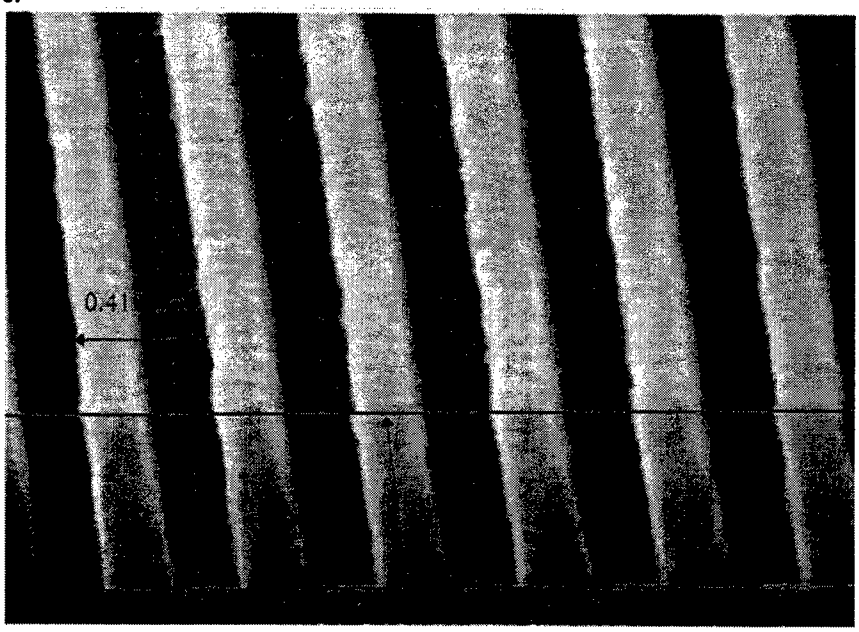

Reference

/1/ - H.T. Nguyen, B.W. Shore, S.J. Bryan, J.A. Britten, R.D. Boyd and M.D. Perry, Optics letters, **22**, 3,1997, p.142-144.

/2/ - Analysis and applications of optical diffraction by gratings, T. K. Gaylord and M.G. Moharam, proceedings of the IEEE viol 73, N°5, may 1985,

Design of diffractive optical elementrs for mode shaping within custom laser resonators

Ian M. Barton and Mohammad R. Taghizadeh
Department of Physics, Herior-Watt University
Edinburgh, EH14 4AS
Tel: +(44)131 451 3646 Fax: +(44)131 451 3136 Email: ianb@phy.hw.ac.uk

Diffractive optical elements (DOEs) have been demonstrated that alter the fundamental mode of a laser resonator to a desired profile, notably by Leger *et al.*[1,2] These, so-called mode-selecting elements (MSEs), usually operate within a Fabry-Pérot laser cavity by replacing one, or both, of the mirrors with a reflecting DOE. They have been mainly applied in solid-state laser systems, e.g., Nd:YAG. The advantages of these customised cavities include superior discrimination against higher-order modes,[3] enabling single-mode operation and the inherently useful properties of the fundamental mode profiles that they can generate, e.g., flattops. These properties are much in demand for many applications including material processing.

Usually MSEs operate as specific phase conjugation devices to select the desired mode profile. In this case, MSEs are designed to phase-conjugate the desired mode profile, once it has been propagated halfway round the cavity, so reforming the profile on return. A single MSE that replaces one mirror in a Fabry-Pérot cavity can generate an arbitrary real mode profile at the opposite mirror.

We use the Fox-Li analysis to calculate the characteristics of the modes of the customised laser resonator.[4] These characteristics include the loss of the fundamental mode, the quality of the mode profile and the discrimination, which is a measure of the difference in the loss of the fundamental mode compared to the next lowest loss mode. The quality of the mode shape is measured in this case by the signal-to-noise ratio (SNR).

The effects of various cavity parameters on the modes within the cavity were evaluated. These included, the size of the input and output mirrors, the size and shape of the desired mode profile, and the number of levels used in the fabrication of the MSE. A number of viable designs where demonstrated for a Nd:YAG laser system with a 1m cavity length.

Various flattop-like profiles (high order super-Gaussian) were generated of around 2mm diameter in size. The typical loss was around 1-2% and the discrimination >20%. MSEs were also used successfully in conjunction with a focussing mirror or lens within the resonator, which was shown to improve the SNR of the fundamental mode.

Quantisation of the MSEs designed above, to enable fabrication, reduces their actual performance. We apply non-linear optimisation algorithms to the design of MSEs, in order to compensate for these quantisation effects and to increase the quality of the mode profile. Two optimisation methods were applied; simulated annealing (SA) and direct binary search (DBS).

A Nd:YAG laser system, with an identical layout to the above was considered. In the optimisation, the initial profile was taken to be the quantised numerical solution as found above. The algorithm then optimised the MSE structure purely in terms of increasing the fidelity of the fundamental mode. Improvement to the fidelity was found to come at the expense of increased intrinsic loss of the cavity. The optimisation process also considered this, setting a maximum acceptable value for the intrinsic cavity loss. The optimisation process did not accept any solution that violated this maximum.

The optimisation was applied to a simpler case with symmetry in one dimension initially and then to the full problem. The standard quantised (16-level) MSE for the two-dimensional case had an intrinsic loss of 2.0% with the SNR = 11350. The next lowest loss mode has an intrinsic (2D) loss of 24%. If the intrinsic loss of the fundamental mode was allowed to increase to 3.0%, then the SNR was similarly increased to 89272. The discrimination of the system was virtually unaffected by the optimisation process. A

comparison of the cross-sections of the fundamental mode profiles of the initial and the optimised MSEs is shown in figure 1.

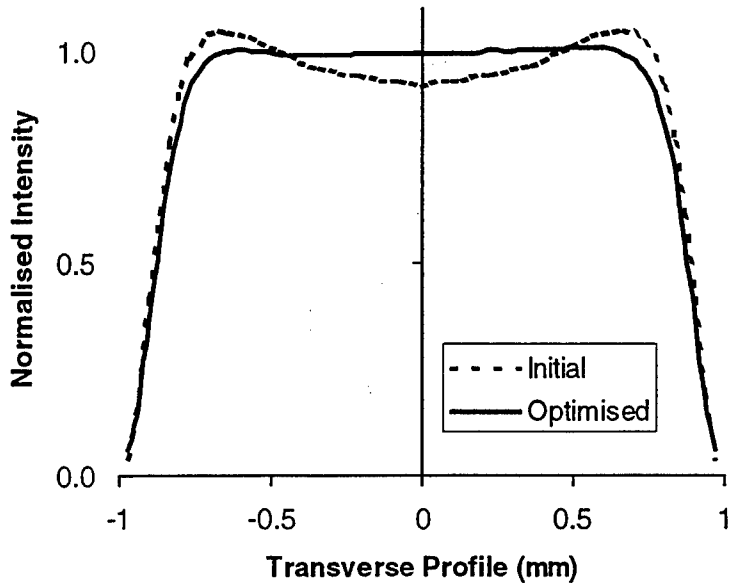

Figure 1. Fundamental mode profiles for the initial and optimised MSE with the maximum allowable loss of the laser resonator = 3%.

The MSEs were fabricated as transmitting 16-level elements in fused-silica using photolithography with reactive-ion etching. Preliminary experimental results show good agreement with that expected from the theory.

References

1. J. R. Leger, D. Chen, Z. Wang, 'Diffractive optical element for mode shaping of a Nd:YAG laser,' *Opt. Lett.* **19** (2) 108 (1993).
2. J. R. Leger, D. Chen, G. Mowry, 'Design and performance of diffractive optics for custom laser resonators,' *Appl. Opt.* **34** (14) 2498 (1995).
3. J. R. Leger, D. Chen, K. Dai, 'High modal discrimination in a Nd:YAG laser resonator with internal phase gratings,' *Opt. Lett.* **19** (23) 1976 (1994).
4. A. G. Fox, T. Li, 'Resonant modes in a maser interferometer,' *Bell Sys. Tech. Journ.* 453 (1961).

Diffractive elements for the generation of propagation-invariant, rotating, and self-reproducing fields

S. N. Khonina, V. V. Kotlyar, and V. A. Soifer

Image Processing Systems Institute, Russian Academy of Sciences, 151 Molodogvardejskaya, Samara 443001, Russia

P. Pääkkönen, J. Lautanen, M. Honkanen, M. Kuittinen, and J. Turunen

Department of Physics, University of Joensuu, P.O. Box 111, 80101 Joensuu, Finland phone +358 13 251 3209 fax +358 13 251 3290 e-mail jari.turunen@joensuu.fi

A. T. Friberg

Department of Physics II - Optics, Royal Institute of Technology, S-100 44 Stockholm, Sweden

Idealized optical fields of infinite spatial extent and energy can display a number of interesting properties, such as exact longitudinal periodicity,[1] propagation-invariance,[2] and rotation of the intensity distribution without any scale change.[3–5] The angular spectra of all these fields consist of one or more rings, known as Montgomery's rings.[1] Therefore finite-aperture approximations can be realized by placing a filter with a set of concentric ringlike apertures (with appropriate complex-amplitude transmission functions) in the front focal plane of a collimating lens and illuminating the filter with a plane wave — this is a direct extension of the method originally proposed for the generation of propagation-invariant fields.[2] However, the method outlined above suffers from poor light efficiency because only a small fraction of the incident light is transmitted by the set of ring apertures. Diffractive optics provides the means to generate propagation-invariant fields with high light efficiency using phase elements analogous to generalized axicons.[6] In this paper we demonstrate experimentally that quite general rotating and self-reproducing optical fields can also be produced by means of diffractive optics.

The general expression for longitudinally periodic fields in polar coordinates (ρ, ϕ, z) may be cast in the form[5]

$$U(\rho,\phi,z) = \exp\left(\mathrm{i}\psi z/z_{\mathrm{T}}\right) \sum_{q\in\mathcal{Q}} \sum_{m=-\infty}^{\infty} C_{qm} J_m(\alpha_q \rho) \exp\left[\mathrm{i}\left(2\pi q z/z_{\mathrm{T}} + m\phi\right)\right], \tag{1}$$

where ψ is an arbitrary phase factor, z_{T} is the longitudinal period (Talbot distance) of the field, $\mathcal{Q}$ is a set of allowed values of q (determined by the requirement that the cone angles of the associated conical waves are between zero and 90°), C_{qm} are arbitrary complex constants, J_m are mth-order Bessel functions of the first kind, and

$$\alpha_q = \left[k^2 - (\psi + 2\pi q)^2 / z_{\mathrm{T}}^2\right]^{1/2}. \tag{2}$$

Paraxial fields are obtained if we choose $\psi \approx 2\pi z_{\mathrm{T}}/\lambda$ and retain only a few lowest-order terms in the q-summation of Eq. (1). Propagation-invariant fields are special cases of longitudinally periodic fields: if $C_{qm} = 0$ for all but one value of q, the field satisfies the condition of propagation-invariance, i.e., $I(\rho,\phi,z) = I(\rho,\phi,0)$ for all values of z. If, on the other hand, we retain only terms with $m = q$ (or any two terms with different values of q and m), the field distributions of all remaining components in the summation in Eq. (1) rotate uniformly.

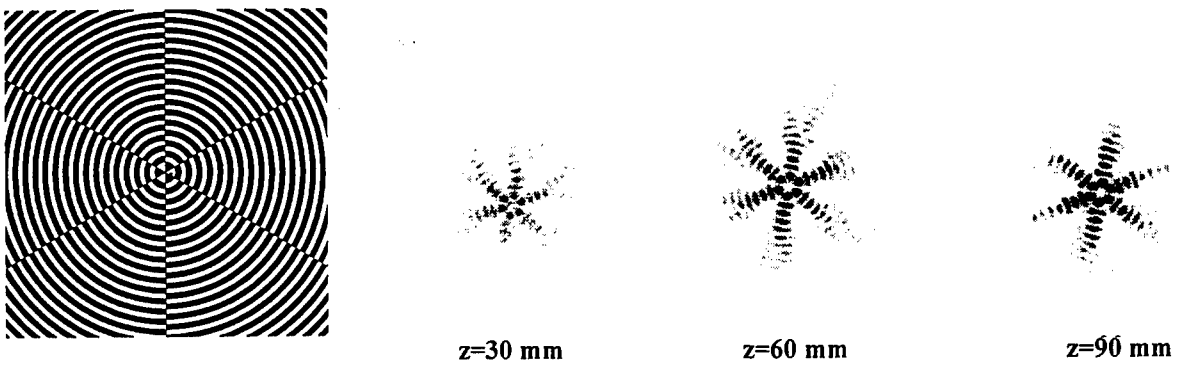

Figure 1: Structure of a diffractive element (left) for the generation of a finite-aperture approximation of a propagation-invariant field, and (right) intensity distributions at three transverse planes.

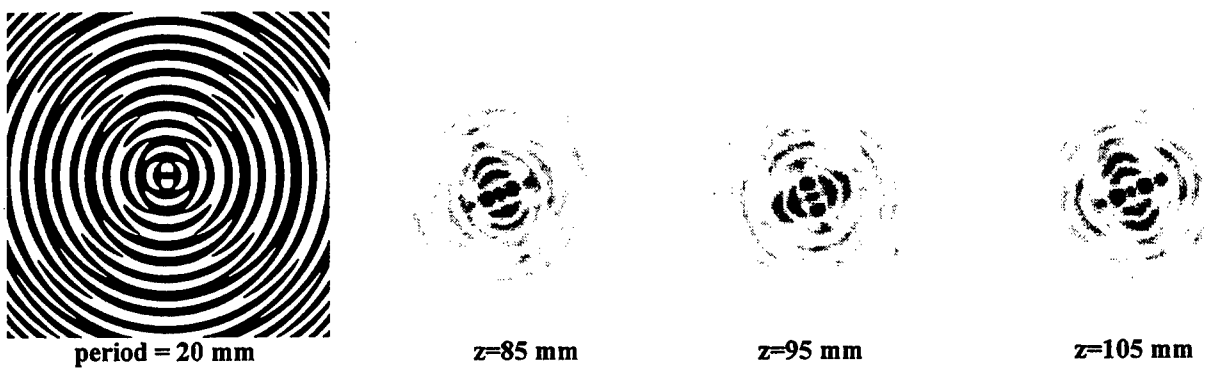

Figure 2: Structure of a diffractive element (left) for the generation of a finite-aperture approximation of a longitudinally periodic field with period $z_T = 20$ mm, and (right) intensity distributions at three transverse planes.

We have employed the methods described in Ref. 5 to design binary-phase diffractive elements for the generation of self-reproducing fields, as well as the special cases of rotating and propagation-invariant fields. The binary-phase diffractive elements used in the experiments to be described below were fabricated by direct-write electron beam lithography, using the Leica LION LV1 low-voltage electron beam pattern generator at the University of Joensuu. After patterning of the resist (PMMA), the phase-relief was transfered in fused silica by reactive ion etching, using a metal mask fabricated by lift-off technology. The optical performance of the elements was tested in a simple arrangement consisting of a collimated He-Ne laser beam and a CCD camera that could be moved along the beam path. It was also established that master elements generated in this manner can be easily replicated, at least in small quantities, by hot embossing in plastic.

Figure 1 illustrates the structure of a binary diffractive element for generation of propagation-invariant fields (the phase difference between black and white regions is π radians), and experimentally observed transverse intensity profiles in three different planes. Despite of the slight modifications of the intensity profile upon propagation, the scale-invariance of the field in the central region is clearly visible. Figure 2 illustrates the structure of a binary diffractive element for the generation of a longitudinally periodic field mode, i.e., a superposition of contributions from more than one Montgomery's ring, and the intensity distributions across three planes separated by one half of the longitudinal period, $z_T/2 = 10$ mm.

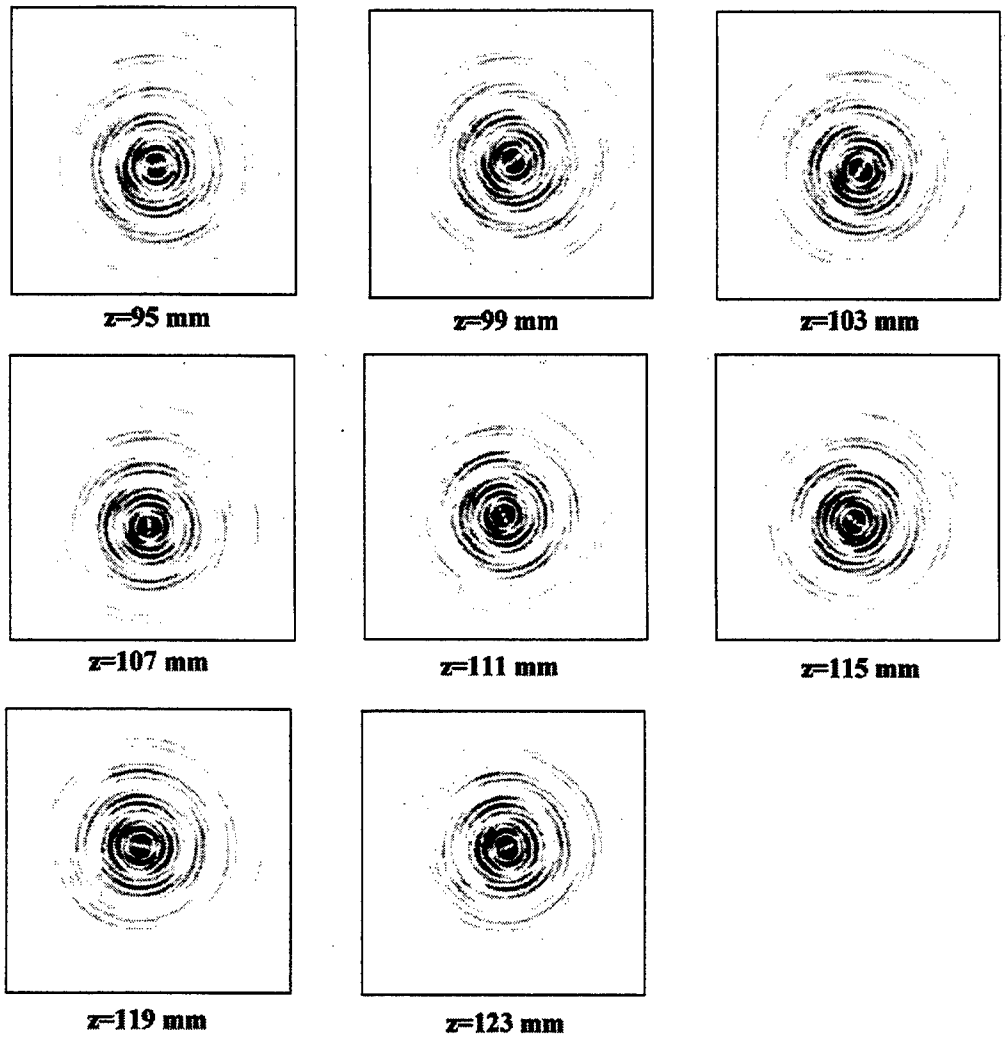

Figure 3: Experimental demonstration of a rotating optical field (superposition of J_1 and J_3 field modes on two Montgomery's rings) over one rotation cycle.

The generation of good-quality rotating fields with binary on-axis diffractive elements is possible only in special cases.[4] Therefore we employed the classic off-axis binary-phase Lohmann coding[7] of amplitude and phase in variations of local diffraction efficiency and lateral fringe shift. However, to improve the total diffraction efficiency, we recorded the amplitude information only partly. The rotating field thus obtained is illustrated in Fig. 3.

References

1. D. Montgomery, J. Opt. Soc. Am. **57,** 772 (1967).
2. J. Durnin, J. J. Miceli, Jr., and J. H. Eberly, Phys. Rev. Lett. **58,** 1499 (1987).
3. S. Chávez-Cerda, G. S. McDonald, and G. H. S. New, Opt. Commun. **123,** 225 (1996).
4. C. Paterson and R. Smith, Opt. Commun. **124,** 131 (1996).
5. V. V. Kotlyar, V. A. Soifer, and S. N. Khonina, J. Mod. Opt. **44,** 1409 (1997).
6. A. Vasara, J. Turunen, and A. T. Friberg, J. Opt. Soc. Am. A **6,** 1748 (1989).
7. A. W. Lohmann and D. P. Paris, Appl. Opt. **6,** 1739 (1967).

Liquid Crystal Blazed Grating Beam Deflector

Xu Wang*, Daniel W. Wilson**, Richard E. Muller**, Paul D. Maker**, and Demetri Psaltis*

*MS 136-93, Dept. of Electrical Engineering
California Institute of Technology
Pasadena, CA 91125
Phone: 626-395-3889
Fax: 626-568-8437
Email: xuwang@sunoptics.caltech.edu

**Center for Space Microelectronics Technology
Jet Propulsion Laboratory
California Institute of Technology
Pasadena, CA 91109-8099

Non-mechanical beam steering devices can play a crucial role in many applications, such as optical interconnects, optical communications and optical data storage.[1] However, current steering devices either require high voltage or complicated fabrication technology.[2][3][4] We have developed a non-mechanical beam steering device using liquid crystal as shown in Figure. 1.

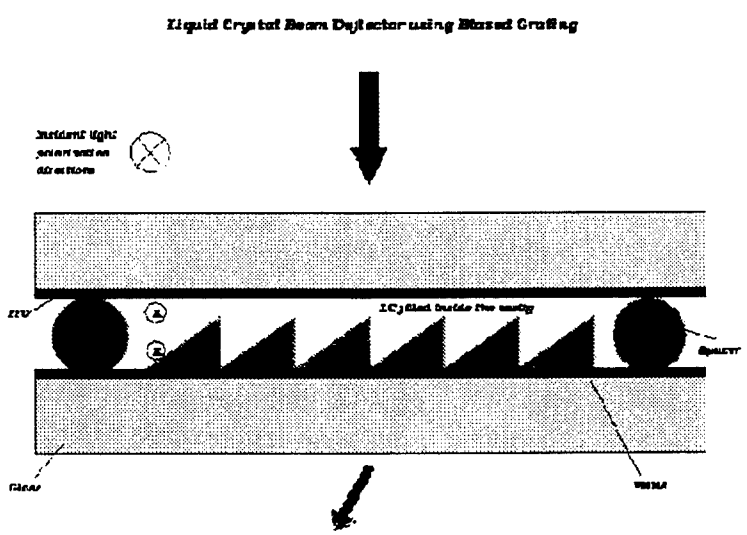

Figure 1. One layer of the liquid crystal beam steering device

A thin layer of nematic liquid crystal is sandwiched between a poly-methyl methacrylate (PMMA) blazed grating and a transparent cover plate. A voltage applied between the transparent electrode patterned underneath the PMMA grating and the

transparent electrode coated on the bottom surface of cover plate electrically drives the liquid crystal. This forms a liquid crystal blazed grating. The way to operate this composite grating is to exploit the electro-optic effect of nematic liquid crystals, whose extraordinary axis's refractive index is changed with the driving voltage. In this way, the resulting dynamic phase grating deflects incident light with a high efficiency into one of two distinct directions depending on the driving condition.

The complete beam deflector consists of a stack of liquid crystal blazed gratings with different grating periods. The period of each layer in the stack is double the previous grating period to make all steering angles clearly resolvable. By applying different driving voltages on each layer, we can easily achieve multiple steering angles. The idea is graphically shown in Figure.2.

Figure 2. Liquid crystal beam steerer's multiple angle addressing concept.

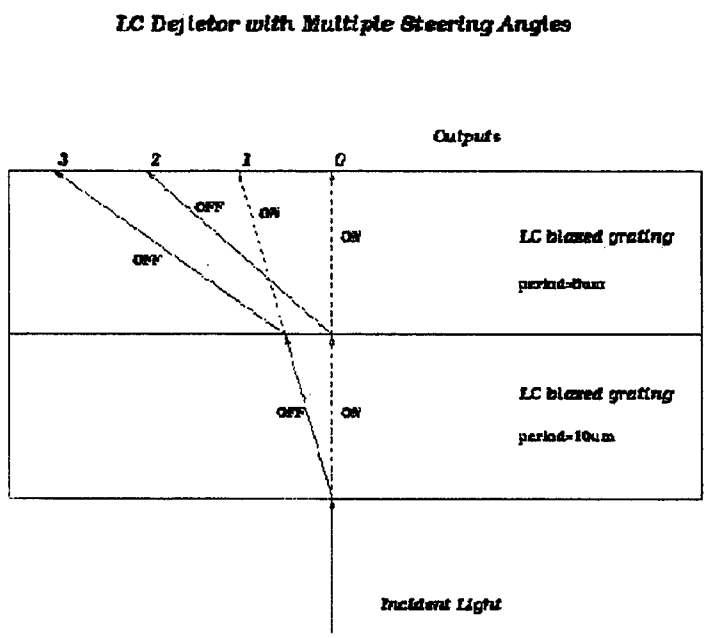

The PMMA blazed grating was fabricated at JPL using analog direct-write electron-beam lithography.[5] The nematic liquid crystal was then filled into the grating at room temperature. To evaluate the performance, we first measured the diffraction efficiency distribution of the 5 μm and 10 μm period samples separately before stacking them together. We then stacked the layers and measured the efficiency of the complete deflector. The measurement results are listed in Table I.

LC Blazed Grating Deflector Performance Summary

10um period sample

D.E. / Order	ON	OFF
1	2.47%	[illegible]
0	[illegible]	2.03%
-1	2.84%	[illegible]
-2	0.57%	[illegible]

5um period sample

D.E. / Order	ON	OFF
1	[illegible]	2.15%
0	[illegible]	[illegible]
-1	[illegible]	[illegible]
-2	1.42%	[illegible]

10um & 5um sample stacking together

Voltage source	Steering angle	Testing D.E.	Calculated D.E.
Both OFF	10.8 degree	65.02%	67.7%
10um ON 5um OFF	7.2 degree	71.21%	[illegible]
10um OFF 5um ON	3.6 degree	72.16%	[illegible]
Both ON	0 degree	75.4%	[illegible]

Table I. Device test results.

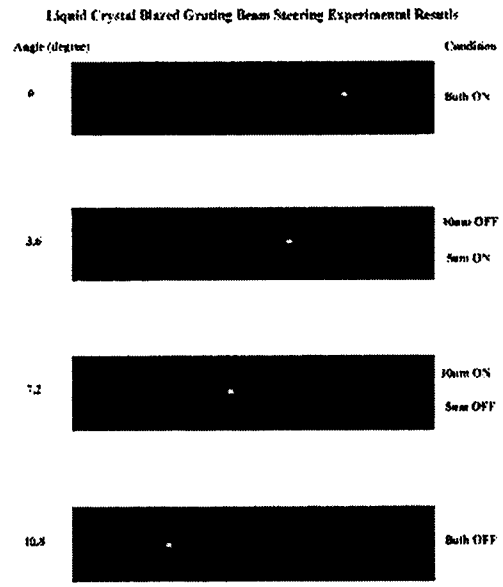

Figure.3 Multiple angle beam steering

Figure 3 shows the multiple beam steering experimental results. Four steering angles (10.8°, 7.2°, 3.6°, 0°) are obtained with very good contrast ratio. The intensity ratio between the strongest and second strongest spots is in the range of 13-21. The steering efficiency ranges from 65% to 75%. The voltage applied to the device is approximately 15V with about 45% of the applied voltage lost across the PMMA layer. A new liquid crystal beam deflector with 16 steering angles capability is currently under development.

References

1. Demetri Psaltis and Fai Mok, *Holographic Memories,* Scientific American, Vol. 273, No. 5, p1-8, 1995

2. Q.Chen, Y.Chiu, D.D.Stancil, *Guide-wave electro-optic beam deflector using domain reversal in $LiTaO_3$,* IEEE J. Lightwave Technology, Vol.12, No.8, p1401-1404, 1994

3. James Thomas and Yeshaiahu Fainman, *Programmable diffractive optical element using a multichannel lanthanum-modified lead zirconate titanate phase modulator,* Opt Lett, Vol. 20, No.13, p1510-1512, 1995.

4. D.Resler, D.Hobbs, R.Sharp, L.Friedman, T.Dorschner, *High-efficiency liquid crystal optical phased array beam steering,* Opt Lett, Vol. 21, No.9, p689-691, 1996.

5. P. D. Maker, D. W. Wilson, and R. E. Muller, *Fabrication and performance of optical interconnect analog phase holograms made be E-beam lithography,* in Optoelectronic Interconnects and Packaging, R. T. Chen and P. S. Guilfoyle, eds., SPIE Proceedings vol. CR62, pp. 415-430, Jan. 1996.

Key to Authors and Presiders

Diffractive Optics and Micro-Optics

Postdeadline Papers

June 8–11, 1998

Kona Surf Hotel
Kailua-Kona, Hawaii

CONTENTS

Electromagnetic Analysis of Axially-Symmetric DOEs Using the FDTD Method

Dennis W. Prather and Shouyuan Shi

University of Delaware
Department of Electrical and Computer Engineering
Newark, DE 19716
phone: (302)-831-8170, fax: (302)-831-4316, email: *dprather@ee.udel.edu*

Many useful diffractive optical elements (DOEs) contain axial symmetry, e.g. lenses and mode shaping elements. Typically these structures are analyzed using scalar-based diffraction methods. However, when the profile of the DOE has variations on a scale comparable to the illumination wavelength scalar theory is not valid. In these cases a rigorous solution to the electromagnetic boundary value problem must be obtained. Unfortunately, most techniques for the rigorous analysis of such DOEs are only applicable to two-dimensional or periodic profiles. An exception to this is our method of moments (MOM) paper included in the technical digest of this conference. Although we have demonstrated the MOM to be a viable method for the analysis of axially-symmetric DOEs, in this paper we present an alternative technique based on the finite-difference time-domain (FDTD) method that is computationally more efficient and has broader application.

Our implementation of the FDTD method differs from most in that we restrict the extent of the solution space to a region just beyond the boundary of the DOE, see Fig. 1. This affords a significant reduction in the computational cost associated with obtaining a solution. However, it does require that the steady state fields be propagated to the plane of observation. Even though this introduces additional computations, those of the propagation algorithm scale with order N whereas those of the FDTD algorithm scale with order N^2, where N represents the number of unknowns in a single direction, thereby rendering it more efficient. In addition to this advantage, the use of a propagation algorithm allows one to determine the electromagnetic field profiles anywhere in space or over discrete regions of space, which provides for a more efficient representation of the diffraction problem. In the remainder of the paper we introduce the formulation of the FDTD method, as it applies to axially-symmetric structures,[1] and the propagation of the steady state fields, using Stratton-Chu integral.[2]

For axially-symmetric problems Maxwell's equations are best represented in cylindrical coordinates where we can represent the azimuthal variation of the fields in terms of a Fourier series expansion,

$$\begin{aligned}\vec{\mathbf{E}}(\rho,\phi,z,t) &= \sum_{k=1}^{\infty} \vec{E}1_k(\rho,z,t)\cos(k\phi) + \vec{E}2_k(\rho,z,t)\sin(k\phi) \\ \vec{\mathbf{H}}(\rho,\phi,z,t) &= \sum_{k=1}^{\infty} \vec{H}1_k(\rho,z,t)\cos(k\phi) + \vec{H}2_k(\rho,z,t)\sin(k\phi)\end{aligned} \tag{1}$$

where the Fourier coefficients, $\vec{E}1$, $\vec{E}2$, $\vec{H}1$, and $\vec{H}2$ are determined from orthogonality. The resulting

angular dependence can be factored out of Maxwell's equations, so that the electromagnetic fields for each Fourier mode can be solved for independently. The resulting form of Maxwell's curl equations can be expressed as

$$\begin{aligned}
\mu\frac{\partial H_{\rho,k}}{\partial t} &= \frac{k}{\rho}E_{z,k} + \frac{\partial E_{\phi,k}}{\partial z} &&, & \varepsilon\frac{\partial E_{\rho,k}}{\partial t} &= -\frac{k}{\rho}H_{z,k} - \frac{\partial H_{\phi,k}}{\partial z} \\
\mu\frac{\partial H_{\phi,k}}{\partial t} &= -\frac{\partial E_{\rho,k}}{\partial z} + \frac{\partial E_{z,k}}{\partial \rho} &&, & \varepsilon\frac{\partial E_{\phi,k}}{\partial t} &= \frac{\partial H_{\rho,k}}{\partial z} - \frac{\partial H_{z,k}}{\partial \rho} \\
\mu\frac{\partial H_{z,k}}{\partial t} &= -\frac{1}{\rho}\frac{\partial(\rho E_{\phi,k})}{\partial \rho} - \frac{k}{\rho}E_{\rho,k} &&, \text{ and } & \varepsilon\frac{\partial E_{z,k}}{\partial t} &= \frac{1}{\rho}\frac{\partial(\rho H_{\phi,k})}{\partial \rho} - \frac{k}{\rho}H_{\rho,k}\,.
\end{aligned} \tag{2}$$

Application of the FDTD method to Eq. (2) results in a set of coupled difference equations, shown below only for the magnetic field components,

$$\begin{aligned}
H_\rho^n(i,j) &= H_\rho^{n-1}(i,j) + \frac{\Delta t k}{\mu\rho_0(i)}E_z^{n-\frac{1}{2}}(i,j) + \frac{\Delta t}{\mu\Delta z}\left[E_\phi^{n-\frac{1}{2}}(i,j+1) - E_\phi^{n-\frac{1}{2}}(i,j)\right] \\
H_\phi^n(i,j) &= H_\phi^{n-1}(i,j) - \frac{\Delta t k}{\mu\Delta z}\left[E_\rho^{n-\frac{1}{2}}(i,j+1) - E_\rho^{n-\frac{1}{2}}(i,j)\right] + \frac{\Delta t}{\mu\Delta\rho}\left[E_z^{n-\frac{1}{2}}(i+1,j) - E_z^{n-\frac{1}{2}}(i,j)\right] \\
H_z^n(i,j) &= H_z^{n-1}(i,j) - \frac{\Delta t k}{\mu_r\rho(i)}E_\rho^{n-\frac{1}{2}}(i,j) - \frac{\Delta t}{\mu\Delta\rho\rho(i)}\left[\rho_0(i+1)E_\phi^{n-\frac{1}{2}}(i+1,j) - \rho_0(i)E_\phi^{n-\frac{1}{2}}(i,j)\right]
\end{aligned} \tag{3}$$

where $\rho_0(i)=(i-1)\Delta\rho$, $\Delta\rho$ and Δz are discretization lengths in ρ and z directions, respectively, and $n\Delta t$ is the time step which satisfies the following dispersion condition $c\Delta t \leq \Delta / s$. The calculation region for Eq. (3) is divided into a total field region, a connecting boundary, a scattered field region, and absorbing boundaries, as shown in Fig.1. The absorbing boundaries used in our formulation are perfectly matched layers (PMLs).[3] The difference equations are then solved using the time marching algorithm.[1]

Once the steady state fields are obtained they are propagated to the observation plane using the Stratton-Chu[2] formulation,

$$\mathbf{E}^s(\mathbf{r}) = -\int_S \left\{ j\omega\mu_0 G\left(\mathbf{r},\mathbf{r}'\right)\left[\hat{n}\times\mathbf{H}^s\left(\mathbf{r}'\right)\right] + \left[\hat{n}\times\mathbf{E}^s\left(\mathbf{r}'\right)\right]\nabla G\left(\mathbf{r},\mathbf{r}'\right) + \left[\hat{n}\cdot\mathbf{E}^s\left(\mathbf{r}'\right)\right]\nabla G\left(\mathbf{r},\mathbf{r}'\right)\right\} ds'$$

where

$$G\left(\mathbf{r},\mathbf{r}'\right) = \frac{e^{-jk\left|\mathbf{r}-\mathbf{r}'\right|}}{4\pi\left|\mathbf{r}-\mathbf{r}'\right|}$$

is the free space Green's function, $\mathbf{E}^s$ and $\mathbf{H}^s$ are the scattered field components of the electric and magnetic fields, S is a closed surface, and $\hat{n}$ is normal unit vector directed outside of S. The propagated incident field is then added to the scattered fields to obtain the total or diffracted fields.

Once confident our model was working properly we applied it to the analysis of binary and 8-level dielectric diffractive lenses. The design parameters for both lenses are: permittivity (ε) = 2.25, wavelength = 1.0μm, $f/number$ = 1.347, diameter = 22.3μm, focal length = 30.0μm, and minimum feature sizes of 1.53μm and 0.2μm, respectively. The incident field was a plane wave having E_x^{inc} polarization. The binary and 8-level lenses are shown in Figs. 2 (a) and (b) and the magnitudes of their electric fields in the focal plane are shown in Figs. 2 (c) and (d), respectively. Even though, in strict sense, scalar theory is not valid for the analysis of these lenses, it is interesting to note that the increase in diffraction efficiencies from 46.64% to 66.74% is consistent with expectations.

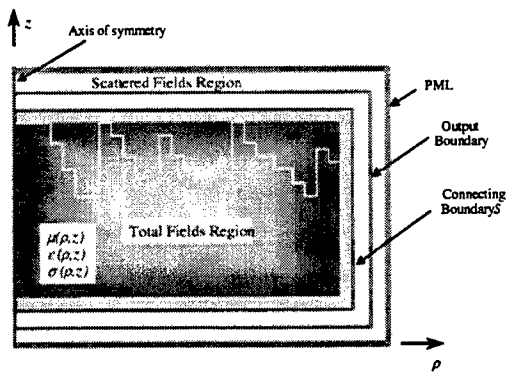

Figure 1: Geometry used for implementing the axially-symmetric FDTD method.

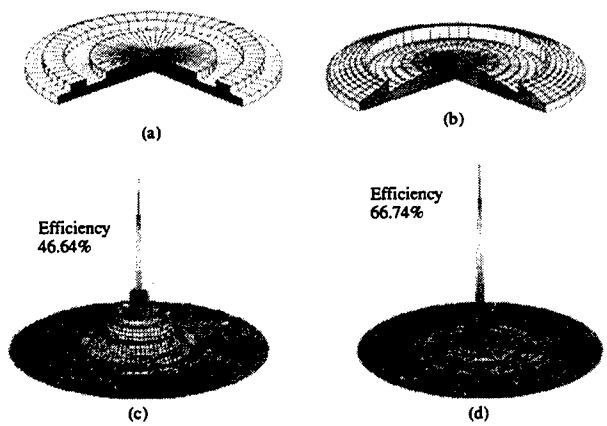

Figure 2: Analysis of (a) binary and (b) 8-level diffractive lenses with the magnitude of the electric field in the focal plane of (a) in (c) and (b) in (d).

1 REFERENCES

[1] A. Taflove, Computational Electromagnetics: The Finite-difference Time Domain Method (Artech House, Boston MA, 1995), chp. 12.

[2] J. A. Stratton, Electromagnetic Theory (McGraw-Hill, New York, NY 1941), pp. 464-470.

[3] F.L.Teixeira and W.C. Chew, "*Systematic Derivation of Anisotropic PML Absorbing Media in Cylindrical and Spherical Coordinates*", IEEE Micrwave and Guided Wave Letters, Vol.7, no.11, 1997, pp.371-373.

Diffractive Optics replicated in Amorphous IR Glasses

Richard D. Rallison
Ralcon Development Lab
8501 So. 400 W. Box 142
Paradise, Utah 84328
ph (435) 245 4623 fax 245 6672
E-mail rdr@ralcon.com

SUMMARY

The spectral region from about 2 microns to far IR has to be covered with only a few materials that are intrinsically transparent. Diffractive optics can be machined into the surfaces of most materials and may be slumped or molded into a few materials. The readily available moldable materials include arsenic Trisulfide (Ar_2S_3) and both AMTIR 1 and AMTIR 2. All three of these amorphous IR glasses may be slumped into lenses and diffractive optics using fused silica and other glass master molds. They all begin to flow at temperatures well below the softening temp of common plate and silica glasses. We have experimented with writing gratings in photo resist, etching the substrates and then heating the IR glasses under pressure in an oven until the pattern is transferred. We have produced zone plates and gratings interferometrically and by using the Postscript language with typesetters and photo reduction. We have etched primarily with HF in solution and with vapors and are in the process of setting up an RIE machine to get better detail and anisotropic etch profiles. Gratings of 35 and 67 l/mm with near square and also sinusoidal profiles have been made recently and prior work was with blazed zone plates reduced from postscript masters. The design and production of binary masks and silica masters is well covered in the literature and won't be reproduced here. The experiments we report on are all dealing with the replication into AMTIR 1 and Arsenic Trisulfide.

Arsenic Trisulfide is an interesting brittle red material with an index of refraction in the IR of about 2.4 and will soften in a bread maker. We initially recorded gratings in 2 to 4 mm thick pieces of the IR glass directly using 488 nm laser light at room temperature. These gratings appeared to be permanent and were easily read out at 670 nm for a few days under florescent lights that eventually erased the fringes. The induced index modulation was apparently only near the surface. The angular bandwidth was large, indicating a shallow grating, and the efficiency was about 10%. Prior work by Ohmachi indicates that delta n can be as high as .1 in 10 micron thick layers, and the volume recording may be converted directly to a permanent surface grating by etching with a basic solution. Our attempts at etching resulted in a less than desirable surface texture, but others report good results. Better controls can be had by etching fused silica and slumping the pattern into the chalcogenide glass. To do this we placed the glass in contact with a master on one side and a piece of polished fused silica on the other side and then weights were stacked to yield about 2 lbs per cm^2 on the IR glass. The oven was brought up to 220 C and held there for 4 hours or until the pattern was uniformly pressed into the surface. Cool down was rather rapid, perhaps as short as 2 hours. A view port was made in the oven to allow monitoring of the pattern growth during the slumping process.

AMTIR 1 was done similarly except that the oven had to be raised to 450 C over 1 hour and the required pressure was only about .2 lbs per cm^2. The flow rate was higher and the embossing took place in about 30 minutes. The AMTIR required a minimum of 12 hours to cool down to avoid fracture. It is a very fragile material. The flow was high enough that we have had to build glass containment boundaries to assure that the pattern was fully embossed before the material spread laterally to an extreme. This material has less of a tendency to outgass and form bubbles than Ar_2S_3 but is not transparent to visible light at room temp. Both materials are available from Amorphous Materials inc of Garland, Texas along with spec sheets and helpful hints to use it in various ways.

Both materials offer a satisfactory means of producing diffractive and hybrid optics for the IR and NIR without the need for machining each piece. Mass produced optics are certainly possible with a simple molding procedure .

High-efficiency guided-mode resonance laser mirror

Z. S. Liu, S. Tibuleac, D. Shin, P. P. Young, and R. Magnusson
Department of Electrical Engineering, The University of Texas at Arlington, Arlington, TX 76019
Phone: (817) 272-3474, Fax: (817) 272-2253, Email: magnusson@uta.edu

Thin-film dielectric waveguides incorporating one or more periodic elements exhibit sharp variations of the externally propagating fields at certain values of the wavelength and angle of incidence that allow coupling of the incident beam to a leaky mode of the waveguide[1,2]. Theoretical studies indicate that with appropriate choice of materials and geometrical parameters, this guided-mode resonance (GMR) effect can be exploited to design polarized, narrowband reflection filters with efficiencies of 100%[3,4]. As practical applications of a filter device with such properties abound[5,6], there is ample motivation for pursuing experimental proofs of these theoretically-predicted characteristics. For example, using a GMR mirror as a polarizing output coupler in a laser may require high-efficiency reflection approaching 100% with corresponding mirror transmission of a few percent yielding the laser output light[7]. During the past few years, experimental resonance efficiencies exceeding 90% have been reported.[8-10] In this paper, a resonance filter with peak efficiency of 98% is presented and its use as output coupler in a laser cavity demonstrated.

The objective of this research is to develop reflection filters with high efficiency, and low, extended sidebands employing simple structures and fabrication methods. The GMR filter structure under study is shown schematically in Fig. 1a. The device is fabricated by depositing a layer of HfO_2 with a thickness d_2 = 270 nm on a fused-silica substrate by e-beam evaporation and subsequent recording of a holographic grating in photoresist on top of the HfO_2 layer. The grating with a period Λ = 487 nm and a thickness of d_1 = 160 nm is recorded with an Ar^+ laser (λ = 364 nm) in a Lloyd-mirror interference setup. An example of a fabricated double-layer structure is illustrated by the scanning electron micrograph of Fig. 1b. The spectral characteristics of the device are measured with a dye laser operating in the 800-900 nm wavelength range pumped with an Ar^+ laser (λ = 514 nm). The beam reflected from the GMR filter is measured automatically while the laser wavelength is scanned across the dye range in increments of 0.1 nm with an intracavity birefringent filter under computer control. The specified linewidth of the dye laser system is 0.05 nm. The reflectance of the GMR filter is obtained by normalizing the power reflected from the device with the power of the incident beam. At small angles of incidence ($\theta \leq 1°$ in this experiment) and at normal incidence, the filter response is found by inserting a beam splitter between the laser and the GMR filter to direct the beam reflected from the device to the detector. The GMR filter reflectance is determined by dividing the power of the beam reflected from the filter by the power of the beam reflected from a mirror with a known reflectance (R = 99.9% for $840 < \lambda < 880$ nm) at each data point in the wavelength range. Figure 2 illustrates the experimentally-measured spectral response of the two-layer GMR filter for a normally-incident TE-polarized probing beam. The GMR filter exhibits a peak reflectance exceeding 98% at the wavelength λ = 860 nm with a linewidth (FWHM) of $\Delta\lambda \sim 2.2$ nm and low sidebands (< 5%) over the wavelength range provided by the dye. The theoretical reflectance curve presented in Fig. 2 is obtained using the rigorous coupled-wave analysis[11] and assuming a grating with a rectangular profile for simplicity. The thicknesses and refractive indices used in the theoretical model are determined by spectral reflectometry measurements. A fill factor, defined as the fraction of the period occupied by the high-refractive-index (n_{1H}) material, f = 0.3, is assumed in the calculations. This fill factor is consistent with Fig. 1b. A close match between the experimental curves and the theoretical calculations is seen in Fig. 2. The main source of measurement error is slight fluctuation of the dye-laser output power; repeated measurements have established the total experimental error to be within ± 1%.

High-efficiency GMR reflection filters with narrow linewidths and inherent polarization selectivity make them suitable for applications as laser mirrors. The polarization selectivity provides a linearly polarized output beam eliminating the need for Brewster windows. The direction of polarization can be changed by rotating the GMR filter about the optical axis of the resonator. Avrutsky et al. performed the first experiments of this kind using a ~50% reflective corrugated-waveguide mirror obtaining lasing within the gain curve of rhodamine 6G in a dye laser.[12] Due to this relatively low mirror reflectance, lasing via Fresnel bulk reflections occurred simultaneously. A similar mirror device with R~50% was applied to reduce a multimode spectrum of a semiconductor laser to a single longitudinal mode using an external cavity configuration.[13]

The high-efficiency GMR reflection filter described above is used to realize a GMR laser mirror. The flat output mirror of the dye laser with broadband output (800 – 920 nm) is replaced with the GMR filter and the birefringent tuning element removed. Lasing is achieved at a wavelength of 860 nm. The laser power is ~100 mW when pumped with an Ar^+ laser emitting a power of ~5 W at a 514-nm wavelength. The linewidth of the output laser beam is measured as ~0.3 nm. This linewidth is set by the GMR filter linewidth at the threshold reflectance for laser oscillation to occur; in this case at ~95% reflectance value in Fig. 2.

In conclusion, a double-layer GMR filter with efficiency approaching the theoretical limit has been presented. The filter exhibits low reflectance sidebands in a 100-nm spectral region and ~2 nm linewidth. Good agreement between theoretical and experimental results is found. This high-efficiency GMR mirror is used as an output coupler in a dye laser cavity. The GMR mirror characteristics are found experimentally to define the laser output wavelength and linewidth. GMR filters fabricated in durable materials may enable a variety of active and passive devices for lightwave communication systems and laser technology.

References

1. A. Hessel and A. A. Oliner, Appl. Opt. **10**, 1275 (1965).
2. R. Magnusson and S. S. Wang, Appl. Phys. Lett. **61**, 1022 (1992).
3. S. S. Wang and R. Magnusson, Opt. Lett. **19**, 919 (1994).
4. D. Shin, S. Tibuleac, T. A. Maldonado, and R. Magnusson, to appear in Optical Engineering, Sept. 1998.
5. S. S. Wang and R. Magnusson, Appl. Opt. **32**, 2606 (1993).
6. S. S. Wang and R. Magnusson, Appl. Opt. **34**, 2414 (1995).
7. A. Yariv, *Optical Electronics in Modern Communications*, Oxford University Press, New York, p. 197 - 201, 1997.
8. M. T. Gale, K. Knop, and R. H. Morf, Proc. SPIE **1210**, 83 (1990).
9. S. Peng and G. M. Morris, Proc. Topical Meeting on Diffractive Optics and Micro-Optics **5**, 257 (1996).
10. R. Magnusson, D. Shin, and Z. S. Liu, Opt. Lett. **23**, 612 (1998).
11. T. K. Gaylord and M. G. Moharam, Proc. IEEE **73**, 894 (1985).
12. I. A. Avrutsky and V. A. Sychugov, J. Mod. Opt. **36**, 1527 (1989).
13. I. A. Avrutsky, A. S. Svakhin, and V. A. Sychugov, J. Mod. Opt. **36**, 1303 (1989).

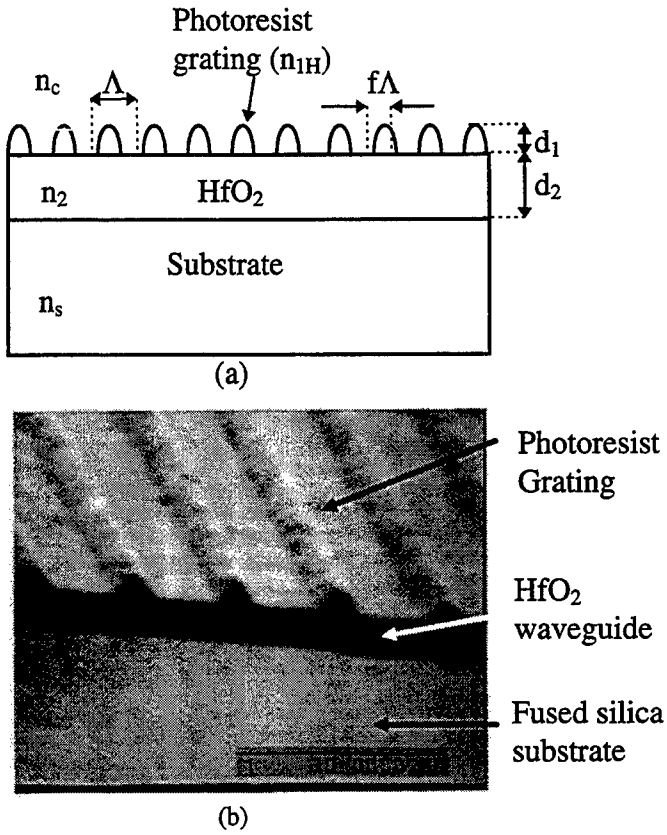

Figure 1. Schematic representation (a) and scanning electron micrograph (b) of a double-layer GMR structure composed of a photoresist grating and an HfO_2 waveguide layer on a fused silica substrate.

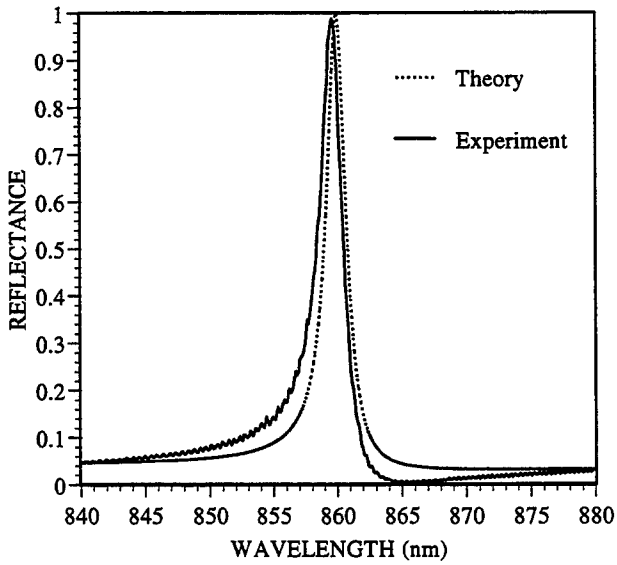

Figure 2. Theoretical and experimental spectral response of a double-layer GMR reflection filter with the structure illustrated in Fig.1. The parameters of the device used in the theoretical modeling are Λ = 487 nm, n_c = 1.0, n_s = 1.48, n_{1H} = 1.63, n_{1L} = 1.0, n_2 = 1.98, d_1 = 160 nm, d_2 = 270 nm. The grating is assumed to have a rectangular profile with a fill factor f = 0.3 in the calculation.

Diffractive Optics and Micro-Optics Technical Program Committee

J. Allen Cox, *General Chair, Honeywell Inc., USA*

Hans Peter Herzig, *Program Chair, University of Neuchatel, Switzerland*

Joseph N. Mait, *Program Chair, U.S. Army Research Laboratory, USA*

Shigeru Aoyama, *Omron Corporation, Japan*

Madeleine B. Fleming, *3M Company, USA*

Michael T. Gale, *Centre Suisse d'Electronique et de Microtechnique (CSEM), Switzerland*

Michael Hutley, *National Physics Laboratory, U.K.*

Juergen Jahns, *University of Hagen, Federal Republic of Germany*

Gina R. Kritchevsky, *Donnelly Corporation, USA*

James R. Leger, *University of Minnesota, USA*

Lifeng Li, *University of Arizona, USA*

Robert Magnusson, *University of Texas-Arlington, USA*

Jim Moharam, *CREOL, University of Central Florida, USA*

G. Michael Morris, *University of Rochester, USA*

Dan Raguin, *Rochester Photonics, USA*

Terry Clark Smith, *Torrance, California, Technical Council Representative*

Donald Sweeney, *Lawrence Livermore National Laboratory, USA*

S. Ura, *Osaka University, Japan*